THE DETECTOR SYSTEM OF THE KATRIN EXPERIMENT

—

IMPLEMENTATION AND FIRST MEASUREMENTS WITH THE SPECTROMETER

Zur Erlangung des akademischen Grades eines

DOKTORS DER NATURWISSENSCHAFTEN

von der Fakultät für Physik
des Karlsruher Instituts für Technologie
genehmigte

DISSERTATION

von

Dipl.-Phys. Johannes Simon Schwarz

aus Öhringen

Erstgutachter:	Prof. Dr. Guido Drexlin
	Institut für Experimentelle Kernphysik, KIT
Zweitgutachter:	Prof. Dr. Ulrich Husemann
	Institut für Experimentelle Kernphysik, KIT

Tag der mündlichen Prüfung: 18. Juli 2014

Declaration of authorship

I declare that I have developed and written the enclosed thesis in hand completely by myself, and have not used sources or means without any declaration in the text.

Erklärung der Selbstständigkeit

Hiermit versichere ich, die vorliegende Arbeit selbstständig angefertigt, alle dem Wortlaut oder Sinn nach entnommenen Inhalte anderer Werke an den entsprechenden Stellen unter Angabe der Quellen kenntlich gemacht und keine weiteren Hilfsmittel verwendet zu haben.

....

Johannes Simon Schwarz

Öhringen, den 20. Juni 2014

Introduction and Objectives

The thesis in hand describes work performed in the context of the Karlsruhe Tritium Neutrino (KATRIN) experiment which is targeted to determine the absolute neutrino-mass scale with an unrivaled sensitivity of $m_\nu = 200\,\text{meV}$ (90 % C.L.).

In the Standard Model of particle physics, neutrinos are established in three active generations and are described as electrically neutral, weakly interacting leptons. They are by far the most abundant and lightest fundamental particles of matter in the universe: each cubic centimeter contains 336 neutrinos. At present, however, their absolute mass scale is not known, but laboratory and cosmological studies imply that neutrino masses reside in the sub-eV range. The significant impact of massive neutrinos on particle physics and cosmology is a central motivation for the ongoing construction of a next-generation large-scale direct neutrino-mass experiment: the KATRIN experiment located at Tritium Laboratory Karlsruhe (TLK) at the Karlsruhe Institute of Technology (KIT) Campus North site.

The experiment will investigate the electron energy spectrum of tritium β-decay close to the kinematic endpoint of $E_0 \approx 18.6\,\text{keV}$ with unprecedented precision in a direct and model-independent measurement in order to search for a minute shape distortion caused by a non-zero neutrino mass. Foray into the sub-eV level will be achieved by combining a high-luminosity windowless gaseous molecular tritium source with a large high-resolution integrating spectrometer based on the MAC-E-filter principle and a segmented 148-pixel silicon wafer housed in a complex detector system. KATRIN relies on an almost background-free, highly efficient, long-term stable, and well-understood detection technique for 18.6-keV electrons, since a generic low signal count rate of only few times 0.01 cps is expected. In addition, detailed signal parameters, such as deposited energy, arrival time, and point of detection, are vital to understand electron-transport and background-generation mechanisms along the entire beam line of the experiment.

With respect to these challenges faced by the KATRIN spectrometer and detector section (SDS), the following objectives were set for this thesis:

- The detector system being an integral main component was to be fully implemented and integrated into the KATRIN beam line. All subsystems were to be optimized and comprehensively characterized. Subsequently, the detector system was to be used as a diagnostic tool for the first SDS commissioning phase to allow a detailed investigation of the transmission characteristics and background behavior of the main spectrometer.

- Detector-based and spectrometer-related backgrounds were to be examined with respect to identifying the specific sources and characteristics to understand the associated background generation mechanisms. In a staged approach, first the intrinsic detector background and second the electron background from the main spectrometer was to be investigated. Special emphasis was to be put on nuclear α-decays of emanated radon atoms and on the quantum-tunneling effect of field emission. The motivation of these studies was to provide a specific background model in order

to establish a solid experimental base for further background optimizations, thereby reaching the ambitious design goal of 0.01 cps for the total background rate to achieve the targeted neutrino-mass sensitivity.

In chapter 1, a brief overview on the history and current status of neutrino physics is given. Based on an introductory survey of natural and man-made neutrino sources, the unique particle properties of neutrinos and in particular the phenomenology of neutrino flavor oscillations are discussed. This is supplemented by a survey of cosmological and laboratory methods to access the absolute neutrino-mass scale.

The focus of chapter 2 is set on a description of the working principle and the status of the main components of the KATRIN experiment. Special attention is given to a detailed description of the experimental setup for the first SDS commissioning phase during a four-month measurement campaign in the middle of 2013, as this represents an important milestone for the experiment. In addition, an overview of expected background processes occurring in the detector system and the main spectrometer is given.

In chapter 3, the complex setup of the KATRIN detector system with its major functional sub-components is described. A special focus is set on the working principle and performance of each sub-component as well as on the required benchmarks and design specifications for the KATRIN experiment.

The characterization of the detector response for different types of radiation is highlighted in chapter 4. In this context, the optimization works to achieve an efficient detector operation are described. Further topics include the determination of crucial detector parameters and the understanding of detector systematics. Of special interest for KATRIN is the description of the long-term detector performance during the first SDS commissioning phase.

The intrinsic detector background from cosmic-ray muons, external radiation, and intrinsic radioactivity is described in chapter 5. Several passive and active strategies are outlined to minimize these background classes. In addition, the level of background contribution of the detector system to the total background rate of the combined SDS system is discussed.

The focus of chapter 6 is on the electron-related background process from the spectrometer. Of particular concern here are nuclear α-decays of emanated radon atoms. In this context, detector properties, such as segmentation and good timing resolution, are used to investigate the characteristics of this background class. This culminates in a determination of the radon activity and emanation rate of the spectrometer. The chapter is concluded by examining contributions from other background sources.

In chapter 7, the quantum-tunneling effect of field electron emission from elevated metal surfaces to a negative high voltage is studied. A very interesting side aspect in this context was the observation of hydrogen anions. The combination of field-emission induced electrons and anions are used as a tool to further characterize important detector parameters, but also to investigate the mapping properties of the SDS system with a well localized particle source. This demonstrates the dual purpose of the investigations of this thesis: to determine crucial detector parameters, such as its alignment relative to the spectrometer axis and the thickness of its insensitive dead-layer volume, as well as to use the excellent detector properties to study background processes and phenomena.

The thesis in hand is completed with chapter 8 by giving a detailed recapitulation of the works performed and by presenting an outlook to the upcoming second SDS commissioning phase which will build on the ground-laying work of this thesis.

Einleitung und Zielsetzung

Die vorliegende Arbeit beschreibt Untersuchungen, die im Rahmen der internationalen Kollaboration des Karlsruher Tritium Neutrino (KATRIN) Experimentes durchgeführt wurden, dessen Ziel die Bestimmung der effektiven Masse des Elektron-Antineutrinos mit einer bisher unerreichten Sensitivität von $m_\nu = 200 \, \text{meV}$ (90 % C.L.) ist.

Im Standardmodell der Elementarteilchenphysik existieren drei aktive Generationen von Neutrinos. Sie werden als elektrisch neutrale, schwach wechselwirkende Leptonen beschrieben, und sind die leichtesten und mit durchschnittlich 336 Neutrions pro Kubikzentimeter gleichzeitig die im Universum am häufigsten vorkommenden Masseteilchen. Obgleich ihre effektive Masse bis heute nicht bekannt ist, deuten Laborversuche und kosmologische Beobachtungen darauf hin, dass sie im sub-eV Bereich liegt. Die Tatsache, dass Neutrinos als massebehaftete Teilchen einen maßgeblichen Einfluss auf die Elementarteilchenphysik und die Kosmologie haben, war und ist einer der Hauptgründe für das Design und den Aufbau des KATRIN Experimentes, einem groß angelegten Laborversuch der nächsten Generation zur direkten und modellunabhängigen Bestimmung der Neutrinomasse, das am Tritium Labor Karlsruhe (TLK) am Karlsruher Institut für Technologie (KIT) Campus Nord angesiedelt ist.

Das etwa 70 m lange Experiment wird das Energiespektrum der emittierten Elektronen des molekularen Tritium β-Zerfalls nahe des kinematischen Endpunktes von $E_0 \approx 18.6 \, \text{keV}$ mit einer einzigartigen Präzision analysieren, um nach einer winzigen Formänderung des Energiespektrums zu suchen, die durch eine nicht-verschwindende Neutrinomasse verursacht wird. Der Vorstoß in den sub-eV Bereich wird erreicht, indem eine fensterlose, gasförmige, molekulare Tritiumquelle hoher Luminosität in Kombination mit einem großen, hochauflösenden, integrierenden Spektrometer betrieben wird, das auf dem Prinzip des MAC-E-Filters basiert. Der Nachweis der transmittierten Elektronen wird durch einen segmentierten Silizium-Wafer bestehend aus 148 Pixeln erreicht, der in ein komplexes Detektorsystem integriert ist. Da eine allgemein niedrige Signalzählrate von nur wenigen 0.01 cps erwartet wird, stützt sich KATRIN auf eine beinahe untergrundfreie, hocheffiziente, langzeitstabile und fest etablierte Technik, um Elektronen mit Energien von 18.6 keV zu detektieren. Außerdem sind detaillierte Signalparameter wie die deponierte Energie, die Ankunftszeit und der Detektionsort des Signals notwendig, um den Elektronentransport und Untergrund erzeugende Mechanismen entlang der gesamten Strahlführung des Experimentes zu verstehen.

Im Hinblick auf die Herausforderungen, denen die Spektrometer- und Detektor-Sektion (SDS) des KATRIN Experimentes gegenübersteht, verfolgt diese Arbeit folgende Ziele:

- Das Detektorsystem als eine wesentliche Hauptkomponente des Experimentes sollte vollständig in die KATRIN Beam Line implementiert und integriert werden. Alle Teilkomponenten des Detektorsystems sollten vollständig optimiert und umfangreich charakterisiert werden. Anschließend sollte das Detektorsystem als Diagnosewerkzeug für die erste Messphase der SDS-Inbetriebnahme genutzt werden, um eine

detaillierte Untersuchung der Transmissionseigenschaften und der Untergrundbedingungen des Hauptspektrometers zu gewährleisten.

- Vom Detektorsystem und vom Spektrometer erzeugter Untergrund sollte untersucht werden, um dessen verschiedene Quellen und Eigenschaften zu identifizieren und um die damit verbundenen Entstehungsmechanismen zu klassifizieren. In diesem Zusammenhang sollte zunächst der intrinsische Detektoruntergrund und anschließend der Elektronenuntergrund des Hauptspektrometers erforscht werden. Hierbei sollte der Fokus auf den α-Zerfall von emanierten Radonatomen sowie auf den Tunneleffekt der Feldemission gelegt werden. Ziel der Untersuchungen war die Definition eines untergrundspezifischen Modells, das als solide experimentelle Basis für weitere Untergrundoptimierungen dient, um das ehrgeizige Ziel von 0.01 cps für die gesamte Untergrundrate und dadurch die angestrebte Neutrinomassensensitivität zu erreichen.

Kapitel 1 bietet einen kurzen Überblick über die Geschichte und den aktuellen Stand der Neutrinophysik. Auf Grundlage einer einführenden Zusammenstellung natürlicher und von Menschenhand geschaffener Neutrinoquellen werden die einzigartigen Eigenschaften von Neutrinos, insbesondere das Phänomen der Neutrinooszillation, diskutiert. Ergänzend wird eine Übersicht über kosmologische und im Labor anwendbare Methoden zur Messung der effektiven Neutrinomasse gegeben.

Das Hauptaugenmerk von Kapitel 2 liegt auf der Beschreibung der Arbeitsweise und des aktuellen Standes der Hauptkomponenten des KATRIN Experimentes. Im Mittelpunkt steht eine detaillierte Beschreibung des experimentellen Aufbaus für die erste SDS-Inbetriebnahme, die eine viermonatige Messphase Mitte 2013 umfasste und einen wichtigen Meilenstein für das Experiment darstellte. Außerdem werden die erwarteten Untergrundprozesse im Detektorsystem sowie im Hauptspektrometer zusammenfassend dargestellt.

In Kapitel 3 wird der komplexe Aufbau des KATRIN Detektorsystems mit seinen individuell funktionierenden Teilkomponenten beschrieben. Im Zentrum des Interesses stehen die Funktionsweise und die Betriebseigenschaften jeder Teilkomponente sowie die notwendigen Vergleichsgrößen und Design-Spezifikationen für das KATRIN Experiment.

Schwerpunkt des Kapitels 4 ist die Charakterisierung der Detektorantwort auf verschiedene Strahlungsarten. Es wird beschrieben, welche Optimierungsarbeiten durchgeführt werden müssen, um einen effizienten Betrieb des Detektors zu gewährleisten. Des Weiteren werden die Bestimmung essentieller Detektorparameter und die Modellierung von Detektorsystematiken besprochen. Insbesondere die Beschreibung des stabilen Langzeitbetriebs des Detektors während der ersten Messphase der SDS-Inbetriebnahme ist für das KATRIN Experiment von großer Bedeutung.

Kapitel 5 behandelt den intrinsischen Detektoruntergrund, der vor allem durch kosmische Myonen, externe Strahlung und intrinsische Radioaktivität verursacht wird. Es werden verschiedene passive und aktive Strategien zur Minimierung der verschiedenen Untergrundarten vorgestellt. Außerdem wird der Beitrag des Detektoruntergrunds zur gesamten Untergrundrate des kombinierten SDS-Systems diskutiert.

Der Fokus von Kapitel 6 liegt auf den elektronenbezogenen Untergrundprozessen des Spektrometers. Interessant sind hier vor allem die α-Zerfälle emanierter Radonatome. Mit Hilfe von speziellen Detektormerkmalen wie räumliche Segmentierung und gute Zeitauflösung können die Eigenschaften dieser Untergrundklasse untersucht werden. Dies erlaubt die Bestimmung der Radonaktivität und -emanationsrate des Spektrometers. Abschließend werden Beiträge anderer Untergrundquellen erforscht.

In Kapitel 7 wird der elektronenbezogene Tunneleffekt der Feldemission von Metallflächen untersucht, die auf dem Potential einer negativen Hochspannung unter exzellenten Vaku-

umbedinungen liegen. Ein höchst interessanter Nebeneffekt trat hier durch die Beobachtung von Wasserstoffanionen auf. Durch die Kombination von durch Feldemission emittierten Elektronen und Anionen konnten nicht nur wichtige Detektormerkmale detaillierter charakterisiert, sondern auch die Abbildungseigenschaften des SDS-Systems mit einer lokalisierten Teilchenquelle untersucht werden. Somit konnte beiden Zielen dieser Arbeit gerecht geworden werden: zum einen der Bestimmung entscheidener Detektorparameter, wie die Ausrichtung des Detektors relativ zur Spektrometerachse und die Dicke der nicht-sensitiven Totschicht, zum anderen der Nutzung der hervorragenden Detektoreigenschaften zur Analyse von Untergrundprozessen und -phänomenen.

Kapitel 8 fasst die durchgeführten Arbeiten abschließend zusammen und gibt einen Ausblick über die anstehende zweite Messphase der SDS-Inbetriebnahme, die auf die grundlegenden Erkenntnisse dieser Arbeit aufbaut.

Contents

Neutrino Physics

Cosmic Gall

Neutrinos, they are very small.
They have no charge and have no mass
And do not interact at all.
The earth is just a silly ball
To them, through which they simply pass,
Like dustmaids down a drafty hall
Or photons through a sheet of glass.
They snub the most exquisite gas,
Ignore the most substantial wall,
Cold-shoulder steel and sounding brass,
Insult the stallion in his stall,
And, scorning barriers of class,
Infiltrate you and me! Like tall
And painless guillotines, they fall
Down through our heads into the grass.
At night, they enter at Nepal
And pierce the lover and his lass
From underneath the bed — you call
It wonderful; I call it crass.

John Updike
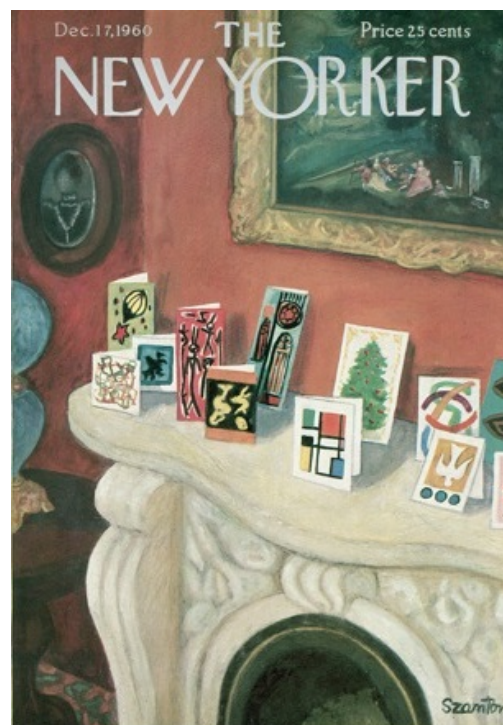
Cover of *The New Yorker* [Upd60]

In 1960, *The New Yorker* published this poem about neutrinos [Upd60] − interpreted as ghostlike particles of the universe with exceptional particle properties [Rie11b] − after their existence was postulated by Pauli three decades earlier [Pau30] and only few years after they were finally discovered by Cowan and Reines in 1956 [Cow56]. Updike's poem was even quoted by the Nobel Prize committee in 1995 [Upd95] when it awarded the Nobel Prize in physics to Reines for his remarkable first detection at the Savannah River Site [Nob95]. Since their discovery, the image of neutrinos has significantly been transformed by important observations in the field of neutrino physics. Two more types of neutrinos were found in 1962 [Dan62] and 2001 [DON01], respectively, and, of particular interest for this theses, flavor transformations from one type into another were experimentally confirmed in 1998 [Fuk98a] [Fuk98b] and in 2001 [Ahm01] [Ahm02]. These breakthrough observations have given incontrovertible evidence for the phenomenon of neutrino oscillations [Pon57a] [MNS62]. Today, neutrinos play a key role in understanding of the Standard Model of par-

ticle physics [Ber13] − *the theory of almost everything* [Oer06]. Neutrinos come in three generations as fundamental, electrically neutral, weakly interacting, leptonic particles: the electron neutrino ν_e, the muon neutrino ν_μ, and the tau neutrino ν_τ. Updike impressively describes many unique neutrino properties using some demonstrative examples, in particular with regard to their weak interaction with other particles of matter. It is this fact that has made and still makes the detection of neutrinos and the examination of their characteristics a challenging task, even today.

When Updike authored his poem, the mass of neutrinos was assumed to be zero. The same applied to the well-established Standard Model of particle physics. However, the discovery of neutrino oscillations has unambiguously proven that the masses are non-zero, giving a hint for physics beyond the Standard Model and representing an important milestone in the field of particle physics. Today, the mass splittings are determined to very high precision, but the absolute mass scale and the associated hierarchy of neutrino masses are still unknown. In this context, neutrino-oscillation experiments on the one hand give at least a lower mass limit defined by the maximum mass splitting [Ber13]. Neutrino-mass experiments on the other hand which have investigated the tritium β-decay spectrum in a direct model-independent way provide an upper mass limit [Kra05] [Ase11]. Cosmological observations [Han10] and the search for the neutrinoless double β-decay [Kla01] provide further more stringent upper mass limits, but are based on approaches being much more model-dependent.

Neutrinos are by far the most abundant and lightest fundamental particles of matter in the universe. The impact of neutrino masses on particle physics and cosmology has been a key motivation in proposing a next-generation large-scale neutrino-mass experiment: the Karlsruhe Tritium Neutrino (KATRIN) experiment. It is targeted to determine the effective mass of the electron (anti)neutrino with an unrivaled sensitivity of 200 meV at 90 % C.L. by performing high-precision electron spectroscopy of tritium β-decay in a direct model-independent way [Ang05].

This chapter gives a brief overview on neutrino physics. In section 1.1, natural and man-made neutrino sources are listed, and the associated source reactions and processes are discussed. In section 1.2, a brief historical overview is illustrated, starting with the postulation and discovery of neutrinos and ending with today's state-of-the-art neutrino experiments. The principle of neutrino oscillations together with the latest experimental results for oscillation parameters are discussed in section 1.3. Finally, in section 1.4, different experimental methods are compared on how to access the absolute neutrino-mass scale. The KATRIN experiment as one of the leading approaches in this field is presented in chapter 2.

1.1 Neutrino Sources

Both natural and man-made neutrino sources are used to investigate neutrino properties, while at the same time using neutrinos as messenger particles to study the sources themselves. In the following, the most important neutrino sources are listed and the associated source reactions are discussed.

1.1.1 Relic Neutrinos

During the freeze-out of the weak interaction in the expanding universe [Sli15] [Lun24] [HH31] a huge number of relic neutrinos was left free-streaming [LP12]. Their origin is of specific interest to the cosmological ΛCDM model which describes the development of the universe from its beginning to its present state, being dominated by dark energy (Λ) and cold dark matter (CDM) [Lid03] [BG06]. In contrast, at a very early stage ($t \ll 0.1$ s) at

high temperatures ($E \gg 1\,\text{MeV}$), the total energy density of the universe was dominated by radiation only. The universe was filled with a relativistic *cosmic soup* [Ott14] including all light fundamental particles in thermodynamical equilibrium as a result of continuous pair production, annihilation and scattering. Neutrinos were kept in equilibrium by the weak interaction:

$$\gamma + \gamma \; \leftrightarrow \; e^- + e^+ \; \leftrightarrow \; \nu + \overline{\nu} \qquad \nu_e + e^- \; \leftrightarrow \; \nu_e + e^- \qquad \overline{\nu}_e + e^+ \; \leftrightarrow \; \overline{\nu}_e + e^+ \; . \qquad (1.1)$$

A comparison between the relativistic number densities of neutrinos, following the Fermi-Dirac statistics of fermions, and photons of the cosmic microwave background (CMB), following the Bose-Einstein statistics of bosons, results in a theoretical ratio of

$$\frac{n_\nu + n_{\overline{\nu}}}{n_\gamma} = \frac{3}{4} \qquad (1.2)$$

for each neutrino flavour at this time epoch. Due to the expansion of space-time, the universe cools down by time. At a certain temperature ($E \approx 1\,\text{MeV}$), the weak interaction rate of neutrinos ($\sim T^5$) dropped below the expansion rate of the universe ($\sim T^2$) so that neutrinos decoupled from the cosmic plasma. This weak freeze-out occurred about $t \approx 0.1\,\text{s}$ after the hot Big Bang. From then on, neutrinos contributed as (relativistic) hot dark matter to the formation and evolution of structures in the early universe by carrying energy out of matter over-densities due to their large free-streaming length. Consequently, they smeared out fluctuations at small scales. Shortly after neutrino decoupling, electrons and positrons annihilated, since the mean photon energy was insufficient to further create electron-positron pairs ($E \approx 0.2\,\text{MeV}$):

$$e^- + e^+ \; \to \; \gamma + \gamma \; . \qquad (1.3)$$

This annihilation of lepton pairs heated up the remaining plasma including the photons but not neutrinos due to their prior decoupling. Put another way, electrons and positrons both dumped their entropy into the photons so that their number density with respect to the one of neutrinos increased by a factor of 11/4. This factor can be calculated by comparing the conserved entropy before and after this process [Ber13]. Thus, the number densities adjusted to a ratio of

$$\frac{n_\nu + n_{\overline{\nu}}}{n_\gamma} = \frac{3}{4} \cdot \frac{4}{11} = \frac{3}{11} \qquad (1.4)$$

for each neutrino flavour. Finally, after a time period of 380000 years ($E \approx 0.3\,\text{eV}$), also the photons of the CMB decoupled from matter since their energy was insufficient to further ionize atomic hydrogen formed by the recombination of electrons and protons:

$$e^- + p \; \to \; \text{H} + \gamma \; . \qquad (1.5)$$

At this stage, the universe became transparent for radiation. While free streaming through the universe, both neutrinos and photons cooled down further so that a resulting cosmic neutrino (CνB) and microwave background (CMB) is expected, both following black body distributions. The cosmic microwave background was first discovered by Penzias and Wilson in 1965 [PW65]. The CMB effective mean temperature was precisely determined by the two NASA satellites COBE and WMAP to $T_\gamma = (2.728 \pm 0.004)\,\text{K}$ [Fix96] and $T_\gamma = (2.7255 \pm 0.0006)\,\text{K}$ [Fix09], respectively. Using the relation $n_\gamma \sim T_\gamma^3$, a present number density of $n_\gamma \approx 411\,\text{cm}^{-3}$ for relic photons is calculated. Although the cosmic neutrino background has not been observed yet, its theoretical temperature and number density for each neutrino flavour can be calculated to $T_\nu \approx 1.9\,\text{K}$ and $(n_\nu + n_{\overline{\nu}}) \approx 112\,\text{cm}^{-3}$ [Ber13], respectively, according to equation (1.4) and making use of the experimental results from the cosmic microwave background. This corresponds to a kinetic mean energy of the CνB of only $\langle E_\nu \rangle \approx 0.5\,\text{meV}$, which makes the detection of relic neutrinos extremely challenging and, most likely, impossible in the near future with the current detector techniques. The influence of relic neutrinos to cosmological observables is discussed in section 1.4.1.

1.1.2 Supernova Neutrinos

Supernovae are transient sources for intense bursts of neutrinos. In the final stage of a massive star ($M > 8 M_\odot$), silicon in the stellar core fuses to iron, cobalt and nickel. At this stage, the mass and the density of its core increases drastically as the thermal pressure in the inner core vanishes after the thermonuclear energy production has stopped. Once, the inner core has reached a mass greater than the Chandrasekhar limit of $\sim 1.44 \, \mathrm{M_\odot}$, the electron degeneracy pressure there is insufficient to balance the gravitational pressure of the outer core shells. Consequently, the core undergoes a rapid gravitational collapse, evolving the star into a gravitationally contracted object, a black hole or a neutron star, depending on its mass. During the collapse, neutrinos are produced by neutronization, thereby leaving the collapsed core. The matter of the inner core rebounds once it reaches the density of nuclear matter. The rebound results in a shock wave which hits the outer infalling matter shells of the star which eventually leads to an explosion of a type-II supernova. Further neutrinos are produced by thermal pair production. For this core-collapse supernova, the following neutrino production mechanisms are relevant [WJ05] [Jan07]:

$$
\begin{aligned}
e^- + p &\rightarrow n + \nu_e & \text{(neutronization)} \\
\gamma + \gamma &\leftrightarrow e^+ + e^- \leftrightarrow \nu_i + \overline{\nu}_i \quad (i = e, \mu, \tau) & \text{(pair production)}
\end{aligned}
\tag{1.6}
$$
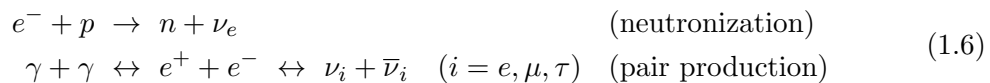
During the described collapse of the core, a total of up to 10^{58} neutrinos can be generated with mean energies of $\langle E_\nu \rangle = (10 - 15) \, \mathrm{MeV}$ carrying 99% of the released binding energy [BDP87]. Due to the high core density of the star, neutrinos diffuse through the core to the outer shells constantly interacting with matter. Finally, after depositing some energy below the (usually) stalled shock front, they reach the outer shells with smaller densities and leave the star. Therefore, a neutrino burst occurs as a distinct pulse for several seconds. The detection of this burst allows to determine the absolute neutrino-mass scale; this is discussed in more detail in section 1.4.2.

1.1.3 Solar Neutrinos

The sun is the most intense natural neutrino source for terrestrial experiments. A huge number of solar neutrinos is created by different nuclear fusion reactions in the solar core, starting with the extremely slow proton-proton (pp) fusion:

$$
p + p \rightarrow \mathrm{D} + e^+ + \nu_e + 0.42 \, \mathrm{MeV} \; .
\tag{1.7}
$$

The theoretical energy spectrum of solar neutrinos as calculated by Bahcall et al. [Bah05] in the standard solar model is shown in figure 1.1, including the corresponding fusion reactions by the dominant proton-proton chain and the subdominant catalytic carbon-nitrogen-oxygen cycle. Although both the ^{8}B- and hep-branches do not result in high fluxes, they generate high-energy solar neutrinos of up to 14.1 MeV and 18.8 MeV, respectively, which are easier to detect than low-energy pp-neutrinos, for example. Over a long time, the solar neutrino flux was measured to be only 1/3 the number expected by the standard solar model. This discrepancy is now explained by the effect of neutrino oscillations (section 1.3). Today, solar neutrinos serve as messenger particles from the core of the sun, allowing an indirect insight into processes occurring inside the nearest star.

1.1.4 Atmospheric Neutrinos

The atmosphere of our planet is another well-known natural neutrino source. Atmospheric neutrinos result from the continuously bombarding of the earth's atmosphere by high-energy particles, mainly protons, from outer space. When interacting with air molecules, cosmic ray produce broad showers of high-energy unstable particles, such as kaons, pions,
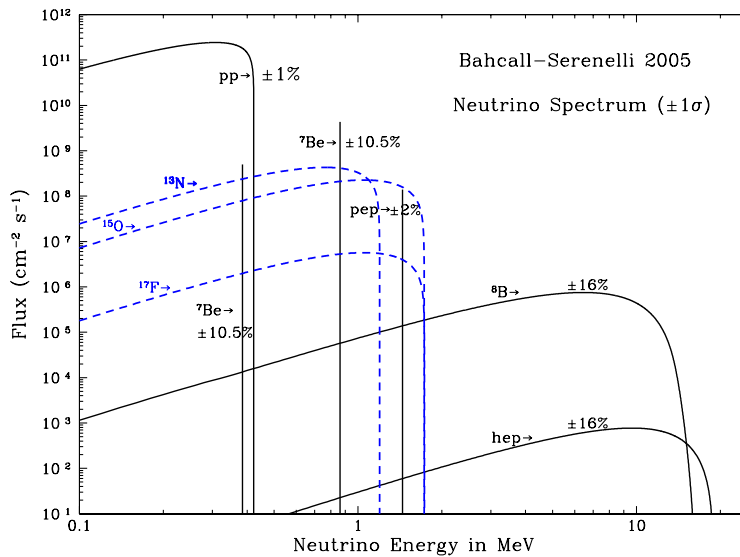
Figure 1.1: Standard solar model. The solar neutrino spectrum as predicted by the standard solar model is illustrated for the different nuclear fusion processes. The neutrino fluxes are given in $\mathrm{cm^{-2}s^{-1}MeV^{-1}}$ for continuous spectra and $\mathrm{cm^{-2}s^{-1}}$ for line spectra. Theoretical errors are stated. Figure adapted from [Bah05] [Ber13].

and muons. The subsequent pure leptonic decay sequences produce neutrinos with energies of up to $\sim 1\,\mathrm{TeV}$:

$$
\begin{aligned}
K^+ &\to \mu^+ + \nu_\mu & \pi^+ &\to \mu^+ + \nu_\mu & \mu^+ &\to e^+ + \nu_e + \overline{\nu}_\mu \\
K^- &\to \mu^- + \overline{\nu}_\mu & \pi^- &\to \mu^- + \overline{\nu}_\mu & \mu^- &\to e^- + \overline{\nu}_e + \nu_\mu
\end{aligned}
\tag{1.8}
$$

Correspondingly, a ratio between muon and electron neutrinos of 2:1 is expected over a large energy range. Cherenkov detectors used this unique neutrino source to search for deviations of this flavor ratio. Indeed, a deficit of atmospheric muon neutrinos was measured and found to be maximal for neutrinos traversing the earth, in contrast to those detected from nearby. This discrepancy is now explained by the phenomenon of neutrino oscillations (section 1.3).

1.1.5 Geoneutrinos

Geoneutrinos result from the natural decay chains of radioactive isotopes, such as $^{40}\mathrm{K}$, $^{232}\mathrm{Th}$ and $^{238}\mathrm{U}$. In each β^--decay

$$
{}^A_Z\mathrm{X} \;\to\; {}^{\;\;A}_{Z+1}\mathrm{Y} + e^- + \overline{\nu}_e
\tag{1.9}
$$

an antineutrino is emitted with an energy in the few MeV-scale, while a mother nucleus X decays into its daughter nucleus Y. As messengers from the earth's interior, geoneutrinos provide valuable information on the distribution of primordial radioactive elements in the crust and mantle of the earth. The experiment KamLAND made the first observation of geoneutrinos in 2005 when 25 events were found during a detector live-time of 749 days [Ara05]. Although the data is statistically limited, this first detection already leads to an upper limit of 60 TW for the radiogenic power of thorium and uranium decays in the earth, in moderate agreement with the expectation of 16 TW suggested from current geochemical and geophysical models [MsS95]. In 2010 and 2011, further experimental evidences for geoneutrinos were obtained by Borexino [Bor10] and KamLAND [Kam11], respecitively.

1.1.6 Reactor Neutrinos

Nuclear reactors are the most intense terrestrial sources for artificially generated neutrinos. Reactor neutrinos are emitted isotropically by the large number of β^--decays of neutron-rich daughter fragments in fission processes, mainly originating from the fissile isotopes $^{233}_{92}$U, $^{235}_{92}$U, $^{239}_{94}$Pu, and $^{241}_{94}$Pu. On average, about six neutrinos are created per fission, so that a typical nuclear power plant generates more than 10^{21} neutrinos per second with a maximum energy of about 10 MeV. Almost 5 % of the released energy by nuclear fission is radiated away as neutrinos and cannot be used for electricity generation. Reactor neutrinos are used to investigate the parameters of neutrino oscillations (section 1.3).

1.1.7 Accelerator Neutrinos

Another artificial source for neutrinos are neutrino beams from particle accelerators. The accelerator collides bunches of protons onto a fixed target, usually made of graphite or beryllium. The protons produce new unstable particles, such as kaons and pions, see equation (1.8), which are magnetically focused by a horn into a long decay tunnel. The powerful magnetic horn sign selects kaons and pions, and focuses them to an evaluated tunnel where they decay in flight into muons and neutrinos. Because of the relativistic boost of the decaying particles, neutrino beams in the GeV-range are produced, typically. An additional block of concrete and steel slows down and absorbs the muons while the neutrinos are sent to a detector located at distances of up to several hundreds of km to study the parameters of neutrino oscillations (section 1.3) [Kop07].

1.2 History of Neutrino Physics and Neutrino Properties

In the following, neutrino properties are illuminated by means of a short history of neutrino physics.

1.2.1 Neutrino Hypothesis

In the β-decay of a mother nucleus X into a daughter nucleus Y, a two-body decay with a discrete spectrum of the electron energy was (incorrectly) expected:

$$^A_Z\text{X} \;\rightarrow\; ^A_{Z+1}\text{Y} + e^- \; . \tag{1.10}$$

A century ago, in 1914, it was Chadwick who finally proofed the energy spectrum of radium β-decay electrons to be of continuous nature [Cha14], as shown in figure 1.2 [Sco35], and not discrete. It took more than a decade until Pauli extended the β-decay of reaction (1.10) to a three-body decay by postulating a hypothetical stable, electrically neutral spin-$^1/2$ particle with a tiny rest mass to explain the shape of the β-spectrum and to conserve electric charge, angular momentum, energy and momentum during the decay process [Pau30]:

$$^A_Z\text{X} \;\rightarrow\; ^A_{Z+1}\text{Y} + e^- + \overline{\nu}_e \; . \tag{1.11}$$

After Pauli's postulate, it was Fermi in 1934 who formulated a coherent theory for the three-body β-decay assuming a weak point-like interaction between the four involved fermions, and gave the neutrino its present name meaning *the little neutral one* [Fer34]. In the same year, Bethe and Peierls calculated the cross section for neutrino interactions with matter to be $\sigma \approx 10^{-44}\,\text{cm}^2$ [BP34]. It is this small cross section which characterizes the weak interaction and which prevented direct detection of the ghostlike neutrino for the following two decades.
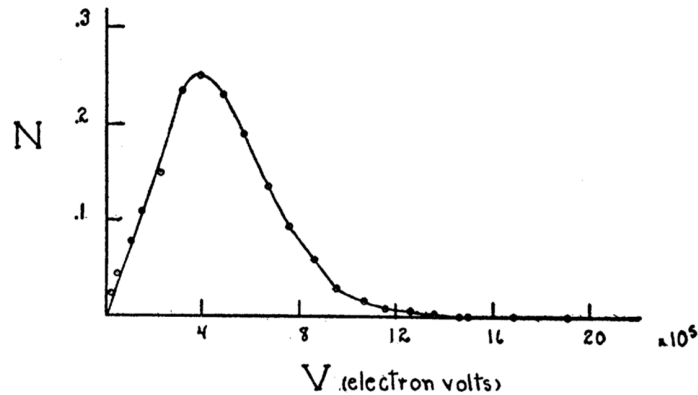
Figure 1.2: Energy distribution curve of the radium β-decay. The measured energy spectrum is continuous but not discrete as expected. Figure adapted from [Sco35].

1.2.2 Neutrino Discovery

Finally, in 1956, the existence of neutrinos was proven by Cowan and Reines in their famous *project poltergeist* using the nuclear reactor P of the Savannah River Site as neutrino source [Cow56] with a calculated reactor-neutrino flux of $5 \cdot 10^{13}\,\mathrm{cm^{-2}s^{-1}}$ at the detector [Gri04]. The latter consisted of two tanks filled with a total of about $200\,\ell$ of water in which about $40\,\mathrm{kg}$ cadmium chloride $CdCl_2$ was dissolved. These tanks were sandwiched between three scintillator layers with photomultiplier readout. The detection process was based on the classical inverse β-decay:

$$\overline{\nu}_e + p \; \rightarrow \; e^+ + n \; . \tag{1.12}$$

In this delayed coincidence, positrons interact electromagnetically in the target and slow down. At rest, they quickly annihilate with electrons into pairs of 511-keV photons being emitted into opposite directions. The neutrons scatter off free protons in the water target and thermalize before being captured by cadmium within a few microseconds. The exited Cd^* state deexcites to its ground state by releasing MeV-scale gamma rays. The characteristic delayed-coincidence signature between the two 511-keV photons and the gamma rays being detected by the surrounding photomultiplier tubes was interpreted correctly as a neutrino-induced signal (see figure fig:CowanReinesScope). With this method, a neutrino rate of up to three events per hour was measured over a total running time of 1371 hours. Therefore, the corresponding cross section of the inverse β-decay was determined to be $\sigma = 6.3 \cdot 10^{-44}\,\mathrm{cm^2}$ [Cow56], in good agreement with the Fermi theory [BP34].

In 1962, Ledermann, Schwartz, and Steinberger discovered a second type of neutrino $-$ the muon neutrino ν_μ $-$ at the Brookhaven National Laboratory. The particle accelerator AGS was used to bombard a beryllium target by protons. The resulting pions decay in flight to neutrinos through

$$\pi^+ \; \rightarrow \; \mu^+ + \nu_\mu \quad \text{and} \quad \pi^- \; \rightarrow \; \mu^- + \overline{\nu}_\mu \; . \tag{1.13}$$
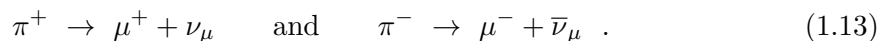
The focused neutrino beam was guided to a 10-ton aluminum spark chamber located behind a 13.5-m thick iron shield absorbing other particles. The observed signals there were different from showers by electrons or positrons but identical to straight tracks as expected for muons. This observation demonstrated that muon-neutrinos and electron-neutrinos are non-identical particles [Dan62].

Only in 2001, the third type of neutrino $-$ the tau neutrino ν_τ $-$ was discovered at the DONUT experiment, although its existence was already implied indirectly in 1975, when its charged partner $-$ the tau lepton τ $-$ and, hence, the third leptonic generation was

(a) **Positron scope**   (b) **Neutron scope**
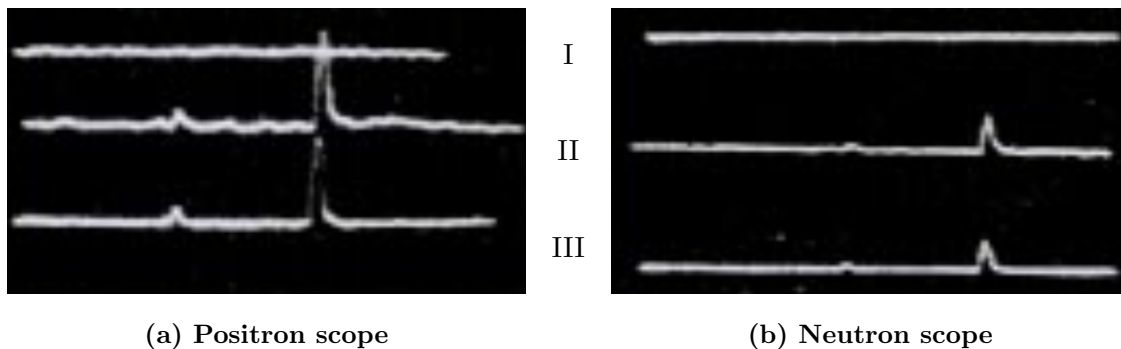
Figure 1.3: The first neutrino signal. The characteristic delayed-coincidence signature of a neutrino-induced signal is shown. In these oscilloscope pictures, traces from the scintillation detectors I, II and III indicate the positron annihilation (left) and the neutron capture (right). The corresponding energy ranges were set with energy discriminators to $0.2 - 0.6\,\text{MeV}$ and $3-11\,\text{MeV}$, respectively. The pulse energies were measured to $0.25\,\text{MeV}$ (II) and $0.30\,\text{MeV}$ (III) in the positron scope and to $2.0\,\text{MeV}$ (II) and $1.7\,\text{MeV}$ (III) in the neutron scope, respectively. The delay between the positron and neutron signal was $13.5\,\mu\text{s}$, in this special case [Rei97]. Such a delayed-coincidence signature was interpreted correctly as a neutrino-induced signal. Figures adapted from [Rei97].

detected [Per75]. The neutrino beam was created using high-energy protons from the Fermilab Tevatron interacting in a tungsten beam dump. The resulting particle shower contained unstable D_S-mesons, with neutrinos originating from the purely leptonic decays

$$D_S \;\to\; \tau + \bar{\nu}_\tau \tag{1.14}$$

and the subsequent leptonic and hadronic decays of the resulting tau leptons into tau neutrinos. Focused to a beam, these neutrinos were detected by a sandwich consisting of stainless-steel sheets interleaved with nuclear emulsion plates. This detector was located behind a shield of concrete, iron, and lead to absorb other produced particles from the initial proton interactions. In the target material, neutrino-induced tau leptons typically decayed within $\sim 2\,\text{mm}$ of their point of creation with a kink in their trajectory, characterizing this decay and giving proof to the existence of tau neutrinos [DON01].

1.2.3 Neutrinos in the Standard Model of Particle Physics

Already in 1955, Davis proved electron neutrinos ν_e to be non-identical with their antiparticle $\bar{\nu}_e$, although both particles were not observed at this stage. At the Savannah River Site, the radiochemical reaction

$$\bar{\nu}_e + {}^{37}\text{Cl} \;\not\to\; {}^{37}\text{Ar} + e^- \;, \tag{1.15}$$

violating the conservation of the lepton number, was investigated using reactor neutrinos. For such a reaction, no evidence was observed [Dav55].

In 1958, Goldhaber proved the left-handed nature of neutrinos by measuring their helicity in the K-electron capture of metastable $^{152\text{m}}\text{Eu}$ and the ensuing fast deexcitation of $^{152}\text{Sm}^*$ ($\tau = 30\,\text{fs}$ [Gro58]):

$$e^- + {}^{152\text{m}}\text{Eu} \;\to\; {}^{152}\text{Sm}^* + \nu_e + 950\,\text{keV} \qquad {}^{152}\text{Sm}^* \;\to\; {}^{152}\text{Sm} + \gamma + 961\text{keV} \;. \tag{1.16}$$

The parameter helicity h is the projection of the particle spin onto the direction of the particle momentum: $h = \vec{s} \cdot \hat{p}$. This physical observable depends on the reference frame, i.e. it is not Lorentz-invariant. In the case of the photon being emitted in opposite direction to the initial neutrino, both have the same helicity, $h(\nu_e) = h(\gamma)$, due to conservation
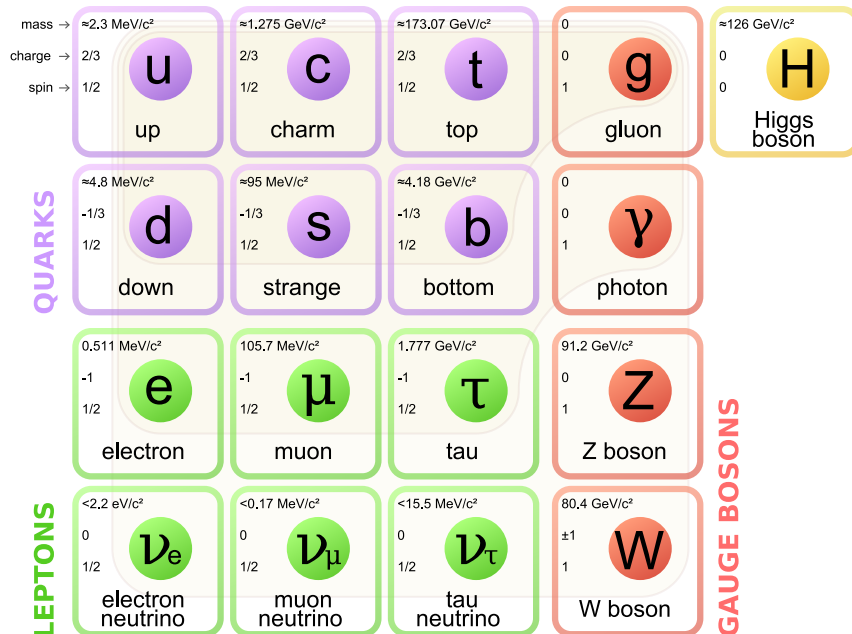
Figure 1.4: Standard model of particle physics. The standard model of particle physics is characterized by three generations of elementary particles of matter ($1^{st} - 3^{rd}$ column), four gauge bosons (4th column), and the Higgs boson (5th column). Each neutrino flavor (ν_e, ν_μ, ν_τ) has an electrically charged leptonic partner of the same flavor (e^-, μ^-, τ^-). The same applies to the antiparticles. Figure adapted from [Kle14]. Particle properties adapted from [Ber13].

of momentum and angular momentum during the decay processes. In the experimental arrangement, such decays were selected by resonant scattering of the emitted photons off a Sm_2O_3 scatterer before their detection with a cylindrical NaI(Tl) scintillation counter shielded by iron and mu-metal. The helicity of the photons was determined by the definition of their polarization. Before reaching the Sm_2O_3 scatterer, the emitted photons had to pass an electro-magnet alternately magnetized in opposite directions in which the ^{152m}Eu source was located. By measuring the photon count rate in dependence on the magnet polarity and, hence, the photon polarization, Goldhaber finally determined the neutrino helicity to be $h = -1.0 \pm 0.3$ [GGS58], showing that the direction of neutrino spin and momentum are opposite. This result confirmed the maximum parity violation of weak interactions, discovered in the Wu experiment already one year earlier [Wu 57], and the corresponding V-A theory [FGM58] [SM58] implying the existence of massless left-handed neutrinos and massless right-handed antineutrinos only.

Already in 1989, the evidence for the existence of only three light, active types of neutrinos was indirectly observed by the ALEPH experiment at the electron-positron collider LEP at CERN. When comparing the total width of the Z^0 resonance with theoretical expectations for all possible decay channels and partial widths, including the invisible decays

$$e^- + e^+ \ \rightarrow \ Z^0 \ \rightarrow \ \nu + \overline{\nu} \ , \tag{1.17}$$

the unknown number N_ν of light neutrino species can be deduced. For neutrinos with mass $m_\nu < m_{Z^0}/2 \approx 45.6 \, \text{GeV}$ and standard coupling to the weak interaction, the best agreement was found for $N_\nu = 3.27 \pm 0.30$ neutrino types [DeC89]. This is consistent with the expectation of $N_\nu = 3$ neutrino generations. Recent combined analyses yield a similar result with $N_\nu = 2.9840 \pm 0.0082$ [ALE06].

Today, the Standard Model of particle physics contains three active types of neutrinos: the neutrino flavours ν_e, ν_μ, and ν_τ. They are described as electrically neutral, weakly

interacting, fundamental fermions with spin-$1/2$. Each neutrino flavour forms a weak doublet with a negatively charged leptonic partner of the same flavour: the electron e^-, the muon μ^-, and the tau lepton τ^-. Analogously, each antineutrino ($\overline{\nu}_e$, $\overline{\nu}_\mu$, $\overline{\nu}_\tau$) forms a doublet with a positively charged lepton (e^+, μ^+, τ^+). Neutrinos have been assigned a lepton number of $L = +1$, and antineutrinos of $L = -1$. The lepton number is an additive quantum number whose sum is a conserved quantity. Neutrinos as the only elementary fermionic particles being electrically neutral, play a unique role in the Standard Model as, in principle, they can be their own antiparticles ($\nu = \overline{\nu}$). In this case, the conserved lepton number would be violated by $\Delta L = 2$ in the associated interaction, representing an evidence for physics beyond the Standard Model. Neutrinos of this type are *Majorana neutrinos*, contrary to *Dirac neutrinos* of the Standard Model [Rod11]. Neutrinos undergo weak interactions via the exchange of massive gauge bosons $W^\pm$ and Z^0 through charged and neutral currents, respectively. Most importantly, however, neutrinos in the Standard Model are assumed to be massless particles, based on the observed maximum parity violation and the associated V-A theory of weak interactions. Figure 1.4 summarizes the role of neutrinos in the Standard Model of particle physics. In 2012, this model was finally completed by the discovery of a massive scalar gauge boson at the LHC by the ATLAS [ATL12] and CMS [CMS12] collaborations, representing an important milestone in the field of particle physics. This spin-0 particle with a mass of $125.9(4)\,\mathrm{GeV}$ [Ber13] is consistent with fundamental properties of the Higgs boson. Based on the principle of spontaneous symmetry breaking, the Higgs mechanism [Hig64] allows to generate non-zero masses for the gauge bosons $W^\pm$ and Z^0 of the weak interaction and leaving the gauge boson γ of the electromagnetic interaction massless. The fermions then obtain their masses through Yukawa-type couplings with the Higgs boson.

1.2.4 The Solar Neutrino Problem

In 1970, the famous Homestake experiment [DHH68], proposed by Davis already in 1964 [Dav64], started its operation to quantitatively confirm the theoretical calculations of the solar neutrino flux worked out by Bahcall et al. in the standard solar model [Bah64a] [Bah64b]. The experiment was located in the Homestake Mine in South Dakota using a tank filled with 615 tons of liquid tetrachloroethylene C_2Cl_4 as target. Solar neutrinos were detected by the transformation of chlorine into argon via the inverse β-decay:

$$\nu_e + {}^{37}\mathrm{Cl} \xrightleftharpoons[\text{capture}]{\text{decay}} {}^{37}\mathrm{Ar} + e^- \ . \tag{1.18}$$
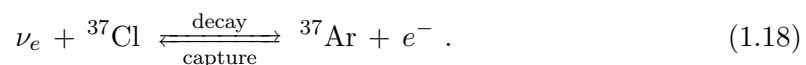
The resulting radioactive isotope of argon has a half-life of about 35 days and was extracted after a solar neutrino exposure of few weeks by bubbling helium gas through the tank. The radiochemical processing then included a cold trap to encapsulate the few ${}^{37}\mathrm{Ar}$ atoms in a counter. Thus, it decayed back to an exited state of chlorine mainly by K-electron capture. The resulting Auger electrons emitted during the deexcitation have a total energy of $2.8\,\mathrm{keV}$ and were detected in a gasfilled proportional counter:

$$e^- + {}^{37}\mathrm{Ar} \rightarrow {}^{37}\mathrm{Cl}^* + \nu_e \qquad {}^{37}\mathrm{Cl}^* \rightarrow {}^{37}\mathrm{Cl} + e^- \ . \tag{1.19}$$
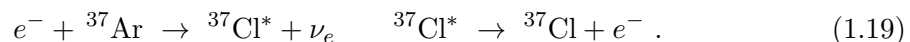
With this stepwise, rather slow radiochemical method, no real-time information about neutrino interactions was available, such as the time of reaction and the neutrino energy. The energy threshold of only $814\,\mathrm{keV}$ allowed to detect ${}^7\mathrm{Be}$ and ${}^8\mathrm{B}$ neutrinos (see figure 1.1). Initial results were presented already in the early 1970s, yielding only 1/4 to 1/3 of the expected solar neutrino flux calculated in the standard solar model [BD76] [DEC79]. The solar neutrino induced production rate of ${}^{37}\mathrm{Ar}$ in the Homestake chlorine detector was measured to ~ 0.48 events per day, averaged over 108 extractions performed from 1970 to 1994 [Dav94] [Cle98]. The deficit of the observed number of electron neutrinos to the

expected one was determined to $\sim 1/3$, establishing the famous *solar neutrino problem*. Initially, it was attempted to trace back this issue to uncertainties in the standard solar model, in nuclear cross sections, or even in the experiment. However, numerous successor experiments based on the transformation of gallium (^{71}Ga) into germanium (^{71}Ge), such as GALLEX [GAL99], SAGE [AVV02], and GNO [GNO05], have confirmed the deficit of solar neutrinos.

The real-time neutrino detectors based on the observation of Cherenkov light from neutrino-electron scattering, such as Kamiokande [Fuk96], Super-Kamiokande [Fuk98a], and SNO [Ahm01], allowed to examine the solar neutrino problem in more detail. Neutrinos interact with matter via elastic-scattering (ES), charged-current (CC), and neutral-current (NC) reactions through the exchange of the weak interaction gauge bosons $W^{\pm}$ and Z^0. These processes give rise to electrically charged particles in the target medium with rather high energies of up to several MeV. This allows to observe characteristic Cerenkov light cones in the target medium, e.g. water, from which the energy, the arrival time, the point of interaction in the target material, and the direction of the incident neutrino can be reconstructed. Cerenkov light cones are detected by the surrounding photomultiplier tubes, enabling a full real-time detection for neutrinos. Compared to radiochemical experiments, Cerenkov-radiation based detectors have the disadvantage of an inherent high-energy threshold of several MeV.

The Super-Kamiokande detector being the largest real-time solar neutrino detector is located in the Kamioka mine in Japan and uses $50000\,\text{t}$ of high-purity water as target material, surrounded by an array of more than 13000 photomultiplier tubes detecting potentially produced Cherenkov light. Solar neutrinos are measured through the ES reaction with atomic shell electrons in the water:

$$\nu_i + e^- \;\rightarrow\; \nu_i + e^- \quad (i = e, \mu, \tau) \qquad \text{(ES)} \tag{1.20}$$

This detection reaction allows to observe all neutrino flavors, in principle, although CC reactions dominate the rate. While confirming the solar neutrino deficit, Super-Kamiokande made its most important discovery in 1998 by observing a discrepancy of the measured number of atmospheric neutrinos (ν_μ) to the expectation as a function of the propagation length through the earth. A smaller number of atmospheric neutrinos was detected going upward, i.e. when the earth is located between the point of origin and the point of detection. Down going atmospheric neutrinos were agreeing with expectations, however. This up-down asymmetry extends the solar neutrino problem by the *atmospheric neutrino anomaly* [Fuk98b].

The SNO detector was located in a nickel mine in Sudbury in Canada and used $1000\,\text{t}$ of heavy water (D$_2$O) as target material surrounded by an array of 9600 photomultiplier tubes. In addition to the ES reaction according to interaction (1.20), incident solar neutrinos did interact via CC and NC reactions with the deuterium nuclei:

$$\begin{aligned} \nu_e + \text{D} \;&\rightarrow\; p + p + e^- && \text{(CC)} \\ \nu_i + \text{D} \;&\rightarrow\; p + n + \nu_i \quad (i = e, \mu, \tau) && \text{(NC)} \end{aligned} \tag{1.21}$$

Due to the limited energy of solar neutrinos, CC reactions are energetically possible only for electron neutrinos, thus the CC-based rate gives the true flux of electron neutrinos. The thermalized neutron arising as signature from the NC reaction has to be captured by a suitable nucleus, thereby releasing photons with known energies which then are detected by the photomultiplier tubes. While the CC reaction gives the rate of electron neutrinos, it is the NC reaction which gives access to the rate of all neutrino flavors. In 2001, SNO discovered that the observed total rate of all neutrino flavors as measured by the NC reaction is consistent with the expected rate of solar neutrinos gained from the standard
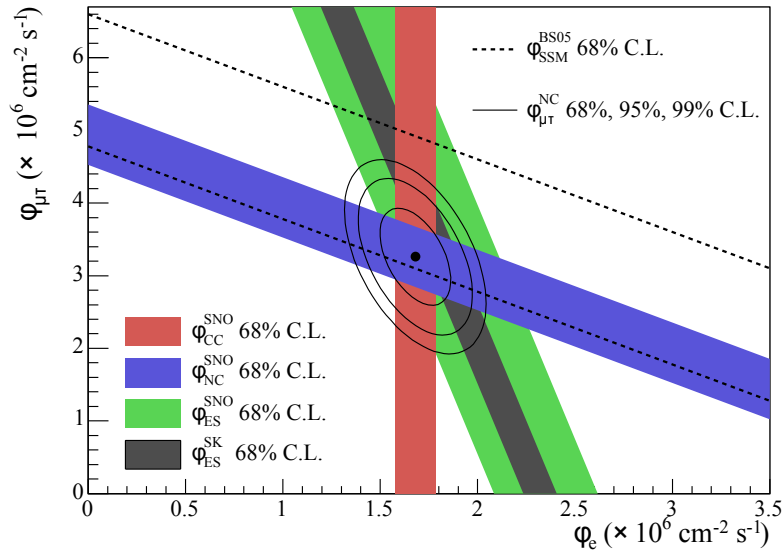
Figure 1.5: Fluxes of ^{8}B solar neutrinos in the SNO experiment. The measured flux $\Phi_{\mu\tau}$ of ν_μ and ν_τ is shown as a function of the measured flux Φ_e of ν_e, gained from the ES, CC, and NC reactions of the SNO detector and from ES reactions of the Super-Kamiokande detector. In addition, the prediction from the standard solar model [Bah05] is illustrated. Figure adapted from [Aha05] [Ber13].

solar model. Apart from that, only a fraction of $\sim 1/3$ of the theoretical solar flux is detected as electron neutrinos [Ahm02]. This remarkable result is illustrated in figure 1.5. Since the sun is a source for electron neutrinos only, SNO unambiguously proved the existence of transformations of neutrino flavors during propagation from the sun to the earth. These transformations are explained by the phenomenon of neutrino oscillations which is discussed in the subsequent section. The solar neutrino problem was solved [Zub11].

Finally, to illustrate the significant progress in neutrino physics with a more recent observation in a state-of-the-art neutrino experiment, one has to mention the detection of transformations of muon neutrinos into electron neutrinos at long baseline in the accelerator neutrino experiment T2K in 2013 [Abe13].

1.3 Phenomenon of Neutrino Oscillations

The theoretical formalism of neutrino oscillations was introduced by Pontecorvo as early as 1957 [Pon57a] [Pon57b] and further developed by Maki, Nakagawa and Sakata in 1962 [MNS62] as well as by Pontecorvo again in 1967 [Pon67]. The following discussion is based on simplified assumptions, resulting however in correct oscillation probabilities [Zub11] [Ber12b].

1.3.1 Neutrino Mixing

Neutrinos being massive particles can mix with each other, i.e. the three weak flavor eigenstates $|\nu_\alpha\rangle$ ($\alpha = e, \nu, \tau$), having well-defined weak interactions, are quantum superpositions of three light, stationary mass eigenstates $|\nu_i\rangle$ ($i = 1, 2, 3$) with well-defined masses m_1, m_2 and m_3. The states are connected via a unitary mixing matrix U ($U_{i\alpha}^\dagger = U_{\alpha i}^*$) through

$$|\nu_\alpha\rangle = \sum_i U_{\alpha i}|\nu_i\rangle \qquad \text{and} \qquad |\nu_i\rangle = \sum_\alpha U_{\alpha i}^*|\nu_\alpha\rangle \ . \tag{1.22}$$

The 3×3 matrix U is called the Pontecorvo-Maki-Nakagawa-Sakata (PMNS) matrix. A convenient parametrization is given in the following form:

$$U = \begin{pmatrix} c_{12}c_{13} & s_{12}c_{13} & s_{13}e^{-i\delta} \\ -s_{12}c_{23} - c_{12}s_{23}s_{13}e^{i\delta} & c_{12}c_{23} - s_{12}s_{23}s_{13}e^{i\delta} & s_{23}c_{13} \\ s_{12}s_{23} - c_{12}c_{23}s_{13}e^{i\delta} & -c_{12}s_{23} - s_{12}c_{23}s_{13}e^{i\delta} & c_{23}c_{13} \end{pmatrix} \cdot \begin{pmatrix} 1 & 0 & 0 \\ 0 & e^{i\alpha_{21}/2} & 0 \\ 0 & 0 & e^{i\alpha_{31}/2} \end{pmatrix}$$

$$(1.23)$$

with $c_{ij} = \cos\theta_{ij}$, $s_{ij} = \sin\theta_{ij}$, three weak mixing angles $\theta_{ij} = [0, \pi/2]$, a Dirac CP violation phase $\delta = [0, 2\pi]$, and two Majorana CP violation phases α_{21} and α_{31}. The mixing angles describe the contribution of the mass eigenstates to a certain flavor eigenstate, and vice versa. Depending on whether massive neutrinos are Dirac or Majorana fermions, one or three non-trivial phases can induce CP violation. This gives 7 or 9 fundamental parameters characterizing three-neutrino mixing: θ_{12}, θ_{23}, θ_{13}, m_1, m_2, m_3, δ, and possibly α_{21}, α_{31}. The latter two parameters, however, cannot be accessed by oscillation studies. Disregarding the phases, the described transformation between neutrino flavor and mass eigenstates can be understood as rotation defined by three rotation angles [Zub11] [Ber12b].

In the general case of n neutrino flavors and n massive neutrinos, the unitary neutrino mixing matrix U has to be extended to an $n \times n$ form which can be parametrized by $n(n-1)/2$ weak mixing angles, $(n-1)(n-2)/2$ Dirac CP violation phases, and $(n-1)$ additional Majorana CP violation phases $\alpha_{21}, \ldots, \alpha_{n1}$ [Ber12b].

1.3.2 Neutrino Oscillations

The stationary mass eigenstates $|\nu_i\rangle$ satisfying $H|\nu_i\rangle = E_i|\nu_i\rangle$ are physical eigenstates of the free Hamiltonian H with energy eigenvalues E_i. Their temporal propagation along a one-dimensional coordinate can be described by plane waves $|\nu_i(x,t)\rangle$ as solutions of the time-dependent Schrödinger equation $i\hbar\frac{\partial}{\partial t}|\nu_i(x,t)\rangle = H|\nu_i(x,t)\rangle$:

$$|\nu_i(x,t)\rangle = e^{-\frac{i}{\hbar}(E_i t - p_i x)}|\nu_i\rangle . \tag{1.24}$$

Neutrinos are produced and detected as flavor states. Therefore, neutrinos of a pure flavor state $|\nu_\alpha\rangle$ develop with time into a superposition of flavor states $|\nu_\beta\rangle$ ($\beta = e, \mu, \tau$):

$$|\nu(x,t)\rangle \overset{(1.22)}{=} \sum_i U_{\alpha i}|\nu_i(x,t)\rangle \overset{(1.24)}{=} \sum_i U_{\alpha i}e^{-\frac{i}{\hbar}(E_i t - p_i x)}|\nu_i\rangle \overset{(1.22)}{=} \sum_{i,\beta} U_{\alpha i}U_{\beta i}^* e^{-\frac{i}{\hbar}(E_i t - p_i x)}|\nu_\beta\rangle .$$

$$(1.25)$$

The spatial- and time-dependent transition amplitude for a flavor conversion $\nu_\alpha \rightarrow \nu_\beta$ is then given by

$$A(\nu_\alpha \rightarrow \nu_\beta)(x,t) = \langle\nu_\beta|\nu(x,t)\rangle \overset{(1.25)}{=} \sum_i U_{\beta i}^* U_{\alpha i}e^{-\frac{i}{\hbar}(E_i t - p_i x)} , \tag{1.26}$$

which finally results into the transition probability

$$P(\nu_\alpha \rightarrow \nu_\beta)(x,t) = |A(\nu_\alpha \rightarrow \nu_\beta)(x,t)|^2 \overset{(1.26)}{=} \sum_{i,j} U_{\alpha i}U_{\alpha j}^* U_{\beta i}^* U_{\beta j}e^{-\frac{i}{\hbar}(E_i t - p_i x)}e^{\frac{i}{\hbar}(E_j t - p_j x)} , \tag{1.27}$$

making the appearance of ν_β spatial- and time-dependent as well [Zub11] [Ber12b].

For ultra-relativistic neutrinos with the total energy $E \approx p_i c \gg m_i c^2$ traveling with the speed $v \approx c$, the energy eigenvalues E_i and the flight distance L between source and detector can be approximated as

$$E_i = \sqrt{p_i^2 c^2 + m_i^2 c^4} \approx p_i c + \frac{m_i^2 c^4}{2p_i c} \approx p_i c + \frac{m_i^2 c^4}{2E} \quad \text{and} \quad x = L = vt \approx ct , \tag{1.28}$$

respectively, which yields

$$E_i t - p_i x \overset{(1.28)}{=} \frac{m_i^2 c^3}{2} \frac{L}{E} \ . \tag{1.29}$$

Finally, the transition probability in (1.27) can be rewritten to

$$P(\nu_\alpha \to \nu_\beta)(x,t) \overset{(1.29)}{=} \sum_{i,j} U_{\alpha i} U_{\alpha j}^* U_{\beta i}^* U_{\beta j} e^{-\frac{i}{\hbar} \frac{\Delta m_{ij}^2 c^3}{2} \frac{L}{E}}$$

$$= \sum_i |U_{\alpha i} U_{\beta i}^*|^2 + 2\text{Re} \sum_{j>i} U_{\alpha i} U_{\alpha j}^* U_{\beta i}^* U_{\beta j} e^{-\frac{i}{\hbar} \frac{\Delta m_{ij}^2 c^3}{2} \frac{L}{E}} = P(\nu_\alpha \to \nu_\beta)(L,E) \tag{1.30}$$

with the difference of squared masses $\Delta m_{ij}^2 = m_i^2 - m_j^2$. This formula demonstrates the quantum mechanical nature of neutrino oscillations as interference phenomenon. The first term describes the average transition probability containing the neutrino-mixing matrix elements of the PMNS matrix (1.23) while the second one characterizes the spatial- or time-dependent neutrino oscillations depending on Δm_{ij}^2 and L/E among others. This causes an oscillatory behavior of the transition probability for stationary mixing among the neutrino flavors, implying non-diagonal terms in U, and of different neutrino masses, implying $\Delta m_{ij}^2 \neq 0$. Therefore, neutrino masses should not be exactly degenerated. Neutrino oscillations are sensitive only to Δm_{ij}^2 but not to the absolute mass scale. The transition probabilities do not depend on the Majorana CP violation phases. Consequently, the latter parameters are unobservable in neutrino oscillations and do not affect them [BHP80] [Lan87]. However, the Dirac phase can cause measurable CP violating effects leading to different transition probabilities for neutrinos and antineutrinos so that $P(\nu_\alpha \to \nu_\beta) \neq P(\overline{\nu}_\alpha \to \overline{\nu}_\beta)$ [Zub11] [Ber12b].

Analogously, the probability of finding the original flavor is given by

$$P(\nu_\alpha \to \nu_\alpha) = 1 - \sum_{\alpha \neq \beta} P(\nu_\alpha \to \nu_\beta) \ , \tag{1.31}$$

describing the disappearance of ν_α [Zub11].

1.3.3 Two-Neutrino Oscillations

In the generic case of two neutrino flavors ν_α, ν_β and two massive neutrinos ν_1, ν_2, the unitary mixing matrix reduces to a simple 2×2 form which can be parametrized by one mixing angle θ only. In this case, there is no CP violation phase affecting neutrino oscillations and the unitary transformation is given by

$$\begin{pmatrix} \nu_\alpha \\ \nu_\beta \end{pmatrix} = \begin{pmatrix} \cos\theta & \sin\theta \\ -\sin\theta & \cos\theta \end{pmatrix} \cdot \begin{pmatrix} \nu_1 \\ \nu_2 \end{pmatrix} \ , \tag{1.32}$$

resulting in the two-flavor transition probability

$$P(\nu_\alpha \to \nu_\beta) = P(\nu_\beta \to \nu_\alpha) = P(\overline{\nu}_\alpha \to \overline{\nu}_\beta) = P(\overline{\nu}_\beta \to \overline{\nu}_\alpha)$$

$$= \sin^2(2\theta) \cdot \sin^2\left(\frac{\Delta m^2 c^3}{4\hbar} \frac{L}{E}\right) = 1 - P(\nu_\alpha \to \nu_\alpha) \tag{1.33}$$

with the difference of squared masses $\Delta m^2 = m_1^2 - m_2^2$. This formula explicitly shows that neutrino oscillations occur only if both θ and Δm^2 are non-vanishing. In (1.33), the first term defines the oscillation amplitude and the second one the oscillation frequency. The latter depends on the given baseline length L between source and detector, and the known total neutrino energy E [Zub11].

Table 1.1: Sensitivity of different oscillation experiments. The table shows the minimal value $\min(\Delta m^2)$ of a generic difference of squared masses $\Delta m^2 > 0$ to which a given experiment is most sensitive, in dependence of neutrino source, neutrino type, average neutrino energy $\overline{E}$, and source-detector distance L. The value $\min(\Delta m^2) \approx \overline{E}/L$ can be understood as figure of merit of the experiment. Table inspired by [GGN03] [Ber12b].

neutrino source	neutrino type	$\overline{E}$ (MeV)	L (km)	$\min(\Delta m^2)$ (eV^2)
reactor	$\overline{\nu}_e$	1	$0.1 - 1$	$10^{-2} - 10^{-3}$
long-baseline reactor	$\overline{\nu}_e$	1	100	10^{-5}
accelerator	$\nu_{e,\mu}, \overline{\nu}_{e,\mu}$	$10^3 - 10^4$	$0.1 - 1$	$\gtrsim 1$
long-baseline accelerator	$\nu_{e,\mu}, \overline{\nu}_{e,\mu}$	$10^3 - 10^4$	$100 - 1000$	$10^{-1} - 10^{-3}$
earth's atmosphere	$\nu_{e,\mu}, \overline{\nu}_{e,\mu}$	$10^3 - 10^5$	$10 - 10^4$	$10^{-1} - 10^{-4}$
sun	ν_e	1	$1.5 \cdot 10^8$	10^{-11}

The characteristic oscillation length

$$L_0 = \frac{4\pi\hbar}{c^3} \frac{E}{\Delta m^2} \tag{1.34}$$

describes the period of one full oscillation cycle. It becomes larger for higher E and smaller Δm^2 [Zub11].

The general formalism in the more realistic scenario with three neutrino flavors and masses can be quite complex. In this case, a set of three differences of squared masses is involved both in magnitude and sign. The sign enters due to both matter effects, modifying the flavor transformation by the MSW effect [Wol78] [MS86], and possible CP violation, which thus can, in principle, be measured. Furthermore, a specific neutrino mass spectrum has to be assumed, expanding the corresponding discussion even more [Zub11].

1.3.4 Experimental Considerations

As described above, the neutrino oscillation probabilities depend on the source-detector distance L, the neutrino energy E, the elements $U_{\alpha i}$ of the PMNS matrix U describing the neutrino mixing angles θ_{ij} among others, and the differences of squared masses Δm_{ij}^2. Thus, a given experiment when searching for neutrino oscillations and investigating the oscillation parameters θ_{ij} and Δm_{ij}^2 can be characterized by its baseline length L between source and detector and by the energy E of the neutrinos being studied. In general, three cases can be considered with respect to a possible observation of neutrino oscillations:

- $L/E \ll 1/\Delta m^2$, i.e. $L \ll L_0$: The detector is placed too close to the source and/or the neutrino energy is too high. The oscillations thus have no time to develop, prohibiting observation of an oscillation signal.

- $L/E \approx 1/\Delta m^2$, i.e. $L \approx L_0$: This is the most sensitive range of the experiment with maximal sensitivity to observe the sinusoidal oscillation pattern.

- $L/E \gg 1/\Delta m^2$, i.e. $L \gg L_0$: The detector is placed too far away from the source and/or the neutrino energy is too low. A large number of oscillations has occurred so that only an averaged transition probability can be measured due to a finite detector resolution and/or source size.

The experimental sensitivity is influenced by a distribution of baseline lengths, e.g. due to an extended source, or by broad neutrino energy, e.g. in a wide neutrino beam. Furthermore, when using natural neutrino sources, the sensitivity is constrained by the given ratio L/E [Zub11] [Ber12b].

Table 1.2: Experimental results of the neutrino oscillation parameters. The following values are obtained through data analyses based on the three-neutrino mixing scheme [Ber12b] [Ber13].

parameter	result	experiment	neutrino source
$\sin^2(2\theta_{12})$	$0.857^{+0.023}_{-0.025}$	KamLAND + solar data [Gan11]	reactor, sun
Δm^2_{21}	$(7.50^{+0.19}_{-0.20}) \cdot 10^{-5}\,\mathrm{eV}^2$	KamLAND + solar data [Gan11]	reactor, sun
$\sin^2(2\theta_{23})$	> 0.95	Super-Kamiokande [Abe11a]	atmosphere
$|\Delta m^2_{32}|$	$2.32^{+0.12}_{-0.08} \cdot 10^{-3}\,\mathrm{eV}^2$	MINOS [Ada11]	accelerator
$\sin^2(2\theta_{13})$	$0.109 \pm 0.030 \pm 0.025$	Double Chooz [Abe12]	reactor
	$0.113 \pm 0.013 \pm 0.019$	RENO [Ahn12]	reactor
	$0.089 \pm 0.010 \pm 0.005$	Daya Bay [An 13]	reactor
	0.095 ± 0.010	combined analysis [Ber13]	reactor

A variety of man-made and natural neutrino sources, covering a wide range of baseline lengths and neutrino energies, is being used to study neutrino oscillations. The most important ones are nuclear reactors and particle accelerators as well as astrophysical sources, such as the atmosphere and the sun [Zub11]. Table 1.1 gives an overview of the sensitivity of oscillation experiments using these sources.

The experimental search for neutrino oscillations can be grouped into two generic cases:

- An appearance experiment searches for new neutrino flavors not being present in the source. Here, the transition probability $P(\nu_\alpha \to \nu_\beta)$ is explicitly measured.

- A disappearance experiment measures a drop in the expected number of neutrinos emitted from the source. It explicitly measures the survival probability $P(\nu_\alpha \to \nu_\alpha)$. To do so, the source activity has to be known precisely, requiring typically a near and a far detector placed at two distances from the source.

In both cases, the flavor identification relies on the detection of the corresponding charged lepton l^- produced in their corresponding charged-current interactions

$$\nu_l + \mathrm{N} \to l^- + \mathrm{X} \tag{1.35}$$

with $l = e, \nu, \tau$, the target material N and the hadronic final state X [Zub11].

1.3.5 Experimental Results

In the past decades, numerous oscillation experiments using different neutrino sources and covering different baseline lengths and neutrino energies, were performed to measure the three mixing angles θ_{12}, θ_{23} and θ_{13} of the PMNS matrix, as well as the differences of squared masses Δm^2_{21} and Δm^2_{32} with high precision. Table 1.2 summarizes the relevant oscillation parameters including the measured best fit values, the associated experiments, and the neutrino sources in use. In the following, the results are discussed based on [Ber12b] [Ber13] [KL13].

From data of the three ongoing reactor disappearance experiments ($\overline{\nu}_e \to \overline{\nu}_e$) Double Chooz [Abe12], RENO [Ahn12], and Daya Bay [An 13], as well as of the accelerator appearance experiment ($\nu_\mu \to \nu_e$) T2K [Abe11b], the neutrino mixing angle $\theta_{13} \approx 9° \pm 0.5° \neq 0°$ has been measured. Hence, the element $|U_{e3}| = \sin\theta_{13} \approx 0.15$ of the PMNS matrix is still surprisingly large. The angles θ_{12} and θ_{23} are traditionally associated with solar and
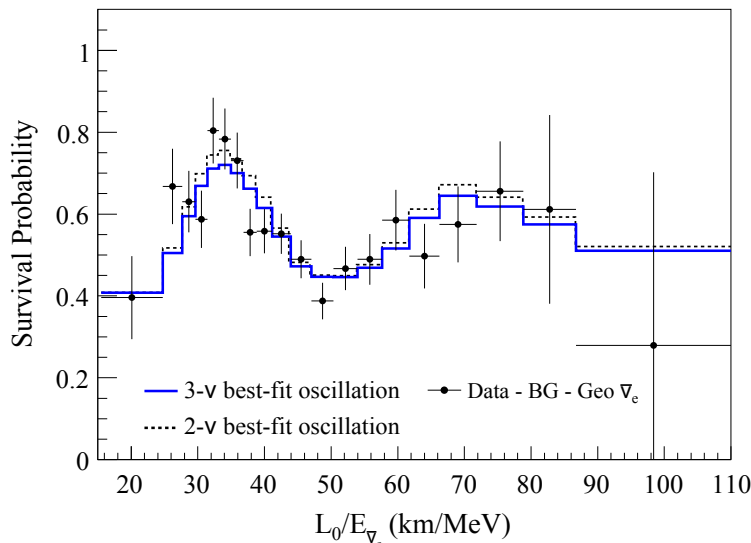
Figure 1.6: Reactor neutrino oscillations. The survival probability of reactor neutrinos as measured by the disappearance experiment ($\overline{\nu}_e \to \overline{\nu}_e$) KamLAND for large values of the ratio L/E is in very good agreement with the theoretical expectation for flavor oscillations (blue line for 3ν oscillation and black dotted line for 2ν oscillation). The data (black dots) are corrected for accidental background events and geoneutrinos. The KamLAND detector at the time of data-taking was surrounded by 53 working Japanese commercial nuclear reactors with various source-detector distances L. Figure adapted from [Ber12b].

atmospheric neutrino oscillations, respectively. Thus, they are often called *solar* and *atmospheric* neutrino mixing angles. Likewise, the same applies to the differences of squared masses Δm_{21}^2 and Δm_{32}^2. Solar neutrino data based on the Cherenkov detection technique from Kamiokande [Fuk96], Super-Kamiokande [Fuk01] and SNO [Aha07] [Aha08], as well as complementary results by the reactor disappearance experiment ($\overline{\nu}_e \to \overline{\nu}_e$) KamLAND [Abe08] (see figure 1.6) show that the *solar* oscillation parameters feature a small mass splitting $\Delta m_{21}^2 \approx 7.5 \cdot 10^{-5}\,\text{eV}^2$ and a large mixing angle $\theta_{12} \approx 34° \pm 1°$. Maximal solar neutrino mixing is ruled out by the data. Atmospheric neutrino data, taken mainly by Super-Kamiokande [Abe11a], as well as results by the accelerator disappearance experiments ($\nu_\mu \to \nu_\mu$) K2K [Ahn06] and MINOS [Ada13] show that the *atmospheric* oscillation parameters feature a large value of mass splitting with $|\Delta m_{32}^2| \approx 2.3 \cdot 10^{-3}\,\text{eV}^2$ and potentially maximum mixing with $\theta_{23} \approx 40° \pm 3°$. However, the data do not allow to determine the sign of Δm_{32}^2. The effects of the atmospheric oscillation scale to solar ν_e and short-baseline reactor $\overline{\nu}_e$ studies, and of the solar oscillation parameters to atmospheric and accelerator $\overset{(-)}{\nu}_\mu$ disappearance are relatively small. They only represent a subdominant modification of the generic two-neutrino case. The solar and atmospheric differences of squared masses differ by approximately a factor of $|\Delta m_{32}^2|/\Delta m_{21}^2 \approx 30$, thereby effectively decoupling both oscillation scales.

However, the undetermined sign of Δm_{32}^2 leaves open the issue of the hierarchy of neutrino masses. In addition, the value of the lightest neutrino mass state is unknown. When using the convention $\Delta m_{21}^2 > 0$, and consider the existing data implying $\Delta m_{21}^2 \ll |\Delta m_{32}^2|$, the neutrino masses can be grouped into the following generic cases:

- Normal hierarchical case: $m_1 \ll m_2 < m_3$
  with $m_2 \cong \sqrt{\Delta m_{21}^2} \cong 0.0086\,\text{eV}$ and $m_3 \cong \sqrt{|\Delta m_{32}^2|} \cong 0.048\,\text{eV}$.

- Inverted hierarchical case: $m_3 \ll m_1 < m_2$
  with $m_{1,2} \cong \sqrt{|\Delta m_{32}^2|} \cong 0.048\,\text{eV}$.

- Quasi-degenerated case: $m_1 \cong m_2 \cong m_3 \cong m_0$
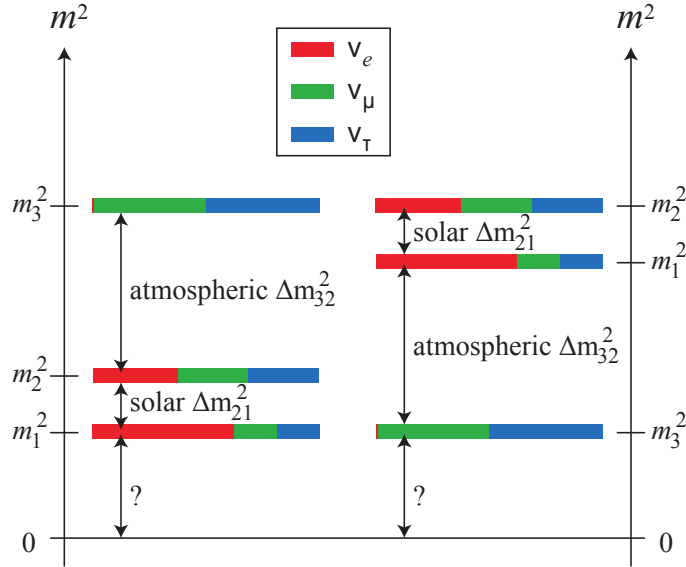
Figure 1.7: Neutrino mass hierarchy. The normal (left) and inverted (right) neutrino mass hierarchy are shown. The solar and atmospheric differences of squared masses are measured with high precision to $\Delta m_{21}^2 \approx 7.5 \cdot 10^{-5}\,\text{eV}^2$ and $|\Delta m_{32}^2| \approx 2.3 \cdot 10^{-3}\,\text{eV}^2$. Neutrino mixing is indicated through different colors with red for electron flavor, green for muon flavor and blue for tau flavor. Figure adapted from [KL13].

with $m_i^2 \gg |\Delta m_{32}^2|$ and $m_0 \gtrsim 0.10\,\text{eV}$.

These cases show that at least a lower limit for the heaviest mass state can be determined for each scenario although neutrino oscillations are not sensitive to the absolute neutrino mass scale [Ber12b] [Ber13] [KL13]. The first two generic cases are illustrated in figure 1.7.

At present, experimental information on the Dirac CP violation phase in the PMNS matrix is limited with 1σ sensitivities for specific parameter cases reached. No information on the Majorana CP violation phases and thus on the nature of the neutrino is available [Ber12b]. When fully exploiting the modifications to flavor transformations of neutrinos and antineutrinos in matter due to the MSW effect [Wol78] [MS86] and comparing the oscillation probabilities for neutrinos and antineutrinos, the neutrino mass ordering and the Dirac CP violation phase can be resolved by oscillation experiments at long baselines of $L \approx 1000\,\text{km}$ [Alb04] [Bar00]. These topics are the primary objectives of the upcoming long-baseline accelerator appearance experiment ($\nu_\mu \to \nu_e$ and $\overline{\nu}_\mu \to \overline{\nu}_e$) NO$\nu$A [Ayr05] [Fel07]. It will make use of certain neutrinos and antineutrinos produced at Fermilab's NuMI beam line by comparing results of two detectors: the near detector being located at Fermilab and the far detector being installed at a distance of $810\,\text{km}$ to the source. Due to operation in neutrino and antineutrino detection mode, a sensitivity to the Dirac CP violation phase is obtained. The NOνA experiment has already observed the first long-distance neutrinos at the time of writing this thesis [Fer14].

1.4 Measurement of the Neutrino Mass

The discovery of neutrino oscillations has unambiguously proven that neutrinos are massive particles. However, due to their inherent nature, neutrino-oscillation experiments are not sensitive to the absolute neutrino-mass scale. Experimental access to the neutrino mass is given by different laboratory approaches, and to a certain degree, by cosmological observations. At present, these studies provide an upper mass limit and imply that the heaviest neutrino mass resides in the sub-eV range. In this context, kinematic methods

are of special interest, since they only rely on the relativistic energy-momentum relation $E^2 = p^2 c^2 + m_0^2 c^4$ with the total energy E, the momentum p, and the rest mass m_0 of the associated particle. This already indicates that it is the squared mass m_0^2 which is the experimental observable in kinematic studies. Model-dependent methods rely on theoretical or modeling assumptions, thereby introducing uncertainties for the neutrino mass. In the following, both kinematic and model-dependent approaches are illustrated.

1.4.1 Cosmology

As briefly discussed in section 1.1.1, relic neutrinos are messengers from the epoch of weak interaction freeze-out and constitute the by far most abundant fermionic matter particles in the universe. In the framework of the cosmological ΛCDM model, only the sum of neutrino masses is of relevance. The contribution Ω_ν of the energy density of neutrinos to the total energy density Ω_{tot} of the universe is given by the sum of the neutrino-mass eigenstates m_i and the Hubble constant H_0 (or the corresponding dimensionless Hubble parameter h) [Ber13]:

$$\sum_i m_i = 93\,\Omega_\nu h^2\,\text{eV} \qquad \text{with} \qquad h = H_0/(100\,\text{km}\,\text{s}^{-1}\,\text{Mpc}^{-1})\ . \tag{1.36}$$

The Hubble constant was determined by several methods of measurement. For instance, the Hubble Space Telescope provides a value of $H_0 = (73.8 \pm 2.4)\,\text{km}\,\text{s}^{-1}\,\text{Mpc}^{-1}$ [Rie11a], whereas recent investigations with Planck result in a much lower value of $H_0 = (67.3 \pm 1.2)\,\text{km}\,\text{s}^{-1}\,\text{Mpc}^{-1}$ [Pla13]. This specific tension for H_0 and from other traditional cosmic distance-ladder methods is currently under investigation [Ber13]. Assuming a neutrino-dominated universe with $\Omega_\nu = \Omega_{\text{tot}}$, the observation of a flat universe with $\Omega_{\text{tot}} = 1$ yields an upper limit for the sum of the neutrino masses of about

$$\sum_i m_i \lesssim 51\,\text{eV}\ , \tag{1.37}$$

with the use of equation (1.36). In addition, figure 1.8 illustrates the contribution of the neutrino energy density to the total energy density of the universe as a function of the neutrino mass.

More realistic mass bounds are provided by detailed cosmological studies based on present values for the contributions of matter (Ω_{m}) and dark energy (Ω_Λ) to the total energy density. This allows to work out the influence of massive neutrinos to the formation of structures on different scales. In this context, the free-streaming length λ_{FS} of non-relativistic neutrinos is of major importance, as it characterizes the scale where neutrinos become non-relativistic [LP06]:

$$\lambda_{\text{FS}} = \frac{8(1+z)}{\sqrt{\Omega_{\text{m}}(1+z)^3 + \Omega_\Lambda}} \left(\frac{1\,\text{eV}}{m_\nu}\right) h^{-1}\,\text{Mpc}\ , \tag{1.38}$$

with z describing the redshift parameter. When free-streaming, neutrinos wash out density fluctuations and perturbations smaller than the free-streaming length λ_{FS} [Zub11], i.e. large scales are less affected by neutrino hot dark matter.

Experimental bounds and constraints on key observables of the cosmological ΛCDM model allow to derive information on the sum of neutrino masses. In 2013, the Planck collaboration published an upper limit of [Pla13]

$$\sum_i m_i \lesssim 0.23\,\text{eV} \quad (95\,\%\,\text{C.L.})\ , \tag{1.39}$$

$$\boxed{\Omega_v = \frac{\Sigma m_i}{h^2 \times 93\ eV}}$$

$\Omega_{tot} = 1.02 \pm 0.02$ (flat universe)

1 — Dark energy — Ω_Λ

Dark matter — Ω_{cdm}

$\Omega_v < 0.14$ (3v)

Tritium experiments
$\Sigma m_i < 6.6\ eV$ (3v)

0.1 —

Structure formation
$\Sigma m_i < 2.2\ eV$ (3v)

Baryons — Ω_b

KATRIN
$\Sigma m_i < 0.6\ eV$ (3v)

0.01 —

Stars & gas

Super-Kamiokande
$\Sigma m_i > 0.06\ eV$ (1v)

0.001 —

$\Omega_v > 0.001$ (1v)

Ω
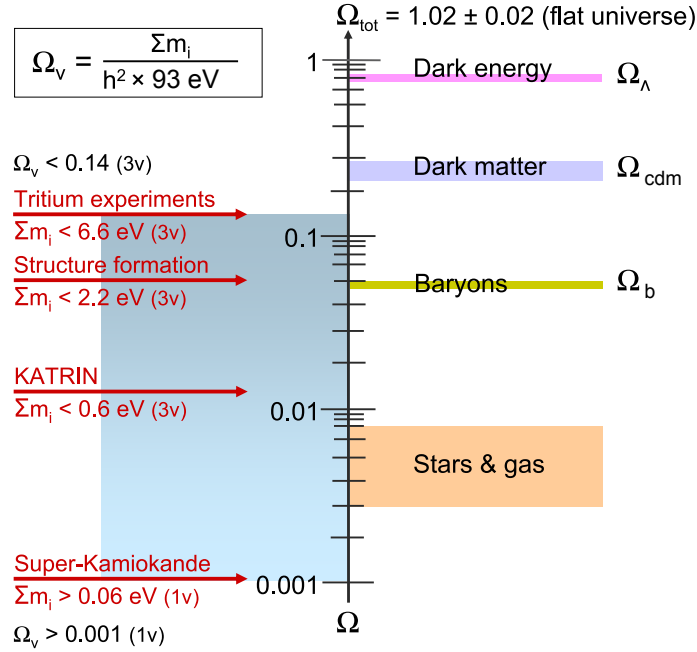
Figure 1.8: Neutrino contribution to the matter energy density. The contribution of the neutrino energy density Ω_ν to the total energy density Ω_{tot} of the universe is compared to the energy density of dark energy (Ω_Λ), cold dark matter (Ω_{cdm}), and baryonic matter (Ω_b). The blue-shaded region denotes the potential neutrino contribution, ranging over two orders of magnitude. The upper limit is provided by tritium-based neutrino-mass measurements performed at Mainz and Troitsk, and the lower limit by neutrino-oscillation experiments on the basis of atmospheric neutrino oscillation. The upper bound will be significantly lowered by the KATRIN experiment, thereby narrowing the contribution of the neutrino energy density to a smaller range. Figure adapted from [Ang05].

obtained from combining the first Planck measurements of the cosmic microwave-background temperature with the lensing-potential power spectrum [Pla13], as well as with polarization measurements from WMAP [Hin13] and surveys of baryon acoustic oscillation [Beu11]. No significant evidence for additional neutrino-like relativistic particles in the early radiation-dominated universe was found. However, these indirect cosmological constraints on the neutrino mass suffer heavily from model-dependent uncertainties and strongly rely on assumptions and priors for other key cosmological parameters. As a consequence, cosmology-based neutrino-mass results show a considerable scatter depending on the data sets selected for the actual analysis. The measurement of the absolute neutrino-mass scale in a direct model-independent way will thus reduce the number of free input parameters required for cosmological models, thereby minimizing the uncertainties for other cosmological observables with the potential to diminish existing discrepancies between different data sets.

1.4.2 Time-of-Flight of Supernova Neutrinos

As described in section 1.1.2, core-collapse supernovae are intense sources of MeV-scale neutrinos, allowing to determine the neutrino mass m_ν in a direct, yet model-dependent way by measuring the time-of-flight T of neutrinos. Neutrinos propagating from the supernova at distance L to the detector located on earth will obtain an energy-dependent time-of-flight [Zub11]

$$T = \frac{L}{v} = \frac{L}{c} \cdot \frac{E_\nu}{p_\nu c} = \frac{L}{c} \cdot \frac{E_\nu}{\sqrt{E_\nu^2 - m_\nu^2 c^4}} \approx \frac{L}{c} \cdot \left(1 + \frac{m_\nu^2 c^4}{2 E_\nu^2}\right), \qquad (1.40)$$

assuming $m_\nu c^2 \ll E_\nu$. In order to deduce information on the neutrino mass, the spread of the arrival time for neutrinos with different energies E_ν is measured. In the case of two neutrinos with energies E_1 and E_2, their temporal delay Δt observed at the detector will depend on the time difference Δt_0 between emission of both neutrinos from the supernova:

$$\Delta t = t_1 - t_2 = \Delta t_0 + \frac{L m_\nu^2}{2c} \cdot \left(\frac{1}{E_1^2} - \frac{1}{E_2^2} \right) \; . \tag{1.41}$$

The parameters Δt, E_1, and E_2 are measured by the supernova neutrino detector from the energy and time signals, while the distance L has to be inferred from astrophysical observations. However, the duration Δt_0 of the neutrino pulse is model-dependent and lead to considerable uncertainties hampering a reliable determination of the neutrino mass m_ν [Fis10].

In February 1987, SN1987A was identified as a type II supernova. The related neutrino burst was observed by the water-based Cherenkov detectors IMB [Bio87] and Kamiokande [Hir88]. Both experiments counted 19 neutrinos within 13 seconds, representing the first direct observation in neutrino astronomy. The neutrino-mass analysis yields an upper bound of [LL02]
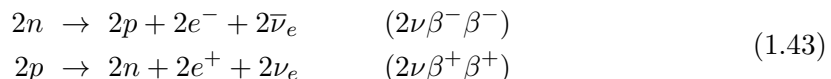
$$m_\nu < 5.7 \, \text{eV} \quad (95\,\% \; \text{C.L.}) \; . \tag{1.42}$$

Up to date, SN1987A has been both the first and the last supernova to provide a neutrino burst observable on earth.

1.4.3 Neutrinoless Double Beta-Decay

In cases where single β-decay is forbidden by energy conservation, a double β-decay process can occur as second-order process of the weak interaction. At present, a total of 35 naturally occurring isotopes with even-even nuclei has been identified, i.e. nuclei with even atomic number Z and even neutron number N. Due to the spin coupling described by the pairing term in the semi-empirical Bethe-Weizsäcker mass formula [vW35], even-even nuclei in general are more stable than the associated odd-odd nuclei with the same mass number A. Consequently, isotopes can undergo the double β-decay only from an even-even nucleus (A, Z) to $(A, Z \pm 2)$.

The Standard Model process of double β-decay with neutrino emission ($2\nu\beta\beta$) involves the simultaneous nuclear transformation of two nucleons as follows:

$$\begin{aligned} 2n &\rightarrow 2p + 2e^- + 2\overline{\nu}_e & (2\nu\beta^-\beta^-) \\ 2p &\rightarrow 2n + 2e^+ + 2\nu_e & (2\nu\beta^+\beta^+) \end{aligned} \tag{1.43}$$

Since the emitted neutrinos carry away a certain fraction of the released energy Q, the energy spectrum of the two emitted electrically charged leptons is continuous as illustrated in figure 1.9 (right). In this decay mode, the total lepton number L is conserved. Isotopes which undergo this decay typically have long half-lives of $\tau_{1/2} \sim 10^{20}$ y due to the second-order nature of the decay. In 1967, first indirect evidence was provided in a geochemical experiment through the $2\nu\beta^-\beta^-$-decay of ^{82}Se into ^{82}Kr occurring with a half-life of $\tau_{1/2} \approx 1.4 \times 10^{20}$ y [KM69]. Up to date, the $2\nu\beta^-\beta^-$-decay has been observed for 12 isotopes in geochemical and laboratory experiments [Ber13].

A far more interesting process is the neutrinoless double β-decay ($0\nu\beta\beta$) describing the simultaneous nuclear transformation of two nucleons without the emission of neutrinos:

$$\begin{aligned} 2n &\rightarrow 2p + 2e^- & (0\nu\beta^-\beta^-) \\ 2p &\rightarrow 2n + 2e^+ & (0\nu\beta^+\beta^+) \end{aligned} \tag{1.44}$$
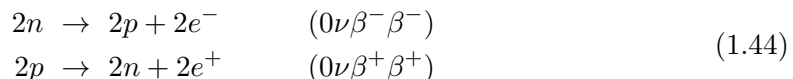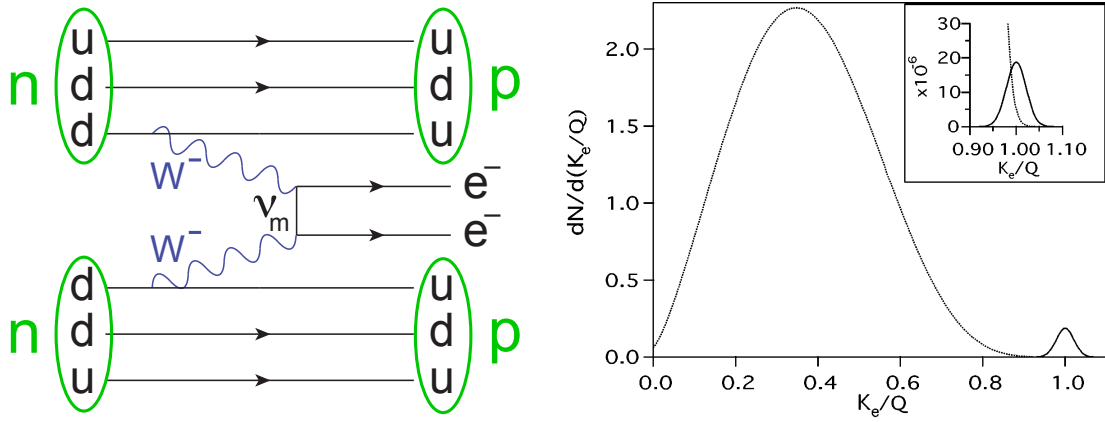
Figure 1.9: Double beta-decay. Left: Feynman diagram of the neutrinoless double beta-decay ($0\nu\beta^-\beta^-$). Two neutrons simultaneously are transformed into two protons via the exchange of a virtual neutrino ν_m of Majorana nature, thereby emitting two electrons. Figure adapted from [Sch13a]. **Right: Energy spectrum of the two emitted electrons from $2\nu\beta^-\beta^-$- and $0\nu\beta^-\beta^-$-decay.** K_e denotes the sum of the electron kinetic energies. The $2\nu\beta^-\beta^-$-spectrum is normalized to 1 and the $0\nu\beta^-\beta^-$-spectrum to 10^{-2} (10^{-6} in the inset), assuming a detector energy resolution of 5 %. Figure adapted from [EV02].

The discovery of the hypothetical $0\nu\beta\beta$-decay would imply direct detection of physics beyond the Standard Model of particle physics. In this decay, neutrinos propagate as virtual particles: one of the involved nucleons absorbs the neutrino by an inverse β-decay, after it was emitted from another nucleon of the nucleus in a single β-decay. This transition in particular requires neutrinos to be their own antiparticles ($\nu = \bar{\nu}$). The exchanged virtual neutrino called a *Majorana neutrino* [DKT85] being emitted and absorbed within the nucleus. This results in the emission of two electrically charged leptons. The Feynman diagram for the special case of the $0\nu\beta^-\beta^-$-decay is shown in figure 1.9 (left). The $0\nu\beta\beta$-decay violates conservation of the total lepton number L, since the initial and final state differ by $\Delta L = 2$. In addition, this process requires a flip of the neutrino helicity h, since a left-handed neutrino with $h = -1$ acts at one vertex and a right-handed antineutrino with $h = +1$ at the other vertex, a fact which strongly suppresses the probability for $0\nu\beta\beta$-decay compared to $2\nu\beta\beta$-decay. However, this helicity flip is only possible for massive neutrinos which have two helicity components [Sch95], or in the presence of right-handed gauge bosons $W_R^\pm$ at one decay vertex [BFP85].

The energy spectrum of the two emitted electrically charged leptons is discrete, manifesting as a single peak with small count rate at the endpoint energy E_0 or the Q-value, see figure 1.9 (right) . This peak represents the characteristic signature for the $0\nu\beta\beta$-decay. The observable is the half-life $\tau_{1/2}^{0\nu}$, given by [EV02]

$$(\tau_{1/2}^{0\nu})^{-1} = G^{0\nu}(E_0, Z) \cdot |M^{0\nu}|^2 \cdot m_{ee}^2 \tag{1.45}$$

with the effective Majorana neutrino mass

$$m_{ee} = \left| \sum_{i=1}^{3} U_{ei}^2 m_i \right| = \left| \sum_{i=1}^{3} |U_{ei}|^2 e^{\alpha_{i1}} m_i \right| \, , \tag{1.46}$$

where $G^{0\nu}(E_0, Z)$ is the phase-space integral. Due to the rather complicated nuclear structure of the nuclei in the initial, intermediate and final state, the nuclear transition matrix elements $M^{0\nu}$ still suffer from considerable theoretical uncertainties. Recent models differ by factors of up to 3 [Dev13], equivalent to an uncertainty of up to ~ 10 in the observable half-life [EV02]. Based on the virtual nature of the exchanged neutrino, $0\nu\beta\beta$-experiments

determine the effective Majorana neutrino mass m_{ee} which is given by the coherent sum of the neutrino-mass eigenstates m_i according to equation (1.46). Cancellations can thus occur due to the two Majorana CP phases α_{21} and α_{31}. By contrast, these phases do not influence the observables of neutrino-oscillation and direct neutrino-mass experiments.

The GERDA experiment [Ack13] searches for the $0\nu\beta^-\beta^-$-decay of ^{76}Ge with a Q-value of 2039 keV:

$$^{76}\text{Ge} \;\rightarrow\; {}^{76}\text{Se} + 2e^- \; . \tag{1.47}$$

The experiment is located at the Laboratori Nazionali del Gran Sasso (INFN, Italy) and uses 21.3 kg of high-purity enriched ^{76}Ge diodes which act both as source and as detector. In 2013, the collaboration published the results from the first measurement phase of 492.3 live days with a total exposure of 21.6 kg y [Ago13]. No signal was observed and the most stringent lower limit for the half-life of ^{76}Ge was derived to

$$\tau_{1/2}^{0\nu} > 2.1 \times 10^{25}\,\text{y} \quad (90\,\%\ \text{C.L.}) \; , \tag{1.48}$$

corresponding to an upper limit on the effective Majorana neutrino mass in the range of

$$m_{ee} < (0.2 - 0.4)\,\text{eV} \; . \tag{1.49}$$

With this result, the GERDA experiment starts to constrain the Heidelberg-Moscow experiment which claims observation of $0\nu\beta^-\beta^-$-events with $m_{ee} = (0.32 \pm 0.03)\,\text{eV}$ [KKK06]. This rather controversial claim has initiated the construction of several further experiments, such as CUORE [Arn04], KamLAND-Zen [Gan13], MAJORANA [Phi12], and SNO+ [Loz14].

1.4.4 Decays of the Pion and the Tau Lepton

A direct model-independent (yet at present outdated) way to measure the absolute neutrino-mass scale is given by the kinematic investigation of the π- and τ-decays, using the relativistic energy-momentum relation.

The π^+-decay ($\pi^+ \;\rightarrow\; \mu^+ + \nu_\mu$) is a two-body decay and allows to determine the effective mass m_{ν_μ} of the muon neutrino by measuring the masses of the pion (m_π) and the muon (m_μ) as well as the momentum of the muon ($\vec{p}_\mu$), assuming the pions decay at rest:

$$m_{\nu_\mu}^2 = m_\pi^2 + m_\mu^2 - 2m_\pi\sqrt{m_\mu^2 + |\vec{p}_\mu|^2} \qquad \text{with} \qquad m_{\nu_\mu}^2 = \sum_{i=1}^{3} |U_{\mu i}|^2 m_i^2 \; . \tag{1.50}$$

The pion mass is obtained from pionic X-ray spectroscopy [JGL94] and the muon mass from measurements of the transition frequencies in muonium [Ber13]. Up to date, the most sensitive value for the muon momentum is being provided by PSI, where a surface muon beam was analyzed in a magnetic spectrometer equipped with a silicon micro-strip detector [Ass96]. The values of the kinematic quantities are well-known on a ppm-scale, leading to the most stringent upper limit for the effective muon neutrino mass of [Ass96]

$$m_{\nu_\mu} < 0.17\,\text{MeV} \quad (90\,\%\ \text{C.L.}) \; . \tag{1.51}$$

Correspondingly, the analysis of τ^--decays

$$\tau^- \;\rightarrow\; \nu_\tau + 2\pi^- + \pi^+ \qquad \text{and} \qquad \tau^- \;\rightarrow\; \nu_\tau + 3\pi^- + 2\pi^+ \; (+\, \pi^0) \tag{1.52}$$

in flight allows to determine the effective mass m_{ν_τ} of the tau neutrino by measuring the visible energy of the decay products. The missing energy is assigned to the energy of the tau neutrino. The ALEPH experiment provides the most stringent upper limit of [Bar98]

$$m_{\nu_\tau} < 18.2\,\text{MeV} \quad (95\,\%\ \text{C.L.}) \; . \tag{1.53}$$
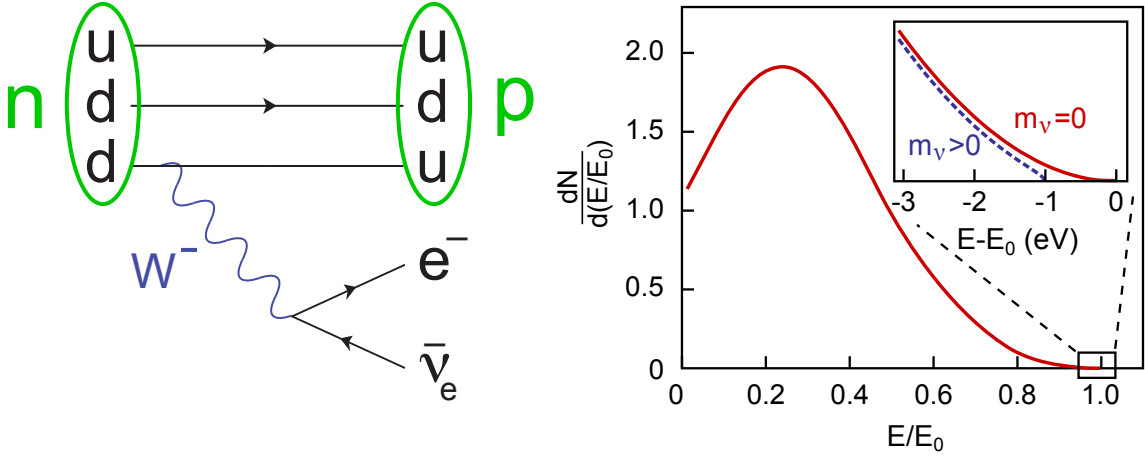
Figure 1.10: Single β-decay. Left: Feynman diagram. A down-quark in a neutron is transformed into an up-quark via the exchange of a W^--boson, thereby forming a proton, and emitting an electron and an electron antineutrino. **Right: Differential electron energy spectrum.** The energy scale is normalized to the endpoint energy $E_0 \approx Q$. The relative intensity is given in arbitrary units. The inset illustrates the endpoint region where the shape of the spectrum is sensitive to the neutrino mass, shown here for $m_\nu = 0\,\text{eV}$ and $m_\nu = 1\,\text{eV}$. Figures adapted from [Sch13a].

Kinematic investigations of the π- and τ-decays give rather large upper bounds for the absolute neutrino-mass scale. It is thus unlikely that these approaches can proceed to a sub-eV sensitivity in the near future. However, the major interest today in studying these experiments is based on the investigation of potential admixtures of the involved neutrinos ν_μ and ν_τ with heavy (sterile) neutrinos beyond the three-neutrino mixing described by the PMNS matrix [Zub11].

1.4.5 Kinematics of the Single Beta-Decay

At present, the most promising direct, model-independent approach to measure the absolute neutrino-mass scale is based on the kinematic investigation of the weak β^--decay process:

$$n \;\rightarrow\; p + e^- + \overline{\nu}_e \; . \tag{1.54}$$

The associated Feynman diagram is illustrated in figure 1.10. This method purely relies on kinematic variables of the particles in this first-order weak interaction process. The only underlying assumption relates to the relativistic energy-momentum equation and conservation of energy and momentum. No further assumptions about the neutrino CP properties with respect to a Dirac or Majorana nature have to be considered. A direct mass experiment performs precision spectroscopy in the endpoint region of the β-decay energy spectrum of electrons of the emitting radioactive isotope. It is only in this narrow region close to the endpoint energy, where the shape of the spectrum depends on the effective mass of the electron antineutrino, see figure 1.10.

The three-body decay shown in reaction (1.54) yields a continuous electron energy spectrum which can be calculated with Fermi's golden rule [Dir27] [Fer34] [Pau85]

$$T_{i\rightarrow f} = \frac{2\pi}{\hbar}|M_{fi}|^2 \rho(E_f) \; , \tag{1.55}$$

where $T_{i\rightarrow f}$ is the transition rate describing the probability of a particular transition from the initial state $|i\rangle$ to a final state $|f\rangle$ per unit time, M_{fi} is the transition matrix element between both states, and $\rho(E_f)$ is the final-state density with energy E_f. This partial transition rate has to be integrated over all possible discrete and continuous final states

to obtain both the total decay constant $\lambda = 1/\tau$, which is directly related to the mean lifetime τ of the initial state, and the total decay width $\Gamma = \hbar\lambda$ of the reaction. Obviously, the decay constant depends on the strength of the coupling between the initial state and final states, described by the individual matrix elements M_{fi}, as well as on the density of final states $\rho(E_f)$ with energies E_f. Finally, after straightforward calculations based on relativistic conservation of energy and momentum [Wei03] [OW08] [Dre13], the differential rate of the electron energy spectrum can be written as

$$\frac{\mathrm{d}N^2}{\mathrm{d}t\mathrm{d}E} = \frac{G_F^2 \cdot \cos^2\theta_C}{2\pi^3 c^5 \hbar^7} \cdot |M|^2 \cdot F(Z+1, E) \cdot p \cdot (E + m_e c^2)$$
$$\cdot (E_0 - E) \cdot \sqrt{(E_0 - E)^2 - m_\nu^2 c^4} \cdot \theta(E_0 - E - m_\nu c^2) \ . \quad (1.56)$$

The Fermi coupling constant G_F, the Cabibbo angle θ_C and the nuclear matrix element M describe the β^--decay as a fundamental nuclear transformation of the weak interaction. The kinetic energy E, the momentum p, and the rest mass m_e of the electron characterize the kinematics of the reaction. The maximum kinetic energy is given by the endpoint energy $E_0 = Q - E_{\mathrm{rec}}$ for the case of a vanishing neutrino mass and energy as a function of the reaction energy Q and the recoil energy E_{rec} of the daughter nucleus. The Fermi function $F(Z+1, E)$ accounts for the Coulomb interaction between the emitted electron and the daughter nucleus with charge $Z + 1$ [Hol92]. The Heaviside step function $\theta(E_0 - E - m_\nu c^2)$ ensures conservation of energy, i.e. a neutrino can be only generated if the available energy is greater than its rest mass m_ν.

The key parameter of interest in the differential spectrum (1.56) is the squared mass m_ν^2 of the electron antineutrino. It is treated as a superposition of three neutrino-mass eigenstates m_i undergoing mixing (section 1.3.1):

$$m_\nu^2 = \sum_{i=1}^{3} |U_{ei}^2| m_i^2 \ . \quad (1.57)$$

This incoherent, weighted sum across the squared mass eigenstates leads to a fine structure in the electron energy spectrum at the endpoint. However, this cannot be resolved with current techniques since the existing differences of masses $\sqrt{\Delta m_{ij}^2}$ are much smaller than the experimental energy resolution ΔE. Therefore, the effective mass of the electron antineutrino characterized by equation (1.57) is the actual observable of the experiment. The incoherent summation renders the neutrino mass m_ν independent from the Dirac CP phase δ and the two Majorana CP phases α_{21} and α_{31} of the PMNS matrix.

In a more detailed consideration, all possible final states of the daughter system have to be included in calculating the differential spectrum. Electronic excitations or, in the case of a molecular structure, rotational and vibrational excitations can lead to a distribution of individual final states with a different phase space for the outgoing lepton pair. Each final state has to be added by its individual transition probability P_j, excitation energy V_j, and specific endpoint energy $E_j = E_0 - V_j$.

Taking into account these modifications by summing up over the neutrino-mass eigenstates and the final states, the differential electron energy spectrum can be rewritten in a more generic form

$$\frac{\mathrm{d}N^2}{\mathrm{d}t\mathrm{d}E} = \frac{G_F^2 \cdot \cos^2\theta_C}{2\pi^3 c^5 \hbar^7} \cdot |M|^2 \cdot F(Z+1, E) \cdot p \cdot (E + m_e c^2)$$
$$\cdot \left(\sum_{i,j} |U_{ei}^2| \cdot P_j \cdot (E_j - E) \cdot \sqrt{(E_j - E)^2 - m_i^2 c^4} \cdot \theta(E_j - E - m_i c^2) \right) \quad (1.58)$$

which is valid for all allowed and super-allowed β^--decays [Dre13].

During β^--decay, the emitted neutrino with energy $E_\nu = \sqrt{m_\nu^2 c^4 + p_\nu^2 c^2}$ can be assessed with a given energy uncertainty δE by the experiment. The resulting mass uncertainty is then given by [Ott10]

$$\delta m_\nu = \frac{1}{c^2} \cdot \frac{E_\nu}{m_\nu c^2} \cdot \delta E_\nu = \frac{1}{c^2} \cdot \gamma \cdot \delta E_\nu \tag{1.59}$$

which directly scales with the relativistic Lorentz factor γ. Therefore, a relativistic neutrino ($p_\nu \gg m_\mu$, $\gamma \gg 1$) hides away its rest mass so that the measurement for determining the neutrino mass has to be performed in the energy region close to the kinematic endpoint where the neutrino looses its ultra-relativistic properties. Obviously, this comes at the expense of strongly decreasing statistics. The favorable region where the generated β-electrons are close to the endpoint energy scales with Q^{-3}. However, this is counteracted by the phase space factor which increases with Q^5 [Gat01]. For actual neutrino-mass measurements, however, it is more advantageous to use a β-emitter with a relatively small Q-value for technical reasons associated with measuring electron energies. In general, there are three major demands on the experiment: maximize the accepted solid angle and thus the luminosity, maximize the energy resolution, and minimize the background rate [Ott10].

Rhenium as β-emitter

Rhenium is, in principle, a rather promising isotope to study the kinematics of the single β^--decay:

$$^{187}\text{Re} \rightarrow {}^{187}\text{Os}^+ + e^- + \bar{\nu}_e \ . \tag{1.60}$$

With $Q = 2.663(19)\,\text{keV}$ [FE04], ^{187}Re has the lowest Q-value of all known β^--emitters. However, a major drawback is its relatively long half-life of $\tau_{1/2} = 4.35(13) \times 10^{10}\,\text{y}$ [FE04], so that significant amounts of the isotope would be required to obtain adequate high source activities [Rob10].

The Milano experiment [Nuc02] studied the β-spectrum of ^{187}Re for about one year using an array of ten cryogenic micro-calorimeters with an energy resolution of $\Delta E = 28\,\text{eV}$, each housing AgReO_4 crystals with a mass of $250 - 300\,\mu\text{g}$. At larger masses in the mg-scale, pile-up effects would occur, since calorimeters have to measure the entire β-spectrum rather than focusing only on the endpoint region. Calorimeters are operated as β-emitter and as energy absorber at the same time. The released energy leads to an increase in temperature, measured by a sensitive thermometer. In total, the Milano experiment observed $\sim 6.2 \times 10^6$ decays, and provides an upper limit for the neutrino mass of

$$m_\nu < 15\,\text{eV} \quad (90\,\%\ \text{C.L.}) \ . \tag{1.61}$$

The successor experiment MARE was targeted to improve the sensitivity to the sub-eV scale in two phases [Nuc12].

Recently, the study of the electron capture on holmium ^{163}Ho has generated a lot of interest. At present, two experiments, HOLMES [Gal12] and ECHo [Gas14], are being prepared to obtain sensitivities in the range of a few eV.

Tritium as β-emitter

With $Q = 18.591(1)\,\text{keV}$, tritium has the second lowest Q-value of all known β^--emitters and a particularly attractive half-life of $\tau_{1/2} = 12.33(6)\,\text{y}$. In tritium β^--decay, the unstable, super-heavy hydrogen isotope tritium ^3H decays into its daughter nucleus helium-3 $^3\text{He}^+$ via emission of an electron e^- and an electron antineutrino $\bar{\nu}_e$:

$$^3\text{H} \rightarrow {}^3\text{He}^+ + e^- + \bar{\nu}_e \ . \tag{1.62}$$
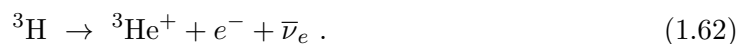
As it will be shown in the next chapter, tritium is ideally suited for high-precision β-electron spectroscopy to obtain sub-eV sensitivities for the absolute neutrino-mass scale.

The KATRIN Experiment

The focus of this chapter is on a description of the working principle and main components of the Karlsruhe Tritium Neutrino (KATRIN) experiment [Ang05] [Dre13] which is targeted to measure the effective mass of the electron antineutrino with an unrivaled sensitivity of $m_\nu = 200\,\mathrm{meV}$ (90 % C.L.). To do so KATRIN will investigate the shape of the electron energy spectrum of tritium β-decay close to the kinematic endpoint of $E_0 \approx 18.6\,\mathrm{keV}$ with unprecedented precision. Pushing forward into the sub-eV level will be achieved by using the unique combination of a high-luminosity windowless gaseous molecular tritium source and a high-resolution integrating spectrometer based on the principle of magnetic adiabatic collimation combined with an electrostatic (MAC-E) filter.

The physics and the measurement principle of high-precision tritium β-spectroscopy are discussed in section 2.1, as well as a brief description of the results obtained by predecessor experiments. Then, the considerable experimental challenges for a next-generation neutrino-mass experiment like KATRIN is outlined. The resulting design requirements and parameters for the experiment are presented in section 2.2. The experimental setup reaches a total length of about 70 m and consists of several main components which have been designed and will be operated at a precision level well above previous efforts in order to ensure reliable neutrino-mass measurements. The features of each component are described in section 2.3 in a compact manner. One of the main components of the beam line is the detector system. The integration and commissioning of this complex system with the main spectrometer forms an essential part of the thesis in hand. It is briefly introduced in this section while its setup, performance, and background contribution are explained in more detail in the subsequent chapters 3, 4, and 5. Another major focus of this thesis has been to realize specific measurements with the integrated beam-line elements of the spectrometer and detector section (SDS) in the framework of the first commissioning measurements. The latter were performed within a four-month measurement campaign starting in mid-2013 and are explicitly highlighted in section 2.4. The commissioning measurements confirmed proper operation of the individual components and verified the working principle of the main spectrometer as a high-resolution MAC-E filter, representing an important milestone for the KATRIN experiment [Bar14] [Thu14]. Finally, the chapter is completed with an overview of background processes occurring in the SDS in section 2.5.

2.1 High-Precision Tritium Beta-Spectroscopy

A high-precision measurement of the tritium β-spectrum close to its kinematic endpoint (section 2.1.1) constitutes the most sensitive, direct, and model-independent approach for determining the absolute neutrino-mass scale. The currently leading technique to do so is

based on the MAC-E filter principle (section 2.1.2) [Ang05] [Wei99] [Thu11] [Dre13]. This well-established technology has yielded the most stringent upper limits of the neutrino mass up to date (section 2.1.3). Accordingly, a next-generation neutrino-mass experiment like KATRIN targeted to improve the present neutrino-mass sensitivity by one order of magnitude has to master considerable experimental challenges and be designed close to current technological limits.

2.1.1 The Ideal Beta-Emitter Tritium

Tritium (^{3}H) is the most favorable and almost ideal β-emitter for a direct, model-independent measurement of the effective mass of the electron (anti)neutrino [Dre13]. This fact has resulted in a long list of neutrino-mass experiments which are and have been based on tritium sources [OW08]. Such experiments perform precision spectroscopy in the kinematic endpoint region of the electron energy spectrum of tritium β-decay. In this weak interaction process, the unstable, super-heavy hydrogen isotope ^{3}H decays into the daughter nucleus helium-3 (^{3}He$^+$), an electron e^-, and an electron antineutrino $\overline{\nu}_e$ via the following semi-leptonic reaction:

$$^3\text{H} \;\rightarrow\; ^3\text{He}^+ + e^- + \overline{\nu}_e \;. \tag{2.1}$$

Tritium has unique characteristics, and in the following its major advantages will be listed [Bor08]:

- **Short half life** of $\tau_{1/2} = (12.32 \pm 0.02)\,\text{y}$ [LU00]. This parameter allows to operate a high-luminosity source while at the same time minimizing the amount of source material, thereby reducing inelastic scattering processes of β-electrons within the tritium source.

- **Low endpoint energy** of $E_0 \approx 18.6\,\text{keV}$ [Nag06]. This allows to technically investigate the electron energy spectrum with the well-established concept of a high-resolution spectrometer of magnetic adiabatic collimation combined with an electrostatic (MAC-E) filter type.

- **Constant recoil correction** of the daughter nucleus of $E_{\text{rec}} = 1.72\,\text{eV}$. The maximum variation of the recoil energy over the full energy region of investigation, about $30\,\text{eV}$ below the endpoint, amounts to $\Delta E_{\text{rec}} = 3.5\,\text{meV}$ only, yielding a quasi-fixed endpoint energy [Mas07].

- **Super-allowed decay.** The mother and daughter nucleus are mirror nuclei. Thus, the nuclear matrix element is energy-independent, so that the β-spectrum is entirely determined by the available phase space. The matrix element has a rather large value of $|M|^2 = 5.55$ [Bel03], close to the one of the β-decay of a free neutron [RK88] [Dre13].

- **Simplest atomic-shell structure.** Tritium and helium are characterized by their low nuclear charge of $Z = 1$ and $Z = 2$, respectively. Both the mother and daughter system have a simple shell configuration. This minimizes the required corrections due to electronic final states or inelastic scattering processes in the tritium source [Bel03]. Furthermore, it allows to exactly calculate individual electronic excitations and their relative probabilities [Dos06] [Dos08]. The Coulomb interaction between the daughter nucleus and the emitted electron can also be reliably calculated via the Fermi function $F(Z = 2, E)$.

- **Gaseous phase** even at cryogenic temperatures $(30\,\text{K})$. In the case of a windowless gaseous tritium source, no solid-state effects have to be considered.
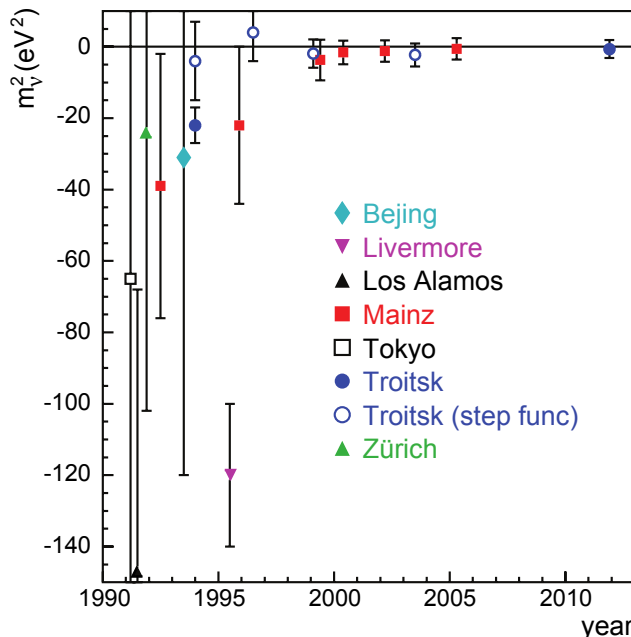
Figure 2.1: Evolution of the results of previous tritium β-decay experiments on the observable m_ν^2. Initial neutrino-mass experiments used magnetic spectrometers [Kaw91] [Rob91] [HFK92] [Che95] [SD95], while only the experiments at Mainz and Troitsk applied electrostatic spectrometers of the MAC-E filter type [Bel95] [Lob99] [Wei99] [Kra05] [Ase11]. The unphysical region of the measurement observable is given by $m_\nu^2 < 0$. Figure adapted from [Dre13].

A specific issue is that all tritium sources up to now were based on its molecular form (T_2), so that the actual tritium β-decay in the experiment is rather given by

$$T_2 \; \to \; {}^3HeT^+ + e^- + \overline{\nu}_e \tag{2.2}$$

than by reaction (2.1). Therefore, the daughter molecule can be excited to rotational and vibrational final states, leading to specific systematic uncertainties on the neutrino-mass measurement.

Over the past three decades, a series of tritium-based neutrino-mass experiments has narrowed the direct and model-independent sensitivity of the effective mass of the electron neutrino down to the few eV-level. This is impressively illustrated in figure 2.1. In this context it is important to note that the most promising results were obtained by experimental setups usin an electrostatic spectrometer of MAC-E filter type. With this approach it is possible to precisely investigate the endpoint region of the electron energy spectrum, as it combines the requirements with regard to high luminosity, excellent energy resolution, and low background [Ott10] [Wei03] [OW08]. Its working principle is explained in the following section.

2.1.2 Measurement Principle of MAC-E-Filter Experiments

The unique measurement principle of combining a stable, high-luminosity tritium source with a large spectrometer of MAC-E filter type with good angular acceptance, high energy resolution, and low background, allows to measure the effective mass of the electron neutrino with unprecedented sensitivity. The fundamental principle of MAC-E filters was proposed first by Kruit and Read [KR83], based on previous works of Beamson, Porter and Turner [BPT80]. This was further refined and adapted for neutrino-mass measurements, such as the Mainz [Pic92] and the Troitsk [Lob85] experiments (section 2.1.3). In general,

a typical MAC-E-filter based experiment consists of the following four system components connected to each other in consecutive order:

- **Tritium source:** A stable, high-luminosity tritium source generates an isotropic flux of β-electrons with well-understood physical parameters and systematic effects, such as temperature influences, scattering effects, and final-states distribution.

- **Transport section:** Active and passive pumping elements remove tritium and other gas species from the beam line, thereby providing good vacuum conditions and separating the tritium-bearing source region from the essentially tritium-free MAC-E filter to prevent background-generating β-decays within the spectrometer.

- **Spectrometer:** Operated under excellent vacuum conditions, an electrostatic retarding spectrometer performs the energy analysis of incoming β-electrons with high energy resolution. The spectrometer operates as high-pass filter with stable retarding potential.

- **Electron detector:** This unit counts the transmitted electrons which have passed through the MAC-E filter, in order to determine the integral electron energy spectrum in an almost background-free way. In the long-term future, the implementation of a high-resolution cryogenic bolometer could allow to measure the differential electron energy spectrum after filtering by the spectrometer.

Typically, a variety of monitoring systems is implemented along the experimental setup to permanently measure and record characteristic parameters and possible variations of experimental conditions, such as the source activity.

In figure 2.2, a simplified sketch of a MAC-E filter and its main features is schematically illustrated using the example of the KATRIN main spectrometer and detector. The operating principle can be divided into the methods of magnetic adiabatic collimation and of electrostatic filtering.

Magnetic adiabatic collimation

Superconducting solenoids located at both ends of the spectrometer provide an axially symmetric magnetic guiding field for signal electrons from the molecular tritium source to the counting electron detector. Both the source and the detector are located in rather strong magnetic fields B_S and B_D, respectively. Signal electrons are isotropically released from the source with individual starting angles θ_S with respect to the direction of the corresponding magnetic field line, and enter the spectrometer with acceptance angles of up to 2π. Due to the acting Lorentz force, the electrons gyrate around the field lines in a cyclotron motion when propagating through the spectrometer. The kinetic energy E_kin along the trajectory of an electron can be divided into a longitudinal component $E_\parallel$ and a transverse component $E_\perp$, relative to the direction of the corresponding magnetic field line:

$$E_\mathrm{kin} = E_\parallel + E_\perp \ . \tag{2.3}$$

In case of the KATRIN spectrometer, the magnetic field drops by several orders of magnitude from the source to the analyzing plane with $B_\mathrm{min} \ll B_\mathrm{S}$. The solenoids are designed and arranged such that the electrons are adiabatically guided through the spectrometer, implying that the first adiabatic invariant

$$\gamma\mu = \frac{\gamma + 1}{2} \cdot \frac{E_\perp}{B} = \mathrm{const.} \tag{2.4}$$

remains constant along the electron trajectories, with γ denoting the relativistic Lorentz factor and μ the orbital magnetic moment of the electron. In the case of tritium β-electrons
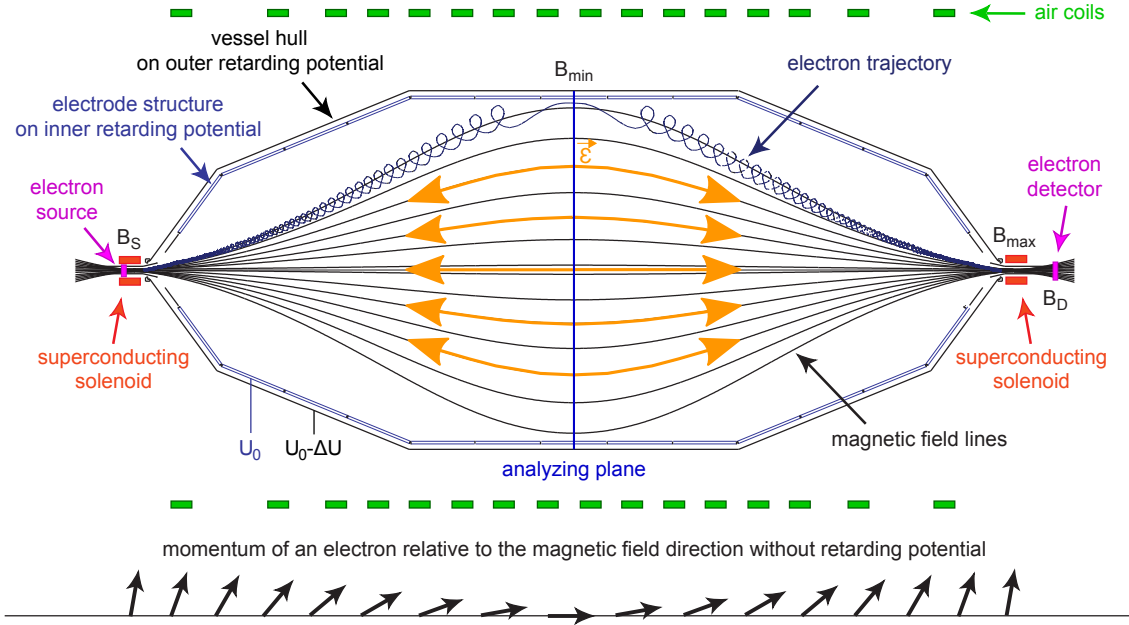
Figure 2.2: Working principle of a MAC-E-filter experiment. The isotropically emitted β-electrons from the source are guided to the entrance side of the spectrometer (left side), and the transmitted electrons are counted by an electron detector at the exit side (right side). The magnetic guiding field is provided by two superconducting solenoids (red) located on both ends of the electrostatic spectrometer. The magnetic field can be fine-tuned by a system of normally conducting air coils (green), surrounding the spectrometer coaxially. Electrons propagate on characteristic cyclotron paths (blue) along magnetic field lines (black) through the spectrometer and undergo an adiabatic transformation of their momentum (see lower part). The electron cyclotron motion is shown in an exaggerated size. In the central analyzing plane with the minimum magnetic field $B_{\min}$ and maximum electric potential U_0, the momentum of electrons is being parallelized in direction of the magnetic field lines. The electric field $\vec{\mathcal{E}}$ (orange) acts only on the longitudinal electron energy component $E_\parallel$, thereby filtering out those electrons with energies lower than the applied retarding potential ($E_\parallel < |qU_0|$). Thus, an electrostatic spectrometer of the MAC-E filter type operates as an integrating high-pass filter. Typically, the negative retarding potential U_0 is applied to an inner system of nearly massless electrodes to fine-tune the electric field and electrostatically shield against surface-induced backgrounds, while the vessel hull is elevated to a slightly more positive voltage of $U_0 - \Delta U$ with $\Delta U \leq 0\,$V. Figure adapted from [Zac09].

with a maximum kinetic energy of $E_{\text{kin}} = E_0 \approx 18.6\,\text{keV}$, the adiabatic invariant of the electron motion is the magnetic moment

$$\mu = \frac{E_\perp}{B} = \text{const.} \tag{2.5}$$

in a non-relativistic approximation in view of $\gamma = 1.04 \approx 1$. The reduction of the magnetic field B leads to an appropriate decrease of the transverse electron-energy component $E_\perp$ in order to keep the adiabatic invariant of the electron motion constant, according to equations (2.4) or (2.5). Due to the conservation of total electron energy according to the relation (2.3), this results in a simultaneous increase of the longitudinal electron-energy component $E_\parallel$. Therefore, the magnetic field gradient enforces an energy transformation $E_\perp \to E_\parallel$ from the source side of the spectrometer toward the analyzing plane ($B_\text{S} \to B_\text{min}$). Analogously, the transformation $E_\parallel \to E_\perp$ from the analyzing plane toward the detector side ($B_\text{min} \to B_\text{max}$) is obtained. This results in three characteristic parameters describing the MAC-E filter:

- **Magnetic flux tube:** The magnetic flux

$$\Phi = \int_A \vec{B} \cdot \mathrm{d}\vec{A} \tag{2.6}$$

  is a conserved quantity. Therefore, a reduction of the magnetic field B results in an appropriate increase of the flux-tube cross sectional area A. As a consequence, the maximum area of transported electrons is reached at minimum field B_min, while the minimum area is reached at maximum field B_max. In other words, the broad parallel beam of electrons in the analyzing plane is reduced to a narrow beam on the source and detector side with large pitch angles.

- **Energy resolution:** A small energy portion ΔE of the transverse component will remain in the analyzing plane due to the finite magnetic field $B_\text{min} > 0$, implying that the transverse component takes on values of $E_\perp = 0 \ldots \Delta E$ in the analyzing plane. Therefore, the momentum of a passing electron with an energy E needs not necessarily be perfectly parallel-aligned to the corresponding magnetic field line. This defines the *energy resolution* or more precisely the filter width of the spectrometer:

$$\frac{\Delta E}{E} = \frac{B_\text{min}}{B_\text{max}} \ . \tag{2.7}$$

- **Magnetic mirror:** When propagating toward an increasing magnetic field strength, the transverse energy component $E_\perp$ increases up to a point where full conversion is reached with $E_\text{kin} = E_\perp$ and $E_\parallel = 0$, so that a magnetic reflection to the opposite direction toward the lower magnetic field is initiated. Accordingly, in a MAC-E filter with maximum magnetic field $B_\text{max} > B_\text{S}$, electrons will be reflected back to the source in case the starting angle θ_S is greater than the maximum accepted angle

$$\theta_\text{max} = \arcsin\sqrt{\frac{B_\text{S}}{B_\text{max}}} \ . \tag{2.8}$$

  This limitation of acceptance is actually beneficial as a large starting angle implies a longer electron trajectory through the entire experimental setup so that the probability for energy losses due to scattering processes and synchrotron radiation increases. Such electrons can conveniently be magnetically pinched back to the source by the above described magnetic mirror effect [Hig07] [Hig08] before reaching the detector, thus suppressing less favorable trajectories for high-precision β-spectroscopy. Further details regarding the magnetic mirror effect are described in section 2.5.2.

Electrostatic filtering

In order to perform a precision analysis of the kinetic energy of the electrons, a negative retarding potential U_0 is applied to the spectrometer vessel as well as to an inner system of electrodes. The retarding voltage typically is close to the endpoint energy, while both the source and the detector are on ground potential. Hence, the generated electric field forms an electrostatic potential barrier which the electrons have to pass in order to reach the detector. Since the direction of the electric field is aligned parallel to the magnetic field lines in the analyzing plane, electrons can be electrostatically filtered according to their longitudinal energy component $E_\parallel$. As described above, the principle of magnetic adiabatic collimation ensures that the energy transformation $E_\perp \to E_\parallel$ is maximal in the analyzing plane. The electrostatic potential barrier can only be passed by electrons whose longitudinal energy component, and thus their kinetic energy, is greater than the applied retarding voltage. After passing the analyzing plane, the electrons are reaccelerated by the decreasing retarding potential and then counted by the detector. Electrons with insufficient energies are electrostatically reflected back to the source and are lost for detection.

MAC-E filter

The combination of magnetic adiabatic collimation and electrostatic filtering allows to analyze the kinetic energies of all isotropically released β-electrons from the tritium source. This characteristic filtering principle of an electrostatic spectrometer of the MAC-E filter type can be analytically described by the transmission probability $\mathcal{T}(E, U_0)$. For an isotropically emitting electron source of energy E, it is given by:

$$\mathcal{T}(E, U_0) = \begin{cases} 0 & \text{for } E < |qU_0| \\ \dfrac{1 - \sqrt{1 - \frac{E - qU_0}{E} \cdot \frac{B_\mathrm{S}}{B_\mathrm{min}}}}{1 - \sqrt{1 - \frac{B_\mathrm{S}}{B_\mathrm{max}}}} & \text{for } |qU_0| \leq E \leq |qU_0| + \Delta E \\ 1 & \text{for } E > |qU_0| + \Delta E \end{cases} \qquad (2.9)$$

Complete transmission corresponds to $\mathcal{T}(E, U_0) = 1$. Due to the operating principle of a MAC-E filter as an integrating high-pass filter, an integral electron energy spectrum is recorded by the detector. By varying the retarding potential around the endpoint region in well-defined increments, the shape of the integrated β-spectrum becomes experimentally accessible.

2.1.3 Neutrino-Mass Limits

The Mainz [Pic92] and the Troitsk [Lob85] experiment were based on the measurement principle of using a molecular tritium source in combination with an electrostatic spectrometer of MAC-E filter type in order to produce β-electrons and analyze their integral energy spectrum close to the kinematic endpoint. Both experiments have reached their intrinsic sensitivity limit resulting in the currently best upper limits for the effective mass m_ν of the electron (anti)neutrino. According to (1.57), the squared effective mass m_ν^2 represents the observable so that an upper limit for m_ν had to be calculated by using the Feldman-Cousins method [FC98].

The Mainz experiment made use of a thin quench-condensed molecular tritium film onto aluminum or graphite substrates operated at $T < 3\,\mathrm{K}$ and a MAC-E filter of $1\,\mathrm{m}$ in diameter. The published result and mass limit are [Kra05]

$$\begin{aligned} m_\nu^2 &= (-0.6 \pm 2.2_\mathrm{stat} \pm 2.1_\mathrm{syst})\,\mathrm{eV}^2 \\ &\to\ m_\nu < 2.3\,\mathrm{eV}\ (95\,\%\ \mathrm{C.L.})\ . \end{aligned} \qquad (2.10)$$

The Troitsk experiment made use of a windowless tritium source and a MAC-E filter of 1.2 m in diameter. The published result and mass limit are [Ase11]

$$
\begin{aligned}
m_\nu^2 &= (-0.67 \pm 1.89_{\text{stat}} \pm 1.68_{\text{syst}})\,\text{eV}^2 \\
&\rightarrow \ m_\nu < 2.05\,\text{eV} \ (95\,\%\ \text{C.L.}) \ .
\end{aligned}
\tag{2.11}
$$

A combined analysis of both results gives the currently most sensitive result for the effective mass of the electron (anti)neutrino of [Ber13]

$$
m_\nu < 2.0\,\text{eV} \ (95\,\%\ \text{C.L.}) \ .
\tag{2.12}
$$

Both experiments could establish impressively precise upper limits on the neutrino-mass scale. However, they do not allow to narrow the neutrino-mass sensitivity down to the sub-eV regime due to the dominating systematic uncertainties and limited source statistics, i.e. these experiments are completed. Therefore, a next-generation experiment with an improved MAC-E-filter based setup is required to push forward into the sub-eV level. In general, such an experiment faces three major technological challenges [Ott10]:

- **Maximizing luminosity:** A windowless gaseous tritium source of highest intensity and stability is essential for a sub-eV sensitivity, as only a tiny fraction of 2×10^{-13} of all tritium β-decays contributes to the electron energy spectrum in the region of 1 eV below the kinematic endpoint. At the same time, the column density[1] of the source can only be increased up to a certain limit so that scattering processes and resulting energy losses of β-decay electrons within the source are small. This leads to a delicate trade-off between increasing statistics or improving systematics.

- **Maximizing resolution:** A high-resolution spectrometer of MAC-E filter type is required to maximize the precision of β-electron spectroscopy close to the kinematic endpoint. As defined by equation (2.7), the energy resolution depends on the minimum and maximum magnetic fields along the MAC-E filter. The latter has to be designed such that the signal electrons are adiabatically guided through the spectrometer, i.e. their magnetic moment needs to be constant in a non-relativistic approximation, according to equations (2.4) or (2.5).

- **Minimizing background:** An experimental setup with a signal-to-background ratio of at least 2:1 few eV below E_0 is essential in order to scan the endpoint region. Both the tritium source and the MAC-E filter have to be designed such that the production of background electrons from internal or external sources is minimized in the region of interest. This demands an almost background-free detection technique.

These design requirements have guided the layout of the KATRIN experiment which is currently under construction at the Tritium Laboratory Karlsruhe (TLK) at the KIT Campus North site. It is targeted to improve the present sensitivity of direct mass experiments by one order of magnitude down to [Ang05] [Dre13]

$$
m_\nu < 200\,\text{meV} \ (90\,\%\ \text{C.L.})
\tag{2.13}
$$

by using a high-luminosity windowless gaseous molecular tritium source with a β-activity of about 10^{11} electrons per second in combination with a high-resolution spectrometer of MAC-E filter type with an energy resolution of $\Delta E = 0.93$ eV to 18.6-keV electrons. Even with a source luminosity which exceeds the forerunner experiments by two orders of magnitude, an effective measurement period of three years is required. In the following, an overview of key KATRIN design parameters will be given.

---

[1]The column density ρd (in cm^{-2}) is defined by the tritium density ρ and the source length d.

2.2 KATRIN Design Parameters

In order to improve the recent neutrino-mass limits by a factor of 10 and reach the targeted sub-eV sensitivity, KATRIN has been designed to meet the following parameters, which are compared to the forerunner experiment at Mainz (Troitsk) [Ang05] [Dre13]:

- **Source luminosity.** The effective source column density is increased by a factor of 2 (3) to 5×10^{17} molecules/cm^2, while the effective source cross section is increased by a factor of 40 (20) to $52.8 \, \text{cm}^2$, and the tritium purity by 1.4 to greater than 95 %. This results in a β-activity of about 10^{11} electrons per second, of which a maximum accepted angle of $\theta_{\max} = 50.8°$ is used by selecting $B_{\text{S}} = 3.6 \, \text{T}$ and $B_{\max} = 6.0 \, \text{T}$. With a detector efficiency of $\epsilon_{\text{det}} \geq 90 \, \%$, this yields an overall improvement of the expected signal rate close to the kinematic endpoint by a factor of about 100.

- **Energy resolution.** The energy resolution of the MAC-E filter is improved by a factor of 5 (4) to $\Delta E = 0.93 \, \text{eV}$ with $E = 18.6 \, \text{keV}$, $B_{\min} = 3.0 \, \text{G}$, and $B_{\max} = 6.0 \, \text{T}$. This requires a spectrometer where the diameter is increased by a factor of 10 (8) to about 10 m. The usable diameter is approximately 9 m resulting in an analyzing plane with $63.6 \, \text{m}^2$ in area. The sensitive magnetic flux transported through the entire system is $\Phi = 191 \, \text{Tcm}^2$.

- **Background rate.** Ideally, the total background rate measured at the detector should not exceed the signal rate in the most important region of few eV below E_0 to first order. Therefore, the reference background rate is limited to be $10^{-2} \, \text{cps}$, which is identical to the value reached in the previous, much smaller neutrino-mass experiments.

- **Statistical uncertainty.** The effective measurement time is extended by a factor of 10 to three net years of data-taking corresponding to five calender years of experimental run time, including calibration phases and maintenance periods. This leads to a statistical uncertainty of $\sigma_{\text{stat}}(m_\nu^2) = 18 \times 10^{-3} \, \text{eV}^2$.

- **Systematic uncertainty.** The expected total systematic uncertainty is reduced by a factor of 100 to $\sigma_{\text{syst}}(m_\nu^2) = 17 \times 10^{-3} \, \text{eV}^2$.

Both statistical and systematic uncertainties contribute about equally to the sensitivity for the squared effective mass m_ν^2, giving a total uncertainty of

$$\sigma_{\text{tot}}(m_\nu^2) = \sqrt{\sigma_{\text{stat}}(m_\nu^2)^2 + \sigma_{\text{syst}}(m_\nu^2)^2} \approx 25 \times 10^{-3} \, \text{eV}^2 \; . \tag{2.14}$$

In case of evidence for a non-zero neutrino mass, the experiment has an expected discovery potential of $m_\nu = 350 \, \text{meV}$ with 5σ significance and of $m_\nu = 300 \, \text{meV}$ with 3σ significance. In case of a vanishing neutrino-mass signal, the upper limit is given by

$$m_\nu < \sqrt{1.64 \cdot \sigma_{\text{tot}}(m_\nu^2)} = 200 \, \text{meV} \; (90 \, \% \; \text{C.L.}) \; . \tag{2.15}$$

2.3 KATRIN Apparatus

The detailed layout of the KATRIN experiment is based on the requirements described in the previous section, and on the experiences gained in the predecessor neutrino-mass experiments. A central element of the site selection for KATRIN is the Tritium Laboratory Karlsruhe (TLK) which offers extensive experience in technologies to handle and process larger amounts of the radioactive hydrogen isotope tritium. Furthermore, it provides both the official license and the appropriate infrastructure required for the handling of a daily throughput of $40 \, \text{g/d}$ of gaseous molecular tritium [Pen00] [Doe08b]. These facts make the TLK an ideal and unique host facility for the KATRIN experiment [Sch13a].
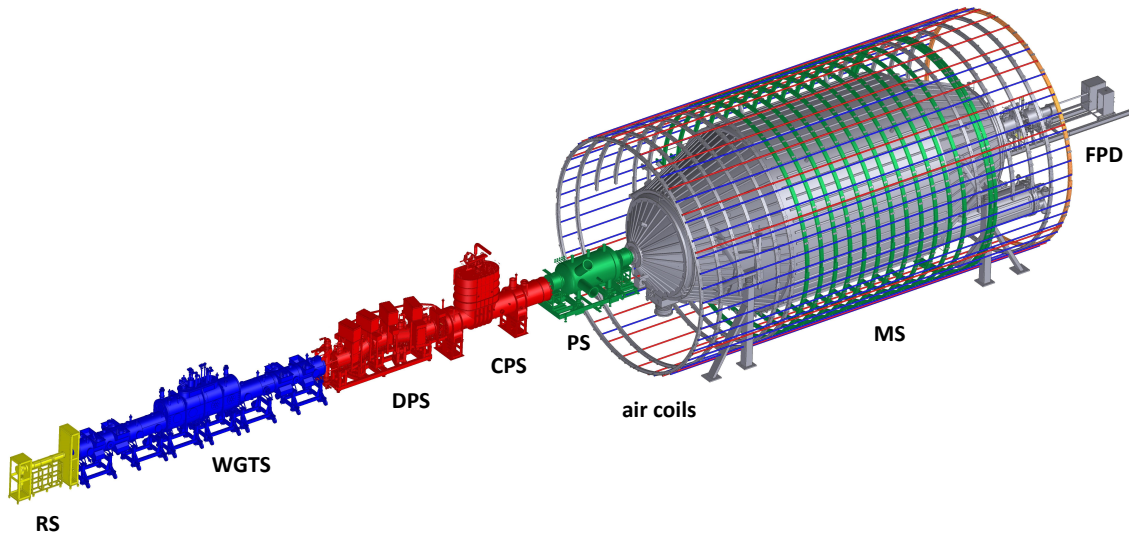
Figure 2.3: The 70-m long experimental setup of the KATRIN experiment. The KATRIN experiment consists of several main components: the rear section (RS) for regular system calibration and permanent source monitoring, the windowless gaseous tritium source (WGTS) for stable tritium injection, the differential pumping section (DPS) and the cryogenic pumping section (CPS) for tritium extraction and adiabatic electron guiding, the pre-spectrometer (PS) for pre-filtering of low-energy electrons, the main spectrometer (MS) for high-resolution tritium β-spectroscopy, and the focal-plane detector system (FPD) for highly efficient counting of transmitted electrons. The main spectrometer is coaxially surrounded by a large-scale air-coil system in order to fine tune the magnetic field and to compensate the earth magnetic field. Further details are given in the continuous text.

A schematic view of the 70-m long experimental setup and its main functional units is illustrated in figure 2.3. In the high-luminosity windowless gaseous tritium source (WGTS), molecular tritium gas is injected under controlled and stable conditions. The injected tritium diffuses to both ends of the WGTS where it is removed from the system by differential and cryogenic pumping within the two-component transport section: the differential pumping section (DPS) and the cryogenic pumping section (CPS). Forward emitted β-electrons are adiabatically guided on cyclotron trajectories by strong magnetic fields provided by an ensemble of superconducting solenoids arranged coaxially to the beam line from the tritium source through the transport section to the spectrometer system consisting of two MAC-E filters connected in series. The pre-spectrometer (PS) offers the option to act as pre-filter, while the high-resolution main spectrometer (MS) precisely analyses the kinetic electron energy in order to measure the shape of the electron energy spectrum close to the kinematic endpoint. Electrons passing both MAC-E filters are guided to and counted by the highly efficient electron detector − the centerpiece of the focal-plane detector system (FPD) − under preferably background-free conditions. The rear section (RS) connected to the rear side of the tritium source provides the hardware components to perform regular calibrations and allows continuous monitoring of characteristic system parameters. The separate beam line of the monitor spectrometer allows to observe fluctuations of the retarding potential applied to the main spectrometer by monitoring of a nuclear standard.

In the following, the relevant subsystems are briefly introduced. Special focus is put on a detailed description of the experimental setup and working principle of the detector system, as its implementation, commissioning, and testing is a major part of the work in hand (chapters 3, 4 and 5). Another essential part of this thesis is focused on the background investigations of the main spectrometer during its first commissioning phase (chapters 6 and 7). For these reasons, the associated experimental setup is discussed in more detail in section 2.4.

2.3.1 The windowless gaseous tritium source

The tritium source is contained in a cylindrical stainless-steel tube of 10 m in length and 90 mm in diameter being housed in the rather complex WGTS cryostat. There, cryogenic molecular tritium gas of high isotropic purity greater than 95 % is injected through a set of capillaries with an inlet pressure of about 10^{-3} mbar at a temperature of 30 K. A total of 5×10^{19} tritium molecules enters the beam tube per second under controlled conditions. Simultaneously, tritium is differentially pumped out of the system by turbomolecular pumps (TMPs) attached to specific pump ports at both ends of the beam tube. The TMPs feed a closed inner loop system [Stu10] where all gas species pumped out are processed by a permeator. The isotopic gas composition is monitored by Laser Raman spectroscopy [Sch13a], and a pressure-controlled buffer is used to reinject high-purity tritium gas to the beam tube. The inner loop will cycle tens of grams of tritium through the WGTS per day to generate a stable column density of 5×10^{17} molecules per cm^2. This number corresponds to a total β-activity of about 10^{11} electrons per second. The isotropically emitted β-electrons are adiabatically guided within a transported magnetic flux of 191 Tcm^2 by a homogeneous magnetic field of 3.6 T, provided by three large superconducting solenoids coaxially arranged around the beam line. The beam tube is kept stable at a temperature of 30 K by a novel cooling concept based on a two-phase liquid neon thermosiphon [Bod11] [Gro11]. This temperature regime (*i*) minimizes the tritium throughput, (*ii*) limits the effect of thermal Doppler broadening of electron energies due to molecular motion, and (*iii*) suppresses the effects of clustering and condensation of hydrogen isotopes. Extensive proof-of-principle measurements at the WGTS demonstrator showed that the peak-to-peak temperature variation is only 3 mK at 30 K over a time period of four hours, which is by a factor of 10 better than required [Hoe12] [Gro13b]. The final assembly of the WGTS cryostat is scheduled to be completed around mid-2015. Further information with regard to the technical setup of the WGTS is provided by [Bab12].

2.3.2 The transport section

The two-component transport section separates the tens of GBq WGTS activity from the low-level (mBq) spectrometer system through a beam line of more than 15 m in length. Since tritium β-decaying within the spectrometer system would lead to an elevated background rate, the transport section in combination with the TMPs of the WGTS has to reduce the tritium flow along the beam line by more than a factor of 10^{14}, from 1.8 mbar ℓ/s at the injection capillaries to a level of about 10^{-14} mbar ℓ/s at the entry of the prespectrometer. This is achieved by the DPS and the CPS. In both cryostats, the beam line is arranged with chicanes of 20° in the DPS and 15° in the CPS to prevent a direct line-of-sight for tritium molecules, thereby suppressing the molecular beaming effect[2] [Luo06] [LD08]. The DPS actively removes tritium by a series of four TMPs attached to corresponding pump ports at the transitions between the chicanes [Luk12], while the CPS passively traps remaining traces of tritium by cryogenic sorption onto an ultra-cold surface (3 K) of specific parts of the beam tube covered by argon frost in order to increase the effective sorption surface and enhance the trapping efficiency [Gil10]. Each section reduces the tritium flow by a factor of about 10^7. Superconducting solenoids surrounding the beam tubes provide adiabatic guiding for the β-electrons in fields of up to 5.6 T. The DPS beam tube also houses two diagnostic units based on the principle of Fourier transform-ion cyclotron resonance to measure the number densities and different species of ions in the transported magnetic flux tube [Ubi09] [Ubi11], while three electrostatic dipole electrodes serve to actively remove these ions [Rei09b] [Win11] originating from the large number of β-decays of molecular tritium in the WGTS. The delivery of the DPS and CPS

---

[2]The molecular beaming effect describes a collimated gas flux which is strongly directed forward.
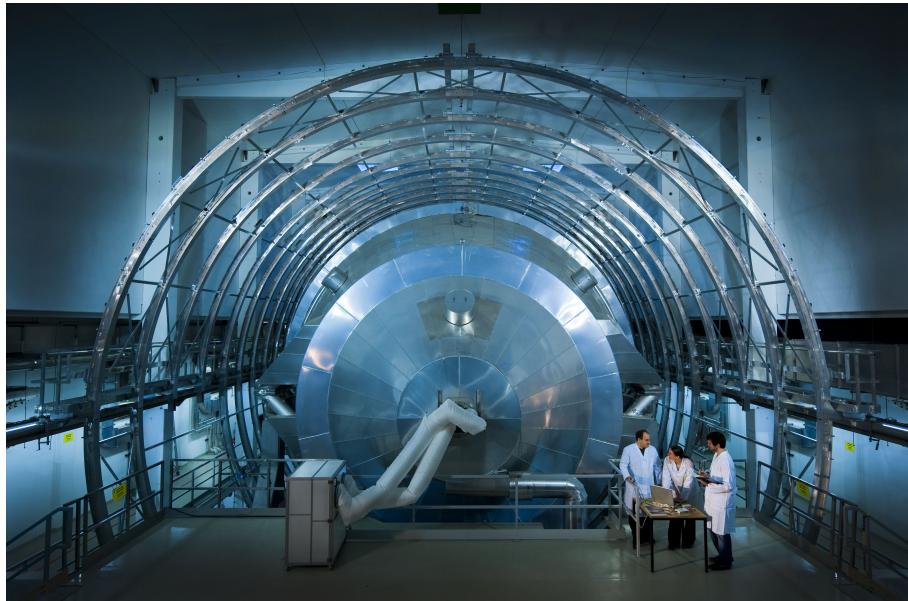
Figure 2.4: Main spectrometer and air-coil system, prior to the main-spectrometer bake-out.

cryostats is scheduled for the end of 2014, followed by acceptance tests and commissioning measurements in order to determine the total gas-flow reduction factor [Luk12], the alignment of the magnetic flux tube relative to the beam line [Sch10], and the efficiency of the dipole electrodes using an ion source [Sch08]. Further information with regard to the technical setup of the transport section is provided by [Kos12].

2.3.3 The spectrometer system

Two tritium-free, high-pass spectrometers of MAC-E filter type will analyze the kinetic energy of the β-electrons under ultra-high vacuum (UHVac) conditions in the 10^{-11}-mbar regime. The smaller pre-spectrometer with a length of $3.4\,\mathrm{m}$, a diameter of $1.7\,\mathrm{m}$, and an energy resolution of $\Delta E \approx 70\,\mathrm{eV}$ at $18.6\,\mathrm{keV}$ offers the option to act as pre-filter with adjustable retarding voltages of up to $-18.3\,\mathrm{kV}$ in order to allow to reject low-energy β-electrons which carry no relevant information on the neutrino mass [PRG12]. The adiabatic guiding field of $4.5\,\mathrm{T}$ is provided by two superconducting warm-bore solenoids. The high-resolution main spectrometer with a length of $23.3\,\mathrm{m}$, a diameter of $10.0\,\mathrm{m}$, and an energy resolution of $\Delta E = 0.93\,\mathrm{eV}$ at $18.6\,\mathrm{keV}$ performs a high-precision electron-energy analysis. In order to scan the β-decay spectrum, the electrostatic retarding potential in the endpoint region is varied within the energy interval of about $30\,\mathrm{eV}$ below and $5\,\mathrm{eV}$ above the kinematic endpoint. In this way, the integral β-electron energy spectrum is measured. The adiabatic guiding field is provided by the downstream solenoid ($4.5\,\mathrm{T}$) of the pre-spectrometer and the upstream solenoid ($6.0\,\mathrm{T}$) of the detector system. A large-scale air-coil system consisting of 16 individually powered, normal-conducting air coils surrounds the main spectrometer in order to fine-tune the magnetic field [Rei09a] [Wan09] [Glu13]. A photograph of the main spectrometer and the air-coil system is shown in figure 2.4. At both spectrometers, the retarding potential can be directly applied to the vessel while an inner quasi-massless wire-electrode system allows to fine-tune the electrostatic retarding field [Val06] [Hug08] [Val09] [Zac09] [Val10] [Pra11]. Until 2011, the pre-spectrometer was extensively investigated as a stand-alone facility to study electron-transport and background-production mechanisms [Fra06] [Hab09] [Lam09] [Fra10b] [Goe10] [Mer12a]. In summer 2013, the main spectrometer was commissioned for the first time in combination with the detector system [Bar14] [Thu14]. Essential parts of this thesis are based on this commis-

sioning phase. The corresponding experimental setup is presented in more detail in section 2.4. Further information with regard to the technical setup of the spectrometer system is provided by [Goe14].

2.3.4 The detector system

At the downstream end of the KATRIN setup, a system of two superconducting solenoids generates a magnetic field of up to $6.0\,\mathrm{T}$ to adiabatically guide the transmitted β-electrons to a so-called *focal-plane detector* (FPD) consisting of a 148-pixel PIN-diode array housed on a monolithic silicon wafer of $9\,\mathrm{cm}$ in sensitive diameter and about $500\,\mu\mathrm{m}$ in thickness. The key objective of the system is to count the signal electrons under almost background-free condition while being operated under UHVac conditions. The intrinsic detector background level is of prime interest, thus a lot of effort was focused on is drastically reducing it by using only hardware components carefully selected and assayed for low intrinsic radioactivity. Another important design feature is a post-acceleration electrode so that the electron signal can be shifted to a window at higher energies with a more favorable background rate. This is complemented by a passive cylindrical shield made of lead and copper to block natural environmental radiation, and by an active veto system based on plastic scintillators to tag incident cosmic rays. Furthermore, the detector itself provides good energy, timing, and spatial resolution in order to map inhomogeneities of the column density or the plasma potential in the tritium source. This also allows to cross-check the transportation mechanisms of the magnetic flux tube along the entire beam line. Last but not least, the radial segmentation enables to map magnetostatic and electrostatic inhomogeneities in the spectrometer system, and to study the radial pattern of different sources of background in the main spectrometer. The detector is thus of central importance for an explicit understanding of the operation of the entire KATRIN apparatus. The detector system houses two calibration sources, a ^{241}Am source as γ-emitter and an illuminated disk elevated to a high potential as photoelectron source, both allowing to perform independent detector calibrations. The technical setup of the detector system is described in more detail in chapter 3. Further information can be found in [Leb10] [Har12] [Wal13] [Ams14].

2.3.5 The rear section

At the rear end of the WGTS cryostat, the rear-section system allows to (*i*) define the plasma potential of the source by a specially developed rear wall [Bab12], (*ii*) monitor the tritium activity via β-induced X-ray spectroscopy [Mau09] [Roe11] [RP13], and (*iii*) measure the actual source column density by an angular resolved electron gun [Hug10] [Val11] in regular intervals via inelastic scattering of the electrons within the source. The technical design of this multi-purpose unit has been approved and the system is expected to be operational in the middle of 2015. Further information on the technical setup of the rear-section system is provided by [Bab12].

2.3.6 The monitor spectrometer

A separate monitor system, the monitor spectrometer set-up, is positioned at a distance of about $20\,\mathrm{m}$ from the KATRIN beam line. This third spectrometer − the refurbished and upgraded MAC-E filter of the former Mainz experiment with a length of $4.0\,\mathrm{m}$, a diameter of $1.0\,\mathrm{m}$, and an energy resolution of $\Delta E \approx 0.93\,\mathrm{eV}$ at $18.6\,\mathrm{keV}$ − precisely monitors high-voltage fluctuations of the retarding voltage applied to the inner wire-electrode layer of the main spectrometer. To do so, a nuclear standard is used as stable β-emitter. At both ends of the monitor spectrometer, two superconducting warm-bore solenoids generate an adiabatic guiding field of $6.0\,\mathrm{T}$ resulting in a 3-G field in the central analyzing plane. There,

Figure 2.5: Monitor spectrometer. The monitor spectrometer is positioned separately from the KATRIN beam line. There, the magnetic guiding field is provided by two superconducting solenoids coaxially arranged on both ends of the spectrometer and by four air coils surrounding the vessel. The middle air coil consists of two layers.

the magnetic field can be fine-tuned by a set of four air coils. The electrostatic retarding potential is applied to an inner solid-electrode and an innermost two-layer wire-electrode system so that the vessel is kept on ground potential. A photograph of the experimental setup is shown in figure 2.5. The nuclear standard for online monitoring of the high-voltage stability is based on 17.8-keV conversion electrons from decay of ^{83m}Kr (K-32 line) in an implanted solid-state ^{83}Rb/^{83m}Kr source [Sle11] [Zbo11] [Sle13]. These monoenergetic electrons are analyzed by the monitor spectrometer with the inner wire-electrode layers being supplied by the same retarding potential as the main spectrometer via a galvanic high-voltage connection. Since the electron energy is significantly lower than the tritium endpoint, the solid-state source is elevated to a potential of about -770 V. Electrons passing the analyzing plane are finally counted by a five-pixel array consisting of individual silicon PIN-diodes arranged on a crosswise geometry. This setup allows to observe high-voltage fluctuations of the main-spectrometer retarding potential on the ppm-scale by continuously recording the K-32 line position, representing a unique atomic and nuclear physics standard [Erh12] [Erh14]. In addition to this method, permanent monitoring of the retarding-voltage is independently achieved by two custom-made precision high-voltage dividers based on the self-compensating principle [Mar01], which are galvanically connected to the main-spectrometer potential. The monitor spectrometer was installed in the period from 2010 to 2012 [Gou10] [Sch11] [Hau13]. Up to now, it has extensively been used to study the long-term stability of the K-32 line with excellent results [Erh14]. Further information on the technical setup of the monitor spectrometer is provided by [Erh14].

2.4 The First Main-Spectrometer Commissioning

A centerpiece of the present thesis has been the first commissioning phase of the main spectrometer in combination with the detector system [Thu14] in the framework of an extensive four-month measurement campaign in mid-2013. This commissioning of the spectrometer and detector section (SDS) has confirmed a proper functioning of the main spectrometer as a MAC-E filter, in particular with regard to its background behavior and transmission characteristics. This success is an important milestone for the KATRIN experiment [Bar14]. A schematic side view of the 30-m long experimental setup is illustrated
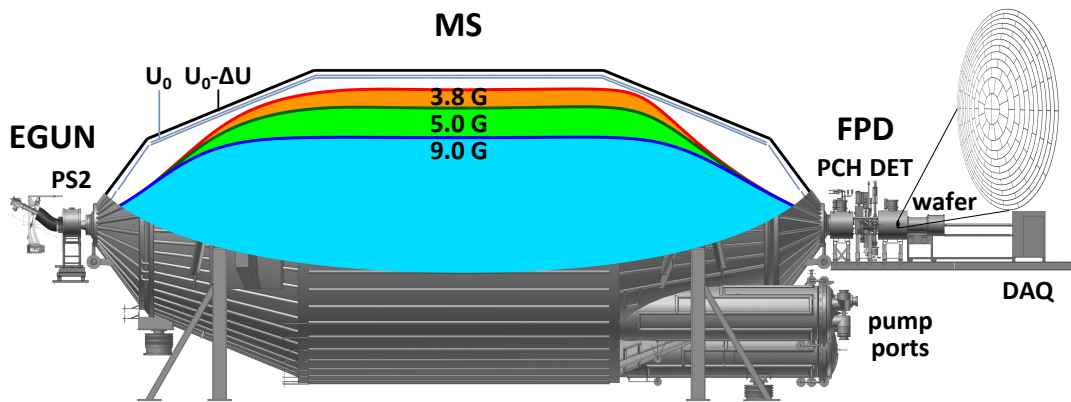
Figure 2.6: The 30-m long experimental setup for the first SDS commissioning phase. The setup consists of several functional units: an angular-selective mono-energetic electron gun (EGUN) to allow for transmission-function and time-of-flight studies, the main spectrometer (MS) as the central component of this commissioning phase, and the focal-plane detector system (FPD) for the almost background-free, highly efficient, and long-term stable detection of transmitted electrons. The three main pump ports house the pumping system required to achieve UHVac conditions. The magnet system consists of four superconducting solenoids (the PS1 magnet is not shown) and a large-scale normally conducting air-coil system (not shown) surrounding the main spectrometer. The shapes of the transported magnetic flux tube for three standard configurations of the first SDS commissioning phase are illustrated. The corresponding flux-tube volumes are as follows: $851.2\,\mathrm{m}^3$ for a field of $B_{\mathrm{ana}} = 3.8\,\mathrm{G}$ (red) in the analyzing plane, $665.1\,\mathrm{m}^3$ for $B_{\mathrm{ana}} = 5.0\,\mathrm{G}$ (green), and $391.8\,\mathrm{m}^3$ for $B_{\mathrm{ana}} = 9.0\,\mathrm{G}$ (blue). The high-voltage system allows to elevate the main-spectrometer vessel and the inner wire electrodes to negative electric potentials with $U_0 < 0\,\mathrm{kV}$. The vessel is typically operated at a slightly more positive voltage than the electrodes with an voltage offset of $\Delta U < 0\,\mathrm{V}$.

in figure 2.6. The main spectrometer as the central component is connected at both ends to individual subsystems. On the upstream side (left side), an angular-selective mono-energetic electron gun [Han13b] is attached, while the detector system (chapter 3) with its segmented 148-pixel silicon wafer is installed at the downstream side (right side). The magnetic guiding and collimation field for the MAC-E filter is provided by four superconducting solenoids. Two of them − the pre-spectrometer magnets PS1 (not displayed in figure 2.6) and PS2 − are located at the entrance side of the main spectrometer, while the other pair − the pinch magnet (PCH) and detector magnet (DET) − is placed at the exit side as an essential part of the detector system. In addition, the main spectrometer is surrounded by two sets of normally conducting air coils [Glu13], the low field correction system (LFCS) and the earth magnetic field compensation system (EMCS). The electric retarding voltage for the MAC-E filter is provided by a complex high-voltage subsystem [Kra14], which allows to elevate both the vessel and the inner double-layered wire electrodes to different potentials. In the following, the vacuum system (section 2.4.1), the magnet system (section 2.4.2), and the high-voltage system (section 2.4.3) are described in more detail as well as typical settings used for commissioning measurements. Further information with regard to the technical setup is provided by [Bar14] [Thu14].

2.4.1 Vacuum System

The main spectrometer is the largest vacuum recipient currently in use and represents the most advanced MAC-E filter for precision electron spectroscopy with energies of up to $35\,\mathrm{keV}$ [Bar14]. Its stainless-steel (grade 316LN/1.4429) vessel, manufactured by *MAN DWE GmbH*, with a maximal outer (inner) diameter of $10.0\,\mathrm{m}$ ($9.8\,\mathrm{m}$), a length of $23.3\,\mathrm{m}$, a volume of $1240\,\mathrm{m}^3$, an inner surface of $690\,\mathrm{m}^2$, and a weight of approximately 200 tons is equipped with a sophisticated vacuum-pumping system [Wol14]. This is based on six

Leybold Turbovac MAG W 2800 turbomolecular pumps (TMPs) and a total of $3\,\text{km}$ of *SAES St 707* non-evaporable getter (NEG) strips with a combined pumping speed for hydrogen of approximately $10^6\,\ell/\text{s}$. The NEG pump, when fully activated, will maintain ultra-high vacuum (UHVac) conditions of $10^{-11}\,\text{mbar}$ for several years [Bar14] [Goe14]. The NEG strips are mounted on a custom-made stainless-steel support structure inside three pump ports which are welded to the downstream conical side of the main spectrometer. Each pump port with an inner diameter of $1.7\,\text{m}$ and a length of $3.0\,\text{m}$ also contains a liquid-nitrogen (LN2) cooled baffle system to prevent the emanation of radon isotopes from the NEG pumps into the vessel by cryogenic sorption. This is an essential passive background-reduction method, since radon emanation generates a non-negligible electron background by α-decays and subsequent ionization of residual gas. In the framework of this thesis, the radon-induced background in the main spectrometer has been investigated in detail (see chapter 6).

A large-scale oil-based heating and cooling system, manufactured by *HTT energy systems GmbH*, stabilizes the vessel at $20\,°\text{C}$ in order to provide long-term stable vacuum conditions. These are permanently monitored by two *Leybold Inficon IE 514* extractor gauges and an *MKS Microvision 2* residual-gas analyzer (RGA), installed at the downstream side of the main spectrometer. The pressure readings of the gauges after thermal bake-out[3] of the entire vessel at $300°\text{C}$ and activation of the NEG pump converged toward a final pressure of $\sim 10^{-10}\,\text{mbar}$. In addition to hydrogen, the vacuum conditions were dominated by water, argon, and nitrogen, due to localized leaks to ambient air [Goe14] and a required venting of the spectrometer after thermal bake-out with gaseous argon [Wol14].

Inside the warm bores of the PS2 and PCH magnets, specially developed beam pipes with in-line flapper valves are installed and attached to the ceramic beam-line insulators of the main spectrometer. This ensures a surge-proof connection of the main spectrometer to the grounded electron gun and detector system, respectively. In addition, full-metal gate valves are installed at the entrance and exit sides to allow a proper separation of the individual subsystems from the main spectrometer in order to perform accurate background measurements and stand-alone detector calibrations.

2.4.2 Magnet System

The major contribution to the magnetic flux tube within the spectrometer and detector section is provided by two pairs of superconducting solenoids, while a smaller part for fine-tuning stems from a complex system of air coils. The magnetic-field lines are oriented into a direction from detector to source.

The solenoids are arranged coaxially to the beam line with the beam tube being installed in their warm bores. The first solenoid pair, PS1 and PS2, manufactured by *Cryogenic Ltd.*, is located at the entrance side of the main spectrometer, while the second pair, PCH and DET, manufactured by *Cryomagnetics Inc.*, is placed within the detector system. Both pre-spectrometer magnets are regulated directly by high-current power supplies in driven mode[4] generating a magnetic field of $B_{\text{PS1}} = 3.0\,\text{T}$ and $B_{\text{PS2}} = 4.3\,\text{T}$, respectively, in the corresponding bore center. By contrast, both detector magnets are operated in persistent mode[5] producing a magnetic field of $B_{\text{PCH}} = 5.0\,\text{T}$ and $B_{\text{DET}} = 3.5\,\text{T}$, respectively. Among the four superconducting solenoids, the PS2 and PCH magnets form the magnetic flux tube

---

[3]A thermal high-temperature bake-out of the main spectrometer is required to artificially release violate compounds and drive off gases from inner surfaces by the active vacuum pumping system, as well as to activate the NEG pump.

[4]In driven mode, the superconducting coil is powered continuously by the magnet power-supply unit.

[5]In persistent mode, the superconducting coil is short-circuited and thus insulated from the magnet power-supply unit. Further details are given in section 3.2.3.

Table 2.1: Common solenoid settings for the first SDS commissioning phase. Shown are the axial design position z, the coil current I and the resulting magnetic field B in the warm-bore center of each superconducting solenoid.

solenoid	z (m)	I (A)	B (T)
PS1	-15.5000	103.8	3.0
PS2	-12.1038	149.7	4.3
PCH	12.1835	72.6	5.0
DET	13.7835	54.6	3.5

within the MAC-E filter. This results in a field asymmetry, since $B_{\mathrm{PS2}} < B_{\mathrm{PCH}}$, so that the accepted solid angle for electrons at the entrance side is larger than at the exit side. Therefore, stored electrons in the main-spectrometer volume will more likely escape toward the source, thereby reducing observable background. The sensitive size of the analyzing plane which is mapped onto the wafer can be changed by varying the magnetic field of the DET magnet. The detector wafer with a sensitive diameter of 90 mm is typically placed in a magnetic field of $B_{\mathrm{wafer}} \approx 3.2\,\mathrm{T}$ at a downstream position within the warm-bore center of the DET magnet, thus covering a magnetic flux of $205\,\mathrm{Tcm^2}$. For future neutrino-mass measurements, the solenoids can be operated at even higher magnetic fields with $B_{\mathrm{PS1}} = B_{\mathrm{PS2}} = 4.5\,\mathrm{T}$, $B_{\mathrm{PCH}} = 6.0\,\mathrm{T}$ and $B_{\mathrm{DET}} = 3.6 - 6.0\,\mathrm{T}$. The actual positions and orientations of the magnet cryostats are referenced relatively to the analyzing plane of the main spectrometer at $z = 0\,\mathrm{m}$. To do so, extensive alignment measurements were performed with a *FaroArm* [Far14] and a laser tracker [Jur12]. This is of special interest for the alignment of the detector system relative to the main spectrometer. This issue is discussed in more detail in section 4.9. The reference currents and design positions of the solenoids for the first SDS commissioning are summarized in table 2.1.

The normally conducting air-coil system with its functional units, the low field correction system (LFCS) and the earth magnetic field compensation system (EMCS), allows to fine-tune the magnetic-field shape in the low-field region of the MAC-E filter. This is essential for the spectrometer transmission properties, as the air coils guarantee the adiabatic transport of electrons through the main spectrometer for each selected electric potential. In addition, the LFCS allows to compensate the field asymmetry caused by the superconducting solenoids PS2 and PCH, and to improve the magnetic field homogeneity and symmetry in the analyzing plane. In contrast, the EMCS is arranged perpendicularly to the beam line. It consists of two cosine coil subsystems: the vertical EMCS, being built of 16 current loops with horizontal planes, and the horizontal EMCS, being made of 10 loops with vertical planes. The task of the EMCS is to compensate the vertical and horizontal transverse component of the earth magnetic field within the MAC-E filter with $B_{\mathrm{ver}} = 436\,\mathrm{mG}$ and $B_{\mathrm{hor}} = 50\,\mathrm{mG}$, respectively. Each of the 16 air coils is connected to an individual *Delta Elektronika SM3000* power supply to allow a flexible and versatile shaping of the magnetic field. Most of the power supplies are limited to a maximum current of 100 A, corresponding to a maximum magnetic field of $B_{\mathrm{ana}} \approx 10\,\mathrm{G}$ in the analyzing plane. During the first SDS commissioning, the main-spectrometer characteristics were investigated at three different settings for the LFCS air-coil currents. As visible in figure 2.6, this results in specific magnetic fields in the analyzing plane and, hence, in different sensitive flux-tube volumes. The EMCS air-coil currents were however static and usually set to $I_{\mathrm{ver}} = 50.0\,\mathrm{A}$ and $I_{\mathrm{hor}} = 9.1\,\mathrm{A}$ to fully compensate the earth magnetic field. The actual alignment of the air-coil system to the main-spectrometer axis is determined by adequate laser-tracker measurements [Jur12]. The adjusted currents[6] and actual positions

---

[6]The optimization of the LFCS air-coil currents is based on magnetic field-line calculations [Sta13], thereby

Table 2.2: Common LFCS settings for the first SDS commissioning phase. Shown are the axial position z and the optimized current (in A) of each LFCS air coil for three different magnetic field strength B_{ana} in the analyzing plane. The LFCS air coils are numbered from the upstream side of the main spectrometer to the downstream side. The EMCS air-coil currents are usually set to $I_{\mathrm{ver}} = 50.0\,\mathrm{A}$ and $I_{\mathrm{hor}} = 9.1\,\mathrm{A}$ to compensate the static earth magnetic field.

LFCS air coil	position z (m)	LFCS air-coil currents (A)		
		$B_{\mathrm{ana}} = 3.8\,\mathrm{G}$	$B_{\mathrm{ana}} = 5.0\,\mathrm{G}$	$B_{\mathrm{ana}} = 9.0\,\mathrm{G}$
#1	-6.788	28.6	60.1	95.2
#2	-4.938	24.0	15.4	99.8
#3	-4.040	17.3	24.3	48.9
#4	-3.139	22.1	41.8	98.8
#5	-2.238	33.5	47.4	100.0
#6	-1.338	36.4	77.4	74.0
#7	-0.442	35.8	29.7	98.2
#8	0.456	54.1	52.1	96.6
#9	1.354	10.2	58.0	80.9
#10	2.256	52.1	48.6	90.4
#11	3.156	32.0	54.8	61.3
#12	4.058	20.1	23.8	99.0
#13	4.952	29.8	46.0	97.6
#14	6.755	-51.8	-50.9	-36.2

of the LFCS air coils are summarized in table 2.2.

A major result of the magnetic guiding field is the extremely effective magnetic shielding which is by far the dominant suppression mechanism for low-energy electron background generated at the inner vessel surface by cosmic rays, natural environmental radiation, intrinsic radioactivity, and field emission. The expected magnetic shielding factor for the sensitive volume of the magnetic flux tube is in the order of 10^5.

In addition, the individual air-coil currents can be inverted on very short time scales by flip boxes [Beh14] plugged in to the power supplies resulting in a short *magnetic pulse*. With this active background reduction method, stored high-energy electrons in the energy range of several keV can be efficiently removed from the magnetic flux tube [Wan13a] at the expense of a small reduction of effective measurement time.

2.4.3 High-Voltage System

The entire vessel is elevated to negative high voltage in order to provide the retarding potential for the main spectrometer. Therefore, the vessel support structures are insulated against high voltage of up to $-35\,\mathrm{kV}$. At both sides, the main-spectrometer beam line is insulated with ceramic cones to allow its connection to the grounded electron gun and the grounded detector system via two custom-built beam pipes housing in-line flapper valves. Inside the vessel, a double-layered quasi-massless electrode system has been installed, consisting of more than 23000 wires with diameters of 200 and 300 μm. The system is mounted on 248 modules distributed on 15 rings arranged coaxially to the beam line. It covers the entire inner surface of the main spectrometer. The actual alignment of the wire-based electrode system relative to the main-spectrometer axis was obtained by adequate laser-tracker measurements [Jur09]. The wire electrodes are elevated to a slightly more negative electric potential than the vessel with a maximum potential difference of 1 kV applicable.

---

ensuring the spectrometer transmission properties.

This allows to electrostatically shield against low-energy knock-on electrons released from the inner vessel surface by cosmic rays, natural environmental radiation, intrinsic radioactivity, and field emission. Therefore, in addition to the dominant magnetic shielding, a further electric shielding factor in the order of up to 10^2 is expected. Analogous to the air-coil system for magnetic fields, the wire-based electrode system is used to fine-shape the applied retarding potential in order to optimize electron transmission conditions and filter properties. It also allows to improve the homogeneity and axial symmetry of the electrostatic field in the analyzing plane, in particular by compensating inevitable deviations from perfect roundness of the main-spectrometer vessel. Furthermore, the generation of Penning traps (section 2.5.2) close to the inner vessel surface and electronic noise originating from devices attached to the vessel are greatly suppressed [Bar14]. The electrode system is divided into two half shells oriented in horizontal direction with a maximum potential difference of $1\,\mathrm{kV}$ to be applied between the two halves. Static or pulsed electric dipole can be applied [Hil14], so that stored low-energy electrons in the sub-keV range are efficiently removed by the resulting $\vec{E} \times \vec{B}$ drift [Wan13a]. The wire-electrode system is complemented at both sides with full-metal ground electrodes made of high-purity aluminum and field-correction anti-Penning electrodes made of titanium.

Due to thermally induced deformations of the inner high-voltage distribution lines made of beryllium copper (BeCu), electrical short circuits between the two wire layers of almost all electrode rings developed [Han13a] during the bake-out phase of the main spectrometer in January 2013 [GTW13]. Therefore, the main-spectrometer characteristics had to be investigated with the same electrical potential applied to both wire layers during the first SDS commissioning phase. Consequently, the large surface of the main-spectrometer vessel can be electrostatically shielded by the two-layer wire electrodes, but the massive support structure of the electrode system is no longer shielded by the innermost wire layer. The short circuit between both wire layers is expected to result in less effective shielding, yielding an increase in the total background rate by a factor of ~ 10 as compared to a fully functional two-layer system. In addition, as it will be shown in chapter 7, parts of this support structure have been localized as a likely source for field electron emission when operating the electrode system at large offset voltages beyond the nominal values required for reliable long-term neutrino-mass measurements. A detailed description of the short circuits [Han13a], the associated consequences for the first SDS commissioning phase [Beh13], and a recently successfully implemented repair for the cylindrical spectrometer part in view of the upcoming second SDS commissioning phase [HT14] can be found in the corresponding references.

Both the main-spectrometer vessel and the inner wire electrodes require precise and stable high voltages at the ppm-level distributed via a sophisticated high-voltage system [Kra14]. It provides up to 46 separate offset voltages as shown in figure 2.7, illustrating the high-voltage scheme for the first SDS commissioning phase. The vessel is operated at a common potential provided by a single high-voltage power supply, while the individual inner electrode rings can be elevated to different potentials, resulting from the sum of the common, dipole, and offset potentials. The latter potentials are delivered by numerous additional low-voltage power supplies working with high precision of $\leq 10\,\mathrm{mV}$ when regulated at voltages above $\sim 0.5\,\mathrm{V}$. However, during the first main-spectrometer commissioning, only the common and dipole power supplies were usually used to apply the retarding potential to the main spectrometer, while the offset power supplies were operated at $\sim 0\,\mathrm{V}$. In this case, the potential difference ΔU between vessel and electrodes is given by the dipole potential. The limited precision and reproducibility in this voltage range resulted in small potential deviations of $\lesssim 0.4\,\mathrm{V}$ appearing between the two half shells of the inner electrodes. This induced a permanent static electric dipole of $\lesssim 40\,\mathrm{mV/m}$ over the main-spectrometer volume [Gro14]. The corresponding influence on the electron background on the basis of a
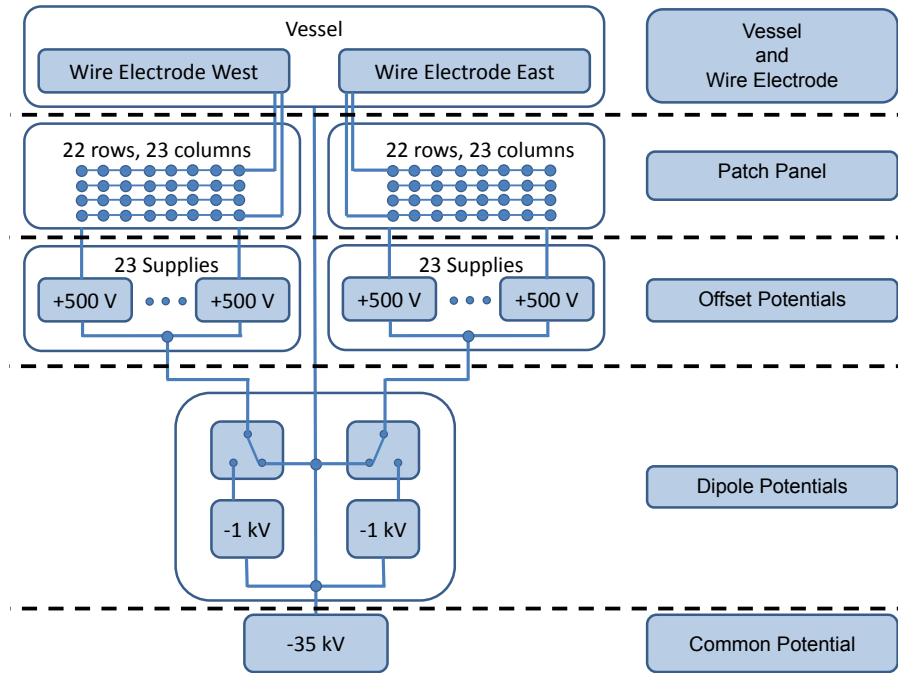
Figure 2.7: High-voltage distribution system for the first SDS commissioning phase. The main-spectrometer vessel is elevated by a single high-voltage power supply (*common potential*). The two half shells of the inner electrodes are separately operated by two power supplies (*dipole potentials*), supported by the common potential. Two high-voltage relays enable the application of a pulsed dipole between the two half shells. Additional offset power supplies allow to elevate the individual inner electrode rings to slightly different potentials (*offset potentials*) via an adequate hard-wired configuration at a patch panel. Sketch taken from [Bar14].

distortion of the axial symmetry of the electrostatic field will be investigated during the upcoming second SDS commissioning phase. There, the application of identical potentials to each electrode ring will be ensured.

2.5 Background Processes in a MAC-E Filter

As outlined above, the KATRIN experiment will investigate the tritium β-decay energy spectrum close to the endpoint in a low statistics region. Thus, it is extremely sensitive to a variety of background processes. Despite the high luminosity of 10^{11} β-electrons per second of the WGTS, generic low signal count rates of only 20 mcps are expected, since only a tiny signal fraction of 2×10^{-13} contributes to the most relevant energy region few eV below the endpoint. In order to achieve a neutrino-mass sensitivity of $m_\nu = 200$ meV at 90 % C.L., a signal-to-background ratio in this region of 2:1 is required, resulting in a maximum tolerable total background rate of 10 mcps only.

The background originates primarily from the inner surface of the main spectrometer through low-energy electrons generated by cosmic-ray muons and by volume-induced processes from radioactive decays of unstable neutral atoms. In both cases, low-energy electrons in the eV-range are being produced in the sensitive volume of the flux tube. Electrons leaving this region are being accelerated by the applied retarding potential and produce a distinct peak in the region of interest of the detector energy spectrum. Thus, they completely overlap the measured energy spectrum of signal electrons. By contrast, the less dominant detector background is an almost featureless continuum. An overview of known background sources including passive and active counter measures within the KATRIN setup is given in the following.

2.5.1 Detector-Related Backgrounds

Two generic and well-known sources of detector-related backgrounds are cosmic rays and natural radioactivity [Sch04] [Leb10]. Each source generates neutral (γ) and charged (e^-) particles with different energy and angular distributions. These particles are not correlated with the beam of signal electrons from the main spectrometer and are expected to result in an almost featureless continuum labeled *detector background*.

Cosmic rays. Major background contributions of cosmic rays at sea level are muons [Miy73], photons and electrons of the electromagnetic component [DS74], and nucleons of the hadronic component [YSP66] [Ber13]. Muons as minimum ionizing particles can easily penetrate through a few centimeters of lead, while the electromagnetic component is reduced in intensity. In a MAC-E filter, these primary particles are usually of less concern. However, primary particles can produce further secondary knock-on particles from the inner surfaces surrounding the detector as additional background component. By contrast, other components like neutrinos and pions make negligible contributions [Leb10].

Natural radioactivity. Natural radioactivity is present in the form of small trace amounts of primordial and cosmogenic radioactive isotopes within the detector components, the experimental hall, and the environment. Such isotopes decay by emitting radiation with energies of up to 3.6 MeV. Low-energy X-rays near the region of interest are of particular concern, while high-energy MeV-gammas can Compton-scatter in or near the wafer. Primordial radionuclides, such as ^{238}U, ^{232}Th, and ^{40}K, feature long half-lives of up to billions of years, thus being a major background contribution not only in the detector system described in the present thesis but in all other low-level background applications. Cosmogenic radioactivity, where cosmic rays interact with nuclei of structural materials near the detector to produce unstable isotopes, plays a minor role however [Leb10].

Background suppression. In order to minimize the detector background ab initio, all construction materials in the proximity of the detector system including both superconducting solenoids are carefully selected and radio-assayed very thoroughly before installation. Furthermore, the detector wafer is spatially separated from the pre-amplifier electronics by a copper-shielded feedthrough flange to suppress incident radiation from the less radio-pure electronic units. The vacuum chamber of the detector system is thus surrounded by a passive, cylindrical radiation shield consisting of 3-cm thick lead and 1.27-cm thick oxygen-free high-conductivity (OFHC) copper to shield incident gammas from natural environmental activity. This is supplemented by an active, cylindrical veto system built of 1-cm thick plastic scintillators to tag incident cosmic muons. A trumpet-shaped post-acceleration electrode made from electro-formed copper is installed in front of the detector wafer to allow the signal electrons to be shifted to higher energies with more favorable background rates. Making full use of the active veto detector, active background-reduction cuts based on anticoincidence methods are applied to the raw background data to reject correlated events. The total intrinsic detector background rate is defined by the recorded rate in a particular region of interest in the measured energy spectrum. However, as will be outlined in more detail later, the width of this acceptance window depends on a trade-off between the background rate, the detection efficiency, and the energy resolution of the detector. By improving the energy resolution, for example, the width of the region of interest is narrowed resulting in a smaller background rate. During commissioning measurements of the standalone detector system, an upper limit of the intrinsic detector background rate of ~ 6 mcps within a 5.5-keV wide region of interest could be established. The detailed investigation of the intrinsic detector background and its characteristics is one of the major objectives of the work in hand; it is discussed in more detail in chapter 5.

### 2.5.2 Spectrometer-Related Backgrounds

There are three generic and well-known background sources that can occur in a MAC-E filter on the basis of different production mechanisms: Penning traps, magnetically stored particles, and electron emission from inner surfaces. Initially, particles from these sources usually have low energies of less than 1 keV when created in the main-spectrometer volume. However, as outlined above, these particles are accelerated by the applied retarding potential toward the detector and produce a distinct peak in the region of interest of the detector energy spectrum. In the following, the spectrometer-related background sources are summarized and described in more detail.

Penning traps   are localized volumes in which charged particles are stored by a combination of electrostatic and magnetostatic fields (see figure 2.8 left). In such traps, particles are electrically confined in axial direction and magnetically in radial direction. This enforces a cyclotron motion of the trapped particles along the magnetic field lines while being repelled by the electric potential wells. These particles can produce background via messenger particles, such as ions or photons, which leave the trap to produce further secondary and tertiary particles inside the sensitive magnetic flux-tube volume. This can result from ionization of residual gas, thus contributing to the measured background at the detector. In an extreme case, unstable plasmas can be generated, even leading to vacuum breakdowns, known as Penning discharges [Pen36] [Hae53a] [Hae53b] [Har89] [Pic92] [Bel95] [Byr05]. The formation of Penning traps is of major concern for KATRIN and has been greatly suppressed by implementing a precise and fine-tuned electromagnetic design [FGV14]. Both the sophisticated wire-electrode system and the complex set of air coils allow a fine-shaping of both the electrostatic and magnetostatic fields inside the main spectrometer. A detailed description of small Penning traps including a model characterizing the mechanisms of trap filling and subsequent background production is provided by [Hil11] [Mer12a].

The tandem filter system in the later neutrino-mass measurements consisting of the pre-spectrometer adjacent to the main spectrometer forms an inherent large-volume Penning trap between the spectrometers when both are operated at highly elevated negative potentials [Ang05]. The installation of a grounded wire scanner wiping through the trap in regular intervals is intended to remove stored electrons in this volume. This should significantly reduce the associated background production [BV10], but it remains to be proven that a stable operation at a background level of 10 mcps is possible in this configuration. When discarding the option to use the pre-spectrometer as a pre-filter by operating it at low or even zero retarding potential, the formation of this Penning trap is completely eliminated [Mer12a].

A major success of the first SDS commissioning measurements was that no evident Penning traps or Penning discharges were observed in the entire main-spectrometer volume when operating the system under nominal electric-field and magnetic-field settings [Bar14] [Kra14]. This is due to a careful electromagnetic design based on *Kassiopeia* [FG14] simulations, experiences, and lessons learned at the pre-spectrometer set-up [Fra10b] [FGV14].

Magnetically stored particles   are electrons trapped inside the volume of a MAC-E filter as a result of the characteristic shape of the magnetic flux tube acting as a magnetic bottle. A magnetic bottle is formed by two magnetic mirrors [Hig07] [Hig08] placed closed together (see figure 2.8 right). The magnetic mirror effect causes a charged particle to be magnetically reflected toward a lower magnetic field when reaching a region with strong magnetic field and its longitudinal momentum completely vanishes. Such a particle can be released from the magnetic trap when its transverse momentum decreases over time, e.g. due to interactions with residual gas atoms and molecules, which induces a cool-down of the particle [Wan14]. In case of the main spectrometer, the magnetic field drops by more

Penning trap   **magnetic-mirror trap**
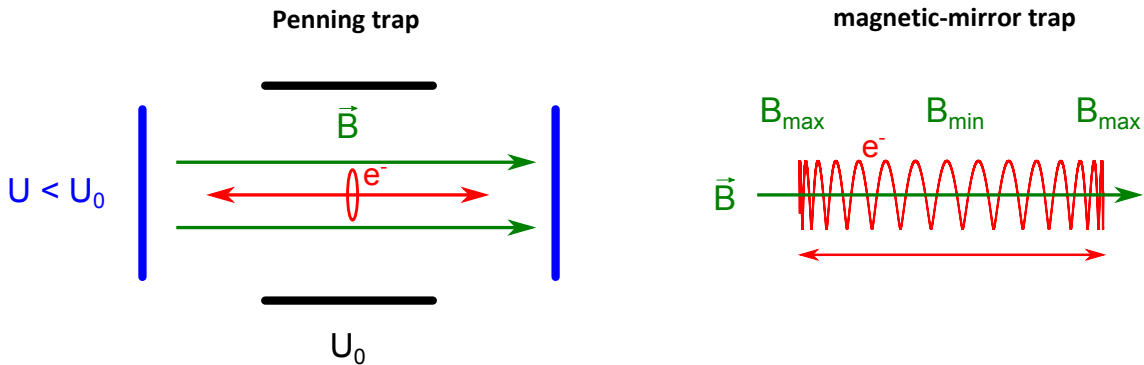
Figure 2.8: Particle trapping in a MAC-E filter. Due to the characteristic electromagnetic design of a MAC-E filter, electrons can be trapped inside a specific region of the spectrometer volume. **Left: Penning trap.** A Penning trap is formed by a combination of electrostatic and magnetostatic fields. **Right: Magnetic mirror trap.** A magnetic mirror trap is formed by a combination of two magnetic mirrors placed closed together. Figures adapted from [Gro10].

than four orders of magnitude from the entrance ($4.5\,\text{T}$) and exit ($6.0\,\text{T}$) to the analyzing plane ($3.0 \times 10^{-4}\,\text{T}$). This magnetic-field configuration forms a strong magnetic bottle where electrons can be stored over long periods of time after being created inside the main-spectrometer volume, e.g. by radioactive decays. Due to scattering off residual gas, the primary electrons cool down over time, thus producing additional secondary electrons along their trajectory. These secondaries can be magnetically stored as well. This continues until the electrons are released from the magnetic bottle and electrostatically accelerated by the retarding potential toward the detector. Owing to the excellent UHVac conditions of $10^{-11}\,\text{mbar}$ inside the main spectrometer, the storage time of primary keV-electrons can reach up to several hours, resulting in hundreds of produced low-energy secondary electrons [Mer12a] [Mer13] [Wan13a]. The major sources of primary electrons are single radioactive decays of tritium and radon, occurring in the main-spectrometer volume:

- **Tritium β-decay:** Although the tritium gas flux from the WGTS is suppressed by 14 orders of magnitude through the transport section and most of the remaining tritiated molecules entering the spectrometer section are pumped out on short time scales by the NEG pumps, a small fraction can decay and produce β-electrons with energies of up to $18.6\,\text{keV}$ inside the sensitive flux-tube volume. Depending on their initial transverse momentum, these electrons are magnetically trapped and produce further secondary electrons. Investigations of tritium-related backgrounds is provided by [Mer12a] [Mer13] [Wan13a].

- **Radon α-decay:** All materials with large surface areas, such as the NEG pumps and the inner main-spectrometer surfaces with their welding seams are major sources of emanation of the neutral radon isotopes ^{219}Rn, ^{220}Rn, and ^{222}Rn. Upon emanation these noble gas atoms propagate through the main spectrometer with thermal velocity. When undergoing α-decay, a radon atom can emit electrons with energies ranging from a few eV to several hundreds of keV. These primary electrons are magnetically trapped and can produce further secondary electrons if their energy is above the ionization threshold of the residual gas species. This background component can be significantly reduced by an LN2 cooled baffle system which is installed between the pump ports housing the NEG pump and the sensitive main-spectrometer volume. This is achieved by cryogenic sorption of emanated radon onto the cold baffle surfaces [Goe10] [Goe14]. Since the baffle system operates as a large-scale cryopump, this passive background-reduction method is highly effective to radon emanation from the NEG material and from the inner structural materials [Bar14]. The in-

vestigation of radon-induced background resulted in a detailed physics models in the pre-spectrometer commissioning measurements described in [Fra10b] [Mer12a] [Wan13a]. Obviously, the experimental investigation of radon-induced background in the first SDS commissioning phase was of major interest for the KATRIN experiment and is also one of the major objectives of the work in hand. The results are presented in chapter 6.

In addition to passive background-suppression approaches, there are several active background-reduction techniques in order to remove remaining magnetically trapped electrons from the flux-tube volume before they can produce further low-energy secondary electrons. In this context, a static or a periodically pulsed electric dipole can be applied [Mue02] [Thu02] [Fla05] [Wan13a] [Hil14] as well as a magnetic pulse [Wan13a] [Beh14], and the method of electron cyclotron resonance has successfully been applied to the pre-spectrometer [Mer12a] [Mer12b]. These active methods typically require only a short duty cycle and reduce data-taking time accordingly.

Electron emission from inner surfaces of the walls of the main-spectrometer vessel and the low-mass wire electrodes with their large areas of $690\,\mathrm{m}^2$ and $460\,\mathrm{m}^2$, respectively, is of primary concern for the KATRIN experiment. These electrons are primarily induced by cosmic rays, and to a much lesser extent by environmental radiation and intrinsic radioactivity. However, in specific cases field electron emission becomes important:

- **Secondary emission:** Cosmic rays, high-energetic gammas from natural environmental radiation, and radioactive decays of primordial and cosmogenic nuclei in the structural materials can produce cascades of low-energy secondary electrons by interactions with the inner stainless-steel surfaces. The background components are described in more detail in [Lei10] [Mer12a] [Wan13a] [Lei14].

- **Field electron emission:** Surface roughness and irregularities as well as sharp edges at the inner wire electrodes being elevated to negative high voltage are capable to generate high electric fields within a narrow volume. This can result in the process of field electron emission [For12], where low-energy electrons leave the stainless-steel surface by quantum tunneling [Raz03]. The investigation of this background component is described in chapter 7 on the basis of measurements from the first SDS commissioning phase.

In both cases, low-energy electrons are released from the inner surface of the main spectrometer. However, these electrons are mostly reflected back to the wall by magnetic shielding, because of the Lorentz force acting. In addition, there is the effect of electric shielding due to a negative voltage offset applied between the vessel and the wire electrodes, forming an electrostatic barrier for low-energy electrons. In general, however, the presence of non-axially symmetric field components [Lei10] from a variety of field disturbances [Rei09a] [Rei13] reduces these shielding effects. Thus, electrons emitted from inner surfaces can propagate into the sensitive flux-tube volume via radial $\vec{E} \times \vec{B}$ and $\vec{\nabla}|\vec{B}| \times \vec{B}$ drift motions. There, they can be magnetically stored and ionize residual gas before escaping, or directly leave the magnetic bottle upon release. They are then accelerated by the retarding potential, and, hence, are adiabatically guided to the detector [Mer12a]. Finally, this results in an electron-emission induced background peak in the same region of interest of the detector energy spectrum as signal electrons. As noted above, the magnetic shielding with an expected shielding factor of 10^5 is more effective than the electric shielding with a factor of 10^2 only. However, the above mentioned drift processes can substantially lower these factors in case of considerable non-axially symmetric field components.

Further spectrometer-related backgrounds originate from the ionization of residual-gas atoms and molecules by signal electrons and by positive ions, leading to the generation

of secondary electrons. These background components are expected to be extremely small with rates of ~ 0.1 mcps because of the excellent UHVac conditions of $\sim 10^{-11}$ mbar inside the main-spectrometer volume. When operating the system at a significantly higher pressure, these background processes could be mitigated by using the pre-spectrometer as an electrostatic pre-filter to limit the number of signal electrons entering the main spectrometer. In this case, however, a wire scanner has to remove electrons from the Penning trap between both spectrometers.

Setup of the KATRIN Detector System

The KATRIN detector system was designed by the international collaboration of the Karlsruhe Institute of Technology (KIT), the Massachusetts Institute of Technology (MIT) (Boston, USA), the University of North Carolina (UNC) (Chapel Hill, USA), and in particular the University of Washington (UW) (Seattle, USA). It was assembled and commissioned with somewhat lessened requirements compared to design specifications for the KATRIN experiment at UW in spring 2011 [Leb10] [Wal13] before being delivered to KIT in summer 2011 [Har12]. This thesis describes the final installation and integration of the detector system into the KATRIN beam line, its optimization by implementing key upgrades, and its subsequent, comprehensive characterization, ending in spring 2013. It also includes the first successful commissioning measurements with the attached main spectrometer performed in summer 2013. An overview of the completely assembled detector system located at the downstream end of the KATRIN experiment is given in figure 3.1.

The major milestones for the detector system after shipping to KIT have been the successful operational readiness review of the detector system in March 2013, doing so as the first main component of the KATRIN experiment. This has been followed by the its successful first attachment to the main spectrometer in May 2013, and its stable long-term operation during the first commissioning of the combined spectrometer and detector section (SDS) over a four-month measurement campaign.

The focus of this chapter is put on the sophisticated setup of the detector system consisting of several major functional components. Section 3.1 gives an overview of the detector system with the setup being schematically illustrated in figure 3.2. A description of the primary system components including the investigation of their performance and performed upgrades is provided in the subsequent sections. Further details are described in [Ams14] [Cen12] [Cen13] [Cen14].

3.1 Overview

The task of the detector system is to count β-electrons which have been high-precision filtered by and transmitted through the main spectrometer in an almost background-free, highly efficient, and long-term stable mode of operation. Transmitted electrons are adiabatically guided toward the detector wafer by the magnetic fields of two superconducting solenoids (section 3.2): the pinch magnet (PCH) and the detector magnet (DET), the latter marking the downstream end of the beam line. Both magnets are aligned coaxially to the beam line with the beam tube being implemented in their warm bores. The electron signal, and thus the region of interest, can be shifted to a higher energy with a potentially

Figure 3.1: Detector system completely assembled, prior to its connection to the main spectrometer. The detector system constitutes the downstream end of the KATRIN experiment. In the background, the main spectrometer is visible. Picture adapted from [Har12].
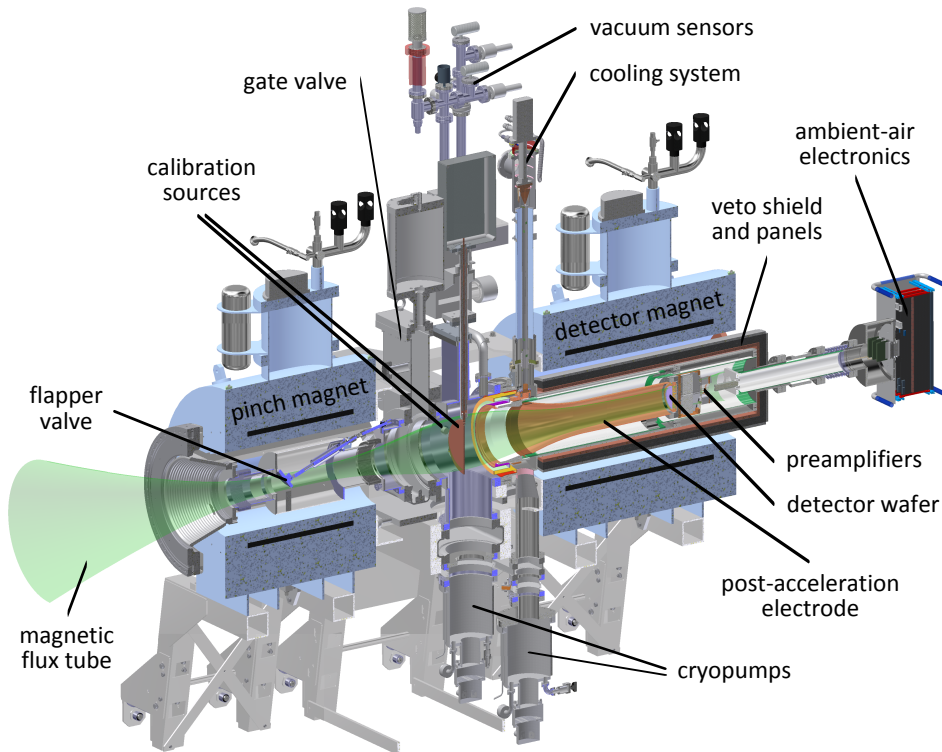
Figure 3.2: Setup of the detector system. The primary components of the detector system are schematically illustrated: two superconducting magnets, an ultra-high vacuum system, a post-acceleration electrode, the detector with its electronics, a cooling system, two calibration sources, a passive shield and an active veto system. In addition, the 191-Tcm^2 flux tube is indicated. The main spectrometer is not shown but located on the left. Drawing adapted from [Ams14].

more favorable intrinsic background rate by a post-acceleration electrode (section 3.4) located in front of the detector wafer. Being an integral component of the vacuum system (section 3.3), this electrode separates the ultra-high vacuum (UHVac) chamber of the detector system from its high vacuum (HVac) chamber, while the whole vacuum system is installed inside and between the warm magnet bores. The UHVac chamber, as part of the KATRIN beam line, is connected to the downstream end of the main spectrometer via a specially developed beam tube with an in-line flapper valve. It also houses the detector wafer, a multi-pixel PIN diode array (section 3.5). The HVac chamber contains the first stage of readout electronics including the feedthrough to the ambient-air electronics (section 3.6) and the data-acquisition (DAQ) system (section 3.7). Both the detector wafer and the preamplifier electronics are continuously being cooled by a custom-built heat pipe (section 3.8) which is attached to the vacuum system between both magnet cryostats. The detector response can be measured and monitored by a modular, independent calibration system (section 3.9) consisting of a γ-emitter and an electron source, both of which can be temporally moved into the magnetic flux tube without breaking the vacuum. A cylindrical passive shield and an active veto (section 3.10) surround sensitive parts of the UHVac and HVac chamber to reduce background originating from natural environmental radioactivity and cosmic rays. The entire detector system is mounted on rails, which simplifies construction work and allows permanent connection to the main spectrometer, even during bake-out phases where the spectrometer thermally expands in the direction of the detector system by several centimeters.

3.2 Magnet System

3.2.1 Electromagnetic Design Constraints

As outline above, the adiabatic guiding field in the detector system is provided by two superconducting solenoids, the pinch magnet (PCH) and the detector magnet (DET). Each solenoid can generate a magnetic field of up to 6.0 T. However, during neutrino-mass measurements, the designed nominal field settings are $B_{\mathrm{PCH}} = 6.0\,\mathrm{T}$ and $B_{\mathrm{DET}} = 3.6\,\mathrm{T}$. The stray field of the pinch magnet is also used to form the downstream part of the magnetic field within the main spectrometer. It delivers the largest guiding field in the entire KATRIN setup so that magnetically stored electrons inside the main-spectrometer volume have a preference to escape toward the source. This fact passively reduces the measured background rate. In addition, the maximum field of the pinch magnet limits the maximum acceptance angle of signal electrons to 50.8° as described in section 2.2. The physical size of the image of the analyzing plane at the wafer can be changed by modifying the magnetic field B_{DET}, i.e. a higher field leads to a smaller image size there, but also to larger impact angles of incident electrons. The wafer is placed 17 cm downstream of the detector-magnet center at a field of 3.3 T, so that it completely covers a flux of 210 Tcm^2. This off-center installation reduces backscattering effects from the wafer. Figure 3.3 illustrates the calculated magnetic field map and the sensitive magnetic flux tube within the detector system, using *Kassiopeia* [FG14].

3.2.2 Magnet Setup and Operation

Both recondenser-type solenoids (PCH, DET) [CB11] were manufactured by the US company *Cryomagnetics Inc.* based at Oak Ridge, Tennessee. The warm-bore cryostats are arranged coaxially to the beam line on individual rollable racks and are made of stainless steel to reduce intrinsic radioactivity. Aluminum spreader bars separate the cryostats and bear up against the attractive magnetic force of 54 kN when both magnets are operated at full field. Each cryostat consists of an outer insulating-vacuum space (0.1 mbar) containing a multilayer thermal shield, and an inner liquid-helium vessel which houses the
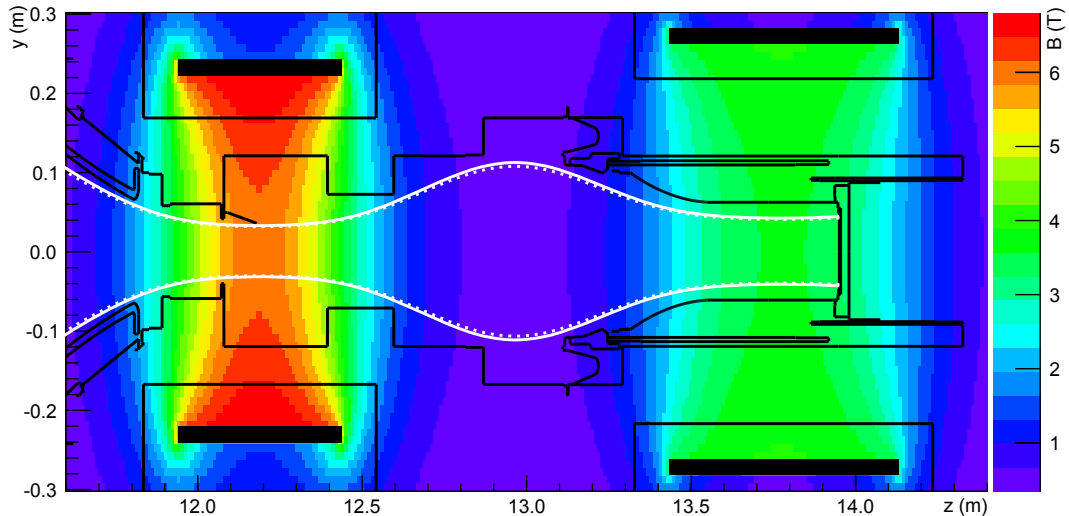
Figure 3.3: Magnetic field map of the detector system. The beam line (black lines) is designed such that the sensitive magnetic flux tube (white solid curve: $210\,\mathrm{Tcm^2}$, white dotted curve: $191\,\mathrm{Tcm^2}$) passes the detector system without touching the inner surfaces. Calculation performed by the author, using *Kassiopeia* [FG14].

mounted superconducting coil. Each coil is made of a twisted multifilamentary NbTi/Cu wire including an attached bare NbTi persistent current switch that allows the operation in either driven or persistent mode (see section 3.2.3). Both coils are cooled to a nominal operating temperature of $4.2\,\mathrm{K}$ with a bath of liquid helium. Each cryostat is equipped with a *Cryomech PT410* two-stage pulse tube cryocooler [Cry14], powered by a *Cryomech CP2800* water-cooled compressor that provides for shield cooling and helium recondensing [Cry11], and a heating element that regulates the pressure inside the inner vessel at $15.10\,\mathrm{psia}$ ($1041.1\,\mathrm{mbar}$), measured by an *Omegadyne PX319-030AI* pressure transducer [Ome14]. The liquid-helium level can be temporarily determined by a mounted single filament of NbTi whose dropped voltage is taped by a *Cryomagnetics LM-500* read-out unit [Cry04]. In addition, a set of Pt-100 and RuO_2 sensors are placed at relevant locations within the cryostats to allow permanent monitoring of temperatures. Each solenoid can be ramped up with a *Cryomagnetics 4G* superconducting magnet power-supply unit (PSU) and is usually operated in persistent mode [Cry09]. In case of a quench, gaseous helium can exit through attached relief valves. Furthermore, an ingenious quench recording system measures the voltage across the coil with a kHz-sampling rate. The characteristics of the two solenoids are summarized in table 3.1. Further details of the magnet setup and operation are described in [CB11].

3.2.3 Magnetic-Field Stability

In principle, a permanent magnet operation in either driven or persistent mode is possible. In driven mode, the superconducting coil is powered continuously by the magnet PSU requiring the persistent current switch to be normally conductive. In persistent mode, however, the coil is short-circuited by the superconducting persistent current switch and thus insulated from the magnet PSU. The field stability in the first mode is limited by the stability performance of the magnet PSU, which is influenced by non-negligible ripples and noise, temperature variations and the technical realization of current regulation. In the second mode, the injected current decreases over time, and so does the provided magnetic field, due to the non-vanishing resistance of the connectors in the superconducting circuit.

Table 3.1: Characteristics of the magnet system. The magnetic field quantities indicated are those of the center of the associated coil. The hardware information are as-built dimensions provided by *Cryomagnetics Inc.* [Bod] [CB11].

characteristic	pinch magnet	detector magnet
coil length (mm)	500	700
coil inner diameter (mm)	454	540
coil outer diameter (mm)	498	580
number of windings	37865.5	45531.5
inductance (H)	432	647
designed coil position (m) [Gro13a]	12.1835	13.7835
cryostat length (mm)	711	910
cryostat inner diameter (mm)	346	448
LHe capacity (l)	65	75
maximum field	6 T (87.15 A)	6 T (93.59 A)
nominal field	6 T (87.15 A)	3.6 T (56.15 A)

In order to investigate the two different operation modes and the resulting long-term magnetic-field stability, a *Metrolab 1062 N° 7* nuclear magnetic resonance (NMR) [Kel11] probe was installed and operated on-axis in the warm-bore center of the pinch magnet while both solenoids were energized to nominal field. The NMR probe is filled with ^{2}H and read out by a *Metrolab PT2025* precision teslameter [Met14a]. An attached *Metrolab ACC-1060* gradient-compensation coil driven by an external constant-current power supply allows to improve the field homogeneity and the performance of the NMR probe [Met14b]. The influence of the stray field of the detector magnet measured by the NMR probe is about 1 %. A picture of the installed NMR probe is shown in figure 3.4.

Stability measurements performed in both operating modes over several hours show the relative deviation from the measured mean value to be $\Delta B/B = 3.2(1) \times 10^{-6}$ in the driven mode and $\Delta B/B = 3.5(2) \times 10^{-8}$ in persistent mode for the pinch magnet [Fis12]. A combination of existing current ripples (20 μA at 100 A, $\Delta I/I = 2.0 \times 10^{-7}$) and temperature drifts (3 mA/K at 100 A, $\Delta I/I = 3.0 \times 10^{-5}$ per K) of the magnet PSU [Cry09] can explain the observed performance in driven mode. Therefore, after both magnets have been energized in driven mode to the desired magnetic field, a continuous operation in persistent mode is advantageous where the coils are not sensitive to a possible malfunction or failure of the magnet PSUs.

However, a quantifiable magnetic field drift over time exists in persistent mode. It can be fitted to the expression [Gil12] [CK77]

$$B(t) = B_0 \left((1 + \alpha)e^{-t/\tau_1} - \alpha e^{-t/\tau_2} \right) , \tag{3.1}$$

where B_0 is the initial magnetic flux density after the energized magnet leaves the driven mode and enters persistent mode, τ_1 and τ_2 are two time constants which parametrize the decays of the transport and screening currents, respectively, and α is the mutually inductive coupling coefficient between both current types. Figure 3.4 shows the measured magnetic field drift within a time window of six days after both magnets have been ramped up from zero to nominal magnetic field. The applied fit ($\tau_1 = 1.885(2) \times 10^6$ d, $\tau_2 = 0.428(1)$ d) slightly overestimates the drift at large times so that an extrapolation over the course of a month will give only an upper limit for the magnetic field drift. Nevertheless, this and other measurements, as summarized in table 3.2, indicate that the drift amounts to less than 20 ppm per month (30 days), well below the KATRIN design goal of 0.1 %. The
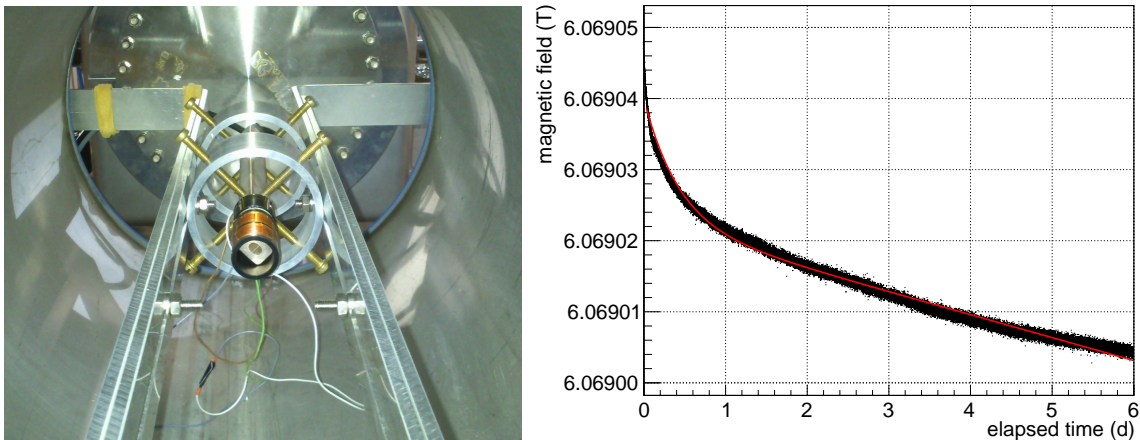
Figure 3.4: Left: NMR probe installed in the pinch-magnet bore, as seen from the upstream face of the cryostat looking downstream. The support structure is made of aluminum bars while the position of the NMR probe can be precisely adjusted by brazed screws. The sensitive volume of the NMR probe is surrounded by an attached gradient-compensation coil. **Right: On-axis magnetic field drift over six days.** The fit according to (3.1) slightly overestimates the drift data so that the extrapolation to large times gives an upper limit for a monthly or yearly drift. The noise reflects the high axial field gradient of the pinch magnet and is in the order of few μT only.

Table 3.2: Long-term magnetic field drift measurements. The fit results according to (3.1) of three measurements differ from each other and are unexplainable by statistical uncertainties. These investigations are most likely dominated by systematic uncertainties since the position of the NMR probe changed between each measurement due to its reinstallation. Nevertheless, all results are compatible with a monthly drift of less than 20 ppm.

date	Feb 2012	Oct 2012	Jan 2013
run time (d)	12.8	6.0	22.8
B_0 (T)	6.06892188(3)	6.06903984(3)	6.06845874(5)
α (10^{-6})	-6.017(9)	-2.862(4)	-5.737(8)
τ_1 (10^6 d)	2.616(6)	1.885(2)	4.338(3)
τ_2 (d)	2.239(7)	0.428(1)	0.756(2)
R^2	0.98975	0.98833	0.97561
monthly drift (ppm)	17.5	18.8	12.7

latter would be reached after a continuous operation of more than four years in persistent mode leading to an increased size of the sensitive 191-Tcm^2 magnetic flux tube of less than 0.1 mm in radius in the high fields of the pinch and detector magnet.

3.2.4 Magnet-Coil Alignment

In order to determine the location of the magnetic center of each coil relative to the physical center of the corresponding cryostat, the magnetic field was measured on-axis in 1-cm steps using a Lakeshore MMA-2536-WL one-axis hall probe [Lak14a] while both magnets were operated at full field. The hall probe was read out by a Lakeshore Model 460 gaussmeter [Lak14b] and carried by a PVC tube mounted inside the cryostats. Figure 3.5 compares the measured values compared to calculations performed with *Kassiopeia*. Assuming an accuracy of 1 mm for the measured axial position, of 1 % for the recorded magnetic field of the hall probe and of 0.1 % for the read-out value of the gaussmeter, the performed measurement is in good agreement with the expectation. In addition, the magnetic center can be localized within a 3-mm window in the warm-bore center of each
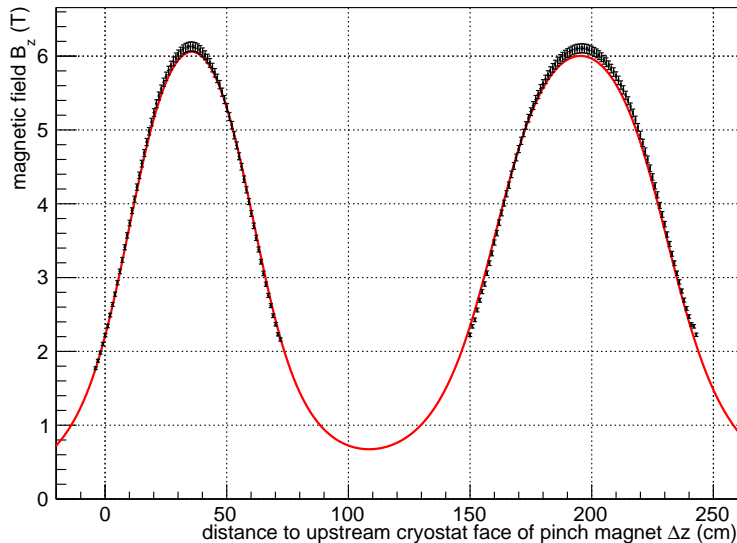
Figure 3.5: Axial magnetic field. A comparison between the measured (black points) and calculated (red line) magnetic field is shown in dependence of the on-axis position with both magnets at full field. The measured field maxima are located at $\Delta z_{\mathrm{PCH}} = (35.42 \pm 0.51_{\mathrm{stat}} \pm 0.10_{\mathrm{syst}})\,\mathrm{cm}$ for the pinch magnet and at $\Delta z_{\mathrm{DET}} = (195.91 \pm 0.30_{\mathrm{stat}} \pm 0.10_{\mathrm{syst}})\,\mathrm{cm}$ for the detector magnet while the calculated field maxima are at $\Delta z_{\mathrm{PCH}} = (35.68 \pm 0.03_{\mathrm{stat}})\,\mathrm{cm}$ and at $\Delta z_{\mathrm{DET}} = (195.41 \pm 0.01_{\mathrm{stat}})\,\mathrm{cm}$, respectively. All positions are measured relative to the upstream face of the pinch magnet. Calculations performed by the author, using *Kassiopeia*.

solenoid by comparing measurements with calculations.

More sophisticated field-alignment studies performed at the stand-alone pinch magnet show similar results [Mue14]. In these studies, a three-axis hall probe recorded the magnetic field on a circular path around the cryostat axis on both ends. The axial displacement between the coil and cryostat center is $(1.1 \pm 0.6)\,\mathrm{mm}$ while the radial displacement is negligibly small. When the detector magnet is operated as well, an additional axial movement of the pinch magnet coil of $(3.6 \pm 0.7)\,\mathrm{mm}$ in downstream direction can be observed, most likely due to the attractive magnetic force between both solenoids.

However, the latter investigations were made after several serious problems of the pinch magnet had occurred, where a non-negligible heat leak developed which slightly increased over time, and where a set of four unexplained quenches during high-field operation in combination with an energized detector magnet were experienced. Currently, these facts limit the operation of both solenoids to a maximum magnetic field of up to $5.0\,\mathrm{T}$ only. Nevertheless, most of the observations indicate that a damage of the tie rods within the cryostat of the pinch magnet leads to a misaligned and moving coil [Mue14]. More details concerning the problems with the pinch magnet are discussed in [Doe13b]. A new pinch magnet with similar specifications has recently been ordered from *Cryomagnetics Inc.* with a guarantee of mechanically robust tie rods.

3.3 Vacuum System

The vacuum system of the detector system must be compatible with the excellent vacuum conditions of the main spectrometer which is operated at a nominal pressure of $10^{-11}\,\mathrm{mbar}$. A benchmark for the former is that the maximum leakage and outgasing rate from external sources must not exceed a value of $10\,\%$ from the total gas load by outgasing hydrogen from stainless-steel surfaces of the main spectrometer [Wol07].
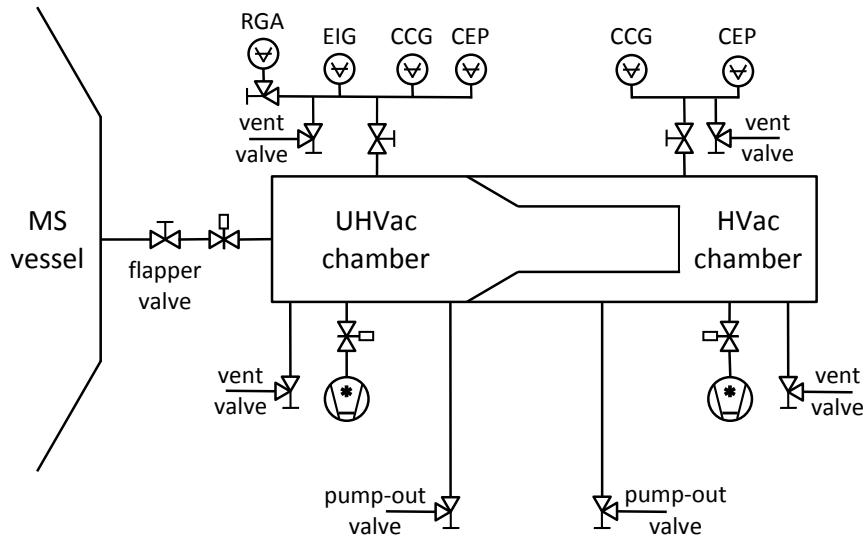
Figure 3.6: Schematic layout of the vacuum system. The post-acceleration electrode spatially separates the UHVac chamber from the HVac chamber. Different sensors monitor the vacuum conditions in both chambers while the CEP gauges operate only in low and medium vacuum ($10^3 - 10^{-3}$ mbar) during initial pump out via turbo-molecular pumps attached to the pump-out valves. The detector system can be isolated from the main-spectrometer (MS) vessel by a manually operated flapper valve and a pneumatically operated gate valve. Drawing adapted from [Ams14].

Spatially separated by the post-acceleration electrode, the detector system incorporates two independent vacuum systems mounted inside and between the warm magnet bores: the UHVac chamber and the HVac chamber. As part of the KATRIN beam line, the UHVac chamber couples to the main spectrometer via a custom-built beam pipe with an in-line beam flapper valve and houses the detector wafer, while the HVac chamber contains the non-UHVac compatible front-end electronics and the feedthrough to the ambient-air electronics and the data-acquisition (DAQ) system. The schematic layout of the vacuum system is shown in figure 3.6. A set of four sensors continuously monitor the pressure and gas composition in the UHVac chamber: an *MKS* convection-enhanced Pirani gauge (CEP), an *MKS* cold-cathode gauge (CCG), a *Leybold Ionivac* extractor-ion gauge (EIG), and an *MKS MicroVision Plus* residual-gas analyzer (RGA). Two sensors permanently monitor the vacuum conditions in the HVac chamber: an *MKS* CEP and an *MKS* CCG. All sensors [AT09] [Doe11] are mounted on extended pipes about 1.5 m from their main chambers of the vacuum system in a low-magnetic-field region. Two Sumitomo Marathon CP-8 cryopumps [Sum08] connected to the bottom of the vacuum chambers maintain the vacuum in each chamber. Both cryopumps are attached via bellows in order to reduce microphonics reaching the detector wafer. The latter process is associated with the mechanically vibrating pulse-tube cryocoolers of the cryopumps. Both manually as well as pneumatically operated all-metal valves allow isolation of the sensors and the cryopumps from their vacuum chambers. The entire detector system can be separated from the main spectrometer by a manually operated flapper valve [Doe08a] and a pneumatically operated DN250 all-metal gate valve by *VAT* [VAT07].

Due to the relatively low conductance through the coupling between the main spectrometer and the detector system, the requirement for the pressure in the UHVac chamber is 1×10^{-9} mbar while the expected pressure in the HVac chamber with 1×10^{-6} mbar is less critical for the required vacuum conditions. After a high-temperature bake-out of the UHVac chamber without the detector wafer (section 3.5) mounted at 150 °C over one week and a subsequent low-temperature bake out including the installed detector wafer

Figure 3.7: Trumpet-shaped post-acceleration electrode, prior to its installation to the detector system. The ceramic insulator is located at the bottom but not visible, since it is surrounded by a copper ring which is enwrapped with superinsulation foil to improve cooling performance (section 3.8). Three temperature sensors are attached along the post-acceleration electrode. The latter is completed by the detector flange with the wafer (section 3.5) attached to the top. Picture adapted from [Har12].

at $70\,^{\circ}\mathrm{C}$ over few days, base pressures of $3 \times 10^{-9}\,\mathrm{mbar}$ and $3 \times 10^{-6}\,\mathrm{mbar}$ in the UHVac and HVac chamber were achieved, respectively. The measured pressures are by a factor of 3 higher than designed, due to existing and localized leaks in both vacuum chambers, which are currently under repair. Therefore, an improvement of the vacuum conditions is expected, and nominal pressures should be achieved after another proper bake-out.

3.4 Post-Acceleration Electrode

After passing the main spectrometer, transmitted electrons can gain further longitudinal energy by post-acceleration, which should result in improved detector performance. Firstly, it shifts the region of interest for signal β-electrons to a possible window with a more favorable intrinsic background rate where less fluorescence lines are generated by surrounding materials close to the detector. Furthermore, low-energy electrons from non-elevated regions on ground potential can be accelerated above the electronic noise threshold of the detector to allow their detailed investigation. Last but not least, the probability for electrons being backscattered from the detector can be reduced since their incident angle decreases with increasing post-acceleration potential [Ren11].

In order to realize this post acceleration, a trumpet-shaped, mechanically robust, 3-mm thick copper electrode manufactured by the *Beverly Microwave Division of Communications and Power Industries*, has been installed in front of the detector wafer. As an integral component of the vacuum system, it forms the physical boundary between both vacuum chambers and can resist a possible pressure gradient of $1\,\mathrm{atm}$. It is brazed to a ceramic insulator on its upstream end to allow its physical attachment to the grounded vacuum

chamber. The detector wafer is mounted on a specially developed feedthrough flange which is connected to the downstream end of the electrode. The electrostatic post-acceleration potential is provided by a *Spellman TOF3000* high-voltage power supply delivering a maximum voltage of 30 kV [Spe04]. Apart from the electrode, the potential is also applied to the detector wafer, the front-end readout electronics, and the ambient-air electronics. In order to prevent Penning discharges and electric breakdowns due to the interplay of high electrostatic and magnetostatic fields, a cylindrical quartz tube with electrodes made of stainless-steel foils on its inner and outer surface surrounds the post-acceleration electrode and separates it from the HVac chamber. The inner foil is at post-acceleration potential while the outer foil is grounded so that the electric field is confined within the quartz insulator.

Although designed to be capable of floating to a level of +30 kV, a stable long-term operation of the post-acceleration electrode at a maximum potential of 11 kV and nominal magnetic fields has only been achieved so far after careful long-term conditioning [SM73] [Bon95]. At potentials above 11.5 kV, high-current spikes and discharges within the vacuum chambers occur which prohibit a long-term use of the post-acceleration electrode. Nevertheless, post-acceleration potentials above 10 kV are sufficient to move the signal of low-energy electrons with thermal energies above the electronic noise threshold of the detector as well as to improve the detector performance (chapter 4) and the intrinsic detector background conditions (chapter 5). In figure 3.7, a picture of the post-acceleration electrode is shown prior to its installation.

3.5 Detector Wafer

3.5.1 Detector-Design Constraints

The design of the detector system is based on a segmented PIN-diode array housed on a monolithic silicon wafer, as this technology represents a well-understood electron-detection device. This silicon PIN diode consists of heavily doped p-type and n-type layers sandwiching a mildly doped or intrinsic silicon layer with high resistivity. The PIN diode operates as a solid-state semiconductor diode detector where ionizing radiation produces electron-hole pairs while passing through the sensitive volume of the detector. If the radiation completely deposits its energy within the depletion zone, the number of electron-hole pairs produced is proportional to the incident energy. Silicon is an indirect band gap semiconductor. Its mean ionization energy is 3.62 eV at 300 K so that a typical 18.6-keV electron will generate more than 5000 electron-hole pairs via ionization and scattering processes within the first few µm of the sensitive detector volume before being absorbed in the bulk. The small ionization energy of the detector material leads to a huge number of electron-hole pairs being created which results in a reduced statistical uncertainty on the measured deposited energy, an improved energy resolution and an increased signal-to-noise ratio. Since the concentration of free charge carriers in the intrinsic layer is non-zero but tiny, the electrical conductivity of the material is low. This results in a dominant leakage current which is superimposed on the detection pulse. There are different ways to decrease the leakage currents to an insignificant sub-nA level in order to improve the signal-to-noise ratio: first, by broadening the intrinsic layer, thus increasing its electrical resistance, second, by cooling the detector material, thereby reducing thermal excitations, and finally, by applying a reverse-bias voltage to the PIN diode, hence depleting the intrinsic layer from free charge carriers. The bias voltage entirely appears across the high-resistivity intrinsic layer. The resulting high electric field is uniform across the i-type region while it drops sharply to zero at the p-i and i-n junctions. Therefore, the dimensions of the i-type region determine the active, sensitive volume of the detector, and the migration of electron-hole pairs to the p-i and i-n boundaries induces the signal pulse. The lifetime of electron-hole

pairs generated within the intrinsic layer is substantially larger than their collection time. The applied bias voltage ensures that only few electron-hole pairs are lost before their fast collection is complete. This leads to highly efficient charge-collection properties of a PIN diode and hence to an excellent timing resolution [DaV03] [Spi05] [SN06] [Kno10] [Spi12].

The capacitance $C = \epsilon A/d$ of a PIN diode with an applied reverse-bias voltage U_b is defined by its cross section A, its thickness d and its permittivity $\epsilon = \epsilon_0 \epsilon_r$ with $\epsilon_r = 11.68$ for silicon if the intrinsic layer is by far the broadest layer. A thicker intrinsic layer results in a lower detector capacitance so that incident ionizing radiation causes a signal with a greater pulse amplitude $\Delta U = \Delta Q/C$ with the total collected charge ΔQ of electron-hole pairs. Moreover, the electrical resistance $R = \rho d/A$ of the intrinsic layer with its material-dependent resistivity ρ increases with its thickness leading to lower leakage currents $I = U_b/R$. Consequently, broadening the detector will improve the signal-to-noise ratio. However, a thicker intrinsic layer reduces the electric field strength $E = U_b/d$ across the i-type region. Therefore, both the mean drift velocity $v = \mu E$ and the transit time $t = d/v = d^2/(\mu U_b)$ of the electron-hole pairs decrease during the charge-collection process, where μ is the fixed charge carrier mobility with $\mu \approx 1350 \, \mathrm{cm^2/Vs}$ for electrons and $\mu \approx 480 \, \mathrm{cm^2/Vs}$ for holes in silicon at room temperature. This leads to less efficient charge-collection properties and hence to a worsening of the timing resolution. Moreover, a thicker intrinsic layer can be a source of lattice defects and impurities, causing an increased intrinsic detector background due to a greater sensitive lateral surface, and representing a higher heat load which has to be cooled. Therefore, an optimized thickness of the intrinsic layer yields the best detector performance [DaV03] [Spi05] [SN06] [Kno10] [Spi12].

In summary, it can be stated that the operation of a semiconductor silicon PIN-diode as electron detectors offers important features such as:

- **Good energy resolution:** This ensures that the region of interest in the measured energy spectrum is small compared to the full energy scale leading to small intrinsic detector background within the acceptance window. KATRIN preferably requires a total background of less than 10 mcps to achieve a signal-to-background ratio of 2:1 in a region few eV below the tritium endpoint [Ang05] [Mer12a]. Energy resolutions of $\Delta E/E < 0.1$ are practical [SN06] [Kno10].

- **Good timing resolution:** This allows to perform time-of-flight measurements through the main spectrometer while the detector operates as stop trigger. A typical 18.6-keV electron needs a few µs to pass the spectrometer, leading to a required timing resolution in the order of 100 ns [Ste13].

- **Spatial resolution:** A segmented PIN-diode array facilitates off-line accounting for spatial electrostatic and magnetostatic inhomogeneities in the analyzing plane or the source region [Ang05] [Dre13].

- **High detection efficiency:** Among other reference parameters, an absolute detection efficiency of at least $\epsilon_{\mathrm{det}} \geq 90\,\%$ is required in order to satisfy the designed statistical error of $\sigma_{\mathrm{stat}}(m_\nu^2) = 0.018\,\mathrm{eV^2}$ after an effective 3-year neutrino-mass measurement [Ang05]. ϵ_{det} depends on background and noise contributions as well as on backscattering and dead-layer effects [Ren11].

- **Monolithic design:** In the case of segmentation, a monolithic design simplifies the detector alignment and installation since all pixels are arranged in the same plane housed on a single wafer [Wal13].

- **UHVac compatibility:** Ultra-clean silicon wafers can be used in an UHVac environment of 10^{-11} mbar which is the nominal absolute vacuum level of the main spectrometer [Wol14].
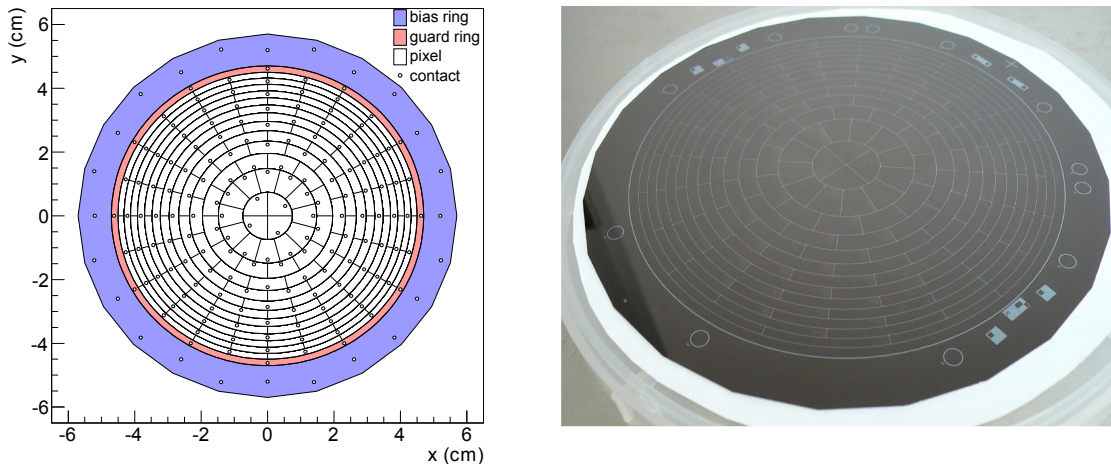
Figure 3.8: Segmented backside of the detector wafer. Both the schematic layout (**left**, adapted from [Ams14]) and a picture (**right**, adapted from [Wal13]) of the segmented contact side of the detector wafer show the sensitive dartboard pixel pattern surrounded by a guard ring and a bias ring, including the positions of the 184 contacts (148 detector-pixel contacts, 12 guard-ring contacts and 24 bias-ring contacts) to the vacuum electronics (section 3.6).

- **High-field compatibility:** PIN diodes with thicknesses of about $500\,\mu m$ can be used in the presence of high electrostatic and magnetostatic fields without any considerable loss of performance. The detector is operated at the potential of the post-acceleration electrode of up to $30\,kV$ while being placed in a magnetic field of up to $6.0\,T$.

- **Variable size, thickness and dimensions:** This allows to design a detector such that it meets the special demands of the experiment, like available space, mechanical robustness, stress-free cooling and complete coverage of the incident radiation. The sensitive 191-Tcm^2 flux tube has a radius of about $4.3\,cm$ at the specified detector position with a designed nominal magnetic field of $3.3\,T$.

3.5.2 Detector Setup

The monolithic silicon wafer of the detector system is architectured as a segmented PIN-diode array. It is $503\,\mu m$ thick with a diameter of $125\,mm$, a resistivity of $80\,\Omega m$, a crystal orientation of $\langle 111 \rangle$ and was manufactured by *Canberra Industries Inc.* via a double-sided process which combines photo-lithography and ion implantation [Evr03]. The sensitive area of the unsegmented, shallowly ion-implanted, n^{++} ohmic entrance side is uncoated with a non-sensitive dead layer of a specified thickness of $100\,nm$ while the segmented, ion-implanted, p-type contact side is entirely coated with non-oxidizing TiN to facilitate electrical connections for signal readout and bias supply. This coating ensures low-background and low-radioactivity properties [Van12] [SN06] [Kno10]. The segmented side has a sensitive area with a diameter of $90\,mm$ which is divided into 148 equal-area pixels arranged on a quad-segmented bullseye and 12 concentric rings of 12 pixels each, according to the dartboard mask shown in figure 3.8. A single pixel has a sensitive area of $44.1\,mm^2$, a capacitance of $8.2\,pF$, and is separated by 50-μm thick boundaries with a specified resistance larger than $1\,G\Omega$ from other pixels. The segmented side is completed by a 2-mm thick guard ring and a 15.5-mm thick bias ring which both surround the sensitive area of the back face. The guard ring minimizes any field distortions originating from the bias ring on the outer rings of pixels. The bias ring is conductively connected to the insensitive, outer areas of the front face via TiN-coating which wraps around the wafer edges to apply the
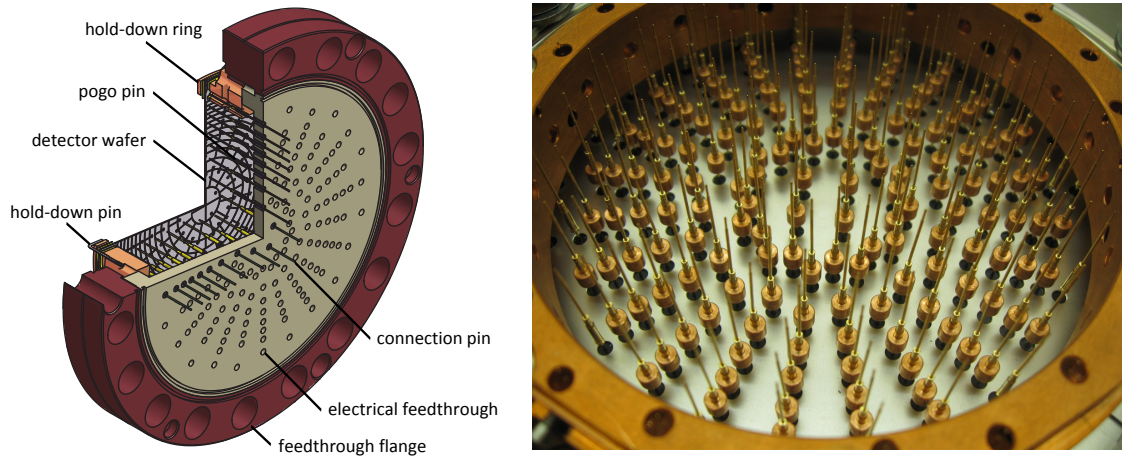
Figure 3.9: Detector feedthrough flange. Both the schematic layout (**left**, back view, adapted from [Ams14]) and a picture (**right**, front view, adapted from [Boy12]) of the detector feedthrough flange show the pogo pins with which contact between the detector pixels and the vacuum electronics is established via feedthrough pins sealed in borosilicate glass. 148 copper sleeves coat those pogo pins which are associated with the pixels to shield background electrons generated within the seals.

bias voltage to the PIN diode from the segmented side. Typical leakage currents are well below 1 nA per pixel at room temperature when a nominal bias voltage of 120 V is applied [Van12] [Wal13].

The electrical connections to the contact side are made by well gold-plated pogo pins, manufactured by *Interconnect Devices Inc.*, with a Ni-Ar barrel, a Be-Cu plunger and a stainless-steel spring. The wafer is placed in a novel mount [Van12], as shown in figure 3.9, by a copper hold-down ring, six L-shaped spring-loaded hold-down pins, and lateral-placed copper stops, so that it compresses the pogo pins by at least 0.38 mm with a total force of 50 N and a corresponding wafer deformation of 0.24 mm in its center. There is no effect on detector resolution and no indication of additional reverse-bias leakage current induced by mechanical stress for wafer deformations of up to 0.41 mm [Van12]. This mounting ensures adequate electrical contact and a fixation of the wafer in its initial position. It is bolted directly to a specially developed UHVac-compatible feedthrough flange, manufactured by *Ametek Hermetic Seal Corp.*, which spatially separates both vacuum chambers from each other and provides low-capacitance and low-microphonic electrical connections between detector pixels and preamplifier contacts. The detector flange consists of a custom-built 184-pin array with well gold-plated *Inconel X-750* pins with 0.5 mm in diameter sealed in type-L21 borosilicate glass in order to realize the feedthrough to 148 detector pixels, 12 guard-ring contacts and 24 bias-ring contacts. All pogo pins are connected via Mill-Max brass-alloy adapter pins to the feedthrough pins of the detector flange while the preamplifier modules make direct contact. The non-negligible potassium content in the borosilicate glass of 3.6 % by weight generates β-electrons with energies of up to 1.3 MeV from the decay of ^{40}K in the feedthrough seals. These electrons can leave the seal, are then magnetically guided to the back face of the detector wafer and could produce significant background at the affected detector pixels. Cylindrical copper sleeves with a height of 3.2 mm and a cross section of 33.5 mm^2 fit over the 148 signal pins to shield such electrons from reaching the detector wafer. Figure 3.9 shows a picture of the front side of the detector flange including the installed copper shields.
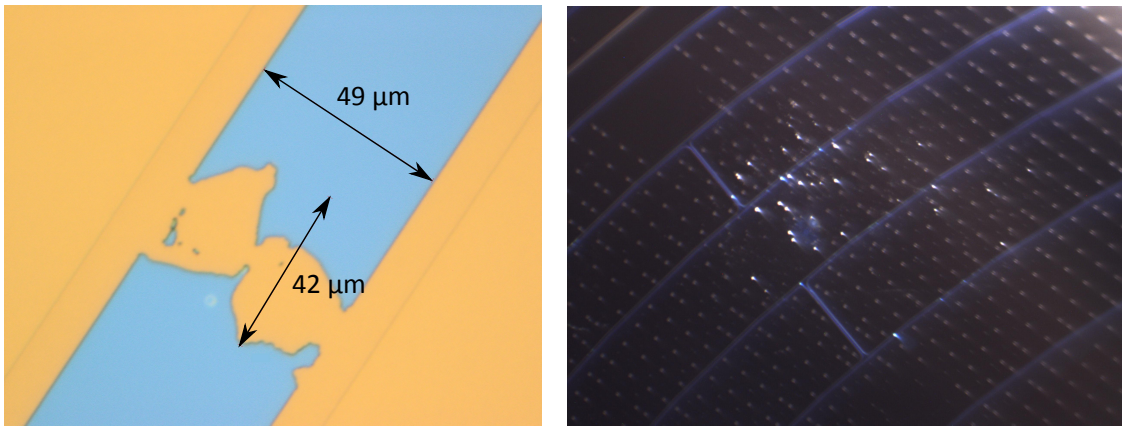
Figure 3.10: Left: Inter-pixel short circuit. A microscopic view of the damaged inter-pixel boundary between pixels #67 and #68 on wafer #96728 is shown. The given dimensions have an accuracy of $\pm 1\,\mu$m Picture adapted from [SW12]. **Right: Wafer contamination.** Wafer #96725 is unusable due to dense contamination by foreign objects. Picture adapted from [Doe13a].

3.5.3 Detector Operation

A set of five wafers were supplied by *Canberra Industries Inc.* in January 2011 with serial numbers #96724 through #96728. Two of these wafers, #96724 and #96728, were installed in the detector system and then characterized in detail. Each tested wafer has two neighboring pixels with an inter-pixel resistance of less than $50\,\Omega$ indicating an inter-pixel short circuit on the associated wafer itself. A microscopic view of the damaged inter-pixel boundary between the two affected pixels #67 and #68 on wafer #96728 is presented in figure 3.10 explicitly demonstrating the inter-pixel short circuit. Wafer #96724 was not yet investigated in detail with a microscope but similar visual observations are expected as described, although two different neighboring pixels #78 and #89 are shorted to each other. As a consequence, only 146 of 148 pixels (98.6 %) could be used for data-taking for detector and SDS commissioning in order to allow the required spatial resolution. In principle, there was the option to modify the readout electronics such that the shorted pixels would be treated as one single pixel with double area and capacitance. Nevertheless, this intervention was not recommended since not only the entire signal chain for this specific pixel would have to be modified significantly but also the corresponding handling in data analysis. Wafers #96725 and #96726 show large amounts of features, dusty deposits, and non-loose pieces of debris on their surface as it is shown in figure 3.10. They are not tested to avoid any contamination of the UHVac chamber. The origin of the foreign objects is unclear. Usually, unused wafers, like the spare wafer #96727, are stored in a dry nitrogen atmosphere. A set of new wafers has thus been ordered. Special attention will be paid to the existing issues with the inter-pixel short circuits and the observed contamination.

3.6 Readout Electronics

Within the sensitive volume of the described detector wafer, a typical 18.6-keV electron generates a short pulse with a length of

$$\Delta t = \frac{d^2}{\mu U_b} = \frac{(503\,\mu\text{m})^2}{1400\,\frac{\text{cm}^2}{\text{Vs}}120\,\text{V}} \approx 20\,\text{ns} \tag{3.2}$$

and an amplitude of

$$\Delta U = \frac{\Delta Q}{C} = \frac{\frac{18.6\,\text{keV}}{3.62\,\text{eV}} \cdot 1.6 \times 10^{-19}\,\text{C}}{8.2\,\text{pF}} \approx 0.1\,\text{mV} \tag{3.3}$$

at room temperature. This tiny signal has to be integrated and amplified in such a way that the data-acquisition system can translate and record the most important information of the signal with high accuracy, e.g. its waveform, deposited energy, time stamp and pixel assignment. This demands a low-noise signal-processing chain. Its design is limited among others by the post-acceleration potential on which the detector floats, the magnetic field in which the detector is operated, the available space in the warm bore of the detector magnet, the required HVac compatibility, and the necessity for detector cooling. Further design constraints are a limited total power dissipation of $\sim 15\,\mathrm{W}$ in the HVac section, a limited operating temperature range of -40 to $+70\,^\circ\mathrm{C}$, a dead-time free operation at variable rates between 10^{-2} and 10^{5} cps, an adjustable energy range of 0.1 to 6.0 MeV, and a linearity and stability of more than 99 %.

The custom-made suite of detector electronics designed and manufactured by the Institute for Data Processing and Electronics (IPE) at KIT reads out the signals from the detector wafer via several stages along the signal path as shown in figure 3.11. Controlling and monitoring are managed bidirectionally along the control paths while the required power is distributed by a set of *Amrel* power supplies along the power paths [Amr09].

As first stage of signal processing, 24 charge-sensitive preamplifier modules are attached directly to the electrical feedthrough pins on the HVac side of the detector flange in order to reduce noise [Wue12]. These modules are arranged in a radial carousel-like pattern with 15° angular spacing according to figure 3.12. Each module consists of either six or seven channels of charge-sensitive preamplifiers and serves pixels from alternating detector rings. A channel contains a low-noise N-channel junction field-effect transistor of type *NXP/Philips BF862* and a high-speed, low-noise operational amplifier of type *Analog Devices AD829JR* to integrate and amplify the signal, respectively. Apart from the preamplifiers, each module houses advanced electrical circuits with switching devices and multiplexers in order to measure its temperature and the reverse-bias leakage current per single pixel as well as to inject an externally applied test pulse per single channel. In addition, a module provides two filtered feedthrough lines which supply the detector wafer with its guard-ring and bias potentials through the detector flange. All modules are built on fitted 0.63-mm thick *Rubalit 710S* aluminum-oxide ceramic boards, manufactured by *CeramTec*, to meet the design specifications of HVac compatibility and active-cooling requirements. In order to limit the power dissipation to $0.6 - 1.0\,\mathrm{W}$ per module, only the first amplification stage is included on the modules. With the help of copper mounting plates and pins, generated heat is conducted to the active cooling system − a custom-built heat pipe (section 3.8) − via the detector flange and the post-acceleration electrode. Two Pt-1000 sensors are installed along the post-acceleration electrode, one at the detector flange, and one at the upstream copper mounting plate in order to monitor the temperatures of the electrode, the detector wafer, and the vacuum electronics. Two 50-Ω heaters attached at the upstream copper mounting plate provide a possible temperature regulation directly at the vacuum electronics. The preamplifier assembly is completed by two additional boards mounted to the downstream side. The inner circular board distributes the preamplifier output signals to a cable harness while the outer ring-shaped board redistributes power and control lines to the preamplifier modules from the ambient-air electronics. Both boards are HVac compatible, are characterized by a low heat dissipation and are made of *Rexolite* plastic. The *Rubalit* ceramic modules and the *Rexolite* plastic boards have been measured in advance regarding intrinsic radioactivity to avoid additional detector background. In figure 3.12, a picture of the vacuum electronics attached to the detector flange as described above is shown. Finally, a cable harness carries the signals via coaxial cables with single-ended transmission lines, a common signal ground, and the filtered power and control lines via flat ribbon cables. This establishes the connection between the vacuum electronics and the ambient-air electronics via a custom-made feedthrough flange with six
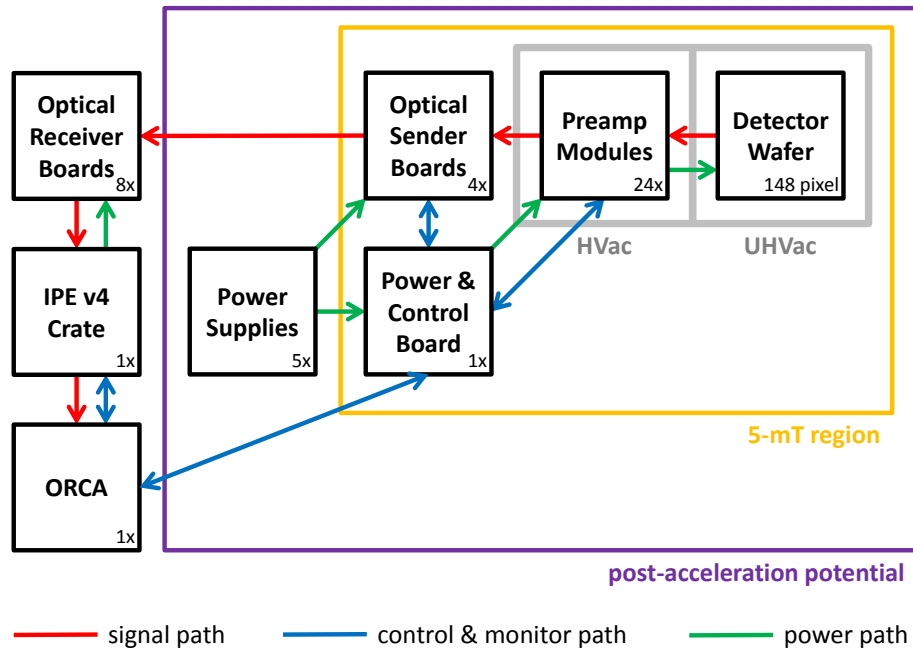
Figure 3.11: Schematic architecture of the detector readout electronics. This block diagram illustrates how the different devices of the readout-electronics system are connected with each other. In addition, it shows which units are located within the 5-mT magnetic-field region and are floating on the potential of the post-acceleration electrode, respectively.

50-pin, vacuum-tight, sub-D type feedthroughs manufactured by *Ametek Hermetic Seal Corp.* which forms the downstream end of the HVac chamber. All other detector-related electronics are mounted on the ambient-air side.

Located on the downstream side of the feedthrough flange and outside the HVac chamber, four 37-channel signal boards, one temperature-monitoring card, and one power-and-control board are enclosed in an inner anti-corona housing and an outer Faraday cage for transient protection and for safety, since the whole set of ambient-air electronics floats at the potential of the post-acceleration electrode. The signal boards provide differential transceivers of type Analog Devices AD8129ARZ to pick up the signals from the HVac chamber such that ground loops across the single-ended signal lines are avoided. These boards also contain programmable, variable gain stages via 8-bit multiplying resistive digital-to-analog converters of type *Analog Devices AD5426YRM* to electronically calibrate the detector pixel-by-pixel and to change the full-scale energy range. The latter can be used to study both keV-electrons from tritium β-decays and MeV-alphas from radon α-decays within the same recorded energy spectrum during neutrino-mass measurements. In addition, the signal boards house a second signal-amplification stage via high-speed, low-noise dual operational amplifiers of type *Texas Instruments LMH6628MA*, and fiber-optical transmitters of type *Avago Technologies HFBR-1527* which convert the analog signals to optical signals in order to finally transmit the translated pixel signals via individual plastic-optical-fiber links to the grounded data-acquisition system. Therefore, the signal boards are labeled as optical sender boards. The temperature-monitoring card can be temporally plugged in without any applied post-acceleration potential to monitor the temperature along the post-acceleration electrode and at the detector flange. The power-and-control board provides the filtered power regulation for the vacuum electronics, and the control and monitoring interface for the vacuum electronics and the optical sender boards. The interface communicates via an RS232 serial connection. The power-and-control board contains power-conditioning circuits, overvoltage protection and temperature readouts for the vacuum electronics, and variable-gain control and monitoring for the resistive digital-
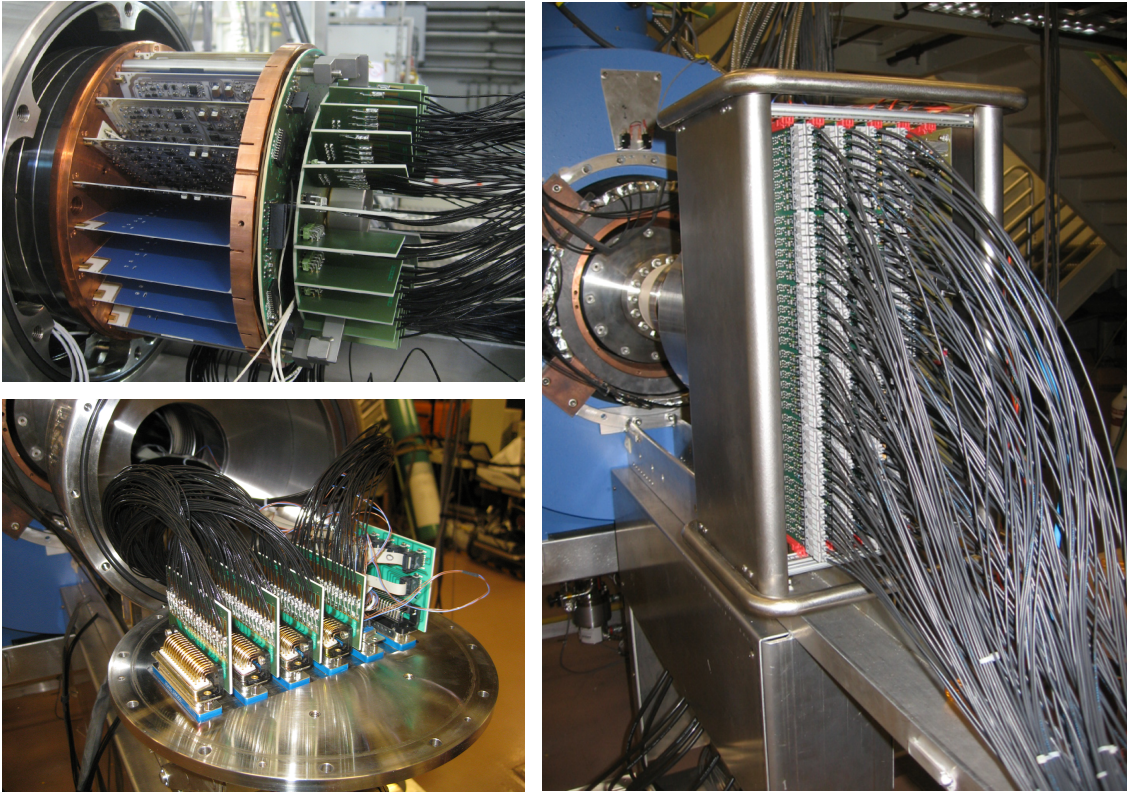
Figure 3.12: Detector readout electronics. In the HVac chamber (**top left**, adapted from [Ams14]), the vacuum front-end electronics is directly mounted on the detector feedthrough flange. A copper mounting plate and a copper support ring complete the carousel-like arrangement of the preamplifier modules. The outer ring-shaped power-and-control distribution board and the inner circular signal distribution board are attached to the downstream end of the carousel. The power and signal lines are guided via ribbon and coaxial cables, respectively, to a feedthrough flange (**bottom left**) separating the HVac chamber from the ambient-air side. The analog signals are converted into optical signals via four optical sender boards mounted in an anti-corona housing (**right**) floating at the potential of the post-acceleration electrode in order to guide the electron signals via individual plastic-optical fibers to the grounded data-acquisition system. The Faraday cages surrounding the floating components are not shown in this picture for better visualization but can be viewed in picture 3.1.

to-analog converters of the optical-sender boards. It further provides monitoring of the leakage current of single pixels, the temperature of individual preamplifier modules, and the reverse bias voltage applied to the detector wafer. An optical test pulse, which can be externally applied by an *Agilent 33220A* waveform generator, is converted to an analog signal on the power-and-control board and can be routed to a selected channel at one of the preamplifier modules by multiplexers mounted on the vacuum electronics. These multiplexers are controlled by the power-and-control board. Two filtered power lines are routed through the power-and-control board and can supply the vacuum heaters with voltages of up to 20 V resulting in a total power of 16 W.

The power of all ambient-air boards is supplied through an insulated metal tube by a set of *Amrel* power supplies positioned in a rack which floats at the potential of the post-acceleration electrode and is thus surrounded by a Faraday cage. An isolation transformer establishes the electrical connection of the power supplies to the 230 V AC mains voltage. The grounded data-acquisition rack and the floated power-supply rack are located 2.5 m downstream from the detector magnet and outside the 5-mT magnetic-field contour to allow a reliable functioning of the power-supply fans. In the analog backplane of the DAQ system, optical receiver boards with fiber-optical receivers of type *Avago Technologies*
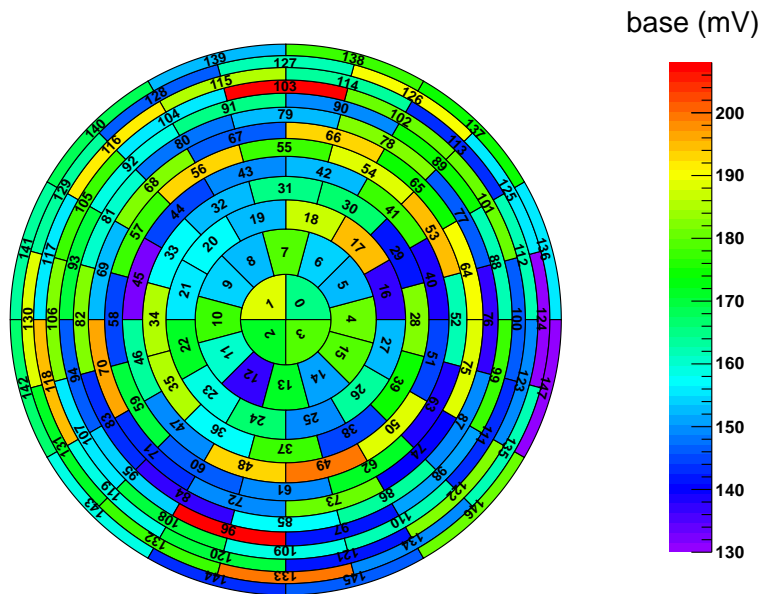
Figure 3.13: Base-line voltages per channel. All channels show working points in the expected voltage range when metering the base-line voltages at the downstream end of the signal-cable harness with a 50-Ω load terminator using a voltmeter. The individual base-line voltages seem to be randomly distributed whereas the different quantities have no influence on the performance in the first approximation. However, the relative full-scale deflection of each channel is limited by the height of the base line. The absolute full-scale deflection is at $\pm 1.75\,\mathrm{V}$ with a 50-Ω load terminator [Wue11].

HFBR-2526 convert the optical signals to analog signals for the digitizers. Finally, the digitized signals are processed by the DAQ crate and the DAQ software as described in section 3.7.

The number of working channels of the readout electronics can be verified by different methods without using the digitization of the DAQ crate:

- Since all modules and boards are identically constructed but underlie electronic tolerances, functional channels should have similar base-line voltages. The latter parameters can be measured with a simple voltmeter at different locations within the signal chain. Non-functional channels could be due to base-line oscillations, defective electronic components, incorrect wiring, short circuits, conductor breaks, or cracked preamplifier modules resulting in significantly different base-line voltages across the channels. As an example, a reasonable voltage output of a single channel at the downstream end of the cable harness is in the order of -200 to $-100\,\mathrm{mV}$ DC with a 50-Ω load terminator [Wue11] indicating a functional channel while damaged channels are short-circuited to ground $(0\,\mathrm{V})$ or floating $(1.8 - 5.0\,\mathrm{V})$ [Wue12]. As it is shown in figure 3.13, all tested channels show similar measured working points in the expected voltage range.

- The heat input through the preamplifier modules into the HVac chamber should be similar per powered quadrant, since the modules are symmetrically constructed and arranged. A power dissipation of about $0.1\,\mathrm{W}$ per channel is expected according to the design specifications resulting in a total heat input of $\sim 15\,\mathrm{W}$. In case of a dead or oscillating channel, a lower or greater heat input is observed, respectively. In table 3.3, the measured heat input for different combinations of powered quadrants is presented, indicating a functionality of the detector electronics as expected, although the mean power dissipation per channel is slightly higher than designed.

Table 3.3: Power dissipation per channel. The vacuum electronics can be powered in individual quadrants by the existing ambient-air electronics. This allows to measure the heat input into the HVac chamber for different configurations of energized quadrants and preamplifier modules. The marks ($\times$) indicate the powered quadrants with the resulting total power and individual power per channel. Systematic uncertainties are in the order of $10\,\mathrm{mW}$. The measured power dissipation is slightly higher than designed, having no influence on the performance if sufficient cooling power is provided.

\#0	\#1	\#2	\#3	total power (W)	mean channel power (mW)
$\times$				4.5	122
	$\times$			4.6	124
		$\times$		4.7	127
			$\times$	4.7	127
$\times$	$\times$			8.9	120
$\times$		$\times$		8.9	120
$\times$			$\times$	8.9	120
	$\times$	$\times$		8.7	118
	$\times$		$\times$	8.7	118
		$\times$	$\times$	8.7	118
$\times$	$\times$	$\times$		13.1	118
$\times$	$\times$		$\times$	13.0	117
$\times$		$\times$	$\times$	13.2	119
	$\times$	$\times$	$\times$	13.2	119
$\times$	$\times$	$\times$	$\times$	16.8	114

(column group header: powered quadrant — \#0, \#1, \#2, \#3)

Both methods show that the readout electronics are measured to be fully functional with $100\,\%$ working channels. More sophisticated studies with the plugged in DAQ crate and the use of calibration sources are presented in chapter 4.

3.7 Detector-Data Acquisition

The DAQ system (section 3.7.1) of the detector system consists of the DAQ hardware (IPE v4 crate) [Gem01a] [Gem01b] and the DAQ software (object-oriented real-time control and acquisition (ORCA)) [How04] [How14], which are closely linked to each other. The digitized detector traces are shaped digitally by a pair of trapezoidal filters in series (section 3.7.2) implemented in field programmable gate arrays (FPGAs) within the DAQ crate to determine both event-energy and event-time information of the associated triggered detector signal. All filter parameters, such as shaping length and gap length, and other measurement parameters, such as run mode and run time, are programmable and can be set by ORCA. All devices which are not part of the detector-signal chain can be controlled and monitored via the slow-controls system (section 3.7.3).

3.7.1 DAQ System

The DAQ hardware follows the same concept as used for the Pierre Auger Cosmic Ray Observatory [Gem01a] [Gem01b]. It consists of a set of first-level trigger (FLT) cards and one second-level trigger (SLT) card mounted in an IPE v4 crate. As for the detector-signal chain, eight FLT cards are in use to process detector signals but more can be added to read out veto signals (section 3.10), external pulsers, or coincidence signals, e.g. from a pulser-controlled electron source.

Each FLT card houses 24 analog channel inputs. The signal is processed through a series of analog differential receivers with programmable offsets, programmable amplifiers, bandpass filters, digitizer drivers, serial ADCs with 12-bit precision and 20-MHz sampling rate, and auxiliary memory for the ADCs. Programmable logic is implemented in four *Altera Cyclone II EP2C35* FPGAs per FLT card which allow to change the digital filtering and trigger system via ORCA at any time. Three of them operate as trigger FPGAs (slave) to control acquisition and preprocessing, each serving eight channels, while the central-control FPGA (master) performs time synchronization and readout for each FLT card. The event-energy and event-trigger information are generated by a two-stage filter through the slave FPGAs. If the energy value is above a programmable threshold, the information is transmitted to the master FPGA. The event-time information is constructed by combining two clock quantities from a pair of counters on each FLT card through the master FPGA. One counter clocks 1-Hz pulses distributed from a GPS receiver on each FLT card as second counter, while the other counts a 20-MHz clock, distributed from the SLT card, as sub-second counter. The second counter is initialized by ORCA at the beginning of each run to UTC time taken from the DAQ computer while the sub-second counter is reset on every start of a second.

The SLT card operates as a single-board computer with an embedded 1.4-GHz Pentium M processor running Linux to initialize and coordinate all connected FLT cards. Communication with the DAQ computer is provided by a Gbit-Ethernet interface, while both systems are synchronized using network time protocol. The SLT clock is synchronized from a high-precision 10-MHz clock supplied by an external, global synchronization unit so that all FLT cards within the KATRIN network receive exactly the same clock phase. The synchronization unit also provides the 1-Hz signal for the individual FLT cards so that the timing of the start of a second is aligned to UTC time. Global synchronization between different DAQ crates within the KATRIN network is realized by GPS signals from the synchronization unit for timing information, by UTC time from the DAQ computers for calender information, and by an additional low-frequency pulser whose signal is injected into the DAQ crates for data synchronization, if required.

The auxiliary memory for the ADCs consists of a circular buffer with 64 pages, each with 2048 samples and four bit-status indicators. Recording stops with every trigger but subsequent event data is acquired in the following page. During recording in one specific page, the DAQ computer prompts to read out the data of all other pages. There are further locations in the data-flow chain where the acquired data is temporarily stored and held for readout. When the incident rate exceeds the system capacity, dead time and loss of event data can occur due to congestion. Therefore, three measurement modes are available in ORCA, each handling various amounts of recorded event information and different sizes of rates. The *energy mode* is the primary operation mode for KATRIN since it records both energy and timing for each event. It can handle a total rate of up to 108 kcps ensuring a dead-time free operation. The *trace mode* is for diagnostics as it adds the 2048-bin digitized waveform of the event, sampled in 50-ns time bins, to the information from energy mode. Thus, it can be operated at a maximum rate of only 8 kcps. The *histogram mode* finally generates 2048-bin energy histograms for each channel in set time intervals so that the ability of event-based analyses is lost, yet a dead-time free operation at very high rates of up to 3.3 Mcps is viable [Kop08] [Phi10] [Ber12a].

Summarized, the detector-signal information is fed through the analog and digital parts of the associated FLT card, the bus of the IPE v4 crate, the SLT card, via a PCI-Express link to a rack-mounted computer, and finally via a Gbit-Ethernet connection to the ORCA DAQ computer, where ORCA stores the data onto the local hard disk drive. Upon completion of a run, the data is automatically transferred to the KATRIN data server which is worldwide accessible. ORCA data streams are converted by ORCARoot [How09] to

ROOT-based files [BR96] [BR97]. Finally, two C++-based data-analysis frameworks, KaLi [Kle14] and Beans [Cen14], allow basic and advanced investigations of the recorded data, respectively.
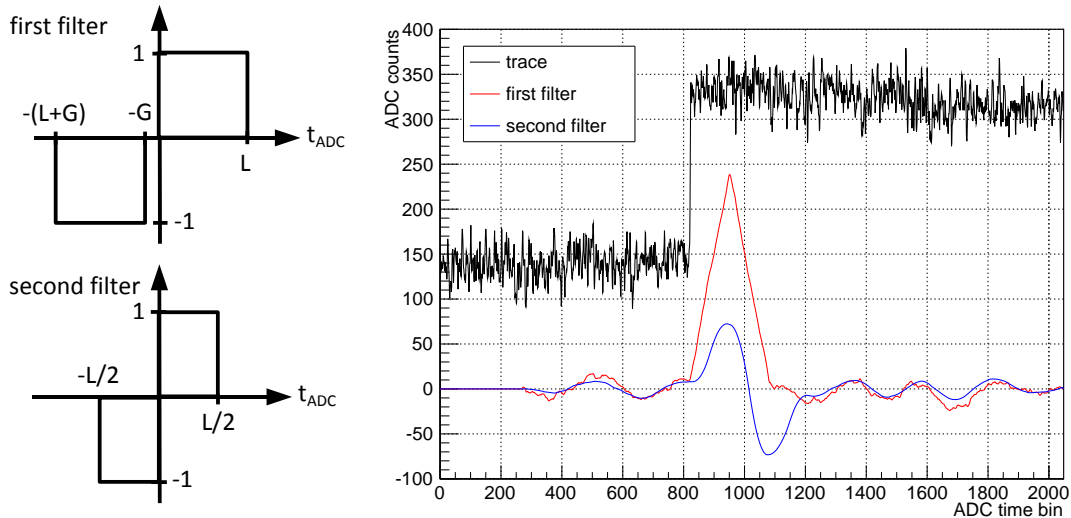
3.7.2 Trapezoidal Filter

Typical detector post-amplification signals have a rise time of 200 ns and a fall time of about 1 ms so that an electron incident on the detector causes a step-like response in the digitized trace whereas the resulting pulse height is proportional to the electron energy. A series of two trapezoidal filters [JK94] detects these steps and determines the event information, such as energy and timing. The functional principle and the application to a sample trace are shown in figure 3.14. One filter stage is defined by its shaping length L and its gap length G, both given in quantities of 50-ns ADC time bins. The filtered signal output S_i at a particular time bin i is computed from the difference between two moving sums of the previous $2L + G$ ADC trace values v_i, whereas each sum is calculated within a time window of length L, both windows being separated by G time bins:

$$S_i = \sum_{j=0}^{L} v_{i-j} - \sum_{k=L+G}^{2L+G} v_{i-k} \ . \tag{3.4}$$

The shaping length defines the amount of filtering and smoothing of the signal while a longer shaping length sums up more trace values averaging out noise. The gap length accounts for the non-vanishing rise time of the detector response to allow a proper energy determination. Due to the applied filter logic, the maximum of the output signal from the first filter stage equals the height of the step in the trace and occurs L time bins after the event signal. The resulting trapezoid has a flat top of length G. The second filter provides the derivative of the first filter by applying the second filter with a reduced shaping length of $L/2$ and no gap length to the output of the first filter. The consequent zero-crossing corresponds to the maximum of the first filter stage and occurs $3L/2$ time bins after the initial signal step. For each zero-crossing in the second filter, a trigger is released if the corresponding peak height from the first filter is above a programmable energy threshold. In this case, the event-energy information is provided by the peak height from the first filter stage while the event-time information is given by the time bin of the zero-crossing from the second filter stage corrected by $3L/2$ time bins. The indirect way via the second filter simplifies searching for the maximum in the first filter since finding a zero-crossing is easier to realize than detecting the highest point of a peak. However, due to existing noise, the determined peak height may not be the actual maximum of the trapezoidal pulse.

3.7.3 Slow-Controls System

All hardware devices which are not part of the detector-signal chain are monitored and controlled by the slow-controls system. Communication between the individual devices and the system is established by compact Field Point (cFP) units from National Instruments. Overall management is provided by a central DAQ and control system, zentrale Erfassung und Steuerung (ZEUS) [LK05]. It consists of the ZEUS engine which communicates with the cFP units to read sensor data and change set points, the ZEUS logger which records relevant data, and the ZEUS VI library which communicates with external software interfaces. A graphical user interface, based on LabVIEW Web UI [Ell07], allows to perform status checks and setting changes of all connected hardware devices. In addition, the local cFP units monitor interlocks, e.g. high-voltage interlocks, and critical components, e.g. magnets, vacuum system, and post-acceleration electrode, such that alarms are generated when interlocks are activated or hardware readouts go out of tolerance. Appropriate messages are then sent via text message or email. In the case of an emergency, a shutdown

Figure 3.14: Trapezoidal filter. Left: Schematic description. The response of the two-stage trapezoidal filter in dependence of time in ADC time bins is visualized where L is the shaping length and G is the gap length. **Right: Filter application to data.** The step-like response in the trace with a 200-ns rise time and a 1-ms fall time of a typical 18.6-keV electron is shown as well as the signal outputs of the two applied trapezoidal filters with $L = 128 = 6.4\,\mu s$ and $G = 4 = 200\,ns$. Each recorded waveform consists of 2048 bins, sampled in 50-ns ADC time bins, with a maximum ADC trace value of 4096 (12 bit). For better visualization, the base line of the represented waveform was reduced by 1850 ADC trace values which is usually located at around 2000 ADC trace values, while the outputs of the first and second filter stage were divided by 10^2 and 10^4, respectively. The second filter detects its zero-crossing at $t_{\mathrm{ADC}} = 1015$ which results in a maximum of the first filter at $t_{\mathrm{ADC}} = 1015 - L/2 = 951$ so that the time window of the initial signal is located between $t_{\mathrm{ADC}} = 1015 - 3L/2 - G = 819$ and $t_{\mathrm{ADC}} = 1015 - 3L/2 = 823$. The peak height of the first filter gives an ADC energy of $E_{\mathrm{ADC}} = 23845/L = 186.289$. This leads to a trigger if the set energy threshold is lower than this value. All channels are electronically adjusted by the variable gains on the optical sender boards such that 1 ADC energy bin corresponds to about 100 eV which results in an initial electron energy of 18.6 keV in the actual example.

of the affected system is initialized. The advanced data extraction infrastructure (ADEI) [Chi10] is a highly modular data-management tool which archives all relevant data centrally. In contrast to ZEUS, which can only be accessed within the local KATRIN network, ADEI provides worldwide, interactive access to the data by the ADEI web-service interface. The latter allows advanced communication between the slow-controls system and ORCA.

Apart from data-taking features, ORCA can control low-level detector tests provided by the power-and-control board, such as leakage-current measurement, temperature readout, bias-voltage metering, and pulser injection to a selected channel. It also allows to control and monitor the variable gain stages of the individual channels on the optical sender boards by the power-and-control-board interface, and regulation of the heaters of the vacuum electronics by a programmable PID loop. In addition, ORCA can communicate with the slow-controls system via the ADEI interface in order to control and monitor all connected hardware devices in the KATRIN network, like pumps, valves, and power supplies. ORCA is fully scriptable to allow continuous data-taking operations with controllable hardware settings. Permanent monitoring of critical components is of huge importance and the reason why ORCA sends out alarm messages if certain limits are undershot or exceeded and in case of an emergency.
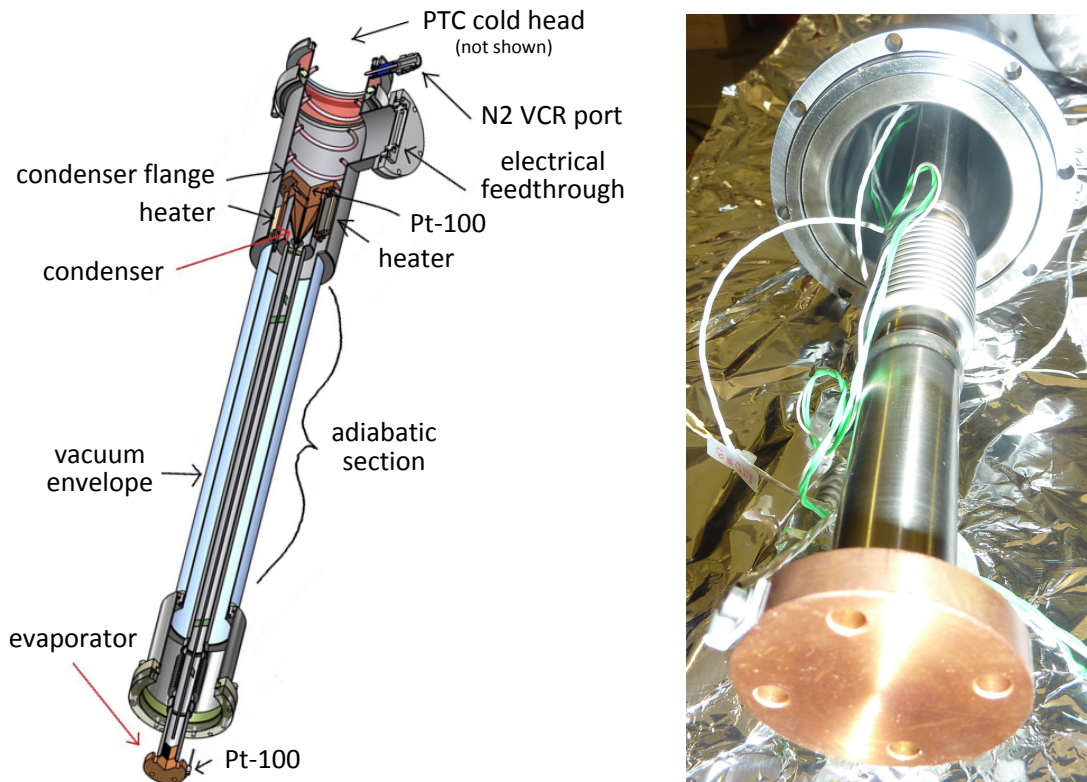
Figure 3.15: Heat pipe. Left: Schematic cross section of the heat pipe. The cold head of the pulse-tube cryocooler (not shown) couples to the top of the condenser and is surrounded by a spiral tube in order to condense nitrogen. Drawing adapted from [Ams14]. **Right: Picture of the evaporator.** The connection between the heat pipe and the evaporator is established by a bellows which reduces microphonics. A Pt-100 sensor is bolted to the end of the evaporator to allow continuous temperature monitoring.

3.8 Cooling System

An active cooling system is required to temperature-stabilize the detector wafer and the front-end electronics below room temperature. Firstly, this reduces leakage currents and thus thermal noise and secondly, it prevents damage to the vacuum electronics by over-heating.

Cooling is provided by a custom-built nitrogen-filled heat pipe [FRA10a] whose cutaway view is shown in figure 3.15. It makes use of a single-stage pulse-tube cryocooler of type *Cryomech PT60-UL*, powered by a water-cooled compressor of type *Cryomech CP830* [Cry07a] [Cry07b], to condense gaseous nitrogen from an external reservoir within a slit-ted conical copper condenser [ABP12]. The external nitrogen reservoir is held at room temperature and is attached to the condenser by a spiral tube with low thermal conductance, surrounding the cold head of the cryocooler. Condensed nitrogen droplets flow to the tip of the condenser and through the inner 3-mm diameter stainless-steel tube in order to reach the evaporator at the end of the heat pipe. The evaporator supports a 60-W boiling rate [Jin09]. In the opposite direction, vaporized nitrogen rises in the outer tube with a diameter of 25 mm and a length of 78 cm, forming the adiabatic region of the heat pipe, and then returns to the condenser. The total nitrogen volume is 4.1 ℓ of which 3.7 ℓ is the external reservoir so that the entire heat pipe is filled with 4.7 g of nitrogen. A transducer of type *Honeywell 19C015PA4K* senses the nitrogen pressure within the system [Cen12]. Two Pt-100 sensors monitor the temperatures at the condenser and the evaporator whereas a pair of heaters (50 W, 1 kΩ) attached to the condenser maintain a favored condenser temperature above the freezing point of nitrogen via a controlled

PID loop. Both heaters are powered by an external power supply of type *TDK-Lambda GEN750W* [TDK08]. The heat pipe operates as a closed circuit and an independent system. It is attached to the HVac chamber between both magnets such that the cold head is mounted 1.2 m above the magnet axis to allow a proper operation of the cold head outside the magnetic field. The evaporator is connected to a copper ring which surrounds the ceramic insulator of the post-acceleration electrode in order to separate the heat pipe from the post-acceleration potential. The copper ring is enwrapped with superinsulation foil that increases thermal performance. Heat generated from the vacuum electronics is thus conducted along the detector flange, the post-acceleration electrode and the copper ring to the evaporator welded to the heat pipe via a flexible bellows to reduce microphonics generated by the cold head.

Due to the long cold chain between the heat pipe and the vacuum electronics, it takes the entire system several days to equilibrate after the initial cool down. An entire cool-down period is shown in figure 3.16. During normal operation, the heat pipe can easily maintain temperatures of the detector flange and the vacuum electronics below room temperature while both condenser heaters are functional. Due to the electronic components mounted on the preamplifier modules, the lowest electronics temperature is limited to $-40\,°C$ which results in a detector-flange temperature of $-90\,°C$. In this case, the heaters provide a power of about 5 W meaning that the heat pipe can generate even more cooling power.

During long-term operation, a particular slow but steady increase of the system temperature can be observed, except for the condenser temperature which holds steady at the desired set value. The temperatures of both the evaporator on the cold end of the cold chain and the preamplifier modules on the warm end rise slowly and steadily in temperature over time with similar behavior, but time-displaced by about half a day due to the long cold chain. At the same time, the nitrogen pressure in the heat-pipe reservoir also rises, consistent with a warming system, as well as the heater power. The cooling stability of the entire system during main-spectrometer commissioning is illustrated in figure 3.17. A possible explanation of this observation is that the emissivity of the HVac chamber is changing with time due to elevated outgassing of the vacuum electronics and cables. This gas load cryogenically adsorbs at the cold surfaces of the post-acceleration electrode and the heat pipe before it can be removed from the system by the cryopump, thereby leading to an increasing heat load of the system over time. In addition, the residual gas spectrum indicates that the vacuum conditions in the UHVac chamber are primarily dominated by water so that water adsorbed at the inner side of the post-acceleration electrode raises the head load as well. Since the same cooling power is provided by the heat pipe, the system slowly and steadily warms up. Moreover, the adsorbed gas can improve the thermal connections between the temperature sensors and the cold surfaces so that actually lower temperatures than those in place are measured. This explains the observed increase of the heat-input power through the heat-pipe heaters. However, it is extremely challenging to verify this hypothesis. The consequences for the detector performance are described in chapter 4. The temperature stability of the front-end electronics and the detector flange can be noticeably improved by using the vacuum-electronics heaters for temperature regulation instead of the heat-pipe heaters due to shorter distances in heat conductance.
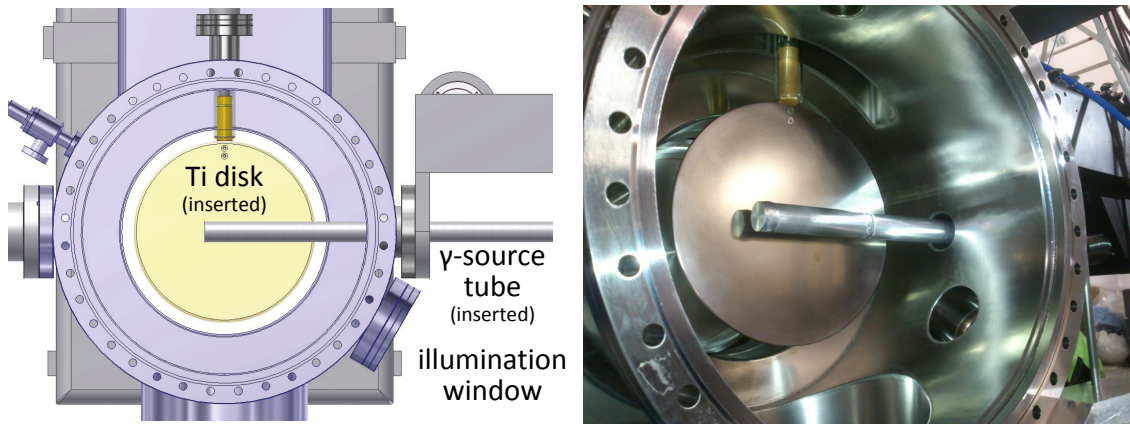
3.9 Calibration System

In order to perform repeated detector calibrations and to investigate the detector response to radiation, two calibration sources are included in the detector system. Both sources are attached to the UHVac chamber between both magnets and can be moved into the detector line of sight without breaking the vacuum via pneumatically operated bellows. Figure 3.18 shows a picture of the calibration system as seen from the detector.
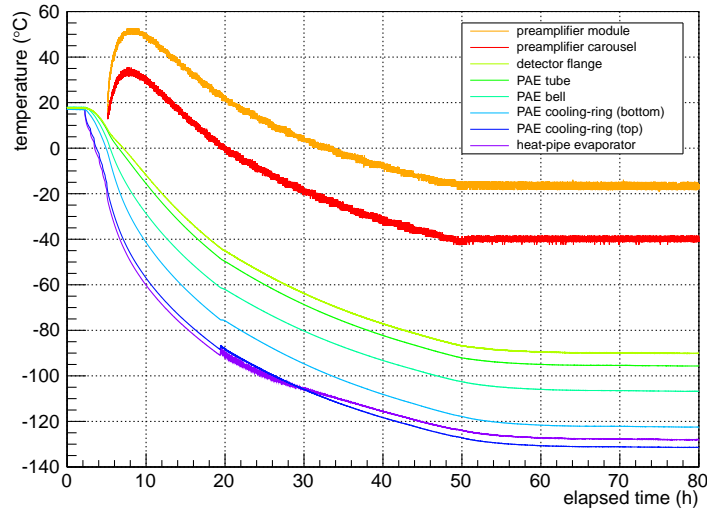
Figure 3.16: Cool-down behavior of the system. A nominal condenser temperature of 76.0 K ($-197.15\,°C$) was set during the diagrammed cool-down curve. It takes about 60 h until the entire system reaches equilibrium when it is cooled down from room temperature. Finally, the preamplifier modules are continuously operated at $-18\,°C$, the vacuum-electronics carousel at $-40\,°C$, and the detector flange at $-90\,°C$. The heat pipe would able to provide even more cooling power but the operating temperature of the front-end electronics is limited to $-40\,°C$.
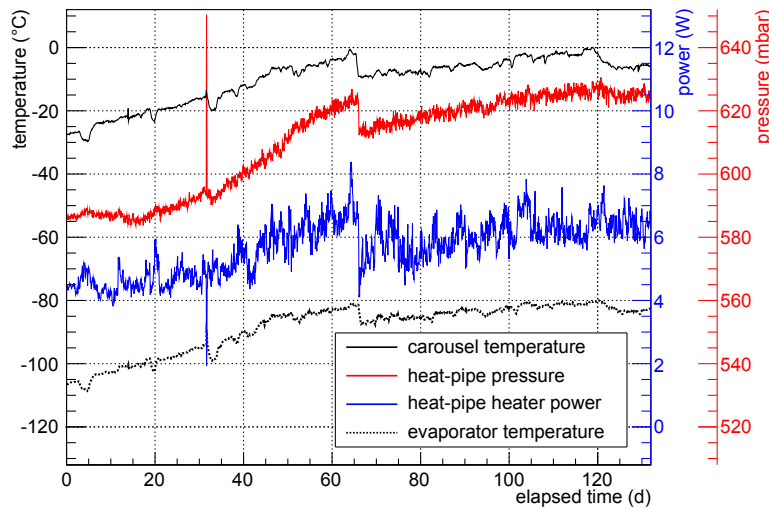
Figure 3.17: Temperature stability of the system during SDS commissioning. Within the first 67 days, the system warmed up by about $30\,°C$. In this example, the temperatures of the vacuum-electronics carousel (black, -30 to $0\,°C$) and the heat-pipe evaporator (green, -110 to $-80\,°C$) are diagrammed since the sensors mounted along the post-acceleration electrode and at the detector flange show a similar behavior. The temperature increase corresponds to a drift of about $0.5\,°C$/day. Moreover, the heat-pipe heater power (blue, 4.5 to 7.5 W) and pressure (red, 590 to 630 mbar) rise correspondingly. At day 67, it was decided to lower the favored set value of the condenser temperature from 76.5 to 76.3 K to counteract the temperature increase of the system. As a consequence, the temperatures, heater power, and pressure abruptly drop. In the following 65 days, the temperatures are stable within a range of $10\,°C$. The visualized quantities have high correlation coefficients between the evaporator temperature and the carousel temperature (0.992), the heat-pipe pressure (0.951), and the heat-pipe heater power (0.822).

Figure 3.18: Calibration system. Both a schematic view (**left**, adapted from [Ams14]) and a picture (right, adapted from [Sch13b]) show the horizontally inserted γ-source tube and the vertically inserted photoelectron-source disk as seen from the detector, looking upstream toward the main spectrometer. The titanium disk can be illuminated with light from an ambient-air UV LED through the illumination window.

The first source is an encapsulated 18.5-MBq γ-source of ^{241}Am ($\tau_{1/2} = 432.2\,\mathrm{y}$) which allows an absolute energy-scale calibration to mono-energetic γs independent of dead-layer effects. This source provides intensive γs at 26.3448 keV and 59.5412 keV via the α-decay of ^{241}Am into ^{237}Np as well as X-rays from the daughter isotope [FE04] and fluorescence lines from the copper post-acceleration electrode [Tho09] as shown in figure 3.19. Therefore, the source is perfect for calibrating the low-energy electron detector. The significant γ-emission lines have small uncertainties of 0.2 eV [FE04] in their energies and create two distinct, separate, Gaussian-like peaks in the ^{241}Am energy spectrum which makes them ideal candidates for detector calibration. The remaining peaks are generated by several individual lines with well-defined energies located within the same single peak due to the relatively large energy resolution of the detector. Thus, these lines are excluded from calibration in the first approximation. The pixel-by-pixel calibration can be understood as conversion from recorded ADC values to measured energies E in the energy spectrum. The two intensive γ-peaks are fitted with individual Gaussian distributions within an energy range of 20 % of the corresponding peak height while the obtained mean ADC values and their statistical uncertainties determine the detector calibration by using a linear fit ($E = m \cdot \mathrm{ADC} + c$) through the two points and the zero point in the KATRIN-relevant energy region well below the saturation energy.

The source can be horizontally moved into the system via a bellows with a thin aluminum window on its end [Ste11]. This window reduces energy-loss effects due to interaction with matter during calibration, since the total mean free path of 60-keV γs is 1.33 cm in aluminum and 0.11 cm in iron [Ber10]. However, γ-radiation liberates a non-negligible amount of photoelectrons from the source holder and the aluminum window. These high-rate photoelectrons are adiabatically guided by the magnetic field to a specific region of the detector wafer so that the resulting photoelectron continuum overlaps the calibration lines in the affected pixels as shown in figure 3.20. This leads to an increased count rate in this region. In figure 3.20, the resulting magnetic shadow of the source on the detector is shown at nominal magnetic field. Its size and location depend on the magnetic-field setting and the position of the source. Therefore, a complete calibration of all pixels under magnetic field requires two calibration measurements at different source positions so that the affected regions do not overlap while the entire wafer is illuminated. Using this strong source, a typical complete detector calibration with sufficient statistics for peak fitting takes a couple of hours depending on the shaping length and the resulting energy
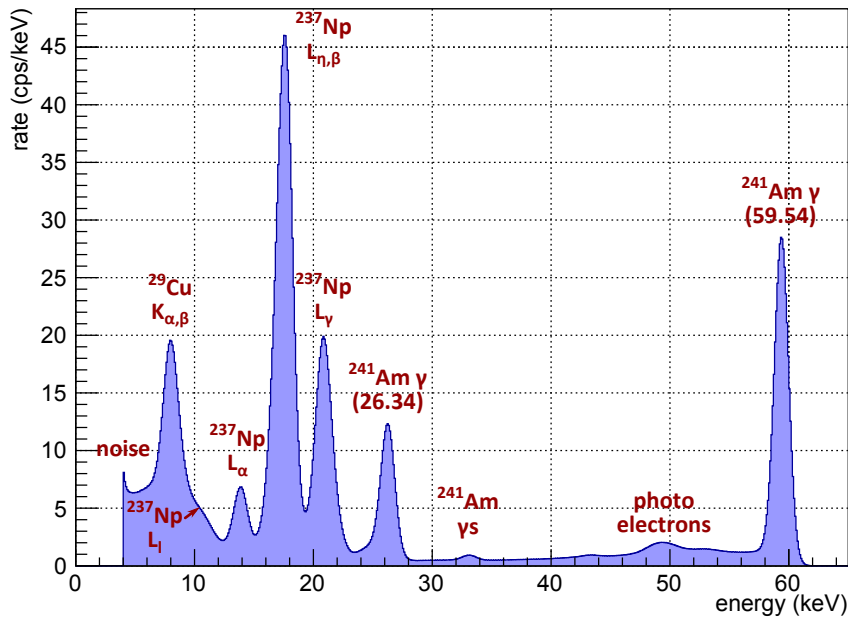
Figure 3.19: Global ^{241}Am spectrum measured with the detector. The global energy spectrum shows several peaks and features when using the ^{241}Am source for detector calibration: the electronic noise threshold (~ 4 keV), a single peak by ^{29}Cu K$_{\alpha 1, \alpha 2, \beta 1, \beta 3}$ fluorescence lines due to the copper post-acceleration electrode, the smeared ^{237}Np L$_l$ X-ray line, a single peak by ^{237}Np L$_{\alpha 1, \alpha 2}$ X-ray lines, a single peak by ^{237}Np L$_{\eta, \beta 1 - \beta 6}$ X-ray lines, a single peak by ^{237}Np L$_{\gamma 1 - \gamma 3, \gamma 6}$ X-ray lines, the first calibration peak by the ^{241}Am γ-line at 26.3448(2) keV, a single peak by three ^{241}Am γ-lines, a characteristic feature by liberated photoelectrons from surrounding materials, and the second calibration peak by the ^{241}Am γ-line at 59.5412(2) keV. Individual fluorescence and X-ray lines cannot be resolved due to the relatively large energy resolution of the detector.

resolution, e.g. 2×1 hours at $L = 6.4\,\mu$s and 2×2 hours at $L = 1.6\,\mu$s. Calibration is usually performed twice a week to monitor long-term stability.

The second source is a photoelectron source which can be vertically moved into the magnetic flux tube via a bellows. It consists of a polished titanium disk with a diameter of about 20 cm which can be energized with variable potentials of up to -30 kV and can be illuminated with light from a 255-nm UV LED from the ambient-air side through a vacuum-tight quartz window. Generated photoelectrons are then adiabatically guided by the magnetic field to the detector wafer so that all pixels can be illuminated at once. Since the photoelectrons gain only longitudinal energy by the applied electrostatic field, their incident angle is $\sim 0°$. The size and location of the image of the disk onto the detector wafer depend on the magnetic-field setting and the position of the source. At nominal magnetic field, the disk is exactly imaged when it is fully driven into the magnetic flux tube. The disk is powered by a *Spellman TOF3000* high-voltage power supply with which the energy of the photoelectrons is set [Mar12]. The illumination device containing the UV LED is adjustable and therefore allows to generate a uniform illumination pattern, both on the disk and the detector. An acceptable homogeneity of better than 1:10 in the individual count rates over the entire wafer is achievable which is shown in figure 3.21. The UV LED can be operated either with a constant voltage powered by an external power supply, or in pulsed mode supplied by an *Agilent 33220A* waveform generator [Agi07]. On top of the support structure of the disk, a pA-scale current meter is installed inside a series of nesting boxes to measure the effective photocurrent induced by photoelectrons emitted from the
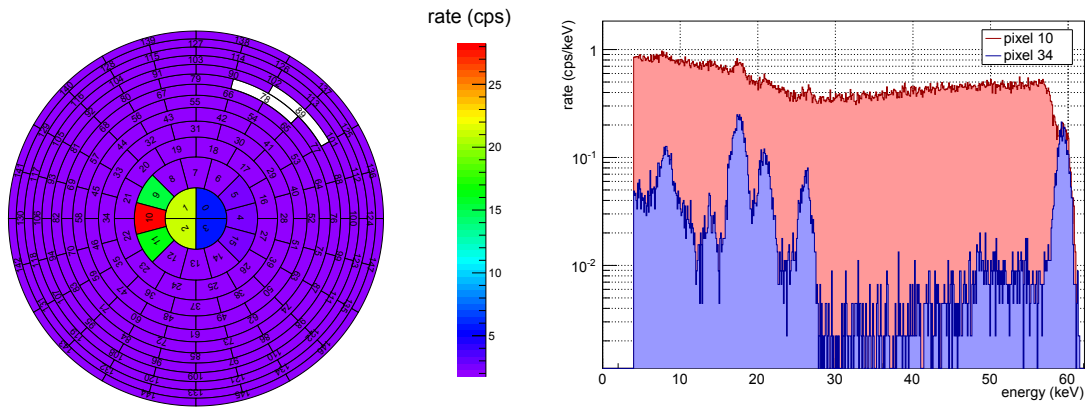
Figure 3.20: Calibration with ^{241}Am source at nominal magnetic field. For a fully inserted γ-source, liberated photoelectrons from the source holder generate a magnetic shadow on the detector (**left**). The resulting photoelectron continuum strongly dominates the ^{241}Am calibration lines in the recorded energy spectrum of the affected pixels. In this case, the histogram of pixel #34 shows definite calibration lines while the histogram of pixel #10 is dominated by the photoelectron continuum (**right**). The electronic noise threshold is at 4 keV.
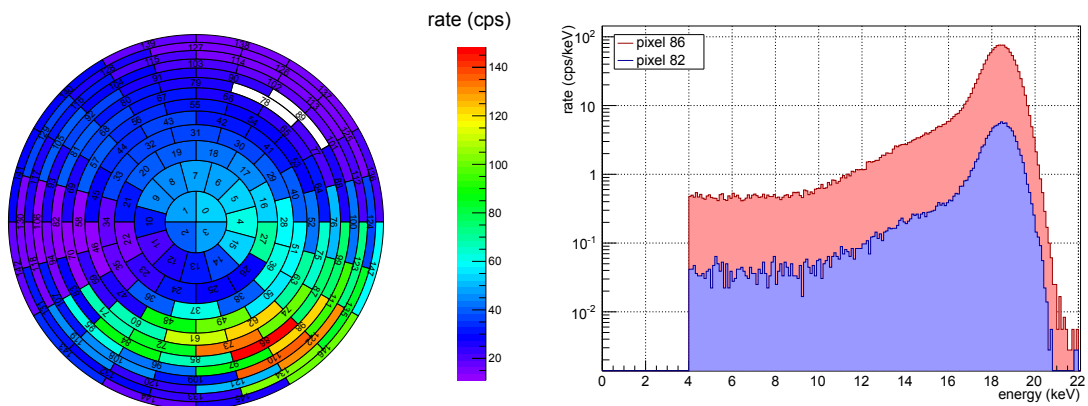
Figure 3.21: Calibration with photoelectron source at nominal magnetic field. Due to the steep angle between the titanium disk and the UV LED, an illumination homogeneity of better than 1:10 is achievable (**left**). Although the uneven illumination pattern does not change the shape of the recorded photoelectron energy spectrum in the first approximation, it has an influence on different count rates (**right**). The electronic noise threshold is at 4 keV.

disk with fA-accuracy [Mar12]. Apart from the UV LED, the illumination device also includes a red LED which can be pulsed with the stated waveform generator. The pulsed light floods the UHVac chamber, reflects and scatters from interior surfaces, and enters the detector wafer. This optical detector illumination allows to investigate the linearity of the detector signal chain since the pulser amplitude can be varied, thereby changing the LED current and hence the light intensity [Pet11].

3.10 Shield and Veto System

The shield and veto system is installed within the warm bore of the detector magnet such that it surrounds the most sensitive part of the vacuum system in which the detector wafer is located. It consists of two nested cylindrical shells built of 1.27-cm thick, oxygen-free, high-conductivity copper and of 3-cm thick lead which both are enclosed by a veto system made of 1-cm thick plastic-scintillator panels of type *Bicron BC-408* manufactured by *Saint-Gobain Industrial Ceramics Inc.* and wrapped in *Gore Diffuse Reflector Product* with an outer layer of adhesive-backed aluminum foil. The shield and veto system is
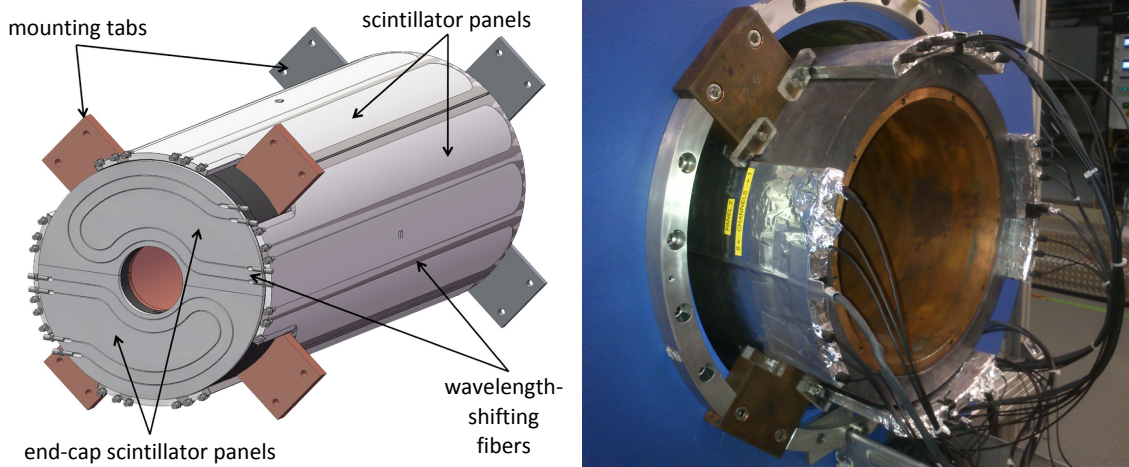
Figure 3.22: Shield and veto system. Both a schematic layout (**left**, adapted from [Ams14]) and a picture (**right**) show the cylindrical setup of the passive-shield and the active-veto system consisting of an inner 1.27-cm copper shield, a middle 3-cm lead shield, and outer 1-cm plastic-scintillator panels. Moreover, the arrangement of the wavelength-shifting fibers inside the veto panels are indicated.

completed by corresponding semicircular end caps attached to the downstream end of the HVac chamber. The entire system is 38 cm in diameter and 106.3 cm in length. Its schematic layout is shown in figure 3.22. The passive shield reduces the γ-background as well as neutrons and blocks X-rays by an estimated factor of 20 [Leb10] while the active veto tags incident cosmic rays and high-energy γs from natural environmental radioactivity.

There are three embedded wavelength-shifting fibers in each of the four long, barrel veto panels and two in each of the two end-cap panels. The fibers are bent into U-shapes according to figure 3.22, and extract generated scintillation light on both ends to 32 clear plastic optical fibers. Finally, the light is detected by individual multi-pixel photon counters (MPPCs) of type *Hamamatsu S10362-11-050P* connected to the fiber ends [For13b]. The devices are mounted on a bar made of aluminum which is maintained in a dry-nitrogen housing at $-18\,^{\circ}$C by two water-cooled thermoelectric coolers by *TE Technology Inc.* in order to reduce dark currents below 5 kcps per channel [TE 12]. The custom-designed suite of veto electronics made by the IPE at KIT consists of four identical front-end circuit boards operated outside the dry-nitrogen atmosphere. Each board serves eight MPPCs with separate preamplifier channels, individually adjustable bias voltages of $60-80\,$V, and single base-line voltages which allow to electronically clip thermally caused, single-photoelectron pulses and noise from the electronics. Power is provided by an *Agilent N6700B* modular power supply [Agi12]. After the electronic signal processing, the amplified veto signals are sent via 50-Ω coaxial cables to two analog summing boards, connected to the analog backplane of the DAQ crate for digitization. Each summing board serves the MPPC pulses of two barrel and one end-cap veto panels. For the DAQ crate, it provides individual readouts for each MPPC channel and an analog sum signal of all MPPC channels connected to the same scintillator panel.

In the veto-signal chain, two FLT cards sharing the same SLT card as for the detector-signal chain are used. ORCA provides a special *veto mode*. Each slave FPGA on the FLT cards handles all MPPC signals associated with a specific, single scintillator panel. Cosmic rays and high-energy γs are identified by coincidences between a certain number of fiber signals from the same panel, typically two, within a particular coincidence interval, typically 100 ns. A trigger is released when such a coincidence occurs at the same time that the sum of all fiber signals in the associated panel exceeds a programmable threshold above the single-photon peak. This summing, performed on dedicated analog summing
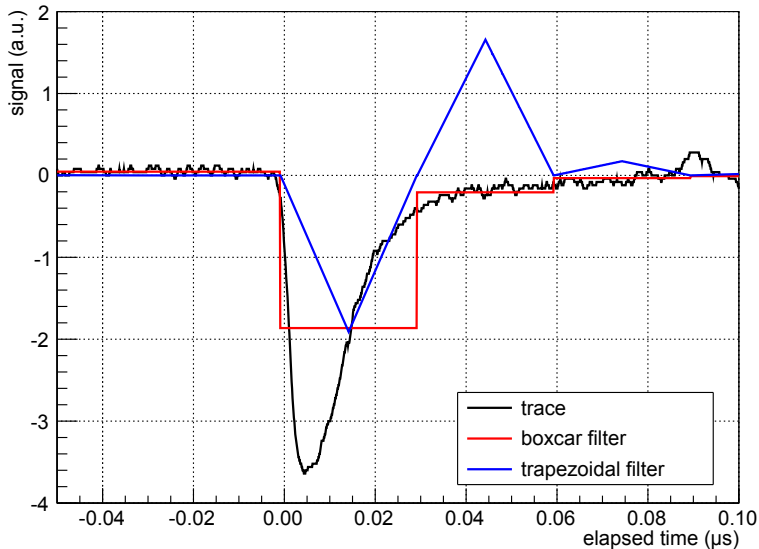
Figure 3.23: Processing of a veto signal. An exemplary illustration of the processing of a typical veto signal is shown using an offline software filter. The trace (black) was recorded by a scope with 10-GHz sampling rate. As first filter stage, the boxcar filter (red) calculates a floating average over a moving time interval of 30-ns length. As second filter stage, the trapezoidal filter (blue) determines the event time stamp via the zero-crossing. Values adapted from [Rin14].

boards as stated above, greatly reduces accidental coincidences caused by high-rate multi-photon dark currents in the MPPCs. Coincidences between different panels are neglected in order to allow tagging the γs which cannot pass the passive shield on the other side but reach the sensitive volume and create background events.

Typical veto post-amplification signals have a short pulse length of only up to $100\,\mathrm{ns}$ (FWHM) with an amplitude of several tens of mV. The pulse length is comparable to the sampling rate of the DAQ crate ($20\,\mathrm{MHz}$) so that the Nyquist criterion ($f_{\mathrm{sampling}} \geq 2f_{\mathrm{signal}}$) is violated when the signals are processed with the trapezoidal filter as used for the detector signals, leading to aliasing. An adjustable boxcar filter with 2 to 4 samples replaces the trapezoidal filter of the first filter stage in the digitized DAQ chain to capture the full veto trace, eliminate signal-clipping effects, reduce aliasing, and provide a more accurate event-energy determination. A trapezoidal filter as second filter stage still determines the event-time information. The processing of a veto signal is illustrated in figure 3.23.

3.11 Conclusion

In this chapter, the sophisticated setup of the KATRIN detector system was described in detail. A special focus was set on the working principle and performance of the individual primary components. It was shown that almost all components fulfill both the required and designed specifications for the KATRIN experiment. In the following, a summary of the most important observations is given:

- **Magnet system:** It has been demonstrated by long-term stability measurements with a NMR probe that the favorable operation mode for both magnets is the persistent mode. In this mode, the magnetic field generated by the pinch magnet was measured to drift less than $20\,\mathrm{ppm}$ per month which is well below the required field stability of $0.1\,\%$. A new pinch magnet has been ordered in 2014 to allow a proper,

long-term stable magnet operation at nominal fields for neutrino-mass measurements from 2016 onward.

- **Vacuum system:** Both vacuum chambers can be operated at base pressures of 3×10^{-9} mbar and 3×10^{-6} mbar in the UHVac and HVac chamber, respectively, close to their designed specifications of 1×10^{-9} mbar and 1×10^{-6} mbar. In the future, vacuum conditions are expected to improve as existing and localized leaks are being repaired.

- **Post-acceleration electrode:** Although a stable post-acceleration potential with a benchmark of $+30$ kV seems to be unrealistic to obtain in the nearer future due to breakdowns and discharges occurring in both vacuum chambers, the achieved value of the post-acceleration potential of $+11$ kV after careful long-term conditioning suffices to accelerate even thermal electrons above the 4-keV electronic noise threshold.

- **Detector wafer:** Two wafers were tested, both showing two neighboring pixels at different locations to suffer from inter-pixel short circuits. This issue seems to trace back to the manufacturing process of the pixel-pattern mask. Therefore, only 146 of 148 pixels (98.6%) of the examined wafers can be used for proper data taking. A set of new wafers has been ordered at the end of 2013 and is currently under investigation.

- **Readout electronics:** The entire signal chain shows 100% working channels with a power dissipation of 114 mW per channel, which is slightly higher than the designed value of 100 mW. As it will be shown in the following chapter, electronic noise contributions primarily characterize the energy resolution of the detector to ~ 1.5 keV (FWHM) for 18.6-keV electrons.

- **DAQ:** In energy mode, which provides both event-energy and event-time information, the detector can be operated at rates of up to 108 kcps without suffering from any detectable dead time. This is slightly above the specified value of 100 kcps.

- **Cooling system:** The heat pipe offers a huge amount of cooling power in order to cool down the vacuum-electronics carousel to $-40\,^\circ$C and the detector flange to $-90\,^\circ$C. The temperature stability of the front-end electronics and the detector flange can be noticeably improved by using the vacuum-electronics heaters for temperature regulation.

- **Calibration system:** Both calibration sources, a γ-emitter and an adjustable photoelectron source, can be used to investigate the detector response on radiation independently from other systems at any time without breaking the vacuum. A proper calibration using γs from the 18.5-MBq ^{241}Am source requires two calibration measurements with different source positions. The electron source shows a suitable illumination pattern with a homogeneity of better than 1:10.

- **Shield and veto system:** The shield and veto system surrounds the sensitive parts of the vacuum system in order to reduce and tag background. The active veto uses 32 MPPCs to detect light from the plastic-scintillator panels. All channels are properly working.

In the subsequent chapter, the detector performance is described in detail while the individual primary components are operated in accordance with each other. The latter fact makes detector investigations and characterizations a quite challenging task.

CHAPTER 4

Detector Characterization

The focus of this chapter is on the detailed characterization of the detector being operated in accordance with the major sub-components of the detector system. The investigations were targeted to verify that the detector allows almost background-free, highly efficient, and long-term stable detection of electrons which have transmitted through the main spectrometer. During neutrino-mass measurements, a signal rate of only 20 mcps is required close to the tritium endpoint, which is much lower than the rates of several kcps during detector calibration where an angular selective electron gun housed in the calibration and monitoring system of the tritium source is used. Therefore, a detailed understanding of both the detector performance under various conditions and the detector response to electrons with different energies and rates is of great importance. In the subsequent sections, specific measurements and results with regard to the detector performance relevant for the KATRIN experiment are presented and discussed. The first part of this chapter (sections $4.1 - 4.6$) describes the detector characterization in a separated stand-alone mode where a gate valve to the main spectrometer was closed at all times. The second part (sections $4.7 - 4.9$) gives an overview of the detector performance during the first main-spectrometer commissioning. If not otherwise stated, all data were recorded with detector wafer #96724 with 146 of 148 functional pixels (98.6 %) (section 3.5). Further details are listed in [Ams14].

4.1 Detector-Response Optimization

The ^{241}Am γ-source described in section 3.9 is an ideal candidate to not only calibrate the low-energy electron detector largely independently from dead-layer effects but also to optimize the detector response by investigating the full width at half maximum (FWHM) energy resolution of the 59.54-keV γ-line experimentally. In each case, the energy resolution was determined as the FWHM of a Gaussian distribution fitted to the portion of the peak interval with more than 20 % of the peak amplitude. At this stage, the optimization of adjustable detector parameters is examined, such as trapezoidal filter settings (section 4.1.1), reverse-bias voltage (section 4.1.2), and operating temperature (section 4.1.3). This is done in the absence of magnetic field and post-acceleration potential for simplification.

4.1.1 Trapezoidal Filter Settings

The trapezoidal filter used for pulse shaping and subsequent determination of event energy and timing in the IPE v4 crate, can be adjusted by two characteristic parameters (section 3.7): The shaping length L defines the amount of filtering and smoothing of the noise-affected, step-like signal, while the gap length G accounts for the non-negligible rise time
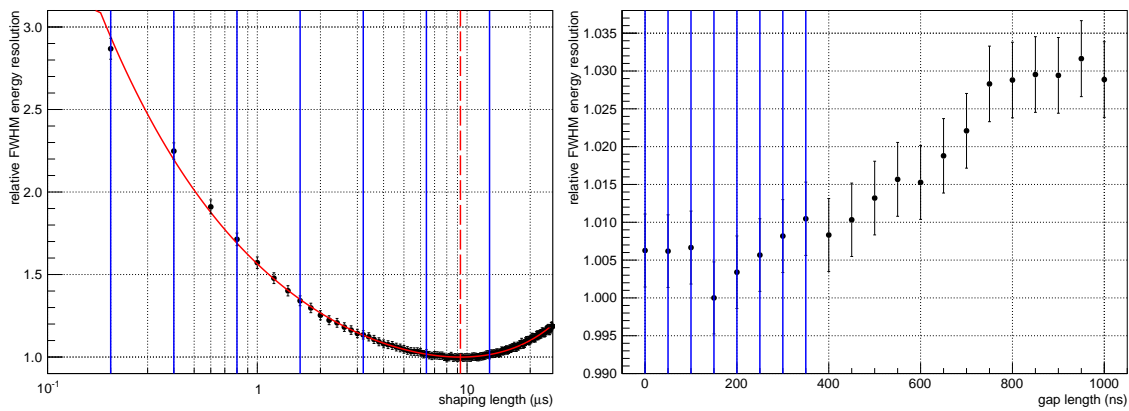
Figure 4.1: Relative energy resolution for different trapezoidal filter settings. Solid-blue vertical lines indicate which filter settings are available in ORCA. **Left: Optimization of shaping length.** The gap length is kept at $G = 200\,\mathrm{ns}$. The combined fit of a power-law relation and an exponential function shows a broad minimum at $L = 9.3(1)\,\mathrm{\mu s}$, illustrated by the dashed-red vertical line. **Right: Optimization of gap length.** The shaping length is kept at $L = 6.4\,\mathrm{\mu s}$.

of the detector response. In the first approximation, a longer shaping length seems to be a reasonable setting to improve the energy resolution of the detector since it integrates over a wider window in the event trace thus averaging out high-frequency noise. However, it may introduce low-frequency noise and disturbing effects based on the 1-ms fall time of the preamplifier modules. A shorter or longer gap length than required underestimates the measured energy. Therefore, an optimal selection of the shaping parameters is necessary to improve the energy resolution significantly depending of the measurement purpose [JK94] [Zha13].

Waveforms of an 1-hour ^{241}Am calibration (run #1829) were investigated with an off-line software trapezoidal filter varying the shaping and gap length in 200-ns and 50-ns increments, respectively, with the objective to improve the global FWHM energy resolution of the 59.54-keV γ-line. The results are shown in figure 4.1. The illustrated energy resolution is normalized to the best value at $L = 9.3(1)\,\mathrm{\mu s}$, including statistical fit uncertainties. Solid-blue vertical lines indicate which filter settings are available in ORCA. Concerning the optimization of the shaping length L at a fixed gap length of $G = 200\,\mathrm{ns}$, the measured behavior is fitted by a combination of a power-law relation and an exponential function describing the energy resolutions ΔE for short and long shaping lengths, respectively, in good agreement ($\chi^2/\mathrm{ndf} = 9.59/124$). However, the slope of the curve close to its minimum is extremely flat so that even shaping lengths of $L = 6.4\,\mathrm{\mu s}$ and $L = 12.8\,\mathrm{\mu s}$, which represent directly adjustable filter settings in ORCA, show a relative γ-line widening of $1.02(02)$ and $1.01(02)$ only, respectively, considering statistical fit uncertainties. Shorter shaping lengths result in extremely broad γ-lines since high-frequency noise dominates which cannot be canceled out, while longer shaping lengths introduce additional noise and artifacts which impair the energy resolution. Concerning the optimization of the gap length G at a fixed shaping length of $L = 6.4\,\mathrm{\mu s}$, the gap length seems to have no clearly

Table 4.1: Noise threshold as a function of shaping length. Longer shaping lengths average out high-frequency noise over a wider integration window, resulting in a lower noise threshold in the resulting energy spectrum.

shaping length L ($\mathrm{\mu s}$)	0.2	0.4	0.8	1.6	3.2	6.4	12.8
noise threshold (keV)	~ 13.5	~ 10.5	~ 8.5	~ 7.0	~ 5.5	~ 4.0	~ 4.0
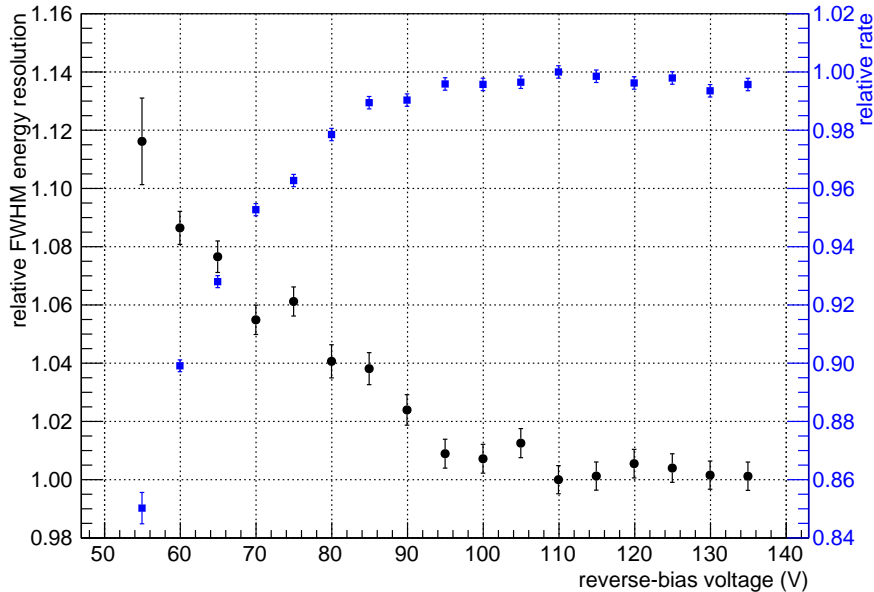
Figure 4.2: Detector response in dependence of reverse-bias voltage. The relative energy resolution (black points, left axis) and the relative rate (blue points, right axis) reach an equilibrium of saturation above a bias voltage of 95 V. *Canberra* quotes an optimized detector operation at 120 V.

discernible optimal value in the range of available filter settings, although the rise time of a typical detector event is 200 ns.

Apart from the energy resolution, the size of the electronic noise threshold is a further characteristic detector quantity. It marks the lowest event energy which can be detected. In this context, short shaping lengths can lead to the detection of more accidental low-energy events due to misinterpretations of high-frequency noise and base-line fluctuations so that the noise threshold will increase accordingly. Using the threshold finder in ORCA with a 1-Hz target frequency and a 20-% safety margin in dependence of available shaping lengths (runs $\#4330 - \#4343$), the electronic noise threshold reaches its minimum value of about 4 keV at $L = 6.4\,\mu s$ and $L = 12.8\,\mu s$ while it increases steadily with shorter shaping lengths, as expected. The conservative relation deduced from the measurements using the threshold finder is shown in table 4.1.

In order to optimize both energy resolution and noise threshold, the filter settings were adjusted to $L = 6.4\,\mu s$ and $G = 200\,ns$ for almost all subsequent detector characterizations.

4.1.2 Reverse-Bias Voltage

In the case of interactions of incident radiation, charge carriers are generated and collected in the depletion zone representing the sensitive detector volume. Its width depends not only on the applied reverse-bias voltage, but also on other detector parameters such as the thickness of the intrinsic layer. The depletion zone is rather narrow when the detector is incompletely biased. This leads to a reduction in charge collection, a loss in detector efficiency, an increase in detector capacitance, and a degradation in noise properties, so that the energy resolution degrades accordingly. Therefore, it seems reasonable to operate the detector in fully depleted mode, where the bias voltage is carefully set to the value of the optimized depletion voltage such that the depletion zone covers the entire thickness of the detector. However, if the bias voltage exceeds a specific breakdown voltage, the over-biased detector suffers a sudden avalanche breakdown across the junctions. There

is a destructive, irreversible hysteresis effect so that the resulting electrical conduction continues even if the bias voltage across the detector drops below the breakdown voltage which renders the detector useless [SN06] [Kno10].

In the datasheet, *Canberra* quotes an optimized and maximum depletion voltage of 120 V and 150 V, respectively. In order to verify these statements, 1-hour ^{241}Am calibrations (runs #8827 − #8843) were performed with the objective to measure both the energy resolution of the 59.54-keV γ-line by the FWHM width and the detector rate within the peak range by the area of the Gaussian fit, while the applied bias voltage was raised from 55 V to 135 V in 5-V increments. Higher voltages were avoided to prevent irreversible damage of the detector. The results are shown in figure 4.2 such that the illustrated values are normalized to their best value, including statistical fit uncertainties. The measured relative energy resolution improves with higher bias voltages, since the depletion zone increases, the detector capacitance decreases consequentially, and the noise properties become better accordingly. The measured relative rate, representing the efficiency in a certain manner, increases likewise with higher bias voltages due to improved charge-collection properties. Both the relative energy resolution and the relative rate reach a specific plateau of saturation starting at an applied bias voltage of around 95 V. Therefore, this voltage can be understood as depletion voltage, in good agreement with the quotes from the datasheet considering some additional margin.

For further detector characterization, a bias voltage of 120 V was applied to the detector, according to the recommendation of *Canberra*.

4.1.3 Operating Temperature

The probability for an electron-hole pair to be thermally generated within the detector is

$$p(T) = C \cdot T^{3/2} \cdot e^{-E_g/(2kT)} \tag{4.1}$$

where C is a proportionality constant characteristic of the material, T the temperature, E_g the band gap energy, and k the Boltzmann constant [Kno10]. Assuming that leakage currents and thermal noise are primarily created by thermal excitations within the detector volume, both quantities can be reduced by three [seven] orders of magnitude by cooling the detector wafer from room temperature to −50 °C [−100 °C], resulting in a better energy resolution. Cooling also improves the charge-collection properties since the charge-carrier mobility of electron-hole pairs increases with decreasing temperature as indicated in table 4.2. However, the performance of the preamplifier modules may degrade with decreasing temperature since the electronic components in use have limited operating temperatures of −40 to 70 °C because of their state in specific casings. The electronics temperature is closely related to the detector temperature due to their direct coupling through the detector feedthrough flange. This limits detector cooling to a lowest temperature of −90 °C.

In order to investigate the temperature-dependent detector response and determine the optimum balance between detector and electronics temperature, individual 1-hour ^{241}Am calibrations were performed continuously during detector cooling (runs #4231 − #4319)

Table 4.2: Charge-carrier mobility in silicon. Cooling improves the charge-carrier mobility of electron-hole pairs in silicon. Values according to [Kno10].

	$T = 300\,\mathrm{K}$	$T = 77\,\mathrm{K}$
electron mobility μ_e (cm^{2}V^{-1}s^{-1})	1.35×10^3	2.1×10^4
hole mobility μ_h (cm^{2}V^{-1}s^{-1})	4.8×10^2	1.1×10^4
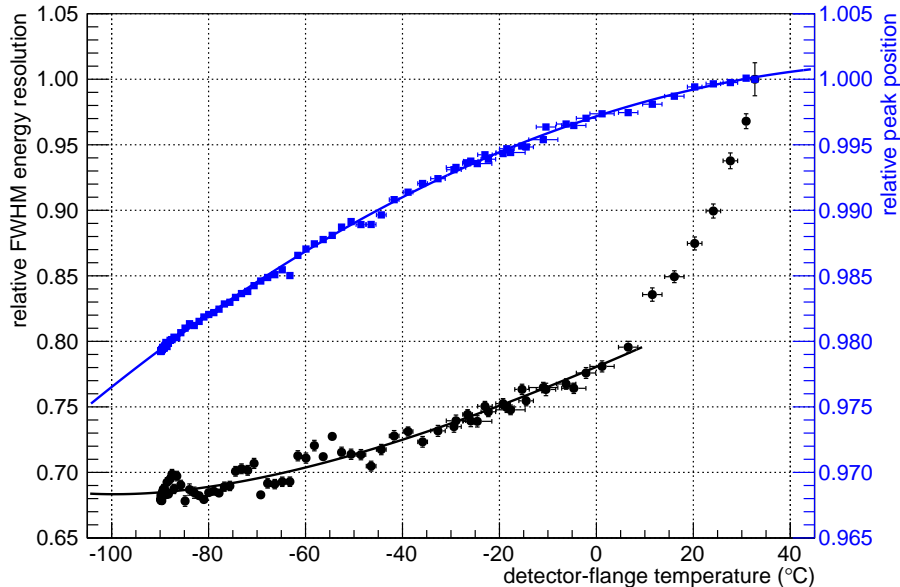
Figure 4.3: Temperature-dependent detector response. Both the relative FWHM energy resolution and the relative peak position are shown during detector cooling to $-90\,°C$. The solid lines represent associated fits to the data.

and warming (runs $\#4207 - \#4229$) within a detector-temperature range from $-90\,°C$ to $33\,°C$. In figure 4.3, the measured detector response is shown as a function of the detector-flange temperature. Here, the energy resolution and the peak position were determined from the FWHM width and the mean of a Gaussian fit to the 59.54-keV γ-line in the ADC energy spectrum, respectively, and are scaled relatively to the calibration with highest temperature. A fit according to 4.1 is applied to the energy-resolution trend ($\chi^2/\mathrm{ndf} = 206.435/68$) while the peak-position behavior follows a quadratic polynomial fit ($\chi^2/\mathrm{ndf} = 392.91/74$) in the first approximation. Within the monitored temperature range, cooling will improve the energy resolution by a factor of about $32\,\%$ and, in comparison to room temperature ($20\,°C$), by about $20\,\%$, whereas the peak position shifts to lower ADC energies by a factor of about $2\,\%$. At higher temperatures, leakage currents and thermal noise dominate due to thermally generated excitations within the detector volume, resulting in a degradation of energy resolution. There seems to be no benefit of cooling below $-80\,°C$ since the energy resolution reaches a constant plateau, and the peak position starts to change more and more significantly. This is most likely due to the fact that the performance of the electronic components does not necessarily improve with decreasing temperatures. It might even degrade on the basis of freeze-out effects of the charge carriers. In addition, the vacuum electronics already operates close to its specified minimum temperature limit, and further cooling may cause irreversible damage. In the case of unintended temperature fluctuations, a shift of the peak position may become a serious issue only if the region-of-interest is fixed within an energy window set unnecessarily narrow. A variation of $\pm 10\,°C$ at $-90\,°C$ does not lead to any obvious change in energy resolution but alters the peak position by about $\pm 0.4\,\%$ or $\pm 0.2\,\mathrm{keV}$ for the 59.54-keV γ-line. However, the energy variation is minor in comparison to the relatively large absolute energy resolution examined in the subsequent section 4.2.

For further detector characterization, detector-flange and vacuum-electronics temperatures were kept at about -70 and $-20\,°C$, respectively.
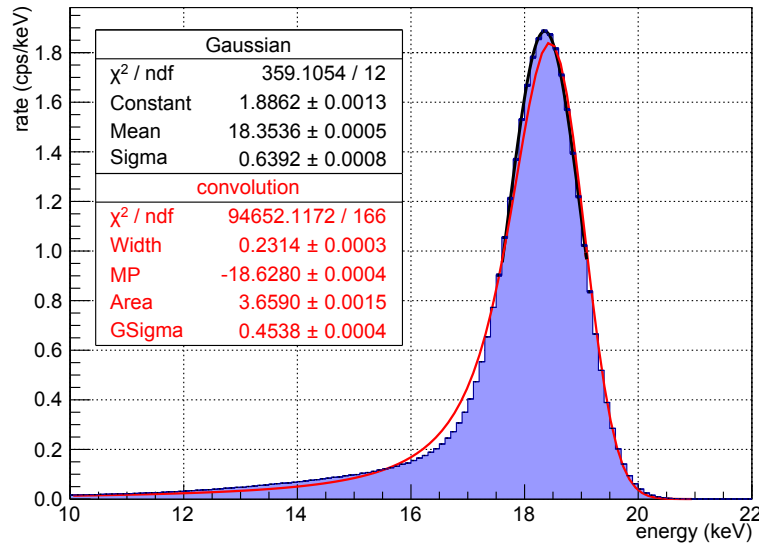
Figure 4.4: Global energy spectrum for 18.6-keV photoelectrons at magnetic field measured with the detector. The characteristic shape of the electron peak with its low-energy tail is fitted by an inverse Landau distribution convoluted with a Gaussian distribution (red line). The Landau distribution with its characteristic tail considers the energy losses of electrons in the insensitive detector dead-layer. The fit parameters show the peak scale (*Width*) and the peak location (*MP*, most probable parameter) of the pure Landau density as well as the total area (*Area*) of the fit and the width (*GSigma*) of the convoluted Gaussian function. The peak position of the pure Landau distribution is at $MP = 18.63\,\text{keV}$, but after convolution with a Gaussian distribution of $GSigma = 0.45\,\text{keV}$, the location of the peak shifts to a lower energy of $18.45\,\text{keV}$. The resulting FWHM energy resolution is $\Delta E = 1.57\,\text{keV}$. Statistical uncertainties are in the eV-scale as indicated. However, a simple Gaussian fit to the peak amplitude only (black line) gives more promising and reasonable results with an FWHM energy resolution of $\Delta E = 1.51\,\text{keV}$. The conversion for the peak width is given by $\text{FWHM} = 2\sqrt{2\ln 2}\,\sigma$.

4.2 Energy Resolution

Two calibration sources (section 3.9), a ^{241}Am source as γ-emitter and an illuminated disk elevated to high voltage as photoelectron source, were used to measure the absolute energy resolution of the detector under optimized detector conditions, as stated in the previous section 4.1. Concerning the ^{241}Am source, the energy resolution was determined as the FWHM of a Gaussian distribution fit to the 59.54-keV γ-line within an energy window where the boundaries are defined by the energy values with 20 % of the peak amplitude. This calibration method is independent from any dead-layer or backscattering effects so that Gaussian noise sources, originating primarily from the electronics, dominate the observed energy smearing. However, it is affected by different impact angles of the incident radiation at the detector, depending on the location of the associated pixel: at the inner-most pixels, the impact angle is negligibly small, while at the outer-most pixels, it is defined by the solid angle of $\sim 2.5°$ from the source to the detector. Detector-response measurements with the photoelectron source provide a variety of electron energies at which the energy resolution can be determined, but suffer from detector-related effects leading to an additional low-energy tail, apart from the Gaussian-smeared electron peak. The electron impact angle at the detector is negligibly small, since the photoelectrons gain only longitudinal energy by the applied electric source potential. As the electron passes an insensitive dead layer with a thickness of $\sim 100\,\text{nm}$ before being stopped after a few μm in the sensitive silicon bulk, the recorded spectrum can be fitted by an inverse Landau distri-
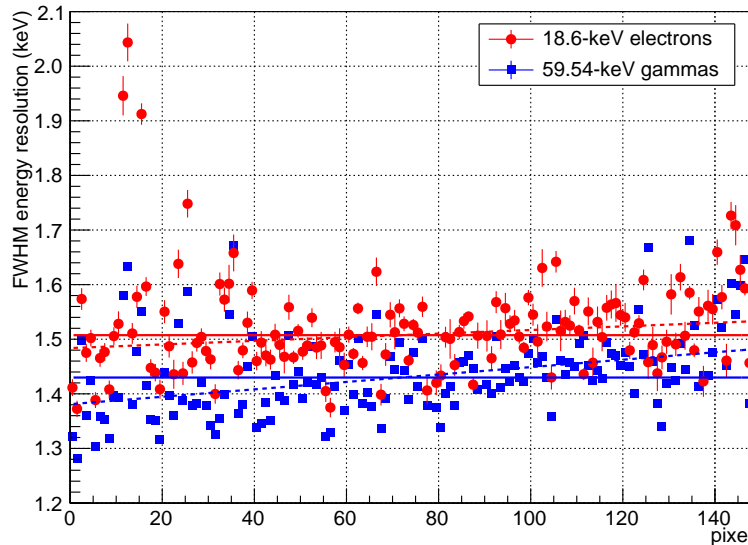
Figure 4.5: Pixel-by-pixel FWHM energy resolution. The energy resolution for 18.6-keV photoelectrons is slightly larger than for 59.54-keV γs. Solid horizontal lines show the averaged energy resolution across 146 of 148 working pixels while dashed lines indicate the tendency that outer pixels (large pixel numbers) suffer from a degraded energy resolution.

bution [Lan44] which theoretically describes the fluctuations of energy losses by ionization of a charged particle in a thin layer of matter. This fit is expected to be convoluted with a Gaussian distribution [Shu66] describing the energy smearing on the basis of dominant electronic-noise and minor Fano-noise [Fan47] effects. The latter characterizes intrinsic detector fluctuations. As illustrated in figure 4.4 showing the global energy spectrum of 18.6-keV photoelectrons at magnetic field (run #8582), the resulting FWHM energy resolution of a Gaussian fit to the electron peak within a restricted energy interval with at least 50 % of the peak amplitude is consistent with the more sophisticated approach of a convoluted Landau-Gaussian fit. Therefore, the FWHM energy resolution can be determined independently from the particle source, considering carefully an appropriate fit interval.

Figure 4.5 shows the FWHM energy resolution for each functional pixel including statistical fit uncertainties both for 59.54-keV γs of ^{241}Am (runs #4005−#4091, 87 h, no magnetic field) and for 18.6-keV photoelectrons (run #8582, 30 min, at magnetic field) under similar conditions. Solid horizontal lines mark the corresponding averaged energy resolution across the working pixels with $\Delta \overline{E}_\gamma = 1.43(08)$ keV for γs and $\Delta \overline{E}_e = 1.51(09)$ keV for electrons. The displayed error bars correspond to the 1-σ variance of the FWHM considering the relatively large spread of individual energy resolutions pixel-by-pixel. The observed scatter in the pixel-by-pixel energy resolutions may originate from different contact pressures between the detector pixels and the associated spring-loaded pogo pins resulting in significant variations of series resistances and noise contributions for each channel. This behavior may be also explained by the tolerances of the electronic parts mounted on the preamplifier modules leading to different performances for single channels. In addition, the dashed lines indicate the tendency that the energy resolution for inner pixels is slightly better than for outer pixels. This is most likely due to a more efficient cooling of the inner pixels since thermal radiation dominates on outer surfaces, reducing the cooling process of the outer pixels. Another hypothesis is based on the unique geometry of the detector wafer. If the guard ring separating the sensitive detector volume from the bias ring (section 3.5) floats on a slightly positive voltage, holes can be injected into the detector bulk and

can diffuse to adjacent pixels, especially to outer pixels, where the charge carriers appear as additional noise current. Adjusting the guard ring to negative voltages may prevent unintended charge-carrier injection. This option will be tested during the next detector commissioning.

A Gaussian fit to the global energy spectrum results in an energy resolution of $\Delta E_\gamma = 1.40(01)\,\text{keV}$ and $\Delta E_e = 1.51(01)\,\text{keV}$, which is consistent with the averaged energy resolution mentioned above. Obviously, the statistical uncertainties are smaller because of the integration over the individual energy spectra of all functional pixels leading to higher statistics. The measured energy resolution for electrons is slightly poorer than for γs due to detector effects which are generated by incident charged particles only, such as energy losses in the insensitive detector dead-layer, backscattering and possible reentries as a result of electrostatic and magnetostatic reflection, and energy-loss fluctuations within the detector material. These effects originate from the different interaction mechanisms of incident particles with the detector material, since keV-γs deposit their energy primarily via the photoelectric effect and multi-Compton scattering through point interactions within the detector volume, while keV-electrons continuously interact with the detector material via ionization and bremsstrahlung, starting at the detector surface, and then moving through the detector entrance window, the insensitive dead layer, and drifting through the sensitive detector volume until they fully deposit their initial energy.

The stated detector effects broaden the electron peak in the energy spectrum, resulting in a larger energy resolution compared to γs. However, they can remarkably be reduced by boosting the electron-disk potential or by applying an additional positive potential to the post-acceleration electrode in order to increase the incident electron energy and electron angle with respect to the detector surface. In particular, the energy loss in the dead layer and the backscattering probability decrease with increasing energy and angle [Ren11]. In figure 4.6, a scan over different total incident electron energies from $E = 7 - 35\,\text{keV}$ with post-acceleration potentials of $0\,\text{kV}$ (runs $\#8582 - \#8601$) and $10\,\text{kV}$ (runs $\#8604 - \#8623$), respectively, at identical magnetic fields shows the expected behavior. The energy resolution worsens notably with decreasing electron energies since backscattering effects and energy losses in the dead layer become more and more dominant. In addition, the signal-to-noise ratio decreases accordingly. A power-law fit to the results describes the observed trend with $\Delta E \sim E^{-2.25(6)}$ in good agreement ($\chi^2/\text{ndf} = 8.65/37$) and allows to extrapolate the expected FWHM energy resolution to higher incident energies E. In this context, it is important to note that the energy resolution can only be improved slightly by applied post-acceleration potentials beyond the present limit of $10\,\text{kV}$. However, higher values are not yet possible without suffering from high-voltage discharges and high-current spikes.

An investigation of the energy resolution using the test pulser shows only a minor improvement in the FWHM energy resolution by few tens of eV (runs $\#4386 - \#4387$). The test pulser injects charge between the signal input and the field-effect transistor at the preamplifier modules. Therefore, the associated preamplifier channel cannot distinguish if this charge originates from the corresponding detector pixel or from the test pulser. Since the detector pixel is connected in parallel to the test-pulser input, the noise-related conditions are similar for a real detector signal and an emulated test-pulser signal, except for Fano noise [Fan47]. The latter describes energy fluctuations of an electric charge obtained in the detector. Thus, in contrast to all other existing dominant noise mechanisms, such as leakage currents, thermal noise of serial resistances, microphonics, and electronic noise of the preamplifiers, there is no contribution of the minor Fano noise to the test-pulser line.
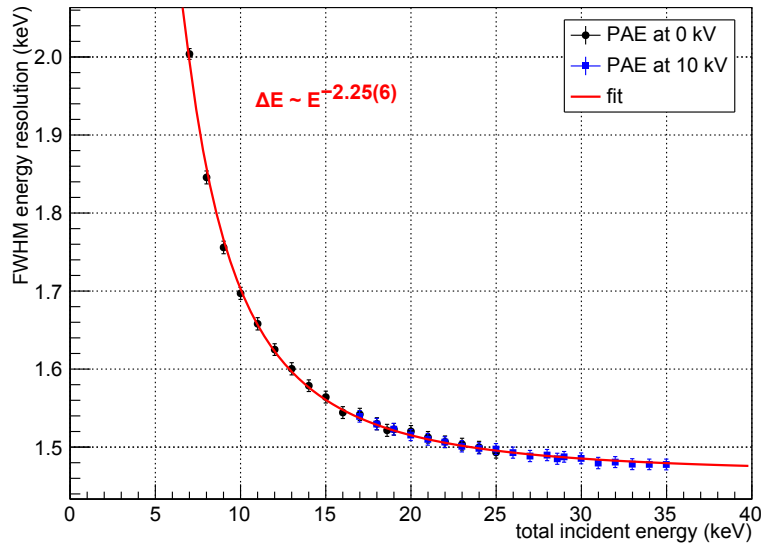
Figure 4.6: FWHM of the energy resolution as a function of the total incident energy at magnetic field. The total incident energy E can be varied by the individual potentials of the photoelectron source and the post-acceleration electrode. This allows to scan energy ranges of up to 35 keV, since the photoelectron disk and the post-acceleration electrode can handle high-voltages of up to -25 and $10\,\text{kV}$, respectively, without suffering from any discharges. A power-law fit ($\Delta E = a \cdot E^b + c$) applied to the results allows to estimate the energy resolution ΔE at higher energies by extrapolation. This is of special interest if the post-acceleration electrode may handle higher potentials: $\Delta E(18.6\,\text{keV}) = 1.51(1)\,\text{keV}$, $\Delta E(28.6\,\text{keV}) = 1.49(1)\,\text{keV}$, $\Delta E(38.6\,\text{keV}) = 1.48(1)\,\text{keV}$ and $\Delta E(48.6\,\text{keV}) = 1.47(1)\,\text{keV}$. However, due to the flat slope of the power-law fit at higher incident energies, the improvement is of minor importance. The fit parameters are $a = (42.3 \pm 5.2)\,\text{keV}$, $b = (-2.25 \pm 0.06)$, and $c = (1.465 \pm 0.003)\,\text{keV}$.

4.3 Linearity

The dynamic linearity of the detector signal chain can be studied by injecting signals of various well-known amplitudes into the system and measuring the mean energy of the associated detector response. The different energy responses are ideally fitted by individual Gaussian distributions so that the resulting mean energies should coincide with incident energies and lie on a best-fit straight line. A strictly linear behavior relates the recorded energies with the incident energies across the observed energy interval. In this context, the largest fractional deviation between the fit and the recorded energies defines the non-linearity of the system [Kno10]. There are two approaches to measure the system linearity independently from any dead-layer and backscattering effects: One approach uses an optical pulse injection with adjustable intensities (section 4.3.1), the other is based on a nuclear standard with defined energies (section 4.3.2). An investigation of the system linearity using the photoelectron source seems to be unreasonable in this case because of energy-dependent dead-layer and backscattering effects.

4.3.1 Red-Light Illumination

When applying this method, the wafer is directly illuminated with pulsed light from a red LED housed in the illumination device on the ambient-air side (section 3.9). During each pulse, the light enters the UHVac chamber through the same window used for the UV illumination of the photoelectron source, floods the chamber, reflects and scatters from interior surfaces, and finally penetrates into the detector wafer. An external *Agilent*

33220A pulser supplies the driving pulse whose amplitude can be varied to change the current through the LED and thus the light intensity. The operation of the LED is stabilized by detecting a particular fraction of the emitted light with a *Hamamatsu S4204* silicon PIN diode and by using its photocurrent in a feedback arrangement to drive the LED. This ensures a precise scaling of the light intensity as a function of the applied pulse amplitude [Pet11]. The pulse amplitude across the LED can be measured using a scope. However, the stabilization requires relatively long driving pulses with minimum pulse widths of 5 μs. The resulting rise time of the detector response of more than 10-μs is longer than the largest shaping length of 6.4 μs available in ORCA, so that the ADC energy value determined by the trapezoidal filter is highly underestimated. Therefore, this approach can only give an upper limit of the system non-linearity.

As a typical example, figure 4.7 shows the measured linearity and fractional deviation of pixel #0 as a function of the pulse amplitude measured across the red LED (runs #9138 − #9208). At each data point, the energy was determined from the mean value of a Gaussian distribution fit to the distinct photon peak in the energy spectrum while the pulse amplitude was metered using a *UTD2052CEL* scope with 50-MHz sampling rate in average mode. Both statistical and systematic error bars are included through peak fitting and amplitude metering, respectively. In order to exclude further uncertainties resulting from ^{241}Am calibration, the measured energies are given in ADC energy values rather than in calibrated energies. One ADC energy bin corresponds to approximately 100 eV so that this investigation covers the KATRIN-relevant energy region of up to ∼ 50 keV if using a 30-kV post-acceleration potential.

In order to maintain its linearity, the external pulser operates in auto-range mode where it automatically selects the optimal settings for the output amplifier and the internal attenuators when the output-voltage amplitude is changed. However, existing tolerances of the internal attenuation network introduce step-like characteristics in the detector-linearity measurement when switching between different attenuator stages. The most distinct step appears as the applied amplitude transitions from 98 to 100 mV due to an adequate change of the output-voltage range. This transition corresponds to amplitudes of 768(8) and 792(8) mV measured at the red LED, respectively. Therefore, two rather than just one best-fit straight lines characterize the system linearity. They have significantly different fit parameters, as indicated by the dashed-line extrapolations to lower energies in figure 4.7. This is a further reason why with this approach only an upper limit of the system non-linearity can be determined. In principle, auto-ranging could be disabled to eliminate these momentary disruptions, but this would lead to side effects. First, the accuracy and resolution of the amplitude as well as the fidelity of the waveform would be adversely affected, and second, the amplitude range would drastically be limited so that specific voltages would be unavailable [Agi07].

Nevertheless, within a specific voltage range where the same attenuator stage operates, the trend of the fractional deviation follows a quadratic behavior with the largest discrepancies at the boundary points, as indicated by the dashed-line quadratic fit in figure 4.7. Toward these boundary points, the attenuator stage and thus the pulser become more and more non-linear, resulting in a degrading detector linearity, before the internal attenuation network switches to another stage. At higher amplitudes, further step-like characteristics indicate internal attenuator switching when changing the output-voltage range. Considering all these aspects, the upper limit of the non-linearity for the signal chain of pixel #0, is 5.1(5) %, defined by the largest fractional deviation. The mean integral non-linearity over all pixels is 5.1(1) % for optical pulsing.

Due to the non-applied calibration, the best-fit parameters like the y-intercept c and the slope m of the linearity straight-line fits drastically differ from channel to channel. Their
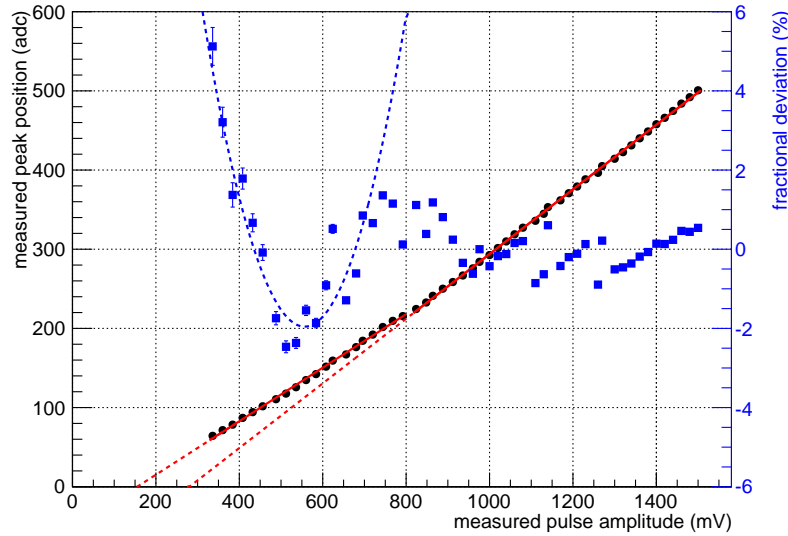
Figure 4.7: Linearity from optical pulse injection for pixel #0. The measured mean ADC energy values (black dots, left axis) are plotted as a function of the pulse amplitude metered across the red LED. One ADC energy value corresponds to approximately $100\,\mathrm{eV}$ so that this investigation covers an energy region of up $50\,\mathrm{keV}$. Two linear fits (solid red lines) consider automatic switching of the internal attenuation network in the pulser when changing the output-voltage range, leading to artifacts in the detector-linearity measurement. Their extrapolations (dashed red lines) to lower energies indicate different fit parameters so that each best-fit straight line covers different energy intervals for linearity investigation. The fractional deviation from the linear fits (blue squares, right axis) features two characteristic behaviors: The quadratic trend (dashed blue line) indicates that the same attenuator stage operates over a specific energy range while the step-like behavior at higher energies shows further attenuator switching. The maximal fractional deviation defines the upper limit for non-linearity.
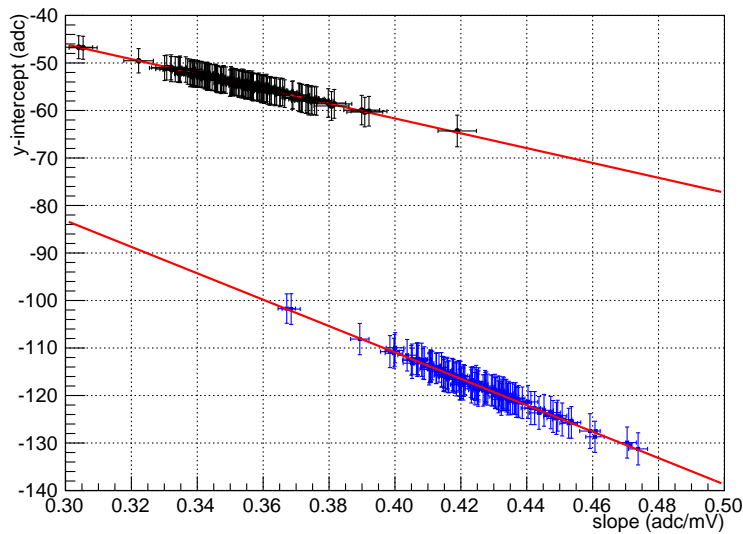
Figure 4.8: Linearity fit parameters from optical pulse injection for all channels. The relation of the pixel-by-pixel linearity fit parameters of the best-fit straight lines for low energies (black) and high energies (blue) is plotted. The energy offset of each channel is defined by the y-intercept and the linearity by the slope. The shown linear fits (red lines, $y = mx + c$) indicate high correlation coefficients of -0.998 (black, $m = -156(16)\,\mathrm{adc/mV}$, $c = 0.75(6)\,\mathrm{adc}$) and -0.808 (blue, $m = -278(19)\,\mathrm{adc/mV}$, $c = 0.17(8)\,\mathrm{adc}$), respectively.

relation is illustrated in figure 4.8. The two shown linear fits ($y = mx + c$) give high correlation coefficients between the fit parameters of -0.998 ($m = -156(16)$ adc/mV, $c = 0.75(6)$ adc) for the individual low-energy linearity fits and -0.808 ($m = -278(19)$ adc/mV, $c = 0.17(8)$ adc) for the individual high-energy linearity fits, indicating a well-understood linearity behavior of the channels. In the case of perfect linearity, the individual y-intercepts of the linearity straight-line fits should match with zero, meaning that an event with no incident energy corresponds to an ADC energy of zero [Kno10]. However, these quantities significantly differ from zero by more than several tens of ADC energies and take on negative values, so that the actual zero energy should be shifted toward higher energies by few keV. Nevertheless, both calibration measurements (section 3.9) and the second method for determining the system linearity (section 4.3.2) show that there is no obvious energy offset in the signal chain. Therefore, this untypical behavior can be traced back to a specific non-negligible voltage offset in the pulse amplitude produced either by the external pulser or by the driving circuit for the red LED.

In the following section, a more elegant method for measuring the system linearity is discussed. It is based on a nuclear standard using ^{241}Am calibration.

4.3.2 241-Americium Energy Spectrum

The second approach to determine the dynamic linearity of the detector signal chain compares the measured positions of the six dominant peaks in the ^{241}Am energy spectrum to the well-known positions of the corresponding ^{241}Am γ, ^{237}Np X-ray, and ^{29}Cu fluorescence lines (section 3.9). Consequently, it covers the KATRIN-relevant energy interval ranging from 8 to 60 keV. The expected location E_{exp} and amplitude A_{exp} of each peak can be calculated on the basis of line energies E_{theo} and intensities I_{theo}, obtained from reference tables for radioactivity [FE04] and fluorescence [Tho09], and with regard to the energy-dependent total mass attenuation coefficients $\mu(E_{\text{theo}})/\rho$ with coherent scattering for silicon where $\rho = 2.33$ g/cm^3 denotes the density of silicon at room temperature [Ber10]. Interaction effects with the source holder and the illumination window made of aluminum are neglected. The expected peak amplitude at a specific energy E_{theo} is defined by

$$A_{\text{exp}}(E_{\text{theo}}) = I_{\text{theo}}(E_{\text{theo}}) \cdot \mu(E_{\text{theo}})/\rho \; , \tag{4.2}$$

where the attenuation coefficient is linearly approximated between the given photon energies. However, in contrast to the two γ-lines used for detector calibration, the individual X-ray and fluorescence lines cannot be resolved due to the relatively large energy resolution of the detector. Therefore, the expected position of a peak in which multiple unresolved lines contribute has to be weighted by the individual peak amplitudes according to (4.2). The expected peak location is then given by

$$E_{\text{exp}} = \frac{\sum_i^N A_{\text{exp}}(E_{\text{theo},i}) \cdot E_{\text{theo},i}}{\sum_i^N A_{\text{exp}}(E_{\text{theo},i})} \tag{4.3}$$

with N unresolvable lines in the corresponding peak. The uncertainty of the peak location is defined by the energy interval spanned by the minimum and maximum line energy within the measured peak:

$$\Delta E_{\text{exp}} = \frac{1}{2}(E_{\text{max}} - E_{\text{min}}) \; . \tag{4.4}$$

This might overestimate the actual error since it is based on a conservative error estimation.

Table 4.3 lists the calculated parameters of the six observed peaks when applying the formulas described above. The single peaks originated by ^{29}Cu K$_{\alpha 1, \alpha 2, \beta 1, \beta 3}$ fluorescence lines and by ^{237}Np L$_{\gamma 1 - \gamma 3, \gamma 6}$ X-ray lines have the largest uncertainties in their expected
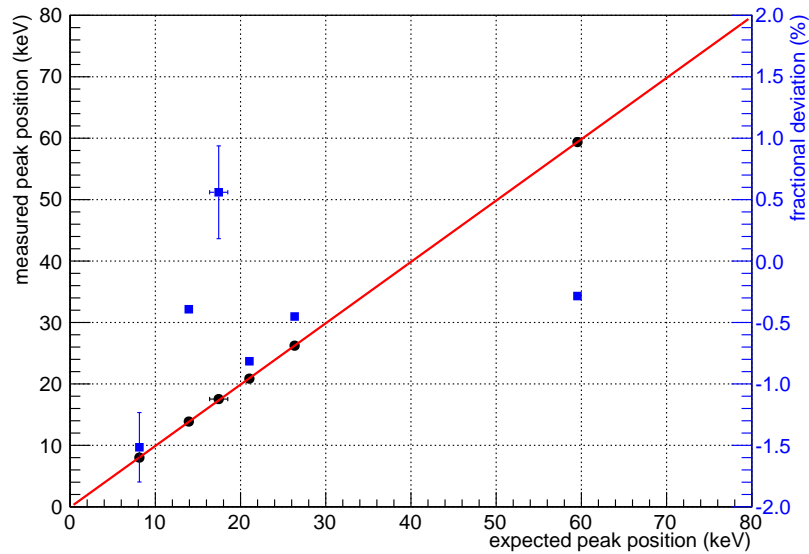
Figure 4.9: Linearity from peaks of ^{241}Am energy spectrum for all pixels. The measured peak locations (black dots, left axis) are plotted as a function of the expected peak locations. The corresponding calculation is described in the continuous text while the results are listed in table 4.3. A linear fit (solid red line) defines the system linearity. The fractional deviation from this fit (blue squares, right axis) describes the system non-linearity. Apart from the fluorescence and X-ray lines, the γ-lines also suffer from a certain deviation concerning linearity since the applied calibration also includes the point $(0, 0)$.
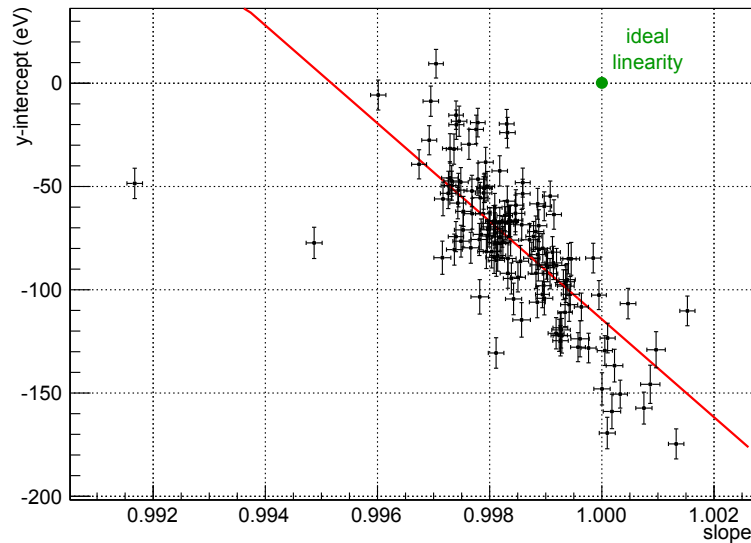
Figure 4.10: Linearity fit parameters from peak positions of ^{241}Am energy spectrum for all channels. The relation between the y-intercept and the slope of the individual linearity fits of all channels is illustrated describing the energy offset and the linearity, respectively. The shown linear fit (red line, $y = mx + c$) indicates a moderate correlation coefficient of -0.703 ($m = -2.371(6) \times 10^4$, $c = 2.360(6) \times 10^4$ eV). This correlation indicates that the slope depends on the pedestal of each pixel.

Table 4.3: Expected peak locations in the ^{241}Am energy spectrum. Both the expected weighted peak positions E_{exp} and their uncertainties ΔE_{exp} are listed. Their calculation is described in the continuous text.

peak	E_{exp} (eV)	ΔE_{exp} (eV)
^{29}Cu K$_{\alpha,\beta}$	8118.8	439.0
^{237}Np L$_{\alpha}$	13926.5	92.5
^{237}Np L$_{\eta,\beta}$	17399.0	1066.0
^{237}Np L$_{\gamma}$	21031.9	354.0
^{241}Am γ	26.3448	0.2
^{241}Am γ	59541.2	0.2

peak locations. The measured peak positions are determined from ^{241}Am calibration using a best-fit straight line through the γ-line positions and the zero point as described in section 3.9.

Figure 4.9 shows the comparison between expected and measured energies of the individual peaks observed in the ^{241}Am energy spectrum averaged over all pixels (runs #4005 − #4091). A best-fit straight line through the six existing data points indicates the system linearity, while the fractional deviation between data and fit denotes the system non-linearity. The largest discrepancy of 1.5(1) % defines the mean integral non-linearity over all pixels using ^{241}Am calibration data. However, this deviation appears at the peak with the largest uncertainty in the expected peak position so that this result represents rather an upper limit for the non-linearity than an exact quantity, as taking into account that an exact energy scale can only be given by a detailed Monte Carlo simulation. The two γ-lines used for ^{241}Am calibration suffer from a non-vanishing deviation since the calibration also includes the zero point. Otherwise, the expected and measured energies would match exactly.

In figure 4.10, the relation of the best-fit straight-line parameters are illustrated on a pixel-by-pixel basis. The y-intercept c defines the energy offset and the slope m the linearity of each channel. In the case of perfect calibration and linearity, the energy offset should be exactly zero and the slope exactly one. The deviation from these ideal values is relatively small since the maximum energy offset is less than $180\,\mathrm{eV}$ while the maximum linearity deviation is less than 0.9 %. The shown linear fit ($y = mx + c$) gives a moderate correlation coefficient of -0.703 ($m = -2.371(6) \times 10^4$, $c = 2.360(6) \times 10^4\,\mathrm{eV}$) for the individual linearity-fit parameters, indicating that the slope of the linearity fit depends on the pedestal. The described aspects indicate a well-understood linearity behavior of the channels.

Finally, figure 4.11 characterizes the maximum fractional deviation from the best-fit linearity and thus the upper bounds for the non-linearity of each channel performing both approaches. The results of almost all pixels are consistent with the mean integral non-linearity shown by a horizontal line. The second method using the distinct peaks of the ^{241}Am energy spectrum leads to more stringent limits for the non-linearity.
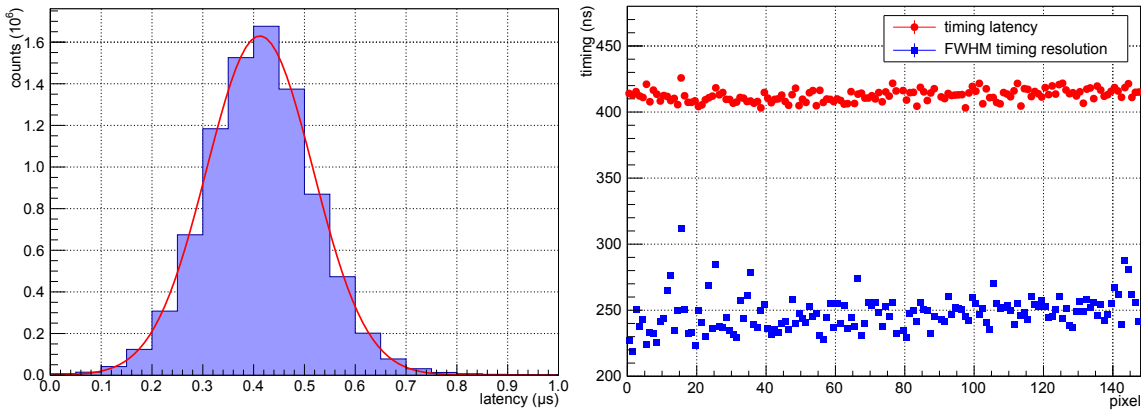
4.4 Timing Resolution

As described in section 3.7, the trapezoidal filter used for pulse shaping in the IPE v4 crate defines the event timing by the zero-crossing of the second filter-stage output. In this context, two characteristic detector properties can be defined. The latency describes the time delay experienced by a system, while the timing resolution refers to the accuracy of a measurement with respect to time. In the ideal case for an exactly step-shaped input
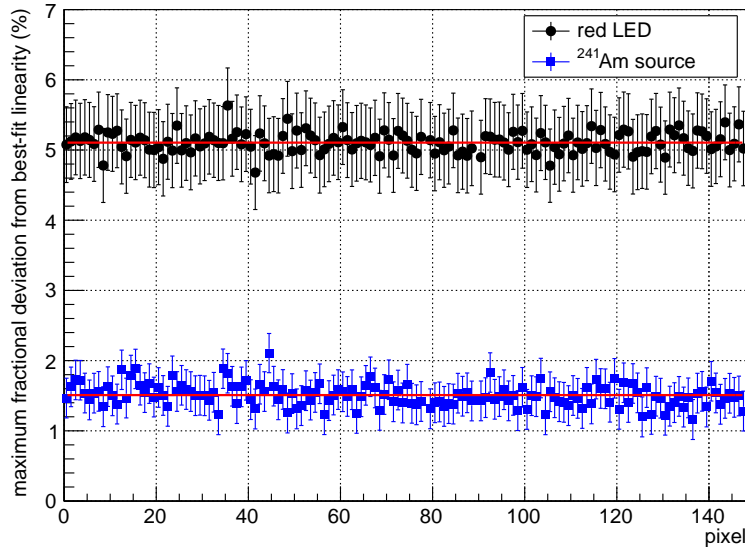
Figure 4.11: Upper bounds for non-linearity of all channels. The first method using optical pulse injection by a red LED (black dots) leads to higher upper limits for the system non-linearity than the second approach investigating the peak locations of the ^{241}Am spectrum (blue squares). Solid-red horizontal lines indicate the mean integral non-linearity of $5.1(1)\%$ and $1.5(1)\%$, respectively.

signal, the stated zero-crossing is delayed by a constant latency of $3L/2 + G/2$ to the actual event time stamp due to the applied filter logic. However, for a real noise-affected signal with the characteristic 200-ns rise time and 1-ms fall time, this may not necessarily be true. In the first approximation, the latency is independent from the signal amplitude and thus of the incident energy, since a corresponding change of the rise time is negligible and the filter logic is linear. However, a lower incident energy leads to a lower signal-to-noise ratio that may affect the latency. Nevertheless, the latency directly depends on the adjusted filter settings so that a particular discrepancy between different shaping and gap lengths is expected if the detector response suffers from uncertainties in event timing, whereas the latter define the timing resolution of the detector. The ns-scale response times of the detector wafer and the preamplifier modules are relatively fast compared to the 50-ns sampling rate of the DAQ system. Therefore, the timing resolution is dominated by the integration interval, primarily described by the shaping length, and by the amount of noise influencing the outputs of the trapezoidal filter stages. In this context, a longer shaping length leads to a degraded timing resolution since the signal integration considers sampled trace values further afar from the signal step. In contrast to the energy resolution, the timing resolution improves with shorter shaping lengths. Just as for latency, larger input signals improve the timing resolution due to the increased signal-to-noise ratio.

The time-dependent detector properties were measured with the photoelectron source elevated to a potential of $-18.6\,\text{kV}$ while it was illuminated by UV light in 20-ns pulses with 5-ns rise and fall times, generated from an external pulser (run #8641). The associated sync pulse was fed to the DAQ system to allow proper coincidence measurements. The averaged time difference between pulse-signal timing and detector-signal timing gives the mean latency of the system, while the resulting FWHM peak width describes the uncertainty in event timing and thus the FWHM timing resolution of the detector. Figure 4.12 shows the corresponding global detector response to 18.6-keV photoelectrons. The resulting spectrum is fitted by a Gaussian distribution where the latency and the FWHM timing resolution are determined to $413.1(1)\,\text{ns}$ and $\Delta t = 245.9(1)\,\text{ns}$, respectively, with very high

Figure 4.12: Latency and timing resolution for 18.6-keV photoelectrons. The shaping length is kept at $L = 6.4\,\mu s$. **Left: Global detector response.** The recorded coincidence data between the signal line and the sync line is fitted by a Gaussian distribution in order to determine an upper limit of $413.1(1)\,$ns for the latency and of $\Delta t = 245.9(1)\,$ns for the FWHM timing resolution. **Right: Pixel-by-pixel detector response.** In contrast to the energy resolution, the spread of the individual latency and timing resolution is remarkably small. The variations are well below the 50-ns sampling rate of the DAQ system.

precision. The reported values are averaged over all functional pixels. The spread of the individual pixel-by-pixel latency and timing resolution is remarkably small and is a proof of the excellent timing conditions of the detector. However, the described method is only sensitive to the upper limits of both quantities since both the signal line and the sync line are affected by the latency and the timing resolution of the system. In addition, the signal pulse has a non-negligible total width of 30 ns, including rise and fall times, which is smaller than the 50-ns sampling rate. Therefore, the actual timing properties of the detector are even better as stated.

In other, more sophisticated studies performed in the framework of the thesis in hand, the timing properties were additionally measured as a function of the incident electron energy within a range from $E = 13.6 - 28.6\,$keV in 5-keV increments as well as in dependence of the shaping length from $L = 0.4 - 6.4\,\mu s$ in specific increments available in ORCA (runs #8624 − #8646). The results are shown in figure 4.13. The timing resolution significantly improves with shorter shaping lengths, while the latency slightly degrades and the energy resolution distinctly worsens accordingly. However, due to a better signal-to-noise ratio, all quantities improve somewhat with higher incident energies when keeping the shaping length constant. At a shaping length of $L = 1.6\,\mu s$, the detector response to typical 18.6-keV electrons, additionally boosted by a post-acceleration potential of $10\,$kV to energies of $E = 28.6\,$keV, gives an excellent FWHM timing resolution of $\Delta t = 88.1(1)\,$ns. This value is smaller than the width of two ADC time bins of the DAQ system, meeting the 100-ns requirement for KATRIN time-of-flight studies [Ams14]. At these conditions, the FWHM energy resolution results in a moderate quantity of $\Delta E = 1.99(01)\,$keV.

Due to the existing trade-off between energy and timing resolution when varying the trapezoidal filter settings, the detector cannot be understood and optimized as all-in-one device suitable for every purpose. Depending on the measurement purpose, the experimentalist has to decide if either energy or timing information is of major importance. Concerning background investigations and neutrino-mass measurements with expected low detector rates, it might be advantageous to choose a relatively large shaping length of $L = 6.4\,\mu s$ in order to keep the region of interest and the background rate within this energy window as small as possible, while tolerating the loss of timing resolution. For coincidence and time-of-flight studies, however, a short shaping length of $L = 0.8\,\mu s$ might be preferable since timing information is much more important in that case. It should be noted however that a
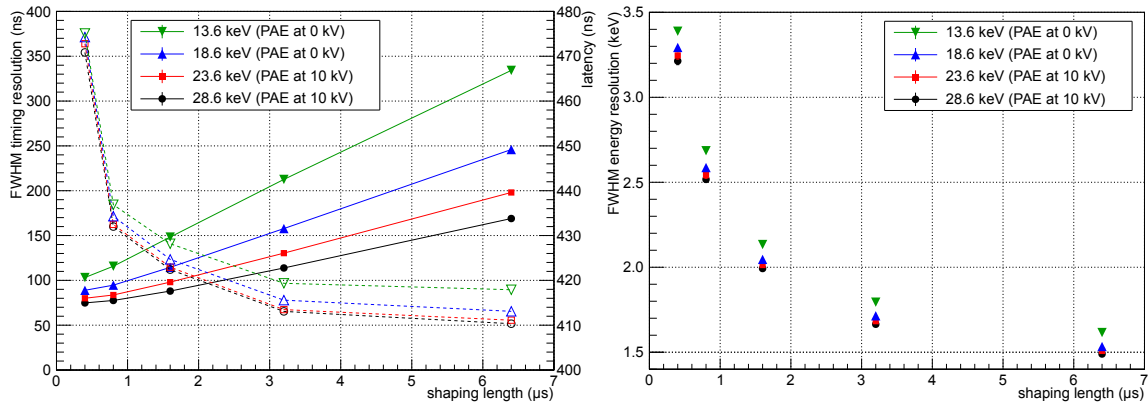
Figure 4.13: Detector response as a function of shaping length and incident energy.
Both the shaping length and the incident energy of photoelectrons were varied to investigate
characteristic detector parameters such as timing resolution, timing latency, and energy reso-
lution. Statistical uncertainties are included, but too tiny to be visible. **Left: Timing res-
olution and latency.** The timing resolution (filled marks, solid lines, left axis) significantly
improves with shorter shaping lengths while the timing latency (blank marks, dashed lines,
right axis) slightly degrades. **Right: Energy resolution.** The energy resolution worsens
significantly with shorter shaping lengths.

shaping length of $L = 0.4\,\mu s$, in general, is not a reasonable and viable filter setting, since
the fixed gap length of $G = 200\,ns$ describing the signal rise time is already in the same
order of magnitude. Nevertheless, a straightforward possibility to optimize the detector
characteristics without sacrificing other detector parameters can be achieved by apply-
ing a post-acceleration potential, on condition that the operation of the post-acceleration
electrode does not increase detector and spectrometer-related backgrounds.

4.5 Rate-Dependent Pile-Up Effects

The detector performance at high incident rates of several kcps and above is of special
interest, although typically only a rather moderate β-electron rate in the order of up to a
few tens of cps and below is expected during KATRIN neutrino-mass measurement. How-
ever, in case of calibrations, commissioning measurements, transmission-function and time-
of-flight studies as well as response-function measurements performed with an angular-
selective electron gun, high rates on single detector pixels are required to increase statistics
and reduce run time.

In order to investigate rate-dependent detector effects, the photoelectron source was ele-
vated to a constant potential of $-18.6\,kV$ and illuminated by UV light with variable DC
voltages, while the corresponding detector response to the generated 18.6-keV photoelec-
trons with adjustable incident rates was investigated on pixel #13 (runs $\#3209 - \#3389$).
Figure 4.14 shows an exemplary demonstration of measured electron energy spectra at four
different rates at a fixed shaping length of $L = 6.4\,\mu s$. It should be noted that the recorded
rates differ from the actual unknown incident rates. More and more distortions appear in
the measured energy spectra with increasing rates, resulting in peak shifting to lower en-
ergies, peak broadening, and the appearance of dominant side peaks which get shifted and
become broader, in contrast to the energy spectrum at moderate rates, e.g. at $0.1\,kHz$. The
main energy peak describes single-electron events while the side peaks indicate multiple-
occupancy events. The changes in the shape of the spectra lead to discrepancies between
acquired and incident parameters, such as electron energies and electron rates. A later
offline correction of these differences is impossible, because the main peak shifts toward
and (partly) below the electronic noise threshold and the broad peaks overlap. In addition,
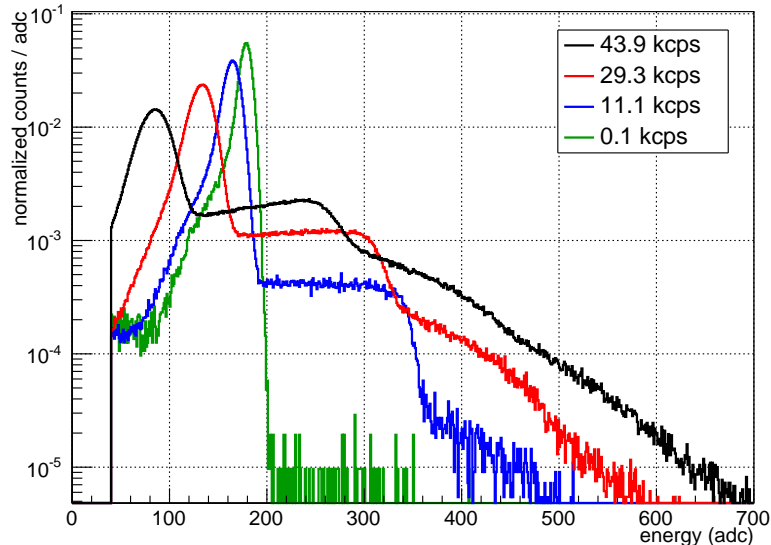
Figure 4.14: Rate-dependent ADC energy spectra of 18.6-keV photoelectrons.
The spectra are normalized to an equal area of one to allow a simplified comparison. The
stated rates are recorded rates and differ from the incident rates. The latter originated from
the photoelectron source and can be varied by adjusting the voltage across the UV LED
illuminating the source disk. With increasing rate, the spectra move toward lower energies,
while the dominant single-electron peak becomes broader and distinct multiple-occupancy
peaks appear. The noise threshold is at 40 ADC energy values.

at these high acquisition rates, trace data cannot be recorded due to the 8-kcps dead-time
limit of the DAQ system (section 3.7). Thus, an appropriate weighting of the individual
peaks seems to be unreasonable in order to calculate the actual rate.

As shown in figure 4.15 which characterizes the parameters of the single-electron peak in
dependence of the shaping length, the described effects strongly depend on the adjusted
shaping length. The distortions become less dominant for decreasing shaping lengths so
that both the peak position and the peak width resist high-rate effects. However, rates
close to the 108-kcps limit at which dead time in energy mode becomes an issue (section 3.7)
cannot be reached without suffering from significant peak shifting and peak broadening,
independently of the shaping length. In general, high-rate effects at moderate rates below
0.1 kHz play a negligible role.

The observed distortions can be explained by pile-up effects [SN06] [Kno10] describing
the interference of signals with each other at short time scales. There are two kinds of
pile-up effects influencing the detector response − peak pile-up and tail pile-up. They are
illustrated in figure 4.16 and explained in the following, based on [Kno10] [Bar14] [Eno14].

4.5.1 Peak Pile-Up

Peak pile-up occurs when the time interval ΔT between two signals is shorter than the
filter shaping length L, resulting in only one single event recorded by the trapezoidal
filter. The determined event energy E can be calculated, assuming two signals with equal
incident energies E_0, neglecting the 1-ms exponential discharging time of the preamplifiers,
neglecting the relatively small gap length compared to the shaping length, and disregarding
noise influences. Under these reasonable conditions, the trigger position is exactly in the
middle of the two events, as illustrated in figure 4.17, so that the recorded energy is given
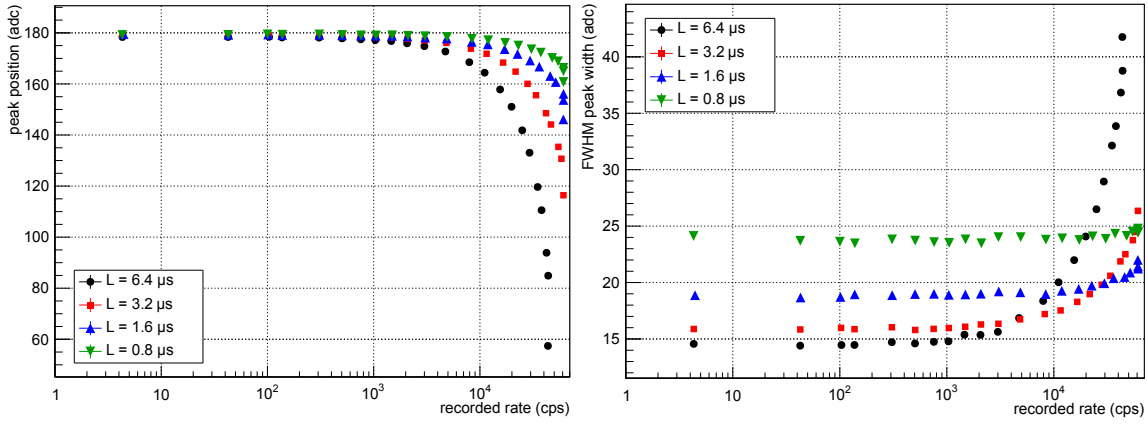
Figure 4.15: Rate-dependent position (left) and width (right) of the 18.6-keV single-electron peak. With increasing rate, the single-electron peak at 18.6 keV moves toward lower energies and becomes broader. The effects become less dominant at shorter shaping lengths.

by

$$E = \frac{S_1 - S_0}{L} = \frac{(E_0(L - \Delta T/2) + E_0 L + E_b L) - (E_0 \Delta T/2 + E_b L)}{L} = 2E_0 \left(1 - \frac{\Delta T}{2L}\right) \tag{4.5}$$

for $\Delta T \leq L$, where S_0 and S_1 denote the moving sums across the trace values from the first trapezoidal-filter stage, and E_b considers the base-line height (section 3.7). At a fixed shaping length, the energy linearly depends on the time interval, so that it can take on values between E_0 and $2E_0$, at $\Delta T = L$ and $\Delta T = 0$, respectively. Interestingly, in the special case of $\Delta T = L$, when two signals arrive with a time difference of exactly the adjusted shaping length, both incident signals look like one single signal with the single-event energy $E = E_0$, losing the information of multiplicity. In the case of more involved signals or different energies, the analytical calculation becomes extremely complicated. As described, peak pile-up results in a plateau-shaped spectrum with broad multiple-occupancy peaks rather than a peak-shaped spectrum with individual distinct peaks [Bar14] [Eno14].

In case of peak pile-up, not only the energy, but also the recorded rate R is different from the incident rate R_0. If signals are time-independent from each other, the probability of a given number of signals occurring within a fixed time interval is given by the Poisson distribution [Hai67]. For a particular mean Poisson rate R_0, the probability that a second event arrives within the shaping length L of a first event is defined by

$$P = \frac{\int_0^L e^{-tR_0} dt}{\int_0^\infty e^{-tR_0} dt} = 1 - e^{-LR_0} . \tag{4.6}$$

With the shaping lengths available in ORCA, this peak pile-up probability is smaller than 1 % for incident rates of up to 1.6 kHz, in the case of Poisson time-distributed signals. Since this probability is defined by the ratio of recorded events to incident events, the acquired rate R can be calculated:

$$\frac{R}{R_0} = 1 - P = e^{-LR_0} \ \rightarrow \ R = R_0 \cdot e^{-LR_0} . \tag{4.7}$$

The recorded rate is always smaller than the incident rate, since $e^{-LR_0} < 1$, so that peak pile-up leads to a general rate drop. However, this is only valid for Poisson-distributed processes and not for calibration measurements using pulsed sources [Bar14] [Eno14].
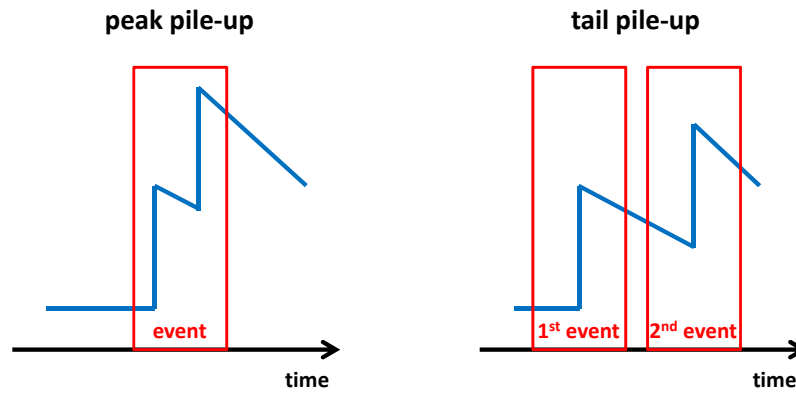
Figure 4.16: Pile-up effects with two signals. The waveforms of two signals suffering from pile-up effects are illustrated. Peak pile-up (**left**) interprets two signals as a single event with twice the energy while tail pile-up (**right**) underestimates the energy of the second event. Figures based on [Sta13].
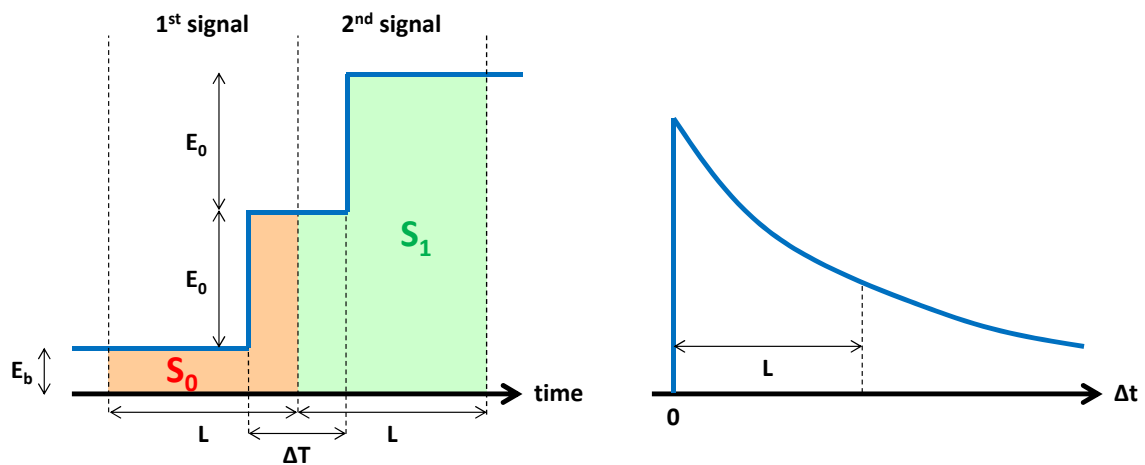
Figure 4.17: Peak pile-up. The simplified waveform for the analytical peak pile-up model (**left**) and Poisson time-distributed signals in the inter-arrival time spectrum (**right**) are shown. Figures based on [Eno14].
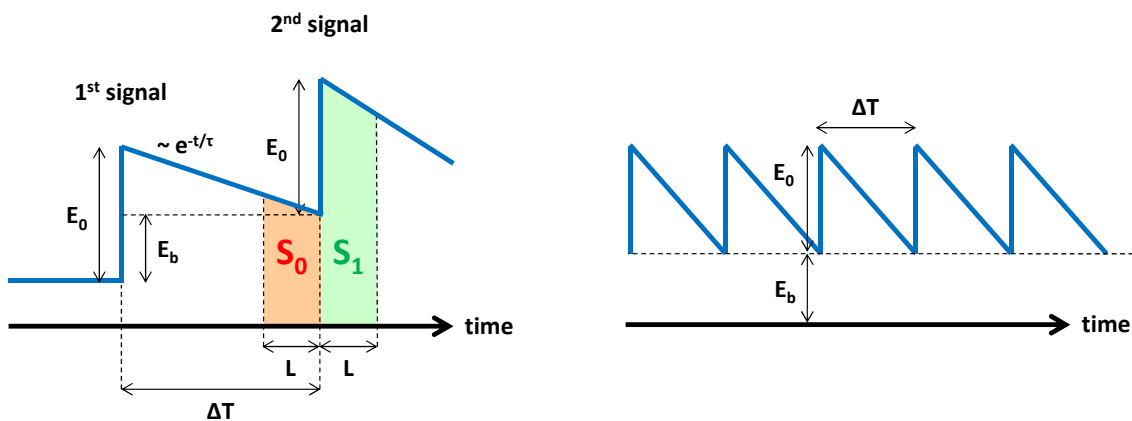
Figure 4.18: Tail pile-up. The simplified waveform for the analytical tail pile-up model (**left**) and accumulated tail pile-up effects in equilibrium (**right**) are shown. Figures based on [Eno14].

4.5.2 Tail Pile-Up

Tail pile-up appears when the time interval ΔT between two signals is shorter than the characteristic discharging time τ of the preamplifiers. The declining tail of the first signal affects the energy determination of the second signal leading to an underestimated energy of the second signal determined by the trapezoidal filter. The resulting energy shift ΔE can be calculated, assuming two signals with equal incident energies E_0, and neglecting analog components, gap length, and noise influences. Under these circumstances, the baseline shift E_b at the second signal is given by the declining tail of the first signal, as illustrated in figure 4.18:

$$E_b = E_0 \cdot e^{-\Delta T/\tau} \ . \tag{4.8}$$

At the second signal at $t = 0$, this baseline shift leads to a baseline slope

$$\frac{\mathrm{d}}{\mathrm{d}t}\left(E_b \cdot e^{-t/\tau} \right)\bigg|_{t=0} = -\frac{E_b}{\tau} \ , \tag{4.9}$$

with which the recorded energy E can be calculated, with the approximation $L \ll \tau$ leading to a constant baseline slope across the moving sums S_0 and S_1:

$$E = \frac{S_1 - S_0}{L} = \frac{(E_b L + E_0 L - E_b \tau^{-1} L \cdot L/2) - (E_b L + E_b \tau^{-1} L \cdot L/2)}{L} = E_0 - \frac{L}{\tau} E_b \ . \tag{4.10}$$

The second term describes the resulting energy shift

$$\Delta E = \frac{L}{\tau} E_b \overset{(4.8)}{=} \frac{L}{\tau} E_0 \cdot e^{-\Delta T/\tau} \tag{4.11}$$

to lower energies. The tail pile-up of two signals is a minor issue, since even in the worst-case scenario of $\Delta T = 0$ and $L = 6.4\,\mu\text{s}$, the relative energy shift $\Delta E/E_0$ is only $0.6\,\%$, with $\tau = 1\,\text{ms}$ [Bar14] [Eno14].

However, tail pile-up plays a major role if it accumulates, meaning that the average time interval $\Delta \overline{T}$ between a certain number of incident events with energies E_0 is shorter than the tail pile-up time scale defined by the preamplifier discharging time τ. The accumulation lowers the average recorded energy $\overline{E}$ by a particular mean energy shift $\Delta \overline{E}$. It can be calculated in state of equilibrium when the mean baseline shift $\overline{E}_b$ asymptotes out and becomes constant, as illustrated in figure 4.18:

$$(\overline{E}_b + E_0) \cdot e^{-\Delta \overline{T}/\tau} = \overline{E}_b \ \rightarrow \ \overline{E}_b = E_0 \cdot \frac{1}{e^{\Delta \overline{T}/\tau} - 1} \ . \tag{4.12}$$

Using the calculated energy shift of two signals according to (4.11), the mean energy shift to lower energies is then given by

$$\Delta \overline{E} = E_0 \cdot \frac{L/\tau}{e^{\Delta \overline{T}/\tau} - 1} \ . \tag{4.13}$$

In contrast to the two-signal tail pile-up, accumulated tail pile-up causes an infinite energy shift to lower energies in the (unrealistic) worst-case scenario of $\Delta \overline{T} = 0$. However, this relation is only valid for the case of equilibrium. Event-by-event baseline fluctuations cause non-negligible variations on the recorded energy E leading to broader peaks in the energy spectrum [Bar14] [Eno14].
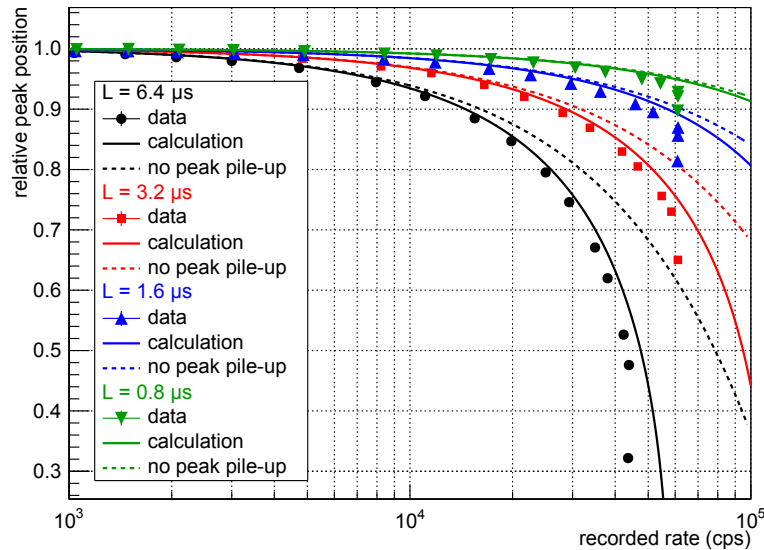
Figure 4.19: Rate-dependent relative peak position of 18.6-keV photoelectrons.
Both the measured (markers) and the calculated (solid lines) relative peak positions are compared at different shaping lengths. In addition, the calculation without regard to peak pile-up (dashed lines) is illustrated, i.e. rate correction is neglected.

4.5.3 Combined Pile-Up Effects in Photoelectron Spectra

The combination of peak and tail pile-up effects in equilibrium allows to model the energy shift of the main single-electron peak at 18.6 keV observed in calibrations performed with a permanently illuminated photoelectron source. In this case, the generated electrons are Poisson time distributed with the average incident rate R_0 while the system is in state of equilibrium in good approximation. This is, however, generally not true for a pulsed photoelectron source. As a consequence of existing pile-up effects, the relative peak position $\overline{E}/E_0$ is defined by

$$\overline{E} = E_0 - \Delta\overline{E} \;\rightarrow\; \frac{\overline{E}}{E_0} = 1 - \frac{\Delta\overline{E}}{E_0} \;. \tag{4.14}$$

Using the rate-drop relation due to peak pile-up described by equation (4.7), and the mean energy shift due to accumulated tail pile-up given by equation (4.13), the relative position of the single-electron peak can be calculated:

$$\frac{\overline{E}}{E_0} = 1 - \frac{L/\tau}{e^{(R_0\tau)^{-1}} - 1} \quad\text{with}\quad R = R_0 \cdot e^{-LR_0} \;. \tag{4.15}$$

This relation allows to determine the relative peak position determined by the trapezoidal filter as a function of recorded rate R and adjusted shaping length L. Figure 4.19 gives a quantitative comparison between measured photoelectron-source data, as described above, and analytical calculations, analyzed at different recorded rates in the range from 10^3 to 10^5 cps and at various reasonable shaping lengths. The agreement is quite good, although smaller discrepancies at very high rates appear which can be explained by the simplification of the calculation and by the assumption of a preamplifier discharging time of exactly $\tau = 1$ ms. The calculation without considering peak pile-up effects ignores the drop of acquired rate compared to incident rate, resulting in an underestimation of the energy shift at a specific rate. The cut-off at a recorded rate of about 60 kcps is due to dead time of the DAQ system handling incident rates of up to 108 kcps dead-time free in energy mode

(section 3.7). However, peak pile-up significantly reduces this limit according to equation (4.7). Dead-time effects emerge only after the cut-off rate, so that data below this rate are not affected by the DAQ system [Bar14] [Eno14].

The shape of the photoelectron energy spectra shown in figure 4.14 can now be qualitatively explained by pile-up effects where signals are influenced by other signals. Peak pile-up lowers the measured event rate and leads to a plateau-shaped spectrum with broad multiple-occupancy peaks, e.g. a two-event peak, a three-event peak, etc., while tail pile-up results in a shift of the entire spectrum to lower energies and in additional broadening of the individual peaks. These distortions become more dominant with increasing rates so that the spectra can be even shifted below the electronic noise threshold. A modification to the FPGA filter logic is currently under development to address this high-rate issue [Ams14] [Eno14].

4.6 Charge Sharing

Charge sharing is a characteristic of a segmented PIN-diode array housed on a monolithic silicon wafer. This effect can appear when an incident particle interacts in the sensitive detector volume near the pixel-boundary region such that the deposited energy is distributed to more than one pixel. In that case, the sum of the recorded energies is equal to the incident energy as long as the individual measured energies are greater than the electronic noise threshold. The detector has a monolithic entrance window and a segmented back side with pixel boundaries of 50-μm in thickness, while a typical 18.6-keV signal electron deposits its entire energy via electron impact ionization only within the first few μm of the detector. Due to the applied bias voltage, generated charge carriers are extracted by the electric field spanned across the whole detector volume to the contact side.

The area ratio of the insensitive pixel-boundary region to the total detector region gives a conservative average upper limit of 2.32 % for the charge-sharing probability between two adjacent pixels. However, this area ratio varies with the detector-pixel rings, since the perimeter for inner pixels is shorter than for outer pixels, owing to the fact that the pixels are equally sized. This leads to a maximum charge-sharing probability of 1.54 % for the thick bullseye pixels and of 2.90 % for the thin outermost pixels. When the electric field in the detector is taken into account, the actual gap between adjacent pixels is of minor importance, regarding potential loss of generated charge carriers. There are always dividing ridges between neighboring pixels so that charge carriers are rather partitioned than lost, meaning that dispersion is of major relevance. Close to the pixel-boundary regions, the charge carriers follow the electric-field lines to individual pixels rather than to the high-resistance boundaries. Therefore, the actual charge-sharing probability is smaller and the actual loss of charge carriers is negligible, especially in the case of incident electrons interacting only at the entrance.

In order to investigate the charge-sharing probability for typical 18.6-keV electrons, the photoelectron source was elevated to a potential of -18.6 kV while it was continuously illuminated by UV light using a constant-current power supply to drive the associated UV LED (run #3462, 90 min). Figure 4.20 shows the resulting inter-arrival time distributions on different time scales for electrons with energies between the electronic noise threshold at 5 keV and the cutoff of the single-electron peak at 20.6 keV. The distributions illustrate the time differences between detector events. For time scales larger than 10 μs, the distributions follow an exponential trend as indicated by the corresponding red-colored fits applied to the data with their time constants being in good agreement with the average recorded count rate of 372.3(3) cps for this measurement. This proves that the produced photoelectrons are indeed Poisson time-distributed signals in this configuration, confirming their independent generation mechanism. However, the distinct peak within the first
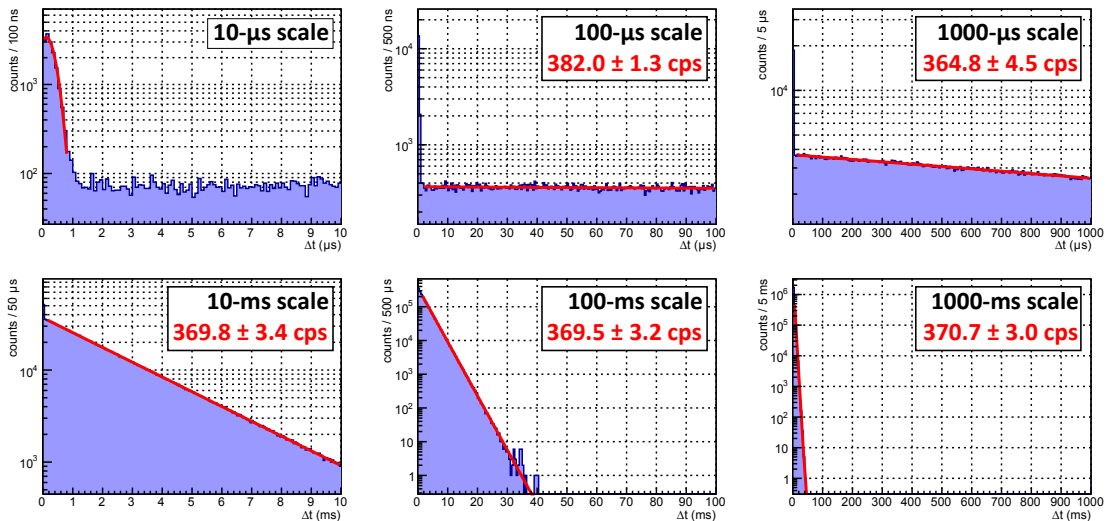
Figure 4.20: Inter-arrival time distributions for 18.6-keV photoelectrons. The inter-arrival time distributions illustrate the time differences between detector events on different time scales. At the 10-µs time scale, the distinct peak describes correlated multi-pixel events, following a Gaussian distribution (red-colored fit). At larger time scales, the distributions are exponential (red-colored fits), while the shown time constants are consistent with the average count rate of 372.3(3) cps for this calibration measurement.

1.5 µs implies correlated events where two events are recorded at the same time. This coincidence peak follows a Gaussian time distribution, being interpreted as multi-pixel events while its standard deviation of 280(5) ns is consistent with the timing resolution of the detector.

These multi-pixel events originate from accidental coincidences, multi-particle events, and charge-splitting events across several pixels. As an illustrative example, figure 4.21 shows those multi-pixel events which are correlated to the events of pixels #0, #94 and #102 within a coincidence window of 1.5 µs. In most cases, the selected pixel underlies a significant self-coincidence. Multiple events recorded in a single channel within the shaping length are strongly suppressed by the peak pile-up of the trapezoidal filter, as described in section 4.5. However, it is still possible to acquire more than one trigger within the shaping length: if the energies of the two events are not equal, if there are more than two events within the shaping length, if there are additional events in close proximity to the event window, and/or if the baseline fluctuates due to noise or other reasons. A further, less dominant effect is the coincidence with an adjacent pixel, most likely caused by charge splitting due to the bounded energy region for this analysis. Charge-splitting events can be classified into charge-sharing events describing internal charge dispersion between neighboring pixels and into external processes, such as backscattering, electrostatic reflection, and magnetostatic mirroring. However, these effects cannot be resolved from each other since the time-of-flight of 18.6-keV electrons through the detector system is in the ns-scale which is less then the sampling rate of the DAQ system. Therefore, only an upper limit for the charge-sharing probability can be given, assuming that all multi-pixel events perform charge-sharing. The observed occasional events can be assigned to accidental events since multi-particle events emerge primarily from high-energy radioactivity and cosmic muons so that they are highly suppressed in the analyzed energy interval.

In figure 4.22, the multi-pixel coincidences between all pixels are illustrated. The radial distance is given in detector rings and the azimuthal distance in angular degrees relative to the selected pixel. Therefore, the center of this plot represents the self-coincidence of a single pixel. The coincidence to adjacent pixels is described by a radial distance of
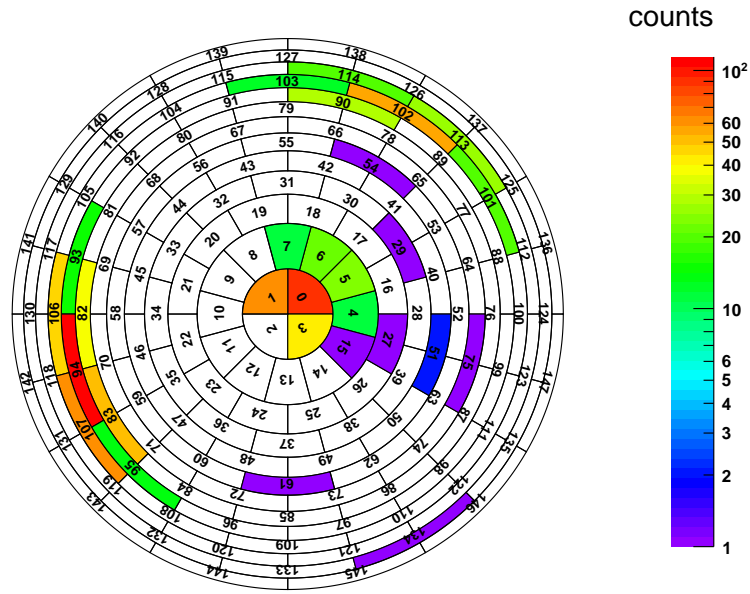
Figure 4.21: Pixel-view of correlated events. Only correlated events to pixels #0, #94 and #102 within a coincidence window of 1.5 μs are shown. This simple example already demonstrates that, in the majority of cases, multi-pixel events occur at the same or at adjacent pixels.
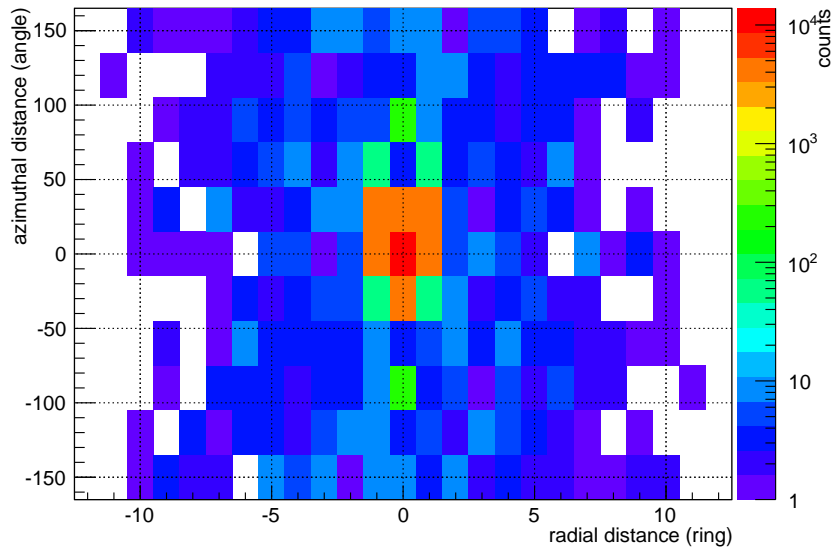
Figure 4.22: Multi-pixel coincidences between all pixels. This plot illustrates all correlated events within a coincidence window of 1.5 μs in respect of the physical distance to the involved pixels. The radial distance is given in detector-pixel rings from −12 to +12 while the azimuthal distance is described in angular degrees from −180° to +180°, each relative to the selected pixel to which the coincidences are investigated. 98.2 % of the multi-pixel events can be assigned to the same pixel and to neighboring pixels.

111
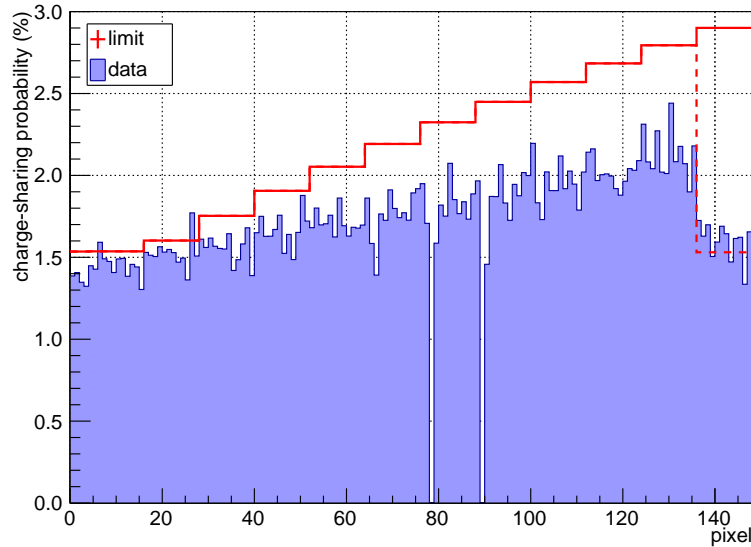
Figure 4.23: Upper limit for charge-sharing probability for each pixel. Both the calculation (red-colored line) and the measurement (blue-colored histogram) of the upper limit for the charge-sharing probability are shown for each pixel. The conservative calculation utilizes the area ratio of pixel boundary and pixel size while the measurement uses the rate ratio of multi-pixel events and total events. The drop in charge-sharing probability for the outermost pixel ring can be explained by neglecting the outermost pixel boundary region in the calculation (dashed-red line). In that case, the area ratio drops from 2.90 to 1.53 %, which is comparable to the bullseye ring and the first 12-pixel ring.

± 1 ring and/or a azimuthal distance of $\pm 30°$. The two hot spots at $\pm 90°$ at the same ring correspond to correlations between adjacent bullseye pixels. Within all multi-pixel events, about 33.4 % underlie self-coincidence, while 64.8 % correlate to adjacent pixels. The remaining 1.8 % of the events are distributed across the other pixels according to the pattern shown in the plot.

The upper limit for the charge-sharing probability for each pixel is given by the ratio of the measured multi-pixel event rate and the recorded total event rate of the associated pixel. Figure 4.23 shows the results gained from the measurement described above, including the calculated upper bound derived from the area ratio of pixel boundary and pixel size. The measured average limit for the charge-sharing probability is 1.74(24) % for the entire detector wafer while the individual probabilities range from about 1.3 to 2.4 %. Both the expected and observed limits are consistent with a higher charge-sharing probability for outer pixels due to the increased pixel-boundary length and the thinner pixel shape. The observed drop for the outermost pixel ring can be explained by fewer available adjacent pixels with which a correlation is realizable since the outermost ring is surrounded by the insensitive guard ring (section 3.5). This effect can be considered in the calculation by neglecting the insensitive area of the outermost pixel boundary region. The non-functional pixels #78 and #89 affect the determined charge-sharing probability of the neighboring pixels, especially of pixel #90 which is adjacent to both pixels. It is important to note that the calculation includes only the geometry of the detector pixels and excludes electric-field effects from the reverse-bias voltage applied to the detector wafer. However, this model is already in moderate agreement with the experimental observations.

Charge-sharing effects can be corrected in the offline analysis when the following criteria are met:

- Involved pixels are adjacent.

- The sum of the split energies is equal to the incident energy, considering the moderate energy resolution of the detector. However, the detector dead layer influences the recorded energy since the incident particle loses a specific amount of undetectable energy in its insensitive volume. In addition, if one of the split energies is below the electronic noise threshold, the event multiplicity reduces accordingly. Therefore, it seems reasonable to apply a high post-acceleration potential to mitigate this effect.

- The coincidence window for charge sharing is $1.5\,\mu s$ when using the standalone detector system. Nevertheless, the time-of-flight for a 18.6-keV signal electron through the main spectrometer is several microseconds. In the case of backscattering, this time window has to be enlarged. However, this effect can also be minimized by applying a high post-acceleration potential.

4.7   Detector Operation During the First Main-Spectrometer Commissioning

In order to investigate whether the main spectrometer operates as a proper MAC-E filter and to study its background behavior and transmission characteristics, the detector system was connected to the downstream end of the main spectrometer via a custom-built beam pipe housing an in-line flapper valve. At each point in time, the detector system could be separated from the main spectrometer by closing the corresponding gate valve or flapper valve, either automatically or manually. On the one hand, this ensured a proper protection of the detector wafer against possible high-voltage and Penning discharges arising from the main-spectrometer volume and against potential water impacts and vacuum failures. These effects can cause irreversible damage to the detector wafer. On the other hand, the separation ensured a proper calibration of the detector using the ^{241}Am source at regular intervals.

Some of the detector parameters were adjusted such that they deviated from the optimized values gained from stand-alone detector commissioning. This was necessary in order to primarily guarantee a stable, long-term operation of the detector system during first main-spectrometer commissioning with the main focus on functionality. Table 4.4 lists the detector parameters realized in comparison to the design values. The most important modifications were the following:

- **Magnetic field:** The field provided by the detector magnet was slightly reduced from 3.6 to 3.5 T so that the size of the imaged flux tube decreased from 210 to $\sim 205\,\mathrm{Tcm}^2$. Due to existing, well-known issues with the pinch magnet, its maximum field was lowered from 6.0 to 5.0 T which led to an associated broadening of the sensitive 191-Tcm^2 flux tube from 3.18 to 3.49 cm in radius within the magnet bore. It will be shown in section 4.9 that this untypical magnetic-field configuration has led to some significant side effects to the transported magnetic flux tube, especially in combination with sub-components, such as the vacuum chamber and the magnets, which were not perfectly aligned relative to the actual beam axis.

- **Post-acceleration potential:** The potential of the post-acceleration electrode was slightly reduced from 11.0 to 10.0 kV since a stable operation could not be guaranteed above 10.5 kV, most likely due to the adjusted magnetic-field configuration. However, this potential is sufficient to boost low-energy electrons from the non-elevated spectrometer parts to an energy above the electronic noise threshold.

- **Vacuum:** The residual gas spectrum shows that the vacuum conditions in the UHVac chamber were dominated by water vapor due to a vacuum incident during the connection process so that a final pressure of $\sim 5 \times 10^{-9}$ mbar was reached.

Table 4.4: Detector parameters during first main-spectrometer commissioning.
The most important detector parameters used during first main-spectrometer commissioning are listed below. The wafer position is given relative to the center of the detector magnet. The detector energy resolution is denoted by ΔE and the incident electron energy by E_0.

parameter	detector comm.	spectrometer comm.	design value
pinch-magnet field (T)	6.0	5.0	6.0
detector-magnet field (T)	3.6	3.5	3.6
imaged magnetic flux tube (Tcm^2)	210	205	≥ 191
post-acceleration potential (kV)	11	10	25
UHVac pressure ($10^{-9}\,\mathrm{mbar}$)	~ 3.0	~ 5.0	1.0
vacuum-electronics temperature (°C)	≤ 0	≤ 0	optimized
functional detector pixels	146 (98.6 %)	146 (98.6 %)	≥ 133 (90 %)
wafer position (cm)	~ 15	~ 15	17.0
wafer bias voltage (V)	120	120	120
shaping length (µs)	6.4	1.6	optimized
gap length (ns)	200	200	optimized
electronic noise threshold (keV)	~ 4	~ 7	$< U_{\mathrm{PAE}} - \Delta E$
region of interest (keV)	optimized & fixed	fixed $[E_0 - 3, E_0 + 2]$	optimized

- **Detector cooling:** The temperatures of the detector wafer and the vacuum electronics were stable within a range of 30°C while the preamplifier modules were permanently held at temperatures below 0°C. It will be shown in section 4.8 that temperature-dependent detector effects are of minor concern in this temperature range, due to the small contributions played by the thermal noise with respect to the detector response and due to periodic detector calibrations.

- **Detector wafer:** During the first phase of the main-spectrometer commissioning, the same wafer (#96724) used for stand-alone detector commissioning providing 146 of 148 functional pixels (98.6 %) was installed about 15 cm downstream of the pinch-magnet center. The bias voltage was kept at 120 V. Nevertheless, it should be noted that electrons and other electrically negative charged particles passing the detector system are boosted in their longitudinal energy by both the post-acceleration potential and the bias voltage.

- **Trapezoidal filter settings:** The shaping length was set to 1.6 µs to ensure a reasonable tradeoff between energy and timing resolution as well as to obtain a reliable detector operation during high-rate transmission-function measurements using the electron gun on the upstream spectrometer side, without suffering from significant pile-up effects with incident rates of up to ~ 5 kcps on a single pixel. Due to the reduced shaping time, the FWHM energy resolution degraded to ~ 2.0 keV for 18.6-keV electrons while the electronic noise threshold increased to ~ 7 keV accordingly. The gap length was kept at 200 ns which represents the typical rise time of a post-amplified detector signal.

- **Region of interest:** The region of interest in the measured energy spectrum corresponds to the acceptance window. Due to the moderate energy resolution of the detector, a fixed asymmetric 5-keV broad region of interest ranging from 3 keV below to 2 keV above the incident electron energy was selected in a rather conservative definition to simplify the associated analysis chains. The total incident energy is

given by

$$E_{\mathrm{INC}} = e(U_{\mathrm{RET}} + U_{\mathrm{PAE}} + U_{\mathrm{BIAS}}) \,, \tag{4.16}$$

where U_{RET} denotes the retarding potential of the inner layer of the wire electrodes, U_{PAE} the post-acceleration potential, and U_{BIAS} the detector-bias voltage. The latter is relatively small compared to the other potentials if applied, so that it can be neglected for the detector response to electrons in good approximation. The asymmetry of the acceptance window considers the characteristic electron-peak profile. However, during stand-alone detector commissioning both fixed and optimized acceptance windows were chosen, using a standard fit with a Gaussian distribution within a specific peak range or an advanced optimization technique such as the figure of demerit as described in section 5.8. The fixed region of interest neglects energy-related effects, such as electron starting energies, potential variations along the analyzing plane, as well as other smaller effects.

During first main-spectrometer commissioning, the detector system was operated continuously for almost four months without any major breakdowns, including all its individual sub-components. Several shorter measurement phases in standalone mode allowed for a detailed characterization of its performance parameters as described in the previous sections. However, the main-spectrometer commissioning campaign provided additional information on the long-term stability of the detector system. In this context, the stability of detector calibration in combination with the performance of detector cooling is expounded in section 4.8. Furthermore, the operation of the detector in interaction with other sub-systems gave a first insight into its capabilities regarding the final KATRIN setup and allowed the technical realization of potential system optimizations at an early stage. In that regard, the alignment of the detector system relative to the main-spectrometer axis is discussed in section 4.9.

4.8 Calibration Stability

In section 3.8, the slow but steady degradation of the performance of the heat-pipe cooling during long-term operation was discussed when using the heat-pipe heaters for temperature regulation instead of the vacuum-electronics heaters. The observed variation in cooling performance is not yet fully understood. As described in section 4.1.3, temperature variations can cause detectable shifts in the absolute positions of the calibration lines and imply significant alterations in the absolute energy resolution of the detector. Within an examined temperature range of about $120\,\mathrm{K}$, the observed energy shift is below $\sim 2.2\,\%$ toward lower energies, becoming more dominant with declining temperatures, while the measured variation in energy resolution is below $\sim 33\,\%$ and converges toward lower temperatures. Both effects influence the stability of the energy position E_0 and the FWHM energy resolution ΔE of the calibration peak and thus affect the properties of the acceptance window in the energy spectrum. Therefore, it is of even greater importance to investigate the resulting consequences for the detector performance. For this purpose, 24 detector calibrations were performed using the ^{241}Am γ-source periodically over the course of the main-spectrometer commissioning. During calibrations, the detector system was separated from the main spectrometer by the closed gate valve. In the meantime, relevant heat-pipe sensor data was recorded, such as evaporator temperature T_{eva}, $\mathrm{N_2}$-reservoir pressure p_{N2}, and heater power P_{heat}, as well as the vacuum-electronics temperature T_{vac}. Figure 4.24 illustrates the relations between these quantities and the characteristics of the 59.54-keV γ-line over all functional pixels. The values are strongly correlated as indicated by the following correlation matrix:
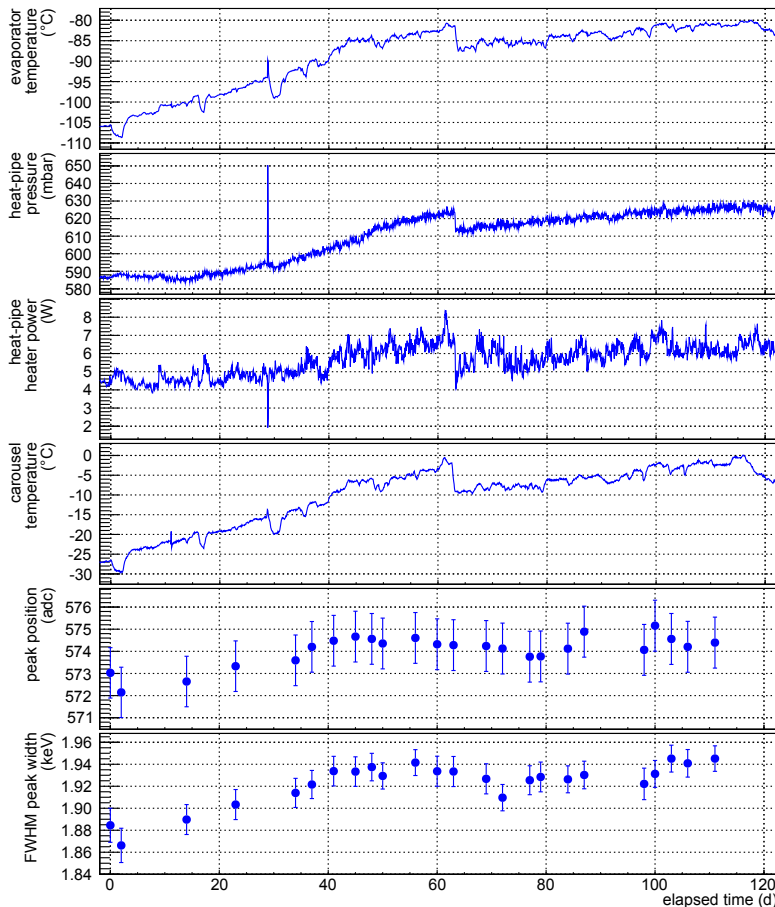
Figure 4.24: Correlation of heat-pipe and detector performance. The imperfect heat-pipe performance affects the temperatures of the detector wafer and the vacuum electronics such that the detector response to position and width of the calibration line is influenced as well. According to the correlation matrix (4.17), all illustrated values are highly correlated. Statistical error bars are included.

$$
\begin{array}{c|cccccc}
 & T_{\text{eva}} & p_{\text{N2}} & P_{\text{heat}} & T_{\text{vac}} & E_0 & \Delta E \\
\hline
T_{\text{eva}} & 1 & 0.951 & 0.822 & 0.992 & 0.885 & 0.936 \\
p_{\text{N2}} & 0.951 & 1 & 0.803 & 0.942 & 0.761 & 0.812 \\
P_{\text{heat}} & 0.822 & 0.803 & 1 & 0.819 & 0.732 & 0.795 \\
T_{\text{vac}} & 0.992 & 0.942 & 0.819 & 1 & 0.893 & 0.934 \\
E_0 & 0.885 & 0.761 & 0.732 & 0.893 & 1 & 0.888 \\
\Delta E & 0.936 & 0.812 & 0.795 & 0.934 & 0.888 & 1
\end{array}
\tag{4.17}
$$

The temperature-related drift of both the absolute global position and width of the calibration peak during the first part of main-spectrometer commissioning can be seen clearly. The variation of the position is relatively small so that it is explicable by the statistical uncertainties originating from peak fitting with a Gaussian distribution. By contrast, the width significantly changes within a specific range. However, due to the high correlation with the heat-pipe parameters and the system temperature, potential drifts in the detector response can be surveilled at any time without necessarily performing detector calibrations. The temperature stability of the front-end electronics and of the detector wafer can be noticeably improved when using the vacuum-electronics heaters for temperature regulation instead of the heat-pipe heaters because of the rather long distances in heat exchange of the latter. A more stable performance and a more robust response of
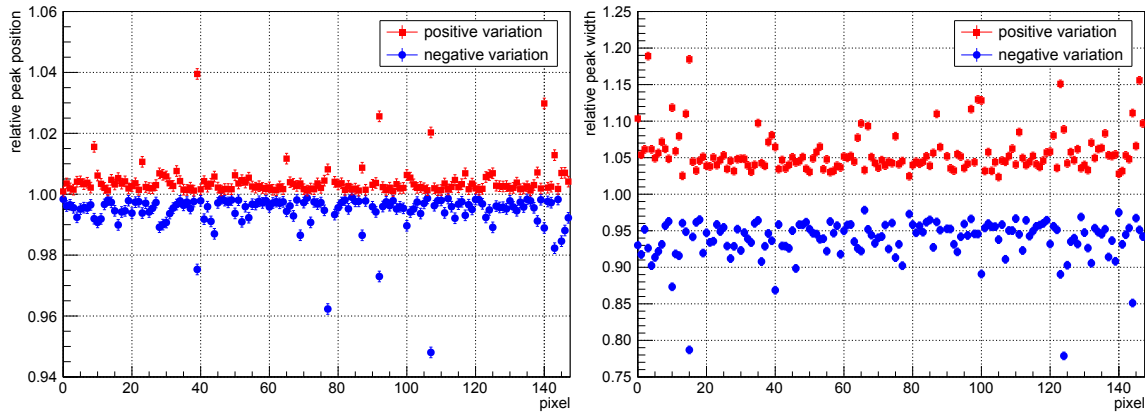
Figure 4.25: Calibration stability per pixel. The maximum relative calibration variation in both positive (≥ 1, red) and negative (≤ 1, blue) direction is shown for each pixel, regarding position (**left**) and width (**right**) of the calibration line. Statistical error bars are included.
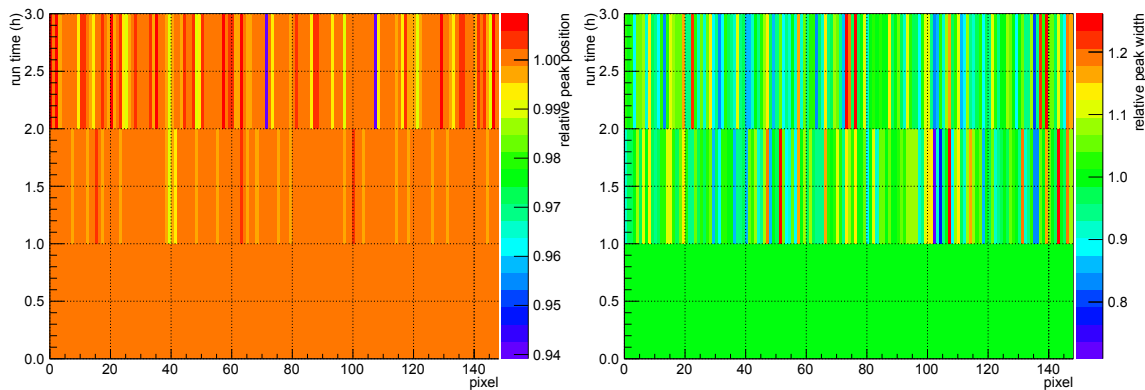
Figure 4.26: Influence of mechanical vibrations to optical-fiber links. The relative peak position (**left**) and peak width (**right**) of the calibration line are shown for each pixel during a 3-h ^{241}Am calibration. After a measurement time of one and two hours, the optical-fiber links were exposed to controlled mechanical vibrations, resulting in a variation of the detector response.

the detector with regard to the stability of the calibration peaks can then be expected. Based on these observations, the permanent use of the vacuum-electronics heaters will be implemented before the upcoming second commissioning phase beginning in summer 2014.

However, compared to the global detector response described above, a different assessment appears in the pixel-by-pixel investigation. Figure 4.25 shows the maximum relative deviation from the mean values of both position and width of the 59.54-keV γ-line in the calibrations performed during main-spectrometer commissioning for each pixel. Pronounced variations in the detector response scattered over the PIN array can be clearly seen. These observations cannot be ascribed to temperature-dependent effects since they occur rather suddenly, and only on single channels. Accordingly, the global detector response at which the individual energy spectra of each pixel are summed up is less affected. This phenomenon can be traced back to mechanical disturbances to single optical-fiber links connecting the optical sender boards with the optical receiver boards (section 3.6), which mainly occurred during the time periods of intensive hardware work on the DAQ system which were progressing, even during main-spectrometer commissioning. Both the optical-fiber links and connections constitute rather fragile parts of the signal chain since small vibrations or narrowing of bends may change the luminous efficiency of the associated fibers, resulting in a different recorded detector response for the corresponding channels. This hypothesis was explicitly verified during a 3-hour ^{241}Am calibration (runs

#4002 − #4004) where the optical fibers were temporarily exposed to vibrations after a run time of 1 and 2 h, respectively. The measured sudden variations for each pixel in peak position and peak width are illustrated in figure 4.26. Such characteristic fluctuations can be counteracted by instantaneous calibrations after the optical fibers were rearranged. Based on these observations, additional strain-relief options will be installed for these connections before the upcoming second commissioning phase.

4.9 Detector Alignment

The alignment of the detector system relative to the main-spectrometer axis is an important issue, since it defines the position of the sensitive magnetic flux tube. This orientation of the transported flux tube has to guarantee that no inner structural surfaces, such as the stainless-steel beam tube or the inner electrode system, are touched. A possible misalignment of a sub-component can be described by a displacement and a tilting from its designed value. Both a misalignment of the beam tube and the solenoids can influence the sensitive magnetic flux tube such that signal electrons hit inner surfaces and are lost for detection. Moreover, the misalignment can lead to additional background. If a sensitive magnetic field line enters the inner surface somewhere along the beam tube, secondary electrons released from cosmic-muon interactions in the structural material can be directly guided along this magnetic field line toward the detector. Depending on the location and the elevated potential of the associated spot of emission, these low-energy background electrons are recorded with different energies at the detector. When liberated in the detector system, they are only boosted by the post-acceleration potential. For background electrons released in the upstream half of the spectrometer (source side), the retarding potential usually is an impenetrable electrostatic barrier, while electrons from the downstream half (detector side) are reaccelerated by the spectrometer before being boosted by the post-acceleration electrode. Therefore, it is reasonable to perform alignment measurements with zero retarding potential and with a specific post-acceleration potential in order to boost the released low-energy electrons above the electronic noise threshold. Due to the spatial resolution of the detector, the resulting background appears on single pixels, most likely on the outermost pixels which map field lines closest to structural materials. The KATRIN design goal is the lossless transportation of a magnetic flux tube with 191 Tcm². At nominal magnetic fields, this flux is covered by the bullseye and the inner 11 12-pixel rings of the detector, excluding the outermost ring. The same applies to the configuration used during main-spectrometer commissioning in the first approximation, where the generated detector-magnet field is 3.5 T rather than 3.6 T.

After the detector system was connected to the main spectrometer during a rather challenging connection process due to the limited hardware-based flexibility of the downstream beam pipe housing the in-line flapper valve [Bar14], the mechanical alignment of the detector system was performed by using a *FaroArm*, a portable coordinate measuring machine [Far14]. This unit meters the absolute positions of the individual sub-components within the global KATRIN coordinate system. A right-handed global KATRIN coordinate system is used in the following such that the z-axis corresponds to the beam axis toward the downstream end of the experiment, where $z = 0$ represents the center of the main spectrometer. The x-axis is the horizontal axis and the y-axis defines the vertical axis pointing from bottom to top. Close to the setup of the detector system, a set of special marker spots for the *FaroArm* are installed at well-known locations to access the coordinate system. The detector system contains three sub-components whose alignment essentially needs to be known in order to model the geometry of the experimental setup correctly:

- **Superconducting solenoids:** The orientation of the pinch and detector magnet was measured via special marker spots mounted on the cryostats. This procedure
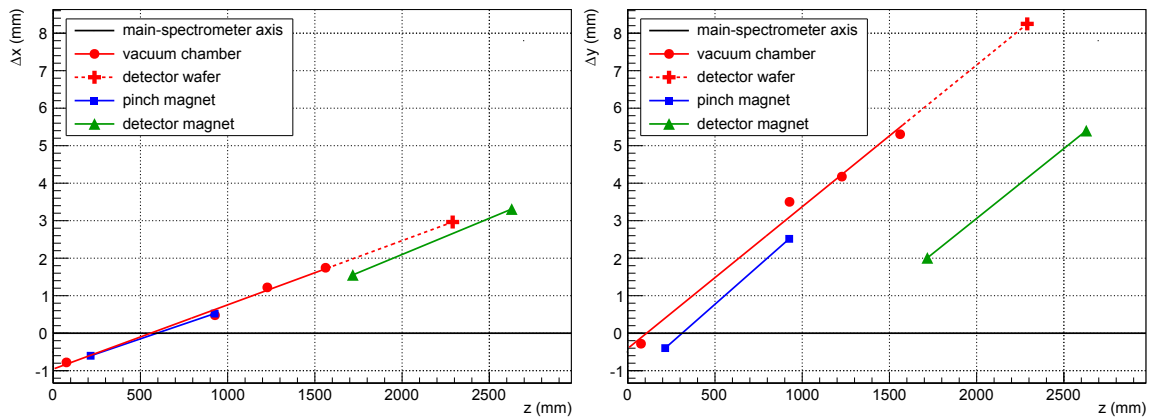
Figure 4.27: Actual displacements of the detector-system sub-components. The actual displacements Δx and Δy of the detector-system vacuum chamber (red), pinch magnet (blue), and detector magnet (green) are illustrated in both the z-x-plane (**left**) and the z-y-plane (**right**) relative to the main-spectrometer axis. The latter is indicated by the solid-black line while the dashed-red line denotes the extrapolation of the vacuum-chamber beam line to the expected wafer position. The z-position is given relative to the downstream face of the main-spectrometer flange on the detector side.

allows to determine the absolute alignment of each cryostat axis while the corresponding coil axis is assumed to be the same as the magnet axis.

- **Vacuum chamber:** The orientation of the vacuum chamber of the detector system, including the custom-built beam pipe housing an in-line flapper valve as part of the KATRIN beam line, was measured in the absence of marker spots, only by scanning the perimeters of selected accessible vacuum flanges along the beam tube. This procedure allows to determine the absolute center of each flange and thus the absolute alignment of the beam-line axis. Since the flapper valve is housed inside the beam pipe, it is impossible to perform direct measurements of its absolute orientation. However, its relative orientation within the beam pipe has been recorded in stand-alone mode before the detector system was connected to the main spectrometer.

- **Detector wafer:** Since the detector wafer is housed inside the UHVac chamber, it is impossible to perform direct measurements of its absolute orientation when the detector system is connected to the main spectrometer. Nevertheless, in stand-alone mode, when the HVac chamber has been partly disassembled, an appropriate scan of the detector-flange perimeter relatively to the vacuum-chamber perimeter allowed to determine the relative orientation within the detector system. As a consequence, the beam-line axis was extrapolated to this relative wafer position in order to identify the absolute wafer position.

The results of these mechanical alignment scans are illustrated in figure 4.27, while the absolute deviations from the design positions are listed in table 4.5. The accuracy is better than $\lesssim 1\,\mathrm{mm}$. The in-line valve has a full opening angle of 7.93° given in the z-y-plane and a rotation angle of 7.5° given in the y-x-plane. In addition, it is displaced and tilted together with the beam line.

The objective was to align both magnets, the detector beam line including the in-line valve, and the detector wafer such that these sub-components share the same axis as the main spectrometer. However, as indicated by the stated results, the alignment could not be performed as expected, due to limited adjustment possibilities the available hardware. After the connection to the main spectrometer had been established, a correction of the detector-system alignment would have resulted in an unacceptable torque acting on the ceramic insulator of the main spectrometer and on the bellows of the custom-built beam

Table 4.5: Absolute deviation from the design position of the detector-system sub-components. For both magnets, the deviation is given relative to the center of the associated cryostat. For the vacuum chamber, the deviation is stated relative to the downstream face of the main-spectrometer flange on the detector side. For the detector wafer, two independent quantities are given. The first one describes the value gained from extrapolation of the vacuum-chamber beam line, while the second value characterizes the intrinsic misalignment of the post-acceleration electrode and the detector wafer, observed in stand-alone mode of the detector system. Thus, the total misalignment of the detector wafer is given by the sum of both values.

component	Δx (mm)	Δy (mm)	Δz (mm)	θ_{zx} (°)	θ_{zy} (°)
pinch magnet	−0.040	+1.059	+0.299	+0.091	+0.235
detector magnet	+2.432	+3.705	+3.184	0.110	0.213
vacuum chamber	−0.779	−0.281	0.000	0.098	0.217
detector wafer	+3.016	+8.361	−0.020	0.098	0.217
	+1.622	+0.088			

pipe, leading to the risk of irreversible damage to the experiment. The associated technical drawing of this setup is illustrated in figure 4.28. Therefore, the main focus was set to functionality at the cost of an ideal alignment. Based on these findings, the adjustment possibilities will be significantly improved before the upcoming second main-spectrometer commissioning phase.

Following the outcome of the alignment results and the corresponding detector-system geometry, the new as-built geometry data were implemented in *Kassiopeia* [FG14] to allow for detailed field-line and electron-tracking simulations through the setup, taking into account the actual misaligned detector-system components. Figures 4.29 and 4.30 illustrate the simulated magnetic flux tube of $\sim 205\,\text{Tcm}^2$ through the main spectrometer and the detector system, respectively, both in the z-x-plane and in the z-y-plane, using the standard magnetic-field setting of 3.8 G in the analyzing plane as described in section 2.4. Each displayed field line ends at a single detector ring so that the innermost field line hits the center of the detector wafer while the outermost field line indicates the boundary of the sensitive entrance window. Due to the misalignment of the detector system relative to the main spectrometer, the transported flux tube is partly blocked by inner surfaces along the beam line at several locations, especially by the main-spectrometer vessel, the main-spectrometer ground electrode on the downstream side, the in-line flapper valve, and the post-acceleration electrode. The misalignment in the z-x-plane leads to minor disturbances of the magnetic flux tube since the pinch magnet, the detector magnet, and the detector beam line approximately share the same axis. By contrast, the misalignment in the z-y-plane results in a distinct shift of the magnetic flux tube such that it touches and even hits the inner surfaces. The actual fully transported flux is significantly reduced.

In order to estimate the size of the magnetic flux which is transported completely through the setup a priori, magnetic field-line simulations were performed with *Kassiopeia* using the parametrized as-built detector-system geometry gained from the *FaroArm* scans and the standard 3.8-G setting as magnetic-field configuration. For this purpose, 10^6 field lines were started on a virtual disk with 4.5 cm in radius placed axially on-axis in the center of the PS2 magnet. This corresponds to a magnetic flux of $274\,\text{Tcm}^2$, meaning that the corresponding cross sectional area of the simulated flux is larger than the sensitive area of the detector. The simulation of a single field line stops when either the field line reaches the detector or the clearance between field line and inner surface along the beam line falls below a distance of 100 μm. The latter seems to be a reasonable limit since the maximum cyclotron radius of a typical 18.6-keV electron in a 5-T field is ~ 65 μm and thus in the same order of magnitude. Figure 4.31 shows the corresponding events hitting the detector
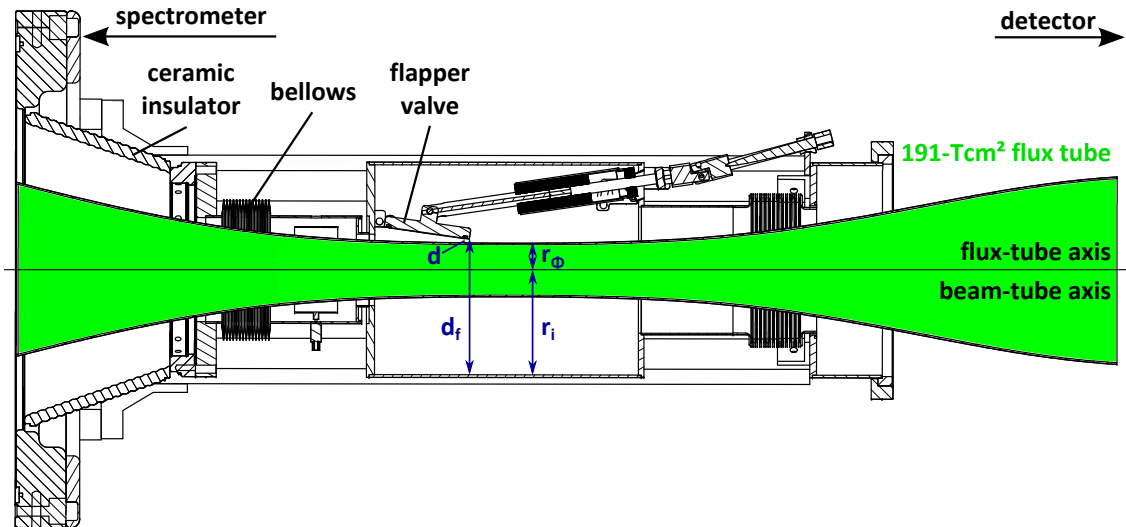
Figure 4.28: Custom-built beam pipe housing the in-line flapper valve. This technical drawing illustrates the given geometry of the ceramic insulator of the main spectrometer, the custom-built beam pipe and the in-line flapper valve with the dimensions $d_f = 16.00\,\text{cm}$ and $r_i = 12.38\,\text{cm}$. The green-colored 191-Tcm^2 magnetic flux tube is illustrated for nominal magnetic field settings with a pinch-magnet field of $B_{\text{PCH}} = 6.0\,\text{T}$ and a detector-magnet field of $B_{\text{DET}} = 3.6\,\text{T}$, so that the flux-tube radius close to the flapper valve is $r_\Phi = 3.18\,\text{cm}$. The associated clearance between flux tube and flapper valve can thus be calculated to $d = 0.44\,\text{cm}$. Details are explained in the continuous text.

wafer, illustrated on a pixel view with the flapper valve both excluded from and included in the simulations. The first configuration indicates that there are no field lines originating from the upstream side of the main spectrometer reaching the three outermost pixel rings at the top of the detector wafer since the main-spectrometer vessel, the ground electrode, and the post-acceleration electrode block the associated flux-tube volume. The second configuration implies the distinct influence of the flapper valve on the detectable flux tube. It prevents field lines from reaching the top of the detector wafer in the seven outermost pixel rings. In this region, the simulations demonstrate that the transported flux tube is significantly reduced to $\sim 90\,\text{Tcm}^2$. Therefore, a pronounced shadow of the inner structural surfaces imaged onto the detector wafer is expected. The simulated displacement of the detector-wafer center to the beam axis is $\Delta x = 1.843\,\text{mm}$ and $\Delta y = 3.111\,\text{mm}$, meaning that the wafer is shifted to the top by Δy and to the right by Δx, measured relative to the central axis of the magnetic flux tube.

The intrinsic detector-system alignment between both magnets, the vacuum chamber, and the detector wafer was experimentally investigated by performing intrinsic detector background measurements with a closed gate valve to the main spectrometer while the post-acceleration electrode was energized to $10\,\text{kV}$ (runs #5258 − #5265, 15 h). Since the simulations imply that the magnetic flux tube covered by the detector touches and even hits the inner surface of the elevated post-acceleration electrode, an increased electron rate is expected at the affected pixels. These electrons can be liberated from the copper material either by secondary emission caused by natural environmental radiation, intrinsic radioactivity and cosmic rays, or by electron field emission. As a consequence, the emitted electrons are immediately boosted by the post-acceleration potential and are directly guided to the associated detector pixels along the corresponding magnetic field lines. This electron-generation mechanism results in a characteristic hot spot on the detector, whose size and rate depends on the surface area of the post-acceleration electrode, which is actually imaged to the detector. The probability that such electrons reach the detector is
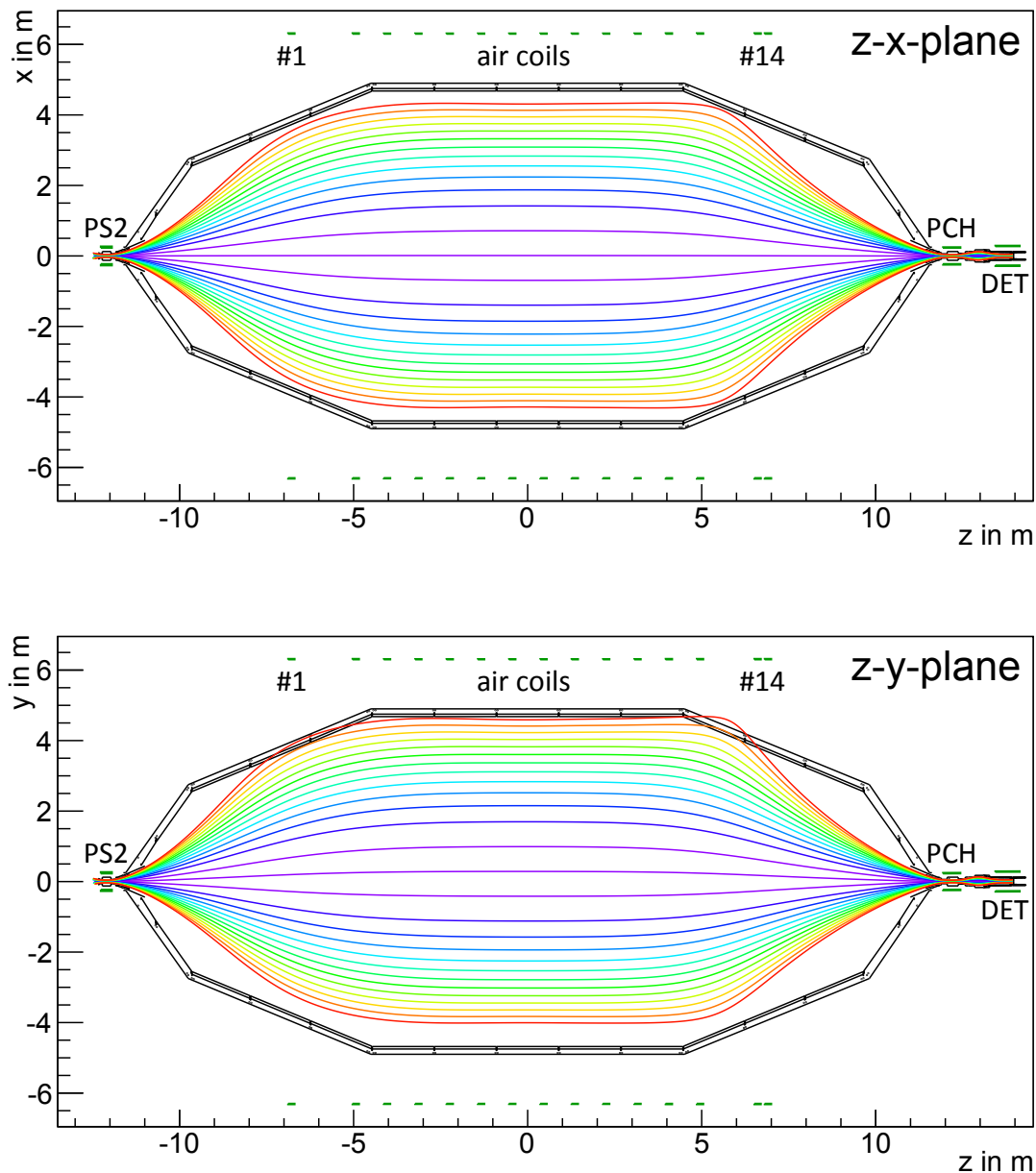
Figure 4.29: Flux-tube visualization in the main spectrometer. The magnetic flux tube is illustrated in both the *z-x*-plane (**top**) and the *z-y*-plane (**bottom**) for the standard 3.8-G setting. Each displayed field line ends at a single detector-pixel ring. The misalignment of the detector system with its solenoids and beam line results in a modification of the flux-tube symmetry within the main spectrometer. At the top of the main spectrometer, the flux tube is significantly blocked. The shape of the magnetic flux tube inside the detector system is shown enlarged in figure 4.30. Simulations performed by the author, using *Kassiopeia*.
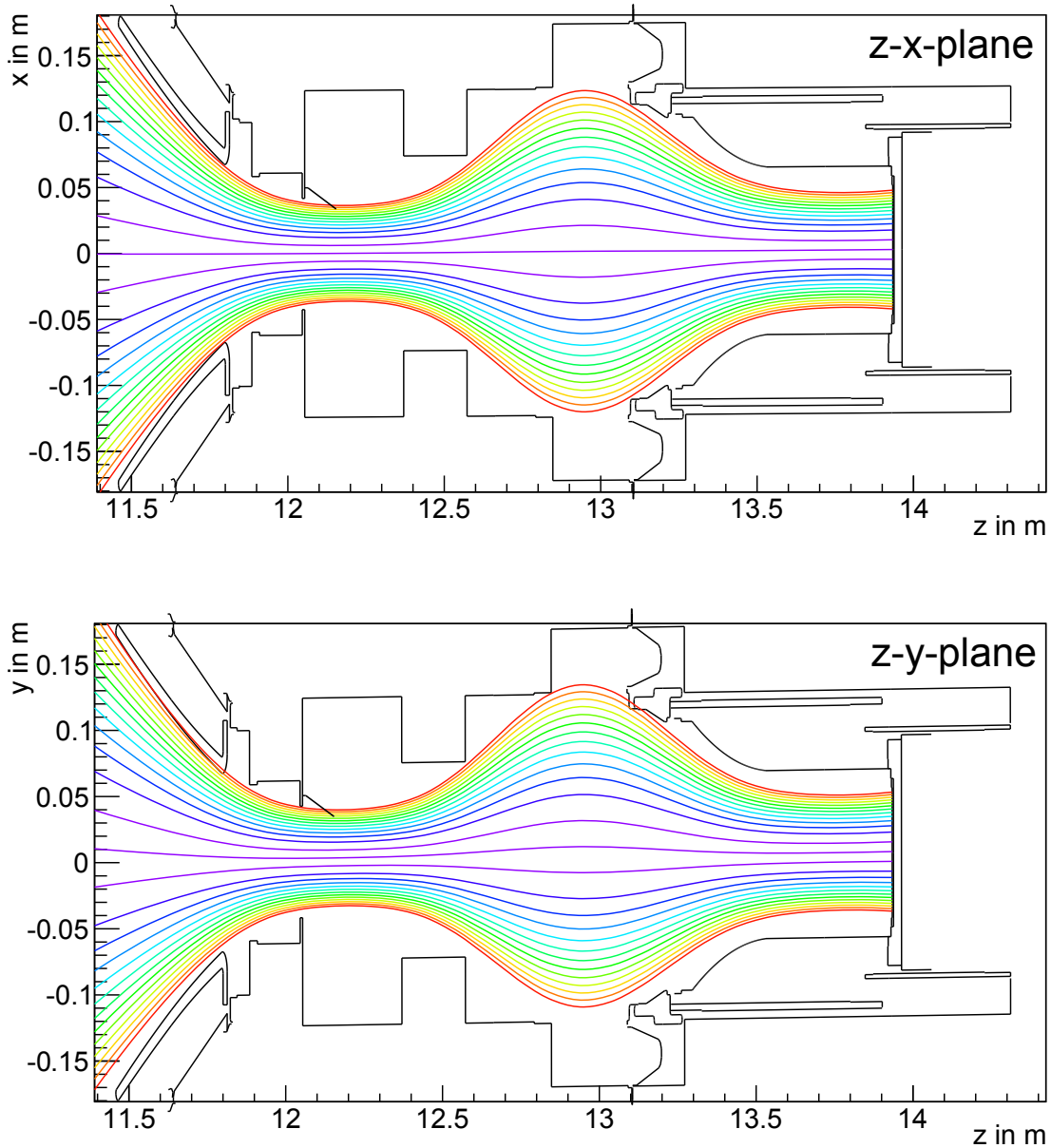
Figure 4.30: Flux-tube visualization in the detector system. The magnetic flux tube is illustrated in both the *z-x*-plane (**top**) and the *z-y*-plane (**bottom**) for the standard 3.8-G setting. Each displayed field line ends at a single detector-pixel ring. The misalignment of the detector system results in a modification of the flux-tube symmetry within the detector system itself. At the top of the ground electrode, at the flapper valve, and at the top of the post-acceleration electrode (from left to right), the flux tube is significantly blocked. Simulations performed by the author, using *Kassiopeia*.
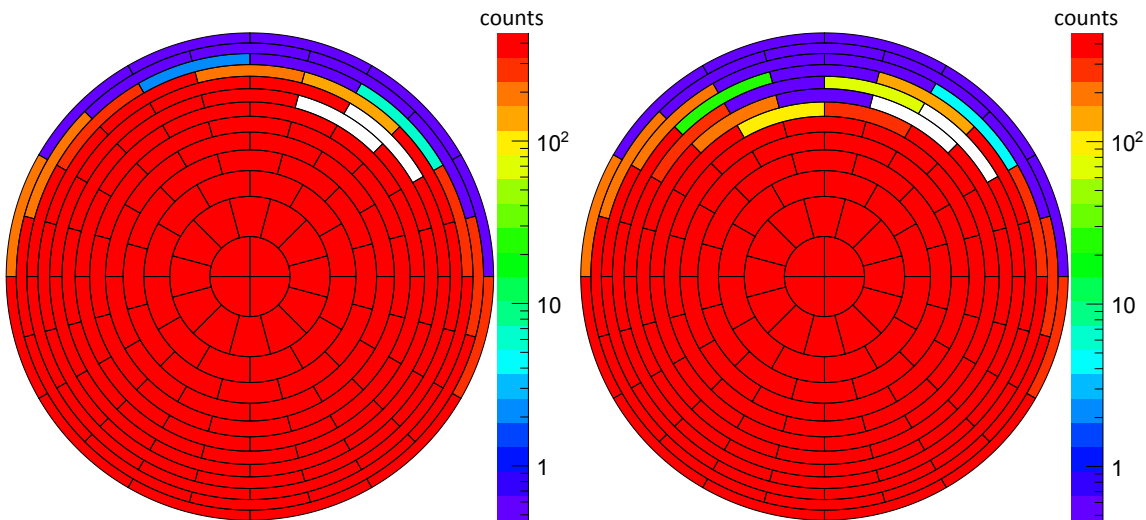
Figure 4.31: Flux-tube simulation through the main spectrometer and the detector system. In this simulation, the actual geometry of the detector system is taken into account while the flapper valve is excluded (**left**) and included (**right**). Simulations performed by the author, using *Kassiopeia*.

increased due to their high initial energy and the strong magnetic field in which they are liberated, in contrast to electrons emitted from inner surfaces on ground potential and in a weak magnetic field. Figure 4.32 (left) shows the electron rate per pixel in the region of interest between 7 and 12 keV. As expected, a distinct increase in rate on the outermost pixel ring can be observed, especially at pixels #136, #137, #138, #139, and #147, and less dominantly at the adjacent pixels #125, #126, and #140. These pixels can be assigned to be affected by electron emission from the post-acceleration electrode. For the other pixels, no obvious statement concerning the alignment can be given.

Finally, the alignment between the detector system and the main spectrometer was experimentally investigated with the main focus set on the influence of the flapper valve to the transported magnetic flux by performing background measurements with opened gate valve to the main spectrometer. For this purpose, the main-spectrometer retarding potential was adjusted to −18.6 kV and the standard 9.0-G setting was used as magnetic-field configuration while the post-acceleration electrode was elevated to 10 kV (runs #7340 − #7352, 13 h). Since the flapper valve is located between the main spectrometer and the detector system, electrons emitted from the flapper are not boosted by the retarding potential, in contrast to background electrons which originate from the main spectrometer. Therefore, the flapper shadow imaged onto the detector can be visualized by setting the region of interest to the expected energy of the main-spectrometer background electrons rather than around the post-acceleration potential. Figure 4.32 (right) shows the electron rate per pixel in the region of interest from 25.6 to 30.6 keV. As expected, the flapper shadow is distinctly visible through a decreased rate of influenced pixels compared to unaffected pixels. The variation in rate around the flapper shadow indicates which pixels are fully or only partly shadowed by the mechanical geometry of the flapper valve. Apart from the two shorted pixels #78 and #89, there are two additional pixels #79 and #91 without any recorded events. These pixels are both shadowed and surrounded by shadowed pixels. Other affected pixels may measure few events due to the effect of charge sharing between neighboring pixels. A total of 16 pixels was shadowed by the flapper valve.

Background measurements using the standard 3.8-G and 5.0-G settings show the same distributions of the observed shadow so that the latter can be fully described by inner mechanical structural parts blocking the sensitive magnetic flux tube. The measurements are
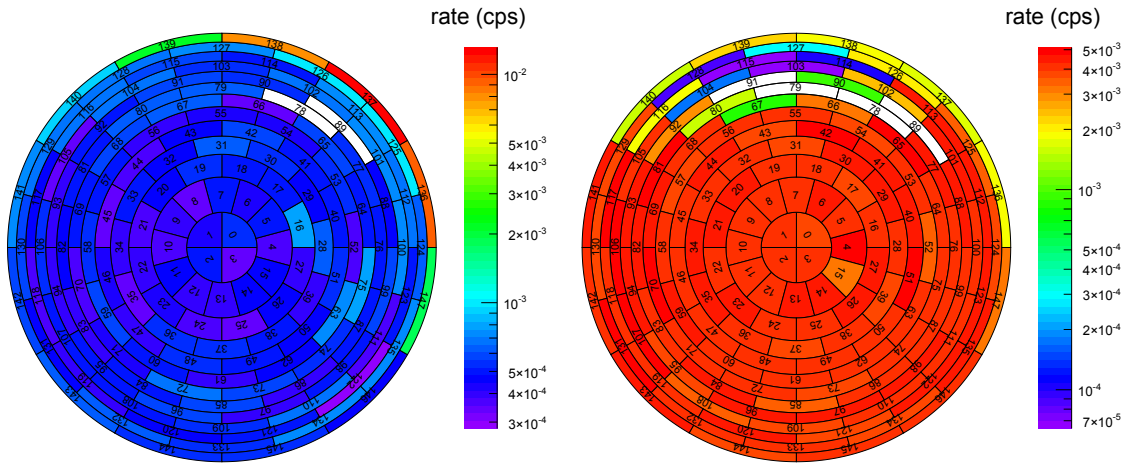
Figure 4.32: Beam-alignment measurements through the main spectrometer and the detector system. The influence of inner surfaces blocking the magnetic flux tube can be investigated by a set of background measurements. **Left: Intrinsic background measurement.** The hot spot at the top right corner of the detector wafer originates from secondary electrons emitted from and boosted by the post-acceleration electrode. **Right: Main-spectrometer background measurement.** The transported flux tube is blocked by the flapper valve resulting in a rate decrease at the shadowed pixels.

in very good agreement with the performed simulations. This fact implies the importance of a well-known parametrized model for the magnets and the beam line in order to fully understand the flux-tube transportation. In addition, it indicates the excellent interplay between mechanical alignment scans using the *FaroArm*, magnetic field-line simulations performed with *Kassiopeia*, and electron-counting measurements using the detector with its energy and spatial resolution. Already these very first measurements underline that the detector characteristics are essential in identifying different background sources and, in this case, in determining the actual system alignment. Although the displacement and the tilting of the individual detector sub-components are only in the mm-scale and below $0.25°$ ($4.4\,\text{mrad}$), respectively, a proper flux-tube transportation cannot be realized. Especially the misalignment in the z-y-plane is critical since the axes of the sub-components differ from each other. Figure 4.33 summarizes the findings described above. It illustrates a pixel view showing which pixels are influenced and which are unaffected by the corresponding shadowing through the post-acceleration electrode and the flapper valve, respectively, by conservatively comparing the measurements with the simulations.

Assuming ideal alignment of the detector system, meaning that the beam tube and the flux tube share the same axial axis, the clearance between the flux tube and the flapper valve can be approximately calculated to

$$d \approx d_f - r_i - r_\Phi \quad \text{with} \quad r_\Phi \approx \sqrt{\frac{\Phi}{B_{\text{PCH}}\pi}} \,, \tag{4.18}$$

where $d_f = 16.00\,\text{cm}$ denotes the smallest distance between the opened flapper valve and the inner surface of the beam tube, $r_i = 12.38\,\text{cm}$ the inner radius of the beam tube, and r_Φ the radius of the sensitive magnetic flux Φ, according to the technical drawing of the custom-built beam pipe shown in figure 4.28. Since the flapper valve is located approximately in the center of the pinch magnet, this clearance is given by the generated field B_{PCH} of the pinch magnet. At nominal magnetic field ($B_{\text{PCH}} = 6.0\,\text{T}$), a clearance of $4.4\,\text{mm}$ [$2.8\,\text{mm}$] is sufficient for a magnetic flux of $191\,\text{Tcm}^2$ [$210\,\text{Tcm}^2$]. However, at the standard magnetic-field configuration used for the first main-spectrometer commissioning ($B_{\text{PCH}} = 5.0\,\text{T}$), the 191-Tcm^2 flux tube barely fit through the beam pipe without touching
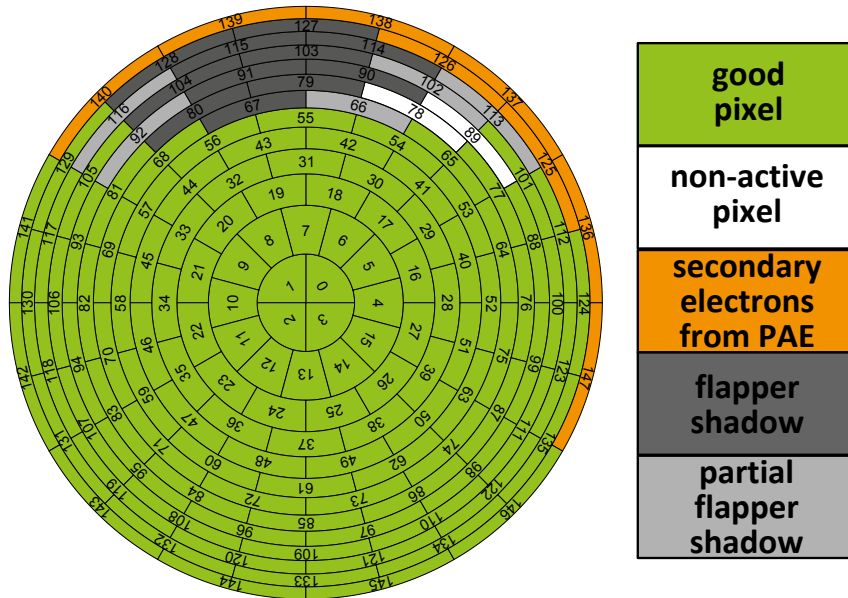
Figure 4.33: Summary of shadowed pixels. This schematic pixel view of the detector wafer indicates the cause of the shadowing on single pixels based on a conservative comparison between measurements and simulations. The behavior of all pixels seems to be understood. In total, 122 of 148 detector pixels cannot be used for the analysis of data recorded during first main-spectrometer commissioning. 2 non-active pixels (white): #78 and #89. 8 pixels affected by secondary electrons liberated from the post-acceleration electrode (orange): #125, #126, #136, #137, #138, #139, #140, and #147. 11 pixels shadowed by the in-line flapper valve (dark gray): #67, #79, #80, #90, #91, #103, #104, #114, #115, #127, and #128. 5 pixels shadowed partly by the in-line flapper valve (light gray): #66, #92, #102, #113, and #116.

the flapper since the clearance is only $1.3\,\mathrm{mm}$. The 210-Tcm^2 flux tube is definitely blocked due to a negative clearance of $d = -0.4\,\mathrm{mm}$. Therefore, it seems quite challenging to guarantee a lossless transportation of the design flux tube when running the pinch magnet below its design field.

Apart from ideal alignment, there are two options to allow for a detector operation where no pixels are shadowed by inner surfaces:

- The magnetic field in the main spectrometer can be increased to compress the magnetic flux tube such that the clearance to the inner layer of the wire electrodes increases at the cost of main-spectrometer energy resolution. The maximum possible magnetic field in the analyzing plane is at present technically limited to $10\,\mathrm{G}$, which would correspond to a filter sharpness of $3.1\,\mathrm{eV}$ for isotropic 18.6-keV electrons.

- The field generated by the detector magnet can be decreased to reduce the sensitive magnetic flux such that the resulting flux tube can pass the detector system without touching the flapper valve and the post-acceleration electrode. As stated above, a lossless transportation of the 90-Tcm^2 flux is guaranteed with the current alignment, corresponding to a required detector-magnet field of $\sim 1.5\,\mathrm{T}$.

4.10 Conclusion

A neutrino-mass measurement would, in principle, only require a simple electron-counting device to determine the number of signal electrons which have passed the analyzing plane for a specific retarding potential of the main spectrometer. However, for all practical purposes, detailed signal information like deposited energy, time stamp, and spatial distribution, represent important features in both understanding the operation of the apparatus

and the generation of background sources. The available detector brings along these characteristics with an adequate performance concerning energy, timing, and spatial resolution. Optimized operation parameters have been established with respect to filter settings, reverse-bias voltage, and temperature. Detector artifacts, such as rate dependence, charge sharing, temperature instabilities, and misalignment, are well-understood effects which can be reproduced by analytical calculations or sophisticated simulations with the *Kassiopeia* framework. As major part of the work in hand, a stable, long-term operation of the detector system has been achieved over a time period of almost four months during the first main-spectrometer commissioning measurement campaign. The system did not suffer from any serious disturbances or breakdowns, demonstrating its reliability for the KATRIN experiment. In the following chapter, the intrinsic detector background and its contribution to the total main-spectrometer background will be discussed in detail.

Intrinsic Detector Background

During the long-term neutrino-mass measurements, the KATRIN experiment will investigate a low-statistics region of the tritium β-decay energy spectrum with a signal rate of 20 mcps in a narrow region of few eV below the kinematic endpoint. Therefore, the mass sensitivity is extremely sensitive to background characteristics, such as rate, event topology, radial distribution, and variability. As source-related background is expected to play a minor role, the dominant background sources are expected to be generated in the main spectrometer and the detector system. All background contributions add to the overall statistical uncertainty of KATRIN and thus need to be minimized. Main-spectrometer related backgrounds originate primarily from low-energy electrons generated by Penning traps, by magnetically stored particles, and by electron emission from inner surfaces. In all cases, the created low-energy electron in the energy range of few eV is boosted by both the retarding potential and the post-acceleration potential, and thus will produce a distinct peak in the region of interest of the detector energy spectrum of the signal electrons, as shown in a more detailed description in section 2.5. Detector-system related backgrounds, however, arise mainly from intrinsic radioactivity, environmental radiation, and cosmic rays, and form a mostly featureless continuous background spectrum (section 5.1). The ambitious design goal for the detector system is to achieve an intrinsic detector background rate of less than 1 mcps within the region of interest [Ang05]. Two active background-reduction techniques can be applied in the offline analysis to reject correlated background events from the raw background spectrum: a multi-pixel cut and a veto cut (section 5.2). Apart from these active methods, passive background reduction is achieved by careful selection of materials used in close proximity of the detector and by substantial shielding (section 5.3). Detailed simulations have allowed to verify the expectations of both the active and the passive background-reduction approaches, and to examine unknown background sources (section 5.4). In order to further reduce the intrinsic detector background, a specific post-acceleration potential allows to shift the region of interest to a higher energy interval with a more favorable background rate (section 5.5). In addition, the magnetic-field settings can be varied to optimize the sensitive size of the magnetic flux tube imaged onto the detector wafer, thus changing the effective detector area (section 5.6). A specific adjustment of both the post-acceleration potential and the magnetic field allows to investigate the secondary-electron emission contributing to the intrinsic detector background (section 5.7). The measured intrinsic detector background influences the statistical uncertainty in the neutrino-mass measurements. Among other experiment-related parameters, it can be described with a detector-related figure of demerit which considers the given detector efficiency, energy resolution, and background rate. A minimization of this crucial parameter requires careful selection of both the position and the width of the region of interest in order to obtain optimum system performance and an almost ideal

detector operation (section 5.8). The contribution of the intrinsic detector background to the total background measured during the first SDS commissioning phase is small at present but will become relevant in later measurements (section 5.9).
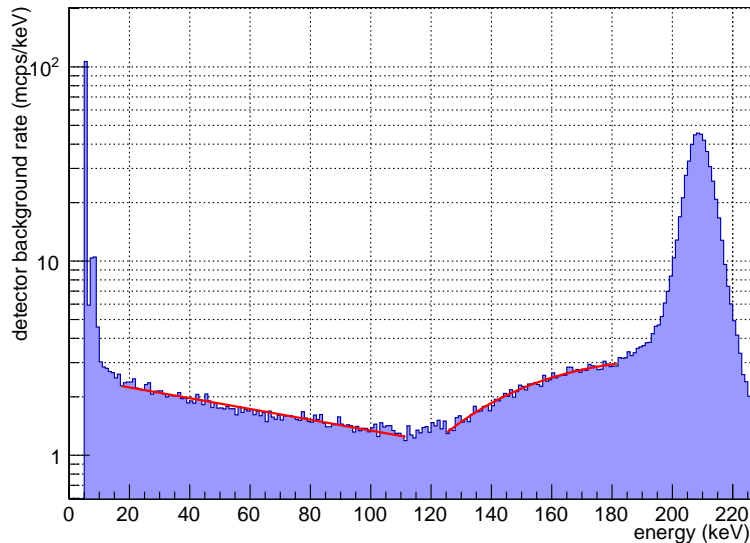
5.1 Raw Background

In order to characterize the intrinsic detector background under similar conditions as the final KATRIN setup, standalone background measurements were performed while the gate valve to the main spectrometer was kept closed to ensure a mechanical separation of the detector system from the main spectrometer. The individual sub-components of the detector system were aligned to an accuracy of $\sim 1\,\mathrm{mm}$ relative to the design values. Both calibration sources were retracted from the magnetic flux tube. The ^{241}Am source was removed from the system and stored in a lead-shielded container whereas the photoelectron disk was kept on ground potential. The illumination window was sealed in a light-tight manner. Detector data were measured in energy mode with filter settings optimized for low rates (section 4.1.1), i.e. $6.4\,\mu\mathrm{s}$ for the shaping length and $200\,\mathrm{ns}$ for the gap length. Veto data were recorded in veto mode with typical filter settings (section 3.10) meaning that at least two coincidences per scintillator panel within a coincidence interval of $100\,\mathrm{ns}$ are required to potentially release a veto trigger. Data were acquired over a total run time of $82\,\mathrm{h}$ while both magnets were operated at nominal magnetic field, i.e. $6.0\,\mathrm{T}$ at the pinch magnet[1] and $3.6\,\mathrm{T}$ at the detector magnet so that the detector wafer covers a magnetic flux of $210\,\mathrm{Tcm}^2$, and the post-acceleration electrode was kept on ground potential (runs $\#3132 - \#3139$ and $\#3142 - \#3175$).

Figure 5.1 illustrates the raw background energy spectrum at nominal magnetic field measured over 146 functional pixels and linearly scaled by a factor of $148/146$ to model a fully working detector. Linear scaling is appropriate as a uniform spatial distribution of the intrinsic background across the detector has been observed, as described in the following sections. The rate is normalized per unit energy interval of $1\,\mathrm{keV}$, so that it is given in mcps/keV. The spectrum shows several features:

- **Electronic noise threshold:** Electronic noise dominates below $6\,\mathrm{keV}$, resulting in a distinct steep rise at the lower end of the energy spectrum.

- **^{29}Cu fluorescence peak:** The individual fluorescence lines $K\alpha_1$, $K\alpha_2$ and $K\beta_{1,3}$ originating from the copper post-acceleration electrode cannot be resolved due to the moderate energy resolution of the detector leading to a distinct peak between 7 and $9\,\mathrm{keV}$.

- **Low-energy tail:** The background rate drops exponentially over a broad range from 15 to $110\,\mathrm{keV}$, indicated by the red-colored exponential fit in figure 5.1. The background in this energy interval is dominated by fluorescence light from surrounding materials [Sch04] [Leb10]. The fluorescence process is triggered by both internal and environmental radioactive impurities as well as cosmic-ray induced. Depending on the adjusted post-acceleration potential, the region of interest for signal β-electrons is located within in this energy interval. Below $40\,\mathrm{keV}$, the raw background rate exceeds a value of $2\,\mathrm{mcps/keV}$ and thus the benchmark. Higher post-acceleration potentials result in lower background rates. However, a background level of $1\,\mathrm{mcps/keV}$ would require unrealistically large post-acceleration voltages.

- **Minimum-ionizing peak:** At $125\,\mathrm{keV}$, a distinct rise in the continuum appears which can be described by a Landau distribution, indicated by the red-colored fit. It characterizes the energy-loss fluctuations caused by ionization of a charged particle

---

[1]At that time, the pinch magnet was still fully operational.

Figure 5.1: Raw background energy spectrum at nominal magnetic field. The experimental background spectrum is linearly scaled by a factor of 148/146 to model a fully working detector. The electronic noise threshold appears at $\sim 6\,\text{keV}$. The individual copper fluorescence lines at $8 - 9\,\text{keV}$ cannot be resolved. Two characteristic fits (solid red lines) describe an exponential drop in the background rate from 15 to $110\,\text{keV}$ and the Landau-distributed energy-loss spectrum of muons in the interval between 125 and $180\,\text{keV}$. The broad overflow peak around $\sim 210\,\text{keV}$ dominates in the high-energy region. Further details are described in the continuous text.

passing a thin layer of matter [Lan44]. In that case, through-passing minimum-ionizing charged particles with high energy like cosmic muons deposit a specific amount of their energy into the $500\text{-}\mu\text{m}$ thick detector wafer. Only the broad peak of the Landau distribution is visible since its long declining tail is cut off by the overflow peak.

- **Overflow peak:** Each pixel has a slightly different energy calibration and each preamplifier channel operates with a slightly different base-line voltage. In addition, the base line is affected by noise. Since the shown background spectrum is integrated over all functional pixels, these effects cause a broad overflow peak above $180\,\text{keV}$ rather than a single overflow bin.

The raw background can be processed by applying two active background-reduction cuts to remove correlated background events. Their implementation is described in the following section.

5.2 Background Cuts

Both an active multi-pixel cut and an active veto cut allow to reject correlated background events from the raw background energy spectrum.

5.2.1 Multi-Pixel Cut

The multi-pixel cut is based on a pixel-to-pixel anticoincidence method. It removes any detector event when additional events are recorded within a certain time window, regardless at which detector pixel the associated events are detected. Those events are interpreted to be correlated, in contrast to the uncorrelated signal electrons from tritium β-decay which
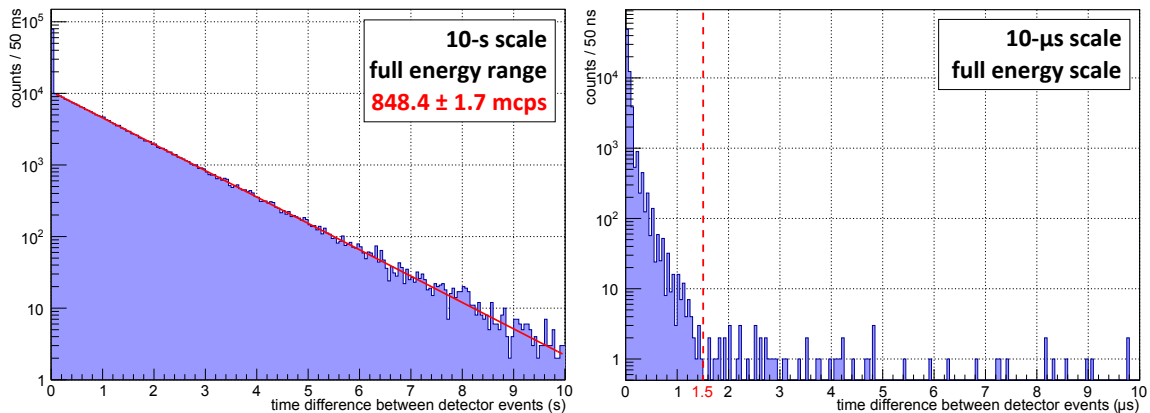
Figure 5.2: Inter-arrival time spectra of raw background. These spectra show the distribution of time intervals between detected events at a scale of $10\,\mathrm{s}$ (**left**) and $10\,\mu\mathrm{s}$ (**right**). The applied exponential fit (solid-red line) at large time scales implies the Poisson-time distributed trend of intrinsic background events with an average rate of $(848.4 \pm 1.7)\,\mathrm{mcps}$ while the base width of the distinct multi-pixel event peak at short time scales defines the coincidence window of the multi-pixel cut to $1.5\,\mu\mathrm{s}$ (dashed-red line).

are expected to trigger only one pixel as the energy deposit in the detector is localized within a volume of typically less than $10 \times 10 \times 10\,\mu\mathrm{m}^3$ [Ren11]. Background events, however, may occur in a correlated manner since cosmic rays and γs from radioactive decays can deposit their energy across the entire sensitive detector volume or can create cascades of secondary particles. These effects result in a multi-pixel detection at different locations and energies within a relatively short time interval whereas the associated multi-pixel events need not necessarily occur at the same or at adjacent pixels. The coincidence window can be determined from the background measurement by investigating the inter-arrival time spectrum which describes the distribution of time intervals between detected events. It is shown in figure 5.2 for a 10-s and a 10-µs scale. For large time scales, the distribution follows an exponential trend, as indicated by the red-colored fit, showing the Poisson-time distributed characteristic of intrinsic background events. For small time scales of a few µs, the distinct peak centered at an time interval of zero corresponds to multi-pixel events. Its base width of $1.5\,\mu\mathrm{s}$ defines the coincidence window for the multi-pixel cut.

The accidental coincidence rate of the multi-pixel cut can be calculated when only two events are involved. In that case, either one pixel or two pixels detect both events within the coincidence interval. For the simplified two-pixel case, the accidental coincidence rate for Poisson-distributed events is given by $r_a = \tau r_1 r_2$, where τ denotes the coincidence window and r_1, r_2 the single rates of the individual pixels [Tso95] [Kno10]. In the generic case of N pixels, there are $\sum_i^{N-1} i = N(N-1)/2$ possible combinations of selecting two different pixels i, j with rates r_i, r_j $(i \neq j)$. Including self-coincidence of a single pixel with both events, the accidental coincidence rate is then defined by

$$r_a = \left(\frac{N(N-1)}{2} + N \right) \tau r_1 r_2 \ . \tag{5.1}$$

For the 148-pixel detector and the 1.5-µs coincidence window, the accidental coincidence rate is $16.5\,\mathrm{mcps}$ for single rates of $1\,\mathrm{cps}$ and $1.65 \times 10^{-8}\,\mathrm{cps}$ for single rates of $1\,\mathrm{mcps}$. The measured single pixel rate is $\lesssim 10\,\mathrm{mcps}$, resulting in an accidental coincidence rate of $\lesssim 1.65 \times 10^{-6}\,\mathrm{cps}$. Therefore, the accidental coincidence rate for the dominant two-event multi-pixel cut becomes an issue for increasing rates but is negligible when applied to detector background measurements. Larger multi-pixel cluster sizes where more than two events are involved are less frequent, as shown in figure 5.3, so that their contributions to
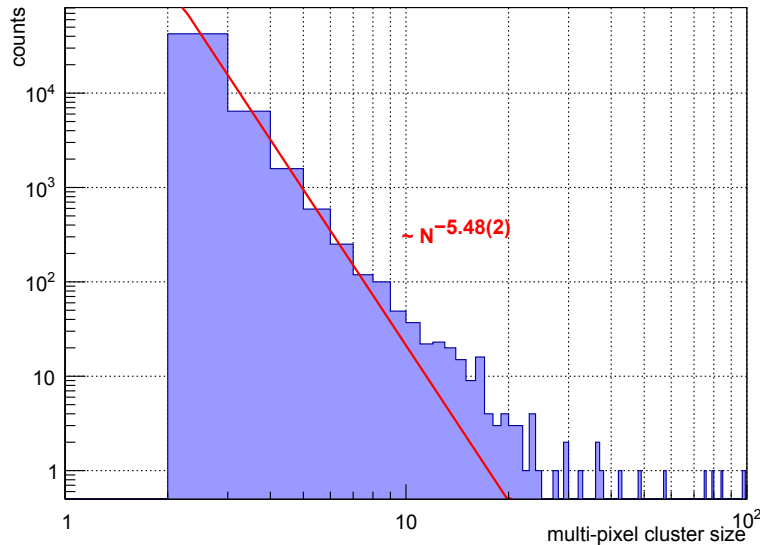
Figure 5.3: Multi-pixel cluster size. This spectrum shows the number of events removed by single multi-pixel cuts with a coincidence window of $1.5\,\mu s$. Two-event multi-pixel signals dominate the associated cut. Even detector signals with almost 100 events can be observed within the adjusted, relatively short coincidence window. The applied power-law fit (red line) indicates a dependence of the number of multi-pixel events, following $\sim N^{-5.48(2)}$, where N denotes the multi-pixel cluster size.

the accidental coincidence rate are negligible.

More importantly, charge-sharing events are definitely rejected by the multi-pixel cut. As described in section 4.6, charge sharing can occur when particles deposit their energy close to the pixel boundary such that adjacent pixels detect parts of the incident energy while the sum of the recorded energy equals the single-event initial energy. An upper limit for the charge-sharing probability of $2.3\,\%$ for the entire detector wafer can be calculated from the area ratio of the boundary region and the pixel region. The experimental investigation gives a smaller average upper limit of $1.74(24)\,\%$ with a decreasing probability for inner pixels. For β-electrons entering at the non-segmented side of the detector wafer, an actual charge-sharing probability being much smaller is expected. The exact value can be estimated by a detailed Monte Carlo simulation using *KESS* [Ren11]. However, this simulation would not include charge-collection effects based on the electric field which is applied across the depletion zone of the detector.

5.2.2 Veto Cut

The veto cut is based on an anticoincidence method between detector and veto events. It removes any detector event in which an additional veto event is recorded within a certain time window, regardless of the position of the detector pixel and veto panel. A veto trigger is released when at least two coincidences at a specific scintillator panel occur within a time interval of $100\,ns$ and simultaneously the analog sum channel of the corresponding panel exceeds the adjusted threshold (section 3.10). The coincidence window can be determined from the background measurement by investigating the time correlation between detector and veto events. The resulting distinct coincidence peak is shown in figure 5.4. Both its base width of $3.0\,\mu s$ and its location approximately centered at a time interval of $-100\,ns$ define the coincidence window for the veto cut, meaning that all detector events are removed from the analysis when at least one veto event is detected $1.5\,\mu s$ before or after the corresponding detector event. The relative coincidence-peak position close to
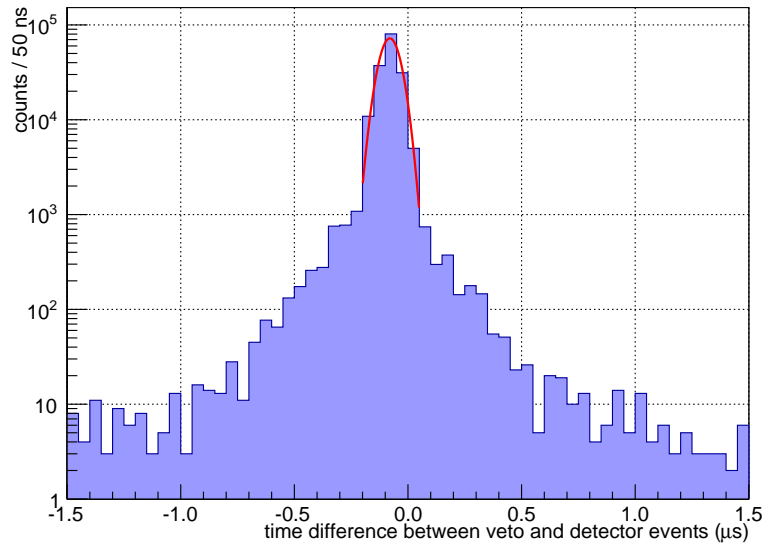
Figure 5.4: Time correlation between detector and veto events. This spectrum shows the time difference between detector and veto events. The base width and relative delay of the distinct coincidence peak define the coincidence window of the veto cut such that a detector event is removed when a veto event is detected within a time interval of $\pm 1.5\,\mu s$ relative to the detector event. The solid-red line indicates a Gaussian distribution fit to the region of the coincidence-peak amplitude. Both the resulting peak location at $-79.8(1)\,$ns and the FWHM of $105.6(3)\,$ns are consistent with the latency and timing resolution of the detector.

zero indicates that no obvious delays between detector and veto events exist, although the readout mechanisms of both subsystems differ from each other, with regard to analog and digital signal processing. In addition, there are no artifacts despite different cable lengths within the veto system.

5.2.3 Cut Background Spectra and Cut Efficiency

Figure 5.5 shows the resulting background spectra after the multi-pixel and veto cut at nominal magnetic field measured over 146 functional pixels and again linearly scaled by 148/146 to model a fully working detector. Both cuts eliminate the correlated events from the background spectrum so that the actual background rate decreases below the benchmark of 1 mcps/keV at energies above 20 keV which is close to the energy region of the 18.6-keV tritium endpoint. The definition and optimization of the associated region of interest for signal β-electrons is discussed in section 5.8.

Figure 5.6 illustrates the relative rate reductions

$$1 - \epsilon = \frac{r_{\text{raw}} - r_{\text{cut}}}{r_{\text{raw}}} \qquad \text{with} \qquad \epsilon = \frac{r_{\text{cut}}}{r_{\text{raw}}} \tag{5.2}$$

for both cuts, where ϵ denotes the individual cut efficiency, r_{cut} the cut detector rate, and r_{raw} the raw detector rate. Within the energy interval around the Landau peak for minimum-ionizing muons, the veto cut is more efficient than the multi-pixel cut, further underlining that the background in this region is primarily dominated by cosmic muons. The observed difference in the veto-cut efficiency between low and high energies is based on the plastic-scintillator efficiency across the entire energy region. The primary radiation detected by the panels are 100-keV to 5-MeV γ-rays caused by natural radiation and cosmic rays, fast neutrons, and charged particles of different energies, such as αs, βs, protons, and cosmic muons [Bic98]. Therefore, low-energy γ-rays have a small probability
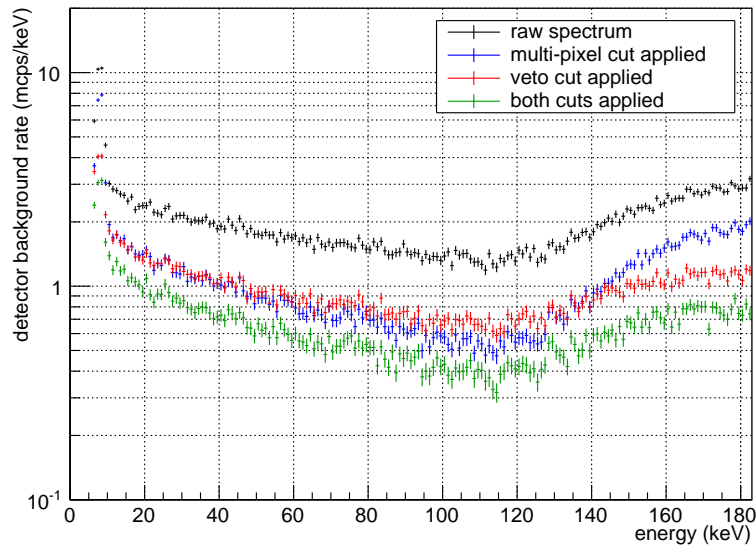
Figure 5.5: Background energy spectra after individual and combined cuts at nominal magnetic field. The spectra are scaled to a fully working detector. The raw spectrum (black) is shown in comparison to the spectra after applying the multi-pixel cut (blue), the veto cut (red), and both cuts (green). If the two cuts are applied, the number of correlated background events drops significantly. Statistical uncertainties given by limited run time are included.
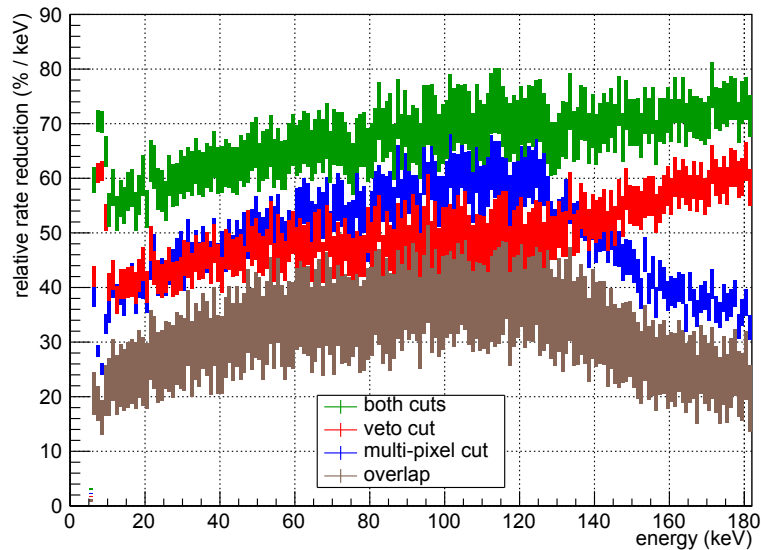
Figure 5.6: Relative rate reduction. The relative rate reductions (in %/keV) of the individual cuts are shown as a function of the visible energy. Statistical uncertainties are included. The total reduction after both cuts (green) rises slightly with increasing energies, while the veto cut (red) is more dominant at higher energies than the multi-pixel cut (blue). There is a certain correlation between both cuts indicated by the overlap (brown). Statistical uncertainties given by limited run time are included.
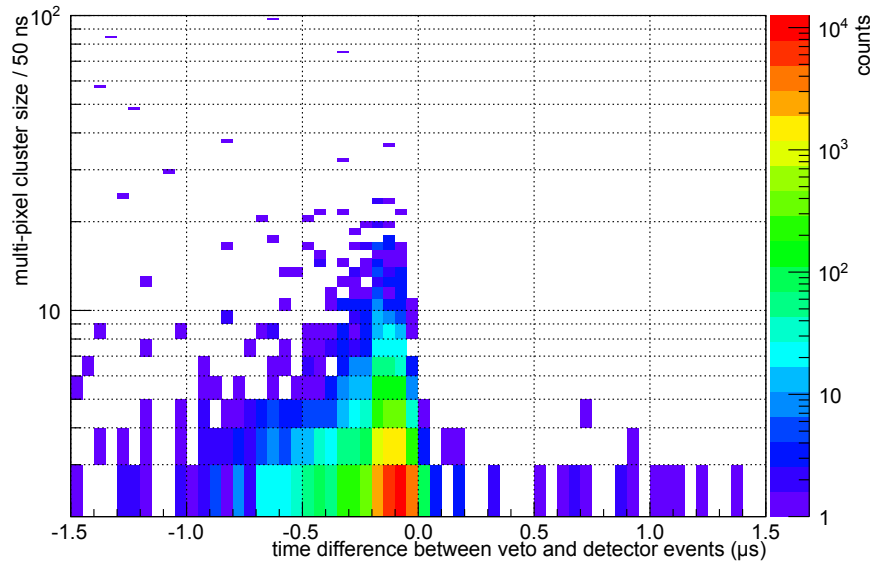
Figure 5.7: Correlation between multi-pixel cut and veto cut. The multi-pixel cluster size describes the multiplicity of events rejected by single multi-pixel cuts. It is shown as a function of the time difference between the veto trigger and the detector events. The hot spot of large multiplicities at the time of a veto trigger proves the correlation between both cuts. The two-event multi-pixel cut marks the dominant cut.

of being detected in the detector and the veto [Leb10]. However, they indirectly contribute to background by secondary emission of low-energy electrons originating from the inner surfaces of the surrounding materials. The actual efficiency of the individual plastic-scintillator panels and the entire veto system is not fully known, but the measured relative rate reduction of the applied veto cut indicates that it is less than the designed value of 90 %, since the Landau peak of minimum-ionizing muons still dominates in the high-energy region.

Both cuts have a significant amount of overlap which is defined by

$$\epsilon_{\text{overlap}} = \epsilon_{\text{multi-pixel cut}} + \epsilon_{\text{veto cut}} - \epsilon_{\text{both cuts}} \cdot \tag{5.3}$$

This overlap is expected since an incident particle which is tagged by the veto can produce multiple events on the detector at the same or at different pixels within a relatively short time interval either by multiple detection of the incident particle within the sensitive detector volume or by production of cascades of secondary particles. Consequently, these correlated events are rejected by both cuts. Again, a smaller overlap is visible for the Landau peak, as expected, while it is largest for the gamma continuum below it due to multi-Compton scattering. This specific correlation between multi-pixel cut and veto cut is illustrated further in figure 5.7 showing the multi-pixel cluster size in dependence of the time difference between a detector event and a veto event. There is a distinct occurrence of high-multiplicity events right at the time of a veto trigger, and a smaller number of multi-pixel hits observed further away from the associated veto time stamps. Both the overlap and the correlation of the two cuts allow a certain robustness against malfunctions and inefficiencies of the veto system.

It should be noted that the intrinsic detector background measured in this configuration can only give an upper limit and thus a worst-case scenario, as the gate valve between the main spectrometer and the detector system is closed. Its massive face forms the upstream end of the magnetic flux tube so that electrons liberated from its stainless-steel surface

by cosmic rays and natural environmental radiation are adiabatically transported to the detector along the magnetic field lines and create additional background events. The gate valve is located within a magnetic field (~ 0.6 T), is much smaller than the field of the detector magnet (3.6 T). The magnetic mirror effect limits the acceptance of isotropically emitted electrons to a maximum angle of 24.1°, according to equation (2.8). This additional source of secondary electrons emitted from the closed gate valve is discussed in more detail in section 5.7. Moreover, as the closed gate valve also has a direct line of sight to the detector, both γs and fluorescence light from the surface of the gate valve are directly transmitted to the detector where they produce an additional background continuum. The distance to the detector is approximately 1.1 m so that the resulting solid angle of 2.3° to the sensitive detector area is quite large. In principle, these additional background effects can be completely removed by installing an inner electrode to the existing custom-built beam pipe, which separates the main spectrometer from the detector. While the gate valve is opened, this electrode can be elevated to a negative potential to electrostatically shield background electrons originating in the main spectrometer. Despite its direct line of sight to the detector, radiation from the closed gate valve on the opposite side of the main spectrometer is only a minor issue, since the associated solid angle of less than 0.1° is quite small. Such an electrode is expected to be used for the next SDS commissioning period to allow a more precise measurement of the actual intrinsic detector background.

5.3 Passive Reduction Methods

The low-radioactivity construction materials used within the detector system were selected and radio-assayed very thoroughly before their installation. Individual components with critically important purities mounted close to the detector wafer were investigated in terms of their intrinsic radioactivity at the *Low Background Facility* of the *Lawrence Berkeley National Laboratory* [CS10]. Table 5.1 illustrates the results, indicating that some components generate considerably more γ-induced backgrounds than others. Passive background reduction is achieved by combining several methods to minimize the intrinsic background by surrounding materials.

- Sensitive parts of the vacuum chamber are externally surrounded by a cylindrical radiation shield consisting of 3-cm thick lead and 1.27-cm thick oxygen-free, high-conductivity copper (section 3.10) to block incident γ-background by an estimated factor of 20 [Leb10] [Ams14]. In this context, the existing suppression of radiation originating from the detector magnet is of special importance since the detector wafer is located within its warm bore.

Table 5.1: Measured activities for selected detector-system components. Radio-assay was performed by direct counting of released γs at the *Low Background Facility* of the *Lawrence Berkeley National Laboratory* [CS10]. The most dominant radioactivity originates from the glass feedthroughs of the detector flange which separates the detector wafer from the vacuum electronics. Values according to [Ams14].

component	^{238}U (Bq/kg)	^{232}Th (Bq/kg)	^{40}K (Bq/kg)
magnet coil	0.25 ± 0.20	0.20 ± 0.04	0.56 ± 0.28
magnet coil banding	10.0 ± 1.2	1.0 ± 0.3	< 0.6
preamplifier modules	3.85 ± 1.31	0.7 ± 0.3	< 2.2
conflat flange	< 0.004	< 0.004	< 0.013
pogo pins	0.86 ± 0.12	< 0.041	< 0.125
glass feedthrough	12.3 ± 1.2	3.66 ± 0.41	1125 ± 31

- The detector wafer is spatially separated from the preamplifier modules by a copper-shielded detector feedthrough flange (section 3.5) to suppress incident radiation from the electronic parts.

- Stainless-steel surfaces, like the detector feedthrough flange itself without its signal feedthroughs, are not shielded due to their low intrinsic radioactivity.

- The spring-loaded pogo pins cannot be completely shielded since they establish the connection between the detector wafer and the detector feedthrough flange. However, cylindrical donut-shaped copper sleeves were installed over the signal-carrying pogo pins to block off radiation arising from the individual glass feedthroughs to the preamplifier modules, see also figure 3.9.

According to the radio-assay results, the dominant component of radiation should originate from the glass seals in the detector feedthrough flange. The glass contains only about 1 ppm each of ^{238}U and ^{232}Th, but is relatively high in ^{40}K by 3.6(1) % in weight [Cen12]. ^{40}K is well-known for undergoing all types of β-decay [EFG62] with a long half life of 1.277×10^9 a. It can decay either to ^{40}Ca via β^--decay with a branching ratio of 89.28(18) % and a Q^--value of 1311.09(12) keV, or to ^{40}Ar via electron capture [β^+-decay] with a branching ratio of 10.72(12) % [< 0.001 %] and a Q^+-value of 1504.9(3) keV [FE04]. The detector wafer is relatively thin ($\sim 500\,\mu s$) and made of low-Z material ($Z = 14$) so that the released 1460.83-keV γs are a minor issue due to the associated small attenuation coefficients in silicon. However, in the presence of a magnetic field, the emitted electrons from the β^--decay to ^{40}Ca with an endpoint energy of 1311.09 keV are directly guided along the corresponding magnetic field lines from the seal to the associated contact side of the detector pixel. Due to their relatively high initial energy following a β-continuum, they easily pass through the TiN-made dead layer on the back side and produce a typical energy-loss spectrum. After scattering, these electrons will leave a specific amount of energy in the sensitive detector volume, leading to additional background in the region of interest, in principle independent of the dead-layer thickness. In order to shield these electrons, the above mentioned donut-shaped copper sleeves with 3.2 mm in height and 3.5 mm in diameter are installed over the signal pins, although a concomitant increase in detector capacitance is expected [Cen12].

In order to investigate the efficiency of the passive background reduction of the copper donuts, two sets of background measurements were performed without post-acceleration potential at nominal magnetic field. All 148 donuts were first installed (runs $\#3132 - \#3139$ and $\#3142 - \#3175$, 82 h) and then removed (runs $\#877 - \#893$, 64 h). However, the second set of measurements suffered from significant issues with the cooling system so that the detector wafer had to be operated above room temperature rather than at optimized conditions (section 4.1) as for the first set. In addition, 19 detector pixels were not functional by then and the veto was operated under different configurations in the second measurement set. Therefore, the analysis includes the same 129 pixels functional in both measurements and linearly scales the acquired background by a factor of 148/129 to model a fully working detector while the veto cut is completely excluded. Figure 5.8 shows the results including the raw background spectra and the spectra after application of the multi-pixel cut with a coincidence window of 1.5 μs. As expected, the raw spectrum using a warm detector suffers from a higher electronic noise threshold, caused by increased leakage currents and more thermal excitations within the sensitive detector volume. These effects result in additional electronic noise which dominates the low-energy background region. However, the noise events appear in significant bursts within relatively short time intervals so that the multi-pixel cut rejects these correlated events from the raw spectrum. Higher detector and electronics temperatures lead to increased baselines in the signal readout chain so that the possible full-scale deflection of the preamplifiers
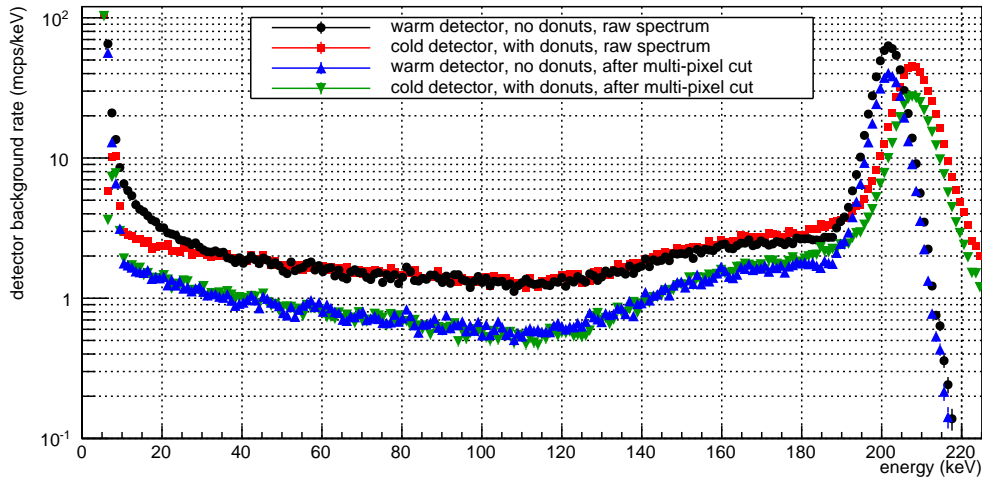
Figure 5.8: Recorded detector background at different configurations. Both the raw background spectra and the spectra after the multi-pixel cut are shown when using a cold [warm] detector with [without] installed copper donuts whose purpose is to shield β-radiation from the glass feedthroughs. The spectra are linearly scaled by a factor of 148/129 to a fully working detector. The veto cut is excluded due to different operation modes used for the veto system in both configurations. Statistical uncertainties given by limited run time are included.

decreases. Consequentially, when compared to a cooled detector, the overflow peak shifts to lower energies. After applying the multi-pixel cut to both raw spectra, they show similar trends. Therefore, the influence of a different operating temperature and presence of the copper donuts to the intrinsic detector background seems to be negligible. In the potential region of interest from 15.6 to 20.6 keV, the background rate before [after] cuts is 2.40(4) mcps/keV [1.43(3) mcps/keV] for the first measurement set using a cold detector and installed donuts, while it is 3.67(6) mcps/keV [1.45(4) mcps/keV] for the second measurement set using a warm detector and no donuts. Even for higher energies above ~ 30 keV where electronic noise is a minor issue, the raw and cut background rates are consistent to each other. There is no obvious improvement in the background rate after cuts, neither by a variation of the operating temperature nor by the presence of copper donuts.

Since a higher temperature causes more thermal noise in the detector volume and the copper donuts are expected to reduce β-electrons from the glass feedthroughs, the presence or absence of the veto cut should make no difference to the above stated conclusion as long as the relative and not the absolute rates between both measurement configurations are of interest. This also applies to the available pixels, since data from the same pixels were analyzed. The difference in the raw background spectra at low energies do not seem to originate from the installed or removed copper donuts, although the background rate for β-electrons from ^{40}K decay should also be noticeable at lower energies in the absence of the copper donuts. But there is no obvious reason for those β-induced events to be correlated and tagged by the multi-pixel cut so that the observed difference is much more likely to be caused by the detector temperature. However, one of the main disadvantages of operating the detector close to room temperature is its degrading performance in terms of a worsening energy resolution (section 4.1). Nevertheless, due to their continuous nature over a wide energy range, this should not affect the background spectra in the first approximation, as long as the temperature is within a moderate range so that contributions of leakage currents and thermal excitations are not dominant, and the vacuum electronics do not suffer from overheating.
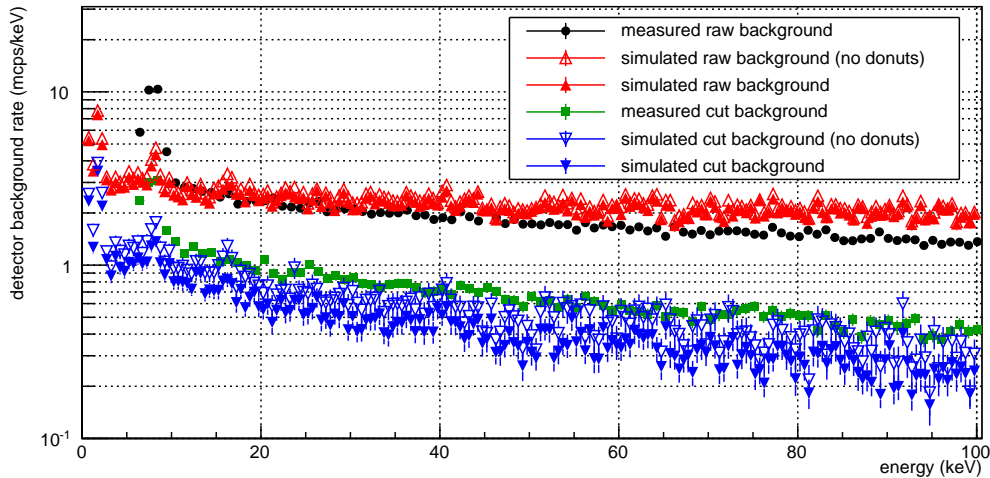
Figure 5.9: Detector-background simulations. The measured raw and cut background spectra are linearly scaled by a factor of 148/146 to a fully working detector to allow a direct comparison to the associated simulated background spectra. Simulations were performed by [Leb10]. Statistical uncertainties are included.

5.4 Comparison with Simulations

Extensive simulations were performed with *Geant4* [Ago03] [All06] to estimate the intrinsic detector background [Leb10]. The input parameters of the simulation include the radio-assay results shown in section 5.3 as well as data recorded by a series of background measurements taken with a ^{241}Am-calibrated, standalone germanium detector at the KATRIN experiment. This method allows to accurately simulate penetrating photons generated in radionuclide decays, in a region within as well as outside of the detector system. The copper donuts were variously excluded from and included in the simulations. In the latter case, full shielding of the β-radiation arising from the glass feedthroughs of the detector feedthrough flange is assumed. In addition, contributions from cosmic rays at sea level, consisting of muons, photons, nucleons, and neutrons, are included in the simulations. However, the actual electronic noise threshold of about $5 - 6\,\mathrm{keV}$, varying from channel to channel, and other detector-related effects were not considered in these simulations. Nevertheless, the region of interest for signal β-electrons is well separated from the electronic noise threshold, and detector effects thus play a negligible role due to the relatively low background rate. Moreover, in comparison to the performed intrinsic detector background measurements, there were minor differences regarding the setup parameters used in the simulations, such as the magnetic field at the detector wafer ($3.0\,\mathrm{T}$ instead of $3.3\,\mathrm{T}$), the FWHM energy resolution of the detector ($0.6\,\mathrm{keV}$ instead of $1.51(1)\,\mathrm{keV}$ for 18.6-keV electrons), the total efficiency of the veto system ($90\,\%$ instead of less than $90\,\%$), and the coincidence windows of the active background-reduction cuts. Nevertheless, the differences in the magnetic field and the energy resolution represent less critical issues since the magnetic field is at least in the same order of magnitude and the energy resolution should not influence a continuous background spectrum in the first approximation, as long as only an average background rate over a specific energy region is determined. Therefore, a comparison of the measured and the simulated raw background spectra seem reasonable while the simulated background spectrum after cuts may underestimate the actual, observed background rate after cuts due to more efficient background-reduction cuts applied in the simulations. Further details regarding the performed simulations on the detector background are given in [Leb10].

Figure 5.9 shows the comparison between background measurements and simulations. In the current region of interest between 15.6 and 20.6 keV around the tritium endpoint, the measured raw background rate is 2.40(4) mcps/keV while the simulated raw background rate is 2.62(5) mcps/keV [2.87(6) mcps/keV] with [without] mounted copper donuts. Obviously, the simulated raw background overestimates the measured raw background, especially at higher energies. A slight overestimate of the cosmic ray flux could be a potential reason, since the background generated by natural environmental radiation and intrinsic radioactivity was recorded beforehand to fine-tune the simulations. It is important to note that the flux of cosmic ray muons is subject to long-term and seasonal variations according to effects of the order of $\pm 10\%$, well in agreement with the observed discrepancy. The copper fluorescence peak is distinctly underestimated in the simulations, indicating that the radiation released from surrounding copper materials, like the post-acceleration electrode, the detector-wafer hold-down ring, and the shielding donuts, is more dominant in the actual setup. However, this peak is distinctly below the region of interest. In the above defined region of interest, the measured background rate after cuts is 1.02(3) mcps/keV while the simulated background rate after cuts is 0.70(3) mcps/keV [0.95(4) mcps/keV] with [without] mounted copper donuts. Obviously, the simulated background underestimates the measured background for identical cuts, most likely due to an overestimated veto efficiency in the simulations. The underestimation of the donut-shielding efficiency by a factor of ~ 1.5 is rather pronounced in view of the agreement of measured and simulated backgrounds after cuts in case of removed donuts, given the scatter in the spectra and including the statistical uncertainties. It seems that either (i) the donuts are less effective as expected in shielding the released β-electrons from the glass feedthroughs, or (ii) there is a detrimental effect due to the additional amount of copper material, which introduces radioactivity and which cancels out the improvement, or (iii) the expected β-radiation is overestimated in the simulations, and shielding actually would be a minor issue. The latter hypothesis is in excellent agreement with the experimental observation of a negligible passive background reduction by the copper donuts, as described in section 5.3. Nevertheless, the comparison indicates the presence of an unidentified background source of low rate of the order of ~ 0.3 mcps/keV which is actually not rejected from the raw background spectrum by neither the multi-pixel cut nor the veto cut.

5.5 Post Acceleration

Apart from the background-rejection cuts, a further active approach to reduce backgrounds in the region of interest is to apply a positive potential to the post-acceleration electrode in order to shift the electron signal to higher energies with a more favorable background rate. As shown in figures 5.1 and 5.5, the intrinsic detector background rate decreases exponentially with increasing energies in the interval of the low-energy tail between 15 and 110 keV. The background rate before [after] cuts around the tritium endpoint energy of 18.6 keV is 2.43(4) mcps/keV [1.03(6) mcps/keV] within a typical 5-keV wide region of interest between 15.6 and 20.6 keV, considering the moderate energy resolution of the detector. Shifting the region of interest by a designed maximum post-acceleration potential of 30 kV to an interval of 45.6 to 50.6 keV results in a significantly reduced background rate of 1.87(8) mcps/keV [0.66(5) mcps/keV], implying a relative background reduction of 23.0 % [35.9 %] compared to the configuration without post-acceleration. However, as stated in section 3.4, instabilities at voltages above 11.5 kV lead to discharges and high-current spikes so that the post-acceleration potential is currently limited to 11.0 kV. In that case, the raw [cut] background rate is 2.17(9) mcps/keV [0.87(5) mcps/keV] in the region of interest from 26.6 to 31.6 keV. This represents a relative background reduction of 10.7 % [15.5 %].
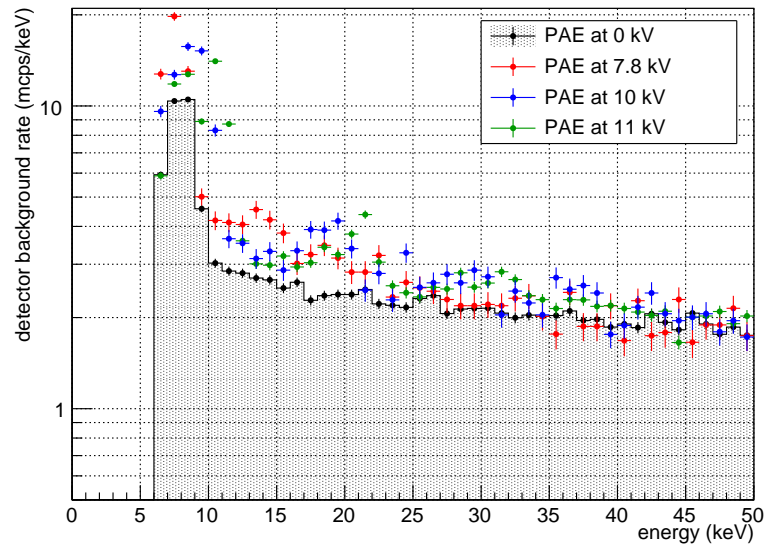
Figure 5.10: Raw detector background at different post-acceleration potentials.
The intrinsic detector background spectra are shown as a function of the applied post-acceleration potential. For comparison, the background spectrum with a grounded post-acceleration electrode is illustrated as well. Statistical uncertainties are included.
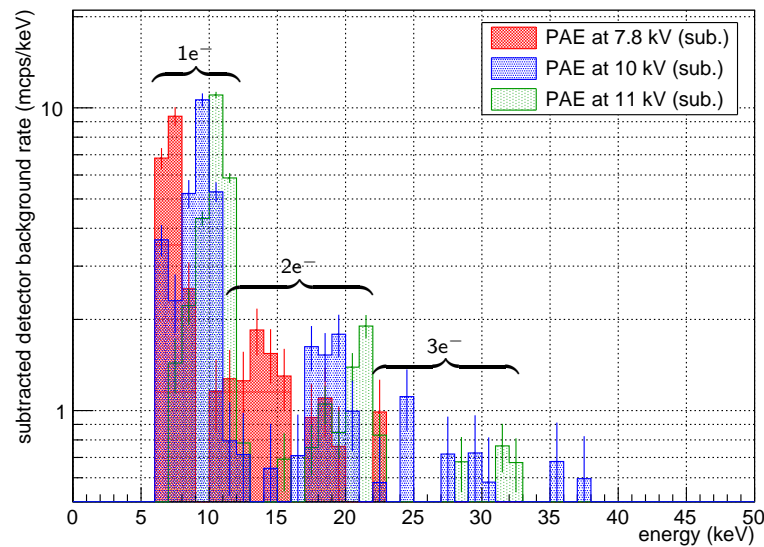
Figure 5.11: Additional detector background at different post-acceleration potentials. The additional background visible at the detector is calculated by subtracting the rather flat background spectrum without post-acceleration potential from the background spectrum with post-acceleration potential. A distinct multiple-peak structure becomes visible. Statistical uncertainties are included.

Table 5.2: Secondary-emission from closed gate valve. The recorded rate of the distinct single-electron peak, the less-dominant two-fold and triple-fold electron peak as well as the weighted rate are listed in dependence of the applied post-acceleration electrode. The secondary-electron rates are in good agreement with each other, although the electronic noise threshold slightly interferes with the single-electron peak at the 7.8-kV configuration. Statistical uncertainties are included.

post-acceleration	additional recorded rate (mcps)			
potential (kV)	1-fold peak	2-fold peak	3-fold peak	weighted sum
7.8	19.17 ± 1.09	7.29 ± 0.73	2.57 ± 0.63	41.48 ± 2.62
10.0	24.94 ± 1.08	6.50 ± 0.64	2.92 ± 0.56	48.59 ± 2.37
11.0	24.52 ± 0.56	5.57 ± 0.36	2.60 ± 0.33	43.46 ± 1.35

In order to investigate the influence of a specific post-acceleration potential to the intrinsic detector background, additional background measurements were performed at nominal magnetic field while the electrode was elevated to $7.8\,\mathrm{kV}$ (runs #3371 − #3377, 13 h), $10.0\,\mathrm{kV}$ (runs #3183 − #3190, 16 h), and $11.0\,\mathrm{kV}$ (runs #3392 − #3423, 64 h). The comparison of the resulting raw background spectra with the raw background spectrum without post-acceleration potential is shown in figure 5.10. Apart from the copper fluorescence peak at around $8\,\mathrm{keV}$, an additional multiple-peak structure appears in the associated energy spectrum at each voltage setting. The major peak is observed at exactly the energy which corresponds to the adjusted potential of the post-acceleration electrode while less dominant broad peaks are located at energies which match to multiples of the set post-acceleration voltage. In the case of the 7.8-kV setting, the major peak overlaps with the copper fluorescence peak. At $10\,\mathrm{kV}$ and especially at $11\,\mathrm{kV}$, the individual peaks are well resolved. Due to the low-energy tails of the separated peaks, the background rate between the individual peaks is slightly higher than without post-acceleration potential. With increasing energies, the spectra show similar trends of exponentially decreasing background rates while high-multiplicity peaks are undetectable.

Figure 5.11 features a more appropriate illustration where the background without post-acceleration potential is subtracted from the background with post-acceleration potential. This subtraction also includes the copper fluorescence peak, whose location is unaffected by the post-acceleration potential as expected. As a result, only the rate originating from the additional background component is shown. The major peak and the individual multiplicity peaks are distinctly separated from each other. This allows to calculate the additional rate as a function of the applied post-acceleration potential considering an appropriate weighting of the multiple-peaks. For this purpose, typical 5-keV wide regions of interest are set from -3 to $+2\,\mathrm{keV}$ around the positions of the associated peaks in which the rates are calculated and weighted by the number of multiplicity. The recorded rate of the additional background component is averaged over the three settings and amounts to $r_{\mathrm{rec}} = (44.51 \pm 2.12)\,\mathrm{mcps}$. Table 5.2 lists further results as a function of the adjusted post-acceleration potential. Assuming that low-energy secondary electrons, liberated from the inner stainless-steel surface of the closed gate valve by interactions with cosmic muons are boosted by the post-acceleration potential to generate this background, an actual emission rate is calculated to be [Ang05]

$$r_{\mathrm{em}} = \frac{r_{\mathrm{rec}}}{1 - \cos\theta_{\mathrm{max}}} \approx 0.5\,\mathrm{cps} \,, \tag{5.4}$$

taking into account the maximum acceptance angle of $\theta_{\mathrm{max}} \approx 24.1°$, as stated in section 5.2. Typically, these electrons are produced within the material, drift to the boundary layer, and tunnel into the vacuum with low energies well below $50\,\mathrm{eV}$ so that they cannot be detected

if the post-acceleration potential is lower than the electronic noise threshold of about 5 keV. Cascades of low-energy electrons generated simultaneously lead to the observed multiplicity peaks ($1e^-$, $2e^-$, $3e^-$, ...) since a bunch of electrons is adiabatically guided by the magnetic field to the same detector pixel where it is recorded within a specific time interval shorter than the 50-ns sampling rate of the DAQ system. Therefore, the individual electrons cannot be resolved in time. This results in a single electron event detected with a multiple energy of the post-acceleration potential. In the final KATRIN setup, the gate valve to the main spectrometer is opened so that the described additional low-energy background component is not an issue when applying a post-acceleration electrode.

5.6 Magnetic Field

A further active method to lower the background level can be achieved by increasing the magnetic field of the detector magnet in the range from 3.6 to 6.0 T. Consequently, the size of the sensitive 191-Tcm^2 flux tube imaged onto the wafer decreases, as the magnetic flux is a conserved quantity according to equation (2.6). This leads to a reduced imaged area at the detector wafer so that the effective background decreases due to a smaller number of pixels used for mapping. However, this comes at the cost of a reduced spatial resolution of the detector in imaging the radial distribution of events in the main-spectrometer analyzing plane. Accordingly, a specific number of outer detector-pixel rings will then map volumes outside the sensitive flux tube or even look at inner surfaces of the beam tube, so that they have to be excluded for neutrino-mass measurements. At nominal magnetic fields, 6.0 T at the pinch magnet and 3.6 T at the detector magnet, the outermost detector-pixel ring covers a magnetic flux-tube volume ranging from 191 to 210 Tcm^2, representing a certain *buffer zone* between the sensitive flux tube and the beam tube, while the inner rings image the relevant 191-Tcm^2 magnetic flux tube. Due to the intrinsic nature of the detector background, it should not be affected by the strength of the magnetic field in the first approximation. If it is not, a magnetic-field dependent background component contributes to the intrinsic detector background. In the long-term neutrino-mass measurements, the field of the detector magnet will be set to a value such that all detector rings map the sensitive magnetic flux tube. At this point in time, it is difficult to estimate the exact value of the transported flux, but the flexibility offered by tuning of the provided field will allow to adapt to any value.

In order to investigate the influence of a specific magnetic-field strength at the detector wafer on the intrinsic detector background, additional background measurements were performed beyond the nominal magnetic-field setting values, and with the post-acceleration electrode being kept at ground potential. For this purpose, the pinch magnet was energized to its fixed nominal field strength of 6.0 T while the detector magnet was operated at 110 % ($\#3497 - \#3506$, 20 h) and at 130 % ($\#3612 - \#3619$, 16 h) of its nominal field setting. In these configurations, the entire detector covers a magnetic flux tube of 231 Tcm^2 and 273 Tcm^2, respectively. The effective wafer area on which the 210-Tcm^2 flux tube is imaged, including the stated buffer volume to the inner beam-tube surface, is reduced to an area of 90.9 % and 76.9 %, respectively, relative to its original size of 63.6 cm^2. In the latter case, the outermost and the three subsequent detector-pixel rings cover non-transported volumes of the flux tube. A comparison of the resulting raw background spectra at nominal and increased magnetic fields is illustrated in figure 5.12. The distinct peak around 8 keV marks the energy-smeared copper fluorescence lines. In figure 5.12 (left), the background spectra summed over all 148 pixels are compared. It is evident that the increasing field strength does not influence the total background rate, as expected for a spectrum dominated by X-rays and florescence lines. In figure 5.12 (right), the effective background rate for a fixed mapped flux tube of 210 Tcm^2 is shown. Due to the reduced effective
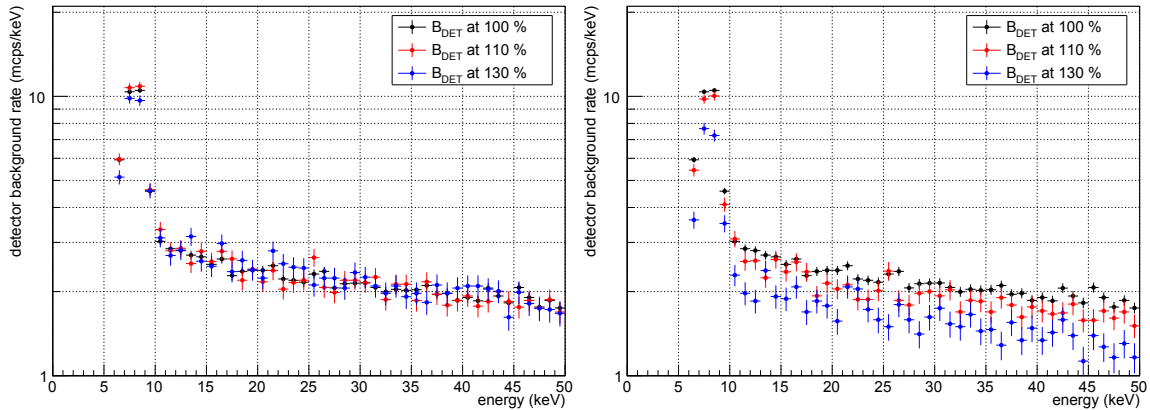
Figure 5.12: Detector background at different magnetic-field settings. The raw detector background spectra are shown for different detector-magnet fields B_{DET} both for the entire wafer (**left**) and for the shrinking part of the effective wafer area covering a 210-Tcm^2 flux (**right**). The nominal field generated by the detector magnet is $B_{\mathrm{DET}} = 3.6\,\mathrm{T}$. Statistical uncertainties are included.

detector area, it decreases with increasing magnetic field. In a possible region of interest between 15.6 and 20.6 keV, the rate drops from 2.43(4) mcps/keV (100 % of nominal detector-magnet field) to 2.27(8) mcps/keV (110 %) and 1.86(8) mcps/keV (130 %), respectively. This represents a reduction of the effective background rate in the 210-Tcm^2 area to $(93.4 \pm 3.6)\,\%$ and $(76.5 \pm 3.5)\,\%$, respectively. Both results are consistent with the expectations, considering the statistical uncertainties. These observations prove the intrinsic nature of the detector background continuum. It should be noted, however, that the background rate is only one criterion when optimizing the magnetic field among others, such as the mapping of radial inhomogeneities in the analyzing plane and the backscattering probability for incident electrons.

5.7 Secondary-Electron Emission

As outlined in section 5.5, the post-acceleration electrode on the one hand boosts low-energy secondary electrons emitted from the inner surface of the closed gate valve to a level above the electronic noise threshold. On the other hand, the field provided by the detector magnet defines the size of the magnetic flux tube imaged onto the detector, as explained in section 5.6. The combination of both methods allows to study the secondary emission rate from the closed gate valve observed by the detector. For this purpose, specific background measurements were performed while the post-acceleration electrode was elevated to a fixed potential of 11 kV and the pinch magnet was energized to a fixed magnetic-field strength of 6.0 T. The detector magnet was again operated at 100 % (runs #3392 − #3423, 64 h), at 110 % (runs #3497 − #3506, 20 h) and at 130 % (runs #3628 − #3635, 16 h) of its nominal field setting. The corresponding shape of the magnetic flux tube for the full wafer surface area is visualized for each configuration in figure 5.13. With increasing magnetic field, the size of the surface area of the closed gate valve mapped onto the entire detector increases. Accordingly, a higher rate of boosted secondary electrons is expected.

The resulting raw background spectra for different magnetic fields are shown in figure 5.14. Analogous to section 5.6, the copper fluorescence peak at around 8 keV and the secondary-electron multiple-peak structure dominate in the associated energy spectra, whereas the two-fold ($2e^-$) and triple-fold ($3e^-$) multiple electron peaks are less pronounced than the single electron peak. While the rate around the fluorescence peak remains unaffected by magnetic-field adjustments as expected, a higher rate of measured secondary electrons is observed with stronger magnetic field, as a result of the increased gate-valve area imaged
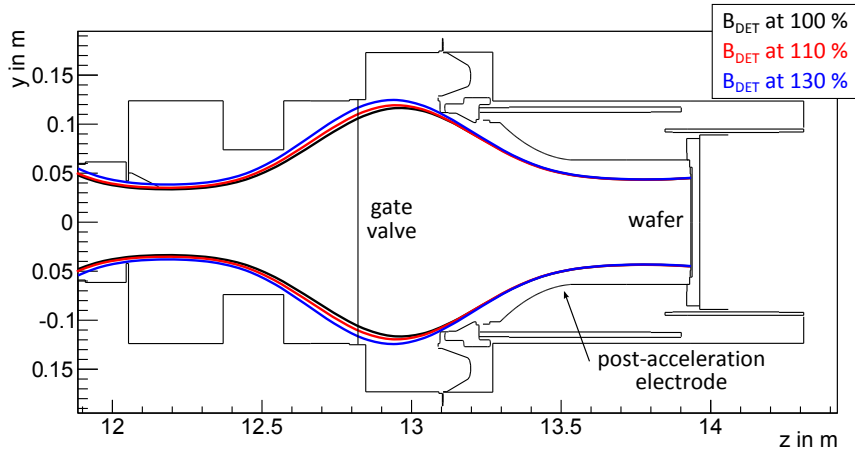
Figure 5.13: Magnetic flux tube within the detector system for different magnetic-field settings. The size of the surface area of the closed gate valve imaged onto the fixed full wafer area depends on the field strength B_{DET} provided by detector magnet. Applying a post-acceleration potential allows to boost emitted electrons from the gate valve above the electronic noise threshold and to study the emission rate.

onto the wafer. This is clearly recognizable in figure 5.15 where the background spectra for different magnetic fields without post-acceleration potential (see section 5.6) are subtracted from the associated background spectra with a post-acceleration potential of 11 kV. The single electron peak of the 130-% setting is the most distinct peak. The individual multiple electron peaks are clearly separated from each other so that the measured secondary-electron rate can be analyzed as a function of the magnetic-field setting by appropriately weighting the multiple peaks, according to the method described in section 5.5. Since the magnetic field at the detector magnet (B_{DET}), detector wafer (B_{WAF}), and gate valve (B_{GATE}) are well-known by adjustments and calculations using *Kassiopeia*, the magnetic flux Φ_{WAF} mapped on the entire detector wafer and the imaged circular surface area of the gate valve given by the radius r_{GATE} can be calculated according to (2.6). This allows to transform the observed rate r_{rec} of electrons reaching the detector to the actual rate r_{em} of emitted low-energy secondary electrons using equation (5.4). Table 5.3 lists the corresponding results. As expected, the observed rate increases for a stronger magnetic field due to a larger imaged surface area, while the normalized secondary-emission rate per unit area keeps constant. The average emission rate of low-energy secondary electrons emitted from the closed gate valve is $1.40(2)\,\mathrm{mcps/cm^2}$. This is in moderate agreement with the emission rate of $0.72(1)\,\mathrm{mcps/cm^2}$ from the closed stainless-steel gate valve on the upstream side of the main spectrometer [Lei14], which was determined during the first SDS commissioning measurements [Bar14] [Thu14]. However, due to most-likely different surface conditions of the two gate valves, an adequate comparison is quite difficult. The character of the emitter surface is of primary importance for the emission probability for secondary electrons [Bun64] [Nis94].

5.8 Figure of Demerit

The optimum detector performance requires a careful balance of several detector-related parameters. A major role is played by the definition of the region of interest describing the acceptance window for β-decay electrons in the energy spectrum. Signal electrons produce a distinct peak in the energy spectrum while the intrinsic detector background forms a characteristic continuum. In principle, three quantities from the detector response affect the position and the width of an optimized region of interest:

- **Detection efficiency:** A more efficient detector will record more signal electrons
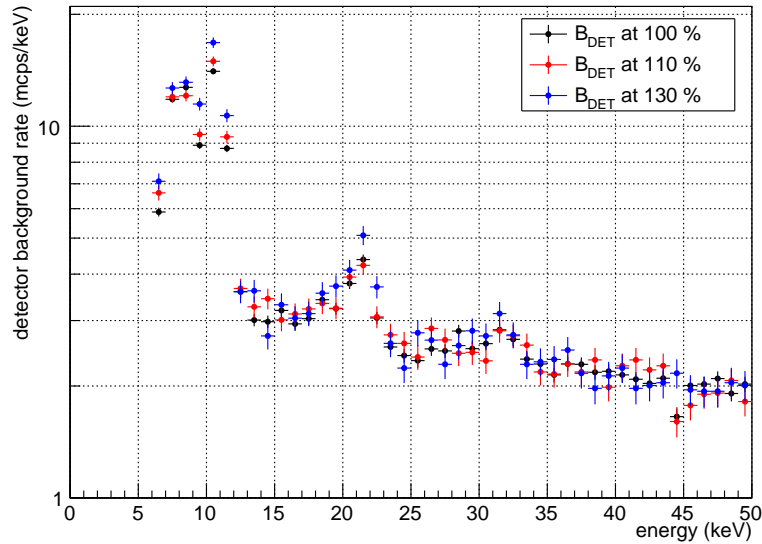
Figure 5.14: Raw detector background for different magnetic-field settings observed with a 11-kV post-acceleration potential. The raw detector background spectra are shown as a function of the detector-magnetic field B_{DET} with applied post-acceleration potential of $11\,\mathrm{kV}$. Statistical uncertainties are included.
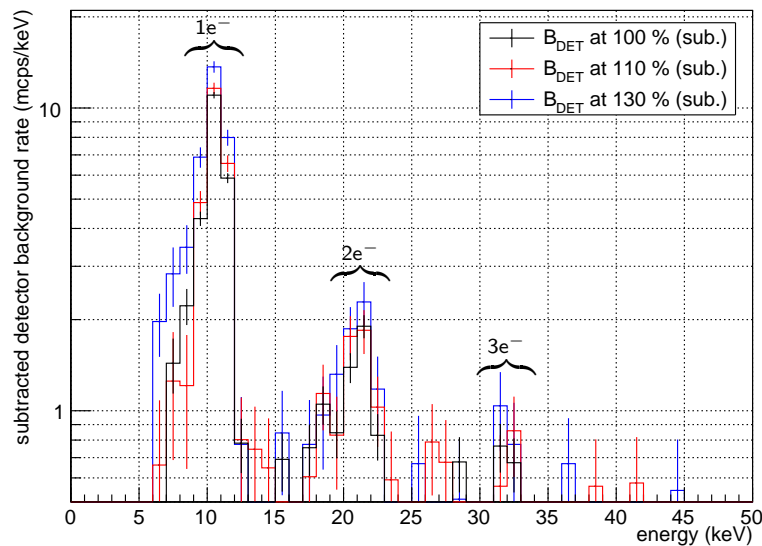
Figure 5.15: Secondary-electron emission background at different magnetic-field settings with a 11-kV post-acceleration potential. The additional background caused by low-energy secondary electrons emitted from the closed gate valve is calculated by subtracting the corresponding background spectrum with zero post-acceleration potential from the background with 11-kV post-acceleration potential for each magnetic-field configuration. The energy spectra correspond to the recorded background rate which is different from the actual emitted secondary-electron rate.

Table 5.3: Secondary-electron emission results. The table lists the calculated rate r_{em} of emitted low-energy secondary electrons per unit area in units of mcps/cm^2 as a function of the detector-magnetic field B_{DET}, the approximate magnetic field B_{WAF} at the detector wafer, the corresponding flux Φ_{WAF} through the detector wafer, the corresponding approximate magnetic field B_{GATE} at the gate valve, the radius r_{GATE} of the surface area of the closed gate valve imaged onto the wafer, and the recorded electron rate r_{rec}. Magnetic-field simulations were performed with *Kassiopeia*.

B_{DET} (T)	B_{WAF} (T)	Φ_{WAF} (Tcm^2)	B_{GATE} (T)	r_{GATE} (cm)	r_{rec} (mcps)	r_{em} (mcps/cm^2)
3.6 (100 %)	3.3	210	0.6	10.5	43.46 ± 1.35	1.42 ± 0.04
4.0 (110 %)	3.6	231	0.6	11.0	45.95 ± 2.54	1.37 ± 0.08
4.7 (130 %)	4.3	273	0.6	12.0	56.29 ± 2.91	1.42 ± 0.07

and more background events, even in case of X-ray photons and fluorescence lines being the dominant intrinsic detector background.

- **Energy resolution:** A detector with a degraded energy resolution requires a broader region of interest to detect signals with high efficiency.

- **Detector background:** A detector with a broad region of interest suffers from a highly intrinsic detector background rate.

Obviously, these parameters influence each other. The detector-related *figure of demerit* combines and balances these parameters with their drawbacks and benefits in a single quantity. It is discussed in the following in more detail.

The observable of the KATRIN neutrino-mass measurement is given by the square of the effective mass of the electron antineutrino m_ν^2. Its statistical uncertainty for a specific region of interest with a lower bound E_L and an upper bound E_U is defined by [Ott94] [Ang05]

$$\sigma_{\mathrm{stat}}(m_\nu^2) = \frac{k}{r^{2/3}t^{1/2}} \cdot b(E_L, E_U) \; , \tag{5.5}$$

where $k = (16/27)^{1/6}$ is a constant, r is the normalized count rate of tritium β-decay electrons analyzed by the main spectrometer and subsequently counted by the detector given in cps/eV^3, t is the effective measurement time in s, and $b(E_L, E_U)$ is the total background rate within the region of interest given in cps. However, this relation is idealized since it assumes that both the background and the endpoint energy are known independently with perfect accuracy [Leb06] [Doe07].

The total background rate b is the sum of the main-spectrometer related background b_{ms}, assumed to be constant in energy for small variations of the retarding potential with the design goal of 10 mcps [Ang05], and the integrated detector background $b_{\mathrm{det}}(E_L, E_U)$, leading to

$$\sigma_{\mathrm{stat}}(m_\nu^2) = \frac{k}{r^{2/3}t^{1/2}} \cdot (b_{\mathrm{ms}} + b_{\mathrm{det}}(E_L, E_U)) \; . \tag{5.6}$$

The total number of recorded signal electrons, given by r, and measured background spectrometer-related events, given by b_{ms}, is reduced by a factor $f(E_L, E_U)$ due to the limited energy resolution and detection efficiency of the detector. This factor defines the fraction of the corresponding recorded spectrum $s(E)$ within the region of interest:

$$f(E_L, E_U) = \int_{E_L}^{E_U} s(E)\mathrm{d}E \; . \tag{5.7}$$

It equals to the areas under the signal and the background spectrum between the boundaries E_L and E_U. This leads to

$$\sigma_{\text{stat}}(m_\nu^2) = \frac{k}{(f(E_L, E_U)r)^{2/3}t^{1/2}} \cdot (f(E_L, E_U)b_{\text{ms}} + b_{\text{det}}(E_L, E_U)) = \frac{kb_{\text{ms}}}{r^{2/3}t^{1/2}} \cdot F(E_L, E_U) \tag{5.8}$$

with the figure of demerit

$$F(E_L, E_U) = \frac{\left(f(E_L, E_U) + \frac{b_{\text{det}}(E_L, E_U)}{b_{\text{ms}}}\right)^{1/6}}{f(E_L, E_U)^{2/3}} \geq 1 \ . \tag{5.9}$$

The signal spectrum has to be normalized to an area of unity since the count rate r is given in normalized units. As for the total statistical uncertainty, equation (5.8) allows to separate the sources from experiment-related parameters, described by the constant prefactor, and detector-related quantities, described by the figure of demerit (5.9). Since the statistical uncertainty scales linearly with the figure of demerit ($\sigma_{\text{stat}}(m_\nu^2) \sim F$), it directly influences the neutrino-mass sensitivity according to relation (2.15). For an optimum detector performance, this figure needs to be minimized ($F \to 1$ is better) in order to reduce the total statistical uncertainty, meaning that the tradeoff between f ($f \to 1$ is better) and b_{det} ($b_{\text{det}} \to 0$ is better) has to be balanced by varying the region-of-interest boundaries. This fact allows to determine the optimum position and width of the region of interest, described by the characteristic energies E_L and E_U. Figure 5.16 illustrates the corresponding process:

- A narrow region of interest decreases f and b_{det} leading to a large F.

- A broad region of interest increases f and b_{det} leading to a large F.

- An optimum region of interest results in a balanced tradeoff between f and b_{det} leading to a minimized F.

An ideal detector has a figure of demerit of $F = 1$ since $E_L = 0$, $E_U \to \infty$, $f = 1$ and $b_{\text{det}} = 0$, independently of the spectrometer-related background b_{ms}.

The actual detector-related figure of demerit can be determined by analyzing background measurements and photoelectron-source calibrations at 18.6 keV for nominal magnetic fields, 6.0 T at the pinch magnet and 3.6 T at the detector magnet, as a function of the applied post-acceleration potential with 0 kV, 7.8 kV, 10 kV, and 11 kV. This set of configurations is similar to the settings to be used for the later neutrino-mass measurements. In a first approach, the global raw and cut background spectra are again linearly scaled by a factor of 148/146 to model a fully functional detector while the global photoelectron-source spectra at the corresponding post-acceleration potential are normalized to an area of 1. The main-spectrometer related background is assumed to be constant with $b_{\text{ms}} = 10$ mcps across the entire detector. The characteristic detector quantities of the global minimized figure of demerit can be determined according to equation (5.9) by varying the lower and upper limit of the global region of interest. In a second approach, the individual pixels are treated as single detectors, so that the individual raw and cut background spectra and the individual normalized photoelectron-source spectra are investigated pixel-by-pixel to determine the figure of demerit for each pixel. In that case, the main-spectrometer background is assumed to be homogeneously distributed across the detector with a constant background of $b_{\text{ms}} = 10/148$ mcps at a single pixel. This is a simplifying assumption, as it will be discussed in the chapters 6 and 7. The pixel-by-pixel investigation requires a variation of the lower and upper bounds of the individual regions of interest. Both methods use the photoelectron source at a fixed potential of -18.6 kV to emulate the signal electrons from the tritium source and the main spectrometer. However, during neutrino-mass measurements, the retarding potential will be varied by several tens of eV around
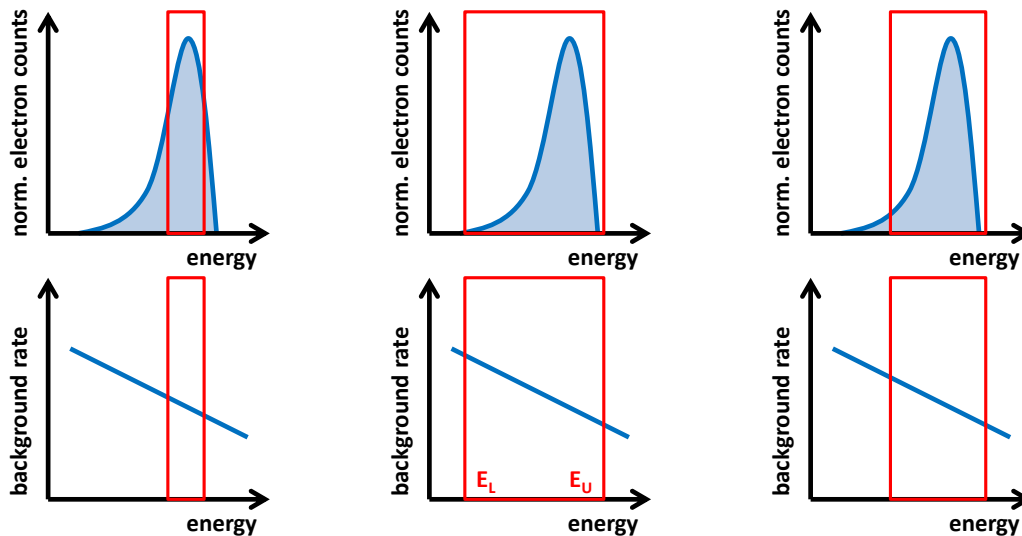
Figure 5.16: Schematic illustration of region-of-interest optimization. The photoelectron spectra (**top row**) at a specific incident energy are normalized to an equal area of 1 while the background spectra (**bottom row**) with their continuum characteristics are given in mcps/keV. Each red-shaded energy interval represents a potential region of interest given by a lower (E_L) and an upper (E_U) energy bound. **Left column: Narrow region of interest.** The fraction f of signal electrons in the acceptance window is small, leading to a large figure of demerit F, although the intrinsic detector background rate b_det is small. **Middle column: Broad region of interest.** b_det is large, leading to a large F, although f is large. **Right column: Optimized region of interest.** In that case, signal and background are balanced such that f and b_det are optimized, resulting in a minimum figure of demerit F_min.

the endpoint energy of tritium. Since the main spectrometer operates as an integrating high-pass filter, the analyzed signal electrons passing the spectrometer will have slightly different energies between the applied retarding potential and the tritium endpoint energy. Nevertheless, compared to the moderate energy resolution of the detector, these variations and differences are small and represent minor issues so that the performed emulation by the photoelectron source seems reasonable.

As for the measurements without post-acceleration potential, figures 5.17 and 5.18 show the corresponding global photoelectron-source and background spectra and the associated minimization curves for the global figure of demerit as a function of the width of the region of interest, including the optimized regions of interest before and after the applications of the veto and multi-pixel cut. In that case, the minimum figure of demerit is 1.195(2) [1.119(2)] for the raw [cut] background while the width of the region of interest is 4.0(1) keV [5.5(1) keV] located between 15.9(1) [14.5(1)] and 19.9(1) keV [20.0(1) keV], the total background rate within the region of interest is 9.88(18) mcps [5.86(14) mcps], and the fraction efficiency of the spectra is 0.897(1) [0.939(1)]. Both background-reduction cuts allow to use a broader acceptance window due to reduced backgrounds compared to the raw background spectrum, leading to an increased efficiency fraction. The stated values for the minimum figure of demerit meet the preliminary commissioning goal of $F_\mathrm{min} < 1.2$ which is motivated by a maximum-allowed enhancement of the total statistical uncertainty for the neutrino-mass measurement of 20 % based on detector-related effects. The final operational goal for the detector is $F_\mathrm{min} < 1.1$ [Ams14].

Figure 5.19 illustrates the minimum figure of demerit within the optimized region of interest for each pixel, using the individual raw and cut background spectrum and the individual detector response to 18.6-keV photoelectrons of single pixels without applied post-acceleration potential. The statistical uncertainties are relatively large due to limited statistics of the intrinsic detector background rate for single pixels. The observed scatter
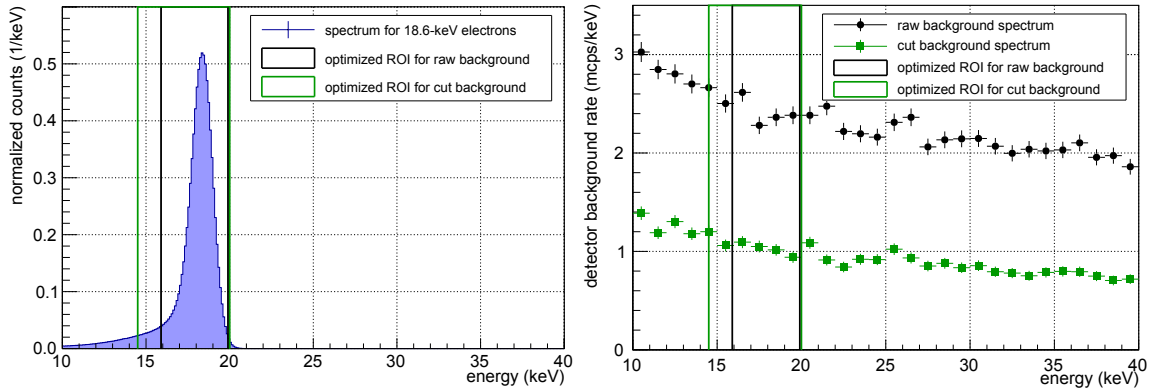
Figure 5.17: Optimized region of interest for raw and cut intrinsic detector background. The 18.6-keV photoelectron spectrum (**left**) and the intrinsic detector background spectrum (**right**) are shown. The optimized acceptance windows using the principle of the figure of demerit for the raw (black-colored boundaries) and the cut (green-colored boundaries) background are included. The signal spectrum is normalized to an area of 1 while the background spectrum is linearly scaled by a factor of 148/146 to a fully working detector. The optimized region of interest spans from 15.9(1) to 19.9(1) keV for the raw background and from 14.5(1) to 20.0(1) keV for the cut background. Statistical uncertainties are included.
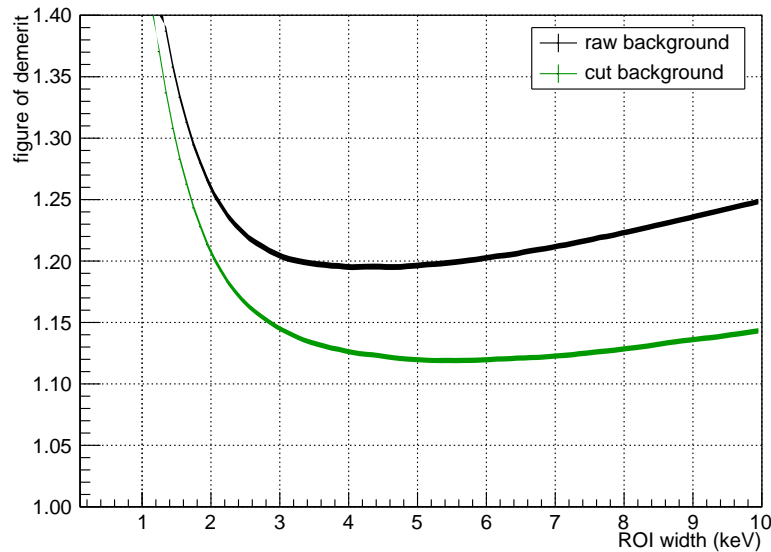
Figure 5.18: Minimization curves for figure of demerit. The minimum figure of demerit is $F_{\min} = 1.195(2)$ with an optimized width of $(E_U - E_L) = 4 \, \text{keV}$ for the region of interest using the raw background, and $F_{\min} = 1.119(2)$ with $(E_U - E_L) = 5.5 \, \text{keV}$ using the cut background. Statistical error bands are included.
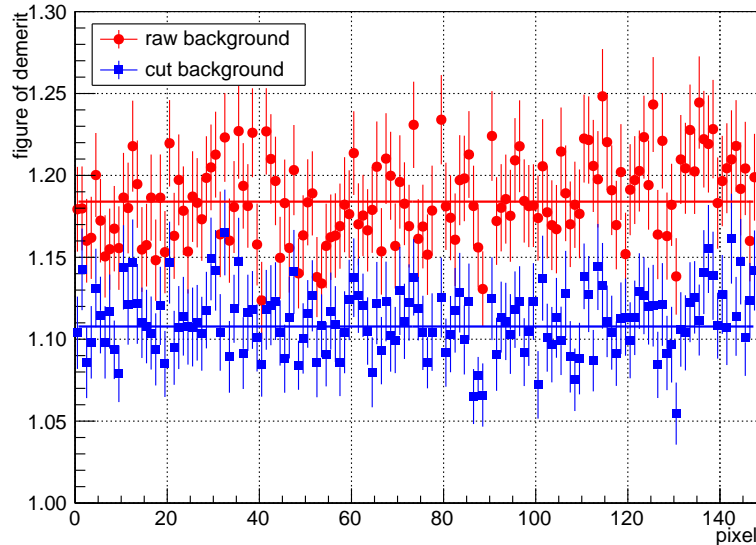
Figure 5.19: Minimum figure of demerit for each pixel. The minimum figure of demerit for each pixel is shown using the individual raw (red) and the cut (blue) background and the individual detector response to 18.6-keV photoelectrons of the associated pixel. The horizontal solid lines indicate the average minimum figure of demerit across all functional pixels.

of the figures between individual pixels can be explained by the pixel-by-pixel spread in the energy resolution, as discussed in section 4.2, which significantly affects the minimization of the figure of demerit. A similar trend is visible for the figure of demerit: It slightly worsens toward outer detector-pixel rings as the corresponding energy resolution degrades. The average minimum figure of demerit across all functional pixels is 1.184(2) [1.108(2)] for the raw [cut] background which is consistent with the results from the global analysis.

In addition, both approaches can be compared by investigating the intrinsic detector background rate for each pixel within globally and individually optimized regions of interest. While the second approach takes into account the energy resolution and the background rate of single channels, the first method averages the energy spectra over all pixels with the same region of interest. The comparison is illustrated in figure 5.20. The average raw background rate is 0.063(1) mcps per pixel using global optimization with a global region of interest between 15.9(1) and 19.9(1) keV while it is reduced to 0.051(1) mcps per pixel in the case of individual optimization. As for the cut background rate, a value of 0.035(1) mcps per pixel is achieved when applying global optimization in an acceptance window from 14.5(1) to 20.0(1) keV, and 0.024(1) mcps per pixel performing individual optimization. Therefore, both the average raw and average cut background rates can be significantly reduced by treating each pixel as single detector during the minimization of the figure of demerit. However, as stated above, the drawback of this pixel-by-pixel approach is the demand of increased statistics, especially in the intrinsic detector background spectrum. Otherwise, the results suffer from large statistical uncertainties.

The minimization curves of the figure of demerit yield trends that are relatively flat for broad regions of interest in contrast to narrow acceptance windows, especially in the case of the cut background. This fact is based on the rather weak influence of the intrinsic detector background rate on the statistical uncertainty, approximately given by $\sim b_{\mathrm{det}}^{1/6}$ according to equations (5.8) and (5.9). Therefore, it seems reasonable to select a relatively broad region of interest rather than a narrow acceptance window in order to achieve a high efficiency and to counteract possible fluctuations or instabilities in the energy resolution,
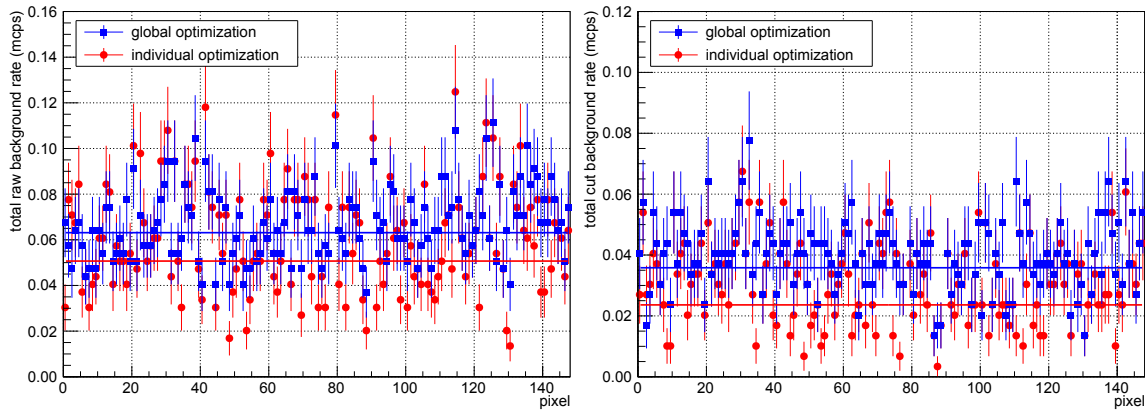
Figure 5.20: Intrinsic detector background in the region of interest for each pixel.
The region of interest is optimized for 18.6-keV photoelectrons. The global optimization
(blue) uses the optimized region of interest from the global detector response of the entire
wafer while the individual optimization (red) uses the optimized regions of interest from the
individual detector response of each associated pixel. The horizontal solid lines indicate the
resulting average background rate across all functional pixels. Individual optimization results
in an improved balance between signal and background for each pixel compared to global op-
timization. This leads to a reduced total detector background rate in the region of interest.
Statistical uncertainties are included. **Left: Raw background.** The raw background rate in
the acceptance window for each pixel is shown, considering global and individual optimization
for the region of interest. **Right: Cut background.** The cut background rate in the accep-
tance window for each pixel is shown, considering global and individual optimizations for the
region of interest.

electron peak position, or detector calibration. However, this comes at the expense of an
increased intrinsic detector background in the region of interest. In this context, the lower
energy bound has to be set carefully in order not to cut off parts of the low-energy tail of
the electron peak. In addition, a broader region of interest considers the observed scatter
in the individual energy resolution and background rate of each channel.

As stated above, the post-acceleration electrode can be used to boost signal electrons
into an energy window with a more favorable background rate. As discussed in section
5.5, different potentials were used to study the resulting background spectra. However,
low-energy secondary electrons are continuously emitted from the inner surface of the
closed gate valve, most likely by interactions with cosmic muons, and are boosted by the
post-acceleration potential as well, so that they contribute significantly to the measured
background and have to be considered when selecting possible positions and widths for the
acceptance window. Due to the slightly increased background rate and the minor improve-
ment in energy resolution (section 4.2) at higher post-acceleration potentials, the minimum
figure of demerit is expected to be similar or even higher than observed in the configura-
tion without post-acceleration potential. Table 5.4 summarizes the associated results in
comparison to the measurements at 0 kV. As expected, both for the raw and the cut back-
ground spectrum, the broadest region of interest and the lowest average background rate
are achieved without post-acceleration potential, due to the absence of boosted low-energy
secondary electrons from the closed gate valve. Each configuration reaches a minimum
figure of demerit of $F_{\min} < 1.2$ while it is further reduced to about $F_{\min} \approx 1.12$ when both
background-reduction cuts are applied. In the latter case, the fraction efficiency is $f > 0.9$.
A post-acceleration potential of 7.8 kV seems a reasonable setting since the signal-electron
peak at 26.4 keV (18.6 + 7.8 keV) is distinctly separated from the less dominant triple-fold
and four-fold multiple electron peaks arising from the boosted background electrons at
23.4 and 31.2 keV (3×7.8 and 4×7.8 keV), respectively. By contrast, at the 10.0-kV
setting, the signal-electron peak at 28.6 keV overlaps partly with the triple-fold peak at

Table 5.4: Figure-of-demerit results. The calculated minimum figure of demerit $F_{\min}$ is shown in dependence of the background and the potential of the post-acceleration electrode (PAE), using global optimization. In addition, the optimized position of the region of interest (ROI) and its width ($E_U - E_L$) are listed as well as the background rate $b_{\det}$ and the fraction f of signal electrons in the acceptance window.

back-ground	PAE (kV)	ROI (keV)	$E_U - E_L$ (keV)	$F_{\min}$	$b_{\det}$ (mcps/keV)	f
raw	0.0	$15.9(1) - 19.9(1)$	4.0	1.195(2)	2.47(04)	0.897(1)
	7.8	$24.4(1) - 27.7(1)$	3.3	1.184(5)	2.50(12)	0.887(1)
	10.0	$26.8(1) - 30.0(1)$	3.2	1.191(5)	2.77(12)	0.888(1)
	11.0	$27.6(1) - 30.9(1)$	3.3	1.187(3)	2.68(06)	0.893(1)
cut	0.0	$14.5(1) - 20.0(1)$	5.5	1.119(2)	1.07(03)	0.939(1)
	7.8	$23.0(1) - 28.0(1)$	5.0	1.120(5)	1.13(07)	0.934(1)
	10.0	$25.8(1) - 30.2(1)$	4.4	1.124(4)	1.24(07)	0.924(1)
	11.0	$26.9(1) - 31.1(1)$	4.2	1.123(2)	1.23(04)	0.920(1)

30.0 keV due to the moderate energy resolution of the detector, thus leading to a higher average background rate. An optimum post-acceleration potential for intrinsic detector background investigation with a closed gate valve would be at 12.4 kV, since the resulting signal-electron peak at 31 keV would be well separated by 6.2 keV from the two-fold and triple-fold electron peaks at 24.8 and 37.2 keV, respectively. However, their non-negligible low-energy tails will contribute to the background spectrum as well.

During the long-term neutrino-mass measurements, the gate valve will of course be opened so that this additional background source will be replaced by spectrometer-related background. Therefore, in a more realistic scenario, the figure of demerit can be determined using both the measured background spectrum without post-acceleration potential and the recorded photoelectron-source spectrum with post-acceleration potential. In that case, the raw and cut background spectra are not contaminated by boosted low-energy secondary electrons. It is even possible to extrapolate the figure of demerit to higher post-acceleration potentials where no photoelectron-source data are available due to the limited operation of the post-acceleration electrode in a stable mode. Since the detector response in terms of the energy resolution only slightly improves for higher energies, as shown in section 4.2, this extrapolation should give a reasonable upper limit for the expectation of a minimum figure of demerit when enhancing the post-acceleration potential beyond the current limits. Figure 5.21 illustrates the results when analyzing the intrinsic detector background without the use of the post-acceleration electrode combined with the 18.6-keV photoelectron-source response as emulation for the signal electrons. Above a post-acceleration potential of 15 kV, a minimum figure of demerit of $F_{\min} < 1.1$ can be reached.

5.9 Detector Background During the First Main-Spectrometer Commissioning

It will be shown in chapter 7 that the total spectrometer-related background rate was measured to be several 100 mcps, depending on the electromagnetic field configuration in use, as a result of current technical limitations in form of a single wire-layer electrode system and a non-permanently operating cryogenic baffle system in the NEG pump ports of the main spectrometer. This background rate significantly exceeds the ambitious design limit of 10 mcps [Ang05] [Dre13]. As one of the initial sets of measurements during the first SDS commissioning phase, the intrinsic background contribution of the detector system
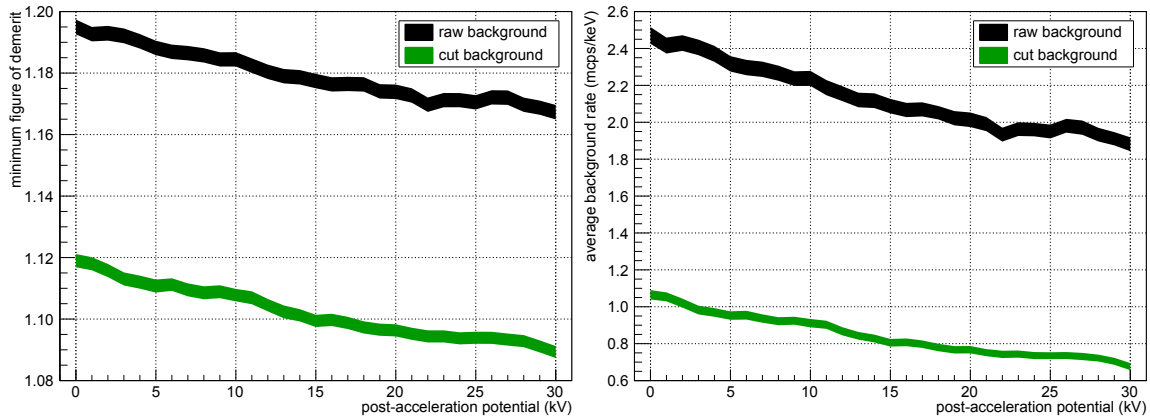
Figure 5.21: Extrapolation to higher post-acceleration potentials. The minimum figure of demerit (**left**) and the average background rate in the optimized region of interest (**right**) are illustrated in dependence of the post-acceleration potential, using the 18.6-keV photoelectron spectrum as signal input and the detector-background spectrum without elevated post-acceleration electrode as background input. Both spectra are extrapolated to higher energies in order to estimate the resulting figure of demerit and background rate for the raw (black) and the cut (green) background. Statistical error bands are included.

to the total main-spectrometer background was investigated with a closed gate valve in order to separate the detector system from the main spectrometer (runs #5258 − #5265, 15 h). In contrast to previous measurements described in this chapter for which the detector system was operated in stand-alone mode, the typical standard detector parameters for the SDS commissioning were used as summarized in table 4.4. In the context of background investigation, specific operational parameters were changed, such as the pinch-magnet field from 6.0 to 5.0 T, the detector-magnet field from 3.6 to 3.5 T, the post-acceleration potential from 11.0 to 10.0 kV, and the filter shaping length from 6.4 to 1.6 μs. In addition, the region of interest was set to a fixed energy window from 25.6 to 30.6 keV, in view of the −18.6-kV retarding potential, the +10.0-kV post-acceleration potential, and the impaired FWHM detector energy resolution of ∼ 2 keV for electrons post-accelerated to an energy of 28.6 keV. Moreover, the number of available pixels was limited to a total of only 122 of 148 because of the shadowing of the flapper valve and the post-acceleration electrode, as described in section 4.9.

The measured intrinsic detector background spectra around the region of interest are illustrated in figure 5.22 as well as the inter-arrival time distributions over the full energy scale. The most important observations are listed in the following:

- The coincidence windows for the two active background-reduction cuts are equal to the ones gained from stand-alone detector commissioning. The multi-pixel cut removes correlated detector events within a time interval of 1.5 μs while the veto cut rejects detector events correlating with veto events within a time interval of ± 1.5 μs.

- In the 5-keV broad region of interest, the raw [cut] background rate is 12.53(48) mcps [7.24(37) mcps] for 122 pixels and 16.88(56) mcps [10.34(44) mcps] for 146 pixels. In this special case, the linear scaling of the detector background does not seem reasonable because of the existing misalignment of the detector-system sub-components and the resulting imaging of the post-acceleration electrode onto the detector wafer. This leads to additional secondary-electron background emitted from the electrode and measured at affected pixels.

- The background spectra are dominated by multiple electron peaks originating from secondary electrons liberated from the closed gate valve and boosted by the post-acceleration potential. The multiplicity peaks are significantly smeared and broad-
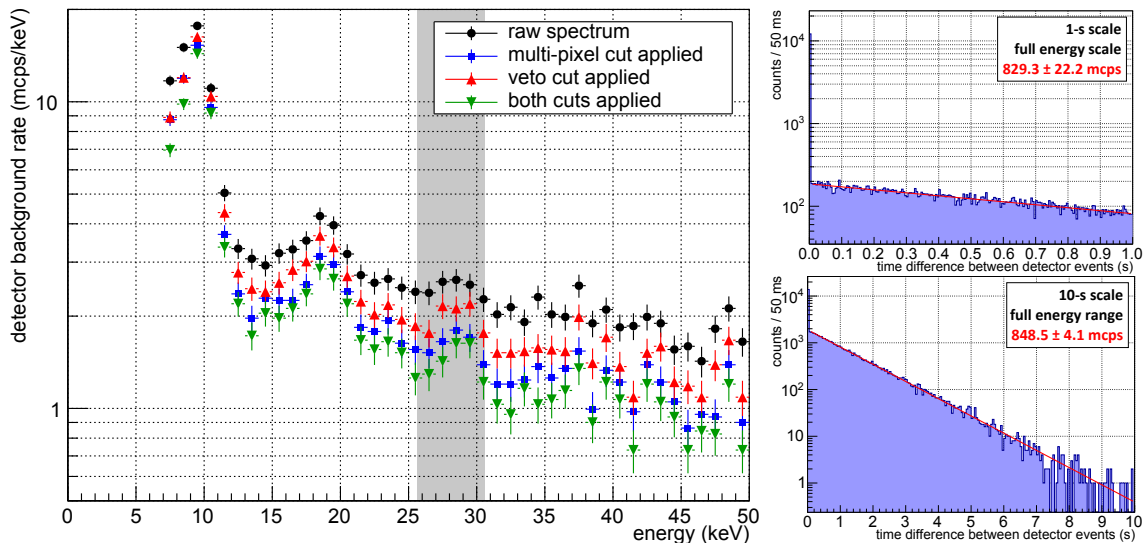
Figure 5.22: Intrinsic detector background during the first SDS commissioning phase.. The detector background spectra around the gray-shaded region of interest from 25.6 to 30.6 keV (**left**) and the inter-arrival time distributions between detector events on different time scales measured over the full energy range (**right**) are shown. The resulting time constants from the exponential fits ($\chi^2/\text{ndf} = 185.9/197$ for 1-s scale and $\chi^2/\text{ndf} = 189.6/178$ for 10-s scale) agree with the average count rate of (842.5 ± 3.9) mcps.

ened due to the degraded energy resolution of the detector. In addition, the triple-fold multiplicity peak overlaps with the region of interest used for main-spectrometer commissioning. Finally, at this magnetic-field configuration, the mapped surface area of the gate valve is larger than at nominal magnetic fields. When combining these effects, the measured detector background is definitely increased compared to the actual detector background. Therefore, the stated background rates can be interpreted as conservative upper limits.

- The upper limit of the detector background is at least two orders of magnitude smaller than typical background rates recorded in combination with the main spectrometer with an opened gate valve.

- The copper fluorescence lines at $8 - 9$ keV overlap with the major post-acceleration electron peak at 10 keV. In addition, they are partly clipped off due to the increased electronic noise threshold at ~ 7 keV.

- At higher energies in the absence of multiple electron peaks, the influence of the impaired filter shaping length is of minor importance due to the characteristic continuum of the background spectrum.

- The total intrinsic detector background is Poisson distributed as follows from the inter-arrival time distributions, showing an exponential trend. The time constants of (829.3 ± 22.2) mcps and (848.5 ± 4.1) mcps for a 1-s and 10-s time scale, respectively, measured over the full energy range, are consistent with the average total count rate of (842.5 ± 3.9) mcps. Correlated events are rejected primarily by the multi-pixel cut and the veto cut. The remaining background events are thus uncorrelated with stochastic arrival times.

Based on these findings, the intrinsic detector background in the region of interest is small for the analysis of spectrometer data in a first approximation. It is even recommended to refrain from applying the 1.5-µs multi-pixel cut and the veto cut since the probability of rejecting accidental events increases with higher rates, as discussed in section 5.2. The

actual intrinsic detector background can be examined during the upcoming second SDS commissioning phase where an additional elevated electrode is expected to be installed within the custom-built beam pipe with the in-line flapper valve. This electrode will allow to electrostatically shield low-energy background electrons and ions originating from the main spectrometer while the gate valve is opened. In that case, the contribution of low-energy electrons liberated from the inner surface of the closed gate valve to the detector background will disappear, as described in section 5.2.

5.10 Conclusion

In this chapter, several strategies to minimize background contributions from cosmic rays, external natural environmental radiation, and intrinsic radioactivity were outlined. Passive background reduction is achieved by a layered lead-copper radiation shield surrounding sensitive parts of the vacuum system on the ambient-air side, by donut-shaped copper sleeves blocking internal radiation, and by carefully selected and radio-assayed components and materials used in close proximity to the detector guaranteeing low intrinsic radioactivity. Active background reduction is accomplished by electrostatic post-acceleration to shift the signal to an energy interval with less background, by magnetic-field variation to optimize the sensitive beam size imaged onto the detector, and by the rejection of correlated detector events through a multi-pixel and veto cut. The latter makes use of plastic-scintillator panels surrounding sensitive parts of the vacuum system. For the detector response to 18.6-keV photoelectrons, a minimum figure of demerit of $F_{\mathrm{min}} = 1.119(2)$ with an average intrinsic detector background rate of $b_{\mathrm{cut}} = 1.07(3)\,\mathrm{mcps/keV}$ and a signal fraction of $f = 0.939(1)$ has been measured within an acceptance window from $E_L = 14.5(1)\,\mathrm{keV}$ to $E_U = 20.0(1)\,\mathrm{keV}$ after both active background-reduction approaches have been applied. A further background reduction to meet the ambitious design goal of $F < 1.1$ can be achieved by improving the veto efficiency and by elevating the post-acceleration electrode beyond its current limits. The measured background rates are still negligible for the first SDS commissioning phase, but there is potential for a slight improvement for later neutrino-mass measurements, e.g. via an enhancement of the post-acceleration performance in form of the maximum potential from 10 to 20 kV which should result in a reduction of the minimum figure of demerit from about 1.110 to 1.095. This leads to a relative improvement of the statistical uncertainty for neutrino-mass measurements by about 1.4 %.

Radon-Induced Background

Measurements performed during the first SDS commissioning phase have confirmed and significantly refined previous observations and results from detailed pre-spectrometer test experiments [Fra10b] [Fra11] [Goe10] [Mer13] [Wan13a]. The latter experiments could demonstrate that radon emanation into the sensitive magnetic flux-tube volume of the spectrometer leads to a significant electron background source due to the MAC-E-filter characteristics. This background component can be traced back to radon α-decays producing high-energy electrons based on a variety of different atomic processes. The resulting electrons with energies up to the multi-keV scale are magnetically trapped inside the large main-spectrometer volume where they can generate up to several hundreds of low-energy secondary electrons which significantly contribute to the measured overall background (section 6.1). Radon-induced background has been experimentally investigated in detail in the framework of this thesis by a variety of methods and measures, such as modifying the vacuum conditions of the main spectrometer and deviating from the standard operating parameters. On the basis of the well-understood detector properties described in the previous chapters, individual radon-induced background events could then be studied in terms of their temporal, spatial and energy-related characteristics (section 6.2). In addition, this modification allowed to determine the overall radon activity and emanation rate inside the main-spectrometer volume (section 6.3). These numbers are of crucial importance for the neutrino-mass measurements. Finally, on the basis of all information obtained in this work, two statistical analysis approaches based on empirical methods were applied (*i*) to estimate the composition of radon-induced and cosmic-ray induced background in standard operating mode (section 6.4), and (*ii*) to study radon-induced background features at nominal vacuum conditions without interference of other background components (section 6.5).

6.1 Radon-Induced Background in MAC-E Filters

Emanation processes of single radon atoms into the main-spectrometer volume result in a serious source of electron background. The different radon isotopes ^{219}Rn, ^{220}Rn, and ^{222}Rn of interest here originate from the α- and β-decay chains of the three primordial isotopes ^{235}U, ^{232}Th, and ^{238}U. Radon as a neutral noble gas is not affected by the magnetic or by the electrostatic shielding of a MAC-E filter. As a result, emanation from the structural material of the inner surfaces or the auxiliary equipment, such as the pumps, to the main-spectrometer volume leads to a homogenous radon distribution and decay vertices where the unstable isotopes α-decay into the polonium isotopes ^{215}Po, ^{216}Po, and ^{218}Po. There are two primary radon sources: the 60-kg material of the non-evaporable getter (NEG) pump with a total length of about 3 km, and the inner spectrometer-vessel
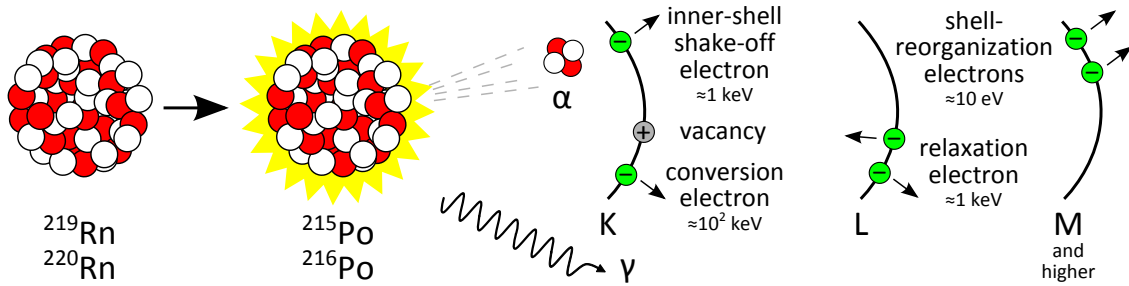
Figure 6.1: Schematic overview of electron-emission processes accompanying α-decay of ^{219}Rn and ^{220}Rn. This sketch visualizes possible atomic processes during α-decay of ^{219}Rn and ^{220}Rn into an excited state of ^{215}Po and ^{216}Po. The stated electron energies can be interpreted as approximate average values. Further details are described in the continuous text. Sketch inspired by [Mer12a].

walls with a total surface area of $690\,\text{m}^2$. Since ^{222}Rn has a relatively long half-life of $\tau_{1/2} = 3.82\,\text{d}$ compared to ^{219}Rn ($\tau_{1/2} = 3.96(1)\,\text{s}$) and ^{220}Rn ($\tau_{1/2} = 55.6(1)\,\text{s}$) [FE04], it is pumped out by the turbomolecular pumps (TMPs) before it can decay within the main-spectrometer volume. Therefore, α-decays of emanated ^{222}Rn atoms are neglected in the following discussion, but are indeed a major background source for other low-level experiments [Sim03] [Sim06].

The α-decay process results in the transition of a mother nucleus ^A_ZX with mass number A and atomic number Z into a daughter nucleus $^{A-4}_{Z-2}$Y through emission of an energetic α-particle:

$$^A_Z\text{X} \;\rightarrow\; ^{A-4}_{Z-2}\text{Y} \;+\; ^4_2\text{He} \;. \tag{6.1}$$

The α-decay can lead to a strong perturbation of the atomic shells, initiating the emission of electrons of different energies via the following atomic processes, also illustrated in figure 6.1:

- **Internal conversion:** If the initial α-decay populates an excited level of the daughter nucleus, it can interact electromagnetically with an inner-shell electron so that the associated electron is released from the atom into the continuum. Typically, these monoenergetic conversion electrons have energies of up to several hundreds of keV. In the case of ^{219}Rn, the most probable electron energies are $178\,\text{keV}$ ($1.27\,\%$, K-shell) and $254\,\text{keV}$ ($0.74\,\%$, L-shell) [Bro01], given in relative probabilities per α-decay. The process of internal conversion competes with radiative processes, where a γ-ray is emitted, due to the fact that both processes result from the deexcitation of the excited daughter nucleus level.

- **Inner shell shake-off:** If the emitted energetic α-particle interacts with the atomic shells via the Coulomb interaction [Fre74] [Han74], it can elevate an inner-shell electron into the continuum (shake-off process) or to an excited level (shake-up process). Typically, ejected shake-off electrons have rather small energies of the same order of magnitude as the associated shell binding energy. Correspondingly, a continuous energy spectrum with a maximum energy of up to few tens of keV is observed.

- **Atomic relaxation:** Both internal conversion and inner shell shake-off leave a vacancy in an inner shell. The atomic electron structure quickly rearranges by filling this vacancy with an electron originating from a higher energetic level. The released binding energy leads to the emission of a γ-ray fluorescence photon (radiative transition) or an electron (non-radiative transition). The ejected electron is labeled *Auger electron* [Bur52], if the vacancy is filled by an initial electron originating from a different higher shell, or *Coster-Kronig electron* [CK35], if the vacancy is filled
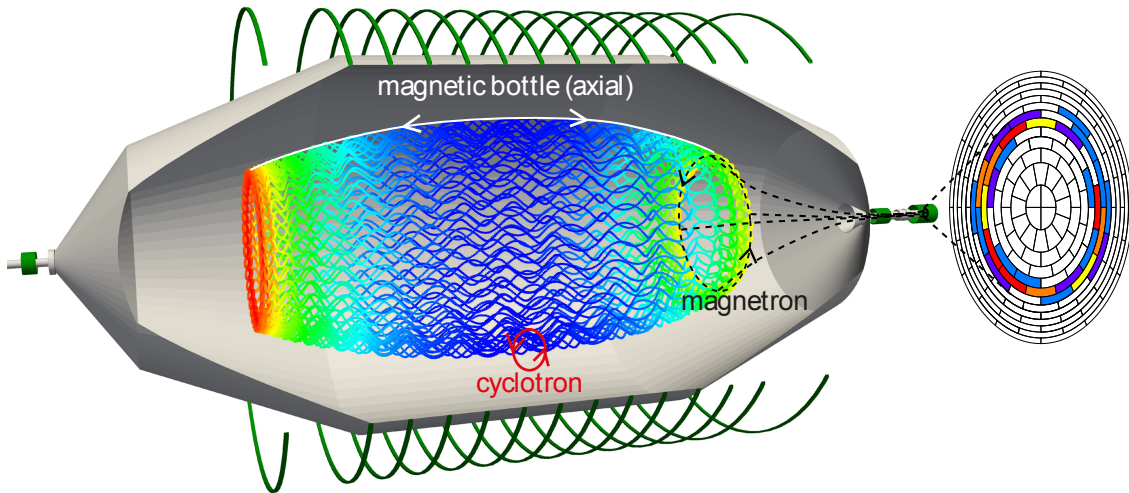
Figure 6.2: Trajectory and background event topology of a magnetically trapped electron. A magnetically trapped primary electron performs a slow azimuthal magnetron motion superimposed on its fast axial oscillation and very fast cyclotron motion. During its cool-down process caused when scattering off residual gas atoms and molecules in the ultra-high vacuum of the main spectrometer [Wan14], it produces low-energy secondary electrons via ionization. A large number of electrons is generated on the same magnetic flux along the circular magnetron path on which the primary electron was created. When escaping from the magnetic-bottle trap by breaking the storage conditions, these electrons produce a characteristic ring-shaped distribution on the detector. Figure adapted from [Bar14].

by an electron originating from a different higher sub-shell of the same shell. This non-radiative transition leaves a second vacancy, initiating a cascade of further photons and electrons being emitted. Atomic-relaxation electrons in heavy nuclei have energies of up to several tens of keV.

- **Atomic-shell reorganization:** The sudden change of the nuclear charge during α-decay is transmitted to the rather slowly moving outer-shell electrons in a non-adiabatic manner, causing the emission of two low-energy shell-reorganization electrons from the atom [Fre75].

A detailed model of the above listed electron emission processes accompanying radon α-decays including the resulting energy spectra of the released electrons is described in [Fra10b] [Mer12a] [Wan13a] [Wan13b].

High-energy electrons emitted in the above described atomic processes during the initial radon α-decay can generate a large number of secondary electrons in the sensitive volume of the main spectrometer, leading to a characteristic background topology. The main spectrometer with its underlying MAC-E-filter principle features a unique precision in measuring the tritium β-decay energy spectrum close to the kinematic endpoint at the expense of operating inherently as a magnetic trap for nearly all electrons created inside the magnetic flux tube. Due to the special magnetic-field configuration (see figure 6.2), the magnetic flux tube has the characteristic form of a magnetic bottle with two magnetic mirrors [Hig07] [Hig08] at the entry and exit regions with high magnetic-field strengths. When an electron propagates from the analyzing plane at low magnetic field toward the entrance or exit region of the MAC-E filter at high magnetic field, its longitudinal energy component $E_\parallel$ is transformed into a transverse energy component $E_\perp$. Meanwhile, the electron is boosted by the electric field generated by the applied retarding potential so that it gains longitudinal energy during the magnetostatic transformation. However, if the initial transverse energy of the electron is above a specific threshold, the magnetostatic

transformation dominates over the electrostatic acceleration, leading to a full conversion of longitudinal into transverse energy. As a consequence, the magnetic mirror effect causes the electron to be magnetically reflected back toward the analyzing plane at a lower magnetic field. This reflection process is then repeated on the opposite side of the main spectrometer, resulting in a stable storage condition for a trapped electron within the spectrometer volume.

However, a magnetically trapped electron can scatter off residual gas atoms or molecules present in small numbers in the ultra-high vacuum of the main spectrometer. At the same time it is emitting synchrotron radiation, thereby losing energy, resulting in a continuous cool-down over time [Wan14]. During this rather long cool-down process, it will produce a cascade of low-energy secondary electrons via consecutive ionization processes of residual gas. Depending on their initial energy and angle relative to the magnetic field line, these secondary electrons are magnetically trapped as well and can produce even further tertiary low-energy electrons. In fact, the primary electron produces a large number of secondary and tertiary electrons during its cool-down time. This number strongly depends on the initial energy of the single stored primary electron as each ionization process results in an average energy loss of $\sim 37\,\mathrm{eV}$ for the primary electron. As illustrated in figure 6.2, a stored electron performs an azimuthal magnetron motion on the same magnetic flux on which the primary electron was created. Superimposed on this are fast axial and cyclotron motions. The associated storage conditions are defined by the storage time. The latter depends on the initial energy of the primary electron, which defines the average number of scattering processes required for the electron to escape the magnetic trap, and on the vacuum conditions inside the main-spectrometer volume, which defines the average time between two subsequent scattering processes. An analytical calculation of these relations is shown in figure 6.3, performed in [Wan13a].

A magnetically trapped electron can leave the magnetic bottle when the storage conditions are finally broken, such as:

- **MAC-E-filter limit:** The transverse electron energy in the analyzing plane eventually drops below the energy resolution of the main spectrometer ($E_\perp \lesssim \Delta E \approx 1\,\mathrm{eV}$) so that the electron can escape the trap toward the source or the detector, thus looking identical to a signal electron.

- **Cyclotron-radius limit:** For large electron energies, the electron cyclotron radius becomes larger than the effective inner spectrometer radius of about 4.5 m, including the inner electrode structures, so that the electron hits inner surfaces. The absolute maximum transverse electron energy is limited to $\sim 320\,\mathrm{keV}$ for an electron propagating in a 3-G field in the analyzing plane on axis, resulting in a cyclotron radius of 4.5 m.

- **Non-adiabatic effects:** If the orbital magnetic moment of the electron is not conserved when propagating through the main spectrometer, non-adiabatic effects can cause the electron to escape the trap.

All electrons which escape the magnetic trap are electrostatically accelerated by the retarding potential of $-18.6\,\mathrm{kV}$ and are then adiabatically guided by the magnetic field to the detector. If the electron only had a small starting energy ($E < 1\,\mathrm{keV}$) before acceleration, it will be detected with the same energy as transmitted signal electrons. Electrons originating from the same primary keV-scale electron are however generated on the same magnetic flux tube along the circular magnetron path and thus produce a characteristic ring-shaped distribution on the detector. This characteristic event topology is of major importance in studying radon-induced background. A major complication arises due to the fact that this electron background is of non-Poisson nature because of the correlation of the electron
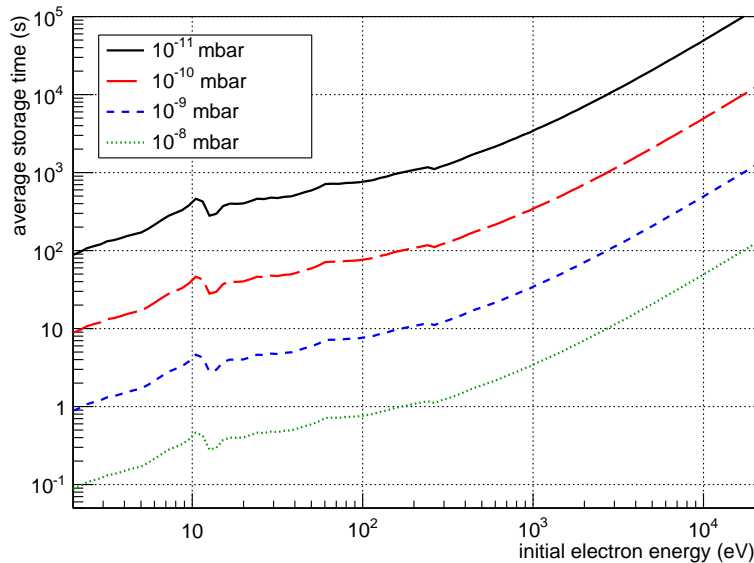
Figure 6.3: Average storage time as a function of the initial electron energy for different main-spectrometer vacuum conditions. The analytical calculations for the average electron storage time at different initial electron energies and main-spectrometer vacuum pressures is discussed in [Wan13a]. Here, only the energy range of relevance for the main-spectrometer is shown. At lower energies, the electron energy drops below the energy resolution of the main spectrometer so that the electron easily escapes the magnetic bottle toward the source or the detector. At higher energies, the electron cyclotron radius will exceed the inner radius of the vessel so that the electron hits the inner surfaces. Since the average time between two subsequent scattering processes scales linearly with the pressure, these curves are parallel to each other. Ideally, a pressure of below 10^{-11} mbar is maintained during neutrino-mass measurements in order to extend the average electron cool-down time to several minutes. This would allow to frequently apply active background-removal techniques with reasonable duty cycles [Mer12a] [Wan13a]. However, when investigating the electron background originating from single radon α-decays, an artificially elevated pressure is highly favorable due to a very short electron cool-down time, resulting in characteristic radon-induced ring patterns on the detector.

production mechanism during the cool-down process of the primary electron. This fact can seriously degrade the neutrino-mass sensitivity of the KATRIN experiment [Hoe12] [Mer12a] [Mer13], if no background-reduction techniques [Mer12b] [Wan13a] [Goe14] are applied.

In order to minimize the radon-induced electron background by means of a passive approach, a liquid-nitrogen (LN2) cooled baffle system was installed in each of the three main pump ports between the NEG pumps and the sensitive spectrometer volume. Its objective is to prevent a direct line of sight for radon emanating from the NEG pumps into the magnetic flux tube, while maintaining a sufficiently effective pumping speed of the NEG pumps with respect to hydrogen and tritium. Therefore, an optimized design of the baffle system requires a careful tradeoff between effective blocking and subsequent adsorption of radon atoms and keeping the vacuum conditions in the main spectrometer. The baffle system operates as a kind of cryogenic pump allowing cryogenic adsorption of radon atoms onto its cold copper surface. In doing so, it traps radon emanating from the NEG pumps before entering the sensitive main-spectrometer volume, and from the inner vessel surfaces before decaying inside the magnetic flux tube. In figure 6.4, the experimental setup of the NEG pump in one of the three main pump ports and the associated baffle system are shown. A more detailed description of the NEG pumps, the baffle system, and the vacuum
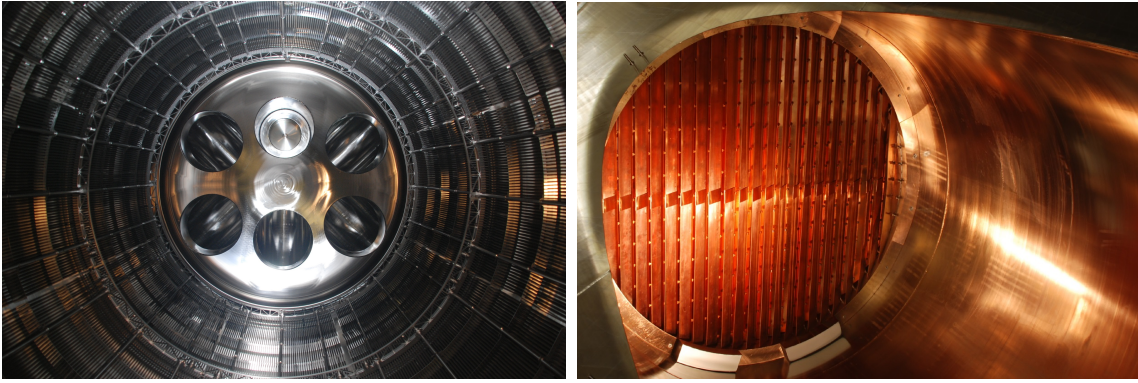
Figure 6.4: View into a main-spectrometer main pump port. Left: NEG pump.
Each of the three main-spectrometer main pump ports contains 16 modules holding 63 NEG
strips. The modules are coaxially arranged in the associated pump port. The 60-kg NEG
pump of the spectrometer has an overall length of about 3 km. **Right: Baffle system.** A
cryogenic copper baffle system is installed between each main pump port and the sensitive
spectrometer volume such that there is no direct line of sight for emanating radon. Pictures
adapted from [Goe14].

technology used in the KATRIN experiment is found in [Goe14].

One of the key goals of the first SDS commissioning phase was to investigate in detail the
characteristics of radon-induced electron background and to test the overall functionality
of the baffle system including its efficiency. Therefore, a set of background measurements
at different magnetic-field settings was performed, while the electric-field configuration
was kept similar to the potential settings used for the later neutrino-mass measurements.
In addition, different configurations of both the baffle system, operating either at room
temperature or at LN2 temperature, and the main spectrometer, operating either under
standard vacuum conditions ($p \approx 10^{-10}$ mbar) or with an artificially elevated pressure
($p \approx 10^{-8}$ mbar), were performed. The latter setup was realized by injecting gaseous
argon into the spectrometer volume. Table 6.1 summarizes the individual measurement
settings. In the following sections, the results of these investigations are discussed in detail.

6.2 Investigation at Artificially Elevated Pressure

During the first SDS commissioning phase, the vacuum conditions inside the main-spectro-
meter volume were dominated by the outgasing of hydrogen from the inner stainless-steel
walls and water originating from localized leaks, resulting in an absolute pressure level
of $p \approx 10^{-10}$ mbar [Bar14]. Since the average cool-down time of a single stored primary
electron reflects the vacuum conditions, as shown in figure 6.3, a considerable number of
primary electrons with energies in the keV-range is trapped inside the spectrometer at
any time for such a low pressure. Depending on the initial energy, average storage times
range from about 10 s to 3 h. During this period of time, they can produce numerous low-
energy secondary electrons via residual-gas ionization. In that case, secondary electrons
originating from different primary keV-scale electrons arrive at the detector within short
time intervals. It is thus difficult to separate individual primary electrons. Accordingly,
a clear identification of the characteristic electron background topology, the ring-shaped
pattern, induced by a single radon α-decay, is quite challenging.

In order to investigate the radon-induced electron background characteristics and event
topologies in more detail, the pressure in the main-spectrometer volume was artificially
elevated by permanently injecting a constant flow of gaseous argon of purity 6.0 (99.9999 %)
via a needle valve attached to the main-spectrometer vacuum system. This implied to keep

Table 6.1: Measurement configuration for radon-induced background investigation. The magnetic field is given for the analyzing plane, using the settings for the superconducting solenoids and the air-coil system according to section 2.4. The baffle system was operated at room temperature (*warm*) and at LN2 temperature (*cold*) while the main spectrometer was operated at a pressure of $p \approx 10^{-10}$ mbar (*normal*) and $p \approx 10^{-8}$ mbar (*elevated*), respectively. For the measurements listed, the spectrometer vessel was kept at -18.5 kV, the wire electrodes at -18.6 kV, and the post-acceleration electrode at 10 kV, resulting in a region of interest ranging from 25.6 to 30.6 keV. Further detector parameters are summarized in section 4.7. Due to a partly shadowed detector, only 122 of 148 detector pixels could be used for data analysis, as discussed in section 4.9. The average background rate is given in mcps. The associated statistical uncertainty is assumed to be Poisson-distributed.

magnetic field (G)	baffle system	pressure	average rate (mcps)	run time (h)	runs
3.8	warm	normal	781.9 ± 2.7	30.7	#6954, #6959, #6991, #7007, #8028, #8029
3.8	cold	normal	472.6 ± 5.7	4.0	#7070, #7072 − #7074
5.0	warm	normal	661.7 ± 9.6	2.0	#8289
5.0	warm	elevated	1264.1 ± 9.1	4.2	#8531 − #8533
9.0	warm	normal	519.6 ± 3.2	14.0	#7340 − #7352, #8479
9.0	warm	elevated	868.3 ± 2.4	42.3	#8545 − #8567
9.0	cold	normal	219.7 ± 4.7	2.8	#7093, #7094, #7096

the baffle system at room temperature and to continuously operate the six TMPs. After equilibrium, the final absolute pressure reached a value of $p \approx 10^{-8}$ mbar, leading to a reduction of the average electron storage time by a factor of ~ 100, now ranging from about 100 ms to 100 s only. It is important to note that the ionization energy of argon (Ar: 15.8 eV) is comparable to the one of hydrogen (H: 13.6 eV, H_2: 15.4 eV) [Nat13]. Under these special conditions, individual radon α-decays can be resolved in time and separated from each other by identifying single bursts of electrons − termed as *radon spike* − arriving at the detector in the region of interest within a relatively short time window. Due to the magnetron motion of the primary and secondary electrons, these events produce a characteristic ring-shaped distribution on the detector.

For the high-field 9.0-G setting, figure 6.5 gives a comparison of the recorded detector rate in the region of interest both at normal and at elevated pressure for a warm baffle system. The corresponding average rates are listed in table 6.1. At elevated pressure, the observed individual bursts of events are clearly identified as electrons arising from a single stored primary electron initiated from a single radon α-decay. In addition, the typical ring-shaped distribution of an exemplary burst is illustrated. On the detector, it is registered within a relatively short time interval, thus proving the characteristic circular magnetron path of stored electrons in the spectrometer. This fact underlines the expected strong correlation of electrons originating from the same primary electron. At normal pressure, the rate trend does not exhibit this burst characteristics, thereby complicating a distinct identification of single radon α-decays.

Since the secondary electrons within a burst are assumed to be generated by a single stored primary electron, a strong correlation not only in space but also in time is expected. Figures 6.6 and 6.7 illustrate the comparison of the corresponding inter-arrival time spectra, both at normal and at elevated pressure for 1-s and 10-s time scales, respectively. In contrast to normal pressure, a distinct non-Poissonian increase of inter-arrival times below $\Delta t \leq 0.2$ s is observed at elevated pressure. At longer time scales the spectra follow exponential trends
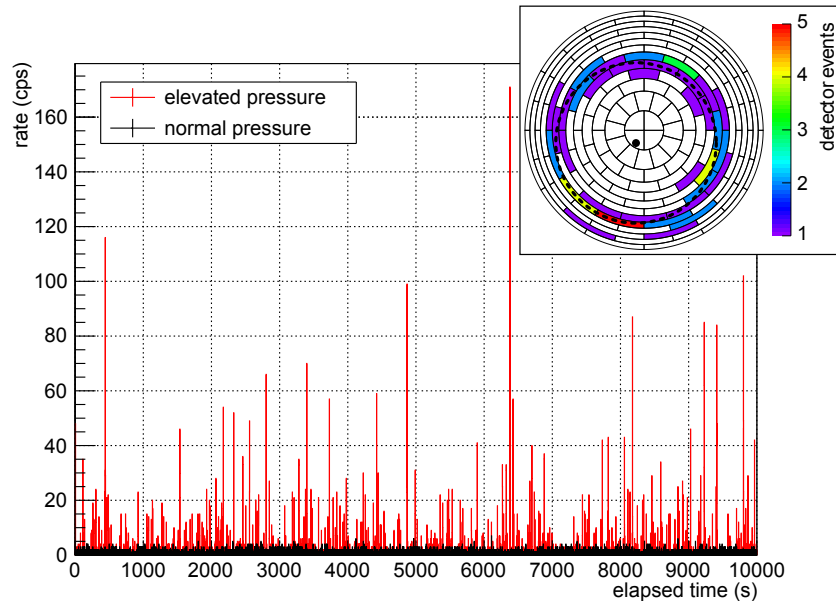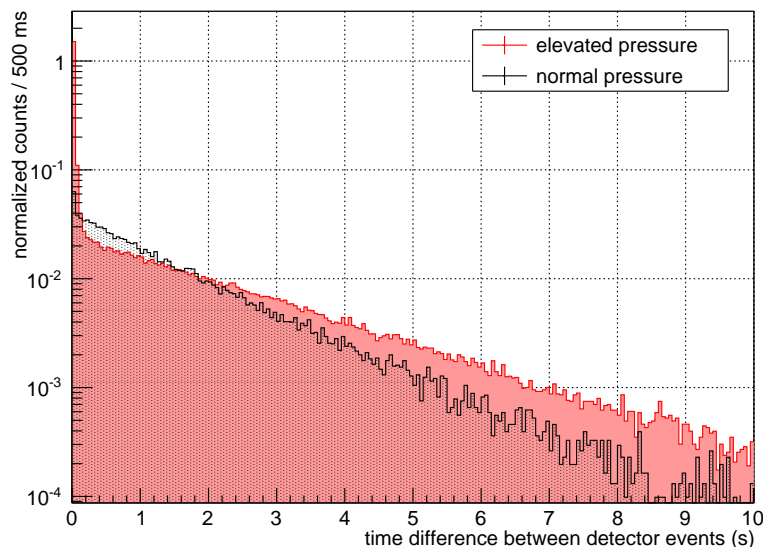
Figure 6.5: Rate trend at normal and at elevated pressure. Within the first 10^4 s of the corresponding measurements, the recorded detector rate in the region of interest over time is shown both at normal (black) and at elevated (red) pressure. At elevated pressure, an individual burst of events can be identified which corresponds to a single radon α-decay. As a typical example, the measured ring-shaped distribution of an individual burst on the detector is shown. It consists of 55 events recorded within a time interval of 672 ms. The distribution of pixel hits follows a circular fit (dashed-black line) with a radius of 30.8 mm whose center is located at $x = -3.3$ mm and $y = -4.8$ mm. A specific misalignment between the spectrometer axis and the detector wafer is visible, as discussed in section 4.9.

due to Poisson-distributed background processes in the first approximation. This feature allows to differentiate between highly correlated radon-induced events − in the following termed as *spike events* for $\Delta t \leq 0.2$ s − and other background events, such as electrons induced by cosmic rays, environmental radiation, intrinsic radioactivity, and field emission − termed as *single events* for $\Delta t > 0.2$ s − by applying an appropriate inter-arrival time cut at $\Delta t_{\mathrm{cut}} = 0.2$ s. This implies that the time difference for events appertaining to a radon-induced electron burst (*radon spike*) is less than 200 ms. At normal pressure, the illustrated inter-arrival spectra indicate that the background components are not strongly correlated, except for detector-related multi-pixel events for $\Delta t \leq 1.5$ μs, as discussed in section 5.2, and cosmic-ray induced multi-pixel events originating from the main spectrometer for $\Delta t \leq 300$ μs [Bar14]. However, these multi-pixel events occur on relatively short time scales compared to the coincidence window of the applied inter-arrival time cut so that a rejection of these events can be performed in a straightforward way. In contrast to background generated by radon α-decays, it is important to note that other background sources originating from electron emission from the inner spectrometer surfaces are not affected by a variation of the vacuum conditions at such low pressures to first order [For12] [Mer12a] [Wan13a] [Lei14].

A further characteristic of the background measurement at elevated pressure is the appearance of a distinct two-electron peak at twice the energy (57.2 keV) of the single-electron peak (28.6 keV) in the energy spectrum, as shown in figure 6.8. This peak originates from the increased probability for double-electron ionization of argon [JKR06], resulting in two electrons arriving at the same detector pixel within a time interval shorter than the filter shaping length of the DAQ system. Due to peak pile-up effects, these two events are recorded as a single event with twice the incident energy, as described in section 4.5.
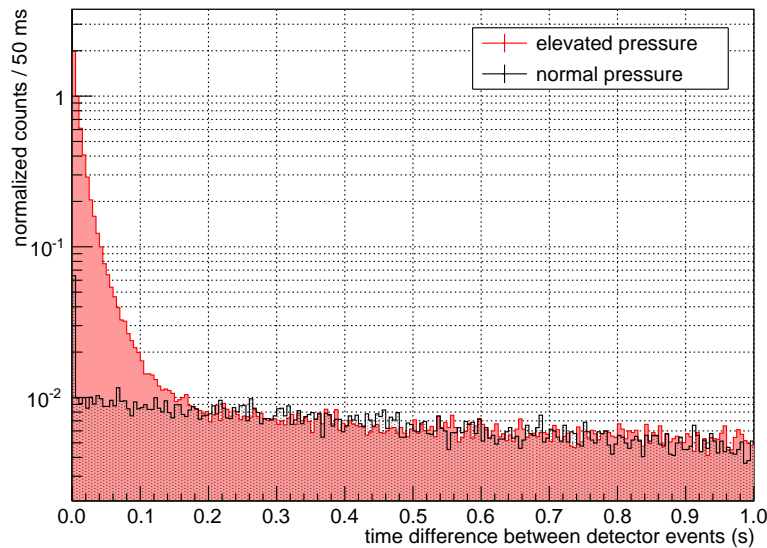
Figure 6.6: Inter-arrival time spectrum for a 1-s time scale at normal and at elevated pressure. The spectra are normalized such that their integrals above $\Delta t > 0.2\,\mathrm{s}$ are equal. At elevated pressure (red), radon-induced electrons (*spike events*) appear as events with inter-arrival times of $\Delta t \leq 0.2\,\mathrm{s}$, while electrons arising from other background sources (*single events*) saturate all events with $\Delta t > 0.2\,\mathrm{s}$. At normal pressure (black), only a small number of multi-pixel events on relatively short time scales can be identified as correlated events, consisting of detector-related multi-pixel events for $\Delta t \leq 1.5\,\mathrm{\mu s}$ and cosmic-ray induced multi-pixel events below $\Delta t \leq 300\,\mathrm{\mu s}$.

Figure 6.7: Inter-arrival time spectrum for a 10-s time scale at normal and at elevated pressure. The spectra are normalized such that their integrals above $\Delta t > 0.2\,\mathrm{s}$ are equal. There, the spectra follow exponential trends in the first approximation, indicating Poisson-distributed background processes. The slopes are different since the radon-induced electrons cannot be separated from other background events at normal pressure.
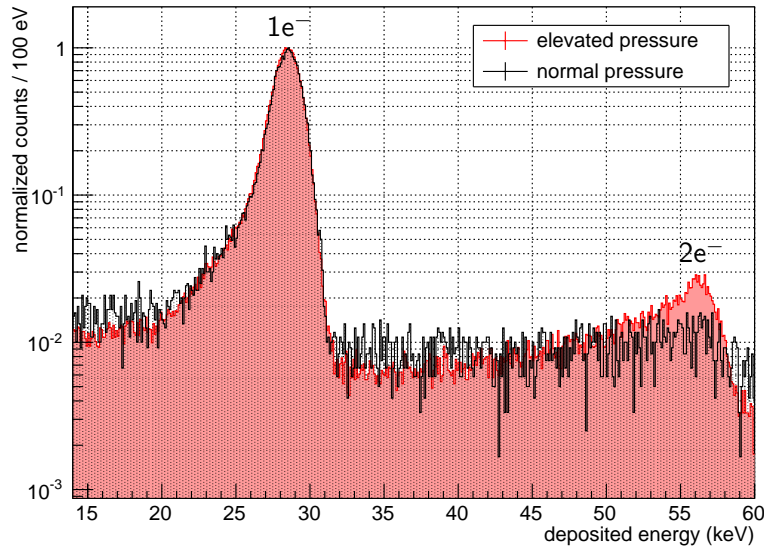
Figure 6.8: Double-electron ionization peak of argon. The energy spectrum at elevated pressure shows single (28.6 keV) and double (57.2 keV) ionization peaks.

In view of the magnetic bottle characteristics of the main spectrometer, the detection of double ionization is remarkable, requiring electrons with almost identical starting energies and pitch angles.

In the following, the background components arising from single (section 6.2.1) and spike (section 6.2.2) events are characterized in more detail in order to further validate the application of the described inter-arrival time cut.

6.2.1 Single Events

At normal pressure, the corresponding inter-arrival time spectra show no obvious features and consequently the correlation between individual single events is less distinct than in the case of spike events. Therefore, electrons induced by cosmic rays, environmental radiation, intrinsic radioactivity, and field emission represent conceivable background candidates for describing these single events.

The electrons are generated at the inner structural surfaces of the main spectrometer, based on different emission processes. In principle, they are quickly reflected back to the surface by the Lorentz force so that magnetic shielding should prevent these electrons from reaching the sensitive magnetic flux tube. However, their initial energy and pitch angle relative to the magnetic field lines can be such that they can enter at least the outermost insensitive flux-tube volume. As a result, they are guided along the magnetic field line to the high-field regions at both ends where they can be reflected by the magnetic mirror effect. Following this, the magnetically trapped electrons can produce low-energy secondary and tertiary electrons via ionization of residual gas. Background is however only pronounced, when the primary, secondary, and tertiary electrons can drift from the outer non-mapped region into the sensitive flux-tube volume via radial $\vec{E} \times \vec{B}$ and $\vec{\nabla}|\vec{B}| \times \vec{B}$ drift motions. These drifts are caused by non-axially symmetric field components due to magnetostatic and/or electrostatic inhomogeneities. Therefore, these electrons are more likely to be detected in the outer volume of the sensitive magnetic flux tube than in the inner volume. More details on the rather complex radial drift motion is given in [Lei10] [Mer12a] [Lei14].
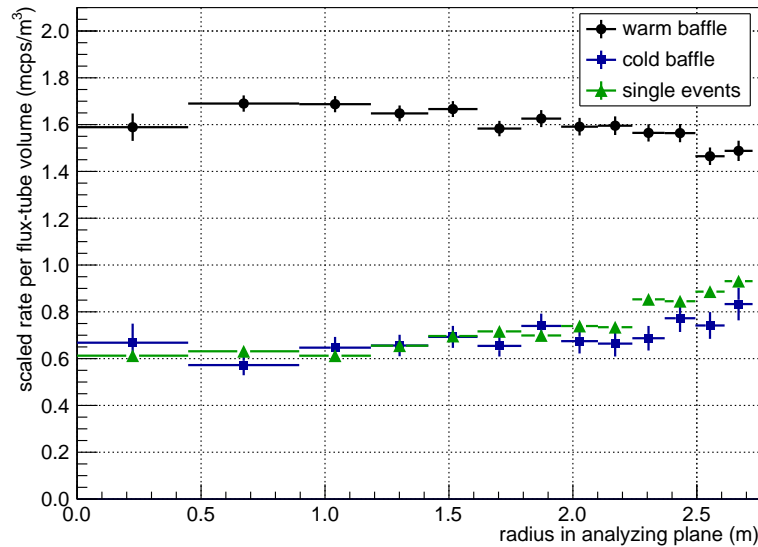
Figure 6.9: Radial distribution of background events at 9.0 G. The observed rate per detector-pixel ring, given in mcps, has been normalized to a unit of observable flux-tube volume, given in m^3. In case of shadowed or non-functional pixels per ring, the rate is scaled linearly to a fully working detector ring. The ring numbers at the detector have been scaled to the corresponding radii in the analyzing plane, given in m. This figure thus shows the normalized radial background distributions for 9.0 G: at normal pressure with warm baffle (black, average recorded rate: (519.6 ± 3.2) mcps), at normal pressure with cold baffle (blue, (219.7 ± 4.7) mcps), and single events only at elevated pressure with warm baffle (green, (234.5 ± 1.3) mcps). Statistical uncertainties are included.

On condition that the baffle system operates in a highly effective manner, the background during a measurement with activated baffle system should be dominated by single-event related electrons. Therefore, the radial distribution of the single events from the elevated-pressure measurement even with a non-activated baffle system should be identical to the overall background spectrum from the normal-pressure measurement with functional LN2 cooled baffle system. In case of the 9.0-G setting, figure 6.9 illustrates that this is indeed the case. At first, it is important to note that the radial distribution for single events indeed decreases from outer to inner flux-tube volumes. However, this reduction is only rather small since the sensitive magnetic flux tube at 9.0 G is strongly compressed (see figure 2.6), implying a rather large clearance to the inner surfaces of the main spectrometer of ~ 2 m.

These observations lead to two important conclusions:

- At normal pressure, the LN2 cooled baffle system at cryogenic temperatures removes practically all emanated radon atoms from the sensitive flux-tube volume before they decay. No surplus of radon-induced events is observed at the detector, equivalent with the statement that the background composition is dominated by single-event related electrons. These are primarily detected in the outer region of the magnetic flux tube.

- At elevated pressure, the applied inter-arrival time cut is a convenient and very helpful approach to distinguish between spike events ($\Delta t \leq 0.2$ s) and single events ($\Delta t > 0.2$ s). The latter event class corresponds exclusively to electrons generated by cosmic rays, environmental radiation, intrinsic radioactivity, and field emission. This allows to separate background classes on an event-by-event basis, which is of vital importance in background studies.

6.2.2 Spike Events

At elevated pressure, radon-induced electrons form spike events due to their origin from subsequent ionization processes and the associated correlation. Each radon spike is characterized by a burst of electrons appearing on the detector within a relatively short time interval of $\Delta t \leq 0.2\,\mathrm{s}$. A proper selection of radon spikes is given by the following assumptions:

- The maximum time difference between two subsequent events is $200\,\mathrm{ms}$, resulting from the inter-arrival time cut of $\Delta t_{\mathrm{cut}} = 0.2\,\mathrm{s}$.

- The number of events in an individual radon spike is $N \geq 3$.

- One radon spike can be traced back to one stored primary electron and is thus caused by one radon α-decay. The temporal overlap of spikes is rather improbable, as it will be discussed below.

Subject to these limitations, radon spikes and their associated electron events can now be characterized in detail.

Radial rate dependence

Figure 6.10 illustrates the radial distributions of different background components at elevated pressure using a 9.0-G setting. Making use of the inter-arrival time cut discussed above, spike and single events were separated on an event-by-event basis and sorted into different radial distributions. First, the pattern of radon-induced spike events is discussed. Here, a high-energy electron emitted from radon α-decays is more likely to be trapped in the inner parts of the flux-tube volume where more favorable storage conditions pertain. By contrast, low-energy electrons generated by cosmic rays, environmental radiation, intrinsic radioactivity, and field emission are more likely to stem from the outer region of the magnetic flux tube. The observed characteristic distributions qualitatively follow the expected distributions and underline the correctness of the above stated assumptions.

However, in case of $\Delta t \leq 0.2\,\mathrm{s}$ and $N = 2$, the background class cannot be assigned unambiguously. This case occurs with a relative fraction of $5.4(7)\,\%$ of the total rate. Also, the corresponding radial distribution of this hybrid class shows no obvious features as expected for events which cannot unequivocally be assigned to either spike or single event category. Nevertheless, at least the relative contribution of both background components can be calculated. Assuming that single events are Poisson-distributed in time with a mean Poisson rate of R, the probability of two events arriving within a certain time interval ΔT is defined by

$$P = \frac{\int_0^{\Delta T} e^{-Rt}\mathrm{d}t}{\int_0^\infty e^{-Rt}\mathrm{d}t} = 1 - e^{-R\Delta T} \ . \tag{6.2}$$

The rate $R = (219.7 \pm 4.7)\,\mathrm{mcps}$ is given here through background measurements with operational baffle system, assuming full efficiency, while the time interval $\Delta T = \Delta t_{\mathrm{cut}} = 0.2\,\mathrm{s}$ corresponds to the inter-arrival time cut. Therefore, the probability for a two-event cluster with $N = 2$ to actually correspond to single events rather than to spike events is $P = 4.3(1)\,\%$. Hence, the individual events of this background component cannot be clearly assigned. However, due to its small contribution to the overall background, this hybrid component will be neglected in the following. By contrast, in a worst-case scenario, the probability of a radon spike consisting of $N = 3$ events with a radon-spike duration of $2 \times \Delta t_{\mathrm{cut}} = 0.4\,\mathrm{s}$ to be accidentally identified as three independent single events is only $P^2 = 0.2\,\%$.
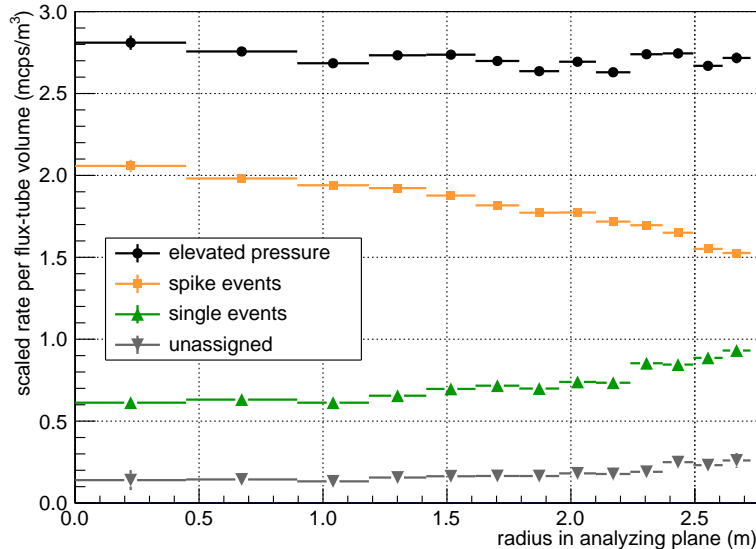
Figure 6.10: Radial rate dependence for measured backgrounds at elevated pressure and at 9.0 G. Different background components are illustrated at elevated pressure and at 9.0 G: total background (black), spike events with $\Delta t \leq 0.2\,\text{s}$ and $N \geq 3$ (orange), single events with $\Delta t > 0.2\,\text{s}$ (green), and unassigned events with $\Delta t \leq 0.2\,\text{s}$ and $N = 2$ (gray). Statistical uncertainties are included.
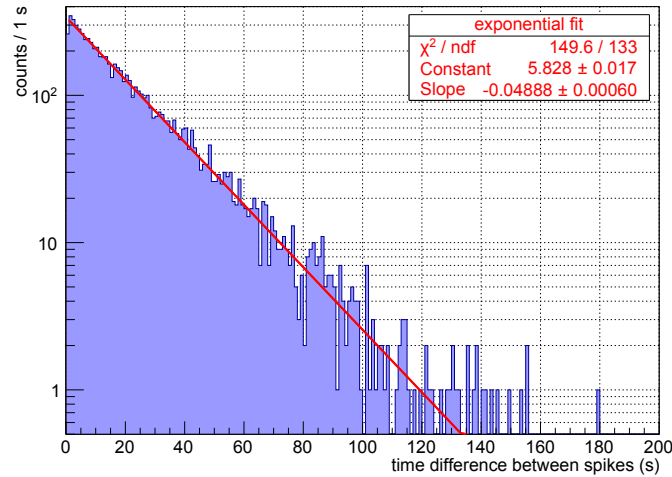
Time difference between radon spikes

Figure 6.11 shows the inter-arrival time spectrum for radon spikes at 9.0 G. As indicated by the associated fit, the distribution follows an exponential trend. This implies that the observed radon spikes are Poisson-distributed in time, which is expected in the case of α-decays of individual radon atoms emanated from the wall or the NEG pump. This Poisson nature of radon spikes allows to determine the radon decay activity inside the sensitive flux-tube volume via the time constant of the applied exponential fit. At 9.0 G [5.0 G], an activity of $(48.9 \pm 0.1)\,\text{mBq}$ $[(78.1 \pm 2.9)\,\text{mBq}]$ is obtained.

The values obtained above can be compared with the radon activities gained from counting the number of radon spikes during the corresponding measurement time. In total, 7162 [1134] radon spikes are identified at 9.0 G [5.0 G] within a run time of 42.3 h [4.2 h], leading to a conservative value for the radon activity of $(47.0 \pm 0.6)\,\text{mBq}$ $[(74.7 \pm 2.2)\,\text{mBq}]$ inside the sensitive flux-tube volume. The two activities measured at the same magnetic-field setting are in good agreement. As the magnetic flux tube is more compressed, the activity at 9.0 G is lower than at 5.0 G. An appropriate scaling of the radon activity to the total main-spectrometer volume, considering both the observable flux-tube volume and the partly shadowed detector wafer, is discussed in more detail in section 6.3.

Duration of radon spikes

Figure 6.12 illustrates the distribution of the duration for radon spikes at 9.0 G. For a spike duration of $t_{\text{spike}} \gtrsim 0.2\,\text{s}$, the spectrum follows approximately a power-law distribution with $\sim t_{\text{spike}}^{-2.20(4)}$. For shorter spike durations, a relatively flat behavior with $\sim t_{\text{spike}}^{0.38(3)}$ is observed. As shown in figure 6.3, the storage time of a multi-keV electron and thus the length of a radon spike depends on the primary electron energy, on the electron cool-down time, and thus on the residual pressure in the spectrometer. However, in view of the rather small magnetic guiding field in the main spectrometer of 9.0 G [5.0 G], non-adiabatic effects

Figure 6.11: Time difference between radon spikes at 9.0 G. The inter-arrival time spectrum for radon spikes follows an exponential trend, indicated by the corresponding fit (red-colored line). This demonstrates that radon spikes are Poisson-distributed in time.
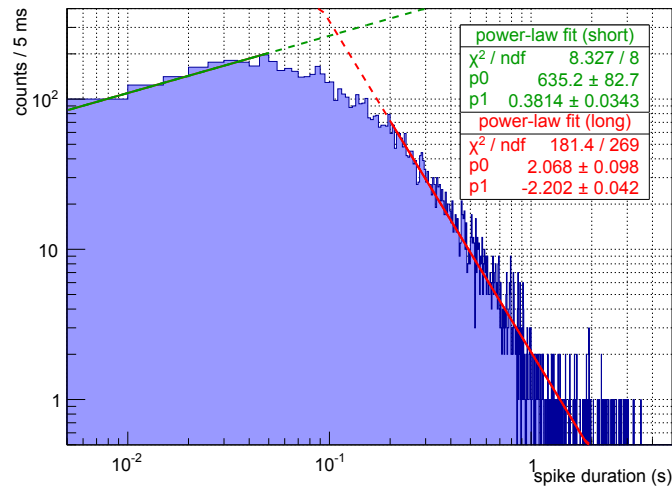
Figure 6.12: Duration of radon spikes at 9.0 G. The observed distribution of the duration t_{spike} of radon spikes follows approximately a power-law fit with $\sim t_{\mathrm{spike}}^{-2.20(4)}$ (red-colored line) for $t_{\mathrm{spike}} \gtrsim 0.2\,\mathrm{s}$, while for shorter time scales a nearly flat distribution with $\sim t_{\mathrm{spike}}^{0.38(3)}$ (green-colored line) is observed.
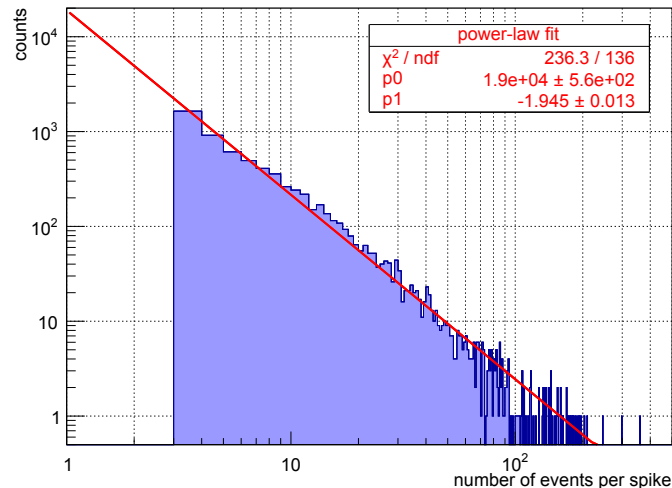
Figure 6.13: Number of secondary electrons per radon spike at 9.0 G. The spectrum shows the number N of secondary electrons per spike which can be described by a power-law fit (red-colored line) with $\sim N^{-1.945(13)}$.

can abruptly terminate the stable storage conditions. The stated effects were included in Monte Carlo simulations [Wan14] performed with *Kassiopeia*. The observed power-law distributions can, in principle, be compared to these simulations in a qualitative manner, but at the time of authoring this thesis corresponding quantitative results were still pending.

The mean spike duration is measured to be (211.7 ± 3.4) ms $[(183.1 \pm 5.3)$ ms$]$ for the 9.0-G [5.0-G] setting. This is in good agreement with the expected electron cool-down time in the elevated pressure region. Since radon spikes are Poisson-distributed in time, these values allow to estimate the probability that two radon spikes are simultaneously detected. For this purpose, equation (6.2) can be applied using the radon activity gained from the inter-arrival time spectrum as mean Poisson rate R and the mean spike duration as time interval ΔT, resulting in a probability of $P \approx 1.0\,\%$ $[P \approx 1.4\,\%]$. Therefore, the effect of radon spikes overlapping in time is negligible to first order.

Number of secondary electrons per radon spike

Figure 6.13 shows the distribution of the number N of secondary electrons per radon spike at 9.0 G. This spectrum closely follows a power-law distribution with $\sim N^{-1.945(13)}$. It reflects to some extent the stochastic nature of the breaking of the storage conditions of the high-energy primary particles. Pending Monte Carlo simulations [Wan14] will allow a detailed comparison.

On average, each detected radon spike contains $12.7(2)$ secondary electrons. The distribution can be extrapolated to low multiplicities at $N = 1, 2$ in order to estimate the total radon activity inside the main-spectrometer volume. This issue is highly non-trivial as the low multiplicities $N = 1, 2$ can also result from a different background class, especially from shell-reorganization electrons. In this case, the power-law distribution cannot be easily extrapolated back. More details with respect to extrapolating to lower multiplicities and determining the total radon activity are given in section 6.3.

Radon-induced ring structures

Due to their slow magnetron drift, trapped electrons will perform azimuthal motions on concentrical trajectories at a specific magnetic flux value, thereby producing numerous low-energy secondary electrons via ionization of residual gas. Figures 6.14 and 6.15 demonstrate the characteristics of the resulting radon-induced ring structures appearing on the detector at 9.0 G. In that case, only high-multiplicity radon spikes with at least $N \geq 10$ spike events are considered, since the fit algorithm for a circle does not yield accurate results due to the distorting effects of the faster cyclotron motion which smears out the magnetron rings, so that the fit accuracy suffers for low multiplicities.

A total of 2383 [323] radon rings was identified at 9.0 G [5.0 G] with mean ring-center coordinates of $x = -1.7(1)$ mm and $y = -4.6(1)$ mm $[x = -1.6(2)$ mm and $y = -4.8(2)$ mm$]$ (see figure 6.14). However, it can be seen that the actual standard deviations of these values are relatively large, resulting in a spread of ring centers: $\sigma_{x,\mathrm{RMS}} = 3.0$ mm and $\sigma_{y,\mathrm{RMS}} = 3.6$ mm $[\sigma_{x,\mathrm{RMS}} = 3.7$ mm and $\sigma_{y,\mathrm{RMS}} = 3.5$ mm$]$. Again, this is due to the distorting effects of the large cyclotron radii in the low-field region of the spectrometer. The observed radon-induced ring patterns are not perfectly centered on the detector due to the previously discussed misalignment between of main spectrometer and detector wafer. This new approach of fitting ring patterns of radon spikes is sensitive to the magnetic alignment of the system relative to the detector wafer, in particular it is independent from cross-referencing via geometries of inner structural surfaces. The results are in moderate
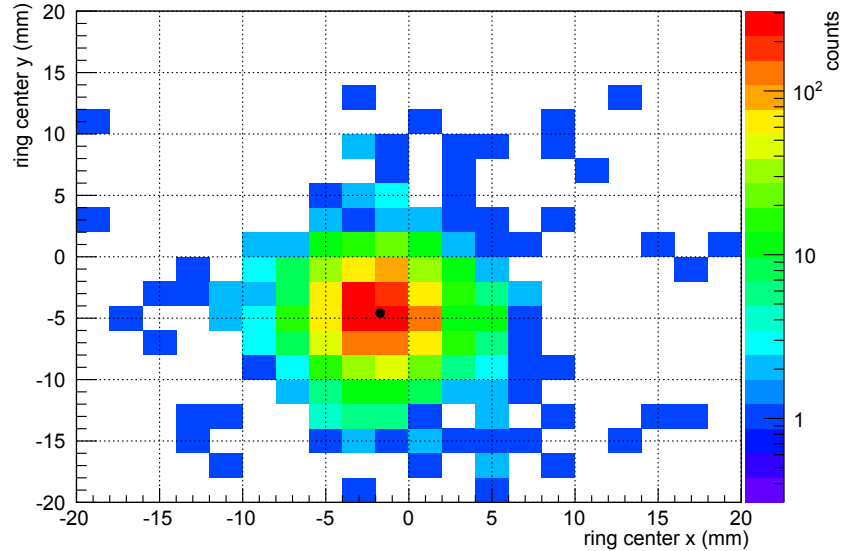
Figure 6.14: Centers of radon-induced ring structures at 9.0 G. The bin width of this histogram is set to 2 mm corresponding approximately to the spatial resolution of the detector wafer in radial direction. The mean ring-center coordinates are $x = -1.7(1)$ mm and $y = -4.6(1)$ mm (black dot), while the standard deviations of these values are relatively large with $\sigma_{x,\mathrm{RMS}} = 3.0$ mm and $\sigma_{y,\mathrm{RMS}} = 3.6$ mm as a result of the distorting cyclotron motion.

agreement with the simulated expectations of $x \approx -2.9$ mm and $y \approx -3.1$ mm, as discussed in section 4.9.

Based on the stochastic thermal motion of radon atoms in the ultra-high vacuum and their rather long half-life of a few seconds, a homogeneous distribution of radon α-decays inside the main-spectrometer volume is expected. The observed linear increase of ring radii toward larger dimensions gives strong experimental backing to this assumption (see figure 6.15 left). Note that the volume element of a generic homogeneous distribution scales with $\Delta V \sim r\,\mathrm{d}r$ in cylindrical coordinates. The observed drop at smaller radii can be explained by the limited dimensions of the detector bullseye and the innermost 12-pixel ring with outer radii of 7.4 and 14.8 mm, respectively. The abrupt drop at larger radii is based on a combination of the limited sensitive detector-wafer radius of 45.0 mm and the existing misalignment of the detector wafer relative to the beam axis so that the four outermost detector rings are affected in this distribution. Again, a comparison with Monte Carlo simulations [Wan14] is pending to quantitatively study this in more detail.

Due to the above mentioned effects related to the large cyclotron radii, the radon-induced ring structures imaged onto the detector wafer are about $4 - 5$ detector rings width (see figure 6.15 right). Since the radial resolution of the detector wafer improves from inner to outer pixels due to the smaller radial width of outer detector rings, this interplay of magnetron and cyclotron motion manifests differently at inner and outer detector rings. In addition, the misalignment of the detector wafer relative to the beam axis has to be considered in follow-up studies based on Monte Carlo simulations.

First events of radon spikes

Figure 6.16 shows the measured and the simulated distributions of the first event within a radon spike at 9.0 G, scaled to a fully working detector and to an equal area of unity in order to visualize the normalized frequency of occurrence. The increased rate of these events at larger radii can be explained by the fact that in this case the detector observes
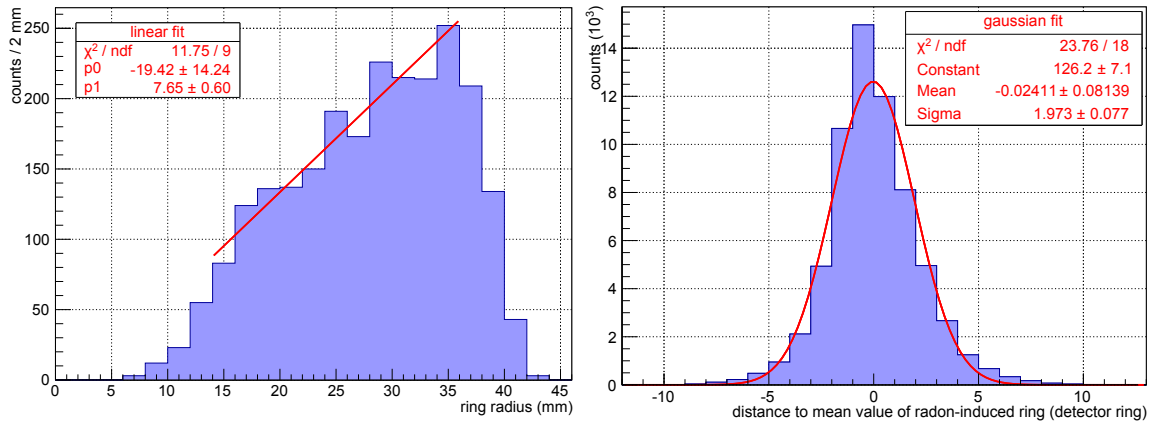
Figure 6.15: Radon-induced ring structures at 9.0 G. Left: Distribution of ring radii. The bin width of this histogram is again set to 2 mm, which approximately corresponds to the spatial resolution of the detector wafer in radial direction. The linear fit (red-colored line) has been restricted to the range from 15 to 36 mm in order to exclude the detector bullseye and the innermost 12-pixel detector ring as well as the four outermost detector rings, in view of the sensitive area of the detector wafer and its misalignment relative to the beam axis. **Right: Distribution of ring widths.** This histogram illustrates the spread of the radial distribution of events within a radon spike relative to the centroidal radius of the ring defined by the magnetron motion of the stored electron. The radial spread results from the superimposed cyclotron motion. The FWHM of the applied fit by a Gaussian distribution (red-colored line) gives an average width of the imaged radon-induced rings of 4.6(2) detector rings.

secondary electrons for which the initial primary electron performs a magnetron motion outside the sensitive magnetic flux tube. Due to the cyclotron motion of the primary electron, ionizing collisions with residual gas and subsequent production of a low-energy secondary electron can however occur inside the sensitive magnetic flux tube, resulting in an increased detection rate of these electrons at larger flux-tube radii.

In that specific case, a simplified two-dimensional simulation of the electron cyclotron motion in the analyzing plane was performed [Rin13] to understand this characteristic pattern in more detail. The model generates primary electrons uniformly distributed over the entire area of the analyzing plane with energies according to the radon-event generator [Wan13a] [Wan13b] implemented in *Kassiopeia*. Then, the resulting cyclotron radius of the primary particle and its respective cyclotron trajectory projected to the analyzing plane were calculated. For each primary electron, a point randomly selected on its superimposed fast cyclotron and slow magnetron path was projected to the plane of the detector wafer. This point corresponds to the point of first ionization and thus can be interpreted as first event of a radon spike. However, as at least three events are required to be counted as radon spike, all simulated events with an observable cyclotron path smaller than twice the average length between two ionization processes were rejected. The resulting simulated radial distribution is in good agreement with the measured radial distribution.

Figure 6.16 also visualizes the calculated probability of the two-dimensional cyclotron trajectory projected to the analyzing plane to be observed by the detector. This is shown as a function of the radius in the analyzing plane where the electron was initially produced. Due to the electron cyclotron motion, this probability smoothly drops to zero for large radii. At 9.0 G, the sensitive magnetic flux tube covers a radius of ∼ 2.72 m in the analyzing plane. However, due to the effects described above, even multi-keV primary electrons gyrating at flux-tube radii of ∼ 3.3 m can be observed by the detector.
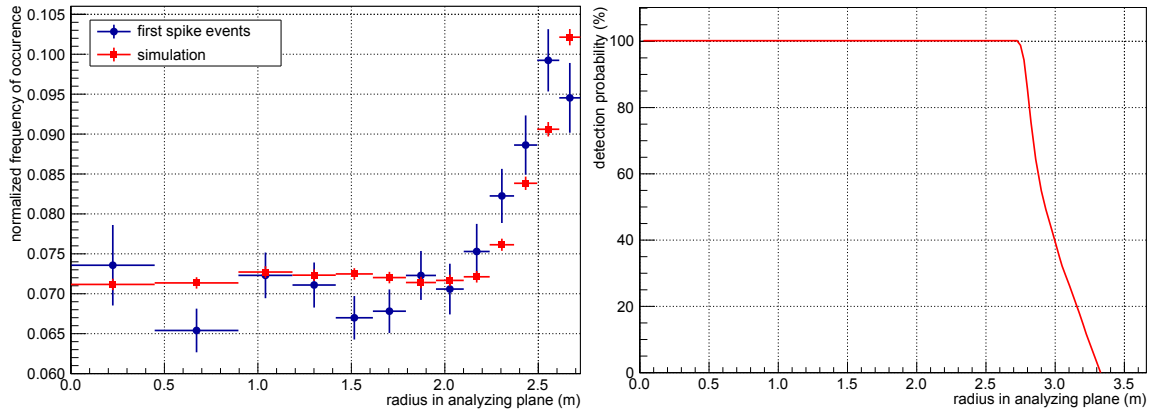
Figure 6.16: Radon spikes at 9.0 G. Left: Radial distribution of the first event in a radon spike. These spectra illustrate the measured (blue) and the simulated (red) radial distributions of the first events to be registered from each radon spike at 9.0 G. The increasing probability for these events at larger flux-tube radii can be explained again by the cyclotron motion. This allows electrons performing their magnetron motion outside the sensitive flux-tube volume to enter the mapped flux-tube via their cyclotron motion. **Right: Detection probability for spike events.** The probability to detect a radon spike as a function of the analyzing-plane radius is shown. At 9.0 G, the radius of the sensitive magnetic flux tube is ~ 2.72 m. However, due to the electron cyclotron motion, electrons up to a radius of ~ 3.3 m can be observed by the detector.

6.3 Radon Activity and Radon Emanation Rate

The total radon activity A_{tot} inside the main-spectrometer volume $V_{\text{MS}} \approx 1240\,\text{m}^3$ is given by the sum over the individual decay rates A_{Rn} of involved radon isotopes:

$$A_{\text{tot}} = \sum A_{\text{Rn}} = A_{219\text{Rn}} + A_{220\text{Rn}} = \lambda_{219\text{Rn}} \cdot N_{219\text{Rn}} + \lambda_{220\text{Rn}} \cdot N_{220\text{Rn}} \qquad (6.3)$$

where $\lambda_{219\text{Rn}}$ [$\lambda_{220\text{Rn}}$] denotes the decay constant and $N_{219\text{Rn}}$ [$N_{220\text{Rn}}$] the number of emanated ^{219}Rn [^{220}Rn] atoms. The generic decay constant is defined by

$$\lambda = \frac{1}{\tau} = \frac{\ln(2)}{\tau_{1/2}} \ , \qquad (6.4)$$

where τ is the mean lifetime and $\tau_{1/2}$ the half-life of the associated decay.

In a state of equilibrium where the radon number density N_{Rn} remains constant over time, the radon emanation rate E_{Rn} can be calculated [Mer12a] [Mer13] via

$$\frac{\mathrm{d}N_{\text{Rn}}}{\mathrm{d}t} = -A_{\text{Rn}} - \frac{N_{\text{Rn}}}{V_{\text{MS}}} \cdot S_{\text{Rn}} + E_{\text{Rn}} \overset{!}{=} 0 \ . \qquad (6.5)$$

This equation takes into account that the number N_{Rn} of radon atoms inside the main-spectrometer volume decreases due to the radon decay rate (first term) and due to the radon pump-out rate S_{Rn} (second term) caused by active and passive pumping through six TMPs and the cryogenic baffle system which operates as a large-scale cryogenic pump. Both pumping processes are included in the effective pumping speed S_{Rn} for radon, measured in ℓ/s. The radon number density increases due to the radon emanation rate (third term) which includes radon emanation both from the NEG pumps and the inner structural surfaces of the main spectrometer. It can be deduced from equation (6.5) to

$$E_{\text{Rn}} = A_{\text{Rn}} \cdot \left(1 + \frac{S_{\text{Rn}}}{V_{\text{MS}} \cdot \lambda_{\text{Rn}}}\right) \ . \qquad (6.6)$$

Finally, the total radon emanation rate E_{tot} is defined by the sum over the individual emanation rates E_{Rn} of the two radon isotopes of interest:

$$E_{\text{tot}} = \sum E_{\text{Rn}} = E_{219\text{Rn}} + E_{220\text{Rn}} \ . \tag{6.7}$$

The background measurement at elevated pressure allows to determine the total radon activity A_{tot} by counting the number of radon spikes within a certain time window or, in a more elegant manner, by measuring the exponential time constant of the inter-arrival times of individual radon spikes, as described in section 6.2.2. However, the individual activities $A_{219\text{Rn}}$ of ^{219}Rn and $A_{220\text{Rn}}$ of ^{220}Rn cannot be resolved by this method so that no conclusions can be drawn from the absolute number of radon atoms emanated into the main-spectrometer volume. As a consequence, a calculation of the individual emanation rates $E_{219\text{Rn}}$ and $E_{220\text{Rn}}$ seems not viable at this time. The total radon emanation rate E_{tot} can be determined as a function of the relative contribution f of ^{219}Rn to the total activity:

$$f = \frac{A_{219\text{Rn}}}{A_{\text{tot}}} \ . \tag{6.8}$$

This leads to

$$E_{\text{tot}} = A_{\text{tot}} \cdot \left[f \cdot \left(1 + \frac{S_{219\text{Rn}}}{V_{\text{MS}} \cdot \lambda_{219\text{Rn}}} \right) + (1 - f) \cdot \left(1 + \frac{S_{220\text{Rn}}}{V_{\text{MS}} \cdot \lambda_{220\text{Rn}}} \right) \right] \ , \tag{6.9}$$

with $A_{219\text{Rn}} = f \cdot A_{\text{tot}}$, $A_{220\text{Rn}} = (1 - f) \cdot A_{\text{tot}}$, and $f \in [0, 1]$. This results in a lower [upper] bound for E_{tot} if $f = 1$ [$f = 0$], since the half-life for ^{219}Rn is significantly shorter than for ^{220}Rn and the estimated effective pumping speeds of both radon isotopes are almost similar with values of $S_{219\text{Rn}} = 3510\,\ell/\text{s}$ and $S_{220\text{Rn}} = 3500\,\ell/\text{s}$ [Mer12a] [Mer13]. Therefore, the emanation rate of ^{220}Rn would dominate, if both radon isotopes had an identical activity.

In the following, the total radon activity A_{tot} (section 6.3.1) and the total emanation rate E_{tot} (section 6.3.2) will be determined by using the background measurement at elevated pressure. Finally, the application of potential correction factors to the activity and emanation (section 6.3.3) will be discussed.

6.3.1 Total Radon Activity

The total radon activity inside the main-spectrometer volume can be determined as a function of the flux-tube volume which is imaged onto the detector. To do so, the measured exponential time constant of inter-arrival times of individual radon spikes for different magnetic-field settings is determined for increasing numbers of detector-pixel rings. The time constant equals the radon activity in the corresponding observable flux-tube volume. The latter can be varied by adjusting the magnetic-field configuration and/or by analyzing sensitive detector areas of different sizes. Figure 6.17 illustrates the results of this approach applied to the background measurement at elevated pressure using the 5.0-G and the 9.0-G settings. The observable flux-tube volume is increased from zero to maximum by successively adding detector-pixel rings to the analysis, starting from the innermost pixels and moving toward outer pixels. Under the plausible assumption that radon α-decays are homogeneously distributed inside the main-spectrometer volume, a linear increase of activity is expected when enlarging the analyzed flux-tube volume according to this method. This is indeed the case for the inner parts of the volume monitored by the bullseye and the five innermost 12-pixel rings of the detector at both magnetic-field settings, as indicated by the corresponding linear fits. In this range, the detector is fully functional and does not suffer from any shadowing effects or non-working pixels, as described in section 4.9. Thus, the distinct flattening of the linear increase of the radon-activity distribution at
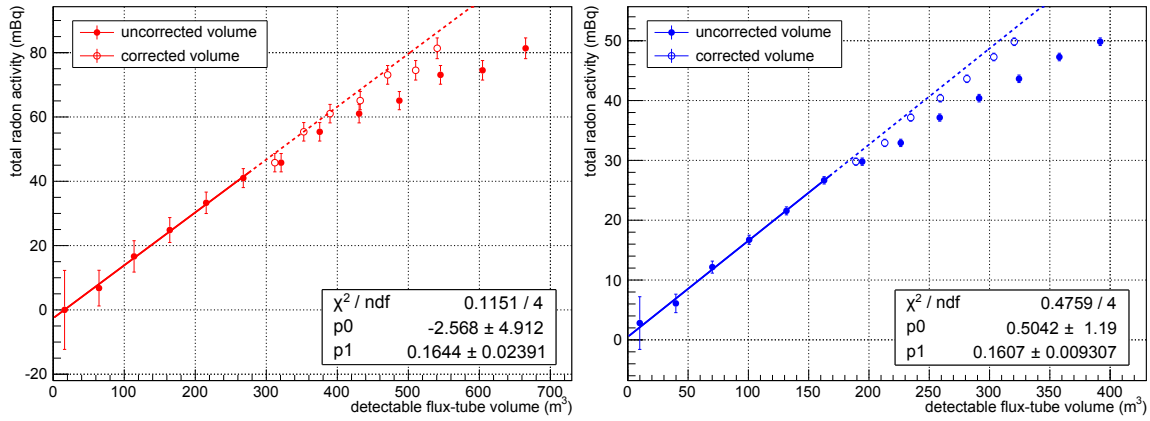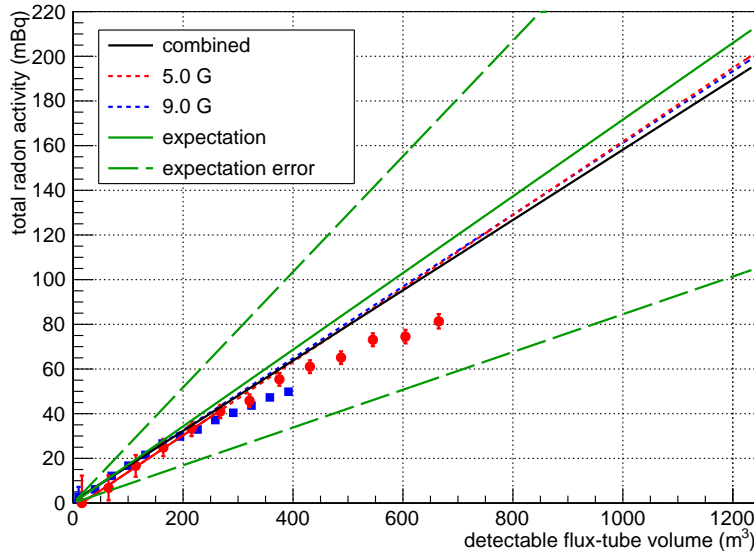
Figure 6.17: Total radon activity as a function of the observable flux-tube volume.
The distribution for the total radon activity is illustrated for a 5.0-G (**left**) and a 9.0-G
(**right**) setting as a function of the observable flux-tube volume. The flux-tube volumes are
calculated from the ring radii at the detector. The first data point of each integral distribution
corresponds to the flux-tube volume observed by the bullseye of the detector, the second data
point to the bullseye plus the innermost 12-pixel ring, and so on. The flattening in the linear
trend in the spectra can be explained by shadowed detector pixels. The bullseye and the
innermost five 12-pixel rings represent a fully working detector so that a linear fit (solid line)
can be applied in the corresponding volume range in order to extrapolate (dashed line) the
total radon activity to larger volumes up to the entire main-spectrometer volume of $\sim 1240\,\mathrm{m}^3$.
The spectra for uncorrected (solid marks) and linearly corrected (blank marks) are illustrated.
In the latter case, a correction was applied for the number of non-functional pixels per detector
ring and the associated flux-tube volumes.

larger volumes can be explained by pixel-ring efficiency factors on the outer detector rings.
When correcting for the number of non-functional pixels per detector ring and for the
associated sensitive flux-tube volumes, the linear trend can be observed up to the larger
volumes. However, still a small discrepancy of the corrected values to the extrapolated
linear increase of the radon activity remains, leading to a small underestimation of the
activity for increasing volumes. This discrepancy can be explained by the width and spread
of radon-induced ring patterns mapped to the detector (see figure 6.15 right). Due to the
cyclotron motion of stored keV-electrons, ionizing collisions can be mapped without losses
only in the inner parts of the flux tube, while the outer flux tube parts are affected in a
more pronounced way based on the flapper shadowing, in particular in view of the required
spike definition. Obviously, the latter effect is more pronounced at the boundary region
between fully mapped and shadowed pixels. Therefore, in view of still ongoing efforts
to obtain full Monte Carlo simulations [Wan14], the extrapolation to the entire main-
spectrometer volume is performed by only using the six innermost detector-pixel rings
and not the entire detector wafer. However, it is important to note that the individual
data points are correlated to each other, since the total radon activity as a function of
the observable flux-tube volume is an integral quantity. Therefore, the individual data
points could include correlated systematic uncertainties, thereby overestimating the stated
uncertainties compared to purely statistical uncertainties.

For the 5.0-G setting, the total radon activity is $A_{\mathrm{tot,\,5G}}(665\,\mathrm{m}^3) = (106.8 \pm 16.6)\,\mathrm{mBq}$ in-
side the observable flux-tube volume and $A_{\mathrm{tot,\,5G}}(1240\,\mathrm{m}^3) = (201.3 \pm 30.1)\,\mathrm{mBq}$ inside the
entire main-spectrometer volume, following the extrapolation described above. Analogous
for the 9.0-G setting, the total radon activity is $A_{\mathrm{tot,\,9G}}(392\,\mathrm{m}^3) = (63.5 \pm 3.8)\,\mathrm{mBq}$ and
$A_{\mathrm{tot,\,9G}}(1240\,\mathrm{m}^3) = (199.7 \pm 11.6)\,\mathrm{mBq}$. For both magnetic-field settings, the determined
total radon activities inside the entire main-spectrometer volume are in excellent agree-
ment in view of statistical uncertainties. In addition, the applied linear fits are consistent
with the fact that no activity is measured at zero volume ($A_{\mathrm{tot}}(0\,\mathrm{m}^3) = 0\,\mathrm{mBq}$) since

Figure 6.18: Total radon activity inside the main-spectrometer volume. The extrapolation of the measured radon activity to the total activity for the entire main-spectrometer volume of $\sim 1240\,\mathrm{m}^3$ (right border) is shown. Apart from the extrapolation using the 5.0-G (dashed-red line) and the 9.0-G (dashed-blue line) settings, a combined analysis using both magnetic-field settings (solid-black line) is shown. This is compared to the expectation based on pre-spectrometer test experiments (solid-green line) including the uncertainty band of the expectation due to limited statistics (dashed-green lines).

$A_{\mathrm{tot,\,5G}}(0\,\mathrm{m}^3) = (-2.6 \pm 4.9)\,\mathrm{mBq}$ and $A_{\mathrm{tot,\,9G}}(0\,\mathrm{m}^3) = (0.5 \pm 1.2)\,\mathrm{mBq}$, taking account of statistical uncertainties. These facts underline the validity and power of this approach to measure the total radon activity. Moreover, it gives strong credit to the model of a homogeneous distribution of α-decaying radon atoms inside the main-spectrometer volume, on the basis of the linear dependence of the radon activity with the sensitive flux-tube volume.

Figure 6.18 summarizes the results obtained here by combining the analysis of both magnetic-field settings. The resulting activities are consistent with the individual results with slightly improved statistical uncertainties with $A_{\mathrm{tot,\,both}}(0\,\mathrm{m}^3) = (0.8 \pm 1.1)\,\mathrm{mBq}$ and $A_{\mathrm{tot,\,both}}(1240\,\mathrm{m}^3) = (195.9 \pm 10.2)\,\mathrm{mBq}$. The expectation trend also displayed originates from pre-spectrometer test experiments [Fra10b] [Goe10]. Their results are extrapolated to the current main-spectrometer setup by scaling the observed radon-induced background events there with respect to the amount of NEG material used and the surface areas of inner structural materials [Mer12a] [Mer13]. In this study, the emanation rates are estimated to be $E_{219\mathrm{Rn,\,NEG}} = (0.12 \pm 0.03)\,\mathrm{s}^{-1}$ for $^{219}\mathrm{Rn}$ emanating from the NEG pumps, $E_{219\mathrm{Rn,\,wall}} = (0.03 \pm 0.03)\,\mathrm{s}^{-1}$ for $^{219}\mathrm{Rn}$ emanating from the inner surfaces, and $E_{220\mathrm{Rn,\,wall}} = (0.08 \pm 0.06)\,\mathrm{s}^{-1}$ for $^{220}\mathrm{Rn}$ emanating from the inner surfaces. Using equation (6.6), these quantities can be transformed into decay rates of $A_{219\mathrm{Rn,\,NEG}}(1240\,\mathrm{m}^3) = (118.1 \pm 29.5)\,\mathrm{mBq}$, $A_{219\mathrm{Rn,\,wall}}(1240\,\mathrm{m}^3) = (29.5 \pm 29.5)\,\mathrm{mBq}$, and $A_{220\mathrm{Rn,\,wall}}(1240\,\mathrm{m}^3) = (65.2 \pm 48.9)\,\mathrm{mBq}$ for the entire main-spectrometer volume. The sum over the individual activities as well as the absolute uncertainties represent the expected radon activity of $A_{\mathrm{tot,\,exp}}(1240\,\mathrm{m}^3) = (212.8 \pm 107.9)\,\mathrm{mBq}$ which is consistent with the measured radon activity. The rather large uncertainty of the estimate results from the highly limited statistics of the pre-spectrometer test experiments [Goe14]. The very good agreement of measured and expected radon decay activities is proof that these processes are well understood and can be adapted to MAC-E filters of different sizes.
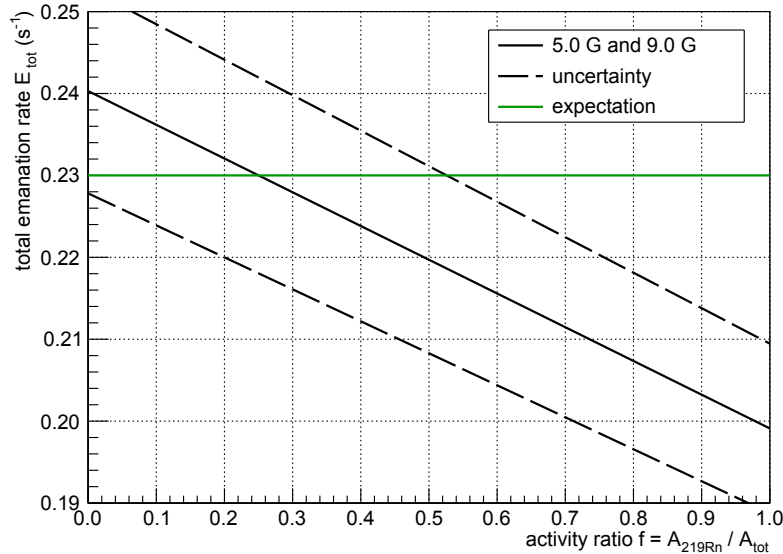
Figure 6.19: Total radon emanation rate inside the main-spectrometer volume.
The total radon emanation rate (solid-black line) with its statistical uncertainty (dashed-black lines) is illustrated as a function of the ratio of emanated ^{219}Rn to the total amount of emanated radon. The measured emanation rate is in excellent agreement with the expectation (solid-green line).

6.3.2 Total Emanation Rate

The total radon activity of $A_{\text{tot, both}}(1240\,\text{m}^3) = (195.9 \pm 10.2)\,\text{mBq}$ for the entire main-spectrometer volume, obtained from background measurements at elevated pressure using a combined analysis for the 5.0-G and 9.0-G data, can be transformed into a total radon emanation rate by varying the unknown ratio $f = A_{219\text{Rn}}/A_{\text{tot}}$ of emanated ^{219}Rn relatively to the total amount of emanated ^{219}Rn and ^{220}Rn, according to equation (6.9). Figure 6.19 shows the corresponding analysis. Due to the fact that the individual activities of ^{219}Rn and ^{220}Rn cannot be resolved, the total radon emanation rate is given as a function of the relative contribution f of ^{219}Rn to the total activity. Varying f within the boundaries $f \in [0, 1]$, gives total emanation rates ranging from $E_{\text{tot, min}} = 0.2036(35)\,\text{s}^{-1}$ to $E_{\text{tot, max}} = 0.2458(42)\,\text{s}^{-1}$. These quantities are in excellent agreement with the expectation of $E_{\text{tot, exp}} = 0.23(12)\,\text{s}^{-1}$ [Mer13]. However, it should be noted that the uncertainty of this expectation is relatively large due to limited measurement statistics. Therefore, the intersection of $E_{\text{tot, exp}}$ with the data band cannot be used to constrain f. As a consequence, the relative amounts of ^{219}Rn and ^{220}Rn to the total radon activity and emanation rate cannot be resolved.

6.3.3 Correction Factors

In principle, the calculated total radon activity and emanation rate inside the main-spectrometer volume are affected by specific mechanisms occurring in a MAC-E filter and are rather underestimated. Therefore, the numbers quoted above represent only lower limits. In order to obtain the actual radon activity and emanation rate, they have to be corrected by the following factors.

Magnetic-field asymmetry

Due to the non-symmetric magnetic-field configuration for both spectrometer hemispheres with the maximum field at the pinch magnet limiting the maximum acceptance angle, only

a fraction of 40 % of all generated secondary electrons will leave the main spectrometer toward the detector system, while the remainder propagates toward the upstream side of the experiment and is lost for detection [Mer12a]. This intentional magnetic-field asymmetry is a passive background-reduction technique of benefit also used for the later neutrino-mass measurements. Therefore, a radon spike consisting of 10 secondary electrons in the flux tube is actually observed as a 4-event radon spike on average at the detector. Nevertheless, in this example, the radon spike would still be detected as a radon spike in most cases. As outlined earlier, a single radon spike has to contain a sufficient number of electrons ($N \geq 3$) and the time difference between these electrons has to be shorter than the limit of the inter-arrival time cut ($\Delta t \leq 0.2$ s). In this case, on average a number of at least 8 secondary electrons in the flux tube is required to ensure the detection of a radon spike with $N \geq 3$ events. This represents a conservative bound where no obvious corrections for radon activity and emanation rate have to be applied to first order. However, for cases with low electron multiplicities, a precise correction factor without detailed Monte Carlo simulations is quite challenging. In order to experimentally obtain a more precise estimate of this correction factor, background measurements at elevated pressure should be performed during the upcoming second SDS commissioning phase in a configuration with magnetic-field symmetry ($B_{\text{PS2}} = B_{\text{PCH}}$) applying similar fields to the PS2 and PCH magnet. Even a reversed magnetic-field asymmetry ($B_{\text{PS2}} > B_{\text{PCH}}$) could be used. A comparison between these settings will allow to determine a precise correction factor for smaller radon-spike multiplicities.

Low-multiplicity radon spikes

Due to the definition of a radon spike to consist of a minimum number of events ($N \geq 3$), the relative number of 1-event and 2-event radon spikes and their absolute contributions to accidental single events is unknown. Each missing low-multiplicity radon spike leads to a systematic underestimation of radon activity and emanation rate inside the main-spectrometer volume. In figure 6.13, a potential extrapolation to lower multiplicities is illustrated based on a power-law fit $y(N)$. The associated correction factor κ necessary to transform the measured radon activity A_{meas} into the actual radon activity A_{real} can be calculated via

$$A_{\text{real}} = \kappa \cdot A_{\text{meas}} \quad \text{with} \quad \kappa = \frac{\int_{N=1}^{\infty} y(N)\mathrm{d}N}{\int_{N=3}^{\infty} y(N)\mathrm{d}N} \ . \tag{6.10}$$

This results in a correction factor of $\kappa_{\text{power-law}} = 2.82(6)$ for the power-law fit. The same factor applies to the actual radon emanation rate since it linearly scales with the activity ($E_{\text{tot}} \sim A_{\text{tot}}$) according to equation (6.9) and thus with the identical correction factor ($E_{\text{tot}} \sim \kappa$). Using this extrapolation, a total radon activity of $A_{\text{tot, real}} \approx 0.55$ Bq is deduced, and a total radon emanation rate ranging from $E_{\text{tot, real}} \approx 0.55 - 0.68$ s^{-1} as a function of the relative fraction f of ^{219}Rn to the total amount of emanated radon. However, as stated above, this extrapolation is afflicted with large uncertainties due to effects arising from a new radon background class, originating from shell-reorganization electrons. A more precise estimate of the total radon activity and emanation rate will only be possible on the basis of detailed Monte Carlo simulations.

Undetectable radon spikes

Monte Carlo methods will also be required to tackle the issues of undetectable radon-induced events. The first effect leading to an underestimation of the total radon activity and emanation rate is defined by the magnetic-field asymmetric described above. The probability that a radon spike with N electrons only leaves the main spectrometer in the direction of the source is $P = 0.6^N$. For a 3-event radon spike, this probability is relatively

large with $P = 21.6\,\%$. Likewise, at least 10 events in a spike are necessary to drop below the 1-% probability limit. The second effect is defined by the cyclotron radius of the electron and the location of its production. High-energy electrons generated outside of the sensitive flux-tube volume and thus close to inner surfaces will hit the inner structural materials and are lost for detection. Especially high-energy primary electrons with large cyclotron radii are affected, so that the associated radon α-decay remains completely undetected. A third effect influencing the present analysis is based on those electrons which undergo a non-adiabatic process shortly after creation, thereby also underestimating the actual radon activity and emanation rate. As the corresponding radon spikes of these effects are invisible for the detector, experimental access is quite challenging.

Radon spikes overlapping in time

As discussed in section 6.2.2, the probability that two radon spikes overlap in time is of the order of $\sim 1\,\%$ for the background measurements at elevated pressure performed at 5.0 and 9.0 G, since the radon activity and the mean duration of a radon spike take on rather small values. In this case, the effect of missing radon spikes due to a certain pile-up effect of radon spikes overlapping in time is of minor importance so that the corresponding reduction of the measured radon activity compared to the actual value is negligibly small.

6.4 Background Composition

As described in section 6.2, the background composition can be determined in the framework of measurements at elevated pressure by applying an inter-arrival time cut of $\Delta t_{\mathrm{cut}} = 0.2\,\mathrm{s}$. This allows to differentiate between highly correlated radon-induced spike events and approximately Poisson-distributed single events originating from electrons induced by cosmic rays, environmental radiation, intrinsic radioactivity, and field emission. However, the optimized setting of this cut strongly depends on the average storage and cool-down time of trapped electrons and thus on the vacuum conditions and the absolute pressure in the main-spectrometer volume. Therefore, a distinct separation of background classes seems not viable for pressures better than $\sim 10^{-10}$ mbar as expected for later neutrino-mass measurements (see figures 6.6 and 6.7). Due to the characteristic magnetron motion of stored high-energy electrons, radon-induced secondary electrons are not only correlated in time but also in space. At elevated pressure, this correlation results in the above described characteristic ring-shaped patterns appearing on the detector within a relatively short time interval. This characteristic event topology arises when low-energy secondary electrons escape from the magnetic bottle: their storage time is short, their point of creation is on the magnetron ring of the stored high-energy primary electron, and they undergo the same magnetron drift as the primary before their release. At normal pressure, this spatial correlation smears out due to the following reasons:

- In an excellent ultra-high vacuum, there are typically several radon-induced primary electrons being magnetically trapped at any point in time. inside the main spectrometer. Accordingly, they produce numerous low-energy secondary electrons on different magnetron paths, which when escaping arrive at the detector to produce a smeared out hit pattern. The affiliation of a secondary electron to a corresponding primary electron seems not viable in the first approximation. However, due to the radial resolution of the detector, the secondary electrons could, in principle, be assigned to their primary electron via the imaged magnetron radius. As shown in figure 6.15, the average width of a measured radon-induced ring is about $4-5$ detector rings due to the distorting cyclotron motion of the high-energy primary electron, thus significantly limiting this approach.

- Depending on the magnetic-field setting, the contribution of single-event related background is of equal size to the contribution of radon-induced background due to the fact that the main spectrometer has to be operated with a single wire-layer potential configuration at present. As a result, correlated radon-induced events do not only overlap in time but also are interspersed with a different background class.

As a consequence, individual radon-induced events cannot be differentiated from events originating from other background classes on an event-by-event basis.

However, the background composition of a specific measurement can be determined even at normal operating pressure by a statistical method: this is based on the spatial distances of individual events instead of the inter-arrival time spectrum. Here, the spatial distance between two subsequent events arriving at the detector is defined as the distance Δring being observed in detector rings.

Figure 6.20 displays corresponding Δring distributions for single-event related background events. In this special case, the events are taken from elevated-pressure measurements where they appear as single events with a minimum time difference of $\Delta t > 0.2\,\mathrm{s}$ to each other, as well as independently from normal-pressure measurements using an operating LN2 cooled baffle system where radon-induced background is strongly suppressed. The distributions are normalized to unit area to allow for better comparison. Considering the statistical scatter, the distribution of these background classes follows a linear trend for Δring ≥ 1, as indicated by the linear fit. At Δring $= 0$, the count rate significantly drops by a factor of ~ 2 compared to the maximum rate reached at Δring $= 1$. Such a trend is expected for both elevated-pressure and normal-pressure LN2-baffle data since the events arise from the same background classes, i.e. from cosmic rays, environmental radiation, intrinsic radioactivity, and field emission. It should be noted that this is true also for different magnetic-field settings.

The observed trend can be phenomenologically explained by events arriving randomly distributed on the detector, as expected in case of magnetic projection of the analyzing plane onto the radially segmented detector wafer. The characteristic drop in rate by a factor of ~ 2 at Δring $= 0$ is trivially caused by the radial segmentation of the detector wafer, since there are twice as many possibilities to obtain a value of Δring $= 1$ than Δring $= 0$ for randomly distributed events, except for events detected on the bullseye and the outermost ring. Therefore, this factor is actually slightly lower than 2. This is verified by a simulation where randomly distributed events in the analyzing plane are magnetically projected onto the detector wafer for different magnetic-field settings. For the 9.0-G setting, figure 6.21 illustrates the comparison between the Δring distributions of simulated events and measured single events at elevated pressure. The distributions are scaled to the same integral. They show good agreement, especially when correcting for unusable detector pixels, which results in a significant improvement for the rate at a large Δring $= 12$. The residuals between measurement and simulation show a maximum deviation of 2σ. As a result, it can be considered that the characteristic distribution of the Δring spectrum for single-event related background events is well understood on a statistical basis.

Similarly, figure 6.22 displays the Δring distribution for radon-induced background events. The data for these events were obtained from elevated-pressure measurements where they appear as spike events with a maximum inter-arrival time of $\Delta t \leq 0.2\,\mathrm{s}$, as well as from normal-pressure measurements with non-operating warm baffle system by subtracting corresponding data taken with a LN2 cooled baffle system. Here, the spectra are not normalized. Considering the statistical scatter, the distributions follow exponential trends for Δring ≥ 1 (note the logarithmic scale), while they transition into linear trends for larger Δring values. In contrast to the single events, both the shape of these distributions and
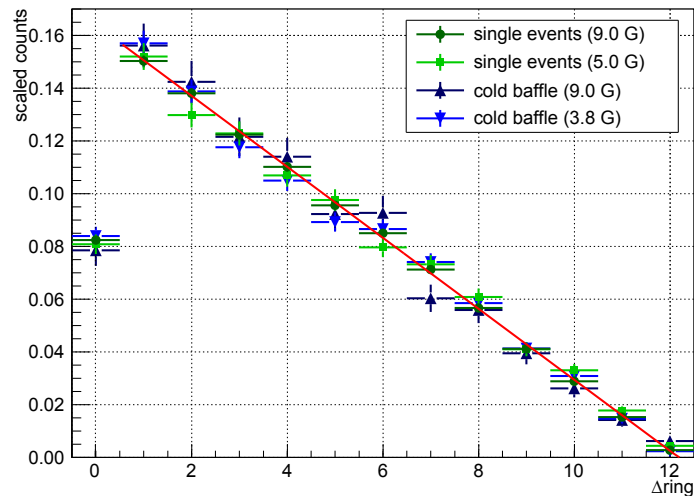
Figure 6.20: Δring distribution for single-event related background. The spectra are normalized to unit area and are described by a linear fit (red-colored line), which excludes Δring = 0.
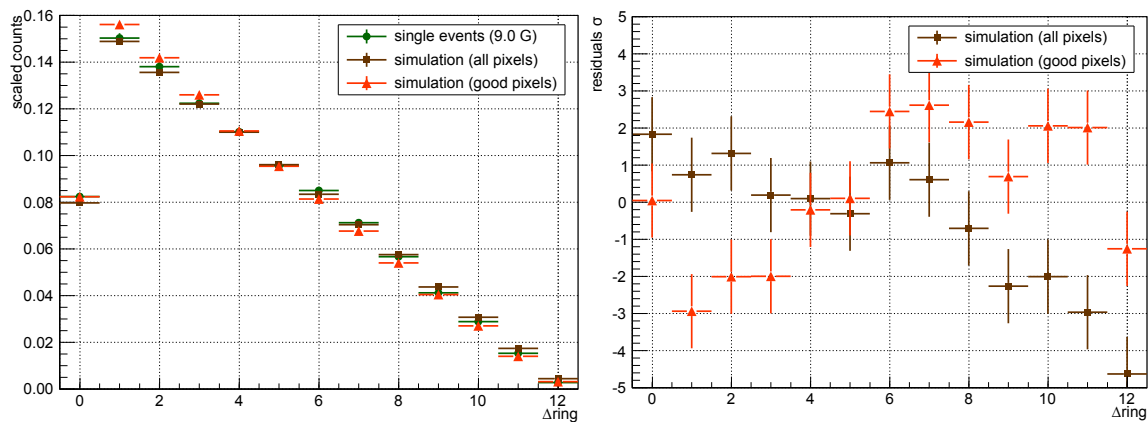
Figure 6.21: Δring distribution for measured and simulated single events. In the Δring spectrum (**left**), the measured rates (green) are compared with simulated events both for all pixels (brown) and for mapped pixels only (orange) together with the corresponding residuals to the data (**right**).
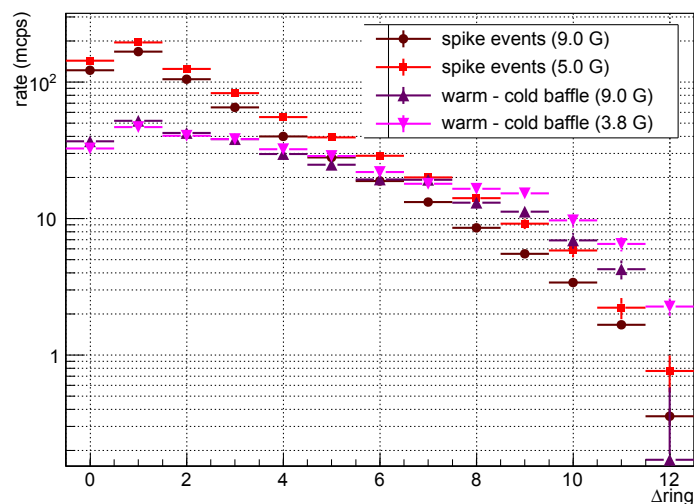
Figure 6.22: Δring distribution for radon-induced events. The spectra are not normalized but display an exponential trend for small Δring values. Note the logarithmic scale.

the rate contribution at Δring $= 0$ depend on the vacuum conditions and the pressure inside the main-spectrometer volume. The exponential increase for smaller Δring values is more dominant at elevated pressure, implying that this describes the spatial correlation of radon-induced background events. Interestingly, this exponential behavior is clearly visible even for normal operating pressure. These facts allow to phenomenologically explain the observed trends: at low Δring values, the spatial correlation of radon-induced background dominates the exponential part, while at larger Δring values randomly distributed radon-induced events are responsible for the linear trend. Here, the vacuum conditions are important but not the adjusted magnetic-field setting.

It is this significant difference in the shape of the observed Δring distributions between single and radon events which allows to empirically distinguish between the two background classes. In doing so, the relative contributions of both background classes for a specific measurement can be determined even at normal pressure. For this purpose, a weighted sum of the Δring spectra is used both for single and radon events. The weighting factors account for the run times of the individual measurements. Since this approach is purely empirical, only recorded data and no simulated events are used. However, data from radon-induced spike events at elevated pressure is not used because of the background investigation at normal pressure. The integrals of the Δring distributions represent free parameters and correspond to the absolute contribution of each background component. The sum of both integrals must then equal the integral of the Δring distribution of the background measurement being examined. The integrals are varied while the relative shapes of the Δring spectra remain unaffected. For each variation the χ^2 value is calculated as a goodness-of-fit indicator [Pea00] via

$$\chi^2 = \sum_i \frac{(r_i^{\mathrm{exp}} - r_i^{\mathrm{inp}})^2}{r_i^{\mathrm{inp}}} \ , \tag{6.11}$$

where r_i^{exp} are the measured Δring rates of the background measurement under investigation at normal pressure, r_i^{inp} the added input Δring rates of single and radon events, and Δring $= i$ with $i \in [0, 12]$. This empirical method is applied to normal-pressure background measurements with a non-operating warm baffle system in order to separate different background classes on this statistical basis .

The comparisons of the measured and the best-fit modeled Δring distributions are illustrated in figures 6.23 (3.8 G), 6.24 (5.0 G), and 6.25 (9.0 G) for different magnetic-field settings, including the associated residuals. The corresponding χ^2 minimization curves are shown as a function of the fraction for single events in figures 6.26 (3.8 G), 6.27 (5.0 G), and 6.28 (9.0 G). The contribution of each background class of course varies with the magnetic-field setting, since the magnetic shielding factor is reduced for a decreasing field in the analyzing plane, while the observable magnetic flux-tube volume increases. Thus, at 3.8 G, the best-fit model is achieved with a relative background composition of 58 % single and 42 % radon events, at 5.0 G with 60 % single and 40 % radon events, and at 9.0 G with 41 % single and 59 % radon events. However, the associated χ^2 values around the minima are not symmetric, especially at the 9.0-G setting, since the statistics for cold-baffle measurements as a major input parameter is strongly limited. For larger fractions of single events, the corresponding χ^2 values increase significantly. In these parameter regions, radon-correlated Δring distributions are strictly limited by the fit so that the characteristic exponential trends in the Δring spectra cannot further be described in an acceptable manner, resulting in poor χ^2 values. A similar but less distinct observation can be made for small fractions of single events where the radon-induced background compositions are overestimated. In these cases, the linear trends in the Δring spectra of the background measurements under examination are not well described, although the Δring distributions for radon-induced events implicate a linear behavior for large Δring values.
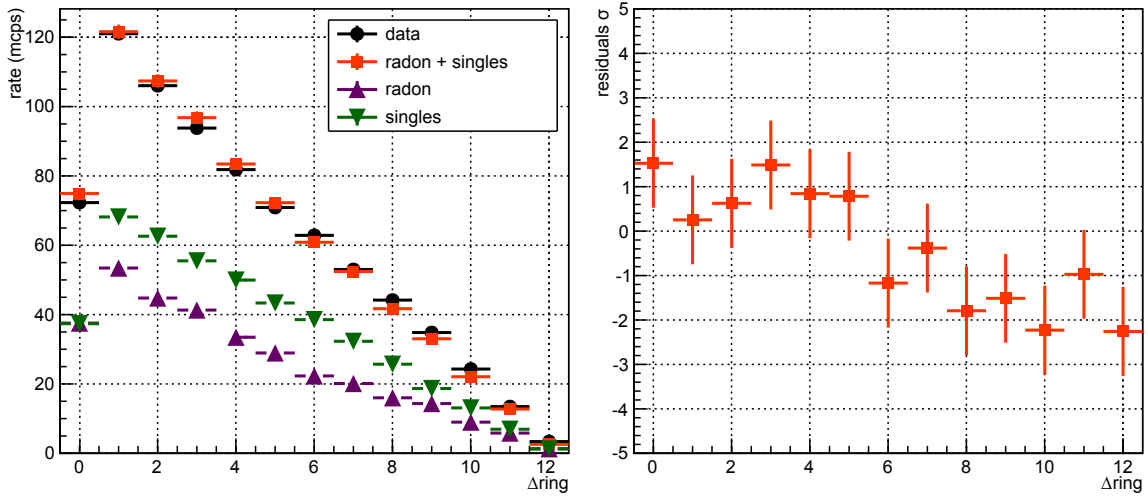
Figure 6.23: Optimized fit to the background composition at 3.8 G, yielding 58 % single and 42 % radon events with a minimum $\chi^2/\text{ndf} = 2.03$. In the Δring spectrum (**left**), data (black) is compared to the model (orange) with the residuals shown (**right**).
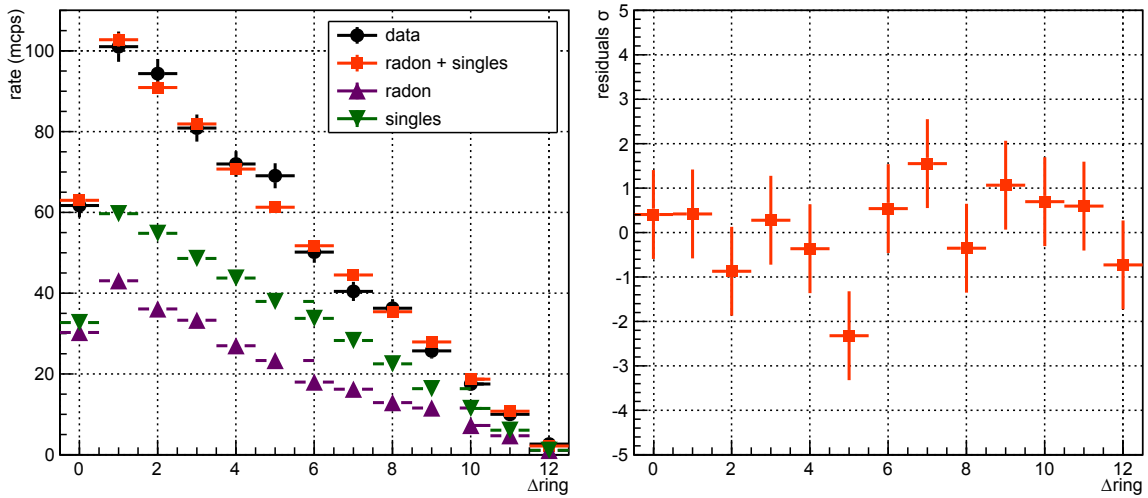

Figure 6.24: Optimized fit to the background composition at 5.0 G, yielding 60 % single and 40 % radon events with a minimum $\chi^2/\text{ndf} = 1.00$. In the Δring spectrum (**left**), data (black) is compared to the model (orange) with the residuals shown (**right**).
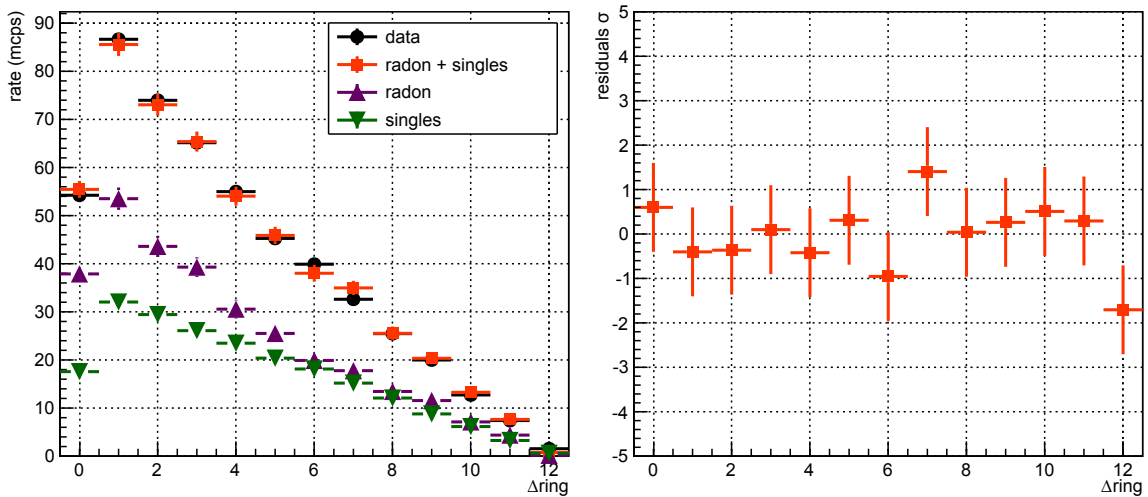
Figure 6.25: Optimized fit to the background composition at 9.0 G, yielding 41 % single and 59 % radon events with a minimum $\chi^2/\text{ndf} = 0.60$. In the Δring spectrum (**left**), data (black) is compared to the model (orange) with the residuals shown (**right**).
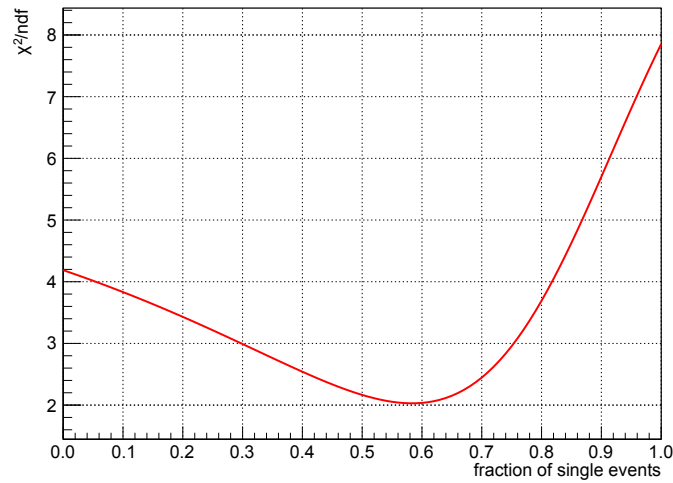
Figure 6.26: Minimization curve for χ^2 as a function of single-event fraction at 3.8 G. The minimum is achieved for a fraction of 58% single events at $\chi^2/\mathrm{ndf} = 2.03$.
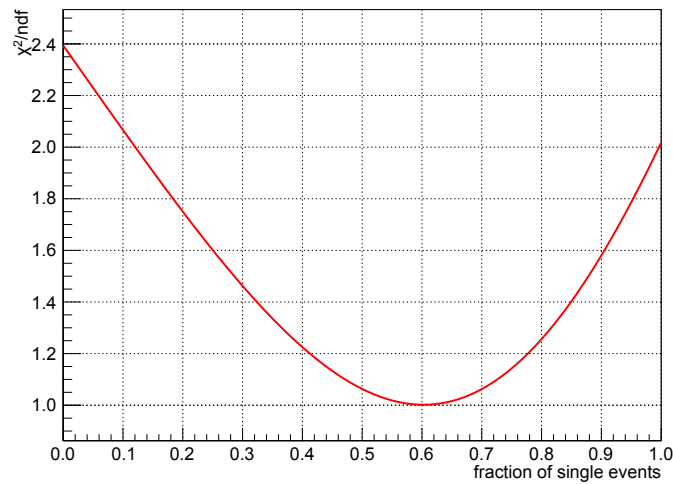
Figure 6.27: Minimization curve for χ^2 as a function of single-event fraction at 5.0 G. The minimum is achieved for a fraction of 60% single events at $\chi^2/\mathrm{ndf} = 1.00$.
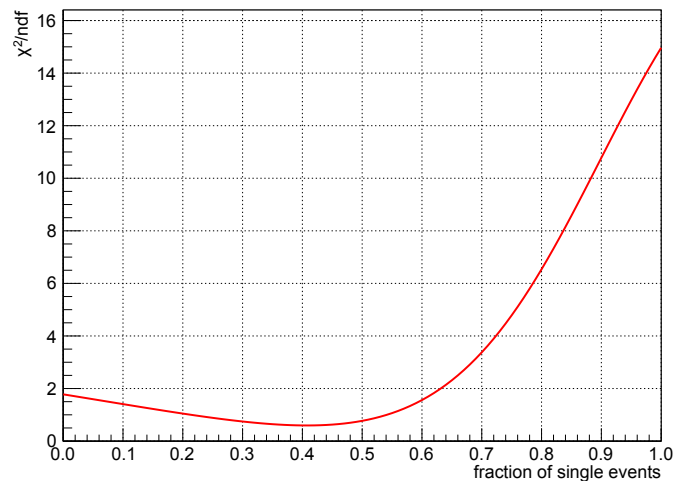
Figure 6.28: Minimization curve for χ^2 as a function of single-event fraction at 9.0 G. The minimum is achieved for a fraction of 41% single events at $\chi^2/\mathrm{ndf} = 0.60$.

The results of this empirical model based on the statistical parameter Δring can be compared with the previously described results at different configurations. Table 6.1 lists the measurements performed and their associated settings. At 3.8 G [9.0 G], the ratio of background rates for measurements with cold and warm baffle at normal pressure indicates a single-event contribution of $(60.4 \pm 0.8)\,\%$ $[(42.3 \pm 0.9)\,\%]$, which is in good agreement with the modeled contribution of 58 % [41 %]. At 5.0 G, no direct benchmark is available, as no cold-baffle measurements were performed at this magnetic-field setting. However, an elevated-pressure measurement allows to determine the acquired single-event rate to be $(409.2 \pm 5.2)\,\text{mcps}$, resulting in a single-event contribution of $(61.8 \pm 1.2)\,\%$. Again, this value is in good agreement with the modeled contribution of 60 %, although no direct input exists for the empirical model at this magnetic-field configuration, i.e. Δring distributions for single events at normal pressure via cold-baffle measurements. The agreement proves the robustness of this statistical approach.

As a conclusion, it can be outlined that the Δring distribution is a powerful tool to separate different background event classes on a statistical basis. In particular, it allows to determine the relative contributions of radon-induced and single-event related backgrounds for excellent ultra-high vacuum conditions, where event-by-event separation as at elevated pressure is no further possible. In general, the Δring distribution enables to examine the relative background composition independently of the magnetic-field settings and the vacuum conditions. It will thus be of great benefit for the upcoming SDS commissioning phases and neutrino-mass measurements to investigate the efficiency of both the baffle system and the double wire-layer and to monitor the background composition in near real-time.

6.5 Radon-Spike Scaling

At elevated pressure, the residual gas was dominated by argon at an absolute pressure of $p \approx 10^{-8}\,\text{mbar}$. At normal pressure, the residual gas species were, however, dominated by hydrogen and water at $p \approx 10^{-10}\,\text{mbar}$. Radon-induced spikes of elevated-pressure measurements can thus be scaled in order to extrapolate the radon-induced background from elevated to normal pressure. The distributions of single-event related background remain unaffected, since the background processes originating from cosmic rays, environmental radiation, intrinsic radioactivity, and field emission proceed on time scales much faster than the time scale for ionization, and are thus pressure-independent. For this scaling, individual radon spikes are identified again via the inter-arrival time cut of $\Delta t \leq 0.2\,\text{s}$ and $N \geq 3$, as described in section 6.2. Analogously, single events are selected via $\Delta t > 0.2\,\text{s}$.

The scaling of radon spikes is performed under the following assumptions, taking into account differences in vacuum pressure and electron cross sections with residual gas:

- The activity of emanated radon remains unaffected, so the number of radon α-decays and primary electrons remains constant.

- Since argon and hydrogen have similar ionization energies [Nat13], each primary electron is assumed to produce the same number of low-energy electrons.

- As the electron storage time scales linearly with the absolute vacuum pressure [Fra10b] [Wan13a], the duration of a radon spike is expected to be enlarged by a factor of ~ 100, implying that the time differences between spike events within an individual radon spike have to be increased accordingly at normal pressure.

- The interaction cross section defines the probability that a stored electron interacts with the residual gas species, e.g. through scattering or ionization. A smaller cross section thus implies that a primary electron has to be stored over longer time scales
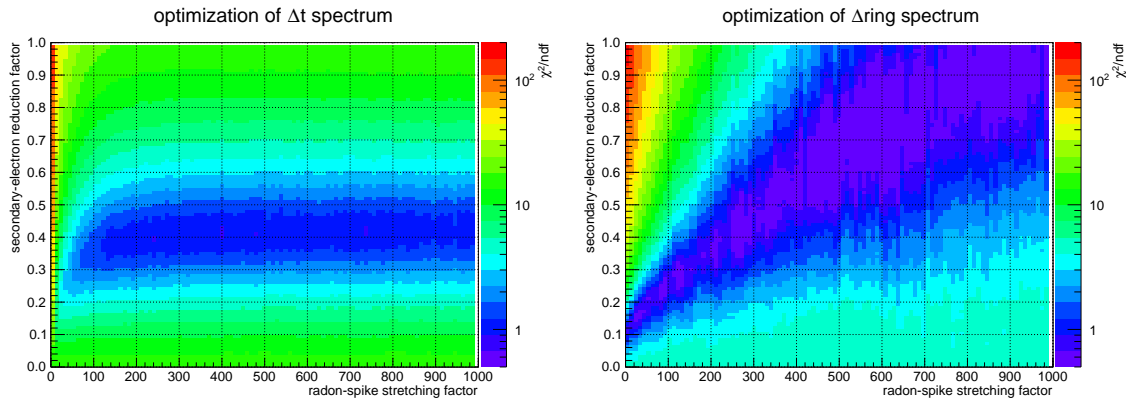
Figure 6.29: Radon-spike scaling. Radon spikes from elevated-pressure measurements are scaled to normal pressure by varying the radon-spike duration (via a *radon-spike stretching factor*) and the relative fraction of secondary electrons remaining in each radon spike (via a *secondary-electron reduction factor*) as free parameters. As goodness-of-fit indicator, a χ^2 test is applied to the scaled inter-arrival time spectra (**left**) and the Δring distributions (**right**), allowing to determine the scaling factors.

in order to produce the same number of low-energy secondary electrons as for a gas species with a larger cross section at the same pressure. Since the electron cross section for argon [Str96] [JKR06] is larger than for hydrogen [Taw90] in the relevant energy interval for radon-induced electrons [Bar95], this fact directly influences the scaling factor with which the radon-spike duration has to be stretched.

- Due to non-adiabatic effects for long cool-down times [Wan13a], the stored primary electron can escape the main-spectrometer trap although its energy would be sufficient to produce further low-energy secondary electrons via ionization of residual gas. This effect can lead to a significant reduction of secondary electrons generated at low pressures in general.

These effects can be taken into account by varying the radon-spike duration and the relative fraction of secondary electrons as free parameters. The first factor can easily be implemented by increasing the time differences between events within each radon spike, while the second factor can be realized by sorting out secondary electrons from all radon spikes, starting from the last event in a radon spike to earlier events. The scaled elevated-pressure model is then compared to the normal-pressure measurement by applying a χ^2 test [Pea00] as goodness-of-fit indicator to the inter-arrival time spectra and the Δring distributions. This was performed for a 9.0-G setting based on the increased measurement time for this configuration.

Figure 6.29 illustrates the corresponding results in the form of two χ^2-optimization curves. The optimum agreement for the observed inter-arrival time spectrum at normal pressure is achieved by an enlargement of the radon-spike duration by a factor of at least ~ 200 and by a reduction of the number of secondary electrons in each radon spike to $\sim 40\,\%$. The radon-spike stretching factor is not well constrained, only a lower bound can be established. In contrast, the secondary-electron reduction factor is significantly narrowed. This results in an optimization band for the corresponding scaling factors. As for the corresponding optimization for the Δring distribution, the χ^2 test results in a broad goodness-of-fit range with a linear dependence of both scaling factors. A constant number of secondary electrons requires a larger radon-spike stretching factor in order to achieve good agreement. Both optimization curves can be combined to narrow the allowed regions of the scaling factors between elevated and normal pressure. In the best-fit case, the radon-spike stretching factor is ~ 250 with a secondary-electron reduction factor of ~ 0.4, resulting in a generic
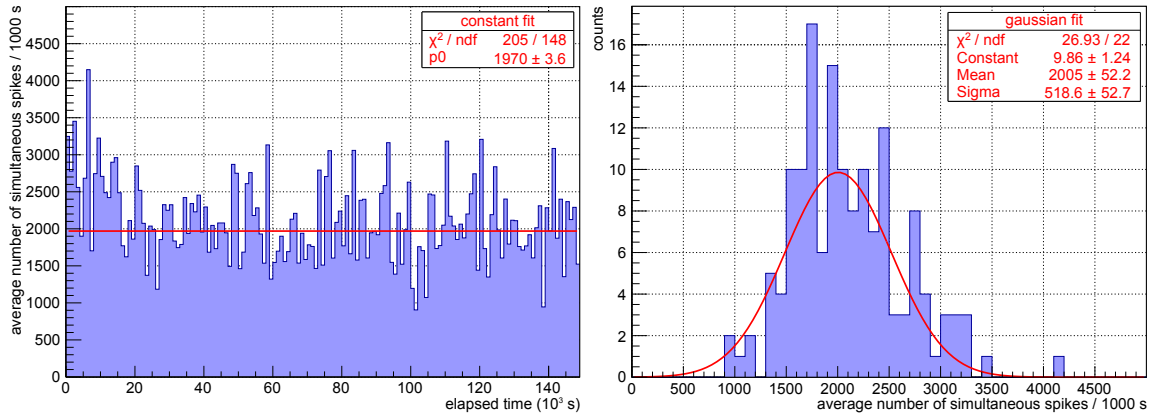
Figure 6.30: Simultaneously stored radon-induced spikes at normal pressure. The temporal trend (**left**) and its projection distribution (**right**) characterize the number of simultaneously stored radon-induced spikes at normal pressure at the 9.0-G setting. The average number is given within a time interval of 1000 s.

scaling factor of $\sim 250 \times 0.4 = 100$. This value is consistent with the expectations. A possible application of this scaling is the investigation of radon-spike characteristics at normal pressure which can be used for detailed modeling of the actual background in order to perform a reasonable neutrino-mass sensitivity evaluation [Kle14]. As an example, figure 6.30 shows that about two high-energy electrons per second are simultaneously stored inside a 9.0-G flux-tube volume. Under these conditions, the most probable spike duration is increased by a factor of ~ 100 to ~ 6.4 s.

6.6 Conclusion

The LN2 cooled baffle system allows to significantly reduce the background rate via cryogenic sorption of radon atoms to a level at which only a very limited number of radon-induced events are detected. While the present measurements have shown that the baffle system is highly efficient, the actual efficiency in removing emanated radon atoms from the sensitive flux tube is difficult to estimate due to the still unknown experimental data for ^{219}Rn and ^{220}Rn emanation from various sources, such as the NEG pump and the vessel surface. During the upcoming second SDS commissioning phase the baffle system will be continuously operated at elevated and normal pressure. In the former case, individual radon-induced events can be resolved − if still present − with the assistance of the well-understood detector properties and analysis methods developed here. As described in this chapter, these approaches were successfully applied to data taken with a non-operating warm baffle system. The methods allow to determine important characteristics of radon-induced background events, such as their temporal and spatial distributions, the average number of generated secondary electrons, or the average storage time of a primary electron. In addition, the analysis showed that radon atoms are homogeneously distributed inside the main-spectrometer volume after emanation from the NEG material and the inner surfaces. The measured total radon activity of $A_{tot} \approx 0.2$ Bq and emanation rate of $E_{tot} \approx 0.20 - 0.25$ s^{-1} follow the extrapolations of pre-spectrometer test experiments. Pending quantitative Monte Carlo simulations [Wan14], these quantities are interpreted as lower bounds. *Kassiopeia* will allow to perform extensive electron-tracking simulations with a detailed radon model at elevated pressure, using electron cross sections for argon in order to examine the relative fraction of undetectable radon events. In this work, it could be demonstrated that the results obtained at elevated-pressure vacuum conditions can be scaled to standard operating mode by using different statistical approaches. The novel implementation of the Δring distribution illustrates that the relative background

composition is quantifiable on a statistical basis at normal pressure. Comparisons show that the modeled contributions of the two background classes, radon-induced and single-event related backgrounds, are in excellent agreement with the actual background rates and patterns. This makes the Δring distribution a powerful statistical tool to investigate spatial correlations between individual background events, complementing the inter-arrival time spectrum for temporal correlations. Moreover, the scaling of radon-induced events allows to model the background characteristics at standard operating mode.

Field Electron Emission and Hydrogen Anions

Field electron emission is commonly observed in experiments in which solid metal surfaces are elevated to a negative high potential under vacuum conditions. In case of the KATRIN spectrometer, surface roughness, irregularities, and sharp edges of the inner wire-electrode system and its support structures have to be considered to be regions where high electric fields occur within a narrow volume. This could result in a non-negligible emission rate of low-energy electrons from the structural materials via the tunneling effect (section 7.1). The first SDS commissioning phase indicated indeed that such electrons are a major source of background in case of non-standard electric-field configurations with field strengths well above the ones required for a successful neutrino-mass determination (section 7.2). Similar observations were made at the detector system (section 7.3). A side benefit of these measurements performed beyond the standard operating mode and with asymmetric magnetic field is to determine the detector alignment relative to the main-spectrometer axis via the detection of field-emission induced electrons from the inner wire-electrode structures (section 7.4). Field electron emission under vacuum conditions is also a likely source of hydrogen anions which allows to measure the thickness of the insensitive detector dead layer (section 7.5).

7.1 Field Electron Emission in MAC-E Filters

In general, field electron emission describes the emission of low-energy electrons with a relatively narrow starting energy window from negatively charged electrodes, induced by strong electrostatic fields. Typically, this emission starts to occur for field strengths above 10^7 V/m while it becomes a dominant effect above $\sim 10^8$ V/m. However, experiments commonly suffer from significant emission rates already for weaker fields of $\sim 10^6$ V/m. This results from complications in the determination of the absolute field strength, as this depends strongly on the geometry of the experimental setup. In this regard, unpolished areas with surface roughness, minute irregularities, and sharp spikes of the elevated regions typically increase the actual local field strength F significantly compared to the expected macroscopic field F_{mac}. This is described by the field-enhancement factor γ

$$F = \gamma F_{\mathrm{mac}} \; , \tag{7.1}$$

which is basically defined by the shape of the elevated object [FN28] [For12].

Field electron emission is a form of quantum tunneling [Raz03] from solid to vacuum. The principle is illustrated in figure 7.1. Due to the intrinsic potential of the lattice, the free
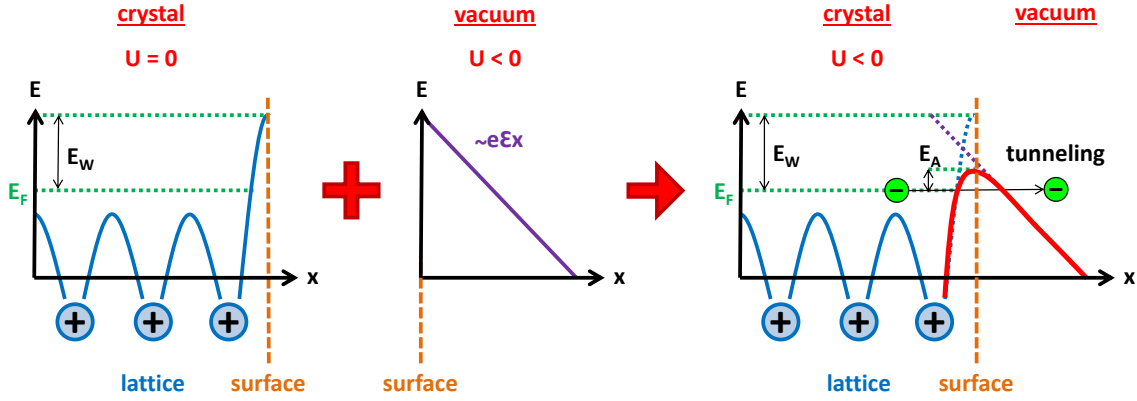
Figure 7.1: Principle of field electron emission. Left: Electron energy levels inside a crystal. If no external voltage ($U = 0$) is applied to the crystal, bound electrons with energies at the Fermi energy E_F have to overcome the potential barrier at the metal surface in order to be extracted as free electrons into the vacuum. The required energy for this process is described by the work function E_W. **Middle: Electron energy outside a crystal.** If a negative electrostatic potential ($U < 0$) is applied to the crystal, the resulting electric field $\mathcal{E}$ is displayed as a function of the distance x to the solid surface. **Right: Electron tunneling.** Due to the applied field, the potential barrier is lowered and narrows, leading to a reduced effective work function of $E_A < E_W$. Bound electrons can overcome the work function by tunneling through the potential barrier into the vacuum. Sketches inspired by [Din14].

electron gas in the metal is bound to the solid, parametrized by the work function E_W which is required to leave the associated material. If a negative potential is externally applied to the crystal, the potential energy of a free electron located outside of the solid is given by $E = e\mathcal{E}x$, where $\mathcal{E}$ denotes the electric field strength and x the approximate electron distance to the surface. In case of a very strong negative potential, the resulting barrier at the crystal surface is significantly lowered and narrowed, thereby allowing electrons to tunnel from the crystal into the vacuum. Therefore, the effective work function is reduced to $E_A < E_W$. As described in section 6.2.1, the low-energy electrons from field emission drift into the sensitive magnetic flux-tube volume via radial $\vec{E} \times \vec{B}$ and $\vec{\nabla}|\vec{B}| \times \vec{B}$ drift motions to produce background in the same energy window as signal electrons. Apart from secondary electrons generated by cosmic rays, environmental radiation, and intrinsic radioactivity, field-emission induced electrons can contribute noticeably to the single-event related background.

The theoretical formalism of field electron emission is based on a Fowler-Nordheim (F-N) type equation [FN28]. Its elementary form describes the local emission-current density J (in A/m^2) as a function of the local surface electric field F (in V/m) and is given by

$$J = \frac{a}{\phi}F^2 \exp\left(\frac{-b\phi^{3/2}}{F}\right) \tag{7.2}$$

[For12], with the unreduced local thermodynamic work function ϕ (in eV) of the elevated material ($\phi \approx 4.4\,\text{eV}$ for stainless steel) and the two constants

$$a \approx 1.541434 \times 10^{-6}\,\text{A eV V}^{-2} \quad \text{and} \quad b \approx 6.830890 \times 10^{9}\,\text{V eV}^{-3/2}\,\text{m}^{-1}\ . \tag{7.3}$$

However, in a MAC-E filter, neither the current density J nor the electric field F can be directly accessed as the experimental observables are the measured electron background rate R (in cps) and the monitored voltage difference ΔU (in V) applied between the spectrometer vessel and the inner electrodes. Therefore, the following linear substitutions [FFM13] are required in order to use the elementary form of the Fowler-Nordheim-type

Figure 7.2: Wire electrodes inside the main spectrometer. Left: View into the main spectrometer. More than 23000 stainless-steel wire electrodes of 200 and 300 μm thickness are mounted on 248 wire modules and cover the inner surface of the main-spectrometer vessel to electrostatically shield against secondary-emission induced background electrons and to fine-tune the electrostatic field. **Right: Support structure of the inner wire electrodes.** The rather complex support structure of the inner wire electrodes is a likely source for field electron emission. For background measurements during the first SDS commissioning, both wire layers and their support structure had to be operated at the same potential of −18.6 kV, while the vessel was elevated to a more positive voltage with a potential difference of ΔU relative to the wire electrodes. This picture shows the exemplary module #1211.

equation to analyze the data:

$$J = \frac{eR}{A} = c_1 R \quad \text{and} \quad F = \frac{\Delta U}{d} = c_2 \Delta U \ , \tag{7.4}$$

where A (in m^2) and d (in 1/m) denote the unknown surface area and distance, respectively, which are affected by local field electron emission, while c_1 (in C/m^2) and c_2 (in 1/m) describe associated geometry factors. The theorem can be converted so that a linear fit ($y = mx + c$) can be applied to the data in the presence of field emission:

$$\underbrace{\ln \frac{R}{\Delta U^2}}_{y} = \underbrace{-\frac{b\phi^{3/2}}{c_2}}_{m} \cdot \underbrace{\frac{1}{\Delta U}}_{x} \underbrace{-\ln \frac{c_1 \phi}{ac_2}}_{c} \ . \tag{7.5}$$

Consequently, the unknown factors c_1 and c_2 are accessible in the characteristic F-N plot showing $y = \ln(R/\Delta U^2)$ as a function of $x = 1/\Delta U$. The geometry factor c_1 is obtained from the intercept c of the linear F-N fit and c_2 from the slope m. This fact allows to calculate the current density and the electric field according to equation (7.4). However, this theory does not contain any description of the energy distribution of field-emission induced electrons emitted from the solid surfaces.

The effect of field electron emission can be significantly reduced by carefully designing the geometry of structural components elevated to negative high voltage [FN28]. This can be achieved by comprehensive electric-field calculation beforehand [Mee13] [FG14]. Moreover, the procedure of conditioning [SM73] [Bon95] can be applied for surface treating in preparation of high-voltage measurements. Field electron emission typically appears as a point-like source on sharp tips with small dimensions leading to local electrostatic spark discharges than over a wide surface area. As a consequence, high current densities heat up the associated material in close proximity. Conditioning performed at higher electric potentials allows to weld surface irregularities, resulting in a smooth, flat surface. The rather complex support structure of the inner wire electrodes which is fully elevated to negative high voltage represents a possible source for field electron emission, in addition

local tips at the vessel surface and the wires. The inner wire electrodes and their support structure are shown in figure 7.2, illustrating the experimental setup. In order to minimize the effect of field electron emission, the electric field can be fine-shaped using optimized field configurations and the inner structural surfaces can be conditioned beforehand using high potentials beyond the standard operating settings. These applications are planned for the beginning of neutrino-mass measurements [Ang05].

7.2 Field Electron Emission in the Main Spectrometer

In order to investigate the process of field electron emission inside the main-spectrometer volume, the total background rate was measured for different magnetic-field configurations and electric-field settings. In this context, as described in section 2.4, the magnetic-field configuration is defined by the field strength in the analyzing plane, whereas the electric-field setting is defined by the potential offset $\Delta U \leq 0\,\mathrm{V}$ between spectrometer vessel and inner wire electrodes. For high-voltage background measurements, the latter were permanently kept on a more negative voltage of $-18.6\,\mathrm{kV}$ than the vessel whose potential was varied accordingly. The post-acceleration electrode was elevated to $+10\,\mathrm{kV}$, leading to an energy region of interest ranging from 25.6 to 30.6 keV.

Figure 7.3 shows the corresponding background rates R measured over the 122 non-shadowed, functional pixels (section 4.9). It illustrates the following characteristics of a MAC-E filter:

- **Magnetic shielding:** For the same voltage offset, the background rate drops with increasing magnetic field because of the improved magnetic shielding effect. On the one hand, the distance between the sensitive magnetic flux tube and the inner surfaces of the main spectrometer increases. As a result, surface-induced backgrounds, such as electrons generated by cosmic rays, environmental radiation, intrinsic radioactivity, and field emission, are suppressed, because not all drift processes allow background electrons to migrate deep into the flux tube. On the other hand, as a result of the smaller volume of the sensitive magnetic flux tube, volume-induced backgrounds, such as radon-induced electrons, are reduced accordingly. However, the latter fact competes with improved storage conditions for magnetically trapped electrons at stronger magnetic fields.

- **Electric shielding:** For the same magnetic-field setting, the background rate first drops for increasing absolute values of potential offsets of $\Delta U \gtrsim -150\,\mathrm{V}$ because of the electric shielding effect. Since the inner wire electrodes are elevated to a more negative potential than the vessel, electrons emitted from the inner vessel surface are electrostatically shielded as long as their energies are below the potential difference. In the current one-potential operation mode of the inner electrodes, only electrons originating from the inner vessel surface are repelled by electric shielding. This is not the case for electrons emitted from the holding structures.

- **Minimum background:** Depending on the magnetic-field configuration, the minimum background rate is achieved at a potential difference of $\Delta U = -200\ldots-100\,\mathrm{V}$. The background composition there can be estimated, as shown in section 6.4 using the example of $\Delta U = -100\,\mathrm{V}$. The background is dominated by radon-induced and surface-induced electrons, while the detector background, showing its characteristic continuum, is negligible (section 5.9). By operating the LN2 cooled baffle system and the two-layer wire electrodes, the background can be significantly reduced.

- **Electron field emission:** Interestingly, the rate rises with increasing absolute potential differences of $\Delta U \lesssim -200\,\mathrm{V}$. This fact indicates the presence of a field-electron
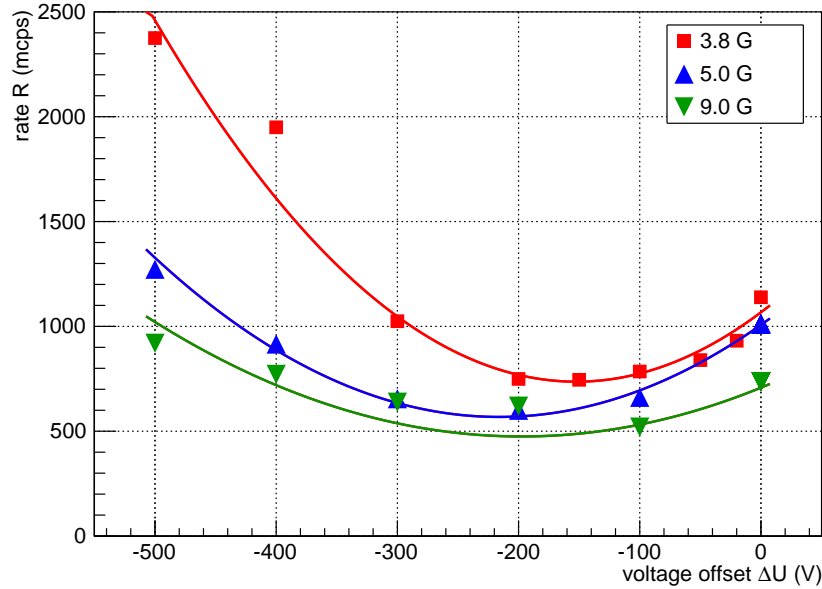
Figure 7.3: Main-spectrometer background rates at high voltage. The background rate R is shown for different magnetic-field configurations (3.8, 5.0, 9.0 G) as a function of the voltage offset ΔU applied between the spectrometer vessel and the inner wire electrodes. Statistical uncertainties are included but not visible.
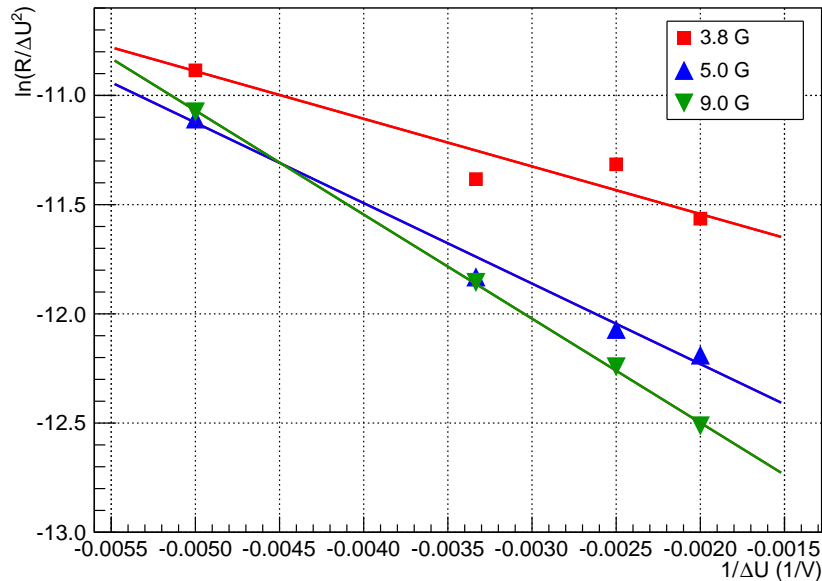
Figure 7.4: F-N plot for main-spectrometer background rates. The Fowler-Nordheim plot shows $y = \ln(R/\Delta U^2)$ as a function of $x = 1/\Delta U$, where R denotes the detector background rate and ΔU the potential difference applied between the spectrometer vessel and the inner wire electrodes. The associated linear F-N fits indicate the presence of field electron emission. Statistical uncertainties are included but not visible.

emission process as additional background component competing with the electric shielding effect in the main spectrometer. It will be discussed in the following.

Using equation (7.5), the R-ΔU plot can be rearranged to the F-N plot for large voltage offsets $\Delta U \lesssim -200\,\mathrm{V}$, with figure 7.4 illustrating the corresponding transformation. The geometry factor c_2 is given by the inverse slope of the related linear F-N fit and establishes the connection to the local surface electric field F which can be calculated:

$$\begin{aligned}
3.8\,\mathrm{G}:\ & c_2 = 2.89(3) \times 10^8\,\mathrm{m}^{-1}\ \rightarrow\ F(\Delta U = -500\,\mathrm{V}) = 145(2)\,\mathrm{GV/m} \\
5.0\,\mathrm{G}:\ & c_2 = 1.71(5) \times 10^8\,\mathrm{m}^{-1}\ \rightarrow\ F(\Delta U = -500\,\mathrm{V}) = 86(2)\,\mathrm{GV/m} \\
9.0\,\mathrm{G}:\ & c_2 = 1.32(3) \times 10^8\,\mathrm{m}^{-1}\ \rightarrow\ F(\Delta U = -500\,\mathrm{V}) = 66(2)\,\mathrm{GV/m}\ .
\end{aligned} \tag{7.6}$$

This analysis indicates that only local electric fields with field strengths of the order of $F \sim 100\,\mathrm{GV/m}$ can explain the observed background behavior and contribution at $\Delta U = -500\,\mathrm{V}$, in principle almost independently from the adjusted magnetic-field configuration. At lower potential differences, the local electric field strength decreases accordingly.

The macroscopic electric field strength can be calculated by static electric-field simulations of objects elevated to negative high voltage using *FEMM* [Mee13] or *Kassiopeia* [FG14]. To do so, only critical sharp-edged parts of the geometry have to be considered, such as the 200-µm thin stainless-steel wire electrodes and their inner support structures with an designed edge radius of 30 µm. For the calculations, these objects were set to a potential of $-18.6\,\mathrm{kV}$ and the surrounding spectrometer-vessel surface to $-18.1\,\mathrm{kV}$. Figure 7.5 shows the corresponding results. These calculations indicate that the maximum macroscopic electric field strength is only in the order of $F_\mathrm{mac} \sim 1\,\mathrm{MV/m}$, well below the measured values of the analysis (7.6). However, this field strength usually is sufficient to produce a measurable amount of field-emission induced electrons [FN28].

Following equation (7.1), the comparison of the measured local field strength F and the calculated macroscopic field strength F_mac points to a field-enhancement factor of $\gamma \approx 10^5$ for the investigated geometry. This factor is $\sim 10^2$ higher than typical values predicted by literature [Smi05] [SS09]. Therefore, the application of the elementary form of the Fowler-Nordheim-type equation to the recorded data seems questionable. Further litera-ture [For12] states that this simplified form might overestimate the field-emission current density and thus the local electric field by a large, highly variable factor ranging from 10^3 to 10^9, when compared to the technically complete form [For13a]. The latter represents the most general form of the Fowler-Nordheim-type equation. Due to additional depen-dencies of the local field strength to material-related correction factors, this form however cannot be converted to an expression which can be applied to the acquired data by cal-culating the associated field strengths in the presented way. Although the values of F obtained from the above quantitative analysis (7.6) might be overestimated, the applica-tion of the Fowler-Nordheim theorem in form of the F-N plot to the observed background rates strongly indicates that from a qualitative point of view, field electron emission is present when applying high negative potential offsets between spectrometer vessel and inner wire electrodes. Nonetheless, it should be noted that other background components, such as electrons induced by radon α-decays, cosmic rays, environmental radiation, and intrinsic radioactivity are included in this kind of analysis, since an event-based separation is not possible. This might affect the outcome of the analysis. For the upcoming second phase of SDS commissioning, however, these background components can be significantly reduced through operating the LN2 cooled baffle system and the two-layer wire electrodes. This will allow to investigate the effect of field electron emission in more detail, even at larger potential offset.
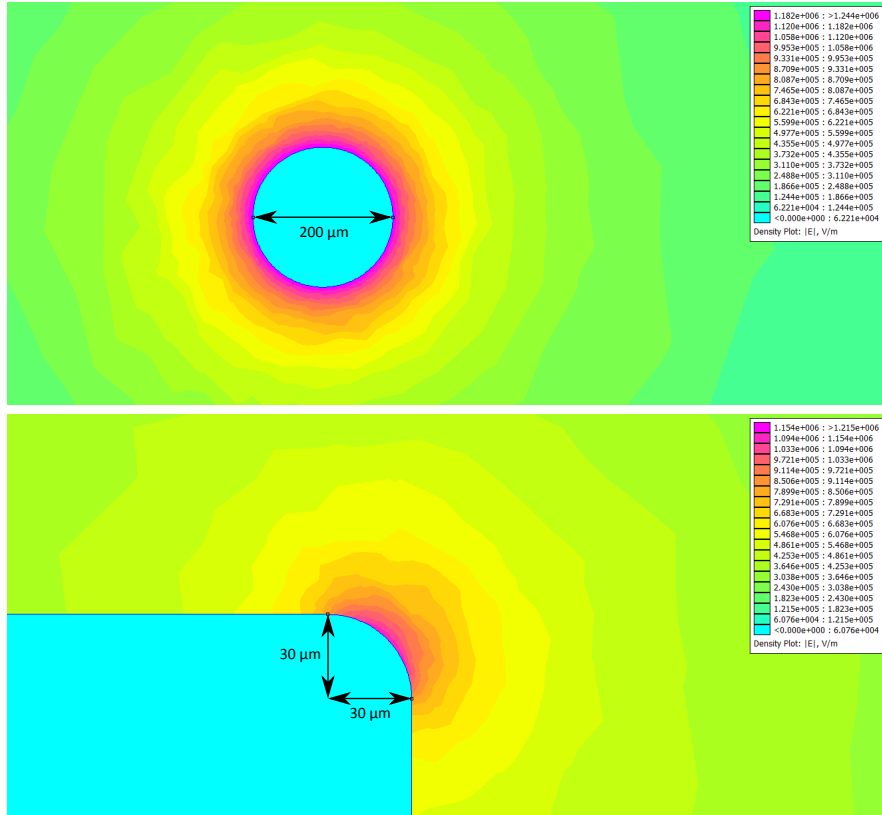
Figure 7.5: Simulation of the macroscopic electric field. The results of a calculation of the macroscopic electric field are shown in close proximity to a 200-μm thin stainless-steel wire (**top**) and its support structure with an assumed edge radius of 30 μm (**bottom**). Both objects are set to $-18.6\,\text{kV}$, while the surrounding geometry is at $-18.1\,\text{kV}$. The calculations were performed with *FEMM* [Mee13]. Similar results were obtained with *Kassiopeia* [Lei14].
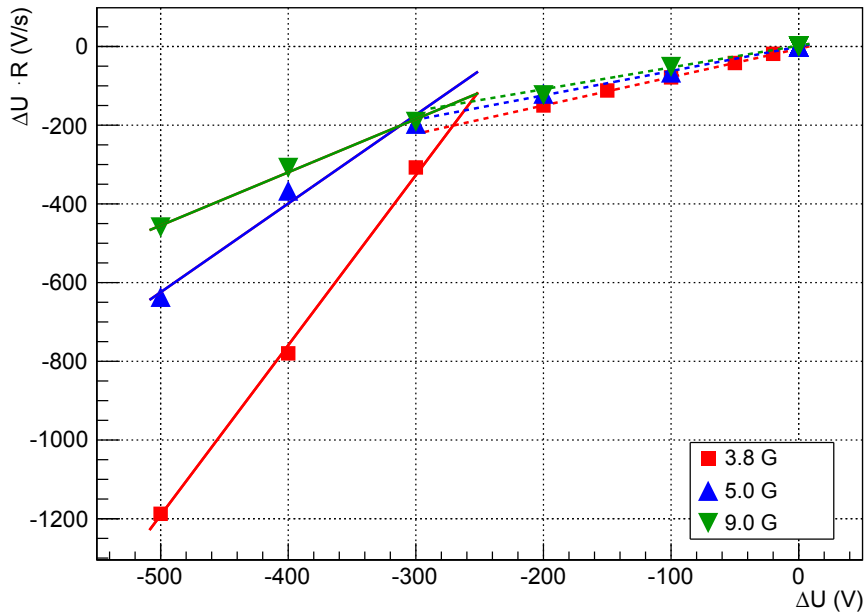
Figure 7.6: Threshold for field electron emission. The $R\Delta U$-ΔU plot illustrates the threshold ΔU_0 of the potential offset of the electrode system for the onset of field electron emission at different magnetic-field configurations. The linear fits at small Δ_U (dashed lines) describe the electric shielding of the electrodes. The linear fits at large Δ_U (solid lines) describe the effect of field electron emission. The intersection of both linear fits define the onset of field electron emission and the corresponding value for the threshold ΔU_0. Statistical uncertainties are included but not visible.

Finally, the linear F-N fit allows to calculate the local emission current density J via the intercept from the fit parameters by applying equations (7.4) and (7.5):

$$
\begin{aligned}
3.8\,\text{G}:\ c_1 &= 63.6(6)\,\text{C/cm}^2 \ \rightarrow\ J(\Delta U = -500\,\text{V}) = 150.9(9)\,\text{A/cm}^2 \\
5.0\,\text{G}:\ c_1 &= 14.0(5)\,\text{C/cm}^2 \ \rightarrow\ J(\Delta U = -500\,\text{V}) = 17.8(9)\,\text{A/cm}^2 \\
9.0\,\text{G}:\ c_1 &= 6.7(3)\,\text{C/cm}^2 \ \rightarrow\ J(\Delta U = -500\,\text{V}) = 6.1(3)\,\text{A/cm}^2 \ .
\end{aligned}
\tag{7.7}
$$

The current densities for the 5.0-G and the 9.0-G setting are in good agreement with calculations based on the technically complete form of the Fowler-Nordheim-type equation [Dol53]. This fact represents another clear indication that field electron emission indeed occurs in the spectrometer when operating the system of the inner wire electrodes beyond its specifications for neutrino-mass measurements. There are further observations of other experiments [DT53], where even current densities of up to $\sim 10^7\,\text{A/cm}^2$ were measured resulting in a strong vacuum arc. This implies a wide range of observed values for the current density. However, in the case of the spectrometer, field electron emission should not produce detectable arcs within the observed voltage range. As stated above, high field-emission induced currents can be used for surface treating when deliberately applying the process of conditioning.

Under the assumption that this type of emission follows an energy-dependent cross section $\sigma(E)$ with a specific threshold energy E_0, the threshold ΔU_0 of the potential difference for field electron emission can be calculated. In general, it is defined by

$$
\sigma(E) = k \cdot \frac{E - E_0}{E}
\tag{7.8}
$$

[For73] [ABL11], where k denotes a reaction-related constant. By replacing $\sigma(E) = R$, $E = \Delta U$, and $E_0 = \Delta U_0$, the threshold of the potential difference is accessible via the parameters of a linear straight-line fit ($y = mx + c$) applied to the converted data in the $R\Delta U$-ΔU plot:

$$
R = k \cdot \frac{\Delta U - \Delta U_0}{\Delta U} \ \rightarrow\ \underbrace{R\Delta U}_{y} = \underbrace{k}_{m} \cdot \underbrace{\Delta U}_{x} \underbrace{-k\Delta U_0}_{c} \ .
\tag{7.9}
$$

Figure 7.6 illustrates the corresponding transformation and the application of the linear fits in the $R\Delta U$-ΔU plot at different magnetic-field configurations. The threshold ΔU_0 of the potential difference for field electron emission is given by the intersection of the linear fit describing field electron emission ($\Delta U \lesssim -250\,\text{V}$) and the linear fit describing electric shielding ($\Delta U \gtrsim -250\,\text{V}$):

$$
\begin{aligned}
3.8\,\text{G}:\ \Delta U_0 &= -271(12)\,V \\
5.0\,\text{G}:\ \Delta U_0 &= -308(24)\,V \\
9.0\,\text{G}:\ \Delta U_0 &= -274(19)\,V \ .
\end{aligned}
\tag{7.10}
$$

Due to the limited data at only a few selected potential differences, the statistical fit uncertainties and thus the uncertainties of the results for ΔU_0 are rather large in this analysis. Therefore, no definite statement can be made as to whether a magnetic-field dependence for ΔU_0 is observed. However, the data convincingly show that field electron emission only becomes a dominant effect where a large amount of background electrons is produced for potential differences of $\Delta U \lesssim -250\,\text{V}$. In the first approximation, this voltage regime must be avoided for later neutrino-mass measurements in the present electrode setup. Nonetheless, it should be noted that field electron emission might locally start already at smaller potential offsets, since the electrons are liberated from the inner surfaces of the spectrometer outside the sensitive magnetic flux tube. They propagate via rather complex radial drift motions into the sensitive flux-tube volume so that there is no direct
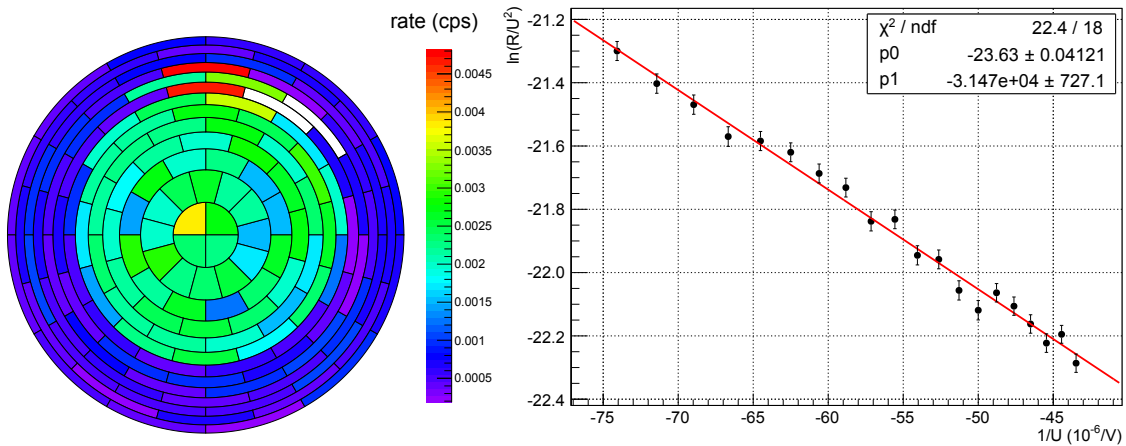
Figure 7.7: Field electron emission from the photoelectron-source disk. Left: Detector pixel view. In case of an untypical magnetic-field configuration of $B_{\mathrm{DET}} = 1\,\mathrm{T}$ and $B_{\mathrm{PCH}} = 0\,\mathrm{T}$, the complete surface of the disk is imaged onto the inner pixel rings of the detector wafer. The corresponding rates are shown for a photoelectron-source disk which is fully inserted into the magnetic flux tube and elevated to a potential of $-23.0\,\mathrm{kV}$ without being illuminated by the UV LED. The field-emission distribution is quite uniform over the disk, except of an increased rate on the top, indicating enhanced field electron emission from the support rod. **Right: The F-N plot** is shown for disk potentials ranging from $U = -23.0 \ldots -13.5\,\mathrm{kV}$. The detector rate R is summed only over the pixels imaging the disk. The linear F-N behavior (red line) strongly hints to the presence of field electron emission over the entire disk. Statistical uncertainties are included.

magnetic line of sight between the source and the detector. In addition, field electron emission strongly competes with the electric shielding effect.

The process of field electron emission for an asymmetric field configuration will be discussed in section 7.4. There, the asymmetric configuration has been used to directly map the areas of field emission. First of all, the application of the Fowler-Nordheim-type equation will be validated by investigating field electron emission in the detector system; this will be discussed in the subsequent section before showing further observations with regard to the main spectrometer.

7.3 Field Electron Emission in the Detector System

The main spectrometer is the first device in the KATRIN setup where field electron emission has been studied in the Fowler-Nordheim theory. There are also two smaller spectrometers – the pre-spectrometer and the monitor spectrometer (see section 2.3) – which require strong negative retarding potentials for the analysis of electron energies based on the MAC-E filter principle. Also the detector system with its photoelectron-source disk made of titanium (see section 3.9) is an ideal candidate to investigate field electron emission in more detail and to validate the observations from the main spectrometer.

In order to examine field electron emission from the photoelectron-source disk, the detector system was separated from the main-spectrometer volume by closing the gate valve. The detector magnet was operated at a moderate magnetic field of $1.0\,\mathrm{T}$ while the pinch magnet was deenergized. The disk was fully inserted into the magnetic flux tube. The intention of the rather untypical magnetic-field configuration was to completely image the disk onto the inner pixel rings of the detector wafer. When doing so, the inner surfaces of the vacuum chamber and the non-operating post-acceleration electrode were projected onto the outer pixel rings. This fact allows to differentiate between pixels mapping the elevated disk and pixels imaging the grounded surfaces, thereby enabling to hunt for local spots of field

electron emission. The photoelectron-source potential U was thus varied from -23.0 to -13.5 kV in 0.5-kV increments, while the external illumination device was replaced by a light-tight cover in order to ensure that the disk was not illuminated by the associated UV LED or by ambient light. The region of interest is then given by the moving energy interval ranging from 3 keV below and 2 keV above the source potential (runs #9764 − #9783, 3 h each).

Figure 7.7 gives a survey of the results of this measurement. The detector rate strongly increases for a more negative source potential in a typical linear F-N behavior. This characteristic feature again strongly indicates field electron emission from the polished titanium disk. The local surface electric field F and the local emission current density J are given by equations (7.4) and (7.5) using the parameters from the applied linear F-N fit:

$$
\begin{aligned}
c_2 &= 2.0(5) \times 10^6 \,\text{m}^{-1} & &\rightarrow\ F(U = -23\,\text{kV}) = 46.1(1)\,\text{GV/m} \\
c_1 &= 3.9(2) \times 10^{-6}\,\text{C/cm}^2 & &\rightarrow\ J(U = -23\,\text{kV}) = 4.3(2) \times 10^{-7}\,\text{A/cm}^2 \ .
\end{aligned}
\tag{7.11}
$$

While the determined electric field is in the same order as the local field emission observed from the inner electrode mounting structure in the main spectrometer (section 7.2), the current density here is quite small. However, this is reasonable, since the disk was treated, polished, and conditioned in advance. Thus, the resulting field-emission induced electron rate is only ~ 0.1 cps, measured over the entire disk. This also indicates that the F-N plot is best suited to a large flat surface. The field electron emission is distributed quite uniformly over the disk, except for an increased rate on the top, implying enhanced emission from the support rod. Secondary electron emission [Bun64] [Nis94] induced by cosmic rays, environmental radiation, and intrinsic radioactivity can be excluded as dominant source due to the clear F-N behavior observed. The advantage of the investigation here is the direct mapping of field electron emission onto the detector. Since similar local electric field strengths can be measured at the main spectrometer and at the detector system, it can be concluded that field electron emission is present in both systems, leading to detectable background rates. The physical process of field electron emission was independently also studied at the monitor spectrometer [Din14] [Lei14].

7.4 Mapping of the Inner Support Structure

With the successful direct mapping of field electron emission at the Ti-disk of the detector system, a similar mapping analysis was performed for the main spectrometer. In order to image the support structure of the inner wire electrodes onto the detector, an asymmetric magnetic-field configuration was used. For this purpose, the pre-spectrometer magnets PS1 and PS2 were deenergized and the LFCS air-coil currents adjusted, such that the upstream cone of the main spectrometer was mapped by the sensitive magnetic flux tube. The related magnetic-field settings and the resulting flux-tube through the combined spectrometer and detector system are shown in figure 7.8 on the left-hand side. In order to promote field electron emission in a significant but still technically safe manner, the spectrometer vessel was grounded and the inner wire electrodes were elevated to an electric potential of $\Delta U = -600$ V, which is far beyond the nominal settings of up to $\Delta U \sim -200$ V and where field emission dominates (see figure 7.6). A post-acceleration potential of $+10$ kV was applied to boost the field-emission induced electrons above the electronic noise threshold of the detector, leading to an energy region of interest ranging from 7.6 to 12.6 keV (run #5193, 30 min).

The resulting detector response is illustrated in figure 7.8 on the right-hand side as a pixel view. A dominant two-ring shaped structure can be observed as pattern which is also
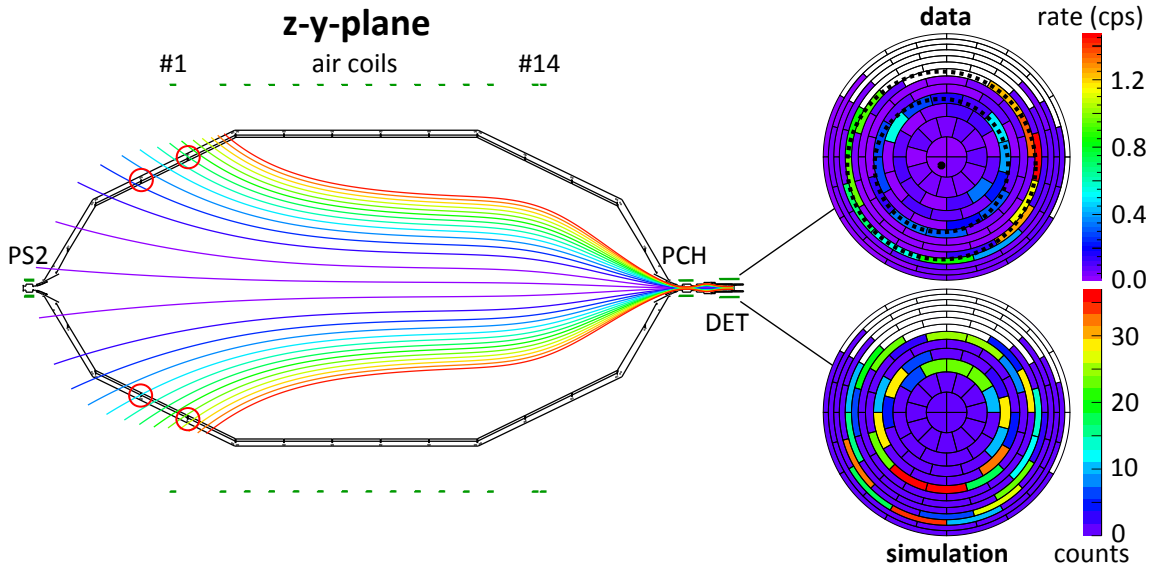
Figure 7.8: Imaging characteristics of the inner support structure onto the detector. In order to map of the holding structure of the wire electrodes at the upstream side of the main spectrometer, an asymmetric magnetic-field configuration was chosen with the following settings: PS1 = 0 T, PS2 = 0 T, LFCS #1 − #3 = 0 A, LFCS #4 = 50 A, LFCS #5 − #13 = 100 A, LFCS #14 = 0 A, PCH = 5.0 T, and DET = 3.5 T. The simulations include the mechanical misalignment of the detector system. The red circles in the magnetic field-line map indicate the positions of the comb-shaped holding structures of the inner wire electrodes. The location and shape of the two-ring structures shown in the pixel view for the measurement (dashed lines) and the simulation are in excellent agreement.

constant over time. In the framework of magnetic field-line simulations with *Kassiopeia*, this characteristic pattern can be traced back to the imaging of the complex comb-shaped holding structure of the inner wire electrodes shown in figure 7.2 onto the detector wafer. For these simulations, the corresponding magnetic field lines were started in close proximity to the support structure using a uniform distribution and then projected to the detector wafer. The simulations include the mechanical misalignment of the detector system as described in section 4.9, but do not include the microscopic field distribution of field electron emission along the holding structure (see figure 7.5). The comparison between measurement and simulation is illustrated in figure 7.8 and indicates that the position of the circular two-ring pattern at the detector can be reproduced in good agreement. However, the simulations do not reproduce the actual count rates measured at the detector correctly, when assuming a uniform distribution for electron emission. However, as stated in section 7.1, field electron emission occurs rather in form of a local point phenomenon, so azimuthal variations along a mapped ring appear feasible. For lower potential offsets approaching the range of standard operating mode with $\Delta U \sim -100$ V, the two-ring shaped structure disappears [Bar14], implying that the comb-shaped structures responsible for field electron emission do not represent major sources of muon-induced secondary-electron backgrounds. This is in excellent agreement with investigations performed in [Lei14] which identified other parts of the holding structures, the so called C-profiles, to play an important part in this respect. Interestingly, the measured field electron emission background shows no unexpected features in the inter-arrival time spectra when different time scales are applied, implying that it is Poisson-distributed in time. Thus, emission of two or more electrons at the same time can be excluded. For a single particle undergoing quantum tunneling effect, this is of course also not expected. Taken together, these findings imply that the source of field electron emission can be localized to the comb-shaped holding structure of the inner wire electrodes. The spectrometer vessel, the wires, or even other structural components

seem not to be affected by field electron emission to first order.

The observation of two-ring shaped structures can be used to deduce the alignment of the detector wafer relative to the system of the inner wire electrodes installed in the observed cone, since the alignment of the individual wire modules is known with an accuracy of better than ≤ 1 mm [Hil11] [Pra11]. This alignment was determined with a laser tracker in advance [Jur09]. The measured center coordinates (x, y) relative to the actual detector-wafer center for the outer [inner] ring are $(-1.3, -3.3)$ mm $[(-1.3, -3.7)$ mm] with a ring radius of 34.5 mm $[23.7$ mm], while the simulated coordinates are $(-1.7, -5.3)$ mm $[(-1.7, -5.3)$ mm] with a radius of 34.3 mm $[23.2$ mm]. The statistical uncertainty of the ring-fit algorithm is of the order of ~ 1 mm. While the results for the x-coordinates and the ring radii agree within the statistical uncertainties, there is a discrepancy of ~ 2 mm between measurement and simulation for the y-coordinates. Based on these findings, it can be argued that the wafer is displaced relative to the inner wire electrodes by a smaller offset than expected, i.e. it is actually located slightly lower than determined in the context of detector-alignment measurements. This, however, is not surprising, since the wafer position was extrapolated from *FaroArm* scans performed at the vacuum chamber of the detector system prior to the first SDS commissioning phase, as described in section 4.9. Table 8.1 in the summary of the thesis in hand gives a comprehensive survey of the results for the detector alignment obtained from different approaches: mechanical *FaroArm* scans (section 4.9), radon-induced ring structures at elevated pressure (section 6.2.2), field electron emission of the coaxially arranged inner comb-shaped holding structure of the wire electrodes, and associated tracking simulations performed with *Kassiopeia*.

7.5 Hydrogen Anions in the Main Spectrometer

During the above described field electron emission studies at symmetric magnetic field of 3.8 G, a second background class can be observed, see figure 7.9. This additional background class produces a distinct peak about 11 keV below the peak of single electrons (28.6 keV). This peak has a FWHM of ~ 3 keV, which is significantly broader than the electron peak (~ 2 keV FWHM). Although the additional background component appears well below the region of interest, it is conceivable to be correlated with the electron background. If such a correlation exists, indeed the investigation of this peak could open a window to not only better understand electron field emission but also transport phenomena in the spectrometer for particles other than electrons. Therefore, this background class will be examined with respect to its potential origin (section 7.5.1), its connection to the electron background (section 7.5.2), and possible production mechanisms (section 7.5.3).

7.5.1 Anion Background

There is a variety of particles which could be responsible for the additional distinct background peak at ~ 17.7 keV and an enlarged FWHM of ~ 3 keV:

- **Electrons:** As incident keV-electrons continuously interact with the detector material via ionization and bremsstrahlung, the variation of the detector energy resolution measured for these particles is relatively small in the observed energy range (see section 4.2). However, the FWHM begins to drastically degrade for incident energies below ~ 10 keV. As the enlarged FWHM is incompatible with electron interactions, this background class cannot originate from electrons with incident energies of ~ 17.7 keV.

- **Photons:** X-ray photons in the keV-range interact through point interactions with the detector material primarily via the photoelectric effect and Compton scattering. As discussed in section 3.9, the FWHM energy resolution of an individual fluorescence
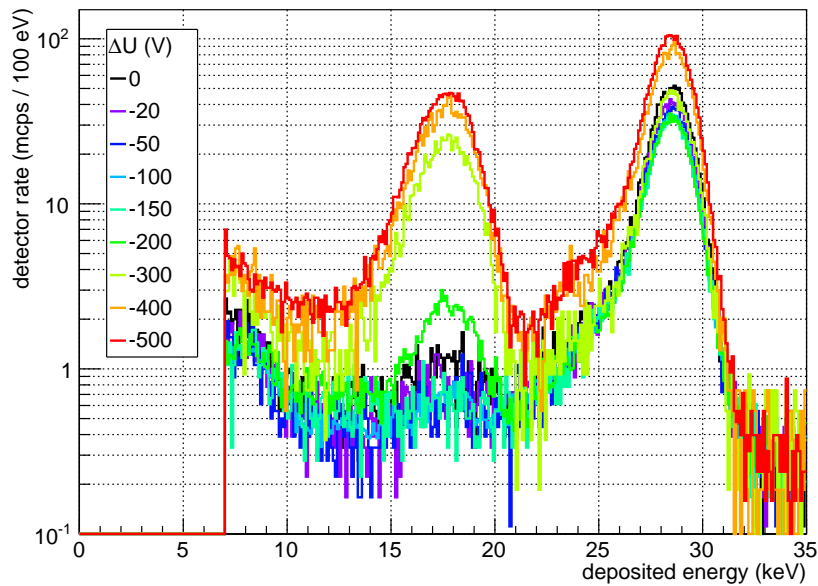
Figure 7.9: Energy spectra for high-voltage background measurements at 3.8 G.
The energy spectra are shown for different voltage offsets $\Delta U < 0$ applied between the spectrometer vessel $((-18.6 - \Delta U)\,\mathrm{kV})$ and the inner wire electrodes $(-18.6\,\mathrm{kV})$ and for a post-acceleration potential of $10\,\mathrm{kV}$ at the 3.8-G setting. In the region of interest, ranging from 25.6 to $30.6\,\mathrm{keV}$ around the single-electron peak at $28.6\,\mathrm{keV}$, the increasing field-emission induced electron background becomes dominant for larger offset values. Interestingly, a second background contribution then appears with a mean energy of $\sim 17.7\,\mathrm{keV}$. This additional background can be traced back to hydrogen anions, as described in the continuous text.

and X-ray line is even narrower than the one of electrons. This is incompatible with the observation, and, as it will be shown below, the position of the observed background peak varies for different incident energies. Therefore, X-ray photons cannot explain the additional background class.

- **Positively charged ions:** Like electrons, positively charged particles, such as ionized atoms (H^+, Ar^+) and molecules (H_2^+) from the residual gas inside the main-spectrometer volume, would experience a continuous energy loss over the detector volume. However, when operating the post-acceleration electrode at a positive potential of $+10\,\mathrm{kV}$, these particles would be decelerated. The resulting peak position at $\sim 8.6\,\mathrm{keV}$ or even below due to additional dead-layer effects would be close to the electronic noise threshold of the detector. Therefore, the positive post-acceleration potential allows to generally exclude positive ions as possible background source for the second background class.

- **Hydrogen anions:** In general, ions will continuously interact with the detector and lose energy via ionization, the production of phonons, and the generation of vacancies and damage. These processes occur directly by incident ions and indirectly by recoiling atoms. The probability for these processes strongly depends on the intrinsic mass and the initial energy of the incident ions. In the case of negatively charged hydrogen atoms (H^-) and molecules (H_2^-, D_2^-) from the residual gas impinging with energies in the keV-scale, the primary energy-loss process is the direct ionization of the detector material [Zie04] [Zie13]. Just as in the case of electrons, hydrogen anions are boosted by the post-acceleration potential. However, due to their higher mass, their energy loss as a function of the target depth significantly differs from the one of electrons with the same kinetic energy. In particular, anions lose a relatively

large amount of energy in the insensitive detector dead layer. This explains why the second peak appears distinctly below the single-electron peak.

As stated above, due to increased energy losses in the insensitive detector dead layer, the second peak at lower energy is supposedly caused by hydrogen anions originating from the residual gas inside the main-spectrometer volume. In order to investigate and corroborate this theory, energy-loss simulations of the relevant hydrogen anions H^-, H_2^-, and D_2^- were performed in silicon using the software package *SRIM-2013.00* [Zie04] [Zie13]. The incident energy of ions is modeled to be zero upon origin, with subsequent acceleration due to the spectrometer retarding potential ($-18.6\,\text{kV}$), the post-acceleration potential ($+10\,\text{kV}$), and the detector reverse-bias voltage ($+0.12\,\text{kV}$), resulting in a total impact energy of $28.72\,\text{keV}$ at the surface of the detector wafer. Figure 7.10 illustrates the corresponding *SRIM* results of the energy loss in silicon for different hydrogen anions at various incident angles as a function of the target depth. The specified thickness of the insensitive dead layer of the installed detector wafer is $100\,\text{nm}$, assuming a complete absence of any charge collection in the dead-layer volume [Ams14]. Within these first $100\,\text{nm}$, the average energy loss for H^- ions with an impact angle of $0°$ is $\sim 11.2\,\text{keV}$, thus in very good agreement with the experimentally observed offset of $\sim 10.9\,\text{keV}$ between the single-electron peak and the additional low-energy peak. For larger incident angles, the energy loss increases, while the average penetration depth decreases accordingly. Compared to other anions, heavy hydrogen anions lose less energy in the dead layer, resulting in a larger penetration depth. Hence, these simulations indicate that the peak at lower energy originates from H^- ions with small impact angles. It is quite reasonable to assume small incident angles close to $0°$, since the applied post-acceleration potential increases only the longitudinal energy component of the ions without affecting their transverse energy. Consequently, their impact angle is reduced accordingly.

The energy deposit of typical 28.72-keV electrons however is localized within the first $\sim 10\,\mu\text{m}$ of the detector [Ren11], which is significantly larger than the insensitive volume of the specified dead-layer thickness of $100\,\text{nm}$. By contrast, as indicated by the examined energy-loss simulations, 28.72-keV H^- ions deposit their energy already in the first $500\,\text{nm}$, implying that a significant amount of their initial energy is lost for detection. This fact allows to determine the dead-layer thickness with rather high accuracy, assuming the absence of a gradual increase of charge-collection effects in the transition zone of the active layer of the dead layer and a zero impact angle for incident hydrogen anions. For this purpose, high-voltage background measurements at the symmetric 3.8-G magnetic-field setting were performed with the inner wire electrodes elevated to $-18.6\,\text{kV}$ and the main-spectrometer vessel elevated to $-18.1\,\text{kV}$, while the post-acceleration potential was varied from $+3$ to $+10\,\text{kV}$. On the one hand, due to the increased potential offset of $\Delta U = -500\,\text{V}$ between vessel and wires, this configuration provides effective and well-controlled production of H^- ions propagating toward the detector. On the other hand, the modification of the post-acceleration potential allows to vary the total incident energy for hydrogen ions, leading to a significant change of the energy loss inside the dead layer. This energy loss manifests as a corresponding shift of the anion-peak position relative to the total incident energy. Finally, the measurements are compared to energy-loss simulations of H^- ions in silicon performed with *SRIM-2013.00* as a function of the total incident anion energy and for different reasonable dead-layer thicknesses. This comparison is shown in figure 7.11, revealing the relative anion-peak position to the total incident energy as a function of the total incident energy. The latter is defined by the sum of the fixed spectrometer retarding potential ($-18.6\,\text{kV}$), the variable post-acceleration potential ($+3\ldots+10\,\text{kV}$), and the fixed detector reverse-bias voltage ($+0.12\,\text{kV}$). The recorded data is in excellent agreement with a simulated dead-layer thickness of $99\,\text{nm}$ which is extremely close to the specification of $100\,\text{nm}$ stated by the manufacturer *Canberra* [Ams14]. In order to underline the power
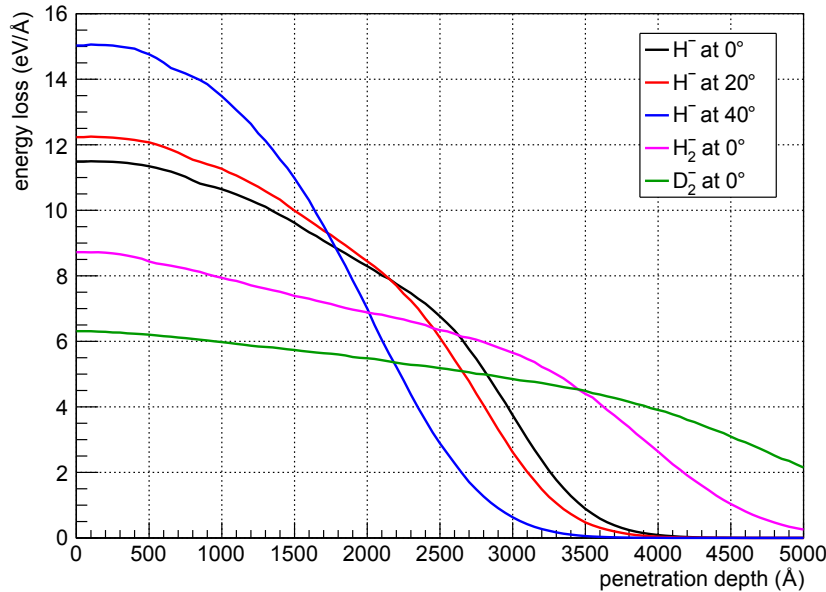
Figure 7.10: Energy loss of hydrogen anions in silicon. The energy loss of H^-, H_2^-, and D_2^- anions in silicon is given as a function of the penetration depth. Apart from the distributions with zero impact angle, the energy loss for H^- ions is shown for incident angles of $20°$ and $40°$ as well. The spectra illustrate the differential energy loss (eV) per unit penetration depth (Å). An H^- ion with zero impact angle loses $11.5\,\text{eV}$ within the first $1\,\text{Å}$. The specified thickness of the detector dead layer is $100\,\text{nm}$ in the absence of any charge collection inside the insensitive dead-layer volume. Within these first $100\,\text{nm}$ ($1000\,\text{Å}$), the average energy loss for H^- (with an impact angle of $0°$) is $\sim 11.2\,\text{keV}$, for H^- ($20°$) $\sim 12.0\,\text{keV}$, for H^- ($40°$) $\sim 14.6\,\text{keV}$, and for H_2^- ($0°$) $\sim 8.4\,\text{keV}$, for D_2^- ($0°$) $\sim 6.2\,\text{keV}$. Simulations were performed by the author with *SRIM-2013.00.*

of this new method, the distributions for a range of dead-layer thicknesses from 98 to $102\,\text{nm}$ are illustrated, indicating the remarkable sensitivity of this measurement approach to determine the dead-layer characteristics. Due to statistical uncertainties originating from the fit of the anion peak with a Gaussian distribution when measuring the mean peak position, the statistical uncertainty for the determined dead-layer thickness is in the order of $\sim 0.5\,\text{nm}$ only. Systematic uncertainties are dominated by the uncertainties of the applied potentials: the retarding potential has been measured with high precision of $10\,\text{mV}$ for the first SDS commissioning phase [Bar14] [Thu14], the post-acceleration potential is known with an overall accuracy of $0.25\,\%$ of the maximum output [Spe04], and the detector reverse-bias voltage is relatively small compared to the other potentials. Therefore, the systematic uncertainty is primarily dominated by the uncertainty of the post-acceleration potential of $\sim 75\,\text{V}$, leading to a systematic uncertainty for the dead-layer thickness in the order of $\sim 0.8\,\text{nm}$. Due to the rather limited statistics of these measurements and the relatively low count rate for H^- ions, only a global detector dead-layer analysis for the entire wafer was possible, instead of a more detailed pixel-by-pixel investigation. However, in the upcoming second SDS commissioning phase, this approach will be followed up with increased statistics and a larger variety of different total incident energies.

Finally, figure 7.12 compares the observed detector energy spectrum with the simulated detector responses for H^-, H_2^-, and D_2^- impinging with incident energies of $28.72\,\text{keV}$ when assuming an insensitive detector dead-layer thickness of $99\,\text{nm}$. The individual peaks resulting from the simulated detector responses are scaled to the same integral as the measured H^- peak and no additional smearing or shifting is considered. This comparison
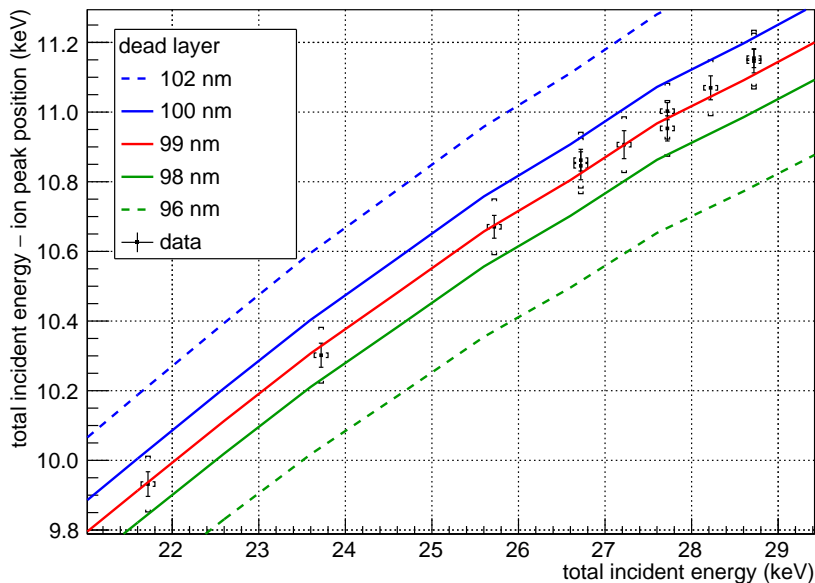
Figure 7.11: Energy loss of H⁻ ions as a function of the detector dead-layer thickness. The distributions illustrate the energy losses of H⁻ ions in the dead layer by plotting the difference of the total incident energy to the mean anion-peak position as a function of the total incident energy for five different dead-layer thicknesses. The data includes statistical uncertainties (black lines) originating from the fit of the recorded H⁻ peak with a Gaussian distribution and systematic uncertainties (black brackets) originating from uncertainties in the applied potentials. The comparison between data and simulation gives a dead-layer thickness of 99 nm, neglecting finite charge collection in the boundary region of the insensitive dead-layer volume. However, considering the combined uncertainties, it seems also to be consistent with the specified thickness of 100 nm. Simulations were performed by the author with *SRIM-2013.00.*

clearly demonstrates that H⁻ ions with small impact angles are responsible for the observed distinct peak at lower energies. Higher incident angles would lead to a shift of the associated peak toward lower energies and to a significant broadening. Heavier hydrogen anions would produce a peak at higher energies. Nevertheless, it should be noted that the shapes of the measured and the simulated H⁻ peak slightly differ from each other, most-likely due to a small distribution of ion impact angles and non-consideration of charge-collection effects in the detector dead layer. Details on a model in which the dead layer might be partly sensitive to incident radiation can be found in [Wal14].

Similar observations of a second peak appearing at energies lower than the single-electron peak were made in the early stages of the Mainz experiment [Pic90] and in initial pre-spectrometer test experiments [Hab09]. Additional investigations at the monitor spectrometer confirmed these findings [Din14]. In all experimental setups, these peaks were identified to originate from H⁻ ions of the residual gas, since detectors with similar dead-layer thicknesses in the order of ~ 100 nm were used, resulting in comparable energy losses. However, for these test measurements, the associated spectrometers were operated at potentials of $U_0 < -18.6$ kV, far beyond the standard operating mode for neutrino-mass measurements, in order to perform high-voltage conditioning. Due to the presence of the post-acceleration electrode within the KATRIN detector system, H⁻ ions can conveniently be observed when operating the main spectrometer at $U_0 = -18.6$ kV close to nominal settings. In the absence of a post-acceleration potential, the H⁻ peak would partly shift below the electronic noise threshold.
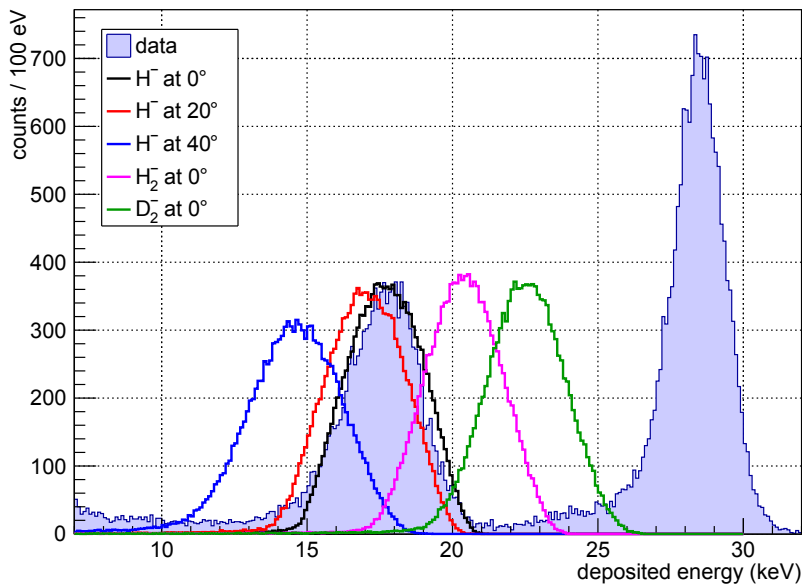
Figure 7.12: Comparison of measured and simulated detector response. The measured energy spectrum is shown for the symmetric 3.8-G magnetic-field setting with the inner wire electrodes elevated to $-18.6\,\text{kV}$, the spectrometer vessel to $-18.1\,\text{kV}$, and the post acceleration electrode to $+10\,\text{kV}$. The H^- peak at $\sim 17.7\,\text{keV}$ and the single-electron peak at $\sim 28.6\,\text{keV}$ are well separated from each other. For the energy-loss simulations, an insensitive detector dead layer with a 99-nm thickness is assumed as described in the continuous text. The individual peaks resulting from the simulated detector responses are scaled to the same integral as the measured H^- peak. Simulations were performed by the author with *SRIM-2013.00*.

7.5.2 Correlation to Electron Background

For high-voltage background measurements with a post-acceleration electrode operating at a potential of $+10\,\text{kV}$, the region of interest for H^- ions is defined as a rather broad energy interval, ranging from 13.7 to 20.7 keV. This is still well separated from the single-electron peak window of 25.6 to 30.6 keV. The difference in the width for the acceptance windows reflects the broader H^- peak. Since the H^- peak is located on top of the low-energy tail of the single-electron peak, the hydrogen-anion rate will be slightly overestimated. However, this effect is negligibly small for higher potential offsets ΔU applied between spectrometer vessel and inner wire electrodes, as the signal-to-background ratio increases for larger offsets. This allows to look for correlations between the rates of hydrogen anions and electrons, in particular for field-emission induced electrons. Figure 7.13 illustrates the measured rates of H^- ions and electrons as a function of the potential offset ΔU applied and for different magnetic-field configurations. Both background rates increase for more negative potential differences, indicating a correlation. This correlation will be examined in the following.

Threshold for H^--ion generation

In close analogy to field electron emission, the threshold ΔU_0 of the potential offset defining the onset of H^--ion generation is given by equation (7.9). Here, it is assumed that the production reaction for anions follows an energy-dependent cross section with a specific threshold energy. Figure 7.14 displays linear fits in the $R\Delta U$-ΔU diagram for different magnetic-field configurations. In this case, the threshold ΔU_0 is given by the intersection of the linear fit describing the onset of the production of anions with the baseline $R \approx 0\,\text{cps}$
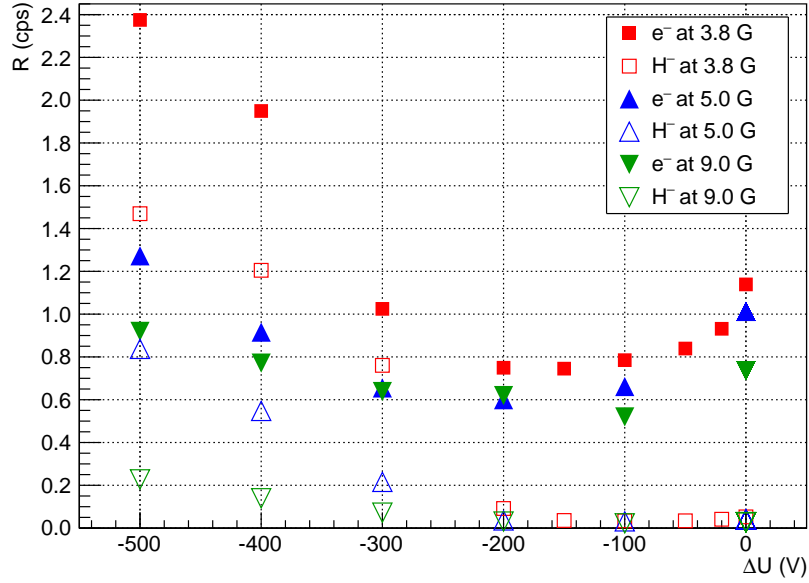
Figure 7.13: Rates for hydrogen anions (H^-) and electrons (e^-). The measured background rates for hydrogen anions and electrons are illustrated as a function of different symmetric magnetic-field configurations and various potential offsets ΔU applied between the spectrometer vessel and the inner wire electrodes. For $\Delta U \lesssim -200\,\mathrm{V}$, both background contributions increase.
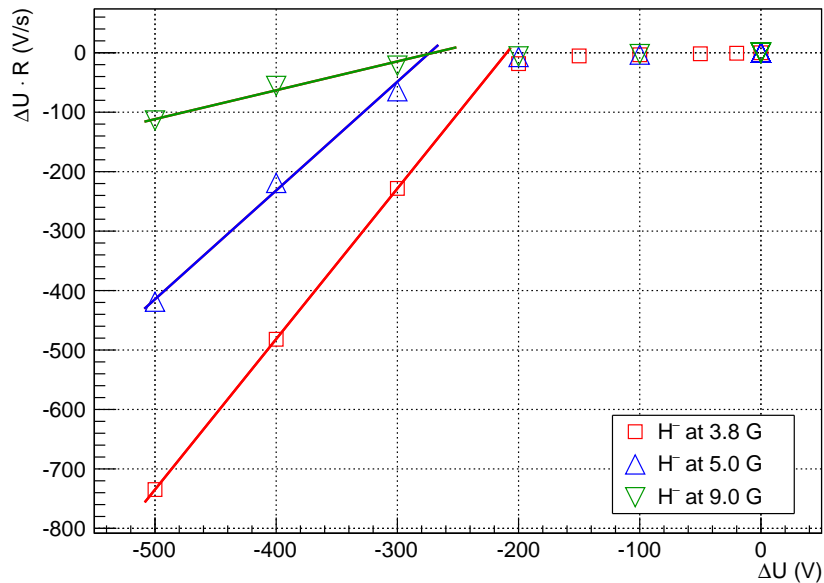
Figure 7.14: Threshold for the generation of hydrogen anions. The $R\Delta U$-ΔU plot illustrates the threshold ΔU_0 of the potential offset for the generation of hydrogen anions for different symmetric magnetic-field configurations. The intersection of the linear fits (solid lines) with the zero line ($R \approx 0\,\mathrm{cps}$) describes the onset of anion production. Statistical uncertainties are included but not visible.

defined by the horizontal axis. The following results are obtained:

$$
\begin{aligned}
3.8\,\text{G:}\ & \Delta U_0 = -210(5)\,V \\
5.0\,\text{G:}\ & \Delta U_0 = -273(11)\,V \\
9.0\,\text{G:}\ & \Delta U_0 = -270(9)\,V\ .
\end{aligned}
\tag{7.12}
$$

At $3.8\,\text{G}$, the sensitive magnetic flux tube is large in size, resulting in a relatively small clearance of a few centimeters relative to the inner surfaces of the spectrometer. Interestingly, the threshold ΔU_0 for the onset of H^--ion generation is significantly lower than the one for field electron emission. Put another way, the rate increase of H^- ions is observed already at a smaller absolute potential offset than observed for field emission of electrons. However, this seems reasonable in view of a common point of origin of field-emission electrons and anion generation, due to the fact that the cyclotron radius of a particle scales directly with its mass. Because of the mass ratio of an H^- ion relative to an electron of ~ 1800, the cyclotron radius of an H^- ion is much larger compared to the one of an electron with the same kinetic energy for a similar magnetic field strength. As a result, H^- ions can propagate more easily into the sensitive magnetic flux tube via radial drift motions, whereas electrons are magnetically shielded. Therefore, the obtained threshold values for ΔU_0 should be interpreted as detection thresholds and not as thresholds for H^--ion generation. For the other magnetic-field configurations, the magnetic flux tube is more compressed so that the clearance of the transported flux to the inner surfaces is increased. Accordingly, the effect of magnetic shielding increases for both H^- ions and surface-induced electrons. Thus, in case of the 5.0-G and the 9.0-G setting, the detection thresholds ΔU_0 for H^- ions and for field-emission induced electrons are consistent with each other within the statistical uncertainties. This fact strengthens the hypothesis of a correlation between field electron emission and the generation of H^- ions.

Spatial correlation

Apart from the observed correlations between the rates and onsets of field electron emission and generation of H^- ions, the mapping of the points of origin by the detector pixels is important. Figure 7.15 shows the background rates for electrons and H^- ions for an inner electrode offset of $\Delta U = -500\,V$ at $3.8\,\text{G}$, illustrated as detector-pixel views. Field-emission induced electrons and H^- ions are preferably detected on the outer pixel rings. As outlined, this can be easily explained as they have to propagate from the region of the spectrometer and electrode surfaces into the sensitive magnetic flux tube. The measured hotspots indicate that both event classes originate from localized sources distributed over the inner surface area. However, due to the use of symmetric magnetic-field configurations, it is quite challenging to physically localize these sources. Moreover, the pixel-rate distribution implies a specific correlation based on similar penetration mechanisms into the sensitive magnetic flux tube.

Time-interval correlation

When analyzing the field electron emission and H^--ion rates for fixed time intervals, correlations of the fluctuations of the background rates of both event classes should manifest. Figure 7.16 (left) shows the corresponding correlation plot illustrating the anion rate as a function of the electron rate within 5-min time intervals for the exemplary voltage offset of $\Delta U = -300\,V$ at $3.8\,\text{G}$. The linear fit indicates a high correlation coefficient of 0.685 for this configuration, thereby implying that variations of the electron rate coincide with variations of the anion rate, and vice versa. Moreover, the correlation coefficients are displayed in figure 7.16 (right) as a function of the potential offsets ΔU applied between vessel
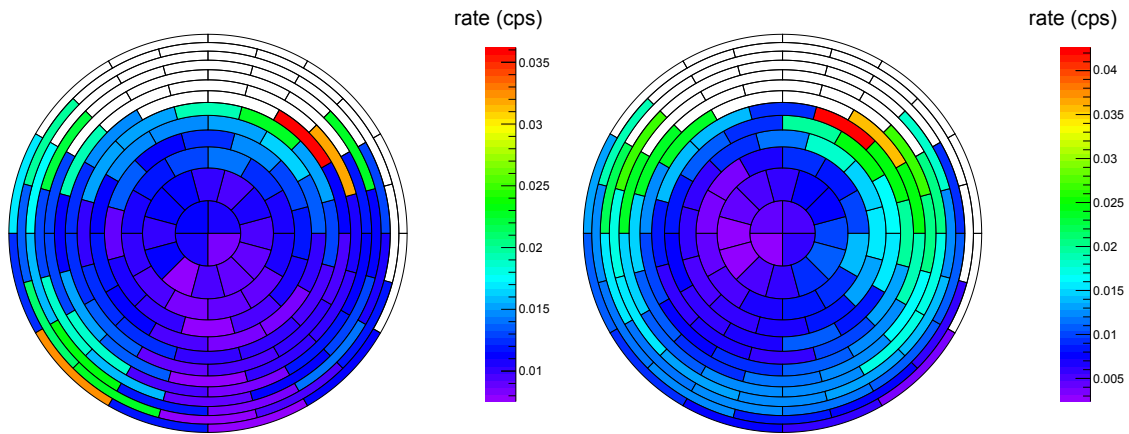
Figure 7.15: Spatial correlation of electrons and H⁻ ions. The pixel-rate distributions are illustrated for electrons (**left**) acquired in the energy interval ranging from 25.6 to 30.6 keV and for H⁻ ions (**right**) from 13.7 to 20.7 keV, using data from the high-voltage background measurement with a potential difference of $\Delta U = -500\,\mathrm{V}$ at the 3.8-G setting.
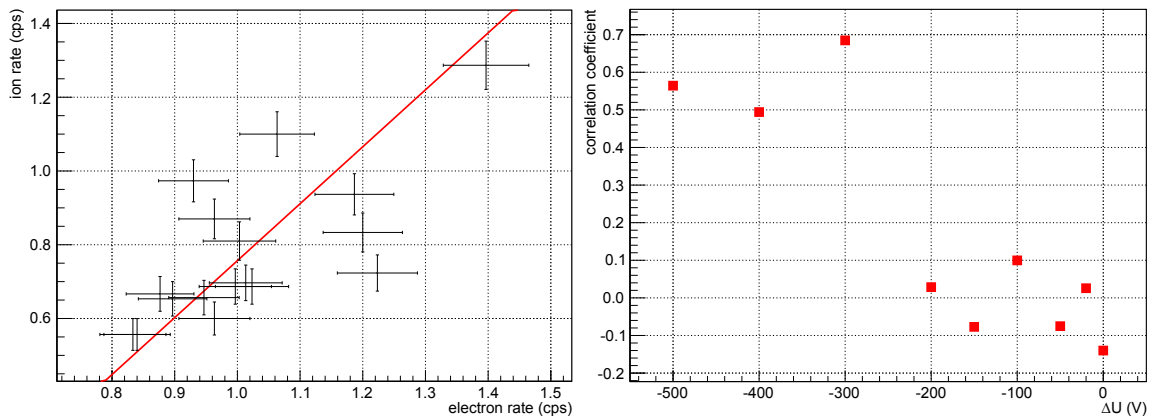
Figure 7.16: Time-interval correlation of electrons and H⁻ ions. Left: Correlation plot for background rates. The anion rate is illustrated as a function of the electron rate over 5-min time intervals for the background measurement with a potential offset of $\Delta U = -300\,\mathrm{V}$ at the 3.8-G setting. The linear straight-line fit (red line) indicates a high correlation coefficient of 0.685. **Right: Correlation coefficients.** The correlation coefficients of the anion rates to the electron rates are shown as a function of the potential offset ΔU at the 3.8-G setting.
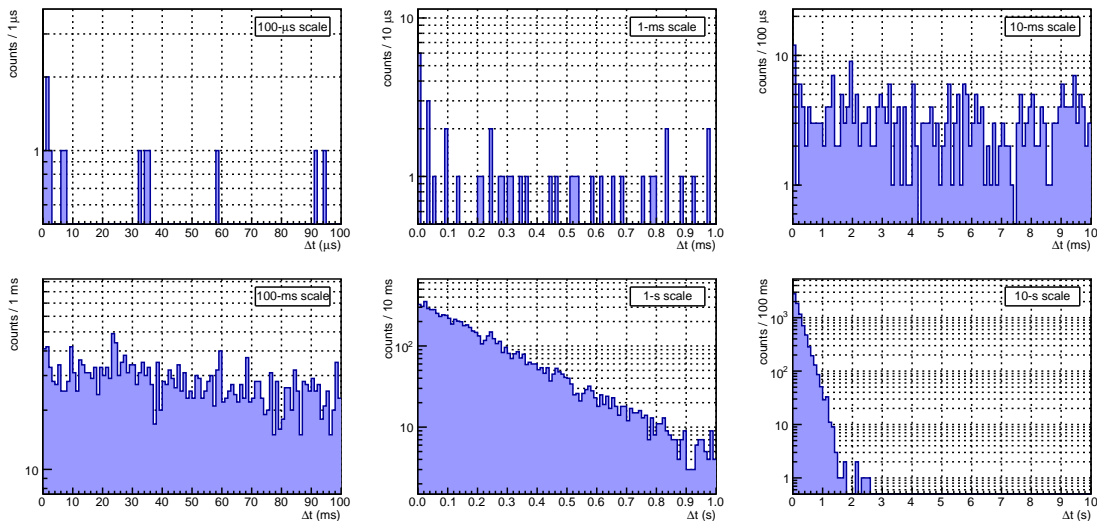
Figure 7.17: Event-based correlation of electrons and H⁻ ions. The distributions of time differences Δt between single electrons and single anions are shown at different time scales ranging from $100\,\mu s$ to $10\,s$.

and wires for the 3.8-G setting. At more negative potential offsets of $\Delta U \lesssim -300\,V$, the correlation coefficient reaches values of $\gtrsim 0.5$, while at smaller absolute potential offsets of $\Delta U \gtrsim -200\,V$, the correlation vanishes with coefficients decreasing toward 0. In the latter voltage region, neither field electron emission nor H⁻ ions contribute, since the detection thresholds for both event classes are $\Delta U_0 < -200\,V$. This observation demonstrates a further clear evidence for the presence of correlated processes between field emission and anion generation. The fact that the correlation coefficient is below unity even for larger voltage offsets ($\Delta U \lesssim -300\,V$) can be traced back to the influence of radon-induced background distorting the correlation analysis.

Event-based correlation

Apart from spatial and rate-based correlations, an event-based analysis allows to investigate correlations of single electrons with single anions, and vice versa. In this context, figure 7.17 illustrates the time differences Δt measured between the occurrence of an electron and the associated anion with shortest time distance to the former. The distributions are shown for different time scales ranging from $100\,\mu s$ to $10\,s$. As expected, no time correlations manifesting in a distinct time peak are visible. The same applies to an analysis where the roles of primary event (electron) and secondary event (anion) are reversed. These findings support the scenario that magnetic shielding suppresses the initial rates of electrons and anions by a large factor, so that the stochastic processes of drifting into the transported flux tube should result in uncorrelated electrons and anions. However, the observed correlation of electron and anion rates as a function of the offset voltage clearly points to a scenario in which electrons and H⁻ ions both originate from the process of field emission.

7.5.3 Production Mechanisms

There are several scenarios for the production of hydrogen anions (H⁻):

- **Dissociative attachment:**

$$\mathrm{H_2} + e^- \;\rightarrow\; \mathrm{H_2^-} \;\rightarrow\; \mathrm{H} + \mathrm{H^-} \tag{7.13}$$

213
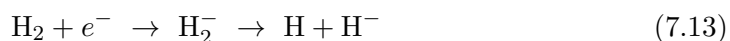
The attachment of a thermal low-energy electron to a hydrogen molecule from the residual gas can lead to the formation of a molecular hydrogen anion H_2^- which has a relatively short lifetime of $(8.2 \pm 1.5)\,\mu s$ [Heb06]. The subsequent fragmentation results in atomic hydrogen and a hydrogen anion H^-. In case of a reaction with residual gas, this volume-based reaction depends on the pressure inside the main-spectrometer volume. The required thermal electrons can arise (*i*) from magnetically trapped low-energy electrons, (*ii*) from surface-induced electrons by interactions through cosmic rays, environmental radiation, intrinsic radioactivity, and field emission, and (*iii*) from filled Penning traps. The exceedingly small number density of H_2 in the spectrometer excludes this reaction channel to be of relevance in view of its cross section.

- **Secondary attachment:**

$$H + e^- \ \to \ H^- \tag{7.14}$$

The reaction of the secondary attachment bypasses the formation of a molecular hydrogen anion. Apart from that, it directly forms a hydrogen anion H^- and is similar to the dissociative attachment. Again, atomic hydrogen column densities are too small to be of relevance.

- **Quantum tunneling:**

$$H_{ad} + e^- \ \to \ H^- \tag{7.15}$$

Metal surfaces are known to be covered in part by atomic hydrogen. This applies to the inner stainless-steel surface elevated to negative high voltage as well. In this case a very promising scenario can be postulated, in which a hydrogen anion H^- is formed by an electron from field emission from the associated surface with a surface-adsorbed hydrogen atom, thus resulting in H^--ion emission. The surface-based reaction strongly correlates with the process of field electron emission.

- **Eley-Rideal mechanism:**

$$H_2 + M \ \to \ H^- + H\text{-}M \tag{7.16}$$

In this case, a hydrogen molecule from the residual gas adsorbs on the inner stainless-steel surface elevated to negative high voltage. It interacts with one atom M of the surface such that a hydrogen anion H^- and a molecule H-M are formed, which desorb from the surface. This surface-related reaction depends on the pressure inside the main-spectrometer volume and on the electric potential applied to the surface. Therefore, it might correlate with the process of field electron emission [JL01] [Dit03].

- **Positive-ion bombardment:**

$$H^+ + M \ \to \ H^- + X \tag{7.17}$$

Signal electrons, surface-induced electrons from cosmic rays, and volume-induced electrons from radon α-decays can ionize residual gas atoms and molecules. The resulting positively charged ions (H^+, H_2^+) will impact on the inner electrodes elevated to negative potential. This volume-based and pressure-dependent bombardment could release hydrogen anions H^- from the surface. In this case, a correlation with the electric field strength between vessel wall and inner electrodes would require the H^+ ion production to take place in the rather small volume between vessel walls and inner electrodes.

The surprisingly large number of H^- ions observed in specific measurements of the first SDS commissioning phase make it rather difficult to establish a concise quantitative scenario to describe the generation of the observed number of H^- ions. The process of quantum

tunneling seems to be the most favorable reaction, since it directly couples the effect of field emission to H^--ion production, and thus might explain the strong correlation between electrons and H^- ions. For the upcoming second SDS commissioning phase, high-voltage background measurements can be performed at elevated pressure using gaseous hydrogen in combination with highly negative potential differences ΔU in order to investigate whether the anion production mechanism is a volume-based or a surface-based process. In addition, the operation at elevated pressure with an LN2 cooled baffle system allows to examine the process of positive-ion bombardment in more detail.

7.6 Conclusion

Field electron emission is a common process occurring in experiments where metal surfaces are elevated to a negative high voltage under vacuum conditions. By application of the Fowler-Nordheim theorem in combination with the magnetic imaging of the support structures of the inner wire electrodes onto the detector, quantum-tunneling origin of field-emission electrons could be demonstrated. For symmetric magnetic fields, the threshold for field electron emission was determined by introducing a $R\Delta U$-ΔU plot to the large value of $\Delta U_0 \lesssim -270\,\mathrm{V}$ applied between the spectrometer vessel and the inner wire electrodes. This large voltage offset region must definitely be avoided for later neutrino-mass measurements, since the field electron emission rate increases faster than the higher efficiency of electric shielding at larger voltage offsets. Other main components of the KATRIN experiment, such as the pre-spectrometer, the monitor spectrometer, and the detector system, also suffer from measurable field electron emission when operating these systems beyond nominal high-voltage values. Finally, a detailed comparison of measurements and energy-loss simulations has revealed a correlation between the process of field electron emission and the generation of H^- ions. These hydrogen anions impact on the detector at relatively small pitch angles, thus depositing a large amount of their initial energy in the insensitive dead-layer volume of the wafer to produce a distinct peak in the detector in a broad region about $11\,\mathrm{keV}$ below the single-electron peak. The post-acceleration potential electrostatically boosts these hydrogen anions above the electronic noise threshold of the detector and thus enables to study their characteristics in more detail. The specific energy loss of H^- ions in silicon allows to determine the dead-layer thickness to $99\,\mathrm{nm}$, ideally matching the specifications of $100\,\mathrm{nm}$ when considering statistical and systematic uncertainties. A variety of viable production mechanisms has been put forward in this thesis, in particular the attractive scenario of H^--ion production of the quantum-tunneled electron by attachment on a surface-adsorbed hydrogen atom on the comb-shaped structures of the inner electrodes. This as well as the other scenarios will be experimentally investigated during the upcoming second SDS commissioning phase.

CHAPTER 8

Summary and Outlook

The thesis in hand describes work performed in the context of the Karlsruhe Tritium Neutrino (KATRIN) experiment which is targeted to determine the absolute neutrino-mass scale with an unrivaled sensitivity of 200 meV (90 % C.L.).

In the Standard Model of particle physics, the three generations of neutrinos are described as fundamental, electrically neutral, weakly interacting leptons, which are predicted to be massless. However, the experimental observation of neutrino flavor oscillations has unambiguously proven neutrinos to have non-zero masses. Since the observables of oscillation experiments are the differences of the squared masses and not the absolute masses, these studies can only set a lower limit for the heaviest mass eigenstate of ~ 48 meV. Up to date, the most promising approach to determine the absolute neutrino-mass scale in a direct and model-independent way is the method of high-precision spectroscopy of tritium β-decay close to its kinematic endpoint at 18.6 keV, using the well-established MAC-E filter technique. With this measurement technique, the most stringent upper limit is set to $m_\nu < 2.0$ eV by two pioneering experiments performed at Mainz and Troitsk. The evidence for massive neutrinos and the ever more evident impact of neutrinos on particle physics and cosmology have initiated the ongoing construction of a next-generation large-scale neutrino-mass experiment: the KATRIN experiment at the KIT Campus North site.

The experiment uses a high-luminosity windowless gaseous molecular tritium source releasing 10^{11} β-electrons per second, and a high-precision electrostatic spectrometer operating as integrating high-pass filter based on the MAC-E filter principle with an energy resolution of $\Delta E = 0.93$ eV to 18.6-keV electrons. This unique experimental setup allows to improve the current neutrino-mass sensitivity by one order of magnitude after an effective measurement time of three years. β-electrons emitted from the source are adiabatically guided by strong magnetic fields from superconducting solenoids along the 70-m long beam line through a differential and cryogenic pumping section to the spectrometer and detector section (SDS). The electron energy in the vicinity of the endpoint is analyzed with sub-eV resolution by the main spectrometer. The characteristics of transmitted electrons is measured by a complex detector system offering very good energy, timing, and spatial resolution. Since only a tiny fraction of 2×10^{-13} of all β-electrons contribute to the relevant energy region of few eV below the endpoint, a generic low signal count rate of typically few times mcps[1] is expected. This contrasts with rates of up to several kcps[2] during periodic detector calibrations. In all cases, the detector parameters of deposited energy, arrival

---

[1] 10^{-3} counts per second
[2] 10^{3} counts per second

time, and point of detection are vital to understand signal-transport and background-generation mechanisms along the entire beam line. Consequently, the experiment relies on an almost background-free, highly efficient, long-term stable, and well-understood detection technique for 18.6-keV electrons. The demands are challenging in view of the stringent benchmarks for detector operation in strong magnetic and electrostatic fields under ultra-high vacuum conditions.

In the framework of the thesis in hand, the detector system has been fully implemented for the KATRIN experiment. It was installed and integrated into the KATRIN beam line as well as optimized by an extensive upgrade program and by adjusting many relevant system parameters. It is now comprehensively characterized. As the first KATRIN main component it successfully passed the operational readiness review. In particular, it was operated very successfully together with the main spectrometer during a four-month commissioning phase performed in the middle of 2013. The first commissioning of the combined spectrometer and detector section demonstrated an extraordinary degree of reliability of system performance with respect to long-term stability. The success of this commissioning has been a crucial milestone for the KATRIN experiment and the international collaboration. As major outcomes of these commissioning measurements, study of the detector characteristics allowed to optimize the alignment of the detector system relative to the main spectrometer. In addition, various sources of background were identified and characterized, such as the intrinsic detector background as well as radon-induced and field-emission induced backgrounds arising from the spectrometer. In the following, a summary of the topics covered in this work is given.

Performance of the KATRIN Detector System

The detector system is a complex yet versatile component of the KATRIN experiment, consisting of several sub-components which have been carefully designed together to meet all requirements: two 6-T warm-bore superconducting solenoids, an ultra-high vacuum and high vacuum system, a post-acceleration electrode, a 148-pixel silicon PIN-diode array with custom-built readout electronics and a DAQ system, including a cooling system, calibration and monitoring devices, and finally a scintillating veto system. A major part of this thesis was devoted to hardware upgrades of all subsystems to guarantee a reliable overall system performance. The main focus of the works was on improved long-term stability and complete functionality of all subsystems. This is exemplified by the following core parameters: a fraction of 98.6 % of working pixels, a magnetic-field stability with a monthly drift of $\lesssim 20\,\mathrm{ppm}$, stable ultra-high vacuum conditions with a base pressure of $3 \times 10^{-9}\,\mathrm{mbar}$, long-term operation of the post-acceleration electrode at a potential of $11\,\mathrm{kV}$ after extensive conditioning, functionality of all channels in the detector and veto readout chains, dead-time free operation of the DAQ system at high rates of up to several tens of kcps, and availability of sufficient cooling power to operate the detector at $-90°\mathrm{C}$ and the vacuum electronics under optimized conditions. This variety of different parameters underlines the complexity of the detector system.

Detector Characterization

The detector performance was fully characterized by investigating the response of each pixel and channel to radiation originating from two inline calibration sources: a 18.5-MBq γ-source of ^{241}Am, and an adjustable planar photoelectron source releasing electrons with energies of up to 25 keV. The detector characterization has yielded very good performance parameters with regard to energy, timing, and spatial resolution. The detector wafer is

functional for 146 of 148 pixels. The non-operational adjacent pixels are short-circuited on the segmented contact side of the wafer because of damaged inter-pixel boundaries. The optimization procedures were targeted with respect to DAQ filter settings, reverse-bias voltage, and operating temperature. A key system variable is the FWHM energy resolution of $\Delta E = 1.51(1)$ keV for 18.6-keV electrons which allows to separate signal electrons close to the retarding energy from the intrinsic detector background continuum. The non-linearity of the detector readout chain is small with an upper limit of $1.5(1)$ %, and the FWHM timing resolution with $\Delta t \lesssim 100$ ns allows to perform accurate time-of-flight studies with the main spectrometer. It is of particular importance that the variance of the timing latency across all pixels is well below the sampling rate of the DAQ system, implying that there are no distorting timing offsets between individual pixels. An important role in the overall optimization of the detector performance was played by the post-acceleration potential, which increases the signal-to-noise ratio and shifts low-energy electrons from the eV-range well beyond the electronic noise threshold. The system thus meets all design requirements with respect to studying background, transmission properties, and time-of-flight characteristics of the main spectrometer.

Detector Systematics

The extensive test program included a detailed investigation of systematics, such as rate dependence of the analog and digital readout chain, charge sharing of adjacent pixels, and calibration stability. All effects are well-understood and can be reproduced by analytical calculations.

Rate Dependence. Rate-dependent effects in energy spectra were traced back to pile-up effects, where signals are influenced by other near-simultaneous signals. This leads to distinct distortions appearing in the energy spectra in the form of peak broadening and peak shifting at high incident rates of $\gtrsim 1$ kcps. In this context, peak pile-up interprets signals with inter-arrival times shorter than the integration time of the DAQ filter as a single event with multiple energy, while tail pile-up underestimates the energies of signals with inter-arrival times shorter than the fall time of the preamplifiers. These effects were suppressed to a large degree by reducing the integration time. For a very high incident rate of 30 kcps, the relative shift of the single-electron peak toward lower energies was measured to be ~ 25 % from its initial value at an integration time of 6.4 μs , and only ~ 5 % at 1.6 μs, in excellent agreement with expectations obtained from calculations.

Charge Sharing. Charge-sharing effects were traced back to incident radiation which interacts in the sensitive detector volume such that the deposited energy is distributed to more than one pixel. The conservative upper limit for the charge-sharing probability between two adjacent pixels was calculated to 2.32 % averaged over the entire wafer. Locally, this varies from 1.54 % for the innermost to 2.90 % for the outermost pixels, as a result of the different pixel shapes. The width of the coincidence window for charge sharing of 18.6-keV electrons was measured to be 1.5 μs This results in an upper limit for the charge-sharing probability of $1.74(24)$ % for the entire detector wafer, with individual probabilities ranging from 1.3 to 2.4 %.

Calibration Stability. During the first four-month long SDS commissioning phase, a total of 24 detector calibrations were performed using the ^{241}Am source in periodic time intervals to investigate the long-term stability of the detector with regard to the position and width of the 59.54-keV calibration line. In order to examine the influence of other system components and operation parameters, a correlation matrix was established showing

the strong correlations between detector-related and heat-pipe parameters, such as drifting temperatures. These correlations allow to monitor drifts in the detector response by observing permanently all heat-pipe parameters, thereby reducing the number of required detector calibrations and increasing measurement times for background studies.

Background Investigation

In the framework of this thesis, two different types of spectrometer-related background were examined in addition to intrinsic detector background: this is radon-induced and field-emission induced background. The intrinsic detector background is at present a small, subdominant component only and can be characterized by an almost featureless continuum. The spectrometer-related background is of the order of 1 cps. This is a small number in view of the more than several 10^4 cosmic-ray muons passing the spectrometer per second and is thus testament to the excellent magnetic shielding of the MAC-E filter. However, the generic rate is two orders of magnitude above the ambitious design value of 0.01 cps, thus necessitating extensive investigations of the background sources and characteristics. Spectrometer-related background originates primarily from low-energy electrons, either generated in the magnetic flux tube by volume-based processes, or being emitted from the inner structural materials by surface-based processes. These low-energy electrons in the eV-range are then accelerated by the retarding potential to produce a distinct peak in the measured energy spectrum with an energy indistinguishable from signal electrons.

Intrinsic Detector Background. The intrinsic detector background is primarily caused by cosmic rays, external natural environmental radiation, and intrinsic radioactivity from primordial or cosmogenic isotopes. In the course of this thesis, several passive and active background-reduction techniques of the detector system were optimized. Passive background reduction is achieved by a layered lead-copper radiation shield surrounding the sensitive parts of the vacuum system on the ambient-air side, supplemented by donut-shaped copper sleeves blocking internal radiation from the readout lines, and by carefully selected and radio-assayed materials used in close proximity to the detector. Active background reduction is accomplished by electrostatic post-acceleration shifting the electron signal to an energy interval with less background, by variation of the magnetic field to tune the sensitive beam size imaged onto the detector, and by the rejection of correlated detector events through a multi-pixel and veto cut. The latter cut makes use of plastic-scintillator panels surrounding the radiation shield. A comparison between background measurements and simulations indicates the presence of an as yet unidentified background component with a rate of the order of ~ 0.3 mcps/keV which is not rejected from the raw background spectrum, neither by the multi-pixel cut nor by the veto cut. The figure of demerit was introduced as a detector-related quantity characterizing the optimum position and width of the region of interest, taking account of the tradeoff between detection efficiency, energy resolution, and detector background rate. In this context, it is important to note that the low signal and background rates as well as the cyclic scanning of the β-decay spectrum with the spectrometer retarding voltage require the definition of a region of interest in the detector energy spectrum. The figure of demerit scales linearly with the statistical uncertainty of the squared neutrino mass and thus directly influences the neutrino-mass sensitivity. For the detector response to 18.6-keV electrons, a minimum figure of demerit of $F_{\min} = 1.119(2)$ with an average intrinsic detector background rate of $b_{\mathrm{cut}} = 1.07(3)$ mcps/keV and a signal fraction of $f = 0.939(1)$ was measured within an acceptance window ranging from $E_L = 14.5(1)$ keV to $E_U = 20.0(1)$ keV after both active background-reduction approaches had been applied. In order to meet the ambitious design goal of $F < 1.1$, further background reduction will require to improve the veto efficiency

and to elevate the post-acceleration electrode beyond its current limits. However, by investigating secondary electron emission from a gate valve mapped onto the wafer for different magnetic field strengths, it could be demonstrated that the true intrinsic background level is below the observed rates. This true intrinsic detector background level can be examined with an additional elevated electrode installed between the spectrometer and the detector system to electrostatically shield low-energy electrons from the main spectrometer after opening the gate valve between both systems.

Radon-Induced Background. The emanation processes of single radon atoms into the spectrometer volume results in a background source of electrons which has the potential to seriously limit the neutrino-mass sensitivity of KATRIN in case of no countermeasures. The radon isotopes ^{219}Rn and ^{220}Rn which are of interest in this context originate from two distinct sources: the 3-km long strips of the non-evaporable getter (NEG) pump and the 690-m^2 surface of the inner vessel walls. Emanation from the structural materials leads to a homogenous distribution of radon atoms in the sensitive magnetic flux-tube volume. The subsequent radon α-decay creates high-energy primary electrons which are magnetically trapped in the flux-tube volume and produce up to thousands of low-energy secondary electrons via residual-gas interactions, thereby cooling down. Accelerated by the retarding potential, these secondary electrons produce a distinct peak with the same energy as signal electrons in the measured energy spectrum. A key measurement technique of this thesis to study this background class was to artificially elevate the spectrometer pressure by injecting argon gas. This allows to identify single radon α-decays occurring inside the magnetic flux tube on an event-by-event basis and to separate them from cosmic-ray muon-induced background. At elevated pressure, radon-induced events manifest as bursts of electrons with inter-arrival times of $\Delta t \leq 0.2$ s for single detector hits (*spike events*), while surface-based background events are Poisson-distributed in time (*single events*). The associated inter-arrival time cut of $\Delta t_{\mathrm{cut}} = 0.2$ s thus allows to separate both background classes to better study their characteristics. Due to their circular magnetron motion, magnetically stored electrons generate a characteristic ring-shaped pattern at the detector. The operation of a LN2 cooled baffle system allows to significantly reduce the radon-induced electron background rate by adsorption of radon atoms onto a cold copper surface so that the subsequent α-decay of the adsorbed radon atom does not produce background. The long-term efficiency of the baffle system in removing radon atoms will be determined during the upcoming second SDS commissioning phase. There, the baffle system will be continuously operated at elevated spectrometer pressure. In this configuration, individual radon-induced events can be observed due to the excellent detector mapping properties. This approach was successfully pioneered during the first SDS commissioning phase with a non-operating baffle system. This allowed to investigate characteristics of radon-induced background, such as the temporal and spatial distributions, the average number of generated secondary electrons, and the average storage time of primary electrons. Moreover, solid evidence was provided for the hypothesis that decaying radon atoms are homogeneously distributed inside the spectrometer volume. The measured total radon activity of $A_{\mathrm{tot}} \approx 0.2$ Bq and emanation rate of $E_{\mathrm{tot}} \approx 0.20 - 0.25$ s^{-1} is consistent with the expectations based on extrapolations of pre-spectrometer test experiments. When scaling data at elevated pressure to standard vacuum conditions, a novel method was implemented based on the spatial Δring distribution. This allows to determine the radon-induced background contribution independently of the actual vacuum conditions inside the spectrometer. The novel method is robust and provides bias-free results, as the modeled contributions are in excellent agreement with the measured background rates. This fact makes the Δring distribution a powerful statistical tool to background events, complementing the inter-arrival time spectrum for temporal correlations. Finally, the scaling of radon-induced events allows to model the background characteristics at standard operating mode. The above

described observations will be further refined in the upcoming second SDS commissioning phase when the baffle system is fully operating, enabling further detailed investigations of radon-induced background.

Field Electron Emission and Hydrogen Anions. In general, field electron emission commonly occurs in experiments where metal surfaces are elevated to negative high voltage under vacuum conditions. In the case of the spectrometer, the rather sharp-edged support structure of the inner wire electrodes is a likely source for field electron emission. Electrons from these well-localized regions propagate via radial $\vec{E} \times \vec{B}$ and $\vec{\nabla}|\vec{B}| \times \vec{B}$ drift motions into the sensitive magnetic flux tube. By applying the Fowler-Nordheim theorem of field emission in combination with the magnetic imaging properties of the support structure onto the detector, it could be demonstrated that field electron emission is present when the voltage offset between spectrometer vessel and inner electrode system was adjusted to a regime beyond the standard operating mode. For a symmetric magnetic field, the threshold for field electron emission was determined to be $\Delta U_0 \lesssim -270\,\text{V}$ via the newly introduced $R\Delta U$-ΔU plot. This threshold is largely independent of the actual magnetic-field configuration. As a consequence of this work, the voltage offsets will have to be minimized and the more negative part of the voltage region explored must definitely be avoided for later neutrino-mass measurements. In this range, field electron emission background rates increase much faster than the background reduction increases due to the electrostatic shielding of the wire electrodes. Therefore, these investigations reveal that the optimum voltage offset is based on a specific tradeoff between a minimum contribution from field electron emission and maximum electrostatic shielding. Other main components of the KATRIN experiment, such as the pre-spectrometer, the monitor spectrometer, and the detector system, also suffer from measurable field electron emission when operating these systems beyond nominal configurations. Finally, by combining these specific measurements with energy-loss simulations, this work revealed that H^- ions are generated as an accompanying process of field electron emission. Hydrogen anions when impacting on the detector with relatively small incident angles will deposit a large amount of their initial energy in the insensitive dead-layer volume of the wafer. Thus, they produce an additional peak in the detector energy spectrum about $11\,\text{keV}$ below the single-electron peak. The post-acceleration potential electrostatically boosts these hydrogen anions above the electronic noise threshold of the detector and thus enables more detailed investigations. The characteristic energy loss of H^- ions in silicon allows to deduce a dead-layer thickness to $99\,\text{nm}$, in excellent agreement with the specification of $100\,\text{nm}$, when considering statistical and systematic uncertainties. Possible H^--ion production mechanisms will be scrutinized during the upcoming second SDS commissioning phase when performing high-voltage background measurements at elevated pressure using hydrogen. The continuous operation of the baffle system will then reduce distorting effects due to radon-induced electrons and the second layer of the inner wire electrodes will enable additional studies with respect to field electron emission.

Detector Alignment

Finally, in the course of this thesis, the alignment of the detector system with the solenoids, the vacuum-chamber beam line, and the detector wafer relative to the spectrometer beam axis was investigated. The following approaches were pioneered:

Mechanical Alignment. The mechanical alignment was performed by scanning the locations of specific components of the detector system with a *FaroArm*. The corresponding results were parametrized for the Monte Carlo package *Kassiopeia* in order to perform

Table 8.1: Results for the detector alignment. The displacement of the center of the detector wafer relative to the central beam axis of the magnetic flux tube is listed for different approaches, measurements, and simulations. In general, the wafer is shifted to the right by Δx and to the top by Δy, looking from the main spectrometer to the detector system. The statistical uncertainty of the ring-fit algorithm used for analyzing data is in the order of $\sim 1\,\text{mm}$.

approach	analysis	Δx (mm)	Δy (mm)	reference (section)
mechanical *FaroArm* scans	simulation at $3.8\,\text{G}$	1.8	3.1	4.9
radon-induced ring pattern	data at $9.0\,\text{G}$	1.7(1)	4.6(1)	6.2.2
	data at $5.0\,\text{G}$	1.6(2)	4.8(2)	
field-emission induced ring pattern	simulation (outer ring)	1.7	5.3	7.4
	data (outer ring)	1.3	3.3	
	simulation (inner ring)	1.7	5.3	
	data (inner ring)	1.3	3.7	

electron-tracking simulations using the actual as-built geometry of the detector system. The observed shadowing from the in-line flapper valve and the post-acceleration electrode due to magnetic imaging onto the detector wafer was reproduced very well by simulations, underlining the important interplay between *FaroArm* scans, simulations, and measurements. In addition, the misalignment of the detector wafer relative to the flux-tube axis for symmetric and asymmetric magnetic-field configurations was determined via simulations.

Radon-Induced Ring Pattern. Background measurements at elevated pressure with symmetric magnetic field allow to observe individual trapped keV-electrons of individual radon α-decays occurring inside the magnetic flux tube. Due to the magnetron motion of magnetically stored electrons, a characteristic ring-shaped pattern is visible at the detector. It was shown that the average ring-center coordinates give experimental access to the magnetic alignment of the detector wafer relative to the axis of the magnetic flux tube.

Field-Emission Induced Ring Pattern. Measurements with asymmetric magnetic field using a strong voltage offset between spectrometer vessel and inner electrodes beyond the standard operating mode allow to map the support structure of the inner wire electrodes by making use of field-emission induced electrons. Since this support structure is circular and coaxially arranged to the main-spectrometer axis, it is imaged as a two-ring shaped structure onto the detector. When calculating the ring-center coordinates, the mechanical alignment of the detector wafer relative to the support structure can be deduced in a third independent way.

The results with respect to the detector alignment are summarized in table 8.1, illustrating general broad agreement of the different approaches.

Outlook

In the framework of this thesis, the complex and versatile detector system was used to acquire data under a large number of different configurations. Detector signal information, such as deposited energy, arrival time, and point of detection, plays a key role in analysis of background processes, system alignment, and signal electron propagation. Of particular importance was the post-acceleration electrode which allows to boost electrons to larger

energies, thus allowing to study eV-electrons being generated at non-elevated regions in the spectrometer and detector section. Despite its rather complicated and compact setup, the detector system is a user-friendly and well-understood facility. Its ability for long-term stable and fail-safe operation was demonstrated successfully over several months of continuous run time. These facts have contributed significantly to the success of the first SDS commissioning phase in summer 2013, representing a major milestone for the KATRIN experiment.

The upcoming second SDS commissioning phase in the middle of 2014 will allow to investigate the background processes described here in more detail. This will be possible due to an aligned detector system, a continuously operating baffle system, and a functional second layer of inner wire electrodes in the central cylindrical part of the spectrometer. The detector system as an integral component of the KATRIN beam line will play a central role in the long-term data-taking. For the first time, the detector system will be operated with 100 % functional pixels. Based on the findings of this thesis, the detector system fulfills all requirements of the KATRIN experiment to measure the effective mass of the electron neutrino with a sensitivity of 200 meV at 90 % C.L. over five calender years.

Appendix

A Detector Channel Map

The following table shows the detector channel map which was used during stand-alone detector commissioning and the first SDS commissioning phase. The assignment of the detector pixels to the electronic channels is important for troubleshooting and reliable data taking.

Table A.1: Detector channel map. The following abbreviations are used: pixel = detector-wafer pixel, cable = plastic-optical-fiber link, quad = detector quadrant, preamp = preamplifier-module slot, preampCh = preamplifier-module channel, osb = optical-sender-board slot, osbCh = optical-sender-board channel, flt = first-level-trigger-card slot, fltCh = first-level-trigger-card channel, air = pin at feedthrough flange on ambient-air side, vac = pin at feedthrough flange on HVac side.

pixel	cable	quad	preamp	preampCh	osb	osbCh	flt	fltCh	air	vac
125	1	0	0	0	0	0	2	0	40	44
101	2	0	0	1	0	1	2	1	39	45
77	3	0	0	2	0	2	2	2	37	47
53	4	0	0	3	0	3	2	3	36	48
29	5	0	0	4	0	4	2	4	35	49
5	6	0	0	5	0	5	2	5	18	33
0	7	0	0	6	0	6	2	6	2	16
136	8	0	1	0	0	7	2	7	19	32
112	9	0	1	1	0	8	2	8	3	15
88	10	0	1	2	0	9	2	9	20	31
64	11	0	1	3	0	10	2	10	4	14
40	12	0	1	4	0	11	2	11	21	30
16	13	0	1	5	0	12	2	12	22	29
124	14	0	2	0	0	13	2	13	6	12
100	15	0	2	1	0	14	2	14	23	28
76	16	0	2	2	0	15	2	15	7	11
52	17	0	2	3	0	16	2	16	41	43
28	18	0	2	4	0	17	2	17	25	26
4	19	0	2	5	0	18	2	18	9	9
147	20	0	3	0	0	19	3	0	26	25
123	21	0	3	1	0	20	3	1	11	7
99	22	0	3	2	0	21	3	2	28	23
75	23	0	3	3	0	22	3	3	12	6
51	24	0	3	4	0	23	3	4	29	22
27	25	0	3	5	0	24	3	5	30	21

pixel	cable	quad	preamp	preampCh	osb	osbCh	flt	fltCh	air	vac
135	26	0	4	0	0	25	3	6	14	4
111	27	0	4	1	0	26	3	7	31	20
87	28	0	4	2	0	27	3	8	15	3
63	29	0	4	3	0	28	3	9	32	19
39	30	0	4	4	0	29	3	10	16	2
15	31	0	4	5	0	30	3	11	33	18
146	32	0	5	0	0	31	3	12	49	35
122	33	0	5	1	0	32	3	13	48	36
98	34	0	5	2	0	33	3	14	47	37
74	35	0	5	3	0	34	3	15	45	39
50	36	0	5	4	0	35	3	16	44	40
26	37	0	5	5	0	36	3	17	43	41
134	38	1	6	0	1	0	4	0	40	44
110	39	1	6	1	1	1	4	1	39	45
86	40	1	6	2	1	2	4	2	37	47
62	41	1	6	3	1	3	4	3	36	48
38	42	1	6	4	1	4	4	4	35	49
14	43	1	6	5	1	5	4	5	18	33
3	44	1	6	6	1	6	4	6	2	16
145	45	1	7	0	1	7	4	7	19	32
121	46	1	7	1	1	8	4	8	3	15
97	47	1	7	2	1	9	4	9	20	31
73	48	1	7	3	1	10	4	10	4	14
49	49	1	7	4	1	11	4	11	21	30
25	50	1	7	5	1	12	4	12	22	29
133	51	1	8	0	1	13	4	13	6	12
109	52	1	8	1	1	14	4	14	23	28
85	53	1	8	2	1	15	4	15	7	11
61	54	1	8	3	1	16	4	16	41	43
37	55	1	8	4	1	17	4	17	25	26
13	56	1	8	5	1	18	4	18	9	9
144	57	1	9	0	1	19	5	0	26	25
120	58	1	9	1	1	20	5	1	11	7
96	59	1	9	2	1	21	5	2	28	23
72	60	1	9	3	1	22	5	3	12	6
48	61	1	9	4	1	23	5	4	29	22
24	62	1	9	5	1	24	5	5	30	21
132	63	1	10	0	1	25	5	6	14	4
108	64	1	10	1	1	26	5	7	31	20
84	65	1	10	2	1	27	5	8	15	3
60	66	1	10	3	1	28	5	9	32	19
36	67	1	10	4	1	29	5	10	16	2
12	68	1	10	5	1	30	5	11	33	18
143	69	1	11	0	1	31	5	12	49	35
119	70	1	11	1	1	32	5	13	48	36
95	71	1	11	2	1	33	5	14	47	37
71	72	1	11	3	1	34	5	15	45	39
47	73	1	11	4	1	35	5	16	44	40
23	74	1	11	5	1	36	5	17	43	41
131	75	2	12	0	2	0	6	0	40	44

pixel	cable	quad	preamp	preampCh	osb	osbCh	flt	fltCh	air	vac
107	76	2	12	1	2	1	6	1	39	45
83	77	2	12	2	2	2	6	2	37	47
59	78	2	12	3	2	3	6	3	36	48
35	79	2	12	4	2	4	6	4	35	49
11	80	2	12	5	2	5	6	5	18	33
2	81	2	12	6	2	6	6	6	2	16
142	82	2	13	0	2	7	6	7	19	32
118	83	2	13	1	2	8	6	8	3	15
94	84	2	13	2	2	9	6	9	20	31
70	85	2	13	3	2	10	6	10	4	14
46	86	2	13	4	2	11	6	11	21	30
22	87	2	13	5	2	12	6	12	22	29
130	88	2	14	0	2	13	6	13	6	12
106	89	2	14	1	2	14	6	14	23	28
82	90	2	14	2	2	15	6	15	7	11
58	91	2	14	3	2	16	6	16	41	43
34	92	2	14	4	2	17	6	17	25	26
10	93	2	14	5	2	18	6	18	9	9
141	94	2	15	0	2	19	7	0	26	25
117	95	2	15	1	2	20	7	1	11	7
93	96	2	15	2	2	21	7	2	28	23
69	97	2	15	3	2	22	7	3	12	6
45	98	2	15	4	2	23	7	4	29	22
21	99	2	15	5	2	24	7	5	30	21
129	100	2	16	0	2	25	7	6	14	4
105	101	2	16	1	2	26	7	7	31	20
81	102	2	16	2	2	27	7	8	15	3
57	103	2	16	3	2	28	7	9	32	19
33	104	2	16	4	2	29	7	10	16	2
9	105	2	16	5	2	30	7	11	33	18
140	106	2	17	0	2	31	7	12	49	35
116	107	2	17	1	2	32	7	13	48	36
92	108	2	17	2	2	33	7	14	47	37
68	109	2	17	3	2	34	7	15	45	39
44	110	2	17	4	2	35	7	16	44	40
20	111	2	17	5	2	36	7	17	43	41
128	112	3	18	0	3	0	8	0	40	44
104	113	3	18	1	3	1	8	1	39	45
80	114	3	18	2	3	2	8	2	37	47
56	115	3	18	3	3	3	8	3	36	48
32	116	3	18	4	3	4	8	4	35	49
8	117	3	18	5	3	5	8	5	18	33
1	118	3	18	6	3	6	8	6	2	16
139	119	3	19	0	3	7	8	7	19	32
115	120	3	19	1	3	8	8	8	3	15
91	121	3	19	2	3	9	8	9	20	31
67	122	3	19	3	3	10	8	10	4	14
43	123	3	19	4	3	11	8	11	21	30
19	124	3	19	5	3	12	8	12	22	29
127	125	3	20	0	3	13	8	13	6	12

pixel	cable	quad	preamp	preampCh	osb	osbCh	flt	fltCh	air	vac
103	126	3	20	1	3	14	8	14	23	28
79	127	3	20	2	3	15	8	15	7	11
55	128	3	20	3	3	16	8	16	41	43
31	129	3	20	4	3	17	8	17	25	26
7	130	3	20	5	3	18	8	18	9	9
138	131	3	21	0	3	19	9	0	26	25
114	132	3	21	1	3	20	9	1	11	7
90	133	3	21	2	3	21	9	2	28	23
66	134	3	21	3	3	22	9	3	12	6
42	135	3	21	4	3	23	9	4	29	22
18	136	3	21	5	3	24	9	5	30	21
126	137	3	22	0	3	25	9	6	14	4
102	138	3	22	1	3	26	9	7	31	20
78	139	3	22	2	3	27	9	8	15	3
54	140	3	22	3	3	28	9	9	32	19
30	141	3	22	4	3	29	9	10	16	2
6	142	3	22	5	3	30	9	11	33	18
137	143	3	23	0	3	31	9	12	49	35
113	144	3	23	1	3	32	9	13	48	36
89	145	3	23	2	3	33	9	14	47	37
65	146	3	23	3	3	34	9	15	45	39
41	147	3	23	4	3	35	9	16	44	40
17	148	3	23	5	3	36	9	17	43	41

B Veto Channel Map

The following table shows the veto channel map which was used during stand-alone detector commissioning and the first SDS commissioning phase. The assignment of the MPPCs to the electronic channels is important for troubleshooting and reliable data taking.

Table B.1: Veto channel map. The following abbreviations are used: MPPC = MPPC slot, cable = *LEMO* cable, panel = plastic-scintillator-panel slot, panelCh = plastic-scintillator-panel channel, amp = front-end-amplifier-board slot, ampCh = front-end-amplifier-board channel, flt = first-level-trigger-card slot, fltCh = first-level-trigger-card channel.

MPPC	cable	panel	panelCh	amp	ampCh	flt	fltCh
1	01	west	1	1	8	15	0
2	02	west	2	1	7	15	2
3	03	west	3	1	6	15	4
4	04	west	4	1	5	15	6
5	05	west	5	1	4	15	8
6	06	west	6	1	3	15	10
7	11	east	1	1	2	15	1
8	12	east	2	1	1	15	3
9	13	east	3	2	8	15	16
10	14	east	4	2	7	15	18
11	15	east	5	2	6	15	20
12	16	east	6	2	5	15	22
13	21	top	1	2	4	16	0
14	22	top	2	2	3	16	2
15	23	top	3	2	2	16	4
16	24	top	4	2	1	16	6
17	25	top	5	3	8	16	8
18	26	top	6	3	7	16	10
19	31	bottom	1	3	6	16	1
20	32	bottom	2	3	5	16	3
21	33	bottom	3	3	4	16	16
22	34	bottom	4	3	3	16	18
23	35	bottom	5	3	2	16	20
24	36	bottom	6	3	1	16	22
25	41	end-cap bottom	1	4	8	15	9
26	42	end-cap bottom	2	4	7	15	11
27	43	end-cap bottom	3	4	6	15	13
28	44	end-cap bottom	4	4	5	15	15
29	51	end-cap top	1	4	4	16	9
30	52	end-cap top	2	4	3	16	11
31	53	end-cap top	3	4	2	16	13
32	54	end-cap top	4	4	1	16	15

List of Acronyms

AC	alternating current
ADC	analog-to-digital converter
ADEI	advanced data extraction infrastructure
ALEPH	Apparatus for LEP Physics
AGS	Alternating Gradient Synchrotron
ATLAS	A Toroidal LHC Apparatus
CC	charged-current
CCG	cold-cathode gauge
CENPA	Center for Experimental Nuclear Physics and Astrophysics
CERN	Conseil Européen pour la Recherche Nucleaire, Europäische Organisation für Kernforschung
CEP	convection-enhanced Pirani gauge
cFP	compact Field Point
CMB	cosmic microwave background
CMS	Compact Muon Solenoid
COBE	Cosmic Background Explorer
CPS	cryogenic pumping section
CUORE	Cryogenic Underground Observatory for Rare Events
CνB	cosmic neutrino background
DAQ	data-acquisition
DC	direct current
DET	detector magnet
DONUT	Direct Observation of the NU Tau
DPS	differential pumping section
EGUN	electron gun
EIG	extractor-ion gauge
EMCS	earth magnetic field compensation system
ES	elastic-scattering

FLT	first-level trigger
FPD	focal-plane detector system
FPGA	field programmable gate array
FWHM	full width at half maximum
F-N	Fowler-Nordheim
GALLEX	Gallium Experiment
GERDA	Germanium Detector Array
GNO	Gallium Neutrino Observatory
GPS	global positioning system
HVac	high vacuum
IMB	Irvine-Michigan-Brookhaven
INFN	Istituto Nazionale di Fisica Nucleare
IPE	Institute for Data Processing and Electronics
K2K	KEK to Kamioka
Kamiokande	Kamioka Nucleon Decay Experiment
KamLAND	Kamioka Liquid Scintillator Antineutrino Detector
KATRIN	Karlsruhe Tritium Neutrino
KHYS	Karlsruhe House of Young Scientists
KIT	Karlsruhe Institute of Technology
LED	light-emitting diode
LEP	Large Electron-Positron Collider
LFCS	low field correction system
LHC	Large Hadron Collider
LN2	liquid-nitrogen
MAC-E	magnetic adiabatic collimation combined with an electrostatic
MARE	Microcalorimeter Arrays for a Rhenium Experiment
MINOS	Main Injector Neutrino Oscillation Search
MIT	Massachusetts Institute of Technology
MPPC	multi-pixel photon counter
MS	main spectrometer
MSW	Michejew-Smirnow-Wolfenstein
NASA	National Aeronautics and Space Administration
NC	neutral-current
NEG	non-evaporable getter
NMR	nuclear magnetic resonance

NOνA	NuMI Off-Axis ν_e Appearance
NuMI	Neutrinos at the Main Injector
OFHC	oxygen-free high-conductivity
ORCA	object-oriented real-time control and acquisition
PAE	post-acceleration electrode
PCH	pinch magnet
PCI	peripheral component interconnect
PID	proportional-integral-derivative
PIN	p-type, i-type, n-type semiconductor
PMNS	Pontecorvo-Maki-Nakagawa-Sakata
PS	pre-spectrometer
PS1	pre-spectrometer magnet 1
PS2	pre-spectrometer magnet 2
PSI	Paul-Scherrer-Institut
PSU	power-supply unit
RENO	Reactor Experiment for Neutrino Oscillation
RGA	residual-gas analyzer
ROI	region of interest
RS	rear section
SAGE	Soviet-American Gallium Experiment
SDS	spectrometer and detector section
SLT	second-level trigger
SNO	Sudbury Neutrino Observatory
T2K	Tokai to Kamioka
TLK	Tritium Laboratory Karlsruhe
TMP	turbomolecular pump
UHVac	ultra-high vacuum
UI	user interface
UNC	University of North Carolina
US	United States
UTC	universal time, coordinated
UV	ultraviolet light
UW	University of Washington
VI	virtual instrument
WGTS	windowless gaseous tritium source
WMAP	Wilkinson Microwave Anisotropy Probe
ZEUS	central DAQ and control system, zentrale Erfassung und Steuerung

List of Figures

List of Tables

Bibliography

[Abe08]   S. Abe et al. (The KamLAND Collaboration), "Precision Measurement of Neutrino Oscillation Parameters with KamLAND," *Phys. Rev. Lett.*, vol. 100, p. 221803, 2008, DOI: 10.1103/PhysRevLett.100.221803.

[Abe11a]   K. Abe et al. (Super-Kamiokande Collaboration), "Search for Differences in Oscillation Parameters for Atmospheric Neutrinos and Antineutrinos at Super-Kamiokande," *Phys. Rev. Lett.*, vol. 107, p. 241801, 2011, DOI: 10.1103/PhysRevLett.107.241801.

[Abe11b]   K. Abe et al. (T2K Collaboration), "Indication of Electron Neutrino Appearance from an Accelerator-Produced Off-Axis Muon Neutrino Beam," *Phys. Rev. Lett.*, vol. 107, p. 041801, 2011, DOI: 10.1103/PhysRevLett.107.041801.

[Abe12]   Y. Abe et al. (Double Chooz Collaboration), "Reactor $\overline{\nu}_e$ disappearance in the Double Chooz experiment," *Phys. Rev. D*, vol. 86, p. 052008, 2012, DOI: 10.1103/PhysRevD.86.052008.

[Abe13]   K. Abe et al. (T2K Collaboration), "Evidence of electron neutrino appearance in a muon neutrino beam," *Phys. Rev. D*, vol. 88, p. 032002, 2013, DOI: 10.1103/PhysRevD.88.032002.

[ABL11]   E. Arimondo, P. R. Berman, and C. C. Lin, "Advances in atomic, molecular, and optical physics," *Academic Press Elsevier*, vol. 60, 2011.

[ABP12]   J. F. Amsbaugh, N. M. Boyd, and D. M. S. Parno, "Heat Pipe Manual: Installation and Operation," 2012, internal KATRIN document. [Online]. Available: https://fuzzy.fzk.de/bscw/bscw.cgi/d746261/Heat%20Pipe%20Manual

[Ack13]   K. Ackermann et al. (GERDA Collaboration), "The Gerda experiment for the search of $0\nu\beta\beta$ decay in ^{76}Ge," *The European Physical Journal C*, vol. 73, p. 2330, 2013, DOI: 10.1140/epjc/s10052-013-2330-0.

[Ada11]   P. Adamson et al. (MINOS Collaboration), "Measurement of the Neutrino Mass Splitting and Flavor Mixing by MINOS," *Phys. Rev. Lett.*, vol. 106, p. 181801, 2011, DOI: 10.1103/PhysRevLett.106.181801.

[Ada13]   ——, "Measurement of Neutrino and Antineutrino Oscillations Using Beam and Atmospheric Data in MINOS," *Phys. Rev. Lett.*, vol. 110, p. 251801, 2013, DOI: 10.1103/PhysRevLett.110.251801.

[Agi07]   Agilent Technologies, "Agilent 33220A 20 MHz Waveform Generator, User's Guide," *Agilent Technologies*, vol. 4, 2007, Publication Number 33220-90002 (order as 33220-90100 manual set).

[Agi12]   ——, "Agilent Technologies, Low-Profile Modular Power System, Series N6700, User's Guide," 2012, internal KATRIN document. [Online]. Available: https://fuzzy.fzk.de/bscw/bscw.cgi/d767566/Agilent-N6700series-PowerSupply.pdf

[Ago03]   S. Agostinelli et al., "Geant4 - a simulation toolkit," *Nuclear Instruments and Methods in Physics Research Section A: Accelerators, Spectrometers, Detectors and Associated Equipment*, vol. 506, no. 3, pp. 250 – 303, 2003, DOI: 10.1016/S0168-9002(03)01368-8.

[Ago13]   M. Agostini et al. (GERDA Collaboration), "Results on Neutrinoless Double-β Decay of ^{776}Ge from Phase I of the GERDA Experiment," *Physical Review Letters*, vol. 111, p. 122503, 2013, DOI: 10.1103/PhysRevLett.111.122503.

[Aha05]   B. Aharmim et al. (SNO Collaboration), "Electron energy spectra, fluxes, and day-night asymmetries of ^{8}B solar neutrinos from measurements with NaCl dissolved in the heavy-water detector at the Sudbury Neutrino Observatory," *Phys. Rev. C*, vol. 72, no. 1, p. 055502, 2005, DOI: 10.1103/PhysRevC.72.055502.

[Aha07]   ——, "Determination of the ν_e and total ^{8}B solar neutrino fluxes using the Sudbury Neutrino Observatory Phase I data set," *Phys. Rev. C*, vol. 75, p. 045502, 2007, DOI: 10.1103/PhysRevC.75.045502.

[Aha08]   ——, "Independent Measurement of the Total Active ^{8}B Solar Neutrino Flux Using an Array of ^{3}He Proportional Counters at the Sudbury Neutrino Observatory," *Phys. Rev. Lett.*, vol. 101, p. 111301, 2008, DOI: 10.1103/PhysRevLett.101.111301.

[Ahm01]   Q. R. Ahmad et al. (SNO Collaboration), "Measurement of the Rate of $\nu_e + d \rightarrow p + p + e^-$ Interactions Produced by ^{8}B Solar Neutrinos at the Sudbury Neutrino Observatory," *Phys. Rev. Lett.*, vol. 87, no. 7, 2001, DOI: 10.1103/PhysRevLett.87.071301.

[Ahm02]   ——, "Direct Evidence for Neutrino Flavor Transformation from Neutral-Current Interactions in the Sudbury Neutrino Observatory," *Phys. Rev. Lett.*, vol. 89, no. 1, 2002, DOI: 10.1103/PhysRevLett.89.011301.

[Ahn06]   M. H. Ahn et al. (K2K Collaboration), "Measurement of neutrino oscillation by the K2K experiment," *Phys. Rev. D*, vol. 74, p. 072003, 2006, DOI: 10.1103/PhysRevD.74.072003.

[Ahn12]   J. K. Ahn et al. (RENO Collaboration), "Observation of Reactor Electron Antineutrinos Disappearance in the RENO Experiment," *Phys. Rev. Lett.*, vol. 108, p. 191802, 2012, DOI: 10.1103/PhysRevLett.108.191802.

[Alb04]   C. Albright, V. Barger, J. Beacom, S. Brice, J. J. Gomez-Cadenas, M. Goodman, D. Harris, P. Huber, A. Jansson, M. Lindner, O. Mena, P. Rapidis, K. Whisnant, W. Winter (The Neutrino Factory, Muon Collider Collaboration), "The Neutrino Factory and Beta Beam Experiments and Development," 2004, arXiv:physics/0411123v2.

[ALE06]   T. ALEPH Collaboration, The DELPHI Collaboration, The L3 Collaboration, The OPAL Collaboration, The SLD Collaboration, The LEP Electroweak Working Group, The SLD Electroweak and Heavy Flavour Groups, "Precision electroweak measurements on the Z resonance," *Physics Reports*, vol. 427, no. 5 - 6, pp. 257 – 454, 2006, DOI: 10.1016/j.physrep.2005.12.006.

[All06]   J. Allison et al., "Geant4 developments and applications," *IEEE Transactions on Nuclear Science*, vol. 53, no. 1, pp. 270 – 278, 2006, DOI: 10.1109/TNS.2006.869826.

[Amr09]   Amrel, "Amrel ePower - Operation Manual," 2009, internal KATRIN document. [Online]. Available: https://fuzzy.fzk.de/bscw/bscw.cgi/d767987/Amrel_PDseries_Manual.pdf

[Ams14] J. F. Amsbaugh et al., "Focal-plane detector system for the KATRIN experiment," *NIM A*, 2014, arXiv:1404.2925 [physics.ins-det].

[An 13] F. P. An et al. (Daya Bay Collaboration), "Improved measurement of electron antineutrino disappearance at Daya Bay," *Chinese Physics C*, vol. 37, no. 1, p. 011001, 2013, DOI: 10.1088/1674-1137/37/1/011001.

[Ang05] J. Angrik et al., "KATRIN Design Report 2004," *FZKA Scientific Report 7090*, 2005.

[Ara05] T. Araki et al., "Experimental investigation of geologically produced antineutrinos with KamLAND," *Nature*, vol. 436, pp. 499 – 503, 2005, DOI: 10.1038/nature03980.

[Arn04] C. Arnaboldi et al., "CUORE: a cryogenic underground observatory for rare events," *Nuclear Instruments and Methods in Physics Research Section A: Accelerators, Spectrometers, Detectors and Associated Equipment*, vol. 518, no. 3, pp. 775 – 798, 2004, DOI: 10.1016/j.nima.2003.07.067.

[Ase11] V. N. Aseev et al., "Upper limit on electron antineutrino mass from Troitsk experiment," *Phys. Rev. D*, vol. 84, no. 11, p. 112003, 2011, DOI: 10.1103/PhysRevD.84.112003.

[Ass96] K. Assamagan et al., "Upper limit of the muon-neutrino mass and charged-pion mass from momentum analysis of a surface muon beam," *Phys. Rev. D*, vol. 53, p. 6065, 1996, DOI: 10.1103/PhysRevD.53.6065.

[AT09] J. Amsbaugh and K. Tolich, "KATRIN Detector Vacuum System Control," 2009, internal KATRIN document. [Online]. Available: https://fuzzy.fzk.de/bscw/bscw.cgi/d767098/Katrin%20Detector%20Vacuum%20System%20Control.pdf

[ATL12] ATLAS Collaboration, "Observation of a new particle in the search for the Standard Model Higgs boson with the ATLAS detector at the LHC," *Physics Letters B*, vol. 716, no. 1, pp. 1 – 29, 2012, DOI: 10.1016/j.physletb.2012.08.020.

[AVV02] J. N. Abdurashitov, E. P. Veretenkin, and V. M. Vermul et al., "Solar neutrino flux measurements by the Soviet-American gallium experiment (SAGE) for half the 22-year solar cycle," *Journal of Experimental and Theoretical Physics*, vol. 95, no. 2, pp. 181 – 193, 2002, DOI: 10.1134/1.1506424.

[Ayr05] D. Ayres et al. (The NOvA Collaboration), "NOvA Proposal to Build a 30 Kiloton Off-Axis Detector to Study Neutrino Oscillations in the Fermilab NuMI Beamline," 2005, arXiv:hep-ex/0503053v1.

[Bab12] M. Babutzka et al., "Monitoring of the operating parameters of the KATRIN Windowless Gaseous Tritium Source," *New Journal of Physics*, vol. 14, p. 103046, 2012, DOI: 10.1088/1367-2630/14/10/103046.

[Bah64a] J. N. Bahcall, "Solar Neutrino Cross Sections and Nuclear Beta Decay," *Phys. Rev.*, vol. 135, no. 1B, pp. B137 – B146, 1964, DOI: 10.1103/PhysRev.135.B137.

[Bah64b] ——, "Solar Neutrinos. I. Theoretical," *Phys. Rev. Lett.*, vol. 12, no. 11, pp. 300 – 302, 1964, DOI: 10.1103/PhysRevLett.12.300.

[Bah05] J. N. Bahcall et al., "New Solar Opacities, Abundances, Helioseismology, and Neutrino Fluxes," *The Astrophysical Journal Letters*, vol. 621, no. 1, p. 621, 2005, DOI: 10.1086/428929.

[Bar95] J. Baro, J. Sempau, J.M. Fernandez - Varea, F. Salvat, "PENELOPE: An algorithm for Monte Carlo simulation of the penetration and energy loss

of electrons and positrons in matter," *Nuclear Instruments and Methods in Physics Research Section B: Beam Interactions with Materials and Atoms*, vol. 100, no. 1, pp. 31 – 46, 1995, DOI: 10.1016/0168-583X(95)00349-5. [Online]. Available: http://pypenelope.sourceforge.net/

[Bar98]   R. Barate et al., "An upper limit on the τ neutrino mass from three- and five-prong tau decays," *The European Physical Journal C - Particles and Fields*, vol. 2, no. 3, pp. 395 – 406, 1998, DOI: 10.1007/s100529800850.

[Bar00]   V. Barger, S. Geer, R. Raja, K. Whisnant, "Long-baseline study of the leading neutrino oscillation at a neutrino factory," *Phys. Rev. D*, vol. 62, p. 013004, 2000, DOI: 10.1103/PhysRevD.62.013004.

[Bar14]   J. Barrett, A. Beglarian, J. Behrens, T. J. Corona, G. Drexlin, S. Enomoto, M. Erhard, F. Fränkle, F. Glück, S. Görhardt, S. Groh, M. Haag, V. Hannen, F. Harms, D. Hilk, A. Kopmann, M. Kraus, M. Krause, B. Leiber, A. Müller, O. Rest, P. Rovedo, J. Schwarz, N. Stallkamp, N. Steinbrink, T. Thümmler, N. Trost, N. Wandkowsky, C. Weinheimer, K. Wierman, J. Wolf, M. Zacher, "Results of the first KATRIN SDS measurement phase," 2014, internal KATRIN document.

[BD76]   J. N. Bahcall and R. Davis Jr., "Solar Neutrinos: A Scientific Puzzle," *Science*, vol. 191, pp. 264 – 267, 1976. [Online]. Available: www.bnl.gov/bnlweb/raydavis/Science-01-23-76.pdf

[BDP87]   J. N. Bahcall, A. Dar, and T. Piran, "Neutrinos and neutrino mass from a supernova," *Nature*, vol. 326, pp. 135 – 136, 1987. [Online]. Available: http://www.nature.com/physics/looking-back/bahcall/Bahcall.pdf

[Beh13]   J. D. Behrens, T. J. Corona, F. Glück, S. Groh, N. Steinbrink, N. Wandkowsky, Ch. Weinheimer, "EMD consequences of electrical shorts at the inner electrode system," 2013, internal KATRIN document. [Online]. Available: http://fuzzy.fzk.de/bscw/bscw.cgi/d775431/EMD%20consequences%20of%20electrical%20shorts%20at%20the%20inner%20electrode%20system.pdf

[Beh14]   J. Behrens et al., "Reduction of stored-particle background by magnetic pulse in the KATRIN spectrometers," *New Journal of Physics*, 2014, paper in preparation.

[Bel95]   A. Belesev et al., "Results of the Troitsk experiment on the search for the electron antineutrino rest mass in tritium beta-decay," *Physics Letters B*, vol. 350, no. 2, pp. 263 – 272, 1995, DOI: 10.1016/0370-2693(95)00335-I.

[Bel03]   E. Bellotti, "Neutrino Physics," *Societa italiana di fisica*, vol. 152, p. 25, 2003.

[Ber10]   M. J. Berger et al., "XCOM: Photon cross sections database, Version 1.5," *National Institute of Standards and Technology, Gaithersburg, MD*, 2010. [Online]. Available: http://www.nist.gov/pml/data/xcom

[Ber12a]   T. Bergmann, D. Bormann, M. A. Howe, M. Kleifges, A. Kopmann, N. Kunka, A. Menshikov, D. Tcherniakhovski, "FPGA-based multi-channel DAQ systems with external PCI express link to GPU compute servers," *Real Time Conference (RT), 2012 18th IEEE-NPSS*, pp. 1 – 5, 2012, DOI: 10.1109/RTC.2012.6418197.

[Ber12b]   J. Beringer et al. (Particle Data Group), "010001 (2012) Review of Particle Physics," *Phys. Rev. D*, vol. 86, no. 1, 2012, DOI: 10.1103/PhysRevD.86.010001.

[Ber13]   ——, "010001 (2012) and 2013 partial update for the 2014 edition," *Phys. Rev. D*, vol. 86, no. 010001, 2013. [Online]. Available: http://pdg.lbl.gov

[Beu11]   F. Beutler et al., "The 6dF Galaxy Survey: baryon acoustic oscillations and the local Hubble constant," *Monthly Notices of the Royal Astronomical Society*, vol. 416, no. 4, pp. 3017 – 3032, 2011, DOI: 10.1111/j.1365-2966.2011.19250.x.

[BFP85]   D. Bogdan, A. Faessler, and A. Petrovici, "Neutrino masses and right-handed current in the neutrinoless double beta decay $^{76}Ge \rightarrow {}^{76}Se + 2e^-$," *Physics Letters B*, vol. 150, no. 1 - 3, pp. 29 – 34, 1985, DOI: 10.1016/0370-2693(85)90131-5.

[BG06]   L. Bergström and A. Goobar, "Cosmology and Particle Astrophysics," *Springer*, 2006.

[BHP80]   S. M. Bilenky, J. Hosek, and S. T. Petcov, "On the oscillations of neutrinos with Dirac and Majorana masses," *Physics Letters B*, vol. 94, no. 4, pp. 495 – 498, 1980, DOI: 10.1016/0370-2693(80)90927-2.

[Bic98]   Bicron, "BC-400/BC-404/BC-408/BC-412/BC-416 Premium Plastic Scintillators," *Saint-Gobain Industrial Ceramics, Inc.*, 1998. [Online]. Available: http://www.phys.ufl.edu/courses/phy4803L/group_I/muon/bicron_bc400-416.pdf

[Bio87]   R. M. Bionta et al., "Observation of a Neutrino Burst in Coincidence with Supernova 1987A in the Large Magellanic Cloud," *Phys. Rev. Lett.*, vol. 58, p. 1494, 1987, DOI: 10.1103/PhysRevLett.58.1494.

[Bod]   L. I. Bodine, "KATRIN Detector Section Magnet Coil Geometry," internal KATRIN document.

[Bod11]   T. Bode, "Optimierung des 2-Phasen-Kühlkonzepts für den WGTS-Demonstrator von KATRIN," *Karlsruhe Institute of Technology*, 2011, diploma thesis.

[Bon95]   B. Bonin, "Field emission and surface conditioning," *Vacuum*, vol. 46, no. 8, pp. 907 – 912, 1995, DOI: 10.1016/0042-207X(95)00069-0.

[Bor08]   B. Bornschein, "Determination of Neutrino Mass from Tritium Beta Decay," *Fusion Science and Technology*, vol. 54, no. 1, pp. 59 – 66, 2008.

[Bor10]   Borexino Collaboration, "Observation of geo-neutrinos," *Physics Letters B*, vol. 687, no. 4 - 5, pp. 299 – 304, 2010, DOI: 10.1016/j.physletb.2010.03.051.

[Boy12]   N. M. Boyd, "Donut Installation (w/pics)," 2012, internal KATRIN elog. [Online]. Available: https://crunch5.npl.washington.edu:8443/KATRIN+Detector+Commissioning+/390

[BP34]   H. Bethe and R. Peierls, "The Neutrino," *Nature*, vol. 133, p. 532, 1934, DOI: 10.1038/133532a0.

[BPT80]   G. Beamson, H. Q. Porter, and D. W. Turner, "The collimating and magnifying properties of a superconducting field photoelectron spectrometer," *Journal of Physics E: Scientific Instruments*, vol. 13, no. 1, p. 64, 1980, DOI: 10.1088/0022-3735/13/1/018.

[BR96]   R. Brun and F. Rademakers, "ROOT - An Object Oriented Data Analysis Framework," *Proceedings AIHENP'96 Workshop, Lausanne*, 1996. [Online]. Available: http://root.cern.ch/

[BR97]   ——, "ROOT - An Object Oriented Data Analysis Framework," *Nucl. Inst. & Meth. in Phys. Res. A*, vol. 389, pp. 81 – 86, 1997. [Online]. Available: http://root.cern.ch/

[Bro01]   E. Browne, "Nuclear Data Sheets for A = 215, 219, 223, 227, 231," *Nuclear Data Sheets*, vol. 93, no. 4, pp. 763 – 1061, 2001, DOI: 10.1006/ndsh.2001.0016.

[Bun64]   R. E. Bunney, "Review of literature, secondary electron emission," *National Aeronautics and Space Administration*, 1964, NASA CR 54366 CER65VAS-REB12a.

[Bur52]   E. H. S. Burhop, "The Auger effect and other radiationless transitions," *University Press Cambridge*, 1952.

[BV10]   M. Beck and K. Valerius et al., "Effect of a sweeping conductive wire on electrons stored in a Penning-like trap between the KATRIN spectrometers," *The European Physical Journal A*, vol. 44, no. 3, pp. 499 – 511, 2010, DOI: 10.1140/epja/i2010-10959-1.

[Byr05]   J. Byrne, "Experience with high electric and magnetic Penning traps," *FZK Karlsruhe*, 2005, released talk. [Online]. Available: https://neutrino.ikp.kit.edu/owncloud/data/katrin/files/Public/Presentations/Byrne-talk-14Apr2005-FZK.pdf

[CB11]   Cryomagnetics Inc. and L. I. Bodine, "User's Manual, 6T Detector and Pinch Superconducting Magnet Pair for University of Washington (KATRIN)," 2011, internal KATRIN document. [Online]. Available: https://fuzzy.fzk.de/bscw/bscw.cgi/d653154/Magnet%20User%27s%20Manual.pdf

[Cen12]   Center for Experimental Nuclear Physics and Astrophysics, "2012 Annual Report," *University of Washington*, 2012. [Online]. Available: http://www.npl.washington.edu/annualreports

[Cen13]   ——, "2013 Annual Report," *University of Washington*, 2013. [Online]. Available: http://www.npl.washington.edu/annualreports

[Cen14]   ——, "2014 Annual Report," *University of Washington*, 2014. [Online]. Available: http://www.npl.washington.edu/annualreports

[Cha14]   J. Chadwick, "Intensitätsverteilung im magnetischen Spektrum der β-Strahlen von Radium B + C / The Intensity Distribution in Magnetic Spectrum of β-Rays of Radium B + C," *Verhandl. Dtsch. phys. Ges.*, vol. 16, p. 383, 1914.

[Che95]   C. Chengrui et al., "A possible explanation of the negative values of $m_{\nu_e}^2$ obtained from the β spectrum shape analysis," *Int. J. Mod. Phys. A*, vol. 10, no. 19, p. 2841, 1995, DOI: 10.1142/S0217751X95001340.

[Chi10]   S. Chilingaryan, A. Beglarian, A. Kopmann, S. Vöcking, "Advanced data extraction infrastructure: Web based system for management of time series data," *Journal of Physics: Conference Series*, vol. 219, no. 4, p. 042034, 2010, DOI: 10.1088/1742-6596/219/4/042034. [Online]. Available: http://katrin.kit.edu/adei/

[CK35]   D. Coster and R. D. L. Kronig, "New type of auger effect and its influence on the X-ray spectrum," *Physica*, vol. 2, no. 1 - 12, pp. 13 – 24, 1935, DOI: 10.1016/S0031-8914(35)90060-X.

[CK77]   L. Cesnak and J. Kokavec, "Magnetic field stability of superconducting magnets," *Cryogenics*, vol. 17, no. 2, pp. 107 – 110, 1977, DOI: 10.1016/0011-2275(77)90107-2.

[Cle98]   B. T. Cleveland et al., "Measurement of the Solar Electron Neutrino Flux with the Homestake Chlorine Detector," *The Astrophysical Journal*, vol. 496, pp. 505 – 526, 1998, DOI: 10.1086/305343.

[CMS12] CMS Collaboration, "Observation of a new boson at a mass of 125 GeV with the CMS experiment at the LHC," *Physics Letters B*, vol. 716, no. 1, pp. 30 – 61, 2012, DOI: 10.1016/j.physletb.2012.08.021.

[Cow56] C. L. Cowan Jr., F. Reines, F. B. Harrison, H. W. Kruse, A. D. McGuire, "Detection of the Free Neutrino: a Confirmation," *Science*, vol. 124, no. 3212, pp. 103 – 104, 1956, DOI: 10.1126/science.124.3212.103.

[Cry04] Cryomagnetics, "Operating Instruction Manual for the Model LM-500 Cryogenic Liquid Level Monitor," 2004, internal KATRIN document. [Online]. Available: https://fuzzy.fzk.de/bscw/bscw.cgi/d713472/LHe-LevelSensor-LM500.pdf

[Cry07a] Cryomech, "Cryogenic Refrigerator: INSTALLATION, OPERATION and ROUTINE MAINTENANCE MANUAL, CP830," 2007, internal KATRIN document. [Online]. Available: https://fuzzy.fzk.de/bscw/bscw.cgi/d768644/Cryomech_PT60_CP830_Manual.pdf

[Cry07b] ——, "Cryorefrigerator Specification Sheet, PT60-UL with CP830," 2007, internal KATRIN document. [Online]. Available: https://fuzzy.fzk.de/bscw/bscw.cgi/d767500/Cryomech_PT60_SpecSheet.pdf

[Cry09] Cryomagnetics Inc., "Operating Instruction Manual for the 4G Magnet Power Supply," 2009, internal KATRIN document. [Online]. Available: https://fuzzy.fzk.de/bscw/bscw.cgi/d653136/Model%204G%20Power%20Supply%20Instruction%20Manual%20-%20Rev%208_1.pdf

[Cry11] Cryomech, "Cryogenic Refrigerator: INSTALLATION, OPERATION and ROUTINE MAINTENANCE MANUAL, CP2800," 2011, internal KATRIN document. [Online]. Available: https://fuzzy.fzk.de/bscw/bscw.cgi/d713454/CryogenicRefrigeratorCP2880_Cryomech.pdf

[Cry14] ——, 2014, Cryomech PT410: specifications. [Online]. Available: http://www.cryomech.com/products/cryorefrigerators/pulse-tube/pt410/

[CS10] Y. D. Chan and A. R. Smith, "Low Background Facility at LBNL," *DUSEL AARM Collaboration Meeting 2010*, 2010. [Online]. Available: https://zzz.physics.umn.edu/lowrad/_media/lbf_faarm.pdf

[Dan62] G. Danby, J.-M. Gaillard, K. Goulianos, L. M. Lederman, N. Mistry, M. Schwartz, J. Steinberger, "Observation of High-Energy Neutrino Reactions and the Existence of Two Kinds of Neutrinos," *Phys. Rev. Lett.*, vol. 9, no. 1, pp. 36 – 44, 1962, DOI: 10.1103/PhysRevLett.9.36.

[Dav55] R. Davis Jr., "Attempt to Detect the Antineutrinos from a Nuclear Reactor by the $Cl^{37}(\overline{\mu}, e^-)Ar^{37}$ Reaction," *Phys. Rev.*, vol. 97, no. 3, pp. 766 – 769, 1955, DOI: 10.1103/PhysRev.97.766.

[Dav64] ——, "Solar Neutrinos. II. Experimental," *Phys. Rev. Lett.*, vol. 12, no. 11, pp. 303 – 305, 1964, DOI: 10.1103/PhysRevLett.12.303.

[Dav94] ——, "A review of the homestake solar neutrino experiment," *Progress in Particle and Nuclear Physics*, vol. 32, pp. 13 – 32, 1994, DOI: 10.1016/0146-6410(94)90004-3.

[DaV03] C. DaVia, "Radiation hard silicon detectors lead the way," *Cern Courier*, 2003. [Online]. Available: http://cerncourier.com/cws/article/cern/28790

[DEC79] R. Davis Jr., J. C. Evans, and B. T. Cleveland, "The solar neutrino problem," *AIP Conf. Proc.*, vol. 52, no. 17, 1979, DOI: 10.1063/1.31802.

[DeC89] D. DeCamp et al. (ALEPH Collaboration), "Determination of the number of light neutrino species," *Phys. Lett. B*, vol. 231, no. 4, pp. 519 – 529, 1989, DOI: 10.1016/0370-2693(89)90704-1.

[Dev13] P. S. B. Dev, S. Goswami, M. Mitra, W. Rodejohann, "Constraining neutrino mass from neutrinoless double beta decay," *Physical Review D*, vol. 88, p. 091301, 2013, DOI: 10.1103/PhysRevD.88.091301.

[DHH68] R. Davis Jr., D. S. Harmer, and K. C. Hoffman, "Search for Neutrinos from the Sun," *Phys. Rev. Lett.*, vol. 20, no. 21, pp. 1205 – 1209, 1968, DOI: 10.1103/PhysRevLett.20.1205.

[Din14] J. Ding, "Electrostatic Field Simulations and Field Emission Measurements at the KATRIN Spectrometers," *Karlsruhe Institute of Technology*, 2014, master thesis.

[Dir27] P. Dirac, "The Quantum Theory of the Emission and Absorption of Radiation," *Proceedings Royal Society A*, vol. 114, p. 243, 1927.

[Dit03] R. Dittmeyer, W. Keim, G. Kreysa, A. Oberholz, "Chemische Technik," *Winnacker-Küchler, WILEY-VCH*, vol. 5, 2003.

[DKT85] M. Doi, T. Kotani, and E. Takasugi, "Double Beta Decay and Majorana Neutrino," *Progress of Theoretical Physics Supp*, vol. 83, pp. 1 – 175, 1985, DOI: 10.1143/PTPS.83.1.

[Doe07] P. Doe, J. Formaggio, M. Howe, M. Leber, R. Robertson, "Optimization criterion for the signal and background in the KATRIN focal-plane detector," 2007, internal KATRIN document.

[Doe08a] P. Doe, "Detector-MS beam line valve," 2008, internal KATRIN documents. [Online]. Available: https://fuzzy.fzk.de/bscw/bscw.cgi/724214

[Doe08b] L. Doerr, U. Besserer, N. Bekris, B. Bornschein, C. Caldwell-Nichols, D. Demange, I. Cristescu, I.R. Cristescu, M. Glugla, G. Hellriegel, P. Schäfer, S. Weite, J.Wendel, "A decade of tritium technology development and operation at the Tritium Laboratory Karlsruhe," *Fusion Science and Technology*, vol. 54, no. 1, pp. 143 – 148, 2008.

[Doe11] P. Doe, "Detector Vacuum System - Users guide," 2011, internal KATRIN document. [Online]. Available: https://fuzzy.fzk.de/bscw/bscw.cgi/d723919/ Detector%20Vacum%20system%20%E2%80%93%20Users%20manual.pdf

[Doe13a] ——, "Checking for shorts on detector wafers," 2013, internal KATRIN elog. [Online]. Available: https://crunch5.npl.washington.edu:8443/KATRIN+ Detector+Commissioning+/534

[Doe13b] P. Doe, F. Harms, H. Robertson, J. Schwarz, M. Steidl, "Quench Report," 2013, internal KATRIN document. [Online]. Available: https: //fuzzy.fzk.de/bscw/bscw.cgi/d857193/4th%20pich%20quench%20report.pdf

[Dol53] W. W. Dolan, "Current Density Tables for Field Emission Theory," *Phys. Rev.*, vol. 91, no. 3, pp. 510 – 511, 1953, DOI: 10.1103/PhysRev.91.510.

[DON01] DONUT Collaboration, "Observation of Tau Neutrino Interactions," *Phys. Lett. B*, vol. 504, no. 3, pp. 218 – 224, 2001, DOI: 10.1016/S0370-2693(01)00307-0.

[Dos06] N. Doss, J. Tennyson, A. Saenz, S. Jonsell, "Molecular effects in investigations of tritium molecule β decay endpoint experiments," *Physical Review C*, vol. 73, p. 025502, 2006, DOI: 10.1103/PhysRevC.73.025502.

[Dos08]   ——, "Excitations to the electronic continuum of ^{3}HeT$^+$ in investigations of T$_2$ β-decay experiments," *Journal of Physics B: Atomic, Molecular and Optical Physics*, vol. 41, no. 12, p. 125701, 2008, DOI: 10.1088/0953-4075/41/12/125701.

[Dre13]   G. Drexlin, V. Hannen, S. Mertens, C. Weinheimer, "Current Direct Neutrino Mass Experiments," *Advances in High Energy Physics*, p. 293986, 2013, DOI: 10.1155/2013/293986.

[DS74]   R. R. Daniel and S. A. Stephens, "Cosmic-ray-produced electrons and gamma rays in the atmosphere," *Reviews of Geophysics*, vol. 12, no. 2, pp. 233 – 258, 1974, DOI: 10.1029/RG012i002p00233.

[DT53]   W. P. Dyke and J. K. Trolan, "Field Emission: Large Current Densities, Space Charge, and the Vacuum Arc," *Phys. Rev.*, vol. 89, no. 4, pp. 799 – 809, 1953, DOI: 10.1103/PhysRev.89.799.

[EFG62]   D. W. Engelkemeir, K. F. Flynn, and L. E. Glendenin, "Positron Emission in the Decay of K^{40}," *Phys. Rev.*, vol. 126, p. 1818, 1962, DOI: 10.1103/PhysRev.126.1818.

[Ell07]   C. Elliott, V. Vijayakumar, W. Zink, R. Hansen, "National Instruments LabVIEW: A Programming Environment for Laboratory Automation and Measurement," *Journal of Laboratory Automation*, vol. 12, no. 1, pp. 17 – 24, 2007, DOI: 10.1016/j.jala.2006.07.012. [Online]. Available: http://www.ni.com/labview/

[Eno14]   S. Enomoto, "Simple Analytical Models of Signal Pile-Up," 2014, internal KATRIN document. [Online]. Available: https://neutrino.ikp.kit.edu:8080/SDS-Analysis/25

[Erh12]   M. Erhard, "Untersuchung der Langzeitstabilität des nuklearen Standards für die Energieskala des KATRIN-Experiments," *Karlsruhe Institute of Technology*, 2012, diploma thesis.

[Erh14]   M. Erhard et al., "High voltage monitoring with a solenoid retarding spectrometer of the KATRIN experiment," *Journal of Instrumentation*, 2014, submitted for review.

[EV02]   S. R. Elliott and P. Vogel, "Double Beta Decay," *Annual Review of Nuclear and Particle Science*, vol. 52, pp. 115 – 151, 2002, DOI: 10.1146/annurev.nucl.52.050102.090641.

[Evr03]   O. Evrard, M. Keters, L. Van Buul, P. Burger, "A novel photodiode array structure for gamma camera applications," *Nuclear Instruments and Methods in Physics Research Section A: Accelerators, Spectrometers, Detectors and Associated Equipment*, vol. 504, no. 1 - 3, pp. 188 – 195, 2003, DOI: 10.1016/S0168-9002(03)00789-7.

[Fan47]   U. Fano, "Ionization Yield of Radiations. II. The Fluctuations of the Number of Ions," *Phys. Rev.*, vol. 72, no. 1, pp. 26 – 29, 1947, DOI: 10.1103/PhysRev.72.26.

[Far14]   Faro, "FaroArm," 2014. [Online]. Available: http://www.faro.com/en-us/products/metrology/measuring-arm-faroarm/overview

[FC98]   G. J. Feldman and R. D. Cousins, "A Unified Approach to the Classical Statistical Analysis of Small Signals," *Phys. Rev. D*, vol. 57, pp. 3873 – 3889, 1998, DOI: 10.1103/PhysRevD.57.3873.

[FE04]   R. Firestone and L. P. Ekstroem, "WWW Table of Radioactive Isotopes, Version 2.1," *LBNL Isotopes Project - LUNDS Universitet*, 2004. [Online]. Available: http://ie.lbl.gov/toi/

[Fel07]   G. Feldman, M. Messier, J. Cooper, R. Ray, N. Grossman (The NOvA Collaboration), "NuMI Off-Axis ν_e Appearance Experiment," 2007. [Online]. Available: http://www-nova.fnal.gov/nova_cd2_review/tdr_oct_23/tdr.htm

[Fer34]   E. Fermi, "Versuch einer Theorie der β-Strahlen. I," *Zeitschrift für Physik*, vol. 88, no. 3 - 4, pp. 161 – 177, 1934, DOI: 10.1007/BF01351864.

[Fer14]   Fermilab, "NOvA experiment sees first long-distance neutrinos," 2014. [Online]. Available: http://www.fnal.gov/pub/presspass/press_releases/2014/NOvA-20140211.html

[FFM13]   R. G. Forbes, A. Fischer, and M. S. Mousa, "Improved approach to Fowler-Nordheim plot analysis," *J. Vac. Sci. Technol. B*, vol. 31, no. 2, p. 02B103, 2013, DOI: 10.1116/1.4765080.

[FG14]   D. Furse and S. Groh et al., "Kassiopeia: A Modern, Extensible C++ Particle Tracking Package," 2014, paper in preparation.

[FGM58]   R. P. Feynman and M. Gell-Mann, "Theory of the Fermi Interaction," *Phys. Rev.*, vol. 109, no. 1, pp. 193 – 198, 1958, DOI: 10.1103/PhysRev.109.193.

[FGV14]   F. Fränkle, F. Glück, and K. Valerius et al., "Penning discharge in the KATRIN pre-spectrometer," *New Journal of Physics*, 2014, submitted for internal review.

[Fis10]   T. Fischer et al., "Protoneutron star evolution and the neutrino-driven wind in general relativistic neutrino radiation hydrodynamics simulations," *Astronomy and Astrophysics*, vol. 517, p. A80, 2010, DOI: 10.1051/0004-6361/200913106.

[Fis12]   J. Fischer, "Analysen zur Langzeitstabilität und den Betriebsmodi des KATRIN Pinch-Magneten," *Karlsruhe Institute of Technology*, 2012, bachelor thesis.

[Fix96]   D. J. Fixsen, E. S. Cheng, J. M. Gales, J. C. Mather, R. A. Shafer, E. L. Wright, "The Cosmic Microwave Background Spectrum from the Full COBE/FIRAS Data Set," *The Astrophysical Journal*, vol. 473, no. 2, 1996, DOI: 10.1086/178173.

[Fix09]   D. J. Fixsen, "The Temperature of the Cosmic Microwave Background," *The Astrophysical Journal*, vol. 707, no. 2, 2009, DOI: 10.1088/0004-637X/707/2/916.

[Fla05]   B. Flatt, "Voruntersuchungen zu den Spektrometern des KATRIN-Experiments," *Univ. Mainz*, 2005, doctoral thesis.

[FN28]   R. H. Fowler and L. Nordheim, "Electron Emission in Intense Electric Fields," *Proc. R. Soc. Lond. A*, vol. 119, no. 781, pp. 173 – 181, 1928, DOI: 10.1098/rspa.1928.0091.

[For73]   W. Forst, "Theory of Unimolecular Reactions," *Academic Press, Inc.*, vol. 1, 1973.

[For12]   R. G. Forbes, "Extraction of emission parameters for large-area field emitters, using a technically complete Fowler-Nordheim-type equation," *Nanotechnology*, vol. 23, no. 9, p. 095706, 2012, DOI: 10.1088/0957-4484/23/9/095706.

[For13a]   ——, "Development of a simple quantitative test for lack of field emission orthodoxy," *Proc. R. Soc. A*, vol. 469, no. 2158, p. 20130271, 2013, DOI: 10.1098/rspa.2013.0271.

[For13b]   J. A. Formaggio, "Temperature Operation for the MPPCs," 2013, internal KATRIN document. [Online]. Available: https://fuzzy.fzk.de/bscw/bscw.cgi/d767967/MPPC_T_dependence.pdf

[Fra06]   F. Fraenkle, "Erste Messungen der elektromagnetischen Eigenschaften des KATRIN Vorspektrometers," *Karlsruhe Institute of Technology*, 2006, diploma thesis.

[FRA10a]   J. Fast, D. Reid, and E. Aguayo, "Majorana Thermosyphon Prototype Experimental Results," *Pacific Northwest National Laboratory*, 2010, pNNL-20065. [Online]. Available: http://www.pnnl.gov/main/publications/external/technical_reports/PNNL-20668.pdf

[Fra10b]   F. Fraenkle, "Background Investigations of the KATRIN Pre-Spectrometer," *Karlsruhe Institute of Technology*, 2010, doctoral thesis.

[Fra11]   F. M. Fraenkle, L. Bornschein, G. Drexlin, F. Glück, S. Görhardt, W. Käfer, S. Mertens, N. Wandkowsky, J. Wolf, "Radon induced background processes in the KATRIN pre-spectrometer," *Astroparticle Physics*, vol. 35, no. 3, pp. 128 – 134, 2011, DOI: 10.1016/j.astropartphys.2011.06.009.

[Fre74]   M. S. Freedman, "Atomic Structure Effects in Nuclear Events," *Annual Review of Nuclear Science*, vol. 24, pp. 209 – 248, 1974, DOI: 10.1146/annurev.ns.24.120174.001233.

[Fre75]   ——, "Ionization by Nuclear Transitions," *Conference: Summer course in atomic physics, Carry-le-Rouet, France*, 1975.

[Fuk96]   Y. Fukuda et al. (Kamiokande Collaboration), "Solar Neutrino Data Covering Solar Cycle 22," *Phys. Rev. Lett.*, vol. 77, pp. 1683 – 1686, 1996, DOI: 10.1103/PhysRevLett.77.1683.

[Fuk98a]   Y. Fukuda et al., "Measurements of the Solar Neutrino Flux from Super-Kamiokande's First 300 Days," *Phys. Rev. Lett.*, vol. 81, p. 1158, 1998, DOI: 10.1103/PhysRevLett.81.1158.

[Fuk98b]   Y. Fukuda et al. (Super-Kamiokande Collaboration), "Evidence for Oscillation of Atmospheric Neutrinos," *Phys. Rev. Lett.*, vol. 81, no. 8, pp. 1562 – 1567, 1998, DOI: 10.1103/PhysRevLett.81.1562.

[Fuk01]   S. Fukuda et al. (Super-Kamiokande Collaboration), "Solar ^{8}B and hep Neutrino Measurements from 1258 Days of Super-Kamiokande Data," *Phys. Rev. Lett.*, vol. 86, p. 5651, 2001, DOI: 10.1103/PhysRevLett.86.5651.

[GAL99]   GALLEX Collaboration, "GALLEX solar neutrino observations: results for GALLEX IV," *Physics Letters B*, vol. 447, no. 1 - 2, pp. 127 – 133, 1999, DOI: 10.1016/S0370-2693(98)01579-2.

[Gal12]   M. Galeazzi, F. Gatti, M. Lusignoli, A. Nucciotti, S. Ragazzi, M. R. Gomes, "The Electron Capture Decay of ^{163}Ho to Measure the Electron Neutrino Mass with sub-eV Accuracy (and Beyond)," 2012, arXiv:1202.4763v3.

[Gan11]   A. Gando et al. (KamLAND Collaboration), "Constraints on θ_{13} from A Three-Flavor Oscillation Analysis of Reactor Antineutrinos at KamLAND," *Phys. Rev. D*, vol. 83, p. 052002, 2011, DOI: 10.1103/PhysRevD.83.052002.

[Gan13]   A. Gando et al. (KamLAND-Zen Collaboration), "Limit on Neutrinoless $\beta\beta$ Decay of ^{136}Xe from the First Phase of KamLAND-Zen and Comparison with the Positive Claim in ^{76}Ge," *Physical Review Letters*, vol. 110, p. 062502, 2013, DOI: 10.1103/PhysRevLett.110.062502.

[Gas14]   L. Gastaldo et al., "The Electron Capture ^{163}Ho Experiment ECHo," *Journal of Low Temperature Physics*, vol. May 2014, 2014, DOI: 10.1007/s10909-014-1187-4.

[Gat01]   F. Gatti, "Microcalorimeter measurements," *Nucl. Phys. Proc. Suppl.*, vol. 91, pp. 293 – 296, 2001, 19th International Conference on Neutrino Physics and Astrophysics - Neutrino 2000, Sudbury, Ontario, Canada, 16-21 June 2000.

[Gem01a]   H. Gemmeke, "The Auger Fluorescence Detector Electronics," *27th International Cosmic Ray Conference*, vol. 27, pp. 737 – 740, 2001.

[Gem01b]   H. Gemmeke, M. Kleifges, A. Kopmann, N. Kunka, A. Menchikov, D. Tcherniakhovski, "First Measurements with the AUGER Fluorescence Detector Data Acquisition System," *27th International Cosmic Ray Conference*, vol. 27, pp. 769 – 772, 2001.

[GGN03]   M. C. Gonzalez-Garcia and Y. Nir, "Neutrino masses and mixing: evidence and implications," *Rev. Mod. Phys.*, vol. 75, no. 2, pp. 345 – 402, 2003, DOI: 10.1103/RevModPhys.75.345.

[GGS58]   M. Goldhaber, L. Grodzins, and A. W. Sunyar, "Helicity of Neutrinos," *Phys. Rev.*, vol. 109, no. 3, pp. 1015 – 1017, 1958, DOI: 10.1103/PhysRev.109.1015.

[Gil10]   W. Gil et al., "The Cryogenic Pumping Section of the KATRIN Experiment," *Applied Superconductivity, IEEE Transactions*, vol. 20, no. 3, pp. 316 – 319, 2010, DOI: 10.1109/TASC.2009.2038581.

[Gil12]   ——, "Status of the Magnets of the Two Tritium Pumping Sections for KATRIN," *Applied Superconductivity, IEEE Transactions*, vol. 22, no. 3, p. 4500604, 2012, DOI: 10.1109/TASC.2011.2175353.

[Glu13]   F. Glueck, G. Drexlin, B. Leiber, S. Mertens, A. Osipowicz, J. Reich, N. Wandkowsky, "Electromagnetic design of the large-volume air coil system of the KATRIN experiment," *New Journal of Physics*, vol. 15, p. 083025, 2013, DOI: 10.1088/1367-2630/15/8/083025.

[GNO05]   GNO Collaboration, "Complete results for five years of GNO solar neutrino observations," *Physics Letters B*, vol. 616, no. 3 - 4, pp. 174 – 190, 2005, DOI: 10.1016/j.physletb.2005.04.068.

[Goe10]   S. Goerhardt, "Reduktion der durch Radon induzierten Untergrundprozesse in den KATRIN Spektrometern," *Karlsruhe Institute of Technology*, 2010, diploma thesis.

[Goe14]   ——, "Background Reduction Methods and Vacuum Technology at the KATRIN Spectrometers," *Karlsruhe Institute of Technology*, 2014, doctoral thesis.

[Gou10]   J. Goullon, "Installation and commissioning of the monitor spectrometer," *Karlsruhe Institute of Technology*, 2010, diploma thesis.

[Gri04]   D. Griffiths, "Introduction to Elementary Particles," *Wiley-VCH*, p. 26, 2004.

[Gro58]   L. Grodzins, "Lifetime of a 1^- Level in Sm^{152}," *Phys. Rev.*, vol. 109, no. 3, pp. 1014 – 1015, 1958, DOI: 10.1103/PhysRev.109.1014.

[Gro10]   S. Groh, "Untersuchung von UV-Laser induziertem Untergrund am KATRIN Vorspektrometer," *Karlsruhe Institute of Technology*, 2010, diploma thesis.

[Gro11]   S. Grohmann, T. Bode, H. Schön, M. Süßer, "Precise temperature measurement at 30 K in the KATRIN source cryostat," *Cryogenics*, vol. 51, no. 8, pp. 438 – 445, 2011, DOI: 10.1016/j.cryogenics.2011.05.001.

[Gro13a]   S. Groh, "Master Document for Kassiopeia Geometries," 2013, internal KATRIN document. [Online]. Available: https://fuzzy.fzk.de/bscw/bscw.cgi/d874183/Master%20Document%20for%20Kassiopeia%20Geometries.pdf

[Gro13b]   S. Grohmann, T. Bode, M. Hötzel, H. Schön, M. Süßer, T. Wahl, "The thermal behaviour of the tritium source in KATRIN," *Cryogenics*, vol. 55 - 56, pp. 5 – 11, 2013, DOI: 10.1016/j.cryogenics.2013.01.001.

[Gro14]   S. Groh et al., "First measurement and simulation of the electromagnetic properties of the KATRIN main spectrometer," *New Journal of Physics*, 2014, paper in preparation.

[GTW13]   S. Görhardt, T. Thümmler, and J. Wolf, "Vacuum Conditioning of the KATRIN Main Spectrometer," 2013, internal KATRIN document. [Online]. Available: https://fuzzy.fzk.de/bscw/bscw.cgi/d875469/430-doc-3-9000-MainSpec-Baking-Report-2013-03-09.pdf

[Hab09]   F. Habermehl, "Electromagnetic measurements with the KATRIN prespectrometer," *Unversität Karlsruhe*, 2009, doctoral thesis.

[Hae53a]   R. Haefer, "Die Zündspannung von Gasentladungen unter dem Einfluss eines transversalen Magnetfeld in Druckbereich von 10 bis 10^{-8} Torr," *Acta Physica Austriaca*, vol. 7, pp. 52 – 90, 1953.

[Hae53b]   ——, "Über den Mechanismus der Zündung einer elektrischen Gasentladung unter der Einwirkung eines transversalen Magnetfeldes in Druckbereich 10 bis 10^{-8} Torr," *Acta Physica Austriaca*, vol. 7, pp. 251 – 278, 1953.

[Hai67]   F. A. Haight, "Handbook of the Poisson Distribution," *New York: John Wiley & Sons*, 1967.

[Han74]   J. S. Hansen, "Internal ionization during alpha decay: A new theoretical approach," *Physical Review A*, vol. 9, no. 1, pp. 40 – 43, 1974, DOI: 10.1103/PhysRevA.9.40.

[Han10]   S. Hannestad, "Neutrino physics from precision cosmology," *Progress in Particle and Nuclear Physics*, vol. 65, no. 2, pp. 185 – 208, 2010, DOI: 10.1016/j.ppnp.2010.07.001.

[Han13a]   V. Hannen, H.-W. Ortjohann, M. Zacher, Ch. Weinheimer, "Electrical short circuits in the main spectrometer wire electrode," 2013, internal KATRIN document. [Online]. Available: https://fuzzy.fzk.de/bscw/bscw.cgi/d875473/430-doc-3-9001-shortcircuit_report.pdf

[Han13b]   V. Hannen, S. Bauer, L. Josten, H.-W. Ortjohann, C. Weinheimer, D. Winzen, M. Zacher, M. Zboril, "Main Spectrometer Electron-Gun Specification," 2013, internal KATRIN document. [Online]. Available: http://fuzzy.fzk.de/bscw/bscw.cgi/d778116/E-Gun_Documentation-2013-04-22.pdf

[Har89]   M. Haraa, H. Shigematsua, S. Yanoa, K. Yamafuji, M. Takeo, K. Funaki, "Influence of transverse magnetic field on breakdown characteristics of vacuum, gaseous helium at low temperature and liquid helium," *Cryogenics*, vol. 29, no. 4, pp. 448 – 456, 1989, DOI: 10.1016/0011-2275(89)90278-6.

[Har12]   F. Harms, "Assembly and First Results of the KATRIN Focal-Plane Detector System at KIT," *Karlsruhe Institute of Technology*, 2012, diploma thesis.

[Hau13]   N. Haußmann, "Development of Analysis Tools and Automatisation of Run Control for KATRIN," *Karlsruhe Institute of Technology*, 2013, diploma thesis.

[Heb06]   O. Heber, R. Golser, H. Gnaser, D. Berkovits, Y. Toker, M. Eritt, M. L. Rappaport, D. Zajfman, "Lifetimes of the negative molecular hydrogen ions: H_2^-, D_2^-, and HD^-," *Physical Review A, atomic, molecular, and optical physics*, vol. 73, p. 060501, 2006, DOI: 10.1103/PhysRevA.73.060501.

[HFK92]   E. Holzschuh, M. Fritschi, and W. Kündig, "Measurement of the electron neutrino mass from tritium β-decay," *Physics Letters B*, vol. 287, no. 4, pp. 381 – 388, 1992, DOI: 10.1016/0370-2693(92)91000-Y.

[HH31]   E. Hubble and M. L. Humason, "The Velocity-Distance Relation among Extra-Galactic Nebulae," *Astrophysical Journal*, vol. 74, pp. 43 – 80, 1931.

[Hig64]   P. W. Higgs, "Broken Symmetries and the Masses of Gauge Bosons," *Phys. Rev. Lett.*, vol. 13, p. 508, 1964, DOI: 10.1103/PhysRevLett.13.508.

[Hig07]   H. Higaki, K. Ito, W. Saiki, Y. Omori, H. Okamoto, "Properties of non-neutral electron plasmas confined with a magnetic mirror field," *Phys. Rev. E*, vol. 75, no. 6, p. 066401, 2007, DOI: 10.1103/PhysRevE.75.066401.

[Hig08]   H. Higaki, K. Ito, K. Kira, H. Okamoto, "Electrons Confined with an Axially Symmetric Magnetic Mirror Field," *AIP Conference Proceedings*, vol. 1037, pp. 106 – 114, 2008, DOI: 10.1063/1.2977830.

[Hil11]   B. Hillen, "Untersuchung von Methoden zur Unterdrückung des Spektrometeruntergrunds beim KATRIN Experiment," *Univ. Münster*, 2011, doctoral thesis.

[Hil14]   D. Hilk et al., "Reduction of stored-particle background in the KATRIN main spectrometer with electric dipole," *New Journal of Physics*, 2014, paper in preparation.

[Hin13]   G. Hinshaw et al., "Nine-Year Wilkinson Microwave Anisotropy Probe (WMAP) Observations: Cosmological Parameter Results," *The Astrophysical Journal Supplement Series*, vol. 208, no. 2, p. 19, 2013, DOI: 10.1088/0067-0049/208/2/19.

[Hir88]   K. S. Hirata et al., "Observation in the Kamiokande-II detector of the neutrino burst from supernova SN1987A," *Phys. Rev. D*, vol. 38, p. 448, 1988, DOI: 10.1103/PhysRevD.38.448.

[Hoe12]   M. Hoetzel, "Simulation and analysis of source-related effects for KATRIN," *Karlsruhe Institute of Technology*, 2012, doctoral thesis.

[Hol92]   E. Holzschuh, "Measurement of the neutrino mass from tritium β-decay," *Reports on Progress in Physics*, vol. 55, no. 7, p. 1035, 1992, DOI: 10.1088/0034-4885/55/7/004.

[How04]   M. A. Howe, G. A. Cox, P. J. Harvey, F. McGirt, K. Rielage, J. F. Wilkerson, J. M. Wouters, "Sudbury neutrino observatory neutral current detector acquisition software overview," *Nuclear Science, IEEE Transactions*, vol. 51, no. 3, pp. 878 – 883, 2004, DOI: 10.1109/TNS.2004.829527.

[How09]   M. A. Howe, J. F. Wilkerson, J. Detwiler, M. Marino, "ORCA, An Object-Oriented Real-Time Data-Acquisition System," *TUNL XLVIII PROGRESS REPORT*, vol. 48, pp. 171 – 172, 2009. [Online]. Available: http://www.tunl.duke.edu/documents/public/tunlxlviii.pdf

[How14]   M. A. Howe, F. McGirt, J. Wilkerson, J. Wouters, "ORCA webpage," 2014. [Online]. Available: http://orca.physics.unc.edu/

[HT14]   V. Hannen and T. Thümmler, "Inner Electrode Repair at Ports 0040 and 0050," 2014, internal KATRIN document. [Online]. Available: https://fuzzy.fzk.de/bscw/bscw.cgi/d894084/30-WKF-3504-03-Inner%20Electrode%20Repair%20at%20Ports%200040%20and%200050%20V2014-04-07.pdf

[Hug08]   K. Hugenberg, "Design of the electrode system of the KATRIN main spectrometer," *Univ. Münster*, 2008, diploma thesis.

[Hug10]   ——, "An angular resolved pulsed UV LED photoelectron source for KATRIN," *Progress in Particle and Nuclear Physics*, vol. 64, no. 2, pp. 288 – 290, 2010, DOI: 10.1016/j.ppnp.2009.12.031.

[Jan07]   H. T. Janka et al., "Theory of core-collapse supernovae," *Physics Reports*, vol. 442, pp. 38 – 74, 2007, DOI: 10.1016/j.physrep.2007.02.002.

[JGL94]   B. Jeckelmann, P. F. A. Goudsmit, and H. J. Leisi, "The mass of the negative pion," *Phys. Lett. B*, vol. 335, no. 3 - 4, pp. 326 – 329, 1994, DOI: 10.1016/0370-2693(94)90358-1.

[Jin09]   T. Jin, J.-P. Hong, H. Zheng, K. Tang, Z.-H Gan, "Measurement of boiling heat transfer coefficient in liquid nitrogen bath by inverse heat conduction method," *Journal of Zhejiang University SCIENCE A*, vol. 10, no. 5, pp. 691 – 696, 2009, DOI: 10.1631/jzus.A0820540.

[JK94]   V. T. Jordanov and G. F. Knoll, "Digital synthesis of pulse shapes in real time for high resolution radiation spectroscopy," *Nuclear Instruments and Methods in Physics Research Section A: Accelerators, Spectrometers, Detectors and Associated Equipment*, vol. 345, no. 2, pp. 337 – 345, 1994, DOI: 10.1016/0168-9002(94)91011-1.

[JKR06]   L. K. Jha, S. Kumar, and B. N. Roy, "Electron impact single and double ionization of argon," *The European Physical Journal D - Atomic, Molecular, Optical and Plasma Physics*, vol. 40, no. 1, pp. 101 – 106, 2006, DOI: 10.1140/epjd/e2006-00158-3.

[JL01]   B. Jackson and D. Lemoine, "Eley-Rideal reactions between H atoms on metal and graphite surfaces: The variation of reactivity with substrate," *Journal of Chemical Physics*, vol. 114, no. 1, pp. 474 – 482, 2001, DOI: 10.1063/1.1328041.

[Jur09]   M. Juretzko, "Positioning of the Electrode Modules of the KATRIN Experiment by Using a Laser Tracker," *Optical 3-D Measurement Techniques IX*, vol. 2, pp. 91 – 98, 2009, A. Grün, H. Kahmen (eds.).

[Jur12]   ——, "Lasertracker-Einsatz beim KATRIN-Experiment des KIT. Industrievermessung - aktuelle Trends und Entwicklungen," 2012, korntal, 12.07.2012.

[Kam11]   KamLAND Collaboration, "Partial radiogenic heat model for Earth revealed by geoneutrino measurements," *Nature Geoscience*, vol. 4, pp. 647 – 651, 2011, DOI: 10.1038/ngeo1205.

[Kaw91]   H. Kawakami, S. Kato, T. Ohshima, S. Shibata, K. Ukai, "New upper bound on the electron anti-neutrino mass," *Physics Letters B*, vol. 256, no. 1, pp. 105 – 111, 1991, DOI: 10.1016/0370-2693(91)90226-G.

[Kel11]   P. Keller, "NMR magnetometers," *Magnetics Technology International*, pp. 68 – 71, 2011. [Online]. Available: http://www.metrolab.ch/uploads/Document/WEB_CHEMIN_105_1158921095.pdf

[KKK06]   H. V. Klapdor-Kleingrothaus and I. V. Krivosheina, "The evidence for the observation of 0nu beta beta decay: The identification of $0\nu\beta\beta$ events from the full spectra," *Mod. Phys. Lett. A*, vol. 21, no. 20, pp. 1547 – 1566, 2006, DOI: 10.1142/S0217732306020937.

[KL13]   S. F. King and C. Luhn, "Neutrino mass and mixing with discrete symmetry," *Reports on Progress in Physics*, vol. 76, no. 5, p. 056201, 2013, DOI: 10.1088/0034-4885/76/5/056201.

[Kla01]   H. V. Klapdor-Kleingrothaus, A. Dietz, H. L. Harney, I.V. Krivosheina, "Evidence for Neutrinoless Double Beta Decay," *Modern Physics Letters A*, vol. 16, no. 37, pp. 2409 – 2420, 2001, DOI: 10.1142/S0217732301005825.

[Kle14]   M. Kleesiek, "A Data Analysis and Sensitivity Optimization Framework for KATRIN," *Karlsruhe Institute of Technology*, 2014, doctoral thesis.

[KM69]   T. Kirsten and H. W. Müller, "Observation of ^{82}Se double-beta decay in selenium ores," *Earth and Planetary Science Letters*, vol. 6, no. 4, pp. 271 – 274, 1969, DOI: 10.1016/0012-821X(69)90167-8.

[Kno10]   G. F. Knoll, "Radiation Detection and Measurement, 4th Edition," *John Wiley & Sons, Inc.*, 2010.

[Kop07]   S. E. Kopp, "Accelerator Neutrino Beams," *Phys. Rept.*, vol. 439, pp. 101 – 159, 2007, DOI: 10.1016/j.physrep.2006.11.004 .

[Kop08]   A. Kopmann, T. Bergmann, H. Gemmeke, M. A. Howe, M. Kleifges, A. Menshikov, D. Tcherniakhovski, J. F. Wilkerson, S. Wüstling, "FPGA-based DAQ system for multi-channel detectors," *Nuclear Science Symposium Conference Record, 2008. NSS 08. IEEE*, pp. 3186 – 3190, 2008, DOI: 10.1109/NSS-MIC.2008.4775027.

[Kos12]   A. Kosmider, "Tritium Retention Techniques in the KATRIN Transport Section and Commissioning of its DPS2-F Cryostat," *Karlsruhe Institute of Technology*, 2012, doctoral thesis.

[KR83]   P. Kruit and F. H. Read, "Magnetic field paralleliser for 2π electron-spectrometer and electron-image magnifier," *Journal of Physics E: Scientific Instruments*, vol. 16, no. 4, p. 313, 1983, DOI: 10.1088/0022-3735/16/4/016.

[Kra05]   C. Kraus et al., "Final results from phase II of the Mainz neutrino mass search in tritium β decay," *The European Physical Journal C*, vol. 40, no. 4, pp. 447 – 468, 2005, DOI: 10.1140/epjc/s2005-02139-7.

[Kra14]   M. Kraus et al., "First commissioning of the KATRIN main spectrometer high voltage system," *JINST*, 2014, paper in preparation.

[Lak14a] Lakeshore, 2014, Lakeshore MMA-2536-WL: specifications. [Online]. Available: http://www.lakeshore.com/products/hall-probes/axial-probes/pages/Specifications.aspx

[Lak14b] ——, 2014, Lakeshore Model 460 3-Channel Gaussmeter: specifications. [Online]. Available: http://www.lakeshore.com/products/gaussmeters/model-460-3-channel-gaussmeter/Pages/Overview.aspx

[Lam09]   M. Lammers, "Untersuchung der Untergrundrate des KATRIN Vorspektrometers im Bereich hoher Feldstärken," *Karlsruhe Institute of Technology*, 2009, diploma thesis.

[Lan44]   L. Landau, "On the energy loss of fast particles by ionization," *J.Phys.(USSR)*, vol. 8, pp. 201 – 205, 1944.

[Lan87]   P. Langacker, S. T. Petcov, G. Steigman, S. Toshev, "Implications of the mikheyev-smirnov-wolfenstein (MSW) mechanism of amplification of neutrino oscillations in matter," *Nuclear Physics B*, vol. 282, pp. 589 – 609, 1987, DOI: 10.1016/0550-3213(87)90699-7.

[LD08]   X. Luo and C. Day, "Test particle Monte Carlo study of the cryogenic pumping system of the Karlsruhe tritium neutrino experiment," *Journal of Vacuum Science and Technology A*, vol. 26, no. 5, p. 1319, 2008, DOI: 10.1116/1.2956628.

[Leb06]   M. L. Leber, "Effect of background rate on minimum statistical error," 2006, internal KATRIN document.

[Leb10]   ——, "Monte Carlo Calculations of the Intrinsic Detector Backgrounds for the Karlsruhe Tritium Neutrino Experiment," *University of Washington*, 2010, doctoral thesis.

[Lei10]   B. Leiber, "Non-axially symmetric field and trajectory calculations for the KATRIN-experiment," *Karlsruhe Institute of Technology*, 2010, diploma thesis.

[Lei14]   ——, "Investigations of background due to secondary electron emission in the KATRIN-experiment," *Karlsruhe Institute of Technology*, 2014, doctoral thesis.

[Lid03]   A. Liddle, "An Introduction to Modern Cosmology," *Wiley*, 2003.

[LK05]   C. H. Lefhalm and V. Krieger, "A full featured monitoring, control and data management system for liquid metal coolant loops," *Real Time Conference, 2005. 14th IEEE-NPSS*, 2005, DOI: 10.1109/RTC.2005.1547521.

[LL02]   T. J. Loredo and D. Q. Lamb, "Bayesian analysis of neutrinos observed from supernova SN 1987A," *Phys. Rev. D*, vol. 65, p. 063002, 2002, DOI: 10.1103/PhysRevD.65.063002.

[Lob85]   V. M. Lobashev, "A method for measuring the electron antineutrino rest mass," *Nucl. Instrum. Meth. A*, vol. 240, no. 2, pp. 305 – 310, 1985, DOI: 10.1016/0168-9002(85)90640-0.

[Lob99]   V. M. Lobashev et al., "Direct search for mass of neutrino and anomaly in the tritium beta-spectrum," *Physics Letters B*, vol. 460, no. 1 - 2, pp. 227 – 235, 1999, DOI: 10.1016/S0370-2693(99)00781-9.

[Loz14]   V. Lozza et al. (SNO+ Collaboration), "Neutrinoless double beta decay search with SNO+," *EPJ Web of Conferences, RPSCINT 2013 - International Workshop on Radiopure Scintillators*, vol. 65, p. 01003, 2014, DOI: 10.1051/epjconf/20136501003.

[LP06]   J. Lesgourguesa and S. Pastor, "Massive neutrinos and cosmology," *Physics Reports*, vol. 429, no. 6, pp. 307 – 379, 2006, DOI: 10.1016/j.physrep.2006.04.001.

[LP12]   J. Lesgourgues and S. Pastor, "Neutrino Mass from Cosmology," *Advances in High Energy Physics*, vol. 2012, no. 608515, 2012, DOI: 10.1155/2012/608515.

[LU00]   L. L. Lucas and M. P. Unterweger, "Comprehensive Review and Critical Evaluation of the Half-Life of Tritium," *Journal of Research of the National Institute of Standards and Technology*, vol. 105, no. 4, pp. 541 – 549, 2000, DOI: 10.6028/jres.105.043.

[Luk12] S. Lukic, B. Bornschein, L. Bornschein, G. Drexlin, A. Kosmider, K. Schlösser, A. Windberger, "Measurement of the gas-flow reduction factor of the KATRIN DPS2-F differential pumping section," *Vacuum*, vol. 86, no. 8, pp. 1126 – 1133, 2012, DOI: 10.1016/j.vacuum.2011.10.017.

[Lun24] K. Lundmark, "The determination of the curvature of space-time in de Sitter's world," *Monthly Notices of the Royal Astronomical Society*, vol. 84, pp. 747 – 770, 1924.

[Luo06] X. Luo, Chr. Day, V. Hauer, O.B. Malyshev, R.J. Reid, F. Sharipov, "Monte Carlo simulation of gas flow through the KATRIN DPS2-F differential pumping system," *Vacuum*, vol. 80, no. 8, pp. 864 – 869, 2006, DOI: 10.1016/j.vacuum.2005.11.044.

[Mar01] R. Marx, "New concept of PTBs standard divider for direct voltages of up to 100 kV," *Instrumentation and Measurement, IEEE Transactions*, vol. 50, no. 2, pp. 426 – 429, 2001, DOI: 10.1109/19.918158.

[Mar12] E. Martin, "Electron Source Users Manual," 2012, internal KATRIN document. [Online]. Available: https://fuzzy.fzk.de/bscw/bscw.cgi/d767648/Pulcinella%20Manual

[Mas07] S. S. Masood, S. Nasri, J. Schechter, M. A. Tortola, J. W. F. Valle, C. Weinheimer, "Exact relativistic beta decay endpoint spectrum," *Phys .Rev. C*, vol. 76, p. 045501, 2007, DOI: 10.1103/PhysRevC.76.045501.

[Mau09] D. Maurel, "Designstudien zur Messung der Aktivität der Tritiumquelle im KATRIN-Experiment mit Röntgenstrahlung," *Karlsruhe Institute of Technology*, 2009, diploma thesis.

[Mee13] D. Meeker, "Finite Element Method Magnetics (FEMM 4.2)," 2013. [Online]. Available: http://www.femm.info/wiki/HomePage

[Mer12a] S. Mertens, "Study of Background Processes in the Electrostatic Spectrometers of the KATRIN experiment," *Karlsruhe Institute of Technology*, 2012, doctoral thesis.

[Mer12b] S. Mertens et al., "Stochastic Heating by ECR as a Novel Means of Background Reduction in the KATRIN spectrometers," *JINST*, vol. 7, p. 08025, 2012, DOI: 10.1088/1748-0221/7/08/P08025.

[Mer13] ——, "Background due to stored electrons following nuclear decays in the KATRIN spectrometers and its impact on the neutrino mass sensitivity," *Astroparticle Physics*, vol. 41, pp. 52 – 62, 2013, DOI: 10.1016/j.astropartphys.2012.10.005.

[Met14a] Metrolab, 2014, Metrolab PT2025: specifications. [Online]. Available: http://www.metrolab.ch/uploads/Document/WEB_CHEMIN_113_1158927562.pdf

[Met14b] ——, 2014, Metrolab ACC-1060: specifications. [Online]. Available: http://www.metrolab.ch/uploads/Document/WEB_CHEMIN_105_1158921095.pdf

[Miy73] S. Miyake, N. Ito, S. Kawakami, N. Hayashida, Y. Hayashi, "A Change of the Interaction Character Around 10^{17} eV," *Proceedings of the 13th International Conference on Cosmic Rays, held in Denver, Colorado*, vol. 5, p. 3220, 1973.

[MNS62] Z. Maki, M. Nakagawa, and S. Sakata, "Remarks on the Unified Model of Elementary Particles," *Progress of Theoretical Physics*, vol. 28, no. 5, pp. 870 – 880, 1962, DOI: 10.1143/PTP.28.870.

[MS86] S. P. Mikheyev and A. Y. Smirnov, "Resonant amplification of ν oscillations in matter and solar-neutrino spectroscopy," *Il Nuovo Cimento C*, vol. 9, no. 1, pp. 17 – 26, 1986, DOI: 10.1007/BF02508049.

[MsS95] W. F. McDonough and S. s. Sun, "The composition of the Earth," *Chemical Geology*, vol. 120, no. 3 - 4, pp. 223 – 253, 1995, DOI: 10.1016/0009-2541(94)00140-4.

[Mue02] B. Mueller, "Umbau des Mainzer Neutrinomassenexperiments und Untergrunduntersuchungen im Hinblick auf KATRIN," *Univ. Mainz*, 2002, diploma thesis.

[Mue14] A. Mueller, "Field Alignment Studies at the KATRIN Pinch Magnet," *Karlsruhe Institute of Technology*, 2014, bachelor thesis.

[Nag06] S. Nagy, T. Fritioff, M. Bjoerkhage, I. Bergstroem, R. Schuch, "On the Q-value of the tritium β-decay," *Europhys. Lett.*, vol. 74, no. 3, p. 404, 2006, DOI: 10.1209/epl/i2005-10559-2.

[Nat13] National Institute of Standards and Technology, "NIST Chemistry WebBook, NIST Standard Reference Database Number 69," 2013. [Online]. Available: http://webbook.nist.gov/chemistry/

[Nis94] K. Nishimura, T. Itotani, K. Ohya, "Influence of Surface Roughness on Secondary Electron Emission and Electron Backscattering from Metal Surface," *Japanese Journal of Applied Physics*, vol. 33, no. 8, p. 4727, 1994, DOI: 10.1143/JJAP.33.4727.

[Nob95] Nobelprize.org. Nobel Media AB 2013., "The Nobel Prize in Physics 1995," 1995. [Online]. Available: http://www.nobelprize.org/nobel_prizes/physics/laureates/1995/

[Nuc02] A. Nucciotti et al., "The Milano neutrino mass experiment with arrays of AgReO$_4$ microcalorimeters," *AIP Conf. Proc.*, vol. 605, p. 453, 2002, DOI: 10.1063/1.1457684.

[Nuc12] ——, "Neutrino mass calorimetric searches in the MARE experiment," *Nuclear Physics B - Proceedings Supplements, Neutrino 2010*, vol. 229 - 232, pp. 155 – 159, 2012, DOI: 10.1016/j.nuclphysbps.2012.09.025.

[Oer06] R. Oerter, "The Theory of Almost Everything: The Standard Model, the Unsung Triumph of Modern Physics," *Penguin Group*, 2006.

[Ome14] Omegadyne, 2014, Omegadyne PX319-030AI: specifications. [Online]. Available: http://www.omegadyne.com/ppt/prod.html?ref=PX309_MA

[Ott94] E. W. Otten, "The Mainz neutrino mass experiment," *Prog. Part. Nucl. Phys.*, vol. 32, pp. 153–171, 1994, DOI: 10.1016/0146-6410(94)90016-7.

[Ott10] E. Otten, "Searching the absolute neutrino mass in tritium β-decay - interplay between nuclear, atomic and molecular physics," *Hyperfine Interactions*, vol. 196, no. 1, pp. 3 – 23, 2010, DOI: 10.1007/s10751-009-0150-2.

[Ott14] R. Otter, "Swimming in Cosmic Soup: Philosophical and Physics Musings on Life in the Twenty-First Century," *iUniverse*, 2014.

[OW08] E. W. Otten and C. Weinheimer, "Neutrino mass limit from tritium β decay," *Reports on Progress in Physics*, vol. 71, no. 8, p. 086201, 2008, DOI: 10.1088/0034-4885/71/8/086201.

[Pau30]   W. Pauli, "Offener Brief an die Gruppe der Radioaktiven bei der Gauvereins-Tagung zu Tübingen," 1930. [Online]. Available: http://www.symmetrymagazine.org/sites/default/files/legacy/pdfs/200703/logbook_letter.pdf

[Pau85]   W. Pauli, A. Hermann, K. v. Meyenn, V. F. Weisskopf, "wissenschaftlicher Briefwechsel mit Bohr, Einstein, Heisenberg u.a., scientific correspondence with Bohr, Einstein, Heisenberg a.o. Band II: 1930 - 1939," *Springer-Verlag, Berlin, Heidelberg, New York, Tokyo*, 1985.

[Pea00]   K. Pearson, "On the criterion that a given system of deviations from the probable in the case of a correlated system of variables is such that it can be reasonably supposed to have arisen from random sampling," *Philosophical Magazine Series 5*, vol. 50, no. 302, pp. 157 – 175, 1900, DOI: 10.1080/14786440009463897.

[Pen36]   F. M. Penning, "Die Glimmentladung bei niedrigem Druck zwischen koaxialen Zylindern in einem axialen Magnetfeld," *Physica*, vol. 3, no. 9, pp. 873 – 894, 1936, DOI: 10.1016/S0031-8914(36)80313-9.

[Pen00]   R.-D. Penzhorn, N. Bekris, P. Coad, L. Dörr, M. Friedrich, M. Glugla, A. Haigh, R. Lässer, A. Peacockc, "Status and research progress at the Tritium Laboratory Karlsruhe," *Fusion Engineering and Design*, vol. 49 - 50, pp. 753 – 767, 2000, DOI: 10.1016/S0920-3796(00)00344-6.

[Per75]   M. L. Perl et al., "Evidence for Anomalous Lepton Production in $e^+ - e^-$ Annihilation," *Phys. Rev. Lett.*, vol. 35, no. 22, pp. 1489 – 1492, 1975, DOI: 10.1103/PhysRevLett.35.1489.

[Pet11]   D. Peterson et al., "Optical pulser for KATRIN focal plane detector," 2011, internal KATRIN document.

[Phi10]   D. G. Phillips et al., "Characterization of an FPGA-based DAQ system in the KATRIN experiment," *Nuclear Science Symposium Conference Record (NSS/MIC), 2010 IEEE*, pp. 1399 – 1403, 2010, DOI: 10.1109/NSSMIC.2010.5874002.

[Phi12]   D. G. Phillips II et al. (MAJORANA Collaboration), "The MAJORANA experiment: an ultra-low background search for neutrinoless double-beta decay," *Journal of Physics: Conference Series*, vol. 381, no. 1, p. 012044, 2012, DOI: 10.1088/1742-6596/381/1/012044.

[Pic90]   A. Picard, "Aufbau und Test eines Solenoid-Retardierungs-Spektrometers zur Bestimmung der Neutrinoruhemasse aus dem Tritium-beta-Zerfall," *Univ. Mainz*, 1990, doctoral thesis.

[Pic92]   A. Picard et al., "A solenoid retarding spectrometer with high resolution and transmission for keV electrons," *Nuclear Instruments and Methods in Physics Research Section B: Beam Interactions with Materials and Atoms*, vol. 63, no. 3, pp. 345 – 358, 1992, DOI: 10.1016/0168-583X(92)95119-C.

[Pla13]   Planck Collaboration, "Planck 2013 results. XVI. Cosmological parameters," *Cosmology and Nongalactic Astrophysics*, 2013, arXiv:1303.5076v3.

[Pon57a] B. Pontecorvo, "Inverse beta processes and nonconservation of lepton charge," *Zh. Eksp. Teor. Fiz.*, vol. 34, p. 247, 1957.

[Pon57b] ——, "Mesonium and anti-mesonium," *Zh. Eksp. Teor. Fiz.*, vol. 33, pp. 549 – 551, 1957.

[Pon67]   ——, "Neutrino Experiments and the Problem of Conservation of Leptonic Charge," *Zh. Eksp. Teor. Fiz.*, vol. 53, pp. 1717 – 1725, 1967.

[Pra11]   M. Prall, "Background Reduction of the KATRIN Spectrometers: Transmission Function of the Pre-Spectrometer and Systematic Test of the Main-Spectrometer Wire Electrode," *Univ. Münster*, 2011, doctoral thesis.

[PRG12]   M. Prall, P. Renschler, and F. Glück et al., "The KATRIN pre-spectrometer at reduced filter energy," *New Journal of Physics*, vol. 14, p. 073054, 2012, DOI: 10.1088/1367-2630/14/7/073054.

[PW65]   A. A. Penzias and R. W. Wilson, "A Measurement of Excess Antenna Temperature at 4080 Mc/s," *Astrophysical Journal*, vol. 142, pp. 419 – 421, 1965, DOI: 10.1086/148307.

[Raz03]   M. Razavy, "Quantum Theory of Tunneling," *World Scientific Pub Co Inc*, 2003.

[Rei97]   F. Reines, C. Cowan Jr., "Celebrating the Neutrino, The Reines-Cowan Experiments - Detecting the Poltergeist," *Los Alamos Science*, vol. 25, pp. 4 – 27, 1997. [Online]. Available: http://www.fas.org/sgp/othergov/doe/lanl/pubs/00326606.pdf

[Rei09a]   J. Reich, "Magnetfeldmessungen und Designarbeiten für das EMCS-Luftspulensystem am KATRIN Hauptspektrometer," *Unversität Karlsruhe*, 2009, diploma thesis.

[Rei09b]   S. Reimer, "Ein elektrostatisches Dipolsystem zur Eliminierung von Ionen in der DPS2-F des KATRIN Experimentes," *Karlsruhe Institute of Technology*, 2009, diploma thesis.

[Rei13]   J. Reich, "Magnetic Field Inhomogeneities and Their Influence on Transmission and Background at the KATRIN Main Spectrometer," *Karlsruhe Institute of Technology*, 2013, doctoral thesis.

[Ren11]   P. Renschler, "A new Monte Carlo simulation code for low-energy electron interactions in silicon detectors," *Karlsruhe Institute of Technology*, 2011, doctoral thesis.

[Rie11a]   A. G. Riess et al., "A 3with the Hubble Space Telescope and Wide Field Camera 3," *The Astrophysical Journal*, vol. 730, no. 2, p. 119, 2011, DOI: 10.1088/0004-637X/730/2/119.

[Rie11b]   K. Riesselmann, "Deconstruction: Cosmic gall," 2011. [Online]. Available: http://www.symmetrymagazine.org/article/february-2011/deconstruction-cosmic-gall

[Rin13]   R. Rink, "2D simulation of first spike events," 2013, internal KATRIN elog. [Online]. Available: https://neutrino.ikp.kit.edu:8080/SDS-Analysis/6

[Rin14]   ——, 2014, master thesis in preparation.

[RK88]   R. G. H. Robertson and D. A. Knapp, "Direct measurement of neutrino mass," *Annual Review of Nuclear and Particle Science*, vol. 38, pp. 185 – 215, 1988.

[Rob91]   R. G. H. Robertson, T. J. Bowles, G. J. Stephenson Jr., D. L. Wark, J. F. Wilkerson, D. A. Knapp, "Limit on ν_e^- mass from observation of the β decay of molecular tritium," *Phys. Rev. Lett.*, vol. 67, p. 957, 1991, DOI: 10.1103/PhysRevLett.67.957.

[Rob10]   H. Robertson, "Kinematic Determination of Neutrino Mass," *The Future of Neutrino Mass Measurements: Terrestrial, Astrophysical, and Cosmological Measurements in the Next Decade*, 2010. [Online]. Available: http://www.int.washington.edu/talks/WorkShops/int_10_44W/

[Rod11]   W. Rodejohann, "Neutrino-less Double Beta Decay and Particle Physics," *Int. J. Mod. Phys. E*, vol. 20, no. 9, pp. 1833 – 1930, 2011, DOI: 10.1142/S0218301311020186.

[Roe11]   M. Roellig, "Studien zu einem Röntgendetektorsystem zur Überwachung der KATRIN Tritiumquelle," *Karlsruhe Institute of Technology*, 2011, diploma thesis.

[RP13]   M. Röllig and F. Priester et al., "Activity monitoring of a gaseous tritium source by beta induced X-ray spectrometry," *Fusion Engineering and Design*, vol. 88, no. 6 - 8, pp. 1263 – 1266, 2013, DOI: 10.1016/j.fusengdes.2012.11.001.

[Sch95]   P. Schmüser, "Feynman - Graphen und Eichtheorien für Experimentalphysiker," *Springer-Verlag GmbH*, 1995.

[Sch04]   F. Schwamm, "Untergrunduntersuchungen für das KATRIN-Experiment," *Unversität Karlsruhe*, 2004, doctoral thesis.

[Sch08]   M. Schöppner, "A Prototype Ion Source for the Functionality Test of the KATRIN Transport Section," *Univ. Münster*, 2008, diploma thesis.

[Sch10]   J. Schwarz, "Design zur Messung der elektro-optischen Eigenschaften der differentiellen Pumpstrecke DPS2-F des KATRIN-Experiments," *Karlsruhe Institute of Technology*, 2010, diploma thesis.

[Sch11]   M. Schupp, "Inbetriebnahme des Monitorspektrometers und erste Messungen," *Karlsruhe Institute of Technology*, 2011, diploma thesis.

[Sch13a] M. Schlösser, "Accurate calibration of the Raman system for the Karlsruhe Tritium Neutrino Experiment," *Karlsruhe Institute of Technology*, 2013, doctoral thesis.

[Sch13b] J. Schwarz, "The Focal-Plane Detector System Of KATRIN," 2013, institute talk. [Online]. Available: https://fuzzy.fzk.de/bscw/bscw.cgi/d767482/The%20Focal-Plane%20Detector%20System%20Of%20KATRIN

[Sco35]   F. A. Scott, "Energy Spectrum of the Beta-Rays of Radium E," *Phys. Rev.*, vol. 48, no. 5, pp. 391 – 395, 1935, DOI: 10.1103/PhysRev.48.391.

[SD95]   W. Stoeffl and D. J. Decman, "Anomalous Structure in the Beta Decay of Gaseous Molecular Tritium," *Phys. Rev. Lett.*, vol. 75, p. 3237, 1995, DOI: 10.1103/PhysRevLett.75.3237.

[Shu66]   P. Shulek, B.M. Golovin, L.A. Kulyukina, S.V. Medved, P. Pavlovic, "Fluctuations Of Ionization Losses," *Yad. Fiz.*, vol. 4, pp. 564 – 566, 1966.

[Sim03]   H. Simgen, C. Buck, G. Heusser, M. Laubenstein, W. Rau, "A new system for the ^{222}Rn and ^{226}Ra assay of water and results in the Borexino project," *Nuclear Instruments and Methods in Physics Research Section A: Accelerators, Spectrometers, Detectors and Associated Equipment*, vol. 497, no. 2 - 3, pp. 407 – 413, 2003, DOI: 10.1016/S0168-9002(02)01823-5.

[Sim06]   H. Simgen, "Ultrapure gases for GERDA," *Progress in Particle and Nuclear Physics*, vol. 57, no. 1, pp. 266 – 268, 2006, DOI: 10.1016/j.ppnp.2005.11.006.

[Sle11] M. Slezak, "The source of monoenergetic electrons for the monitoring of spectrometer in the KATRIN neutrino experiment," *Charles University in Prague, NPI Rez*, 2011, diploma thesis.

[Sle13] M. Slezak et al., "Electron line shape of the KATRIN monitor spectrometer," *Journal of Instrumentation*, vol. 8, p. T12002, 2013, DOI: 10.1088/1748-0221/8/12/T12002.

[Sli15] V. M. Slipher, "Spectrographic Observations of Nebulae," *Popular Astronomy*, vol. 23, pp. 21 – 24, 1915.

[SM58] E. C. G. Sudarshan and R. E. Marshak, "Chirality Invariance and the Universal Fermi Interaction," *Phys. Rev.*, vol. 109, no. 5, pp. 1860 – 1862, 1958, DOI: 10.1103/PhysRev.109.1860.2.

[SM73] G. F. Steib and E. Moll, "High-voltage conditioning at large gaps in industrial vacuum," *Journal of Physics D: Applied Physics*, vol. 6, no. 2, p. 243, 1973, DOI: 10.1088/0022-3727/6/2/311.

[Smi05] R. C. Smith, R. D. Forrest, J. D. Carey, W. K. Hsu, S. R. P. Silva, "Interpretation of enhancement factor in nonplanar field emitters," *Appl. Phys. Lett.*, vol. 87, p. 013111, 2005, DOI: 10.1063/1.1989443.

[SN06] S. M. Sze and K. K. Ng, "Physics of Semiconductor Devices, 3rd Edition," *John Wiley & Sons, Inc.*, 2006.

[Spe04] Spellman, "TOF3000 Modular Mass Spectrometry Power Supply," 2004, product description, 128032-001 REV. J. [Online]. Available: www.spellmanhv.com/~/media/Files/Products/TOF3000.ashx

[Spi05] H. Spieler, "Semiconductor Detector Systems," *Oxford University Press*, 2005.

[Spi12] ——, "Silicon Detectors. Many different applications, but built on the same basic physics," *IEEE 2012 Nuclear Science Symposium, Medical Imaging Conference Refresher Course*, 2012. [Online]. Available: http://www-physics.lbl.gov/~spieler/NSS_2012_Refresher_Course/Refresher-Course_Silicon-Detectors.pdf

[SS09] R. C. Smith and S. R. P. Silva, "Interpretation of the field enhancement factor for electron emission from carbon nanotubes," *Appl. Phys. Lett.*, vol. 106, p. 014314, 2009, DOI: 10.1063/1.3149803.

[Sta13] N. Stallkamp, "Optimierung und erste Messung der Transmissionseigenschaften des KATRIN-Hauptspektrometers," *Karlsruhe Institute of Technology*, 2013, diploma thesis.

[Ste11] M. Steidl, "Manual for using the FPD Gamma Ray Source," 2011, internal KATRIN document. [Online]. Available: https://fuzzy.fzk.de/bscw/bscw.cgi/d717901/Manual%20for%20using%20the%20FPD%20Gamma%20Ray%20Source.pdf

[Ste13] N. Steinbrink, Volker Hannen, Eric L. Martin, R. G. Hamish Robertson, Michael Zacher, Christian Weinheimer, "Neutrino mass sensitivity by MAC-E-Filter based time-of-flight spectroscopy with the example of KATRIN," *New Journal of Physics*, vol. 15, no. 11, p. 113020, 2013, DOI: 10.1088/1367-2630/15/11/113020.

[Str96] H. C. Straub, "Absolute partial cross sections for electron-impact ionization of argon, hydrogen, nitrogen, oxygen, and carbon dioxide from threshold to 1000 eV," *Rice University*, 1996, doctoral thesis. [Online]. Available: http://hdl.handle.net/1911/16994

[Stu10]   M. Sturm, "Aufbau und Test des Inner-Loop-Systems der Tritiumquelle von KATRIN," *Karlsruhe Institute of Technology*, 2010, doctoral thesis.

[Sum08]   Sumitomo, "Marathon CP-8 Cryopump - Technical Manual," 2008, internal KATRIN document. [Online]. Available: https://fuzzy.fzk.de/bscw/bscw.cgi/d724433/Marathon%20CP-8%20Cryopump%20%28Manual%29.pdf

[SW12]   J. Schwarz and S. Wüstling, "Feedthrough Flange and Wafer #96728 Inspection," 2012, internal KATRIN elog. [Online]. Available: https://crunch5.npl.washington.edu:8443/KATRIN+Detector+Commissioning+/485

[Taw90]   H. Tawara, Y. Itikawa, H. Nishimura, M. Yoshino, "Cross Sections and Related Data for Electron Collisions with Hydrogen Molecules and Molecular Ions," *Journal of Physical and Chemical Reference Data*, vol. 19, no. 3, p. 617, 1990, DOI: 10.1063/1.555856.

[TDK08]   TDK-Lambda Americas Inc., "TECHNICAL MANUAL FOR GENESYSTM 750W/1500W Programmable DC Power Supplies," 2008, internal KATRIN document. [Online]. Available: https://fuzzy.fzk.de/bscw/bscw.cgi/d746830/Manual_TDKLambda.pdf

[TE 12]   TE Technology Inc., "Instruction Manual for Model TC-48-20 and Model TC-48-20 OEM, Thermoelectric Cooler Temperature Controller," 2012, internal KATRIN document. [Online]. Available: https://fuzzy.fzk.de/bscw/bscw.cgi/d767915/PeltierCooler_Controller_Manual.pdf

[Tho09]   A. C. Thompson et al., "X-Ray Data Booklet," *Center for X-ray Optics and Advanced Light Source, Lawrence Berkeley National Laboratory*, 2009, pUB-490 Rev. 3. [Online]. Available: http://xdb.lbl.gov

[Thu02]   T. Thuemmler, "Entwicklung von Methoden zur Untergrundreduzierung am Mainzer Tritium-β-Spektrometer," *Univ. Mainz*, 2002, diploma thesis.

[Thu11]   ——, "Direct neutrino mass measurements," *Phys.Part.Nucl.*, vol. 42, no. 4, pp. 590 – 597, 2011, DOI: 10.1134/S1063779611040149.

[Thu14]   T. Thuemmler et al., "System setup for the first commissioning measurements with the KATRIN main spectrometer," *JINST*, 2014, submitted for internal review.

[Tso95]   N. Tsoulfanidis, "Measurement and Detection of Radiation," *Taylor & Francis*, 1995.

[Ubi09]   M. Ubieto-Diaz, D. Rodriguez, S. Lukic, Sz. Nagy, S. Stahl, K. Blaum, "A broad-band FT-ICR Penning trap system for KATRIN," *International Journal of Mass Spectrometry*, vol. 288, no. 1 - 3, pp. 1 – 5, 2009, DOI: 10.1016/j.ijms.2009.07.003.

[Ubi11]   M. Ubieto Diaz, "Off-line commissioning of a non-destructive FT-ICR detection system for monitoring the ion concentration in the KATRIN beamline," *Ruprecht-Karls-Universität, Heidelberg, Germany*, 2011, doctoral thesis.

[Upd60]   J. Updike, "Cosmic Gall," *The New Yorker*, vol. Dec.17, p. 36, 1960. [Online]. Available: http://www.newyorker.com/archive/1960/12/17/1960_12_17_036_TNY_CARDS_000268214

[Upd95]   ——, "Cosmic Gall," 1995. [Online]. Available: http://www.nobelprize.org/nobel_prizes/physics/laureates/1995/illpres/cosmic-call.html

[Val06]   K. Valerius, "Electromagnetic design and inner electrode for the KATRIN main spectrometer," *Progress in Particle and Nuclear Physics*, vol. 57, no. 1, pp. 58 – 60, 2006, DOI: 10.1016/j.ppnp.2005.11.011.

[Val09]   ——, "Spectrometer-related background processes and their suppression in the KATRIN experiment," *Univ. Münster*, 2009, doctoral thesis.

[Val10]   ——, "The wire electrode system for the KATRIN main spectrometer," *Progress in Particle and Nuclear Physics*, vol. 64, no. 2, pp. 291 – 293, 2010, DOI: 10.1016/j.ppnp.2009.12.032.

[Val11]   K. Valerius et al., "Prototype of an angular-selective photoelectron calibration source for the KATRIN experiment," *Journal of Instrumentation*, vol. 6, p. P01002, 2011, DOI: 10.1088/1748-0221/6/01/P01002.

[Van12]   B. VanDevender et al., "Performance of a TiN-coated monolithic silicon pin-diode array under mechanical stress," *Nuclear Instruments and Methods in Physics Research Section A: Accelerators, Spectrometers, Detectors and Associated Equipment*, vol. 673, pp. 46 – 50, 2012, DOI: 10.1016/j.nima.2012.01.033.

[VAT07]   VAT, "All-Metal Gate Valve - Installation, Operating, and Maintenance Instructions," 2007, internal KATRIN document. [Online]. Available: https://fuzzy.fzk.de/bscw/bscw.cgi/d724077/DN250%20Gate%20valve,%20users%20manual,%20operating%20instructions..pdf

[vW35]   C. F. v. Weizsäcker, "Zur Theorie der Kernmassen," *Zeitschrift für Physik*, vol. 96, no. 7 - 8, pp. 431 – 458, 1935, DOI: 10.1007/BF01337700.

[Wal13]   B. L. Wall, "Karlsruhe Tritium Experiment: Detector System Commissioning and In-Situ PIN-Diode Array Dead-Layer Measurement," *University of Washington*, 2013, doctoral thesis.

[Wal14]   B. L. Wall et al., "Dead layer on silicon p-i-n diode charged-particle detectors," *Nuclear Instruments and Methods in Physics Research Section A: Accelerators, Spectrometers, Detectors and Associated Equipment*, vol. 744, pp. 73 – 79, 2014, DOI: 10.1016/j.nima.2013.12.048.

[Wan09]   N. Wandkowsky, "Design and Background Simulations for the KATRIN Main Spectrometer and Air Coil System," *Karlsruhe Institute of Technology*, 2009, diploma thesis.

[Wan13a]   ——, "Study of background and transmission properties of the KATRIN spectrometers," *Karlsruhe Institute of Technology*, 2013, doctoral thesis.

[Wan13b]   N. Wandkowsky, G. Drexlin, F. M. Fränkle, F. Glück, S. Groh, S. Mertens, "Modeling of electron emission processes accompanying radon-α-decays within electrostatic spectrometers," *New Journal of Physics*, vol. 15, p. 083040, 2013, DOI: 10.1088/1367-2630/15/8/083040.

[Wan14]   N. Wandkowsky, G. Drexlin, F. Fränkle, F. Glück, S. Görhardt, S. Groh, S. Mertens, J. Schwarz, N. Trost, J. Wolf, "Electron cooling mechanisms in electrostatic spectrometers," *New Journal of Physics*, 2014, submitted for internal review.

[Wei99]   C. Weinheimer, B. Degenddag, A. Bleile, J. Bonn, L. Bornschein, O. Kazachenko, A. Kovalik, E.W. Otten, "High precision measurement of the tritium β spectrum near its endpoint and upper limit on the neutrino mass," *Physics Letters B*, vol. 460, no. 1 - 2, pp. 219 – 226, 1999, DOI: 10.1016/S0370-2693(99)00780-7.

[Wei03] C. Weinheimer, "Springer Tracts in Modern Physics, Laboratory Limits on Neutrino Masses," *Springer*, vol. 190, pp. 25 – 52, 2003. [Online]. Available: http://f3.tiera.ru/2/P_Physics/PQft_Quantum%20field%20theory/Altarelli%20G.,%20Winter%20K.%20%28eds.%29%20Neutrino%20Mass%20%28broken%20hyperlinks%29%20%28STMP0190,%20Springer,%202003%29%28ISBN%203540403280%29%28258s%29_PQft_.pdf

[Win11] A. Windberger, "Berechnungen und Simulationen zum Verhalten von Ionen in der differenziellen Pumpstrecke des KATRIN-Experiments," *Karlsruhe Institute of Technology*, 2011, diploma thesis.

[WJ05] S. Woosley and T. Janka, "The physics of core-collapse supernovae," *The physics of core-collapse supernovae*, vol. 1, pp. 147 – 154, 2005, DOI: 10.1038/nphys172.

[Wol78] L. Wolfenstein, "Neutrino oscillations in matter," *Phys. Rev. D*, vol. 17, p. 2369, 1978, DOI: 10.1103/PhysRevD.17.2369.

[Wol07] J. Wolf, "Vacuum Performance of the Main Spectrometer," 2007, internal KATRIN talk, 13th collaboration meeting. [Online]. Available: https://fuzzy.fzk.de/bscw/bscw.cgi/d425773/95-TRP-4302-S1-JWolf.pptx

[Wol14] J. Wolf et al., "Commissioning of the vacuum system of the KATRIN Main Spectrometer," *JINST*, 2014, paper in preparation.

[Wu 57] C. S. Wu , E. Ambler, R. W. Hayward, D. D. Hoppes, R. P. Hudson, "Experimental Test of Parity Conservation in Beta Decay," *Phys. Rev.*, vol. 105, no. 4, pp. 1413 – 1415, 1957, DOI: 10.1103/PhysRev.105.1413.

[Wue11] S. Wuestling, "KATRIN Main Detector (Focal Plane Detector) Electronics Design Description," 2011, internal KATRIN document. [Online]. Available: https://fuzzy.fzk.de/bscw/bscw.cgi/d732369/Description%20of%20FPD%20readout%20electronics.pdf

[Wue12] ——, "KATRIN Main Detector (Focal Plane Detector) Electronics Design Description," 2012, internal KATRIN document. [Online]. Available: https://fuzzy.fzk.de/bscw/bscw.cgi/d732369/Description%20of%20FPD%20readout%20electronics.pdf

[YSP66] M. Yamashita, L. D. Stephens, and H. W. Patterson, "Cosmic-ray-produced neutrons at ground level: Neutron production rate and flux distribution," *Journal of Geophysical Research*, vol. 71, no. 16, pp. 3817 – 3834, 1966, DOI: 10.1029/JZ071i016p03817.

[Zac09] M. Zacher, "Electromagnetic design and field emission studies for the inner electrode system of the KATRIN main spectrometer," *Univ. Münster*, 2009, diploma thesis.

[Zbo11] M. Zboril, "Solid electron sources for the energy scale monitoring in the KATRIN experiment," *Univ. Münster*, 2011, doctoral thesis.

[Zha13] H. Zhang, L. Ge, B. Tang, T. Liu, "Optimal choice of trapezoidal shaping parameters in digital nuclear spectrometer system," *Nuclear Science and Techniques*, vol. 24, no. 6, p. 60407, 2013. [Online]. Available: http://www.j.sinap.ac.cn/nst/EN/Y2013/V24/I6/60407

[Zie04] J. F. Ziegler, "SRIM-2003," *Nuclear Instruments and Methods in Physics Research Section B: Beam Interactions with Materials and Atoms*, vol. 219 - 220, pp. 1027 – 1036, 2004, DOI: 10.1016/j.nimb.2004.01.208.

[Zie13]   ——, "SRIM-2013, SRIM - The Stopping and Range of Ions in Matter," 2013. [Online]. Available: http://www.srim.org/

[Zub11]   K. Zuber, "Neutrino Physics," *CRC Press*, vol. 2, 2011.

Danksagung

Abschließend möchte ich mich ganz herzlich bei allen bedanken, die mich die letzten Jahre während meiner Promotion begleitet und zum Gelingen meiner Doktorarbeit beigetragen haben. Ein ganz besonderes Dankeschön gebührt hierbei folgenden Personen.

- Vielen Dank PROF. DR. G. DREXLIN für die abwechslungsreiche Arbeit, die motivierenden Gespräche und die stete Unterstützung, sowie für die Möglichkeit meine Dissertation am KATRIN Experiment mit dem Schwerpunkt des Spektrometer- und Detektorsystems durchführen zu können.

- Vielen Dank PROF. DR. U. HUSEMANN für die freundliche und umfangreiche Unterstützung als Korreferent dieser Arbeit.

- Vielen Dank der PRÜFUNGSKOMMISSION für die Begutachtung und Beurteilung dieser Arbeit.

- Thank you PROF. DR. PETER DOE and PROF. DR. HAMISH ROBERTSON for giving me the opportunity to stay at CENPA for several weeks and for supporting the installation, commissioning and characterization of the focal-plane detector system at KIT.

- Thank you PROF. DR. SANSHIRO ENOMOTO for answering all my detector-related and analysis-based questions, and for providing Beans just at the right time.

- Vielen Dank PROF. DR. ÁNGEL GONZÁLEZ UREÑA and DR. MAGNUS SCHLÖSSER for the fruitful discussions about hydrogen anions and reaction thresholds.

- Vielen Dank DR. UDO SCHMITT und DR. MARKUS STEIDL für die vorbildliche Betreuung, die motivierenden Gespräche und die stete Unterstützung.

- Vielen Dank DR. SASCHA WÜSTLING, ARMEN BEGLARIAN, JULIUS HARTMANN und LARS PETZOLD für die Bereitstellung der Elektronik zur Signalauslese.

- Vielen Dank RAINER GUMBSHEIMER, SIEGFRIED HORN, BERNARD BENDER, LUISA LA CASCIO, HOLGER FRENZEL, MARTIN JÄGER, MONIKA KAISER, ALAN KUMB, KLAUS MEHRET und HENDRIK WEINGARDT für die technische Unterstützung während des Auf-, Ab- und Umbaus des Detektorsystems und dessen Anflanschen an das Hauptspektrometer.

- Vielen Dank DR. LUTZ BORNSCHEIN und DR. KLAUS SCHLÖSSER für den Strahlenschutz.

- Vielen Dank MARTIN MARK für die Sicherheit.

- Vielen Dank MARTIN BABUTZKA für einfach alles!!!!!

- Vielen Dank FABIAN HARMS für die tatkräftige und zuverlässige Unterstützung am Detektorsystem und für das Organisieren einer Mikrowelle.

- Vielen Dank Dr. Florian Fränkle und Florian Heizmann für die kompetente Unterstützung bei der Analyse.

- Vielen Dank Marco Kleesiek für die Bereitstellung von KaLi, das Organisieren eines Kaffeevoll-automaten und die angenehme Arbeitsatmosphäre im *Sekretariat für alles*.

- Vielen Dank Stefan Groh für die Bereitstellung von Kassiopeia und die Einführung des Pizza-Tags.

- Vielen Dank Moritz Erhard, Marcel Kraus und Nikolaus Trost für die Sicherstellung der Kaffee-Versorgung.

- Vielen Dank Moritz Hackenjos für das Organisieren der unvergesslichen Doktorfeier.

- Vielen Dank Jan Oertlin für die Einführung eines Süßigkeiten-Ladens.

- Vielen Dank Dr. Stefan Görhardt und Benjamin Leiber für die Motivation in den letzten Monaten.

- Vielen Dank allen Young Scientists des KATRIN Experimentes für die tolle Zeit während und außerhalb meiner Arbeitszeit.

- Vielen Dank dem Karlsruhe House of Young Scientists (KHYS) für die Förderung meines zweimonatigen Auslandsaufenthaltes an der University of Washington und des Gastaufenthaltes von Thomas Corona.

Ein ganz herzliches Dankeschön geht an meine Eltern Uta und Walter, die mich während meines Studiums und meiner Promotion sowohl finanziell als auch moralisch unterstützt und ständig an mich geglaubt haben, sowie an meine beiden Brüder Maximilian und Christopher.

Der größte Dank geht an meine Herzallerliebste Sarah Fünfer, die trotz manch schlafloser Nächte meinerseits immer zu mir gehalten, sich liebevoll um mich gekümmert und mir gezeigt hat, dass es erstaunlicherweise auch noch ein Leben neben KATRIN gibt. Vielen lieben Dank hierfür!!!